

**THE DEFORMATION CAPACITY OF
REINFORCED CONCRETE ELEMENTS SUBJECT TO
SEISMIC LOADING:**

Determination of Empirical Equations for Assessment

A thesis submitted to the University College London for the degree of Doctor of Philosophy

Randolph Carl Borg

March 2015

Department of Civil, Environmental and Geomatic Engineering,

Declaration

I, *Randolph Carl Borg*, confirm that the work presented in this thesis is my own. Where information has been derived from other authors, I confirm that this has been indicated in the thesis.

Randolph Borg

March 2015

Abstract

This project aims to enhance relationships that quantify earthquake induced damage in reinforced concrete (RC) structures, in terms of Engineering Demand Parameters (EDPs) and/or Damage Indices (DIs). In the seismic vulnerability assessment process structures are classified onto Damage Scales (DS) based upon their expected performance. The damage level is quantified by Damage Indices (DIs) as a function of Engineering Demand Parameters (EDPs). This research aims to enhance the relationships that quantify damage in Reinforced Concrete (RC) structures in terms of empirically derived EDPs equations as a function of material properties, geometrical properties of sections and detailing aspects. Current relationships found in literature are generally defined at yield and ultimate damage states, or at the occurrence of a particular failure mechanism in terms of chord rotation. Assessment procedures have however evolved from these two limit states onto multiple state assessment. Relationships referring to intermediate states of damage are therefore proposed.

EDP relationships are derived from datasets of low cycle fatigue tests on columns found in literature. The number of elements with design and detailing aspects referring to old design practices are limited. Recent earthquakes have shown that such structures are very vulnerable. Hence, an experimental campaign consisting in RC elements with varying detailing aspects, material properties and geometric properties, designed to old design codes was conducted to enhance the dataset, act as a benchmark, and to investigate failure mechanisms. Low cycle fatigue tests generally refer to monotonic or cyclic loading patterns without any direct reference to earthquake loading or response. A procedure describing the determination of the loading history based on earthquake demands is therefore considered. The experiments also indicate that the loading pattern is a function of chord rotation capacity. This effect is taken into account in the development of the EDP relationships.

Multivariable stepwise regression was used for the development of the EDP relationships. The selection of the explanatory variables was based on significant parameters used in existing EDP relationships, parameters found in existing relationships describing particular failure modes, and dimensional analysis. A comprehensive model of chord rotation and stiffness are provided at yielding, maximum force, 10% maximum force reduction, 20% maximum force reduction and 50% maximum force reduction. Relationships that relate residual stiffness, chord rotation and energy dissipation are derived. The testing campaign on columns not only highlights the behaviour of reinforced concrete designed without seismic detailing, but adds to the database in literature. The beam-column connection tests indicate that the behaviour at the nodes affects the behaviour of RC structures, and stress the importance of their inclusion in further investigations. Finally, proposing a method to determine low-cycle fatigue loading regimes based on seismic response is an attempt to address an anomaly where tools that are used to quantify seismic damage are not linked in any way with earthquakes.

To Mary, Paul, Marija, Bernard and Julian



The research work disclosed in this publication is partially funded by the Strategic Educational Pathways Scholarship (Malta). This Scholarship is part-financed by the European Union – European Social Fund (ESF) under Operational Programme II – Cohesion Policy 2007-2013, “Empowering People for More Jobs and a Better Quality Of Life”.



Operational Programme II – Cohesion Policy 2007-2013
*Empowering People for More Jobs and a Better Quality of
Life*

Scholarship part-financed by the European Union
European Social Fund (ESF)
Co-financing rate: 85% EU Funds; 15% National Funds



Investing in your future

Acknowledgements

Firstly I would like to thank my main supervisor Professor Tiziana Rossetto for her encouragement, support advice and guidance. I would also like to thank my second supervisor, Professor Humberto Varum (formerly University of Aveiro) for accepting me as a visiting student at the University of Aveiro, and also for his advice and discussions.

I would like to thank my main sponsors:

- **EPSRC** for funding the project under EP/F012179/1 Grant name: EPICENTRE - Earthquake and People Interaction Centre
- **STEPS** – Malta which is part financed by the European Union – European Social Fund (ESF) under Operational Programme II – Cohesion Policy 2007-2013, “Empowering People for More Jobs and a Better Quality of Life”.

I would like to thank Dr. Peter Domone and Dr. C. Arya for their help when required.

Thanks also to Dr. Ioanna Ioannou for the discussions on statistics.

I would like to thank the people I met while in Aveiro, particularly Jose Melo. Particular thanks also to Antonio Figueredo, Vitor Rodriguez, Jorge Catarino and Ricardo Santos. I would like to thank the people in room 1M01 in the Chadwick building at UCL for their friendship during the course of the studies.

I would also like to show my appreciation to Gillian Noel for the time spent at Woodlea Road, and to her dog Hero for the early morning walks at Clissold Park.

I would like to thank my parents for their constant unconditional support and encouragement, and for the good example they have been. I would also like to show gratitude to my mother-in-law.

I would like to thank my wife Marija, for her patience and for accepting to share the Ph.D. experience and burden with me. Thanks also to my children, Bernard and Julian who found themselves in this world while I was conducting this project.

Table of Contents

Declaration	ii
Abstract	iii
Acknowledgements	vii
List of Figures	xiii
List of Tables	xx
List of Symbols	xxiii
List of Acronyms	xxvii
Chapter 1. INTRODUCTION	1
1.1 Background.....	1
1.2 EN1998-3 (2005): Deformation Capacity Recommendations for Assessment	3
1.3 The Aim of the Thesis.....	4
1.4 The Structure of the Thesis.....	4
Chapter 2. RC STRUCTURE ASSESSMENT AND DAMAGE ESTIMATION	7
2.1 Introduction.....	7
2.2 Mechanical Properties and Damage Development of Reinforced Concrete Elements.....	10
2.2.1 Code Provisions and Detailing.....	10
2.2.2 Properties and Behaviour of Concrete	12
2.2.3 Properties and Behaviour of Steel Reinforcement	13
2.2.4 Characteristics of Bond-slip.....	15
2.2.5 Strain Rate Effects	17
2.2.6 Failure Modes of Reinforced Concrete	18
2.2.7 Determination of Damage Levels	21
2.3 Tools in the Assessment Procedures	23
2.3.1 Engineering Demand Parameters (EDPs)	23
2.3.2 Damage Indices.....	35
2.3.3 Damage Scales	41
2.3.4 Application of Seismic Assessment.....	44
2.4 Experiments for the Development of EDP relationships	52
2.4.1 Types of Tests and Testing Configurations	52
2.4.2 Databases Considered	53
2.4.3 Loading Considerations	54
2.5 General Conclusions and Requirements.....	55
Chapter 3. DESIGN OF EXPERIMENTS AND DIAGNOSTICS	57

3.1	<i>Introduction</i>	57
3.2	<i>Experiments for the assessment of RC structural elements</i>	57
3.2.1	Collection of Material and Geometric Properties	57
3.2.2	Data Distribution Requirements	59
3.2.3	Design of a Reference Structure	65
3.2.4	Experimental setup for the experimental campaign	66
3.3	<i>Experimental schedule and testing requirements</i>	70
3.3.1	Scheme of RC Column Experiments	70
3.3.2	Construction of specimens and tests on the properties of materials	75
3.3.3	Data acquisition and instrumentation	86
3.4	<i>Data processing requirements and diagnostics</i>	91
3.4.1	Definition of General Parameters	91
3.4.2	Accounting of P- Δ and non-linear geometric effects	95
3.5	<i>General Conclusions and Requirements</i>	111
Chapter 4.	RESULTS OF EXPERIMENTS: COMPARISONS AND INTERPRETATIONS	
	114	
4.1	<i>Introduction</i>	114
4.2	<i>General Observations on the Behaviour of RC Columns</i>	115
4.3	<i>Comparison of Experimental results with Analytical Considerations</i>	119
4.4	<i>Observations and Comparisons of the Results of Column Tests</i>	121
4.4.1	Comparison of the Behaviour of RC Columns with Different Span-Depth Ratio 121	
4.4.2	Comparison of the Behaviour of RC Columns Subject to Different Loading Patterns 125	
4.4.3	Comparison of the Behaviour of RC Columns with Transverse Reinforcement Having 90° or 135° Hooks	132
4.4.4	Comparison of the Behaviour of RC Columns with Different Reinforcement Ratio and Confinement Considerations	137
4.4.5	Comparison of the Behaviour of RC Columns with Symmetric and Un- symmetric Distribution of Longitudinal Reinforcement	145
4.4.6	Comparison of the Behaviour of RC Columns with Different Axial Load Ratio 149	
4.4.7	Comparison of the Behaviour of RC Columns with Different Detailing Aspects at the Column –Foundation Interface	155
4.4.8	Comparison of the Behaviour of RC Columns with and without Lap-splicing. 160	
4.5	<i>General Conclusions and Requirements</i>	166
Chapter 5.	PROCEDURE FOR EMPIRICAL DETERMINATION OF ENGINEERING DEMAND PARAMETERS	167
5.1	<i>Introduction</i>	167

5.2	<i>Methodology for the development of a new model</i>	167
5.3	<i>Consideration of variables for model development</i>	173
5.3.1	Requirements for Explanatory Variables	173
5.3.2	General Combined Variables	174
5.3.3	Dimensional Analysis	175
5.4	<i>Database Considerations for EDP Model Development</i>	185
5.4.1	Treatment of missing data.....	185
5.4.2	Data variability between datasets.....	187
5.4.3	Corrections and filtering of data	191
5.5	<i>Categorization and classification of data</i>	192
5.5.1	Loading pattern	192
5.5.2	Failure mode	198
5.5.3	Building Class	198
5.6	<i>Identification of trends</i>	202
5.6.1	Correlation matrices.....	202
5.6.2	Density distribution.....	204
5.6.3	Scatter plots.....	204
5.6.4	Plots of single test series with only one variable changed	205
5.7	<i>The Regression Analysis Process and Associated Statistical Considerations</i>	206
5.7.1	General Requirements for the Regression Analysis Process	206
5.7.2	Selection of Regression Analysis Process.....	208
5.7.3	Criteria for Model Selection and Validation.....	210
5.7.4	Regression Diagnostics	213
5.7.5	Removal of outliers and Extreme Values of Variables	214
5.7.6	Statistics for the Comparison of Models.....	216
5.7.7	Summary of the Regression Analysis Procedure	216
5.8	<i>Form of the regression model</i>	217
5.8.1	Form of the model relating different EDPs.....	217
5.8.2	Form of the Model Relating Chord Rotation or Stiffness Ratio with Material and Physical Properties.....	218
5.9	<i>General Conclusions and Requirement</i>	223
Chapter 6.	NEW EMPIRICAL EDP MODELS	226
6.1	<i>Introduction</i>	226
6.2	<i>Range of Application of the EDP Models</i>	226
6.3	<i>Relationship between Chord Rotation (θ_{dmg}), Residual Stiffness (K_{dmg}) and Energy Dissipation (E_{dmg})</i>	232
6.4	<i>Chord Rotation Model</i>	245

6.4.1	Chord Rotation at Yielding.....	245
6.4.2	Chord Rotation at Maximum Force.....	248
6.4.3	Chord Rotation at 10% Maximum Force Reduction	251
6.4.4	Chord Rotation at 20% Maximum Force Reduction	255
6.4.5	Chord Rotation at 50% Maximum Force Reduction	259
6.5	<i>Stiffness Ratio Model</i>	263
6.5.1	Stiffness Ratio at Yielding.....	263
6.5.2	Stiffness Ratio at Maximum Force	266
6.5.3	Stiffness Ratio at 10% Maximum Force Reduction	268
6.5.4	Stiffness Ratio at 20% Maximum Force Reduction	271
6.5.5	Stiffness Ratio at 50% Maximum Force Reduction	274
6.6	<i>Comparison of Different EDP Models at Various Damage States</i>	276
6.7	<i>Comparison of EDP Models with Other Models in Literature</i>	281
6.7.1	Stiffness Ratio at Yielding.....	281
6.7.2	Chord Rotation at Yielding.....	287
6.7.3	Chord Rotation at 20% Maximum Force Reduction	291
6.8	<i>Validation of Proposed EDP Relationships</i>	294
6.9	<i>Application to Seismic Assessment</i>	296
6.10	<i>General Conclusions on the EDP Models Proposed</i>	297
Chapter 7.	CONCLUSIONS AND FUTURE RECOMMENDATIONS	299
7.1	<i>General Conclusions</i>	299
7.2	<i>Limitations and Future Research</i>	301
	REFERENCE LIST	303
Appendix A:	Detailing requirements by Different Guidelines.....	A.1
Appendix B:	Auxiliary Testing Campaigns.....	B.1
Appendix C:	Low-cycle Fatigue Tests on Beam-Column Connections.....	C.1
Appendix D:	Experimental Results of Column and Beam-Column Specimens.....	D.1
Appendix E:	Distribution of Data of Regression Variables Using the Selected Database.....	E.1
Appendix F:	Correlations of Explanatory Variables with Dependent Variables.....	F.1
Appendix G:	Scatter-plots of Regression Variables Using the Selected Database.....	G.1
Appendix H:	Trends between Variables by Isolating Effects of Individual Variables	H.1
Appendix I:	Diagnostics of the Statistical Regression Chord Rotation Models.....	I.1
Appendix J:	Diagnostics of the Statistical Regression Stiffness Ratio Models	J.1
Appendix K:	Diagnostics of the Statistical Regression Models relating Chord Rotation Energy Dissipation and Stiffness.....	K.1

List of Figures

Figure 2-1 <i>Performance based earthquake engineering criteria. A) Vision 2000, b) FEMA 273.</i>	7
Figure 2-2 <i>General aspects that affect seismic assessment procedure of RC structures.</i>	9
Figure 2-3 <i>Theoretical bond-slip and bond-split model (Harajli et al., 1995).</i>	15
Figure 2-4 <i>Bond-slip mechanism due to monotonic loading (Eligenhausen et al., 1983)</i>	16
Figure 2-5 <i>Amplification of concrete strength under uni-axial stress due to different strain rates based on recommendations by Penelis et al. (1997).</i>	17
Figure 2-6. <i>Classification of reinforced concrete column failure modes according to ATC-6 (1981)</i>	19
Figure 2-7. <i>Determination of parameters relating with: a) displacement ductility; b) Longitudinal steel ratio; c) aspect ratio.</i>	19
Figure 2-8 <i>Determination of parameters relating with displacement ductility.</i>	20
Figure 2-9 <i>Distribution of maximum force reduction ratio for various damage phenomena.</i>	22
Figure 2-10 <i>Distribution of chord rotation for various damage phenomena.</i>	23
Figure 2-11 <i>Comparison of the damage phenomena data with the DI proposed by Rossetto et al. (2004).</i>	23
Figure 2-12 <i>The plastic hinge concept as presented by Fardis (2007) and as adopted in EN1998-3 (CEN, 2005).</i>	27
Figure 2-13 <i>Comparison of global damage indices.</i>	42
Figure 2-14 <i>Structural configuration of the considered buildings.</i>	44
Figure 2-15 <i>Acceleration response spectra (5% damping).</i>	47
Figure 2-16. <i>The damage indices for each storey (L1,L2,L3) and earthquake for: a) Building 1, b)Building 2.</i>	48
Figure 2-17. <i>The global DI corresponding to each earthquake for: a) Building 1, b)Building 2.</i>	49
Figure 2-18 <i>The evaluation of β for each element as provided by Park et al. (1985) and Kunnath et al., 1990 for: a) Building 1, b)Building 2.</i>	50
Figure 2-19 <i>Damage distribution in Building 1 following response to earthquake 440, and capacity requirements according to EN1998-3(2005).</i>	52
Figure 2-20. <i>Low cycle fatigue tests on piers, using different cyclic loading histories (Takemura et al., 1997).</i>	55
Figure 3-1 <i>Density distribution of data from the databases provided by Rossetto et al., 2002 and Berry et al., 2003, and the experimental campaign presented in Chapter 4, for various explanatory variables.</i>	64
Figure 3-2 <i>Elevation of the RC frame that is used as a reference structure.</i>	65

Figure 3-3. Design details of column (section A.A.) and beam (section B.B.) for the reference RC frame designed according to: a) EN1998-1 (CEN,2005), b) BS8110 (British Standards, 1985).	66
Figure 3-4 Test setup for column specimens	67
Figure 3-5 Detail of the restraint of the foundation and hinging of the rods: a) from the front; b) from behind.	68
Figure 3-6 a) the axial load actuator and lateral load actuator setup; b) Frame with applied pre-stress connecting the column with lateral load actuator; c) Specimens are supported on universal ball bearings.	68
Figure 3-7 Schematic representation for the determination of the experimental schedule for columns.	71
Figure 3-8 a) A general layout of the apparatus for the tensile test of steel reinforcement; b) Measurement of deformation by an LVDT on a 12mm A400NRSD reinforcing bar sample.	76
Figure 3-9 Reinforcement samples used for the construction of the specimens: a) 8mm A235NL; b) 8mm A400NRSD; c) 12mm A400NRSD ; d) 12mm A500NRSD; e) 16mm A400NRSD; f) 20mm A400NRSD.	76
Figure 3-10 Stress strain relationship for: a) 8mm A235NL; b) 8mm A400NRSD; c) 12mm A400NRSD ; d) 12mm A500NRSD; e) 16mm A400NRSD; f) 20mm A400NRSD.	78
Figure 3-11 Details of the reinforcement layout and form work for various columns specimens: a) T14; b) T4; c) T6; d) T10; e) T12; f) T16-D1.	80
Figure 3-12 Aggregate for the concrete mixture: a) Coarse aggregate I; b) Coarse aggregate II; c) Sand; d) Fines.	81
Figure 3-13 Monitoring of the climatic conditions with respect to casting and curing of the testing specimens: a) Average temperature; b) Average relative humidity; c) Sky clearance; d) rainfall.	82
Figure 3-14 A general layout of the instrumentation that measures the deformation of column-foundation specimens.	88
Figure 3-15 Instrumentation that was used to measure the deformation of the specimens during testing, and some of the corresponding mounting setups: a) Potentiometer (Gefran) measuring deformation in column, and deformation close to and including the node panel joint; b) Bridge potentiometer (Truck) measuring lateral movement of the specimens ; c) LVDTs on the upper surface of column specimens; d) LVDTs on the lower surface of column T13.	90
Figure 3-16 General overview of the deformation instrumentation in critical areas of: a) column-foundation specimens with 300x300mm sections; b) column-foundation specimens with 500x300mm sections.	90
Figure 3-17 Monitoring that can be a source of error: a) Rotation of the foundation in column specimens; b) Rotation of the rods and frame connection at the column-foundation interface.	91
Figure 3-18 Determination of yielding based on equilibrium of minimum areas: a) until the maximum force, b) until the ultimate.	92
Figure 3-19. a) Determination of yielding based on equilibrium of minimum areas: a) until the maximum force, b) until the ultimate.	92

Figure 3-20	<i>The interpretation of ultimate displacement as defined by Saatcioglou (1991) based on 20% maximum force reduction.</i>	93
Figure 3-21	<i>Anomalies in the definition of the ultimate.</i>	94
Figure 3-22	<i>Interpretation of deformation, energy dissipation and residual stiffness at a particular % of maximum force reduction.</i>	94
Figure 3-23	<i>P-Δ corrections for column tests with different axial load application set-ups.</i>	96
Figure 3-24	<i>Schematic diagram for P-Δ corrections for the column test setup carried out in this research and described in section 4.2.2.</i>	99
Figure 3-25	<i>Schematic representation for the assumptions of the actuator load vector and the maximum lateral displacement obtained from the bridge potentiometers.</i>	100
Figure 3-26	<i>Details of the action (a) by the axial load actuator on the column, (b) by the lateral load actuator on the column, resolved in components about the axis of the column.</i>	101
Figure 3-27	<i>The set-up of the column specimen and instrumentation, indicating the position of each “i” section and “j” sub-element.</i>	102
Figure 3-28	<i>The rotation of the foundation.</i>	103
Figure 3-29	<i>Considerations of potentiometer deformations for the determination of the rotation of a general sub-element.</i>	104
Figure 3-30	<i>Displacement and rotation considerations at corresponding sections and sub-elements for the determination of shear and flexural moment distribution.</i>	105
Figure 3-31	<i>Determination of the angle of rotation at the top of the column by considering displacements of the bridge potentiometers B1, B2 and B3.</i>	107
Figure 3-32	<i>Definition of the length of the sub-element at the base: a) before considerable flexural cracking in the foundation, b) after considerable flexural cracking in the foundation.</i>	108
Figure 3-33	<i>Definition of top displacement contribution by each section.</i>	110
Figure 4-1	<i>a) Model of the column specimen (T13) under monotonic loading, used in the numeric analysis. b) Comparison of the force-displacement response from the monotonic experiment and analysis.</i>	119
Figure 4-2	<i>The development of damage as observed at the end of each damage level for column specimen T14, T2, T4, T5 and T8.</i>	123
Figure 4-3	<i>Comparison of T2, T14, T5, T4 and T8 in terms of :a) Shear force-chord rotation, b) Cumulative energy dissipation – chord rotation, c) Residual stiffness-chord rotation, envelopes.</i>	124
Figure 4-4	<i>The development of damage as observed at the end of each damage level for column specimen T13, T14, T1a and T1b.</i>	130
Figure 4-5	<i>Comparison of T1a, T1b, T13 and T14 in terms of: a) Shear force-chord rotation, b) Cumulative energy dissipation – chord rotation, c) Residual stiffness-chord rotation, envelopes.</i>	131
Figure 4-6	<i>The development of damage as observed at the end of each damage level for column specimen T14 and T1c.</i>	135

Figure 4-7 Comparison of T1c and T14 in terms of: a) Shear force-chord rotation, b) Cumulative energy dissipation – chord rotation, c) Residual stiffness-chord rotation, envelopes.	136
Figure 4-8 The development of damage as observed at the end of each damage level for column specimen T14, T2, T3, T9, T11 and T12.	143
Figure 4-9 Comparison of T2, T3, T9, T11, T12 and T14 in terms of: a) Shear force-chord rotation, b) Cumulative energy dissipation – chord rotation, c) Residual stiffness-chord rotation, envelopes.	144
Figure 4-10 The development of damage as observed at the end of each damage level for column specimen T14, T9 and T10.	147
Figure 4-11 Comparison of T9, T10 and T14 in terms of: a) Shear force-chord rotation, b) Cumulative energy dissipation – chord rotation, c) Residual stiffness-chord rotation, envelopes.	148
Figure 4-12 The development of damage as observed at the end of each damage level for column specimen T14, T14, T2 and T7.	153
Figure 4-13 Comparison of T7, T2, T15 and T14 in terms of: a) Shear force-chord rotation, b) Cumulative energy dissipation – chord rotation, c) Residual stiffness-chord rotation, envelopes.	154
Figure 4-14 The development of damage as observed at the end of each damage level for column specimen T14 and T6.	158
Figure 4-15 Comparison of T6 and T14 in terms of: a) Shear force-chord rotation, b) Cumulative energy dissipation – chord rotation, c) Residual stiffness-chord rotation, envelopes.	159
Figure 4-16 The development of damage as observed at the end of each damage level for column specimen T14, T16-D1 and T17-D2.	164
Figure 4-17 Comparison of T14, T16-D1 and T17-D2 in terms of: a) Shear force-chord rotation, b) Cumulative energy dissipation – chord rotation, c) Residual stiffness-Chord rotation, envelopes.	165
Figure 5-1 Schematic representation of the procedure that is followed to determine chord rotation and stiffness ratio empirical models at various damage states in terms of material and geometrical properties with loading considerations.	172
Figure 5-2 a) Scatter plot of $f_{t1} - f_{y1}$ showing complete observed data, and data with the imputation of f_{t1} b) Distribution of the residuals of observed f_{t1} only, and observed f_{t1} with the addition of missing values after imputation.	187
Figure 5-3 Scatter plots of experimental values of θ_V for common records in different databases. The values measured in this research plotted against the values as reported in a) Berry et al., 2003, b) Rossetto et al., 2002 and c) Panagiotakos et al, 2001.	188
Figure 5-4 Scatter plots of experimental values of θ_{u-20} for common records in different databases. The values measured in this research plotted against the values as reported in a) Berry et al., 2003, b) Rossetto et al., 2002 and c) Panagiotakos et al, 2001.	190
Figure 5-5 Scatter plots of $\theta_{u-20} - \theta_V$ from common records in different databases. Each record is represented by a quadrilateral enclosing the different values of chord rotation as used in this research, and as provided by Rossetto et al., 2002, Panagiotakos et al., 2001 and Berry et al., 2003.	191

Figure 5-6a Distribution of effective inelastic cycles (n_{cy}) considering 20% maximum force reduction, for different effective load patterns.	194
Figure 5-6b Distribution of chord rotation at 20% maximum force reduction (θ_{u-20}), for different effective load patterns.	195
Figure 5-6c Distribution of energy dissipation at 20% maximum force reduction (E_{u-20}), for different effective load patterns.	195
Figure 5-7 Scatter plot of dissipated energy against chord rotation at 20% maximum force reduction, distinguishing between failure in shear, shear-flexure and flexure.	198
Figure 5-8 Scatter plots of chord rotation at 20% maximum force reduction against different explanatory variables. The data is separated in groups distinguishing between the different building class characteristics, and between the possibility of having considerable bond-slip.	200
Figure 5-9 Scatter plot of dissipated energy against chord rotation at 20% maximum force reduction, distinguishing between different building classes.	202
Figure 5-10 The plot shows the effects of variable X_n on EDP. Each line connects crosses corresponding to single test series in which X_n was the only variable changed.	206
Figure 5-11. The permutations of possible non-linear trends between EDPs (Z_{dmg}) and explanatory variables (X_n) and corresponding linear conversion using logarithmic transformation.	220
Figure 6-1 Experimental chord rotation at maximum force plotted against predictions from a) equation 7.1a and b) equation 7.1b, based on the inclusion and exclusion of extreme data-points respectively. The chord rotation is a function of dimensional terms of residual stiffness and energy dissipation.	237
Figure 6-2 Experimental chord rotation at 10% maximum force reduction plotted against predictions from a) equation 7.2a and b) equation 7.2b, based on the inclusion and exclusion of extreme data-points respectively. The chord rotation is a function of dimensional terms of residual stiffness and energy dissipation.	238
Figure 6-3 Experimental chord rotation at 20% maximum force reduction plotted against predictions from a) equation 7.3a and b) equation 7.3b, based on the inclusion and exclusion of extreme data-points respectively. The chord rotation is a function of dimensional terms of residual stiffness and energy dissipation.	239
Figure 6-4 Experimental chord rotation at 50% maximum force reduction plotted against predictions from a) equation 7.4a and b) equation 7.4b, based on the inclusion and exclusion of extreme data-points respectively. The chord rotation is a function of dimensional terms of residual stiffness and energy dissipation.	240
Figure 6-5 Experimental chord rotation at maximum force plotted against predictions from a) equation 7.5a and b) equation 7.5b, based on the inclusion and exclusion of extreme data-points respectively. The chord rotation is a function of non- dimensional terms of residual stiffness and energy dissipation.	241
Figure 6-6 Experimental chord rotation at 10% maximum force reduction plotted against predictions from a) equation 7.6a and b) equation 7.6b, based on the inclusion and exclusion of extreme data-points respectively. The chord rotation is a function of non- dimensional terms of residual stiffness and energy dissipation.	242
Figure 6-7 Experimental chord rotation at 20% maximum force reduction plotted against predictions from a) equation 7.7a and b) equation 7.7b, based on the inclusion and exclusion of extreme data-points respectively. The chord rotation is a function of non- dimensional terms of residual stiffness and energy dissipation.	243
Figure 6-8 Experimental chord rotation at 50% maximum force reduction plotted against predictions from a) equation 7.8a and b) equation 7.8b, based on the inclusion and exclusion	244

of extreme data-points respectively. The chord rotation is a function of non-dimensional terms of residual stiffness and energy dissipation.

Figure 6-9. Experimental yield chord rotation of members plotted against predictions from a) equation 7.9a and b) equation 7.9b, based on the inclusion and exclusion of extreme data-points respectively. The chord rotation is a function of physical and material properties. 247

Figure 6-10 Experimental chord rotation at maximum force plotted against predictions from a) equation 7.10a – variables from dimension analysis b) equation 7.10b – variables as used in literature and c) equation 7.10c – includes an energy dissipation term. 251

Figure 6-11 Experimental chord rotation at 10% maximum force reduction plotted against predictions from a) equation 7.11a – variables from dimension analysis b) equation 7.11b – variables as used in literature and c) equation 7.11c – includes an energy dissipation term. 255

Figure 6-12 Experimental chord rotation at 20% maximum force reduction plotted against predictions from a) equation 7.12a – variables from dimension analysis b) equation 7.12b – variables as used in literature and c) equation 7.11c – includes an energy dissipation term. 259

Figure 6-13 Experimental chord rotation at 50% maximum force reduction plotted against predictions from a) equation 7.13a – variables from dimension analysis b) equation 7.11b – variables as used in literature and c) equation 7.13c – includes an energy dissipation term. 262

Figure 6-14. Experimental yield stiffness ratio plotted against predictions from a) equation 7.14a and b) equation 7.14b, based on the inclusion and exclusion of extreme data-points respectively. The stiffness ratio is a function of physical and material properties. 265

Figure 6-15 Experimental stiffness ratio at maximum force plotted against predictions from a) equation 7.15a and b) equation 7.15b, based on the inclusion and exclusion of extreme data-points respectively. The stiffness ratio is a function of physical and material properties. 267

Figure 6-16 Experimental stiffness ratio at 10% maximum force reduction plotted against predictions from a) equation 7.16a and b) equation 7.16b, based on the inclusion and exclusion of extreme data-points respectively. The stiffness ratio is a function of physical and material properties. 270

Figure 6-17 Experimental stiffness ratio at 20% maximum force reduction plotted against predictions from a) equation 7.17a and b) equation 7.17b, based on the inclusion and exclusion of extreme data-points respectively. The stiffness ratio is a function of physical and material properties. 273

Figure 6-18 Experimental stiffness ratio at 50% maximum force reduction plotted against predictions from a) equation 7.18a and b) equation 7.18b, based on the inclusion and exclusion of extreme data-points respectively. The stiffness ratio is a function of physical and material properties. 276

Figure 6-19 Experimental stiffness ratio at yield plotted against predictions from equation 7.19a determined by Biskinis et al., 2010a, using the selected database a) including and b) excluding extreme data-points. 283

Figure 6-20 Experimental stiffness ratio at yield plotted against predictions from a) equation 7.19b –including outliers and extreme data-points, b) equation 7.19c – excluding outliers and extreme data-points. The form of model is based on Biskinis et al., 2010a, but coefficients are determined by regression analysis on the available data from the selected database. 284

Figure 6-21 Experimental stiffness ratio at yield plotted against predictions from a) equation 7.20a – model as determined by Haselton et al., 2008, b) equation 7.20b – model form as determined by Haselton et al.2008, but coefficients are obtained from regression analysis using the available data. 285

Figure 6-22 *Experimental chord rotation at yield plotted against predictions from equation 7.21a. The model as determined by Haselton et al., 2008. The data a) includes, b) excludes outliers and extreme data-points.* 288

Figure 6-23 *Experimental chord rotation at yield plotted against predictions from: a) equation 7.21b –includes outliers and extreme data-points, b) equation 7.21c- data excludes outliers and extreme data-points. The form of the model is the same provided by Haselton et al., 2008, but the coefficients are determined from regression analysis using the available data.* 289

Figure 6-24 *Experimental chord rotation at 20% maximum force reduction plotted against predictions from a) equation 7.22a – model as determined by Biskinis et al., 2010b, b) equation 7.22b – model form as determined by Biskinis et al., 2010b, but coefficients are obtained from regression analysis using the available data.* 292

Figure 6-25. *Damage distribution in Building 1 following response to earthquake 414, and capacity requirements according to EN1998-3(2005).* 296

List of Tables

Table 2-1. Geometric and material properties of some representative buildings that suffered damage in Europe due to recent or past earthquakes.	11
Table 2-2 Stiffness model proposed by Miranda et al., (2005)	34
Table 2-3. Comparison of various damage indices (DI) found in literature.	37
Table 2-4. Criteria requirements for Dis and general categorization	39
Table 2-5 Requirements of a damage scale as modified from Hill et al. (2008).	42
Table 2-6 Comparison of different damage scales in literature compiled by Rossetto (2004).	43
Table 2-7 Member cross-sections and reinforcement schedule of Building 1 and Building 2.	46
Table 2-8 Characteristics of selected accelerograms from Ambraseys et al., (2002).	46
Table 2-9. Chord rotation capacity at NC, DS and DL.	51
Table 2-10 Comparison of the number of tests in the databases considered.	54
Table 2-11 The evolution of damage as a cumulative process.	54
Table 3-1 Un-combined explanatory variables that describe constitutive models of steel and concrete.	58
Table 3-2. Un-combined explanatory variables that are used to differentiate between shear, flexure and shear-flexure failure mechanisms.	58
Table 3-3 Un-combined explanatory variables that are used to differentiate between shear, flexure and shear-flexure failure mechanisms.	58
Table 3-4 Nominal properties for column specimens.	72
Table 3-5 Detailing and nominal properties for the column specimens.	74
Table 3-6 Properties of the reinforcement that is used for the construction of the specimens.	77
Table 3-7 Quantity of material required for the production of concrete C16/20	80
Table 3-8 Characteristics of aggregate that is used for C16/20 concrete.	81
Table 3-9 Quantity of material required for the production of concrete C30/37.	81
Table 3-10 Compression strength and splitting test results for column specimens.	85
Table 3-11 The instruments used to measure forces and deformation according to the column schedule.	89
Table 4-1 The drift ratio of the cycle at which various damage phenomena are observed in each column specimen.	118

Table 4-2 Analytical quantities of initial stiffness, and chord rotation and force at first cracking, first yielding and ultimate capacity for each specimen, compared with experimental results.	120
Table 5-1 Combination of variables for θ_{dmg} and EI_{dmg}/EI_g where $dmg = \{Y\}$.	175
Table 5-2 Combination of variables for θ_{dmg} and EI_{dmg}/EI_g where $dmg = \{m, u - 10, u - 20, u - 50\}$	175
Table 5-3a Substituting variables for general equation 6.2b and equation 6.3b.	177
Table 5-3b Substituting variables for general equation 6.2c and equation 6.3c.	177
Table 5-4a Compact solutions for the chord rotation at yielding - θ_Y .	152
Table 5-4b Compact solutions for the stiffness ratio at yielding - EI_Y/EI_g .	152
Table 5-5a Compact solutions for the chord rotation θ_{dmg} at various damage states after yielding, using confinement factor (a).	183
Table 5-5b Compact solutions for the chord rotation θ_{dmg} at various damage states after yielding, using confinement variable ω_w .	183
Table 5-6a Compact solutions for stiffness ratio EI_{dmg}/EI_g at various damage states after yielding, using confinement factor (a).	184
Table 5-6b Compact solutions for stiffness ratio EI_{dmg}/EI_g at various damage states after yielding, using confinement variable ω_w .	184
Table 5-7 Compact solution for the relationship between θ_{dmg} , E_{dmg} and K_{dmg} .	185
Table 5-8 Missing data in the database from Rossetto et al., 2002.	186
Table 5-9. Summary of statistics on the ratio of values of θ_Y reported in common records of different databases.	189
Table 5-10 Summary of statistics on the ratio of values of θ_{u-20} reported in common records of different databases.	190
Table 5-11 Statistics on the correction of the maximum force of a force displacement history due to P- Δ effects due to different test setups.	192
Table 5-12a Summary of statistics for the distribution of the number of cycles at 20% maximum force reduction (n_{cy}), for different effective load patterns.	196
Table 5-12b. Summary of statistics for the distribution of chord rotation (θ_{u-20}) and energy dissipation (E_{u-20}) at 20% maximum force reduction, for different effective load patterns.	197
Table 5-13 Logarithmic transformation of for the m number of permutations of explanatory variables that can possibly form the empirical model of the EDP (Z_{dmg}) at the relevant damage state.	222
Table 6-1 Range of explanatory variable values for empirical models at yielding damage state.	228
Table 6-2 Range of explanatory variable values for empirical models at maximum force.	228

Table 6-3 Range of explanatory variable values for empirical models at 10% maximum force reduction.	229
Table 6-4 Range of explanatory variable values for empirical models at 20% maximum force reduction.	229
Table 6-5 Range of explanatory variable values for empirical models at 50% maximum force reduction.	230
Table 6-6 Range of chord rotation and stiffness ratio for all empirical models at each damage state.	230
Table 6-7 Range of stiffness and energy dissipation for all empirical models at each damage state.	231
Table 6-8 Statistics of experiment-to-predicted chord rotation in terms of stiffness and energy dissipation.	236
Table 6-9a Statistics of experiment-to-predicted chord rotation in terms of explanatory variables determined from dimensional analysis.	279
Table 6-9b Statistics of experiment-to-predicted chord rotation in terms of variables as combined and used in literature.	279
Table 6-9c Statistics of experiment-to-predicted chord rotation in terms of explanatory variables determined from dimensional analysis including an energy dissipation term.	279
Table 6-10a Statistics of experiment-to-predicted stiffness ratio. Database including outliers extreme variable values.	280
Table 6-10b Statistics of experiment-to-predicted stiffness ratio. Database excluding outliers extreme variable values.	280
Table 6-11 Statistics of experiment-to-predicted stiffness ratio at yielding. Comparison of models in literature with the model provided by equation 7.14.	286
Table 6-12 Statistics of experiment-to-predicted chord rotation at yielding. Comparison of models in literature with equation 7.9.	290
Table 6-13 Statistics of experiment-to-predicted chord rotation at 20% maximum force reduction. Comparison of models in literature with equation 7.12.	293
Table 6-14 Comparison of expected and predicted values of empirical models for records not utilized in the regression analysis.	295
Table 6-15. Chord rotation capacity at Y, m, u-10, u-20, u-50.	296

List of Symbols

$\frac{E_Y}{E_g}$	Stiffness ratio at yielding.
$\frac{E_m}{E_g}$	Stiffness ratio at maximum force capacity.
$\frac{E_{u-10}}{E_g}$	Stiffness ratio at 10% reduction of maximum force capacity.
$\frac{E_{u-20}}{E_g}$	Stiffness ratio at 20% reduction of maximum force capacity.
$\frac{E_{u-50}}{E_g}$	Stiffness ratio at 50% reduction of maximum force capacity.
A_{bh}	Cross sectional area of RC section.
A_e	Effective area of RC section
E_c	Elastic modulus of concrete.
E_{dmg}	Energy dissipation at a particular damage level.
E_m	Energy dissipation at maximum force capacity.
E_s	Young's modulus of steel
E_{tot}	Total energy dissipation capacity.
E_{u-10}	Energy dissipation at 10% reduction of maximum force capacity.
E_{u-20}	Energy dissipation at 20% reduction of maximum force capacity.
E_{u-50}	Energy dissipation at 50% reduction of maximum force capacity.
F_{max}	Maximum lateral force.
$ISD_{max\%}$	Inter-storey drift expressed in %.
I_e	Moment of inertia based on effective sectional properties.
I_g	Moment of inertia based on gross sectional properties.
K_{fe}	Elastic stiffness due to flexural deformation.
K_{ff}	Stiffness due to flexural deformation when section is cracked in flexure and shear.
K_{fy}	Stiffness due to flexure deformation after yielding.
K_{se}	Elastic stiffness due to shear deformation
K_{sf}	Stiffness due to shear deformation when section is cracked in flexure.

K_{ss}	Stiffness due to shear deformation when section is cracked in shear.
K_{dmg}	Residual stiffness at a particular damage level.
K_m	Residual stiffness at maximum force capacity.
K_{tot}	Combination of stiffness due to shear and flexure deformation.
K_{u-10}	Residual stiffness at 10% reduction of maximum force capacity.
K_{u-20}	Residual stiffness at 20% reduction of maximum force capacity.
K_{u-50}	Residual stiffness at 50% reduction of maximum force capacity.
L_{pl}	Plastic hinge length.
L_s	Shear span of a cantilever, measured from the point of fixity to a point of contra-flexure.
M_p	Plastic moment of section.
M_y	Yield moment.
V_{RC}	Shear force at diagonal cracking.
V_a	Shear strength of RC section
V_c	Shear strength contribution due to concrete.
V_n	Shear strength of the column.
V_p	Shear strength contribution due to axial load.
V_p	Shear demand at flexural yielding.
a_{1-4}	Mechanical properties of steel obtained experimentally to determine R .
a_{cy}	Zero-one variable for the presence of cyclic loading.
a_{sl}	Zero-one variable for considerable slip of longitudinal reinforcement from their anchorage zone beyond the end section.
a_v	Zero-one variable for diagonal cracking before flexural yielding of the end section.
d_{bh}	Diameter of transverse reinforcement.
d_{bl}	Diameter of main longitudinal reinforcement
f'_c	Maximum strength of un-confined concrete
f'_{cc}	Maximum strength of confined concrete.
f_{cr}	Stress in a bar at the instance of buckling.
f_{tl}	Maximum strength of longitudinal steel reinforcement.

f_{yl}	Yield strength of longitudinal steel reinforcement.
f_{yw}	Yield strength of transverse steel reinforcement.
k_y	Compression zone depth normalised with h .
n_{cy}	Number of cycles in a loading history pattern.
s_n	Parameter defining buckling.
s_r	Spacing between ribs of reinforcement.
ε_{c0}^*	Strain rate of concrete.
ε_{cc}	Strain of confined concrete at maximum strength.
ε_{co}	Strain of unconfined concrete at unconfined maximum strength.
ε_{cu}	Ultimate strain of unconfined concrete.
ε_{st}	Strain at maximum tensile strength of steel reinforcement.
ε_{su}	Ultimate strain of longitudinal steel reinforcement.
ε_{sy}	Yield strain of steel reinforcement.
$\theta_{Y,slip}$	Chord rotation due to bond slip at yielding.
θ_{bb}	Chord rotation at longitudinal bar buckling.
θ_{dmg}	Chord rotation at a particular damage level.
θ_m	Cord rotation at maximum force capacity.
θ_{sp}	Chord rotation at spalling.
θ_{u-10}	Cord rotation at 10% reduction of maximum force capacity.
$\theta_{u-20,slip}$	Chord rotation due to bond slip at 20% reduction of maximum lateral force capacity.
θ_{u-20}	Cord rotation at 20% reduction of maximum force capacity.
θ_{u-20}^{pl}	Plastic chord rotation between yielding and ultimate.
θ_{u-50}	Cord rotation at 50% reduction of maximum force capacity.
μ_Δ	Displacement ductility.
ρ_1	Tension reinforcement ratio at extreme fibres
ρ_2	Compression reinforcement ratio.
ρ_d	Diagonal reinforcement ratio in diagonally reinforced members (ratio of cross-sectional area of reinforcement along one diagonal to bh)

ρ_s	Minimum transverse reinforcement ratio among the two transverse directions.
ρ_v	Ratio of “web” longitudinal reinforcement uniformly distributed between tension and compression reinforcement.
ω_1	Mechanical tension reinforcement ratio.
ω_2	Mechanical compression reinforcement ratio.
ω_T	Mechanical total reinforcement ratio.
ϕ_Y	Curvature at yielding.
ϕ_u	Curvature at 20% reduction of maximum lateral force capacity.
b	Width of RC cross-section.
c	Concrete cover to transverse reinforcement.
E	Energy dissipation
e	Eccentricity of axial force.
h	Depth of RC cross section.
N	Axial force applied on RC elements
N	Axial force
P	Power index for strain hardening.
R	Parameter that influences the shape of transition during cyclic deformation of steel.
R^o	The value of R during the first cycle.
s	Spacing between transverse reinforcement.
G	Elastic shear modulus of concrete.
z	Internal lever arm.
λ	Normalized energy dissipation capacity

List of Acronyms

<i>AIC</i>	Akaike Information Criteria
<i>BIC</i>	Bayesian Information Criteria
<i>CoV</i>	Coefficient of Variation
<i>DCH</i>	Ductility class: high
<i>DCL</i>	Ductility class: low
<i>DCM</i>	Ductility class: medium
<i>DI</i>	Damage Index.
<i>DL</i>	Damage limitation level as defined in EN1998-3 (2005).
<i>DS</i>	Damage Scale.
<i>EDP</i>	Engineering demand Parameters.
<i>ELP</i>	Effective loading pattern
<i>ILP</i>	Input loading pattern
<i>LVDT</i>	Linear variable differential transformer
<i>m</i>	Damage level at maximum lateral force resistance at first yielding of component.
<i>MAR</i>	Missing (data) at random.
<i>MCAR</i>	Missing (data) completely at random
<i>MCFT</i>	Modified compression field theory.
<i>MNAR</i>	Missing (data) not completely at random
<i>MRF</i>	Moment resisting frame.
<i>NC</i>	Near collapse damage level as defined in EN1998-3 (2005).
<i>P-Δ</i>	P-delta effect, ie. The effect of the axial load on the component when deformed with respect to its original position.
<i>PEER</i>	Pacific earthquake engineering research
<i>PGA</i>	Peak Ground Acceleration
<i>RC</i>	Reinforced Concrete.
<i>SD</i>	Significant damage level as defined in EN1998-3 (2005).
<i>SDOF</i>	Single degree of freedom
<i>SRCC</i>	Spearman rank correlation coefficient

- u-10* Damage level at 10% maximum lateral force resistance of component.
- u-20* Damage level at 20% maximum lateral force resistance of component.
- u-50* Damage level at 50% maximum lateral force resistance of component.
- Y* Damage level at first yielding of component.

LOOCV Leave-one-out cross-validation.

SST Total sum of squares.

Chapter 1. INTRODUCTION

1.1 Background

Natural and man-made hazards including earthquakes have claimed the lives of more than 3 million people between 1976 and 1996, and adversely affecting the lives of more than 800 million people, and causing more than \$50 billion in property damages (Noji, 1996). Recent European earthquakes (e.g., Southern Italy 1980, Turkey 1999, L'Aquila 2009, Emilia Romagna 2012) have shown that the structural performance of Reinforced Concrete (RC) buildings has played a crucial role in terms of earthquake losses and urban resilience. This is particularly true for moment resisting frame structures (Vona, 2014). It is observed that the number of masonry or adobe buildings that collapse in an earthquake are more than RC structures (Coburn and Spence, 2002). Nevertheless, when RC structures collapse, they are associated with a higher mortality rate since RC structures tend to be multi-family dwellings or apartment blocks with high occupancy rates (Coburn and Spence, 2002). This was particularly observed in the collapse of a RC student residence house in L'Aquila during the 2009 earthquake (EEFIT, 2009) and in Cavezzo during the 2012 Emilia Romagna earthquake (Ioannou et al., 2012).

It is estimated that up to 50% of existing reinforced concrete (RC) structures in European countries, particularly in the Mediterranean, were constructed between the 1940s and late 1970s (Cosenza *et al.*, 2003). During this period, most RC structures were constructed with smooth longitudinal reinforcement bars (Verderame *et al.*, 2010). In subsequent years, ribbed reinforcement was introduced. In some Mediterranean countries, during the 1980s and early 1990s, whilst ribbed bars were used for longitudinal reinforcement, smooth bars were used for transverse reinforcement. It is observed that various MRF RC structures constructed during these periods have suffered extensive damage in recent historical earthquakes since they were constructed according to codes that at the time did not recommend either sufficient reinforcement or adequate detailing for the structure to resist strong seismic shaking (EEFIT, 1999; EEFIT, 2003; EEFIT, 2009).

Framed RC structures are commonly found and represent 75% of building stock in Turkey and 30% in Greece (Yakut, 2004) and other studies by Dolce, 2006; Goretti, 2008; Masi, 2014 that these are also significant in other European countries. In order for a society or a community to be resilient, it needs to be aware of the effects of hazards, prepare, and take remedial action. Consequently, in European and other Mediterranean earthquake-prone countries, the seismic performance of the building stock particularly RC frame structures needs to be investigated (Vona, 2014).

Part of the process involves the assessment of structures. The seismic assessment in Europe is carried out following EN1998-3 (2005) and amendments EN1998-3 (2009). The code provides a performance based approach to evaluate the seismic performance of existing individual structures. This evaluation through an assessment procedure is required as an input in the selection of necessary corrective measures and to set criteria for the design of retrofitting measures.

Fundamental requirements for assessment and intervention refer to states of damage in the structure. The response of a structure following analysis is compared with these damage limit states. Within EN1998-3 (2005) three damage limit states are defined. The near collapse damage limit state refers to the condition where a structure is heavily damaged with lower residual lateral strength and stiffness, although vertical elements are still capable of sustaining vertical loads. At this level, most elements of the structure would have collapsed and large permanent drifts are present. A structure that would have reached this level would probably not survive another earthquake/aftershock even of a moderate intensity.

The significant damage level (SD) refers to a structure that is significantly damaged with some residual lateral strength and stiffness. This damage level is characterised by large permanent drifts but the vertical elements are capable of sustaining vertical loads. The structure is considered to be able to sustain aftershocks of moderate intensity.

A structure which does not exceed the damage limitation level (DL) is considered to be lightly damaged with structural elements prevented from significant yielding. Structural elements are considered to retain their strength and stiffness properties. Permanent drifts are considered negligible.

The capacity of RC elements is defined in terms of deformation by EN1998-3 (2005) where Appendix A provides chord rotation equations in terms of material and geometrical properties of the RC structural elements that define the deformation capacity at damage limitation level and collapse damage limit. The chord rotation capacity corresponding to the limit state of significant damage is assumed to be 0.75 of the chord rotation capacity at the limit state of near collapse. The chord rotation expressions are either empirically or semi-empirically based, and are derived on regression analysis of results of low-cycle fatigue tests on column specimens. These equations essentially provide the basis on which RC structure assessments are made, and hence are key to the assessment of the overall seismic risk in European countries.

1.2 EN1998-3 (2005): Deformation Capacity Recommendations for Assessment

Many damage scales in literature that are used for the assessment of RC structures define damage states, not only at yield and ultimate but also at various other states, which are useful for damage quantification, possible loss estimation and intervention requirements. However, damage limit states as defined in EN1998-3 (2005) only refer to only one intermediate damage state between yield and ultimate. The definition of this damage state is not considered independently but is coupled with a subsequent damage state (e.g. the deformation level is defined as a proportion of the collapse deformation). As defined by damage scales, damage at a particular damage state builds upon previous occurring damage, following the behaviour of a RC element or a structure. Nevertheless, the significant damage level defined in EN1998-3 (2005) is not defined independently, but in terms of a subsequent damage state.

Apart from deformation, the description of damage limit states in EN1998-3 (2005) make reference to residual stiffness and strength degradation. The limit state of near collapse is defined as a function of strength degradation. However, the provided relations that define the limit states do not make reference to residual stiffness, apart from a relation that describes the effective stiffness ratio at yielding. Moreover, permanent drifts are used to describe damage limit states. However, these are also not quantified by any relation in EN1998-3 (2005).

The explanatory variables in current chord rotation expressions refer to forms of combined variables as found in literature referring to specific damage phenomena or deformation characteristics. The combination of variables in the existing empirical or semi-empirical models does not involve analysis of relationships between the different physical quantities. This is required to check whether the structure of the explanatory variables has an optimal structure in terms of the basic variables. It is also required to check that the structure of the explanatory variables is optimal with respect to the structure of the other variables in the same set forming the model.

In current relations, considerable bond-slip is considered through a dummy variable such that each explanatory variable is assumed to have the same contribution towards bond-slip. However, specific relations that describe the bond-slip phenomenon indicate that different variables have different effects on the phenomenon.

The results of low-cycle fatigue tests on column specimens upon which the existing EDP relations are derived are collected from literature, where in many cases not the same rationale is used when presenting values of parameters and associated definitions. Moreover, different testing setups are used which are associated with different error characteristics, and induce different $P-\Delta$ effects in

the experimental tests. This adds to the uncertainty with which existing EDP relations are determined.

The low cycle fatigue tests constituting the database upon which EDP relations are derived, were not specifically designed and conducted for the exercise. Hence, there are possibly ranges of data, which are characteristic to existing RC structures that generally require assessment, but which are underrepresented in low-cycle fatigue experimental campaigns. This further increases the uncertainty about the applicability of some existing EDP relations.

Particularly in the case where low cycle fatigue tests in the database are used to calibrate analytical procedures, or to describe specific damage phenomena, loading regimes used do not necessarily reflect the demand that is induced by an earthquake in a particular RC structure. In addition, experimental evidence shows that the behaviour of RC elements including the chord rotation capacity is a function of the loading pattern and its associated characteristics. However, this phenomenon is generally ignored in the development of EDP relations.

1.3 The Aim of the Thesis

At the onset of new revisions to EN1998-3 (2005) that will be made in the coming years, an attempt will be made to address some of the issues that are highlighted above. The aim of the research is therefore to develop tools for predicting RC element deformation capacity at different damage limit states that can be used within the context of a full structural performance based assessment.

Developed tools will consist in EDP relations mainly describing chord rotation and stiffness ratio capacity of RC elements with ribbed reinforcement, expressed in terms of material and geometric properties. However, independent relations will also be developed at intermediate damage states between yield and ultimate, in order to define better damage scale requirements and definitions. As a result, since residual stiffness and strength degradation are used in the definition of damage states, associated relationships that define the interaction between these EDPs will also be determined.

1.4 The Structure of the Thesis

In order to develop the EDP relationships various considerations have to be made. These mainly refer to identification of properties that define deformation, requirements by structures on which assessment can be made, data to develop models and a statistical procedure. This section outlines the structure of the thesis that is used to satisfy the aim.

In **Chapter 2** material and geometric properties that characterise RC building stocks that generally require assessment or that have shown to perform badly in earthquakes are identified (Section 2.2). The properties that define constitutive models of materials and damage phenomena

that contribute to the overall deformation of RC elements are identified and discussed. A combination of these variables can form possible explanatory variables to the models. Further requirements for the development of new EDP models are discussed by assessing the advantages, limitations and boundaries of existing EDP models in literature (Section 2.3). While material and geometric properties describe damage and the deformation capacity, quantification is done through Damage Indices (DIs) on a Damage Scale (DS). Associated requirements for EDP relations are therefore discussed to identify damage levels at intermediate damage states, and through an example, where the existing EDP relations recommended by EN1998-3 (2005) are used to assess a MRF RC structure. Chord rotation, energy dissipation and residual stiffness are identified as the most relevant parameters.

The EDP models will be determined on the basis of experimental data. Databases available in literature are discussed. However, these are characterised by gaps in the range of application of explanatory variables that characterise building stocks of MRF RC structures. The number of available records is also small.

A low cycle fatigue experimental campaign is proposed in **Chapter 3**. This is extended on RC columns which represent a range of elements in existing structures, but have material and geometric characteristics which are underrepresented in databases and previous experimental campaigns in literature (section 3.2). The main explanatory variables are based on the observations from literature in Chapter 2. These included v , a , ρ_T , L_S/h and detailing aspects. The experimental campaign consists in 19 column-foundation RC specimens tested on a horizontal setup (section 3.3). A hyper static system provides axial loads which do not simulate P- Δ realistically. Hence, an instrumentation layout is proposed, not only to determine the EDPs, and material and geometric properties, but also to monitor and account for the P- Δ effects and other sources of error (section 3.4). A rational approach to determine the dependent and explanatory variables which will help in the reduction of uncertainty associated in determining EDP models is defined.

The results of the experimental campaign are then discussed in **Chapter 4** mainly in terms of the EDPs, the occurrence of damage phenomena, and the associated capacity at each damage level (section 4.4). Diagnostic considerations discussed in Chapter 3 are applied. The experimental campaign is also used to evaluate different trends in terms of the behaviour of RC elements and damage development, which can be useful in the development of EDP models. Section analysis is used to verify and compare analytical quantities such as initial stiffness, initial cracking, first yielding and the ultimate capacity, with the experimental response (section 4.3). The data that is required for regression analysis to develop EDP models is determined.

A procedure for empirical determination of engineering demand parameters is then proposed in **Chapter 5**. Existing relationships indicate that a semi-empirical approach provides a better

logical understanding of damage development with respect to mechanics of deformation than empirical models. However, the former provide worse models in terms of fit and parsimony. This is due to reference of physical phenomena in semi-empirical models which are still being developed in literature. Hence, for the purpose of this research, an empirical approach is considered. Regression analysis will be used in determining EDP models, based on data from the experimental campaign obtained in Chapter 4 and an identified database in Chapter 2. Some data is retained for cross validation. Statistical techniques and associated methodologies will be identified to determine an optimal combination and form of explanatory variables in a general model form that also allows the expression of variable contribution by each explanatory variable towards considerable bond-slip. Since the permutations and combinations of variables is extensive, stepwise regression is considered where different models describing the same EDP at the same damage level are considered with different explanatory variables determined using different techniques. Selection criteria is chosen keeping balance between best-of-fit and parsimony characteristics.

Selected regression models are then discussed in **Chapter 6** in terms of their ability to fit data and their range of application. The assumptions used in the regression analysis process are also checked. The models are then compared with other models in literature, including the relationships recommended by EN1998-3 (2008). Proposed models are also validated with experimental data that were not used for their development in order to assess their applicability. The proposed models are also used to determine the damage levels of the example in Chapter 2. The damage classification following the response of the analysed structure in the example is compared with corresponding damage classification based on the relationships proposed by EN1998-3 (2005).

Chapter 2. RC STRUCTURE ASSESSMENT AND DAMAGE ESTIMATION

2.1 Introduction

In this Chapter, general aspects that somehow influence the seismic assessment process are discussed in order to identify and understand requirements for the development of new empirical relations of EDPs.

Both structures that are designed or not designed to resist earthquakes have to be checked and satisfy criteria which are based on their performance. As shown in Chapter 1, performance based criteria adopted in EN1998-3 (2005) are required to be satisfied such that under frequent earthquakes, no damage is observed in structures, under a rare event damage a structure can be repaired and under an extreme event, life safety can be secured. Other fundamental Performance Based Design and Assessment procedures criteria are illustrated in figure 2-1. The process therefore involves linking the seismic hazard, performance and capacity of the structure.

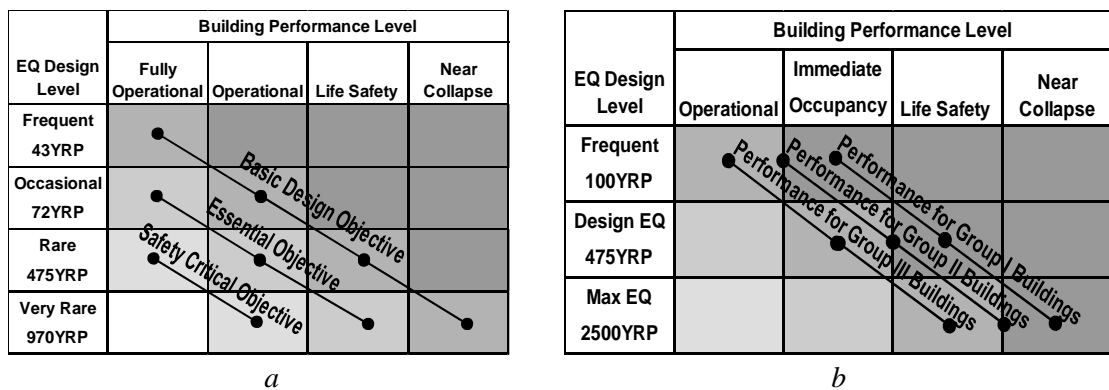


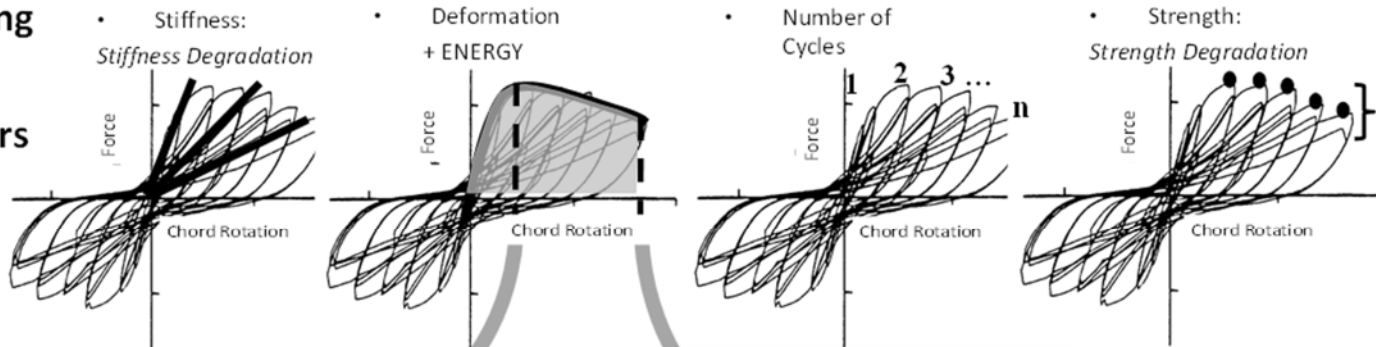
Figure 2-1 Performance based earthquake engineering criteria. A) Vision 2000, b) FEMA 273.

As illustrated in figure 2-2, in general, an assessment process involves the analysis of structures where the response is compared with the capacity of structural elements for a particular damage level through EDP relationships. The relative magnitude of the two quantities defines the damage index, which maps the state and degree of damage of the structure defined by a damage scale.

Hence, in this Chapter, the material and geometric properties that influence the constitutive behaviour of RC elements and structures, and which are required to define deformation capacity are discussed. Seismic assessment is required to be conducted on a range of structures. As a result, detailing considerations, and material and geometrical properties that characterise RC structural configurations in Europe are identified to understand application requirements of EDP models. Since for the purpose of this research only models referring to failure in flexure will be developed, approaches which identify failure modes of RC structural elements will be discussed for selection purposes. Existing EDP relationships are discussed and compared, also with respect to damage

indices and scales in order to identify further requirements in new models. Since existing EDP models are determined on low-cycle fatigue test results, information from existing databases will be evaluated for possible requirements in developing EDP models.

Engineering Demand Parameters



$$\theta_y = \phi_y \frac{L_V + a_V z}{3} + 0,00135 \left(1 + 1,5 \frac{h}{L_V} \right) + \frac{\varepsilon_y}{d - d'} \frac{d_b f_y}{6 \sqrt{f_c}}$$

$$\theta_{um} = \frac{1}{\gamma_{el}} 0,016 \cdot (0,3^v) \left[\frac{\max(0,0; \omega)}{\max(0,0; \omega)} f_c \right]^{0,225} \left(\frac{L_V}{h} \right)^{0,35} 25^{\left(\frac{\alpha_{\rho_{xx}} f_{yw}}{f_c} \right)} (1,25^{100 \rho_d})$$

(Example: Fardis, 2009)

DAMAGE INDEX

Example:

$$DI = \frac{\delta_m}{\delta_u} + \frac{\beta}{Q_y \delta_u} \int dE \quad DI_{storey, j} = \frac{\sum w_i D_i^b}{\sum w_i D_i} \quad DI_{global} = \frac{\sum w_{storey, j} D_{storey, j}^b}{\sum w_{storey, j} D_{storey, j}}$$

(Example: Park et. al., 1986)

DAMAGE SCALE

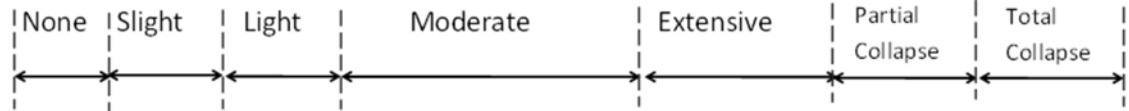


Figure 2-2 General aspects that affect seismic assessment procedure of RC structures.

2.2 Mechanical Properties and Damage Development of Reinforced Concrete Elements

2.2.1 Code Provisions and Detailing

The degree of damage development of RC structures as observed in recent historical earthquakes is a function of detailing aspects, material properties with which they were designed and built Booth et al., 2006. Table 2-1 shows and compares various case studies of RC structures that have suffered damage during earthquakes in Europe and which are also representative of populations of similar structures in terms of geometry and material properties. Many RC structures in the case studies are constructed with poor construction techniques and inadequate materials or detailing that is not even according to the code at the time. The RC structures are characterised with low concrete strength; inadequate confinement consisting in large spaces between stirrups, small diameter of transverse reinforcement and stirrups ending with 90° hooks; inadequate longitudinal reinforcement where the reinforcement ratio is not sufficient, the diameter of the bars is too small and the tensile strength is small particularly when mild steel is used. The cross-sectional dimensions of the columns mostly vary between 200mm and 400mm. Beams are generally deep and stiffer than columns. In general beams span between 3.5m and 6.5m. The height of the ground floor is larger than 3m, while the height of other floors is in the range of 2.75m and 3m. The height of most buildings in table 2-1 varies between 2 and 6 storeys. Bad workmanship as a result of corruption or fraud was sometimes remarked as the reason for inadequate detailing, and hence failure of structures.

Appendix A synthesises important detailing aspects and design recommendations by some guidelines with which many RC structures were built in various European countries. The recommendations by codes before the 1990s do not account for seismic considerations and justify the damage of the RC structures in Table 2-1. The detailing recommendations by EN1998-1(2004) is more robust where the expected behaviour and performance is controlled through the design. The synthesised detailing aspects are a representation of the characteristics of the existing building stock on which seismic assessment is expected to be conducted. Hence, EDP relations are required to cover the referred magnitude ranges of material and geometric properties.

Table 2-1. Geometric and material properties of some representative buildings that suffered damage in Europe due to recent or past earthquakes.

Country	Construct. period	Number of storeys	Column dimensions	Beams dims.	Ground floor height	Other floors height	Beam spans	Slab depth	Concrete strength	Concrete mix Proportions	Cover	Reinforcement Yield Strength	Reinforcement	Code	Past earthquakes.	General Comments	Reference
			(mm x mm)	(mm x mm)	(m)	(m)	(m)	(m)	(cube - MPa)		(mm)	(Mpa)					
Turkey	>1970	2 - 5	variable; high-aspect ratio	200-250 x 500-600	3.5 - 4.5	2.7 - 3	2.5 - 6	0.12	10-20; 25	1:2:3(Cement:sand:gravel); Old structures use >1cm aggregate	<25	n.a.	Beams: 4x12-16mm ϕ bars; Transverse: 6-10mm ϕ @ 200-250mm cc, 90° hooks. Column lapping = 40-70 ϕ of corner bars only and intermediate bars are terminated with 180° hooks.	Turkish Code 1975; TS-500.	Damage during the 1999 Kocaeli and Duzce earthquakes.	R.C. frames with infill masonry, known as Beskas. Generally reinforcing detailing and material properties do not follow code requirements. Irregular grid arrangement. Clay tile or aerated concrete block infill panels.	Gulkan et. al., 2002; EEFIT, 2000; EERI, 2000
Turkey	1980's; 1990's	<5	230 x 390; 300 x 500; 600 x 360 (5 storeys); 890 x 390 (5 storeys)	500 x 525-625	2.8 - 4.5	2.8 - 3	<5	0.125	<25	Aggregate maximum size >30mm	<25	Main reinforcement: Mild smooth Steel in older buildings, high-strength corrugated in more recent buildings. Transverse reinforcement: smooth mild steel.	Columns: <1.5%, 8-10 x 18mm ϕ bars (terminated in hooks); Column transverse: <0.3%, 8mm ϕ @200-300mm cc, 90° hooks. Beams: 5 x 16mm ϕ single layer top. Beam Transverse: 8mm ϕ @ 150-300 c.c.	Turkish Code 1975; TS-500.	damage during the 2003 Bingol earthquake.	R.C. frames with infill masonry. Column width is generally twice the thickness of the infill panel. Code requirements not always followed. Beams were generally either not continuous or if continuous, they were not always in a straight line.	EEFIT, 2003
Romania	1960 - 1990	5 - 10	Example: 300 x300; 300 x 650; 500 x 500	>150 x 300	(sometimes higher than upper floors)	3	4 - 6.5	0.06 - 0.21	ca. 13	Large quantity of fine aggregate (0-3mm); 240-270kg/m ³ cement.	n.a.	Smooth round reinforcement	Columns: <0.5-0.6% longitudinal reinforcement. Longitudinal reinforcement including <10mm ϕ . Typical arrangement includes 8x 16mm ϕ bars. Transverse reinforcement: 6-8mm ϕ @ 250-300mm c.c. connecting corner bars only. Poorly confined sections include up to 1m reinforcement spacing; 100-120kg of steel/m ³ concrete	DIN; Seismic design codes (1977, 1981, 1992)	1940 Vrancea (M=7.4); 1977 Vrancea (M=7.2); 1986 Vrancea (M=7.0); 1990 Vrancea (M=6.7).	Irregular in plan and elevation, with unevenly distributed columns. Make use of R.C. secondary beams spanning on primary beams. 50% of buildings damaged in 1977 earthquake were of this typology. Infilled thick masonry walls.	Prager, 1979; Bostenaru, 2003; Balan et. al., 1982.
Romania	1960-1990	4 - 18	600 x 700-800 at lower levels. Reduced at higher levels.	Interior: 300 x650; Exterior: 300 x 550	4	2.75	Grids: 4.5 x 5; 6 x 6; 5.4 x 3.6	0.13	n.a.	n.a.	n.a.	250	n.a.	DIN; Seismic design codes (1977, 1981, 1992)	1940 Vrancea (M=7.4); 1977 Vrancea (M=7.2); 1986 Vrancea (M=7.0); 1990 Vrancea (M=6.7).	Poor construction material quality. Formation of cold joints at beam column interfaces. Concrete bursting due to corrosion. During earthquakes, damage included horizontal cracks along cold joints, concrete spalling, reinforcement buckling, and X-shaped cracks.	Bostenaru, 2003; Balan et. al., 1982.
Ex-Yugoslavia (also used in Cuba, Georgia and Philippines)	>1970	5 - 10	n.a.	n.a.	n.a.	2.9 - 3.2	3 - 12	n.a.	40	Concrete mix design: 3 fractions of gravel and 400kg/m ³ of cement	n.a.	400	n.a.	Yugoslav National building Code-1964, 1987.	Few damages during: 1969 Bosnia earthquake (M=6.4); 1977 Vrancea (M=7.2); 1979 Montenegro (M=7.2); 1980 Kopaonik (M=5.7)	R.C. frames, some including precast elements. The constructions are generally regular in shape.	Dimitrijevic et. al., 2002.
Former USSR countries	1974-1976; 1980's and 1990's	9	n.a.	n.a.	n.a.	3	n.a.	n.a.	30-35	n.a.	ca. 35	390	n.a.	SNiP II-7-81	No damage in the 1984 Severobaikalsk earthquake. MSK=5	This is a load bearing R.C wall and column system, consisted in a very rigid wall system generally R.C. wall panels connected to a frame system.	Eisenberg et. al., 2002.
Greece	1977-2000	4 - 5	Examples: 300 x 300; 200 x200; 400 x 400; 300 x 600	n.a.	n.a.	3	3.5 - 4.5	n.a.	25	n.a.	n.a.	500	n.a.	National Building Code, 1955; NKOS,1985, 1995; NEAK, 1995.	1999 Athens earthquake (Ms=5.9)	Multistorey reinforced concrete structures using a dual system of frames and shear walls. .	Tassios et. al., 2002.
Greece	part 1960's, part 1980's.	3	200 - 500 x 200 - 500	n.a.	3.5	3.5	<5	0.15	16	n.a.	>10	Year 1960: 220; year 1980: 400	n.a.	National building Code, 1959	2000 Athens earthquake (Ms=5.9)	These are low R.C. frame structures which were extended with additional floors decades later.	Koumouis et. al., 2002.
Cyprus	part 1960's, part 1980's.	3 - 5	n.a.	n.a.	3; >3	3	3.5 - 4.5	0.15	15-25	n.a.	15 -25	220 - 500	Longitudinal reinforcement: >1960 use mild steel; >1980 high strength steel	CP114, CP110, BS8110, ACI318, BAEL, DIN, SNiP.	1995 Paphos (M=5.7); 1996 Paphos - Limassol (M=6.5); 1999 Limassol (M=5.8).	Irregular positioning of columns. Covers 30% of the dwelling stock. Shear failure in columns was the most common mode of failure. Eccentric compression and shear cracking were factors that enhanced this failure mode. Reinforcement corrosion was also a common phenomenon that enhanced failure of concrete columns during past earthquakes.	Levtchitch et. AL, 2002
Italy	1970's - 1990's	<6	Common examples: 300 x 300; 400 x 300; 350 x 300.	Common examples: 300 x 500; 800x200; 500x200	3; >3	3	4.5 - 6.0	0.1 - 0.3	20	n.a.	15-25	440	Columns: 4-6 x 16mm ϕ bars; Transverse : 6-8mm ϕ @ 200mm c.c., no hook anchor; Beams: sometimes hooks in nodes, 3-5 x 12-16mm ϕ diameter top/bottom - 2 x 12-16mm ϕ diameter bottom/top.	D.M. 30/05/72; D.M. 26/03/80; D.M. 09/01/96	1976 Friuli; 1980 Irpinia; Umbria Marche 1997; 2009 Aquila	R.C. frames sometimes with infilled masonry. Eccentricities are sometimes present. Slab may not be completely continuous due to the use of precast elements.	Manfredi et. al., 2007

2.2.2 Properties and Behaviour of Concrete

The constitutive model of concrete changes depending on the context the material is being used. The stress-strain relationship varies with the size of the concrete specimen (Van Mier, 1986). It also depends on the pressure that it is confined with and affects the strength, deformability and failure mode (William *et al.*, 1986). Being weaker in tension than compression, concrete fails under developing tensile stresses when in compression due to Poisson effects. The size and type of surrounding pressure then manifest the mode of failure of how this happens. A wider account of how this happens is beyond the scope of this thesis, however a more detailed account is given by Powasrusron (2003). While models by Vecchio *et al.*, 1982 give account on the behaviour of concrete through the modified compression field theory (MCFT), other models give an account of the concrete under confinement. There are various models in literature that give confinement models for different applications. The first is given by Richart *et al.*, (1928). The number of models is substantial, and comparison is beyond the scope of this research. However a study of such models is carried out by Fattah *et al.*, (2000). What is relevant, are however the parameters the material and geometric parameters that affect the behaviour of concrete in an RC scenario. As observed from the study by Fattah *et al.* (2000), many are common in different models. A popular and widely used model is provided by Mander *et al.*, (1988). The ultimate confined strain (ε_{cu}) is given by equation 2.1a, the maximum confined stress (f'_{cc}) is given by equation 2.1b and the strain at maximum stress (ε_{cc}) is given by equation 2.1c.

$$\varepsilon_{cu} = 0.004 + \frac{1.4\rho_s f_{yh} \varepsilon_{su}}{f'_{cc}} \quad [2.1a]$$

$$f'_{cc} = f'_c \left(-1.254 + 2.254 \sqrt{1 + \frac{7.94f_l}{f'_l} - \frac{2f_l}{f'_c}} \right) \quad [2.1b]$$

$$\varepsilon_{cc} = 0.002 \left(1 + 5 \left(\frac{f'_{cc}}{f'_c} - 1 \right) \right) \quad [2.1c]$$

In EN1998-3 (2005) the maximum strength of concrete is based on the model by Newman *et al.*, (1982) and is given by equation 2.2a and refers to a confinement factor a given by equation 2.2b. The strain at maximum strength and the ultimate strain are then given by equation 2.2c and equation 2.2d respectively. The models therefore depends on other properties of concrete under uniaxial loading, axial load, strength of transverse steel, and density and arrangement of transverse steel.

$$f'_{cc} = f'_c (1 + K) \quad \text{where} \quad K \approx 3.7 \left(\frac{a\rho_s f_{yw}}{f_c} \right) \quad [2.2a]$$

$$a = \left(1 - \frac{s}{2b_o}\right) \left(1 - \frac{s}{2h_o}\right) \left(1 - \frac{\sum b_i^2/6}{b_o h_o}\right) \quad [2.2b]$$

$$\varepsilon_{co} = \varepsilon_{co}(1 + 5K) \quad [2.2c]$$

$$\varepsilon_{cu} = 0.0035 + \left(\frac{10}{h_o}\right) + 0.4 \left(\frac{\alpha \rho_s f_{yw}}{f_c}\right) \quad [2.2d]$$

The models therefore depends on other properties of concrete under uniaxial loading, axial load, strength of transverse steel, and density and arrangement of transverse steel.

2.2.3 Properties and Behaviour of Steel Reinforcement

There are various widely used models that describe the constitutive behaviour of steel (Examples; Peterson and Popov, 1997; Ramberg and Osgood, 1993; Sozen *et al.*, 1973; Kato *et al.*, 1997; Menegotto and Pinto, 1973 and Ma *et al.*, 1976). It is beyond the scope of this research to compare these models. However it is important to highlight the physical parameters and the geometrical properties utilised by the models that are used to define the behaviour of steel at various levels of deformation.

The elastic region can be defined by the elastic modulus (E_s), the yield strain (e_{sy}) and the yield stress (f_y). In the inelastic range, the model by Menegotto *et al.* (1992) consider parameter R given by equation 2.3 as the parameter that influences the shape of the transition curve in cyclic deformation. ξ_p^n is the plastic excursion at the n th semi-cycle. a_1 and a_2 are mechanical properties which can be obtained experimentally. R_0 is the value of R during the first loading. The larger the value of R the larger is the transition curve. R is a function of other steel properties and the stress strain inversion of previous cycles. It also defines the Bauschinger effect. Dodd and Restrepo-Posada (1995) shows that the Bauschinger effect also depends on the chemical composition of the reinforcing steel, is also a function of the carbon content.

$$R^n = R_0 - \frac{a_1 \xi_p^n}{a_2 + \xi_p^n} \quad [2.3]$$

The model by Monti *et al.*, (1992) is based on the model by Menegotto *et al.*, (1992) accommodating post-elastic buckling based on a threshold of s/d_{bl} . For very large values of s/d_{bl} , buckling is assumed to occur just after yielding. The hardening rule is considered to be a function of a weighting coefficient (P_w), the yield stress (f_y), a hardening ratio (b_p^0) and the elastic modulus (E_s). In the presence of buckling, the isotropic hardening is considered to be less. Isotropic hardening is represented by four experimentally calibrated parameters. In this model, the presence of either isotropic hardening or kinematic hardening depends on the presence or exclusion of buckling. Gomes *et al.*, (1997) is also based on the Manegotto *et al.*, model and assumes that buckling occurs only between two stirrups and occurs when failure of the cover

takes place. The stress strain ($f_s - \varepsilon_s$) relationship for a buckled bar is given by equation 2.4 where M_p refers to the plastic moment, A_s is the cross-sectional area of the bar.

$$f_s = \frac{2\sqrt{2}M_p}{A_s s \sqrt{\varepsilon_s}} \quad [2.4]$$

The Mander model (Mander, 1994) is based on a power law for strain hardening. This power index P is defined by the initial slope E_h of hardening curve h given in equation 2.5.

$$P = E_h \frac{\varepsilon_u - \varepsilon_h}{f_u - f_y} \quad [2.5]$$

Buckling failure is an important phenomenon in the overall behaviour of steel which depends on both internal and external factors. Papia *et al.*, 1989 defines the external conditions of ultimate concrete ε_{cu} at which buckling occurs in terms of d_{bl} , f_y , $\frac{f_t}{f_y}$, s , f_{yw} and d_{bt} . The problem of elastic buckling was first reported by Euler (1959) where the general critical axial stress in a bar associated with buckling failure mechanism is given by equation 2.6

$$f_{cr} = \frac{\pi^2 E_s I_{lb}}{s' A_{lb}} \quad [2.6]$$

E_s is the yield modulus of steel, I_{lb} is the moment of inertia of the bar, s' is the buckling length which may not necessarily be equal to the transverse reinforcement spacing s , and A_{lb} is the cross sectional area of the bar. However, for seismic engineering purposes, inelastic buckling is generally more of a concern. Typical sectional analysis for columns does not account for buckling. Hence the behaviour at large inelastic deformations may be over predicted with respect to strength and ductility (Bae *et al.*, 2005). On the initiation of buckling in a column, the reinforcing bar strain would be different from the concrete core strain at that section. Hence, this strain would not correspond to the longitudinal strains calculated from a sectional analysis. Buckling is generally but not exclusively observed after spalling where high compressive stresses develop in steel. The occurrence of buckling also depends on the diameter of the longitudinal reinforcement (d_{bl}) the spacing of the stirrups (s) and their strength (f_{yw}). Buckling depends also on whether 90° or 135° hooks are used. The latter provides better restraint. In the analytical model proposed by Urmson *et al.*, 2012, defines buckling capacity as the maximum stress after buckling initiation. For ribbed bars, the phenomenon of buckling may be more complicated to interpret as these have a strong and weak axis due to the ribs and is influenced by the f_t/f_y and e/d_{bl} ratio. The dependence on f_t is also observed by Mau and El-Mabsout (1989).

2.2.4 Characteristics of Bond-slip

Bond failure between steel bars and concrete occurs either in splitting mode if the cover is small or pull-out mode if the cover is large Eligenhausen *et al.*, 1983. The former occurs by shearing off of the concrete keys. On the other hand, if either the concrete is moderately confined or the longitudinal steel bars are closely spaced, failure in splitting mode is expected before shearing off of the keys. A comparison of the two mechanisms in terms of bond stress and deformation are shown in figure 2-3 based on the model by Haralji *et al.*, (1995).

Bond slip failure has widely been investigated by Ciampi *et al.*, (1982) and Eligenhausen *et al.*, 1983. The mechanism described by the latter is shown in figure 2-4. The initial bond stress between steel and concrete is due to chemical adhesion between the two materials. It is then followed by friction and the wedging action between the cement paste and pitting of the reinforcement contribute to the bond action. Interlock between the ribs and the concrete lead to internal bond cracks which coincide with the separation of concrete from the bars Eligenhausen *et al.*, 1983. (In a model proposed by Eligenhausen *et al.*, 1983 which is an extension of a model by Tassios (1979), the maximum bond stress is considered to depend on $\sqrt{f'_c}$. Haralji *et al.* (2006) expresses bond slip in terms of spacing between ribs (s_r). The interlock and friction between the reinforcing bars and concrete is considered negligible when the slip is equal to the spacing between the ribs.

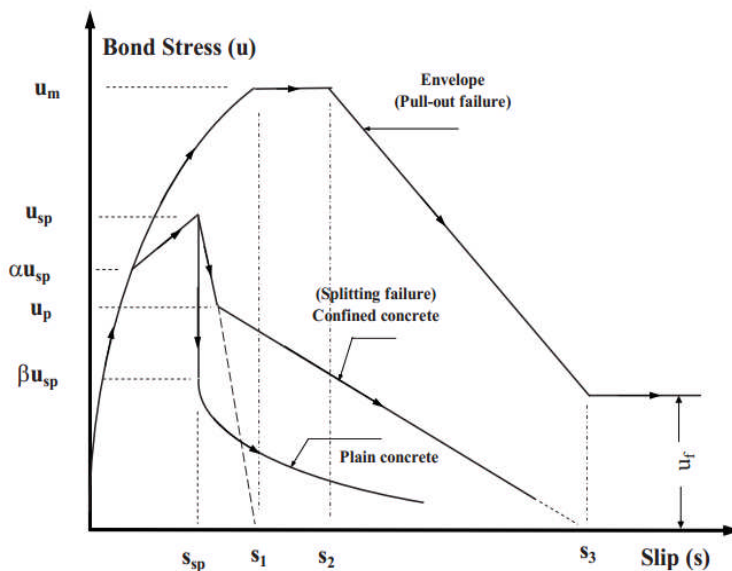


Figure 2-3 Theoretical bond-slip and bond-split model (Haralji *et al.*, 1995).

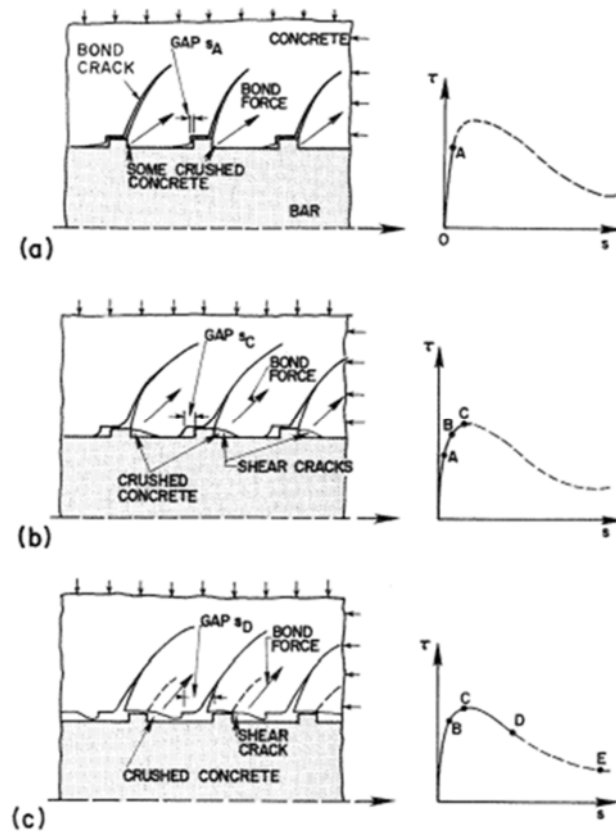


Figure 2-4 Bond-slip mechanism due to monotonic loading (Eligenhausen et al., 1983)

Eligenhausen et al., 1983 observed that bond-slip increases with the number of cycles in cyclic loading. Most of the experimental data in literature describing local effects and individual failure phenomena such as bond-slip, bond splitting and buckling are conducted at slow strain rates. However, f_{yt} is a function of strain rate and hence also the mechanism of these phenomena. However, this phenomenon is rarely accounted for in literature.

Most of the existing RC structures experience more splitting mode failure over bond slip failure (Harajli, 2009). This may not be observed by localised pull-out tests as generally in these tests, concrete is not confined, and bars are not restrained. The parameters that are considered to influence this failure mode include the diameter of the longitudinal reinforcement bars (d_{bl}), the concrete cover (c) and confinement parameters or factors (Harajli, 2006). The non-dimensional parameter c/d_{bl} is generally considered.

The compression slip under negative bending is lower than the tension slip mobilized under positive bending (Harajli, 2009). This indicates that unless the loading pattern on the element is symmetrical with very small increments and the reinforcement in tension and compression are equal, the bond failure mechanism is not symmetrical. Hence since low cycle fatigue tests are generally characterised by symmetrical loading patterns this phenomenon which can occur in a structure due to earthquake loading is not simulated by low-cycle fatigue tests.

During cyclic tests investigating bond splitting, Haralji (2009) observed that ratios of bond stress at the instant of unloading for successive cycles are similar for all types of confinement ratios and cover. For small slip values before splitting, the reduction in bond resistance is small. In the post splitting stage, this is increased.

2.2.5 Strain Rate Effects

As shown in figure 2-5, based on experimental testing, Penelis *et al.* (1992) indicate that the strength and corresponding strain of concrete increases with the rate of applied strain following equations 2.7a and 2.7b respectively. Penelis *et al.*, (1992) also indicates that the yield strength of reinforcement increases with the strain rate, while the range of the yielding plateau decreases with an increasing strain rate. Large strain rates are induced in RC structures during earthquakes. However, these are not simulated by low-cycle fatigue tests.

$$\varepsilon_{cl,dyn} = \varepsilon_{cl,stat} \left(\frac{\varepsilon_c^*}{\varepsilon_{c0}^*} \right)^{0.2} \quad [2.7a]$$

$$f_{c,dyn} = f_{c,stat} \left(\frac{\varepsilon_c^*}{\varepsilon_{c0}^*} \right)^{1.026/5+0.9f_c} \quad [2.7b]$$

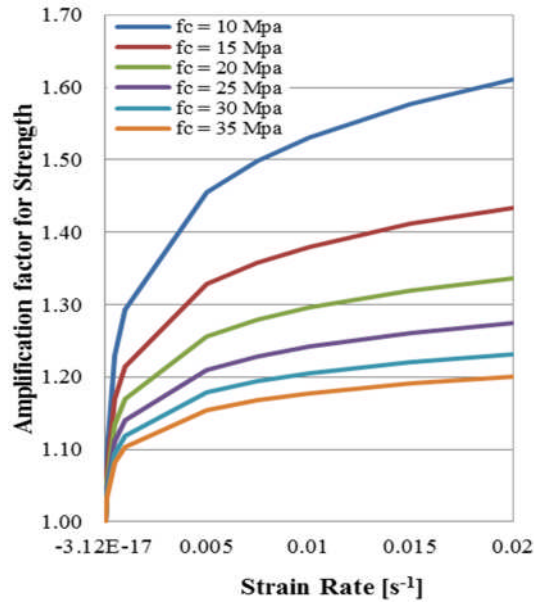


Figure 2-5 Amplification of concrete strength under uni-axial stress due to different strain rates based on recommendations by Penelis *et al.* (1997).

2.2.6 Failure Modes of Reinforced Concrete

Reinforced concrete fails in three general modes of failure: flexure, shear and flexure-shear. The determination of the latter two is complex and hence seismic design guidelines emphasise that adequate structures should be flexure dominant. However, this is not always the case particularly for existing structures not designed with recent codes.

For a flexural failure scenario, a one dimensional stress field in fiber modelling or in the traditional stress block analysis gives generally acceptable predictions of deformations at yield and ultimate limit states, such that this is the bases of design in many design codes such as Eurocode-2, considering that flexural failure occurs before shear failure. However this approach alone cannot estimate deformations of shear or shear-flexure failure accurately. Empirical equations such as Arakawa (1970) have been developed and truss models have been used to simulate shear deformation, yet, the accuracy is not generally acceptable. The modified compression field theory (MCFT) (Collins *et al.*, 1980), incorporated further the effect of the inclined cracks, and the effect of concrete tensile stresses in the non-linear range. The theory is applied in a model by dividing a structural element into small bi-axially stressed elements (Vecchio *et al.*, 1986,1989)

Mostafei *et al.*, 2007 extends and simplifies the model by considering that the total drift ratio (θ_t) of a column between two sections is equal to the summation of the shear drift ratio (θ_s), and flexural drift ratio (θ_f). The compression constitutive law is considered in the axial-flexure and axial shear parts of the model. The secant stiffness method is used in the constitutive laws of steel and concrete in the MCFT. The method by Kent and Park is used for the confinement. Springs of flexural and shear mechanisms, and an equivalent pull-out strain are considered to represent bond slip. The MCFT incorporates tension stiffening effects, softening effects and crack conditions consideration, where the transfer of tensile forces in concrete are transferable across the crack through interlocks, capped by the maximum shear stress. The shear rotation (θ_s) and flexural curvature (ϕ) are a function of shear axial and flexural strains based on constitutive models of steel and confined concrete and with respect to lines of action positions of lines of action along the cross sections. The model considers axial failure or gravity collapse as the stage where equilibrium in the vertical direction cannot be satisfied any more under the applied axial load. This analytical approach identifies that the main problem with reinforcement lies in its interaction with cracked sections which is generally not accounted by pull-out models and hence also underestimated by this model.

Flexure, shear and flexure-shear failure can also be determined by the intersection of shear-deformation capacity approximation, and the shear-flexure limit envelope as shown in figure 2-6. The model provided in ACI318 Code Equation (1999), is modified by Kowalsky *et al.*, (2000). A similar model is provided by Sezen *et al.*, (2002). The consideration of confinement is very limited in these parameters due to limited variability of experiments.

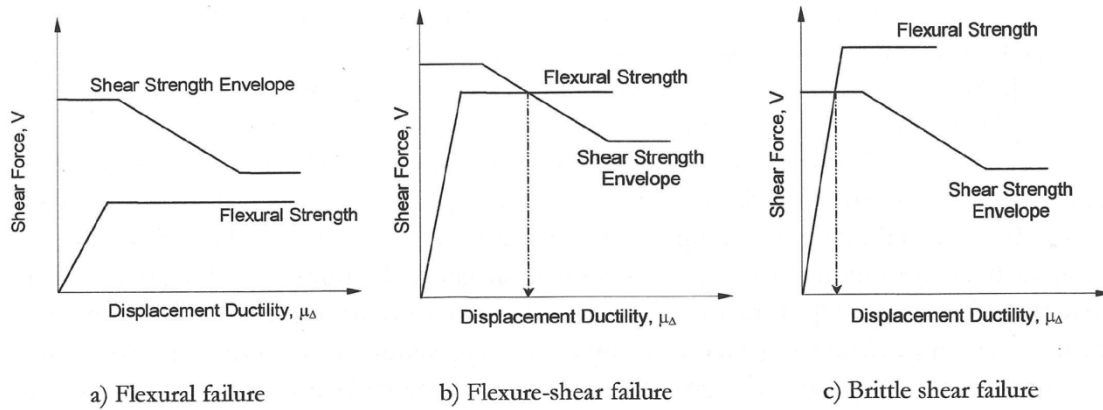


Figure 2-6. Classification of reinforced concrete column failure modes according to ATC-6 (1981)

The shear strength (V_A) of a RC member in the model by Kowalsky *et al.*, 2000 is given by equation 2.8.

$$V_A = V_c + V_S + V_p$$

$$V_c = \alpha\beta\gamma\sqrt{f'_c}(A_e)$$

$$V_S = \frac{A_{st}f_{yh}D'}{s} \cot \theta \quad [2.8]$$

$$V_p = P \tan \alpha = \frac{D - x}{2L} N$$

The shear concrete mechanism (V_c), and the axial load contribution (V_p). These shear capacity components are considered distinct and independent from each other. The shear concrete mechanism (V_c) depends on the effective area (A_e) assumed to be 0.8 the gross area concrete shear strength ($\gamma\sqrt{f'_c}$) determined from following figure 2-7a, the aspect ratio based on figure 2-7b, and the longitudinal steel ratio based on figure 2-7c.

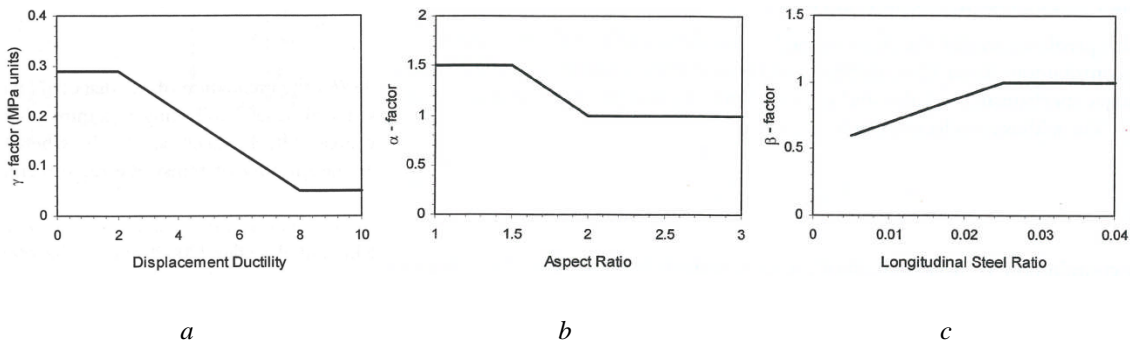


Figure 2-7. Determination of parameters relating with: a) displacement ductility; b) Longitudinal steel ratio; c) aspect ratio.

The steel truss mechanism (V_S) component depends on the angle of the diagonal cracks (θ) assumed to be 30°, the total cross-sectional area of the shear reinforcement (A_{st}) crossing the

shear diagonal crack. The diagonal shear cracks are closed in the compression zone and no shear strength is assumed to mobilise in the transverse reinforcement. The tension zone (D') is where the shear strength of the steel truss mechanism is effectively mobilised, and is the sectional depth (d) region excluding the cover (c) and the compression zone (x) such that $D' = d - x - c$.

The model provided by Sezen *et al.* (2002) is based on the concrete mechanism and the steel truss mechanism as given by equation 2.9. Whereas in the UCSD method the axial load is accounted separately, in the model proposed by Sezen (2002), this is accounted by the concrete. As the ductility increases, the shear resistance provided by the steel truss mechanism decreases due to possible anchorage degradation and irregular arrangement of reinforcement.

$$V_n = k_{\Delta}[V_c + V_s]$$

$$V_c = \frac{f_{c,s} \cdot A_e}{a/d} ; \quad f_{c,s} = 0.5\sqrt{f'_c} \sqrt{1 + \frac{N}{0.5\sqrt{f'_c}A_g}} \quad [2.9]$$

$$V_s = \frac{A_{st} f_{yh} d}{s}$$

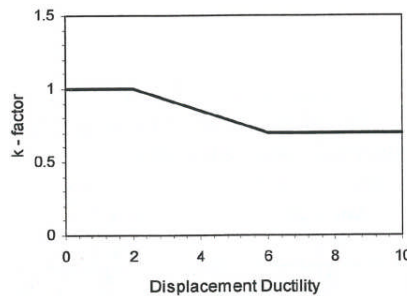


Figure 2-8 Determination of parameters relating with displacement ductility.

The shear strength and the ductility are linked with parameter “ k_{Δ} ” which is determined from figure 2-8. The shear strength due to the concrete (V_c) given by equation 2-9, depends on the column aspect ratio (a/d), concrete strength ($f_{c,s}$), the effective shear area ($A_e = 0.8A_g$) and the axial load (N). The Ritter-Morsch truss model is used for the steel truss mechanism relationship in equation 2.9 where inclined shear cracks at 45° are considered, which is realistically higher.

Biskinis *et al.*, (2010a) considers the possibility of having adverse shear effects on flexural yielding based on the proximity of the experimental yield of 2350 specimens to the theoretical flexural yield moment. In order not to have flexure-shear coupling at yielding, Biskinis *et al.*,

(2010a), suggest that all criteria in equation 2.10 have to be satisfied in order not to have flexure-shear coupling.

$$\frac{L_s}{h} > 3 \quad [2.10a]$$

$$2 \leq \frac{L_s}{h} \leq 3 \quad \text{and} \quad N < N_1 \text{ or } N > N_2$$

$$\text{where} \quad N_1 = 0.5bhf'_c - A_{sl}f_{yl} + \rho_w b_w f_{yw} \left[2L_s - \frac{(h-z)(\rho_{tot} - 0.5\rho_v)}{\rho_{tot}} \right] \quad [2.10b]$$

$$N_2 = 0.5bhf'_c + A_{sl}f_{yl} - \rho_w b_w f_{yw} \left[2L_s + \frac{(h-z)(\rho_{tot} - 0.5\rho_v)}{\rho_{tot}} \right]$$

$$\frac{L_s}{h} < 2 \quad \text{and} \quad \frac{\omega_{tot}}{\omega_w} \frac{h}{2L_s} < 1 \quad [2.10c]$$

The columns in the PEER database compiled by Berry *et al.*, 2003 and used by Berry *et al.*, (2004) in the determination of chord rotation equations are classified into shear, flexure and flexure-shear failure mechanisms by Camarillo (2003). For specimens that are reported to have flexural damage only are automatically exempted from failing in shear. If the maximum force is less than 95% of the force interpolated on a bilinear envelope when the strain is 0.004, or when the displacement ductility is less than 2, then the column is classified to be shear critical. Otherwise, the column is classified as flexure-shear critical.

The criteria suggested by Biskinis *et al.*, (2003) is applied to the PEER database. It is observed that approximately 94% of the classification for shear and flexure is similar to the classification by Camarillo (2003).

2.2.7 Determination of Damage Levels

The damage data used in section 2.2, compiled by Berry *et al.*, (2003) is used to compare the distributions of each damage phenomenon for chord rotation (figure 2-9) and maximum force reduction (figure 2-10). Based on this data, the dispersion of the chord rotations is larger than the dispersion of maximum force reduction. The data was also compared with the displacement based damage index and damage scale proposed by Rossetto *et al* (2004). However due to data available, this could only be done for $DI > 6$. As shown in figure 2-11, the two models show some discrepancies. Considering the larger dispersion of the chord rotation vis-à-vis maximum force reduction, considering that the ultimate damage is defined in terms of reduction of maximum force, and considering that trends of damage phenomena occurrence that relate with maximum force reduction, the damage levels are expressed in terms of maximum force reduction. The

damage levels considered will be yielding (Y), maximum force (m), 10% maximum force reduction (u-10), 20% maximum force reduction (u-20) and 50% maximum force reduction (u-50) which Padilla et al., (2005) claims that it approximately corresponds to the total collapse of a RC structure.

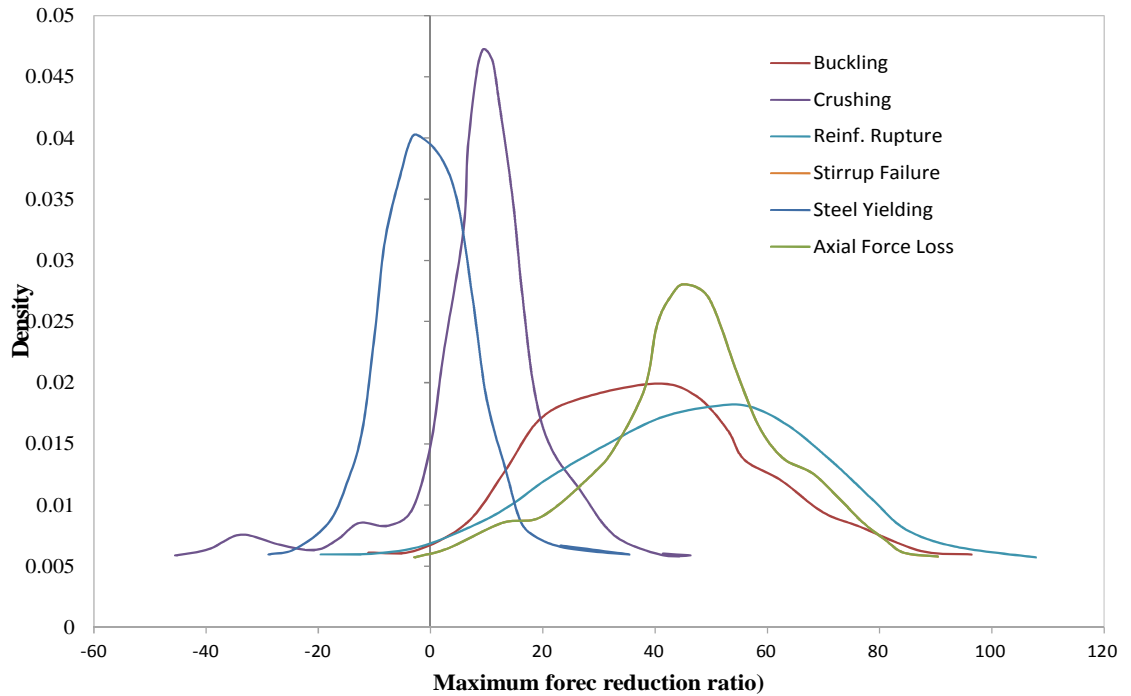


Figure 2-9 Distribution of maximum force reduction ratio for various damage phenomena.

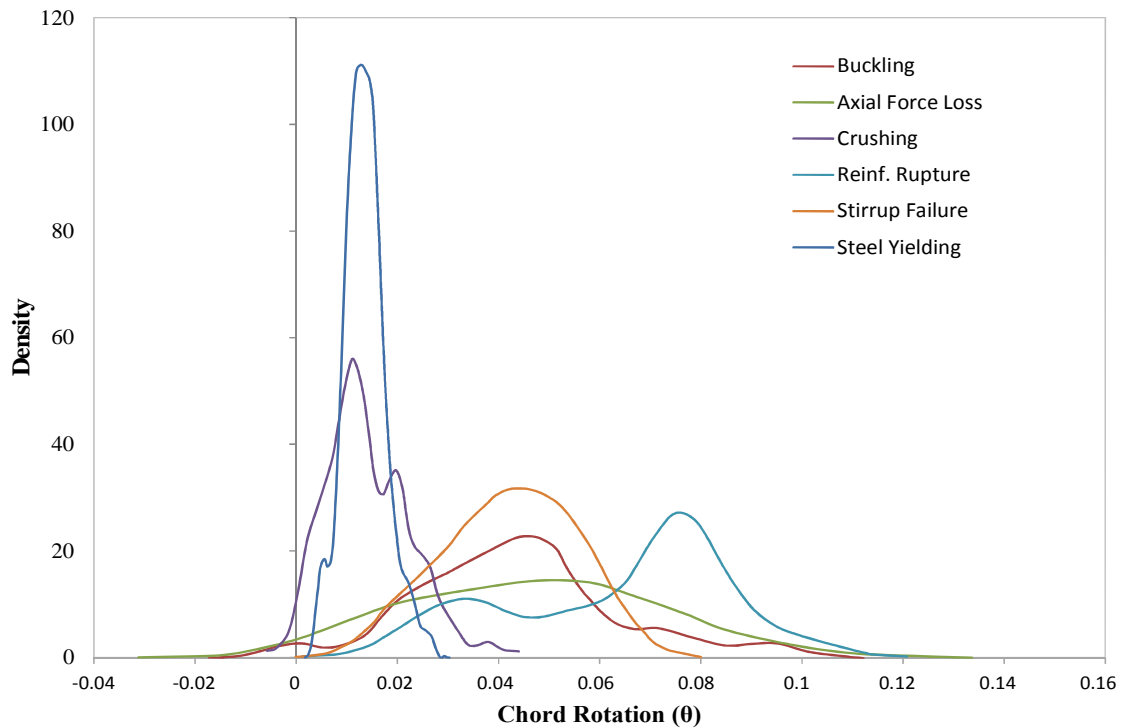


Figure 2-10 Distribution of chord rotation for various damage phenomena.

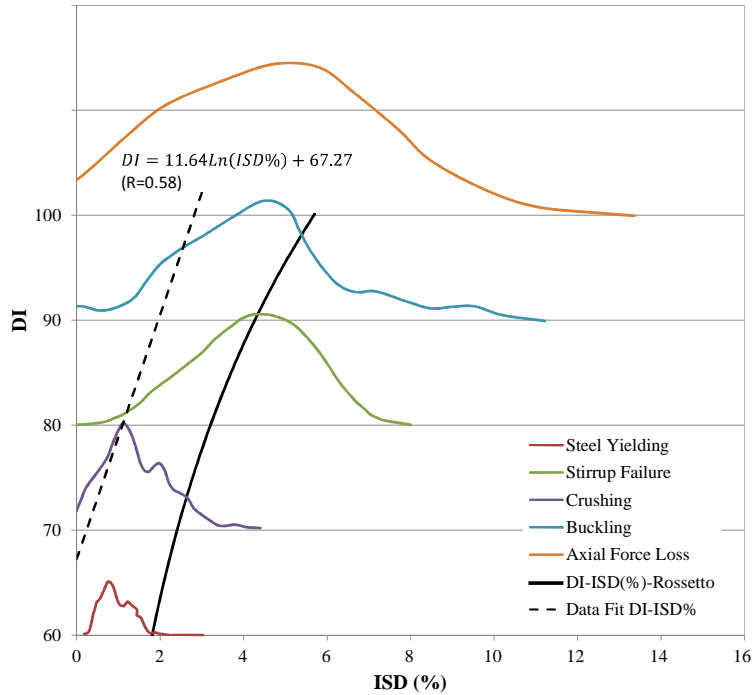


Figure 2-11 Comparison of the damage phenomena data with the DI proposed by Rossetto et al. (2004).

2.3 Tools in the Assessment Procedures

2.3.1 Engineering Demand Parameters (EDPs)

The seismic capacity of existing reinforced concrete (RC) structures is determined by non-linear analysis methodologies according to EN1998 (CEN, 2005). Real inelastic information of the deformation capacity of beams and columns is required in the analysis process. In the case of non-linear static analysis, monotonic response is required, while in the case of non-linear dynamic analysis, cyclic response is required. In the latter, the cyclic response is required to define strength degradation, stiffness degradation and hysteretic models. This is a very difficult process since the number of mechanical and material parameters may not be exhaustive. In general, the type of loading considered is ignored. Although calibrations are done with data on experiments with cyclic loading, the loading is not calibrated with earthquake demand. Moreover, most code prescriptions are at yield and collapse damage states only. Hence unless more information on the demand parameters at intermediate damage state is given, it is not possible to define properly the strength degradation and the hysteretic behaviour.

Chord Rotation at Yielding

The chord rotation at yielding provided by Panagiotakos et al., (2001) and reproduced in equation 2.11 is based on a semi empirical approach. It is made up of three main components. The first

refers to flexural deformations. The second refers to shear deformation and is given by a constant only due to lack of statistical significance, particularly when bond-slip is very significant. The third term refers to bond slip.

$$\theta_Y = \phi_Y \frac{L_S}{3} + 0.0025 + a_{sl} \frac{0.25 \varepsilon_y d_{bl} f_{yl}}{z \sqrt{f'_c}} \quad [2.11]$$

where

$$\phi_Y = \frac{f_{yl}}{E_s (1 - k_y) h} \quad (\text{steel}) \quad \phi_Y \approx \frac{1.8 f'_c}{E_c k_y h} \quad (\text{concrete})$$

Fardis (2007) and Biskinis et al., 2010a extend the model by Panagiotakos et al., 2001 into the model provided by equation 2.12. The length of the shear span has an extension equal to the length of the lever arm (z) if the shear force at diagonal cracking (V_{Rc}) which is taken equal to the shear resistance of members without shear reinforcement in EN1992-1 (2004) is lower than the value of the yield force given by M_Y/L_S . In this other model, shear deformation is not represented by a constant only, while the bond slip component is now considered to depend more on ϕ_Y than z and ε_y .

$$\theta_Y = \phi_Y \frac{L_S + a_v z}{3} + 0.0014 \left(1 + 1.5 \frac{h}{L_S} \right) + a_{sl} \frac{\phi_Y d_{bl} f_{yl}}{8 \sqrt{f'_c}} \quad [2.12]$$

where

$$\phi_Y \approx \frac{1.75 f_{yl}}{E_s h}$$

The regression of the model proposed by Panagiotakos et al., 2001 is performed on 963 tests on column specimens, while the model proposed by Biskinis et al, 2010a is based on 1617 tests on column specimens. The mean of the test-to-predicted values is 1.05 for the former model, while for the latter it is 1.06. The CoV of the model proposed by Biskinis *et al.*, 2010a is 32.1%, about 4% lower than the corresponding value for the model proposed by Panagiotakos et al., 2001. In the case of not having considerable bond slip, the CoV of the former is even 26.3%. Hence the model proposed by Biskinis *et al.*, 2010a shows improvement over the model proposed by Panagiotakos *et al.*, 2001.

Chord Rotation at 20% Maximum Force Reduction

The ultimate is based on a fixed strength decay of 20% of the maximum force capacity of the element. In literature and in EN1998-3 (CEN,2005; CEN, 2009), two methods are generally used to determine the ultimate chord rotation (θ_{u-20}). The first is a semi-empirical approach based on the plastic hinge concept. Some examples in literature include Panagiotakos et al., 2001; Rossetto, 2002; Lam et al., 2003; Perus et al., 2006, Perus et al., 2007, Haselton et al., 2007, Fardis, 2007

and Zhu et al., 2007. The other method is empirically based and some relations are given by Panagiotakos et al., 2001 and Berry et al., 2004.

Semi-empirical relations of θ_{u-20} are generally based on the mechanics of deformation and the empirical determination of the plastic hinge length (L_{pl}). In general, ultimate chord rotation (ϕ_{u-20}) is given by equation 2.13, where the plastic hinge length is made up of flexure, shear and bond-slip components.

$$\theta_{u-20} = \theta_Y + (\phi_{u-20} - \phi_Y)L_{pl} \quad [2.13]$$

As indicated in figure 2-12, while the plastic hinge region (l_{pl}) is the zone over which either yielding of the reinforcement, or crushing of concrete, or both takes place, the plastic hinge length is the zone where the plastic curvature ($\phi_{pl} = \phi_{u-20} - \phi_Y$) is assumed to be constant (Fardis, 2007). The regions have different magnitudes, and while the first is real but difficult to determine, the latter is hypothetical but easier to determine with assumptions. Both ϕ_{u-20} and ϕ_Y are computed based on section equilibrium, using constitutive behaviour of materials and on Bernoulli's assumption that plane sections remain plane. The plastic hinge length cannot be based entirely on a mechanical deformation approach. Else, full interaction between the steel and concrete would have to be assumed where after the maximum moment is reached, the curvature should increase at the base of the section resulting in a plastic hinge with zero length (Verderame et al., 2010; Daniell et al., 2008). As a result, shear and bond slip deformation which can be responsible for approximately 30% and 40% of the deformation (Sezen, 2002) would not be accounted for in a mechanical deformation approach without empirical considerations based on experimental results. The determination of yield curvature (ϕ_Y) and ultimate curvature (ϕ_{u-20}) are associated with a lot of uncertainty due to inadequate consideration or exclusion of buckling of reinforcing bars and spalling. Moreover, there are a large number of confinement models in literature which can lead to different plastic hinge lengths. There are also a large number of plastic hinge equations which can therefore give a different values of θ_{u-20} . Some plastic hinge length relations include Baker (1956), Mattock (1964), Corley (1966), Mattock (1967), Park et al., (1982), Priestley et al., (1987), Pauley et al., (1992), Panagiotakos et al., (2001) and Fardis (2007). However, from these relations it is observed that the shear span (L_s) and the section depth (h), together with the yield strength (f_{yl}) and diameter of reinforcement (d_{bl}) are the major variables.

EN1998-3 (CEN, 2005) provides equation 2.14. The relation is valid for members with ribbed longitudinal bars without lap-splicing. The plastic hinge length is provided by equation 2.15a if the concrete confinement relation in EN1998-3 is used, while equation 2.15b is used if the concrete confinement relation in EN1992-1 section 3.1.9 (CEN, 2004) is used.

$$\theta_{u-20} = \frac{1}{\gamma_{el}} \left[\theta_Y + (\phi_{u-20} - \phi_Y) L_{pl} \left(1 - 0.5 \frac{L_{pl}}{L_s} \right) \right] \quad [2.14]$$

$$L_{pl} = \frac{L_s}{30} + 0.2h + 0.11 \frac{d_{bl} f_{yl}}{\sqrt{f_c'}} \quad [2.15a]$$

$$L_{pl} = \frac{L_s}{10} + 0.17h + 0.24 \frac{d_{bl} f_{yl}}{\sqrt{f_c'}} \quad [2.15b]$$

Equation 2.16 is another relation similar to equation 2.14 and is proposed by Panagiotakos et al., 2001. The associated L_{pl} is obtained from equation 2.17a and is valid for cyclic loading while equation 2.17b is valid for monotonic loading.

$$\theta_{u-20} = \frac{\phi_Y L_s}{3} + (\phi_{u-20} - \phi_Y) L_{pl} \left(1 - 0.5 \frac{L_{pl}}{L_s} \right) \quad [2.16]$$

$$L_{pl} = 0.12L_s + 0.014d_{bl}f_{yl} \quad [2.17a]$$

$$L_{pl} = 0.18L_s + 0.021d_{bl}f_{yl} \quad [2.17b]$$

Equation 2.18 is another relation provided by Fardis (2007) which is based on the plastic hinge mechanism. It is based on 1307 tests which is much more than the number of tests used by Panagiotakos et al., (2001).

$$\theta_{u-20} = \theta_Y + a_{sl}(\theta_{u-20,slip} - \theta_{Y,slip}) + (\phi_{u-20} - \phi_Y) L_{pl} \left(1 - 0.5 \frac{L_{pl}}{L_s} \right) \quad [2.18]$$

where:

$$L_{pl} = 0.09L_s + 0.02h$$

$$\theta_Y = \frac{\phi_Y L_s}{3} + 0.0013 \left(1 + 1.5 \frac{h}{L_s} \right) + \frac{\phi_Y d_{bl} f_{yl}}{8\sqrt{f_c'}}$$

$$(\theta_{u-20,slip} - \theta_{Y,slip}) = 5.5d_{bl}\phi_{u-20} \text{ (Cyclic loading)}$$

$$(\theta_{u-20,slip} - \theta_{Y,slip}) = 9.5d_{bl}\phi_{u-20} \text{ (Monotonic loading)}$$

The relation provided by Panagiotakos et al. (2001) has a mean and CoV of 1.23 and 83% for monotonic tests on the test-to-prediction ratio. The mean and CoV for cyclic loading are 1.37 and 94% respectively. The calibration of the relation by Fardis (2007) shows improvement. The mean and CoV on the test-to-prediction ratio are 1.105% and 53.6%.

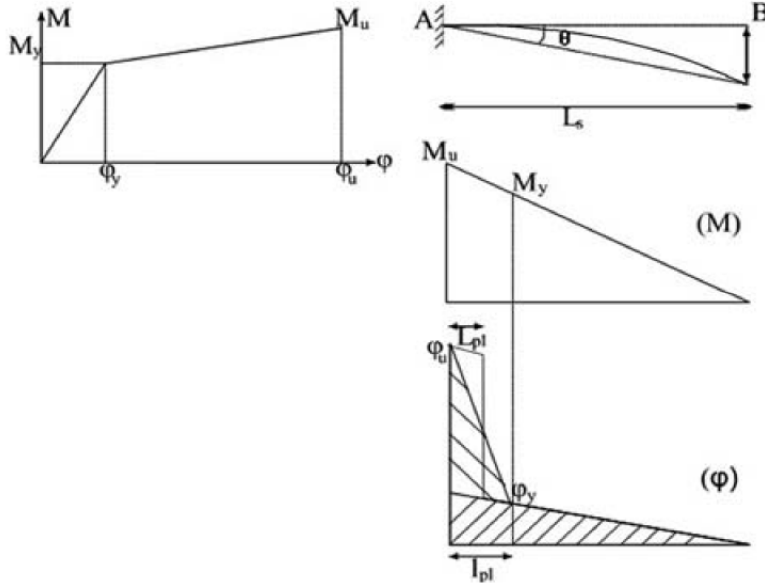


Figure 2-12 The plastic hinge concept as presented by Fardis (2007) and as adopted in EN1998-3 (CEN, 2005).

There are various other ways on how empirical relations are provided. Perus (2006) and Perus et al., 2007 provide an empirical model that describes the whole force drift envelope using a multi-dimensional non-parametric regression approach. The model is based on the database provided by PEER (Berry et al., 2003) and a subset that is adopted in the computation of relations by Fardis (2007). The statistical summary of this model on the test-to-prediction ratio shows improvement over the EN1998-3 (CEN, 2005) formulations. Lam et al., (2003) provides an empirical model of calibrated on θ_{u-20} a few number of experiments, but is specific for rectangular sections with low lateral confinement and high axial load ratios.

Another chord rotation in EN1998-3 (CEN,2005) is given by equation 2.19, where γ_{el} is 1.5 and 1.0 for primary and secondary seismic elements respectively. The aim of these parameters is to transform mean into mean minus one standard deviation so that that the equation is conservative. Equation 2.20 is another expression provided by EN1998-3 (CEN, 2005) that provides the plastic chord rotation. The ultimate chord rotation (θ_{u-20}) is then the sum of plastic and corresponding yield equations.

$$\theta_{u-20} = \frac{1}{\gamma_{el}} 0.016 (0.3^v) \left[\frac{\max(0.01, \omega_2)}{\max(0.01, \omega_1)} f_c^t \right]^{0.225} \left(\frac{L_s}{h} \right)^{0.35} \frac{\rho_s f_{yw}}{25 f_c} 1.25^{100\rho_d} \quad [2.19]$$

$$\theta_{u-20}^{pl} = \theta_{u-20} - \theta_Y \quad [2.20]$$

$$= \frac{1}{\gamma_{el}} 0.0145 (0.25^v) \left[\frac{\max(0.01, \omega_2)}{\max(0.01, \omega_1)} \right]^{0.3} f_c'^{0.2} \left(\frac{L_s}{h} \right)^{0.35} 25^{\frac{\alpha \rho_s f_{yw}}{f_c'}} 1.275^{100 \rho_d}$$

Both equation 2.19 and 2.20 that are used to ultimately determine θ_{u-20} apply to RC elements that have seismic detailing, do not have lap-splicing and ribbed longitudinal reinforcement. In case of non-seismic detailing a multiplication factor of 0.825 is applied. Where lap-splicing is involved, the reinforcement ratio should be doubled, while if the lap-splicing length (l_{ou}) is less than the minimum ($l_{ou,min}$), provided by equation 2.14 another reduction factor should be applied in equation 2.15 equal to $l_{ou,min}/l_{ou}$. In case of smooth bars, equation 2.19 is multiplied by 0.575 and equation 2.20 by 0.375, and include the correction factor 0.825. In update provisions to EN1998-3(CEN, 2005) given in “Corrigenda to EN1998-3” (CEN, 2009), these coefficients are respectively changed to 0.80 and 0.75, and also incorporate the correction factor 0.825, which has been reduced to 0.833.

In case of having both smooth bars and lap-splicing, another coefficient α_{ou} is applied. This is based on the assumption that the effective shear span that controls the ultimate deformation is then based on the region between the end of the lap-splice and the point of contra flexure. Equation 2.21a applies for θ_{u-20} , and equation 2.21b applies for θ_{u-20}^{pl} of EC8 (CEN,2005).

$$\alpha_{ou} = 0.0025[180 + \min(50, l_{ou}/d_{bl})](1 - l_{ou}/L_s) \quad [2.21a]$$

$$\alpha_{ou} = 0.0035[60 + \min(50, l_{ou}/d_{bl})](1 - l_{ou}/L_s) \quad [2.21b]$$

In CEN, 2009, equations 2.21a and 2.21b has respectively been changed to equation 2.22a and 2.22b, eliminating the lap-splice length to shear span ratio. These do not incorporate the 0.833 ratio.

$$\alpha_{ou} = 0.0019[10 + \min(40, l_{ou}/d_{bl})] \quad [2.22a]$$

$$\alpha_{ou} = 0.0019 \min(50, l_{ou}/d_{bl}) \quad [2.22b]$$

A model proposed by Panagiotakos et al., 2001 given in equation 2.23. It is calibrated with 633 cyclic and 242 monotonic tests that exclude brittle failure. Linear regression is conducted on the log of θ_u and the logs of the explanatory variables without coupling them. It is assumed that the variance of the scatter of $\log \theta_u$ about the regression is independent of θ_u . This means that

the coefficient of variation CoV of the experimental value is constant for every predicted value. In the regression analysis all parameters were assumed to be control variables, but were dropped if turned out to be not statistically significant.

$$\theta_{u-20} = \frac{1}{100} a_{st,cy} \quad [2.23a]$$

$$\times \left(1 + \frac{a_{sl}}{2}\right) (0.2^v) \left[\frac{\max(0.01, \omega_2)}{\max(0.01, \omega_1)}\right]^{0.275} f_c'^{0.175} \left(\frac{L_s}{h}\right)^{0.4} 1.1 \frac{100a_{ps}f_{yw}}{f_c'} 1.3^{100\rho_d}$$

$$\theta_{u-20} = \frac{1}{100} a_{st,mon} \left(1 + \frac{a_{sl}}{8}\right) (0.15^v) \left[\frac{\max(0.01, \omega_2)}{\max(0.01, \omega_1)} \frac{L_s}{h} f_c'\right]^{0.425} \quad [2.23b]$$

The parameter a_{st} refers to the type of steel where $a_{st,cy}$ is 1.125 for hot-rolled ductile steel, 1.0 for heat-treated (tempcore) steel and 0.8 for cold worked steel, and $a_{st,mon}$ is 1.25 for hot-rolled ductile steel, 1.0 for heat-treated (tempcore) steel and 0.5 for cold-worked steel. The mean and CoV of the test-to-prediction ratio of equation 2.23a and equation 2.23b are 1.05 and 41%, and 1.17 and 57% respectively. Equation 2.24 is another model based on the regression of both cyclic and monotonic tests. In this case $a_{st,mon}$ is 1.5 for hot-rolled ductile steel, 1.25 for heat-treated (tempcore) steel and 0.8 for cold-worked steel. The latter model has a mean and CoV of 1.06 and 47% respectively.

$$\theta_{u-20} = \frac{1}{100} a_{st} a_{cy} \quad [2.24]$$

$$\times \left(1 + \frac{a_{sl}}{2.3}\right) (0.2^v) \left[\frac{\max(0.01, \omega_2)}{\max(0.01, \omega_1)} f_c'\right]^{0.275} \left(\frac{L_s}{h}\right)^{0.45} 1.1 \frac{100a_{ps}f_{yw}}{f_c'} 1.3^{100\rho_d}$$

Two other models, equation 2.25a and 2.25b are proposed by Rossetto (2002). In the first model, the type of steel is represented by a different coefficient, where a_{st} is 1.2 for high ductility steel of grade S400 or lower, 0.9 for tempcore steel, and 0.37 is for cold worked steel. In the second model, the steel is represented by the maximum stress to yield stress ratio (f_{tl}/f_{yl}) and the ultimate steel strain. These parameters are respectively 1.5 and 0.12 for high ductility steel of grade S400 or lower, 1.2 and 0.08 for tempcore steel, and 1.1 and 0.05 for cold worked steel.

$$\theta_{u-20} = \frac{1}{100} \left(1 + 0.65 \varepsilon_{su}^{0.6} \left(\frac{f_{tl}}{f_{y1}}\right)^4\right) (1 - 0.45 a_{cy}) \quad [2.25a]$$

$$\times \left(1 + \frac{5}{18} a_{sl}\right) (0.2^v) \left(\frac{\max(0.01; \omega_2)}{\max(0.01; \omega_1) + \omega_v} f_c'\right)^{\frac{7}{20}} \left(\frac{L_s}{h}\right)^{\frac{4}{11}} (1.26^{\omega_w}) (1.05^{\rho_d})$$

$$\theta_{u-20} = \frac{a_{st}}{100} (1 - 0.35a_{cy})(0.16^v) \quad [2.25b]$$

$$\times \left(\frac{\max(0.01; \omega_2)}{\max(0.01; \omega_1) + \omega_v} \right)^{\frac{2}{5}} f_c^{\frac{1}{2}} \left(\frac{L_s}{h} \right)^{\frac{2}{5}} (1.33\omega_w)(1.06\rho_d)$$

These two models are calibrated with 674 member tests. While equation 2.25a has a mean of 1.02 and a CoV of 55%, equation 2.25b has a mean of 1.05 and a CoV of 50%. The statistics are therefore slightly worse than Panagiotakos et al., 2001.

Other models are provided by Fardis (2007) and are reproduced by equation 26. Further details on the models are found in Biskinis et al., 2010b. Equation 2.26a and 2.26b are the special cases of equation given by EN1998-3 (CEN, 2005).

$$\theta_{u-20} = a_{st} (1 - 0.43a_{cy}) \left(1 + \frac{a_{sl}}{2} \right) (1 - 0.42a_{w,r}) \left(1 - \frac{2}{7}a_{w,nr} \right) \quad [2.26a]$$

$$\times (0.3^v) \left[\frac{\max(0.01; \omega_2)}{\max(0.01; \omega_1)} f_c \right]^{0.225} \left[\min \left(9; \frac{L_s}{h} \right) \right]^{0.35} 25^{\left(\frac{a_{psf} f_{yw}}{f_c} \right)} 1.25^{100\rho_d}$$

$$\theta_{u-20} = \theta_Y + a_{st}^{pl} (1 - 0.52a_{cy}) \left(1 + \frac{a_{sl}}{1.6} \right) (1 - 0.44a_{w,r}) \left(1 - \frac{a_{w,nr}}{4} \right) \quad [2.26b]$$

$$(0.25^v) \left[\frac{\max(0.01; \omega_2)}{\max(0.01; \omega_1)} \right]^{0.3} f_c^{0.2} \left[\min \left(9; \frac{L_s}{h} \right) \right]^{0.35} 25^{\left(\frac{a_{psf} f_{yw}}{f_c} \right)} 1.275^{100\rho_d}$$

$$\theta_{u-20} = \theta_Y + a_{st}^{hbw} (1 - 0.525a_{cy})(1 + 0.6a_{sl}) \quad [2.26c]$$

$$\times \left(1 - 0.052 \max \left(1.5; \min \left(10, \frac{h}{b_w} \right) \right) \right)$$

$$\times (0.2^v) \left[\frac{\max(0.01; \omega_2)}{\max(0.01; \omega_1)} \min \left(9; \frac{L_s}{h} \right) \right]^{\frac{1}{3}} f_c^{0.2} 25^{\left(\frac{a_{psf} f_{yw}}{f_c} \right)} 1.225^{100\rho_d}$$

The three models in equation 2.26 provide similar accuracy. For of the three models, the mean varies between 1.06 and 0.98, while the CoV varies between 50% and 32.6%, depending on whether monotonic or cyclic or both is considered, and depending on whether bond slip is present or not. The statistics indicate considerable improvement over Panagiotakos et al., 2001. In total, the database refers to approximately 2049 beam or column tests. While model in equation 2.26a, give a direct interpretation of θ_{u-20} , equation 2.26b and 2.26c depend also on the uncertainty in determining θ_Y . The explanatory variables of equation 2.26a and 2.26b are very similar, while equation 2.26c also incorporates the slenderness ratio h/b_w .

Chord Rotation at Maximum Force

Haselton *et al.*, 2008 proposes chord rotation equations at maximum force capacity which is defined based on the hysteretic model by Ibarra *et al.*, 2003 where the effective chord rotation at maximum force is considered larger than the maximum point on the response of the tested column if the stiffness is positive. The considered maximum response is termed as the capping of the hysteretic envelope Haselton *et al.*, 2008.

$$\theta_{cap,pl} = 0.12 \left(\frac{\max(0.01, \omega_1)}{\max(0.01, \omega_2)} \right)^{0.225} (1 + 0.55a_{sl})0.16^v \quad [2.27a]$$

$$\times (0.02 + 40\rho_{sh})^{0.43} 0.54^{0.01f'_c} 0.66^{0.1s_n} 2.27^{10\rho_{bl}}$$

$$\theta_{cap,tot} = 0.14 \left(\frac{\max(0.01, \omega_1)}{\max(0.01, \omega_2)} \right)^{0.175} (1 + 0.4a_{sl})0.19^v \quad [2.27b]$$

$$\times (0.02 + 40\rho_{sh})^{0.54} 0.54^{0.01f'_c}$$

Equation 2.27a gives the plastic chord rotation model only, while equation 2.27b gives the total range of chord rotation including the elastic region. The test-to-predicted ratio associated with equation 2.27a has a mean and a standard deviation of 1.18 and 0.61 respectively with outliers removed. The standard deviation for equation 2.27b is 0.45 where outliers are removed, and hence it is slightly better fit. The model is calibrated with 255 column test results obtained from Berry *et al.*, (2003). Since the database does not include a lot of tests with specimens having un-symmetric reinforcement, the second term where the longitudinal reinforcement ratios are separated between ω_1 and ω_2 may not be very significant.

Chord Rotation on the Occurrence of different Damage Phenomena

Berry *et al.*, 2004 provide two chord rotation models on the onset of spalling (θ_{sp}) given by equation 2.28a and onset of buckling (θ_{bb}) given by equation 2.28b. The models are semi-empirical and are based on the plastic-hinge approach. The model is calibrated with experiments from the PEER database compiled by Berry *et al.*, 2003. The models are calibrated with 62 tests on rectangular columns and 42 tests on circular columns where buckling is observed, and with 102 tests on rectangular columns and 40 tests on circular columns where cover spalling is observed. The mean and CoV on the test-to-predicted ratio for the spalling model are 0.97 and 43% respectively, while the same statistical properties for the buckling model are 1.0 and 29% respectively.

$$\theta_{sp} = 0.016(1 - \nu) \left(1 + \frac{l_s}{10h} \right) \quad [2.28a]$$

$$\theta_{bb} = 0.0325(1 + 2.84\omega_w)(1 - \nu) \left(1 + \frac{l_s}{10h} \right) \quad [2.28b]$$

Stiffness

Relations in literature that are used to determine the stiffness that characterises the response of a RC element at a particular stage of damage refer to the parameter either in its basic form as a function of lateral force divided by the displacement of the element (K_{eff}), or normalised by the stiffness of the gross-section when un-cracked (EI_{eff}/EI_g). There are two main approaches in literature on how the stiffness is determined.

The first approach is empirically based and mainly refers to the normalised secant stiffness (EI_Y/EI_g) that passes through the yield point. Equation 2.29 gives the effective secant stiffness at yielding as determined by Elwood et al., 2006.

$$\begin{aligned} \frac{EI_Y}{EI_g} &= 0.2 & \frac{N}{A_{bh} f_c'} &\leq 0.2 \\ &= \left(\frac{5}{3} \frac{N}{A_{bh} f_c'} \right) - \frac{4}{30} & 0.2 &\leq \frac{N}{A_{bh} f_c'} \leq 0.5 \\ &= 0.7 & 0.5 &\leq \frac{N}{A_{bh} f_c'} \end{aligned} \quad [2.29]$$

Another model given by equation 2.30, is provided by Biskinis et al., 2010.

$$\frac{EI_Y}{EI_g} = a_{EI} (1 - 0.25 a_{sl}) \left\{ 0.8 + \ln \left[\max \left(\frac{L_s}{h}; 0.6 \right) \right] \right\} \left[1 + 0.048 \left[\min \left(\frac{N}{A_{bh}}; 50 \right) \right] \right] \quad [2.30]$$

Both models are derived on the presumption that flexure, bond-slip and shear are the main three components responsible for deformation of a column fixed against rotation at both ends. The model determined by Elwood et al., (2006) has a semi-empirical approach where first each displacement component is derived separately, and then combined in the final regression model. As a result, a variable that has to determine whether bond-slip is present or not does not feature in the model. The model determined by Biskinis et al., 2010 is empirically based and the user has to determine whether bond slip is present or not through the binary variable (a_{sl}) where $a_{sl}=1$ means that bond slip is present and $a_{sl} = 0$ means that bond slip is not present. This relation distinguishes also between beams and columns where $a_{EI} = 0.108$ in case of columns and $a_{EI} = 0.133$ in case of beams. From the experimental results, Elwood et al., 2006 observes that for columns with low axial load, the steel stress f_s can be assumed to be equal to the yield stress f_{yl} . As the axial load increases, f_s converges to zero as the neutral axis and the effective depth become equal. Hence, equation 2.29 is divided in three parts depending on the range of axial load ratio. The axial force ratio ($\nu = N/(A_{bh} f_c')$) is the only explanatory variable in the equation by Elwood et al., 2006. However, the equation by Biskinis et al., 2010 also includes the span-depth ratio as a variable, while the combined variable representing the axial load does not include the concrete strength (f_c'). The relation provided by Elwood et al., 2006 is calibrated with 120 column experimental data, while the other relation is calibrated with 142 column experimental data. The

mean and the coefficient of variation (CoV) of the test-to-prediction ratio of the former equation are 0.99 and 35% respectively, while the same statistics of the latter are 1.1 and 42.6%.

Another model defining stiffness at yielding is proposed by Haselton et al., (2008). However, this model which is given in equation 2.31 is empirically based. The data to calibrate the model is provided obtained from Berry et al., (2003). The standard deviation of the test-to prediction data without outliers is 0.28, and the mean is 1.23 which is slightly high.

$$\frac{EI_Y}{EI_g} = -0.07 + 0.59 \left[\frac{N}{A_{bh}f'_c} \right] + \left[\frac{L_s}{h} \right]; \quad 0.2 \leq \frac{EI_Y}{EI_g} \leq 0.6 \quad [2.31]$$

A post yield hardening stiffness is also proposed by Haselton et al., 2008. However, this is based on the ratio of the maximum moment capacity and the moment at yielding ($M_{m,cap}/M_Y$). The point of maximum capacity may not coincide with the maximum point in the moment-rotation response of the model but can be extrapolated as defined in the hysteretic model Ibarra et al., 2003. The model is provided by equation 2.32.

$$\frac{M_{m,cap}}{M_Y} = 1.25 \cdot 0.89^v \cdot 0.91^{0.01f'_c} \quad [2.32]$$

The standard deviation and mean of the test-to predicted values when the outliers are removed from the regression are 1.01 and 0.10 respectively. When this model is combined with chord rotation models at yielding and maximum capping, and stiffness at yielding, the entire envelope of deformation can be determined.

Table 2-2 shows a model proposed by Miranda et al., 2005 for a shear-flexure mechanism which also provides the entire envelope. This model, highlights the main four phases that lead to the ultimate failure. Table 2-2 underlines the corresponding stiffness as a flexure and shear contribution to deformation. These are based on Dilger (1966) and Pauley (1975) as a function of material properties mainly the modulus of elasticity of steel (E_s), modulus of elasticity of concrete ($E_c = 4700\sqrt{f'_c}$), elastic shear modulus ($G = 0.43E_c$ for a Poisson ratio $\nu = 0.17$). The model is also in terms of geometric properties mainly the height of the column (L_s for single bending), moment of inertia (I_g : based on gross sectional properties, I_e : based on effective sectional properties), shear area ($A_v = \frac{5}{6}bh$), density of transverse reinforcement (ρ_{sh}) and inclination of compression struts from the axis of the member (α_s). The flexural first yield is based on Priestley et al., 1992. The secant stiffness E_cI_y after the first yield is expressed in terms of moment and curvature at yield and spalling since the moment of inertia after concrete cracking is difficult to define independently. The total stiffness (K_{tot_i}) is then determined according to equation 2.33 as a combination of the shear stiffness (K_{f_i}) and flexural stiffness (K_{s_i}).

Table 2-2 Stiffness model proposed by Miranda et al., (2005)

Phase		Flexural Stiffness	Shear Stiffness
I	Elastic	$K_{fe} = \frac{3E_c I_g}{l_s^3}$	$K_{se} = \frac{G A_v}{l_s}$
II	Cracked in flexure	$K_{ff} = \frac{3E_c I_e}{l_s^3}$	$K_{sf} = \frac{G A_{ve}}{l_s} = \frac{G A_v \frac{I_e}{I_g}}{l_s}$
III	Cracked in shear		$K_{ss} = \frac{\rho_{sh} \sin^2 \alpha_s \cos^2 \alpha_s E_s b h}{\sin^4 \alpha_s + \rho_{sh} \frac{E_s}{E_c}} \frac{1}{l_s}$
IV	After first yield	$K_{fy} = \frac{3E_c I_y}{l_s^3} = \frac{3(M_{spall} - M_y)}{l_s^3(\phi_{spall} - \phi_y)}$	

$$K_{toti} = \frac{1}{\frac{1}{K_{fi}} + \frac{1}{K_{si}}} \quad [2.33]$$

The approach proposed by Miranda et al., 2005 follows an earlier model by Calvi et al., 2005 and ATC-6. Although for the test-to-predicted data of this model the mean is 0.95 and the CoV is as small as 20.3%, it is only calibrated with 9 tests. Unlike many other models, the model is useful in the assessment of RC elements with limited shear resistance. This damage typology is very characteristic of many past RC structures lacking seismic detailing. Nevertheless, the original model by Calvi et al., 2005 is defined for column piers and its.

Energy Dissipation

In spite energy is considered as an important parameter that quantifies damage and is widely used in the determination of damage indices (DIs), there are not a lot of expressions that define this EDP in terms of material parameters and physical properties are very limited. Haselton et al., 2008 provides a relation that determines the normalized energy dissipation capacity (λ) which forms part of the hysteretic model defined by Ibarra et al., 2003. It is defined by equation 2.34, where E_{tot} is the total energy dissipation capacity, M_Y is the yield moment and θ_Y is the yield chord rotation.

$$\lambda = \frac{E_{tot}}{M_Y \theta_Y} \quad [2.34]$$

Haselton et al., 2008 observe that the significant explanatory variables are the axial force ratio (ν), the stirrup-to-column depth ratio (s/d), the confinement density of the transverse reinforcement (ρ_{sh}) and the ratio between the shear demand at flexural yielding and the shear

strength of the column (V_p/V_n). The model is given in equation 2.35a and a simplified model is given in equation 2.35b.

$$\lambda = 127.2 (0.19)^v 0.24^{\frac{s}{a}} 0.595^{\frac{V_p}{V_n}} 4.25^{\rho_{sh}} \quad [2.35a]$$

$$\lambda = 170.7 (0.27)^v 0.10^{\frac{s}{a}} \quad [2.35b]$$

The difference in the statistical accuracy between these two models is negligible. On average, the standard deviation (S.D.) is 0.5 when outliers are removed, and the mean is 1.25. The latter is slightly high. However, the median is 1.01.

2.3.2 Damage Indices

Damage Indices (DI) can themselves be independent EDPs that quantify or describe damage, or they can be formed from one or more EDPs. In both cases, they generally form non-dimensional indices that quantify damage on a numeric damage scale, generally continuous and which correspond to damage description.

DIs can be grouped in *local damage indices* which describe damage of an individual member and *global damage indices* where damage endured by the whole structure is quantified. It is also possible to have a DI procedure where provisions are given to quantify both local and global damage. Depending on the nature of the EDPs and the derivation of the DI, DIs are further classified in *deformation based indices*, *energy based indices* and *force based indices*, or a combination of any of these three (Williams *et.al.*, 1995 and Ghobarah *et.al.*, 1999). A non-exhaustive list of DIs found in literature are classified and compared based on their advantages and disadvantages as shown in Table 2-3.

The seismic response of RC structures during earthquake action is cyclic. The damage build-up during this seismic response is however increasingly monotonic. The problem in the quantification of damage lies in mapping this cyclic expression onto the monotonic expression. There are three systems of how this mapping can be done. Damage indices can therefore be classified accordingly. Table 2-4 indicates the system used for various DIs. In the first system *A* the dynamic response of the structure is substituted with an equivalent monotonic response for the analysis process. EDPs used in the DI are based on this monotonic response of the structure. An equivalent SDOF structure may be used. In the second system *B*, EDPs for DIs are measured after the completion of the dynamic analysis of the actual structure. In the third system *C*, cumulative measures of EDPs are collected as a function of damage after each cycle during dynamic response of the actual structure. While system *A* is simple, it may not be as reliable as other systems if oversimplification is involved. System *C* may be very complicated, and errors at

each cycle are inherited. Although system *B* is simpler than *C* but more robust than system *A*, it lacks the build-up process of damage knowledge which can also be important.

The DIs found in literature are quite various, and the ability of a DI to relate with damage depends on many conditions. There are various structural configurations, and damage indices are expected to detect the different kinds of damage experienced by these structures. A DI should also be able to detect various forms of failure mechanisms either due to shear or flexure (Dymiotis *et.al.*, 1999). A damage index should not only be able to quantify the global damage of a structure, but also be able to identify the location where damage occurs within a structure. This is important for repair and retrofit considerations. DIs should also be accessible and easy to use. From the reviews on damage indices given by Ghobarah *et.al.*, 1999, Williams *et.al.*, (1995) and Padilla *et.al.*, (2009), *member deformation*, *stiffness degradation*, *strength degradation* and the *number of response cycles* in the inelastic range are identified as the main EDPs that mostly relate with damage. It is difficult to determine the best parameter since each has its own importance, depending on the type of failure mechanism, loading pattern and structural typology. Deformation is however one of the most important. This is generally expressed in terms of *material strain*, *deflection*, *curvature*, and *chord rotation*. Strain is a parameter that can be used to describe deformation at a local place within a cross section. Curvature can describe deformation of the whole section, while local drift or chord rotation can describe deformation of a whole element. Most of these parameters are considered relative to the ultimate and yield criteria. The determination of DI using deformation parameters has become more accurate due to recent developments on relationships of ultimate and yield deformations (Biskinis, 2007; Fardis, 2009).

Table 2-3. Comparison of various damage indices (DI) found in literature.

<i>DI</i>	<i>Description</i>	<i>Parameters</i>	<i>Advantages</i>	<i>Disadvantages</i>
Park and Ang (1985)	Based on a linear combination of maximum displacement and total hysteretic energy dissipation.	B Maximum deformation or rotation; Yield strength or moment; hysteretic energy per cycle.	Deformation and hysteretic energy directly relate with damage. Simple. Widely used.	Ignores direct considerations of stiffness and strength degradation. Based on monotonic loading. Cyclic effect considered through β which varies in literature.
Di Pasquale and Cakmak (1987)	Based on the ratio of the final and initial period of an equivalent SDOF system to the structure.	A Initial period; final period after earthquake.	Indirectly considers stiffness degradation.	Ignores displacement, number of cycles and strength degradation, which directly relate with damage. A SDOF is not an exact representation of a MDOF, where secondary effects are ignored.
Chung et. al., (1988)	Considers the number of cycles, and the stiffness degradation associated with it, at a given curvature.	C Moment; curvature; stiffness; number of cycles	Considers a cumulative response and sequence of events. Considers stiffness, strength degradation and the number of cycles causing damage.	An iterative process and involves a large number of calculations. Curvature is not able to express strain penetration, reinforcement slippage and member plasticity. Not calibrated with experimental or observed data.
Powell and Allahabadi (1988)	This is either based on displacement or ductility demand and capacity under monotonic conditions	A Maximum displacement ductility demand; maximum displacement ductility capacity under monotonic loading.	Considers maximum displacement which directly relates with damage. The demand can also affect damage control.	Does not take into account stiffness and strength degradation, and cyclic effects which directly relate with damage.
Bracci et. al., (1989)	Based on a combination of factors: difference in hysteretic area between cyclic and monotonic conditions, strength degradation and permanent deformation effects. Linear hardening is assumed after yielding.	C Maximum and yield curvature; Energy; change in strength.	Considers cyclic effects and strength degradation which directly relate with damage. Calibrated with experimental tests.	Iterative process. Cumbersome process. Experimental models are scaled. Curvature is not able to express strain penetration, reinforcement slippage and member plasticity.
Kunnath et. al., (1990)	Similar to Park and Ang (1985) but uses curvature values which are corresponding to damage levels.	B Curvature; hysteretic energy	Considers energy which can be directly related with damage. Simple.	Curvature is not able to express strain penetration, reinforcement slippage and member plasticity.
Fajfar (1992)	Based on energy dissipation in terms of displacement ductility, assuming an elastic-perfectly plastic (EPP) hysteresis.	A Hysteretic energy under monotonic loading; total hysteretic energy.	Considers effects of energy which may relate to damage.	Ignores directly effects of strength and stiffness degradation. Cyclic effects ignored. An EPP hysteresis is generic and approximate.
Fardis (1995)	Based on Park and Ang (1985). Concentrates on the effect of cumulative response of deformation in terms of energy.	B Maximum energy; Cumulative energy;	Deformation and hysteretic energy directly relate with damage. Simple. Calibrated with experiments.	Ignores direct considerations of stiffness and strength degradation. Based on monotonic loading. Cyclic effect considered through β which varies in literature.

Continued...

...Continued

DI	Description	Parameters	Advantages	Disadvantages	
Ghobarah, Abou-El Fath and Biddah (1999)	The damage index is based on the ratio of the final and initial stiffness of the structure.	A Initial stiffness before earthquake; Final stiffness after earthquake.	Tries to directly relate the behaviour of the structure with damage. Stiffness degradation directly relates with damage.	Ignores displacement, number of cycles and strength degradation, which directly relate with damage.	
Mehanny and Deierlein (2000)	Based on ductility, taking into account cumulative effects and loading history of the structure.	C Rotation capacities	Considers loading history and cumulative effects.	Slightly complicated to compute. Relationship of rotation with damage is not calibrated with experimental data or observed damage.	
Bozorgnia and Bertero (2003)	For inelastic SDOF systems based on maximum ductility, with the use of various calibrated coefficients.	B Maximum displacement ductility demand; maximum displacement ductility under monotonic loading; Total and effective hysteretic energy dissipated by component under monotonic loading.	Considers displacement indirectly, and energy which both relate with damage. Takes into account cumulative effects of the hysteresis development.	Ignores strength and stiffness degradation which directly relate with damage. Cyclic effects are ignored. A SDOF is not an exact representation of a MDOF, where secondary effects are ignored.	
Rossetto and Elnashai (2003)	Based on interstorey drift	B Interstorey drift	Simple, can detect soft storey, calibrated with experiments and can be used to describe global damage. Very useful in fragility functions.	Ignores strength and stiffness degradation. Since experimentally based, it may be valid to the range of the limited number of experiments with which it is calibrated.	
Erduran and Yakut (2004)	Based on the interstorey drift ratio for various levels of ductility. The method mainly refers to columns.	A Given drift; yield drift	Particular reference to slenderness effects, yield strength of reinforcement and axial force that may contribute to damage.	The effect of displacement history is not considered. Refers to RC columns only.	
Colombo and Negro (2005)	Based on the ratio between the initial and the reduced resistance capacity of a structure, evaluated by using an evolution equation for the yield strength in which the structural damageability is included.	B Displacement ductility; energy dissipation	Considers ductility and energy dissipation which directly relate with damage. Independent of material. Distinguishes between energy based and displacement based damage.	Generalised approach. Cyclic effects and strength degradation not considered directly.	
Kim, Lee and Chung (2005)	Proposes a damage based methodology on results from finite element analysis. Considers progression history to failure.	B Hysteretic properties	Considers damage at element level inside the structural component. Supports outcome with experiments.	Developed for bridge piers which are SDOF. Hence, the methodology might underestimate MDOF effects when applied to other structures.	
Rodriguez and Padilla (2009)	Baesd on Park and Ang (1985), using hysteretic energy dissipation through drift and stiffness parameters.	A Maximum rotation; Maximum drift ratio; Parameter based on energy dissipation, mass, frequency , maximum rotation and height.	Considers displacement history. Calibrated with experiments. Parameter g represents structural and ground motion parameters that may affect damage.	Derived on a SDOF system. Parameters used are dependent of each other. Does not consider cyclic effects directly. Experiments on columns only.	
KEY	Energy based DI	Energy Based DI	Deformation based DI	Combined DI	A= EDPs measured from a monotonic equivalent of the dynamic response of the structure; B=EDPs measured after the completion of the dynamic analysis of the actual structure; C= EDPs are a cumulative measure, function of damage, measured after each cycle response

Table 2-4. Criteria requirements for Dis and general categorisation

Criteria		Description of criteria characteristics	
1	Ability of parameters to detect failure	a	The system makes use of parameters that relate directly with damage in terms of deformation, stiffness and strength degradation, and accounts for failure mechanisms in shear and flexure.
		b	System relates to some of the parameters only, but accounts for different failure mechanisms.
		c	System relates to some of the parameters indirectly through other parameters, and may not necessarily account for different failure mechanisms, or expression is oversimplified.
2	Ability of DI to describe member damage	a	The DI is directly developed from parameters that relate directly with damage development of individual members. Parameter refers to the behaviour of the whole member rather than a cross-section only.
		b	The DI is developed from parameters that relate to the behaviour of a group of members. Parameter used may refer to damage at a cross-section level rather the whole element.
		c	The DI is developed from parameters that express the global behaviour of the structure.
3	Ability of DI to describe global damage	a	Method directly describes the global damage of the structure, or method combines local damage indices to obtain global damage index. It is able to detect soft storey failure.
		b	Method uses local damage indices which can be combined to obtain the global damage, but the method does not give a method on how this can be done. May not necessarily be able to detect soft storey failure.
		c	Damage index cannot be used to assess the global damage performance of the structure.
4	Ability and ease of use	a	Method makes use of simple but reliable analytical procedures. Parameters are easily and directly retrieved from the analysis. Involves no iteration.
		b	One of the characteristics in 4a is missing
		c	Two of the characteristics in 4a are missing.
5	Experimental calibration	a	Various experiments are directly used for the calibration of the method.
		b	Indirect reference to experimental calibration, or reference to experimental calibration with a large degree interpolation
		c	No reference to experimental calibration
6	Ability to account for cyclic effects	a	Can measure the development of damage over a time series, or direct measure of damage incurred after each cycle.
		b	Damage development can be measured at few discrete stages, or indirect consideration of cyclic effects through cumulative parameters such as maximum displacement, energy and stiffness.
		c	Only the ultimate value of damage is obtained. Based completely on monotonic considerations or equivalent.

Six major criteria that are required for the success of a DI are identified. These criteria are listed in table 2-4. Each DI does not satisfy the criteria equally. Each criteria is then subdivided into different sections depending on how this is satisfied by the different DIs. While description “a” refers to the criteria when best satisfied, “c” refers to the criteria when least satisfied. No damage index falls within “a” or “c” for all criteria, and hence it is difficult to choose between DIs. Nevertheless, many combined DIs such as Park and Ang (1985) and Kunnath *et al.* (1990) satisfy most of the criteria in the better way. Many DIs which are only force based do not satisfy many aspects of the criteria. As shown in table 2-4, other DIs such as Rossetto and Elnashai (2003) and

Colombo *et al.*, (2005) satisfy well some criteria but do not perform well on others.

This comparison on such criteria may be subject to interpretation. An analytical comparison is therefore made. DIs including Park and Ang (1985) given in equation 2.6, Kunnath *et al.* (1990) given in equation 2.7, Colombo *et al.*, 2005 given in equation 2.8 and Rossetto and Elnashai (2003) given in equation 2.9 are used to quantify damage of structures analysed for various earthquake loadings.

$$DI = \frac{\delta_m}{\delta_u} + \frac{\beta}{Q_y \delta_u} \int dE \quad ; \quad \beta = \left(-0.447 + 0.073 \frac{l}{d} + 0.24n_0 + 0.314P_t \right) 0.7^{p_w} \quad [2.36]$$

$$DI = \frac{\phi_m - \phi_y}{\phi_u - \phi_y} + \beta \frac{\int dE}{M_y \phi_u} \quad ; \quad \beta = [0.37n_0 + 0.36(s_r - 0.2)^2] 0.9^{p_w} \quad [2.37]$$

$$DI = 1 - \left\{ \left[\left(1 - \frac{u_{max}}{u_u} \right)^{1/0.15} \right] \cdot \left[0.5 \left(1 - \tanh \left(0.1 \frac{\int dE}{E_u^*} \right) \right) \right] \cdot \left[\exp \left(-9 \frac{\int dE}{E_u^*} \right) \right] \right\} \quad [2.38]$$

$$DI = 34.89 \ln(ISD_{max\%}) - 39.9 \quad (R^2 = 0.991) \quad [2.39]$$

δ_m is the maximum deformation under the earthquake, δ_u is the ultimate deformation under monotonic loading, dE is the incremental absorbed hysteretic energy, Q_y is the calculated minimum strength in the inelastic range, M_y is the yield moment, ϕ_u is the ultimate curvature, ϕ_y is the yield curvature, n_0 is the normalized axial stress, p_w is the confinement ratio, $\frac{l}{d}$ is the span-depth ratio, s_r is the normalized steel ratio, P_t is the longitudinal steel ratio, d_i is the maximum relative displacement between two floors, and h_i is the floor-to-floor height.

The DIs provided in equation 2.36 to 2.39 are local damage indices. The storey damage index is determined as a function of the sum of the weighted local damage indices. Energy absorption or load-bearing weights are considered as weighting parameters. The storey DI is further weighted with storey absorbed energy or structural weight carried by that level, to determine a global damage index. For the purpose of this investigation, the damage index proposed by Bracci *et al.* (1989) is used. This is easy to apply hence it is widely used in literature. The computation of weighting based on structural weight is faster than that based on energy. This DI is given by equation 2.40.

$$DI_{storey,j} = \frac{\sum w_i D_i^b}{\sum w_i D_i} \quad [2.40]$$

$$DI_{global} = \frac{\sum w_{storey,j} D_{storey,j}^b}{\sum w_{storey,j} D_{storey,j}}$$

In the given relationship of global DI, w refers to structural weight on the member or storey as appropriate, while D is the DI at member or storey level as appropriate. The parameter b is generally taken as “1”. It can also be taken as “2” to give greater emphasis on severely damaged elements. By considering the structure situations and combinations 1-3 in figure 2-13, it is observed that this damage index is very sensitive on b as it gives quite distinct values for the cases $b=1$ and $b=2$. Whereas the first consideration is sensitive to the level at which soft-storey is taking place, the damage value is very small and does not represent total collapse mechanism. In the second consideration of this damage index, the values obtained indicate ultimate failure. Nevertheless, it does not distinguish between soft-storey failures at different levels. For the purpose of this investigation, comparison of damage between different storeys for various local damage indices is required. A value of $b=1$ was therefore assumed.

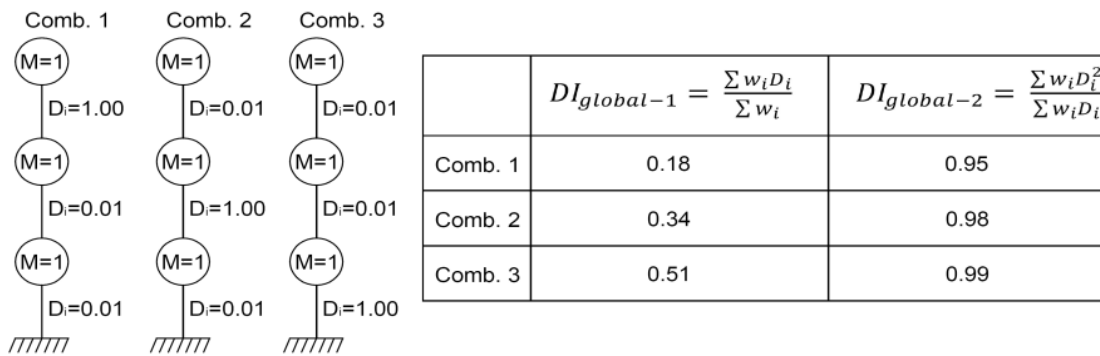


Figure 2-13 Comparison of global damage indices

2.3.3 Damage Scales

Seismic damage scales are used to assign performance limit states to buildings and are used within vulnerability studies. A damage scale is divided in gradual levels. The difference between each level should also be very clear in terms of damage. As a result the loss and corresponding repair costs can be clearly quantified, and will be characteristic to that particular level.

In a study prepared by Hill *et al.* (2008) various damage indices are reviewed and compared using a scoring system. Blong *et al.*, 2003a highlights important characteristics of a damage scale which are based only on seismic loss estimation considerations. According to Hill *et al.*, a seismic damage scale should also be well divided in levels where damage and failure mechanisms are well identified. These levels should also be associated with a measurable threshold physical

structural response parameters (DI's or EDP's). The characteristics required by a damage index are summarised in table 2-5.

Table 2-5 Requirements of a damage scale as modified from Hill et al. (2008).

<i>Characteristic</i>	<i>Subcategory</i>	<i>Definition</i>
Damage Description	Ease of measurement	Clarity in distinguishing states, that can be easily applied to a population of buildings
	Coverage	Ability of description to capture the range of damage to the building typology.
	Global	Ability to incorporate global damage.
	Local	Ability to incorporate local damage.
	Non-structural	Ability to incorporate non-structural damage.
	European Relevance	Relevance of the damage description to the European scenario.
Physical Parameter	Ease of measurement	Ability and ease to measure the physical parameter form analytical analysis or from populations of buildings.
	Relationship with damage	Ability of parameter/s to describe and relate with damage.
	Global	Ability to incorporate global damage.
	Local	Ability to incorporate local damage.
	Quantity	Ability to derive values from significant quantity of data.
	Calibration	Ability to calibrate with experiments and observed data, analytical data and judgement (These 3 factors are given in the order of importance, the most important first)
	European Relevance	Relevance of the values to European building types.
Repairs/ Retrofitting	Degree	Ability to define and specify the repair/retrofit.
	Repair/retrofit type	Ability to associate with repair/retrofit types and quantities correspondent to the level of damage / performance level required.
	Quantity	Ability to derive values from significant quantity of data.
	European relevance	Relevance of repair/retrofit types to the European construction practice.
Retrofit/Damage cost	Cost	Ability to associate the damage scale to actual or possible financial losses.
	Cost parameter	Suitability of cost parameter for loss modelling over a substantial period of time.
	Quantity	Derivation of values from significant quantity of financial data.
	European relevance	Relevance of the cost data to European construction practice.

Table 2-6 Comparison of different damage scales in literature compiled by Rossetto (2004).

DI _{HRC}	HRC	HAZUS 1999 [17]	VISION 2000 [18]	FEMA 273 [19]	EMS98 [20]	MSK [2]	ALJ [5]	ATC-13 [7]	ATC-21 [21]	EPPO [22]
0	None	No damage limit state								
10	Slight	Slight damage	Fully operational	Immediate occupancy	Grade 1	D1	Light	Slight	Green Tag	Green Tag
20	Light		Operational	Damage control	Grade 2	D2	Minor	Light		
30								Moderate		
40	Moderate	Moderate damage	Life safe	Life safe	Grade 3	D3	Moderate	Heavy	Yellow Tag	Yellow Tag
50										
60										
70	Extensive	Extensive damage	Near collapse	Limited safety	Grade 4	D4	Major	Major	Red Tag	Red Tag
80				Collapse prevention						
90							Collapse	Partial collapse		
100	Partial Collapse									
	Collapse	Collapse limit state								

Table 2-6 shows the comparison (Rossetto *et al.*, 2004) of different damage scales found in literature. The HAZUS scales contain a detailed description of reinforced concrete building types. It also has a methodology for the calculation of physical parameter values. It also refers cost through cost ratios. It is considered as the damage scale that fulfils most criteria by Hill *et. al.* (2008). RISK-UE does not give a lot of information with regards to data used for the derivation of cost ratios. The damage scale proposed by Rossetto *et al.*, 2003 relates well with damage parameters, and hence its classification of damage and its description is very distinguishable. This is however done without reference to repairs, retrofitting and costs. It is divided in 12 sections, 2 less than Vision 2000. HAZUS'99 has 5 sections. Many engineers prefer a scale which does not have more than 6 divisions since it reduces anomalies in their interpretation (Abbott *et. al.*, 2007). Moreover, although scales with a larger number of scale divisions are required in order to have cost efficient repair and retrofit strategies, the relationship of damage with physical parameters describing damage is not yet developed to offer that sensitivity and accuracy. With regards to cost considerations in their approach, this is only done by HAZUS, Milutinovic and Trendafiloski (2003), Rocca *et. al.* (2006), Bommer (2002) and Blong (2003). Few of the damage scales relate with repair considerations. This is slightly done by GNDT, Milutinovic and Trendafiloski (2003), FEMA 356, and Crowley *et. al.*, 2002. EMS-98, Okada and Takai (2000) and GNDT (2007) have a very detailed damage description since they were specifically developed for post earthquake field investigation and hence have a very detailed damage description. Yet, these do not relate to physical damage parameters such as damage indices, cost or repair criteria. An advantage of the scale proposed by Rossetto and Elnashai (2003) is that the former considers the local damage effects in more detail.

Vision 2000, GNDT, HAZUS and FEMA 356 omit the initial definition of no-damage. The transition between light and moderate damage is not clear in Vision 2000, EMS-98 and GNDT. Overall, it can be observed that when considering the detailed descriptions and common levels of damage of each scale, there are inconsistencies between damage states. This may be due to different references of damaged building cases when developing the damage scale. This means that a successful damage scale should be one which considers an exhaustive number of R.C. typologies and damage situations.

Different scales contain damage states with similar names to define the damage level, but imply very different degrees of sustained physical damage in their descriptions. This means that either equivalences of damage vary between damage scales, or damage levels have different equivalences between damage scales. (Hill *et al.*, 2008)

2.3.4 Application of Seismic Assessment

Two structures are considered for this investigation. The first structure consists in a regular 3 x 3-bay, 3 storey frame system. The floor-to-floor height is taken as 3m. Each bay approximately measured equal spans of 4.5m. This structure is adopted from the vulnerability analysis conducted in Rossetto (2004). The second structure is an irregular structure, having a similar configuration as the first structure. Nevertheless, this second structure has an open plan at the bottom level; over two spans in one direction and across the three spans in the perpendicular direction. Figure 2-14 shows the frame configuration of each building. The structures are designed according to Italian design codes of 1982. The structures are assumed to be in seismic Zone 2 with a corresponding peak ground acceleration (*pga*) of 0.07g with an associated exceedence probability of 10% in 50 years. Table 2-7 shows the reinforcement schedule and member dimensions of the member sections. The steel grade considered is FeB38. Transverse reinforcement of 6mm diameter is considered with spacing varying between 175mm and 300mm.

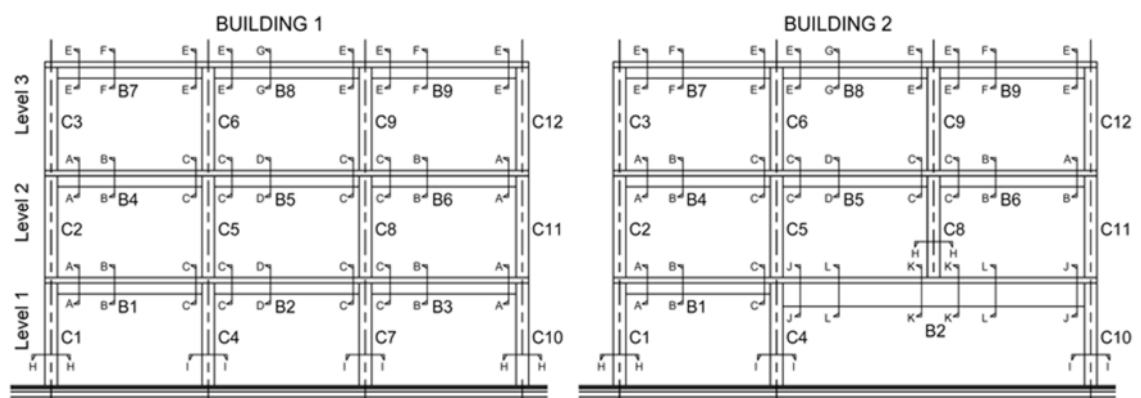


Figure 2-14 Structural configuration of the considered buildings.

For the purpose of this investigation, three suites of 2 accelerograms each are selected from the European Strong-Motion database (Ambreseys et. al., 2002). Each suite of accelerograms corresponds in turn to target spectra characteristic to 95 return period (associated with serviceability limit state), 475 years return period (associated with damage control limit state) and 2475 years return period (associated with collapse prevention limit state). The target spectra are based on provisions by Albarello et. al. (1999) and OPCM-3519 (2006). The amplitude scaling of the accelerograms is kept within 40% variation of the original *pga* of the original record. Table 2-8 and figure 2-15 show data on the selected accelerograms and corresponding response spectra. The records in each suite are selected with different characteristics in order to investigate the effect of dynamic input on the response of the structures as detected by the DIs.

Table 2-7 Member cross-sections and reinforcement schedule of Building 1 and Building 2.

Section	Height (mm)	Width (mm)	BUILDING 1				BUILDING 2			
			Internal Frame		Extrenal Frame		Internal Frame		Extrenal Frame	
			Top (m)	Bottom (m)	Top (m)	Bottom (m)	Top (m)	Bottom (m)	Top (m)	Bottom (m)
A.A.	450	250	3x12; 2x16	2x16	5x12; 3x10	2x12	4x20; 4x12	2x16	4x20	2x16
B.B.	450	250	2x12	3x16	2x10	2x12	2x12	3x14	2x12	2x16
C.C.	450	250	3x12; 2x16	3x12; 2x16	5x12; 3x10	2x12	5x16; 3x12	2x16	4x20	2x16
D.D.	450	250	2x12	3x16	2x10	2x12	2x12	2x16	2x12	2x16
E.E.	450	250	3x12	2x16	5x12; 3x10	2x12	4x18	2x16	4x20	2x16
F.F.	450	250	2x12	3x16	2x10	2x12	2x12	3x16	2x12	3x14
G.G.	450	250	2x12	2x12	2x10	2x12	2x12	2x16	2x12	2x16
H.H.	400	400	4x16; 8x12		12x14		8x18	4x16; 4x12		
I.I.	350	350	4x18		4x16; 8x12		4x18	12x18		
J.J.	800	350	/	/	/	/	4x20	2x18	4x20	2x18
K.K.	800	350	/	/	/	/	2x18	5x20	2x18	4x20
L.L.	800	350	/	/	/	/	2x18	4x20	2x18	4x20

Key: No. of bars x bar diameter in mm.

Table 2-8 Characteristics of selected accelerograms from Ambraseys et al., (2002).

Return period hazard scenario (yrs.)	Record Ref.	Earthquake Name	Date	Ms	r (km)	Soil	pga	Duration (s)	Effective Duration (s)
4275	414x	Kalamata, Greece	13/09/1986	5.75	5	stiff	0.272	29.73	5.2
4275	147y	Aftershock of Friuli, Italy	13/09/1976	5.98	9	stiff	0.236	16.75	2.75
475	440x	Aftershock of Spitak	07/12/1988	5.8	10	soft	0.147	21.42	6.03
475	138x	Aftershock of Friuli, Italy	15/09/1976	5.98	19	alluvial	0.142	24.56	6.43
95	368y	Lazio Abruzzo	07/05/1984	5.79	31	rock	0.068	32.4	18.33
95	246x	Valnerina, Italy	19/09/1979	5.84	21	rock	0.061	13.76	10.35

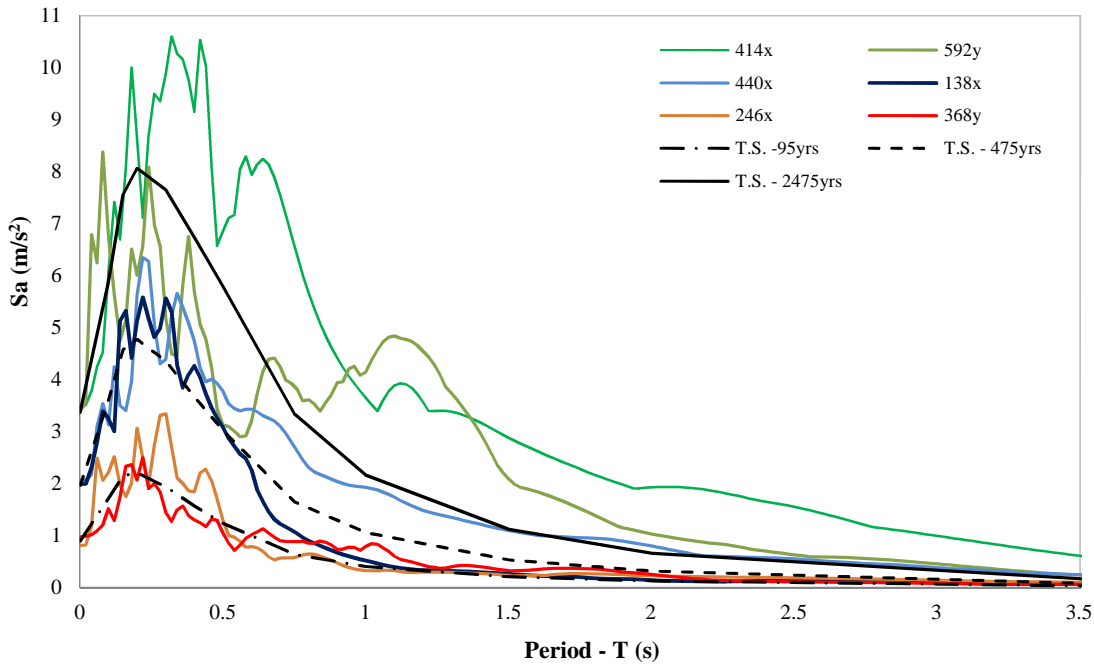


Figure 2-15 Acceleration response spectra (5% damping).

For the time history dynamic analysis, the fibre element based package SeismoStruct V5.03. (Seismosoft, 2010) is used. Since both structures are symmetrical at least in one direction, each model consisted in superimposed frames representing structural cross-sections, connected together with links. Nodes on the Gauss point and at the full length of the plastic hinge are also used as additional nodes.

After the time history analysis of each structure for the several excitations, local damage indices, storey damage indices and global damage indices were computed by equations 2-40. Figure 2-16 shows the weighted storey damage indices for each building. Figure 2-17 shows the weighted global damage indices for each building. At both storey and global level, Colombo *et al.*, (2005) and Park *et al.*, (1985) are observed to yield similar results. The value of yield curvature is slightly higher than the actual value, since a bi-linear approximation is used. As a result in the method presented by Kunnath *et al.*, (1990), the computed ratio of maximum plastic curvature ductility and ultimate plastic curvature is slightly lower than the actual value. It is therefore not excluded that the DI values obtained by this method are excessively low due to this reason.

During the computation of the damage indices corresponding to earthquake “414” and Building 2, it is observed that all columns in the lower level go beyond yielding. Some reach the ultimate state. As a result, it is expected that a damage index close to “1” is obtained. Nevertheless this is not the case. Many beams do not form hinges, and hence in the global damage computation unrealistically contribute as if part of the structure has not failed. As a result during the computation of global damage indices, hierarchal distinction between different elements depending on their position in the structure should be further developed.

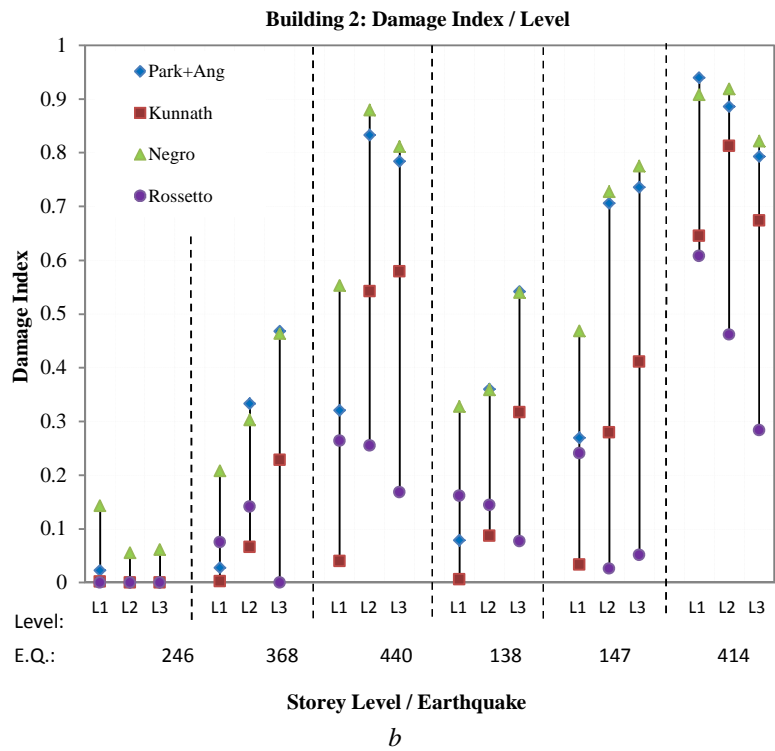
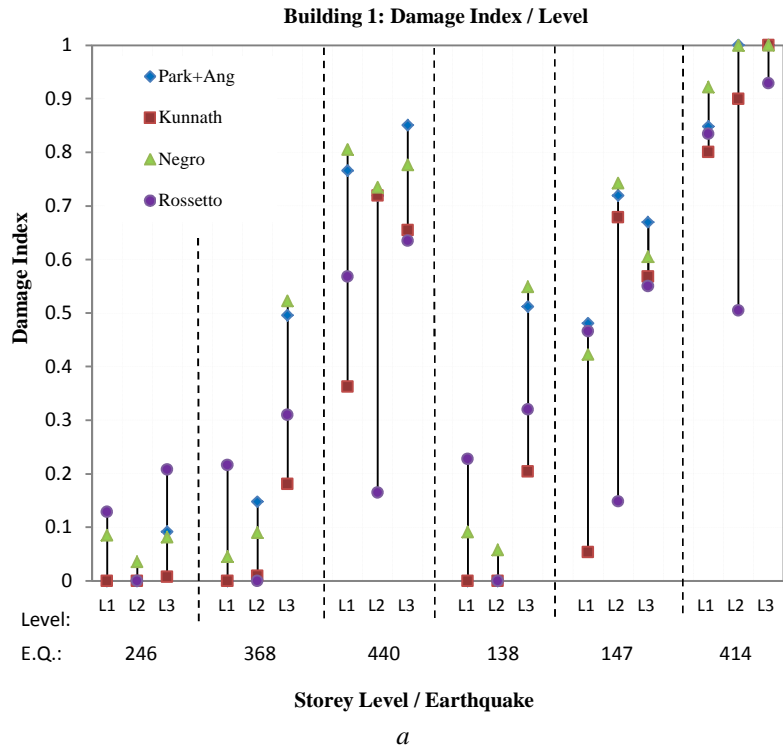
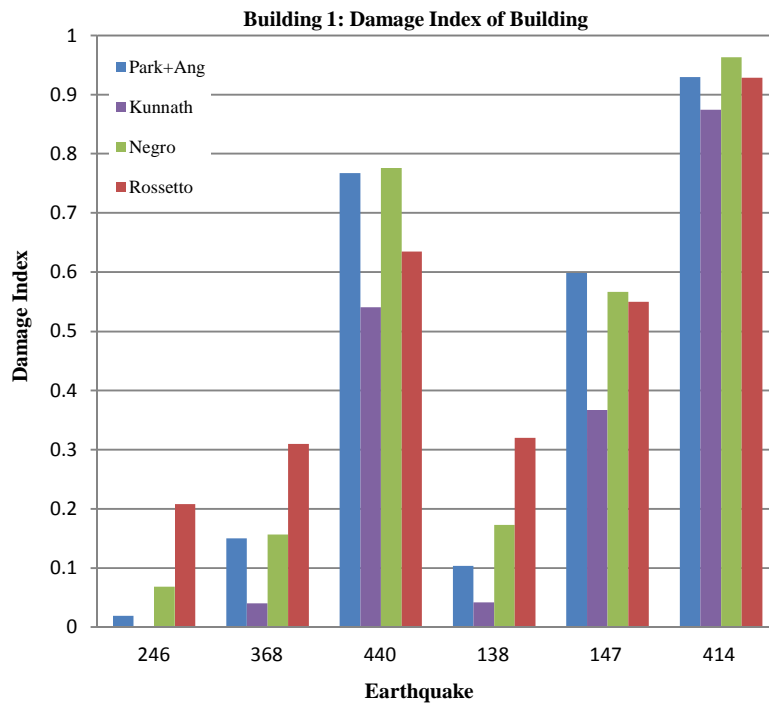
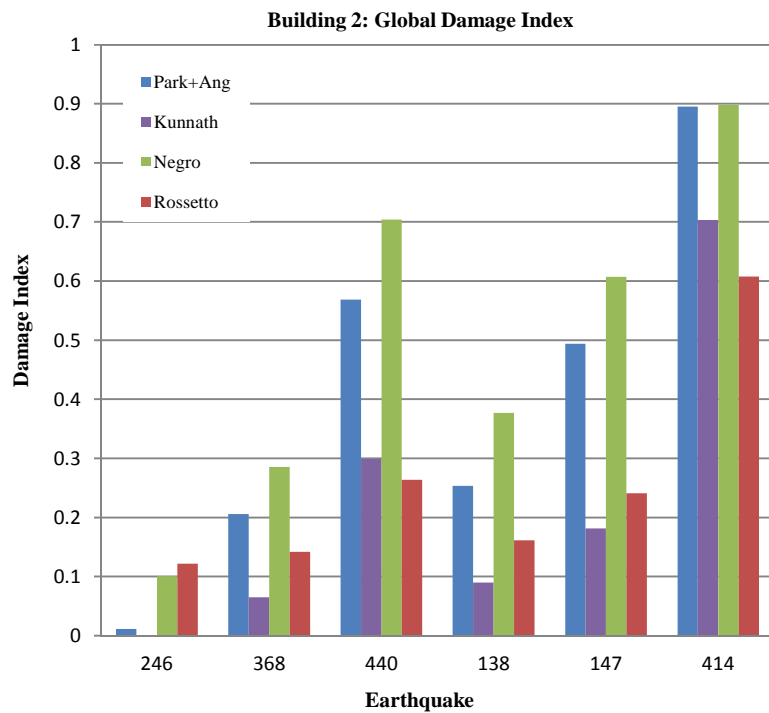


Figure 2-16. The damage indices for each storey (L1,L2,L3) and earthquake for: a) Building 1, b)Building 2.



a



b

Figure 2-17. The global DI corresponding to each earthquake for: a) Building 1, b) Building 2.

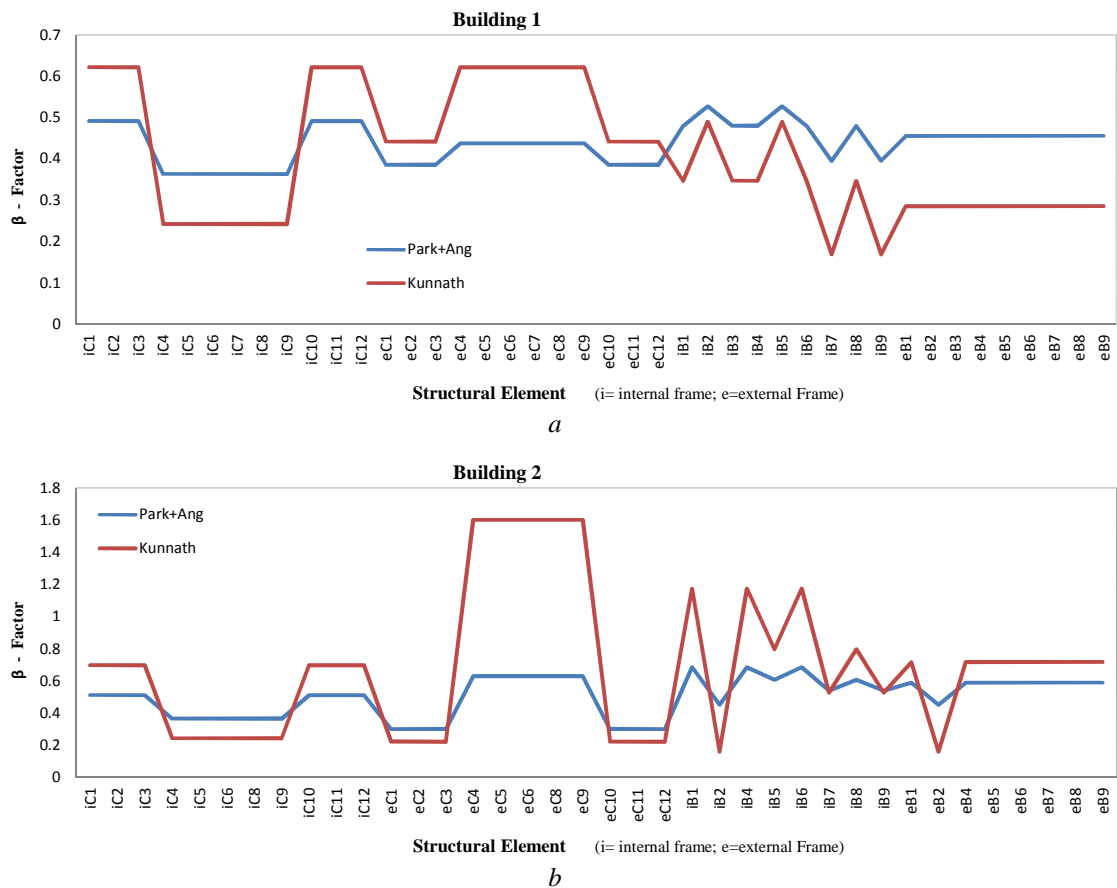


Figure 2-18 The evaluation of β for each element as provided by Park et al. (1985) and Kunnath et al., 1990 for: a) Building 1, b) Building 2.

The value of “ β ” for each element varies considerably between Park et. al., (1985) and Kunnath et. al., 1990 as shown in figure 2-18. In some cases, values in excess of unity are obtained for the DI proposed by Park and Ang (1985). This shows that although this DI may be perceived as one of the best DI, its factual relationship with damage may be questionable. The fact that a different value was obtained for each DI method for the same earthquake and building, indicates that the significance of the value vis-à-vis the damage is specific for the particular DI method. This means that a particular value of a damage index may signify different quantification of damage for different DI methodologies. Hence, rationalisation of the significance of damage is required. From Fig. 2-17 it is observed that the scatter in the four DI values for a particular earthquake and building is not uniform for other earthquakes. This shows that different DI methods respond differently to different earthquakes. As a result the reliability of DIs, may also depend on frequency, magnitude and duration contents of the earthquake.

The degree of scatter amongst the 4 DIs is more evident in the irregular building “2”. This shows that some DIs are not able to detect damage due to the irregular features of the structure. The failure mechanism of building “2” is associated with the failure progression of beam “B2”. Consequently this causes the failure of the supported two levels. Since the damage index of Rossetto et. al. (2003) is a function of the interstorey drift, it is not able to detect this failure

mechanism. This damage index gives underestimated values for all the seismic excitations on irregular building “2”. As a result, this method will be more effective if it is adjusted such that member rotations, of beams and columns are incorporated in the computation. Nevertheless, this should not be at a cost to the ease of use of this DI. Experimental calibration in this regard is also essential to calibrate the parameters. An experimentally calibrated DI based on regression, can be advantageous over the other 3 approaches as it may reduce the uncertainty associated with weighting of local damage indices to determine the global damage index. For a particular earthquake loading, the scatter between values of different DI is least for earthquake cases characteristic to 2475 years return period, and slightly higher for 95 years return period. The scatter between values of different DI is large for earthquakes characteristic to 475 years return period. For the former two situations the response of the structure or an individual member is close to the ultimate and the yielding point respectively. Although improvement is still required, it is evident that relationships of EDPs describing these damage limit states are effective. It is therefore required to develop deformation formulations that are able to define intermediate stages along the plastic range, between the ultimate and the yield limit states. These are essential in order to quantify damage accurately between these two limits. In spite of all the differences in the score across different Dis, one has to keep in context that the DIs are calibrated differently and hence a score by a particular DI may represent a level of damage, while the same level of damage is represented by another score in the case of another DI. Nevertheless, this would still indicate that there is lack of rationalisation.

The response of the structure is also checked in terms of the chord rotation capacity relationships provided in EN1998-3 (2005) and discussed in section 2.3.1. As an example the response of building 1 to earthquake 414 representing a hazard with a return period of 2475 years, corresponding to a probability of exceedance of 2% in 50 years is considered. According to EN1998-3 (2005), for this hazard level the structure is expected to be associated with a response resulting in heavy damage to the structure. For this damage level, very low residual lateral strength and stiffness are expected and components should not exceed θ_{u-20} . Table 2-9 shows the chord rotation capacity requirements for each damage level, and figure 2-19 maps the corresponding exceeded level of damage from the response of each element in the column.

Table 2-9. Chord rotation capacity at NC, DS and DL.

Section	θ_Y	$\theta_{75\%;u-20}$	θ_{u-20}
	<i>Eq. 2.7</i>	(= $0.75 \cdot \theta_{u-20}$)	<i>Eq. 2.21a</i>
A.A.; C.C.; E.E.	0.0080	0.029	0.038
H.H.	0.0068	0.028	0.037
I.I.	0.0072	0.022	0.030

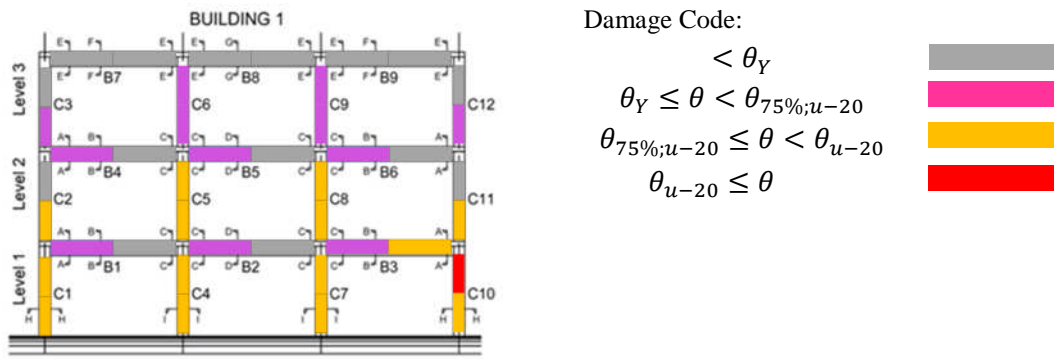


Figure 2-19. Damage distribution in Building 1 following response to earthquake 440, and capacity requirements according to EN1998-3(2005).

It is observed that quite a few elements in the lower two levels exceed 75% of θ_{u-20} and hence the structure is characterised with significant damage. However, one element even exceeds θ_{u-20} . Hence the criteria of NC is not followed for this building. The expected heavy damage is concentrated at the lower levels and concentrated more in columns and beams, including the element that exceeds θ_{u-20} . This compromises the overall stability of the structure. Although a unique retrofiting strategy is followed for the whole structure (FIB, 2006), the damage distribution indicates that the second and lower level require similar intervention, while the upper levels require fewer intervention.

2.4 Experiments for the Development of EDP relationships

2.4.1 Types of Tests and Testing Configurations

In seismic engineering there are four testing techniques (Sullivan *et al.*, 2004). These include free-vibration shaking table tests for structural identification, full dynamic shaking table tests, low-cycle fatigue tests and pseudo-dynamic tests. EDP relations in literature are determined on results from low-cycle fatigue tests. These types of tests refer to physical sub-element models of complete structures supported by pin or fixed supports, where loads are applied at points where contra-flexure or points that define a particular mode of deformation of the element are assumed (FEMA, 2007). The load is applied at slow rate increments such that dynamic effects are not simulated. The initial loading pattern is generally of a low amplitude such that elastic properties and the efficiency of the apparatus is tested (Sullivan *et al.*, 2004). Incremental loading continues until failure is reached. The loading pattern can be either cyclic or monotonic. External forces are generally lumped at a particular node (Harris *et al.*, 1999).

Since EDP relationships whether empirical or semi-empirical, require a large dataset and referring to multiple variables, low-cycle fatigue tests are very suitable. Experiments can be performed on various elements with different variables. It is possible to conduct a large number of tests, where RC elements with different geometrical and material properties, and detailing aspects can be

compared, and extrapolate and interpolate to similar components (FEMA, 2007). The other sophisticated tests, such as shaking-table tests offer dynamic simulation that is associated with an earthquake scenario. This is lacking in low-cycle fatigue tests. Nevertheless, shaking table tests are expensive, and capacity information is obtained on few components only and with limited variability.

2.4.2 Databases Considered

Three databases of low-cycle fatigue tests on RC are available to the author. The contents of these databases are accounted and defined in Rossetto et al., 2002, Panagiotakos *et al.*, 2001 and Berry *et al.*, 2003. The more extensive database utilised by Biskinis *et al.*, 2010a,b is not available for this research, however this is a built-up on Panagiotakos *et al.*, 2001, and hence inherits most of the advantages and disadvantages of the latter. The three available databases are compared.

In the database available from Panagiotakos *et al.*, 2001, it is not possible to distinguish between different types of elements. Moreover, the data describing confinement is limited and certain relevant explanatory variables discussed in section 5.3 such as the confinement ratio (a) cannot be determined. Other relevant data, such as the cover width (c) is not available. This information is completely missing for all the records, and hence cannot be recovered using statistical approaches. The database provided by Rossetto *et al.*, 2002 is a subset of that utilised by Panagiotakos *et al.*, 2001.

Table 2-10 shows the number of tests for each type of specimen in each database. For the purpose of this research, only beams and column tests are relevant. As indicated in the table, the number of relevant tests provided by the database in Berry *et al.*, 2003 is much less than that provided by Rossetto et al., 2002 and Panagiotakos *et al.*, 2001. Having a small number of records in a dataset, effects negatively the precision of the regression analysis. The data compiled in Berry *et al.*, 2003 referring to parameters and associated explanatory variables is directly obtained from the original source in a rational format. The data of the other two databases is obtained by the compilers by looking at data from experiments reported in literature. The rational of data presentation and interpretation varies in literature and there is no indication how this has been accounted for in Rossetto et al., 2002 and Panagiotakos *et al.*, 2001. For example, as discussed in section 2.2, the strength of concrete varies slightly depending on the test, and size and shape of the specimens in case of destructive tests.

Table 2-10 Comparison of the number of tests in the databases considered.

Type of specimen	Database Reference		
	Berry <i>et al.</i> , 2003	Rossetto <i>et al.</i> , 2002	Panagiotakos <i>et al.</i> , 2001
Unknown:	/	72	
Slabs:	/	30	
Walls:	/	27	
Beams:	9	216	Not available
Columns:	266	399	
Total	Beams and columns:	275	615
	All typologies:	275	744

2.4.3 Loading Considerations

From direct field investigation, it is also observed that earthquake cyclic loading induces damage cumulatively, and is not always proportional to the maximum displacement. Table 2-11 summarises damage development in RC structures after an earthquake which was further enhanced by aftershocks of lower magnitude and intensity that induced further energy in the system but not necessarily forcing the structure into larger displacements.

Table 2-11 The evolution of damage as a cumulative process.

Earthquake	RC Frame Structure	Damage after Main Event	Damage after Aftershocks	Reference
Loma Prieta, California, 1989	Palmor Hotel at Santa Cruz	Cracks in concrete	Further opening of cracks	EEFIT, 1989
Luzon, Philippines, 1990	Hyatt Terraces Main Hotel	Moderate damage	Collapse of structure	EEFIT, 1991
Erzincan, Turkey, 1992	General structures	Moderate damage	Severe damage	EEFIT, 1992
Emilia Romagna, 2012	Water tower at San Felice sul Panaro	Moderate damage	Severe damage	EPICentre, 2012(a); EPICentre, 2012(b)

In low-cycle fatigue tests, the applied load forces the RC elements to deform using a particular loading regime. Traditionally, the most common and popular loading regime used in low cycle fatigue tests on RC components refers to Krawlinker (1996) where the loading regime consists in a series of incremental loading cyclic steps, and each incremental steps consists of about 3 cycles at the same amplitude. However, this loading regime is not calibrated according to general earthquake loading characteristics which will actually force the element to deform in case of an earthquake. Takemura *et al.*, (1997), shows through low cycle fatigue tests, that the deformation capacity is not only a function of displacement parameters but also a function of the energy input as a result of the loading regime. Figure 2-20 shows that failure occurs at lower values of drift when a large number of cycles is employed. The existing EDP relationships discussed in section 1.3 do not take into account the effect of loading pattern on the deformation capacity, apart from distinguishing between general monotonic and cyclic effects.

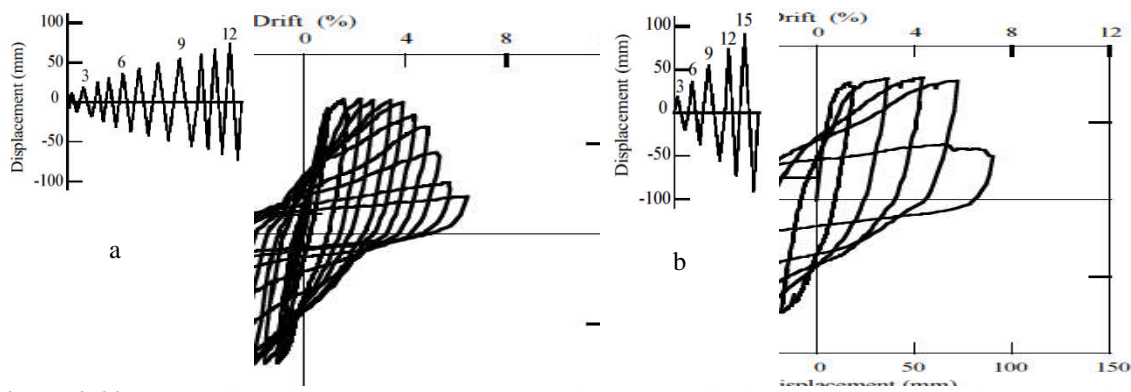


Figure 2-20 Low cycle fatigue tests on piers, using different cyclic loading histories (Takemura et al., 1997).

2.5 General Conclusions and Requirements

The literature review and discussions in this chapter show that several phenomena affect damage development in RC elements and that these need to be included in any relationship that aims to link EDPs to the RC element material and geometric properties.

There are a large number of variables that describe different damage phenomena when considered individually. However, not all of these variables are included in existing relationships of EDPs. Material and geometric properties are observed to give different contributions to deformation in the presence or exclusion of considerable bond-slip. However, existing EDP relationships do not account for this effect. In addition, different combined variables are used as explanatory variables to account for a particular phenomenon in different models of EDPs by different authors. Some variables in discussed models feature several times in the same model within different explanatory variables. In the reviewed literature, there is a general lack of reporting of the procedures followed for constructing the form of the adopted equations and for regressing the empirical coefficients. Hence, it is not possible to determine whether the inclusion of each variable provides an optimal representation of the explanatory variables within the model (and hence reduces the possibility of overfitting) or not.

It can therefore be concluded that an improvement on the existing models would lie in defining a rigorous approach for the development of new EDP models that looks at how variables should be included in a systematic way, and which considers approaches for determining the best fit model to the data. Such a procedure is proposed in Chapter 5, where developed models also consider different variation of geometric and material properties in the presence, and not, of considerable bond slip. Existing EDP relations are determined on low-cycle fatigue tests which do not simulate the dynamic characteristics of structures subject to earthquakes. The new models proposed in this thesis still refer to such tests, and hence the exclusion of dynamic considerations is a limitation. In most existing databases of low cycle fatigue tests, with the exception of Berry

et al., 2003, EDP information is not retrieved using a rational approach. This increases the uncertainty in model development. As a result, the database proposed by Berry et al., 2003 together with other complimentary data found in literature is selected for the development of EDP models in Chapter 5. The size of the database is not very large. Like the other databases, test records that refer to RC structures that characterise RC building stocks susceptible to earthquake damage as discussed in section 2.2 are very limited. As a result, Chapter 3 presents a new testing campaign of low-cycle fatigue tests on RC columns that specifically includes specimen material properties, geometric aspects and detailing aspects that are underrepresented or not popular in the database provided by Berry et al., 2003.

Most of the EDP relationships discussed in literature refer to yielding and ultimate damage states. However, damage scales are defined in terms of intermediate damage levels and hence, EDP relations are required at such levels. Some damage scales, such as HRC (Rossetto et al. 2003), are defined in terms of expected damage phenomena. The recommended damage states are based on the same philosophy adopted in EN1998-(2005), which is defined in terms of strength degradation and residual stiffness requirements.

The existing EDP relationships discussed in section 2.3 do not take into account the effect of loading pattern on the deformation capacity, apart from distinguishing between general monotonic and cyclic effects, despite it being shown in section 2.4 that the loading pattern has an effect on the deformation capacity of RC elements. Reference to Borg *et al.*, 2012 is made to utilise a loading regime for the experimental campaign that is based on seismic requirements. Moreover, the experimental campaign is extended to investigate the effect of loading pattern on the deformation capacity of RC elements. On this basis, variables that can characterise the loading pattern are required to be identified and included in the development of new EDP models.

Chapter 3. DESIGN OF EXPERIMENTS AND DIAGNOSTICS

3.1 Introduction

The aim of the quasi-static testing campaign is to conduct tests whose results could be used as a benchmark to other tests and corresponding results that are obtained from literature and various data sets such as Rossetto, 1999 and Berry, 2003. The data sets are described in Chapter 2. As discussed in chapter Chapter 2, the integration of the benchmark tests with further data from the described datasets will assist in the derivation of empirical formulation of EDPs which define and quantify damage as a function of parameters that describe the geometrical aspects of the component, material properties and detailing aspects.

In this chapter, the most suitable type of test that fits the required criteria will be identified. Since benchmark tests are required, the type of test should give the possibility to carry out a considerable number of tests considering different variations. Associated types of setups are then selected based on their ability to simulate realistically loading and response patterns, and their ability to simulate important physical characteristics that influence the development of damage as discussed in chapter 2.

An experimental schedule is designed for each setup. Detailing aspects and material properties are modified such that a specimen differs from at least one other specimen by one property only. The range of properties considered are based on the distribution of properties of the tests in the considered databases. The variables that are initially assumed refer to the variables that are considered a function of EDPs in existing relationships in literature.

The specimens are produced with selected materials based on tests such that the characteristic and nominal properties of the specimens are uniformly and consistently conserved. For each type of specimen an instrumentation layout is devised in order to be able to monitor the required parameters with which EDPs could be determined. Sources of error are identified and ways and means of how to monitor them and mitigate their effect is proposed. Diagnostics on how the raw data is filtered and used to give the respective EDPs as benchmark values is described.

3.2 Experiments for the assessment of RC structural elements

3.2.1 Collection of Material and Geometric Properties

The base variables of material and geometric properties that define the constitutive models of steel and concrete, and other properties that describe failure mechanisms such as bond slip and buckling are collected and grouped in table 3-1. All of these variables contribute participate in the behaviour of RC elements. However, some are difficult to determine when doing assessment of

structures. For example, the chemical adhesion is difficult to define and is only important either for plain bars or at the initial stages of deformation when ribbed bars are used. Strain values for concrete are close to constant and hence will be assumed to be expressed indirectly in terms of stress and modulus variables. Other parameters such as the strain rate value (ϵ_{co}^*) although relevant, is insignificant when low-cycle fatigue tests are concerned. Table 3-2 provides the list of base variables that are used in formulations to differentiate between shear, flexure and flexure-shear failure mechanisms.

Table 3-1 Un-combined explanatory variables that describe constitutive models of steel and concrete.

Constitutive Model	Explanatory Variable
Confined /Unconfined concrete:	$f'_c, f_{tl}, \epsilon_{co}, \epsilon_{cu}, f_{yw}, k_{conf}, \epsilon_{co}^*, n_{cy}$, loading pattern, Transverse reinforcement anchorage (90° or 135°).
Steel and Buckling:	$f_{yl}, f_{tl}, d_{bl}, E_s, a_1, a_2, a_3, a_4, s', s, \epsilon_{sy}, \epsilon_{st}, \epsilon_{su}, R^o, R, P, r, e, c, f_{yw}, k_{conf}, f'_c, f'_{cc}, \epsilon_{cu}, L_s, b, h, N, {}^x C, \epsilon_{co}^*, n_{cy}$, loading pattern, Transverse reinforcement anchorage (90° or 135°), Ribbed-plain.
Bond:	$f'_c, s_c, c, L_a, d_{bl}, f_{yl}, k_{conf}, \epsilon_{co}^*$, loading pattern, Chemical adhesion, Ribbed-plain.

Table 3-2. Un-combined explanatory variables that are used to differentiate between shear, flexure and shear-flexure failure mechanisms.

Shear, Flexure, flexure-shear deformation and failure: Explanatory Variables
$E_s, E_c, L_s, b, h, G, \alpha, f'_c, \vartheta, k_{conf}$

Table 3-3 Un-combined explanatory variables that are used to differentiate between shear, flexure and shear-flexure failure mechanisms.

Equation	Explanatory Variables
Rossetto et al., 2002	$f_{tl}, f_{yl}, \epsilon_{su}, a_{cy}, a_{sl}, \epsilon_{su}, N, b, h, n_2, n_{1*}, n_v, f'_c, f_{yw}, b_{xo}, b_{yo}, s, d_{bl}, d_{bh}, n_{yo}, n_{xo}$
Biskinis et al., 2010a,b Panagiotakos et al., 1999,2001	$a_{st}, a_{cy}, a_{sl}, N, b, h, f_{yl}, f'_c, n_2, n_1, L_s, b_{xo}, b_{yo}, b_i, f_{yw}, d_{bh}, s, d_{bl}, n_{yo}, n_{xo}$
Berry et al., 2003	$N, b, h, f_{yl}, f'_c, L_s, h, f_{yw}, n_{yo}, d_{bh}, s, n_t, d_{bl}$
Haselton et al., 2008	$a_{sl}, N, b, h, f_{yl}, f'_c, d_{bl}, n_{yo}, b_{yo}, s, n_2, n_1,$

Table 3-3 provides the list of base variables that are used in EDP relationships in terms of material properties, geometric aspects and detailing that are found in literature. Equations 3.1, provide three alternatives on how the longitudinal reinforcement is accounted for in different chord rotation relationships.

$$\text{Alternative 1:} \quad \omega_1 = (\rho_1 + \rho_v) \frac{f_{yl}}{f'_c}; \quad \omega_2 = \rho_2 \frac{f_{yl}}{f'_c} \quad [3.1a]$$

$$\text{Alternative 2:} \quad \omega_v = \rho_v \frac{f_{yl}}{f'_c}; \quad \omega_{1*} = \rho_1 \frac{f_{yl}}{f'_c}; \quad \omega_2 = \rho_2 \frac{f_{yl}}{f'_c}; \quad [3.1b]$$

Alternative 3

$$\omega_T = (\rho_1 + \rho_2 + \rho_v) \frac{f_{yl}}{f'_c} ; \frac{\omega_2}{\omega_1} ; \frac{\omega_2}{\omega_1} f'_c \quad [3.1c]$$

The axial force ratio is generally considered as N/bhf'_c or N/bh . Confinement is considered as either ρ_s or $a\rho_s f_{yw}/f'_c$ or $\omega_w = \rho_w f_{yw}/f'_c$. Although buckling depends on the type of confinement, this is considered separately since while confinement refers to concrete, buckling refers to steel and the parameters affect the buckling behaviour of steel and confinement of concrete separately. The main parameters that define buckling are identified as either s/d_{bl} or $s_n = s/d_{bl} \sqrt{f_{yL}/100}$. Parameters that characterise the geometry of the elements are grouped as aspect ratios in h/b and L_s/h . The concrete strength f'_c is used in various combined parameters that define confinement, and the quantity of longitudinal and transverse reinforcement when defined as mechanical ratios. The main combined variables that influence bond slip include c/d_{bl} and f_{tl}/f_{yl} . The latter is also used to define the type of steel. The binary variable a_{st} is also used to define the grade of steel and the binary variable a_{sl} is used to differentiate between considerable bond slip and none. Variables referring to loading considerations are rarely used. The binary variable a_{cy} is used to differentiate between cyclic and monotonic loading, n_{cy} refers to the number of cycles and E_d refers to the energy dissipation.

A variable can be classified in being quantitatively continuous, quantitatively discrete or descriptive (Sonin, 2001). In the above tables 3-1 to 3-3, variables measuring quantities on a continuous scale such as length, stress, strain, force are considered as a continuous quantity. The variables f'_c and d_{bl} are amongst such continuous quantities which describe the bond-slip phenomenon amongst others. However, a_{sl} indicates the presence or the exclusion of bond-slip with respect to the nature of the column anchorage. It involves description of the phenomenon, through a discrete numerical binary representation (Baker et. al., 1981) and is considered a discrete quantity. Other similar discrete quantities include having ribbed or plain bars, having 90° or 135° stirrups, and a_{cy} . The loading pattern is a descriptive quantity since it involves descriptive categorical classification. Descriptive quantities refer to numerical continuous and discrete quantities as criteria for classification. In the case of loading pattern, energy dissipation E and number of loading cycles n_{cy} are continuous quantities, and a_{cy} is a discrete quantity indicating the presence or not of cycles in the loading pattern which are included in the descriptive categorical classification further discussed in Chapter 6. The distinction between parameters is relevant when considering the position of variables and form of the model in the regression analysis procedure.

3.2.2 Data Distribution Requirements

In this section the distribution of the data of some important parameters of the selected database provided by Berry *et al.*, 2003 is compared with the distribution of the corresponding data from

the experimental campaign discussed in Chapter 2, to highlight the latter's contribution to the dataset for the regression analysis in having a more uniform distribution, filling gaps in the data range that are not available. Reference to the corresponding data available from the Rossetto et al., 2002 database is made to highlight the differences in the data used for regression purposes, with data used to define other equations in literature.

Figures 6-6 indicate the distribution of data for some explanatory variables for the three datasets. In general the distribution of data from Berry *et al.*, 2003 is very similar to Rossetto et al., 2002 for most variables considered. The larger the standard deviation (SD) the better is the distribution of data for regression analysis. The database available from Rossetto et al., 2002 expresses a better continuity of data in a range than Berry *et al.*, 2003 since it has more records.

The data from Rossetto et al., 2002 covers a broader cross section aspect ratio range. As shown in Figure 3-1a. The data by Berry *et al.*, 2003 is normally distributed around $d/b=1$. The skewness in and a mean and median larger than 1, are indicative that Rossetto et al., 2002 is more representative of elements that were tested in the stronger direction. This can be misleading since elements fail in the direction with the weaker moment of inertia ie. $d/b < 1$ if the cross section is not a square.

The reinforced concrete strength (f'_c) data from Berry *et al.*, 2003 is bi-modal, with peaks round normal concrete 27MPa and higher strength 80MPa. Rossetto *et al.*, 2003 covers the high strength concrete range as well, however the distribution is skewed such that the average is lower. As discussed in Chapter 2, un-seismically designed structures susceptible to damage are characterised with low strength concrete. This is underrepresented by both databases, however, the distribution from the experimental campaign covers the lower range of f'_c .

The distribution of the axial force ratio (ν) from Berry *et al.*, 2003 and Rossetto et al., 2002 is very similar in terms of range covered, SD and skewness towards lower values. The average in Rossetto et al., 2002 is lower than that by Berry *et al.*, 2003 due to a lower average of the axial force (N) in the former. The experimental campaign provides a larger average of ν which is more characteristic to older structures designed to un-seismic codes.

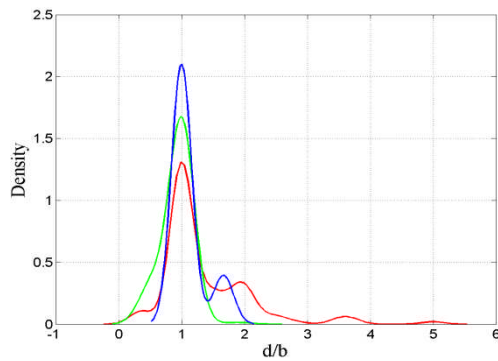
The distribution of L_s/h for the data from Rossetto et al., 2002 is skewed towards low values which are typically associated with shear failure. This research focuses on flexural failure and hence, such distribution would have been undesirable had the Rossetto et al., 2002 database been selected for the regression analysis. Although low values of L_s/h are also covered by Berry *et al.*, 2003, the distribution density in this range is very small. The distribution of the experimental campaign is skewed towards larger values of L_s/h , and hence contributes in having a more uniform representation of data, which also characterises flexural failure.

Data from Rossetto et al., 2002 and Berry *et al.*, 2003 databases is similarly distributed in terms of transverse reinforcement strength (f_w), the longitudinal reinforcement strength (f_{yl}) and the tensile strength ratio (f_{tl}/f_{yl}). The average and median f_{tl}/f_{yl} from the Rossetto et al., 2002 data is larger than Berry *et al.*, 2003. The distribution of f_{tl}/f_{yl} has its peak at a value of 1.1 for the former database. As discussed in Chapter 2, old RC structures most vulnerable to seismic damage are characterised with low reinforcement strengths and tensile strength ratios. In this regard, the database by Rossetto et al., 2002 can provide a more adequate representation. However, there is a discontinuity in the f_{tl}/f_{yl} distribution by the latter database. The range of the experimental campaign covers this discontinuity. The average f_{yl} and f_{tl}/f_{yl} are also low and representative of steel used in old structures as indicated in Chapter 2. As a result, this data from the experimental campaign combined with the corresponding data from Berry *et al.*, 2003 towards a more desirable distribution for regression analysis of EDPs in terms of material and geometrical properties.

Berry *et al.*, 2003 and Rossetto et al., 2002 have similar distributions of the transverse reinforcement ratio (ρ_s) in terms of mean, median, SD and skewness towards the lower values. The distribution of variables from the experimental campaign is relatively lower on average, but it enhancing the range which is more representative of older structures more vulnerable to damage as discussed in Chapter 2.

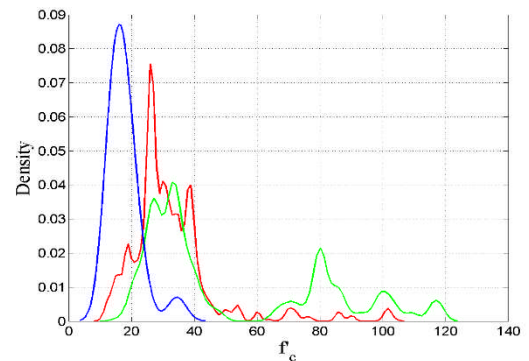
As discussed in Chapter 2, s/d_{bl} is associated with the susceptibility to longitudinal reinforcement buckling. The higher the value, the higher is the susceptibility. Both distributions from the Berry *et al.*, 2003 and Rossetto et al., 2002 databases are skewed towards low values. Specimens with the susceptibility for buckling are underrepresented. This is countered by the distribution of the experimental campaign whose skewness is towards higher values and the mean falls in a range characteristic to buckling susceptibility as discussed in Chapter 2. Rossetto et al., 2002 also contains very large s/d_{bl} which are associated with shear failure mechanisms as discussed in Chapter 2 and section 5.5, and which are undesirable to the scope of this research.

d/b	Rossetto <i>et al.</i>	Berry <i>et al.</i>	Exp. Camp.
Max.	5.00	2.00	1.67
Min.	0.30	0.50	1.00
Mean	1.36	0.93	1.11
Median	1.00	1.00	1.00
S.D.	0.72	0.20	0.24



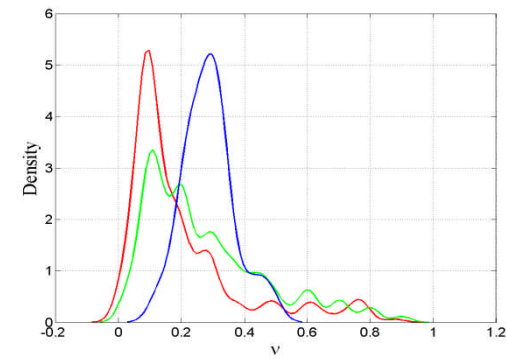
a

f'_c (MPa)	Rossetto <i>et al.</i>	Berry <i>et al.</i>	Exp. Camp.
Max.	103.7	118.0	34.5
Min.	11.0	16.0	12.6
Mean	32.6	51.6	17.6
Median	30.0	35.7	17.2
S.D.	14.4	29.1	4.9



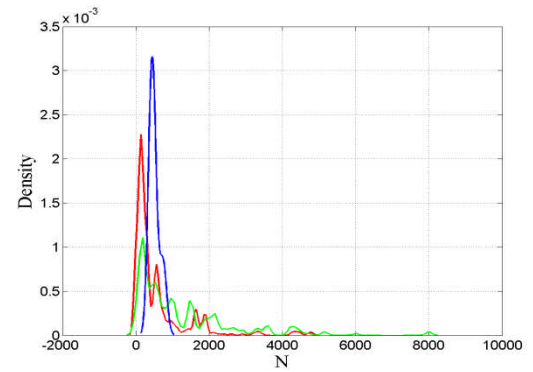
b

ν	Rossetto <i>et al.</i>	Berry <i>et al.</i>	Exp. Camp.
Max.	0.889	0.90	0.48
Min.	0.01	0.03	0.13
Mean	0.202	0.27	0.29
Median	0.130	0.21	0.28
S.D.	0.184	0.19	0.08



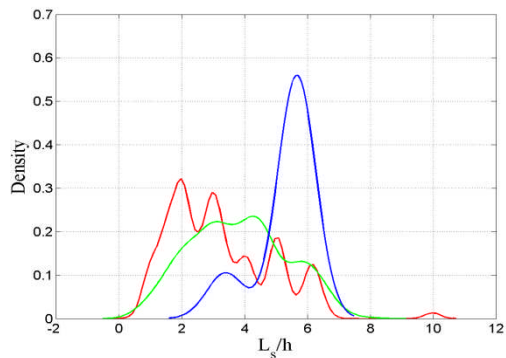
c

N (kN)	Rossetto <i>et al.</i>	Berry <i>et al.</i>	Exp. Camp.
Max.	4800	8000	740
Min.	50	55	437
Mean	575	1226	506
Median	277	744	446
S.D.	817	1345	119



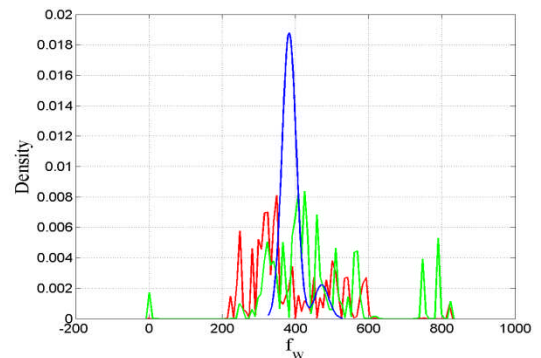
d

L_s/h	Rossetto <i>et al.</i>	Berry <i>et al.</i>	Exp. Camp.
Max.	5.67	7.64	5.67
Min.	3.40	1.00	3.40
Mean	5.31	3.82	5.31
Median	5.67	3.92	5.67
S.D.	0.83	1.49	0.83



e

f_w (MPa)	Rossetto <i>et al.</i>	Berry <i>et al.</i>	Exp. Camp.
Max.	825	825	472
Min.	201	210	383
Mean	404	449	392
Median	377	426	383
S.D.	113	135	27

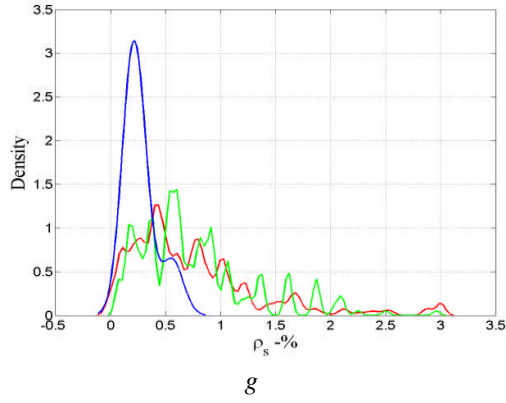


f

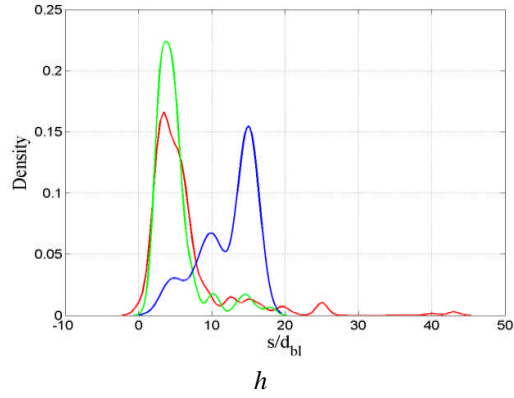
Continued...

...Continued

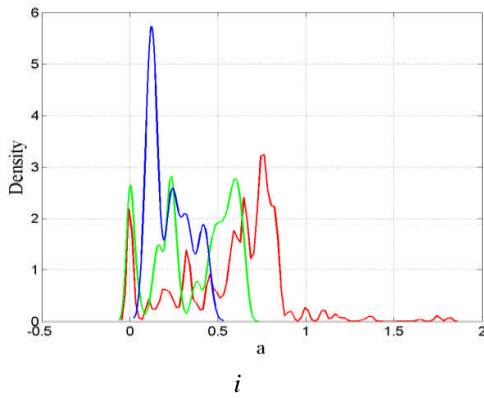
ρ_s (%)	Rossetto <i>et al.</i>	Berry <i>et al.</i>	Exp. Camp.
Max.	3.00	2.96	0.56
Min.	0.02	0.07	0.19
Mean	0.74	0.76	0.27
Median	0.60	0.61	0.21
S.D.	0.60	0.52	0.13



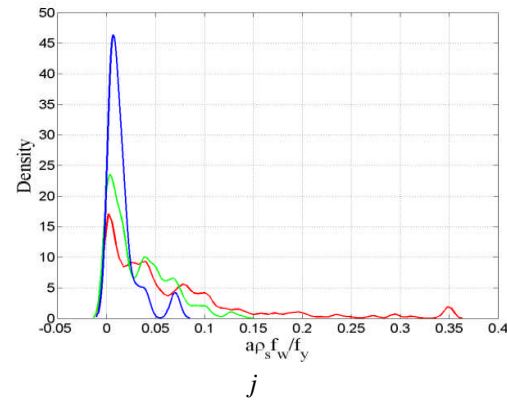
s/d_{bl}	Rossetto <i>et al.</i>	Berry <i>et al.</i>	Exp. Camp.
Max.	40.00	18.00	15.0
Min.	0.4	1.57	4.5
Mean	6.18	5.13	12.2
Median	5.00	4.21	15.0
S.D.	4.97	3.17	3.6



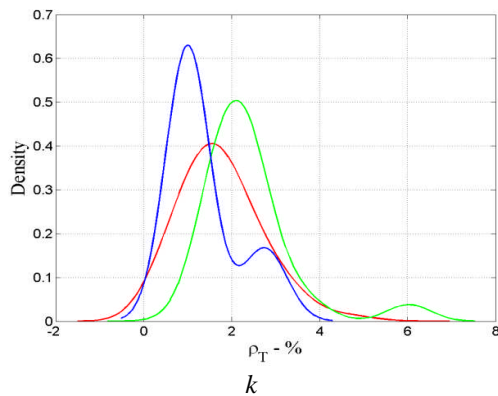
a	Rossetto <i>et al.</i>	Berry <i>et al.</i>	Exp. Camp.
Max.	1.81	0.67	0.43
Min.	0.01	0.01	0.12
Mean	0.58	0.36	0.23
Median	0.65	0.39	0.23
S.D.	0.30	0.22	0.11



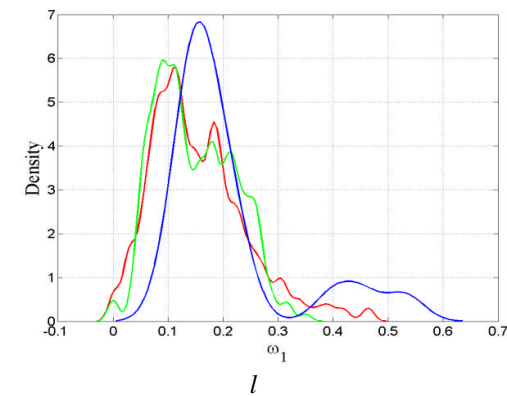
$a\rho_s \frac{f_w}{f_c}$	Rossetto <i>et al.</i>	Berry <i>et al.</i>	Exp. Camp.
Max.	0.350	0.137	0.070
Min.	0.003	0.003	0.004
Mean	0.064	0.032	0.015
Median	0.039	0.020	0.011
S.D.	0.075	0.030	0.016



ρ_T (%)	Rossetto <i>et al.</i>	Berry <i>et al.</i>	Exp. Camp.
Max.	5.46	6.03	2.79
Min.	0.05	0.68	0.99
Mean	1.75	2.37	1.37
Median	1.67	2.22	1.01
S.D.	0.92	1.00	0.71



ω_1	Rossetto <i>et al.</i>	Berry <i>et al.</i>	Exp. Camp.
Max.	0.47	0.35	0.53
Min.	0.01	0.01	0.11
Mean	0.15	0.15	0.21
Median	0.14	0.14	0.17
S.D.	0.09	0.07	0.11



Continued...

...Continued

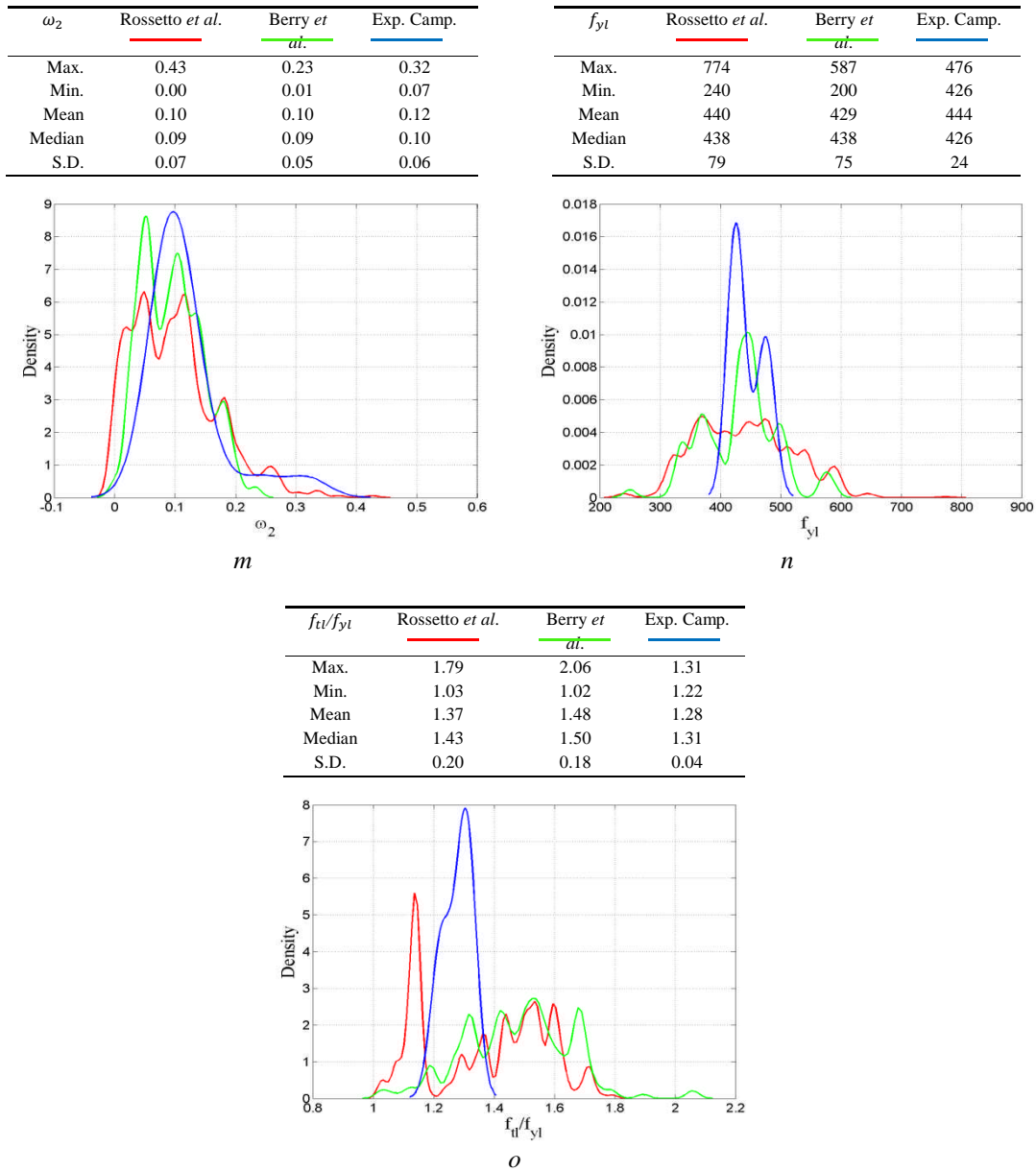


Figure 3-1 Density distribution of data from the databases provided by Rossetto *et al.*, 2002 and Berry *et al.*, 2003, and the experimental campaign presented in Chapter 4, for various explanatory variables.

The database from Rossetto *et al.*, 2002 covers a large range of confinement ratios (a) and associated combined parameters ($a\rho_s f_w/f_{yl}$). However the density with high values is low, and skewness is towards low values. Berry *et al.*, 2003 ranges over lower values characteristic to structures which, as discussed in Chapter 2, are more vulnerable to seismic damage. The latter has a lower average than Rossetto *et al.*, 2002 for both parameters. The distribution of Berry *et al.*, 2003 is discrete around 3 peaks. The distribution of the confinement ratio (a) from the experimental campaign covers the intermediate range where the distribution of Berry *et al.*, 2003 has a low density between the peaks. This enhances the uniformity of data distribution of this parameter for the regression analysis.

The distribution of reinforcement ratio (ρ_T) from Berry *et al.*, 2003 has a higher mean than the distribution from Rossetto *et al.*, 2002. However the distribution of this parameter as used in the experimental campaign has a much lower mean, and covers a range which is less represented by the distributions from Berry *et al.*, 2003 and Rossetto *et al.*, 2002, and is more characteristic to vulnerable RC structural elements as discussed in Chapter 2. The ratios distribution of the compression (ω_2) and tension (ω_1) longitudinal reinforcement is similar for all sets of data.

3.2.3 Design of a Reference Structure

Reference columns are required in the process to determine loading regimes where the procedure by Borg *et al.*, 2012 is followed, and in the development of the experimental campaign. Two reference columns are required: one representing columns of structures without seismic detailing typical of years before the 1990s, and the other representing modern practice. An infilled RC frame structure is considered. The geometry is based common characteristics of buildings discussed earlier. It consists in a three-by-three frame and its geometry is described in figure 3-2. The frame is designed following two guidelines, one for each column.

BS8110 Part 1,2,3 (British Standards, 1985) is used for the design of the frame without seismic detailing. Most of the provisions of this code looked representative of many detailing aspects that are found in similar codes. A typical design procedure discussed in MacGinley *et al.* (1991) is followed. EN1998-1 (CEN,2004) is used for the design of the frame with seismic considerations. The design follows the procedure suggested by Fardis (2007). In the case where seismic loading is considered a moderate seismic load $a_g R = 0.18g$ is considered. Masonry infills are assumed typical of southern Mediterranean regions with a dead load 1.5kN/m. The screed and tiles are assumed 1.5kN/m², and a live load of 2kN/m² for a normal occupancy building is considered. All values are provided not factored. Figure 3-3 shows the resulting reinforcement schedule of the structure designed according to each code. A concrete grade of C16/20 is considered for the building designed according to BS8110 (British Standards, 1985) and a concrete grade C30/37 is considered for the building designed according to EN1998-1 (CEN,2004).

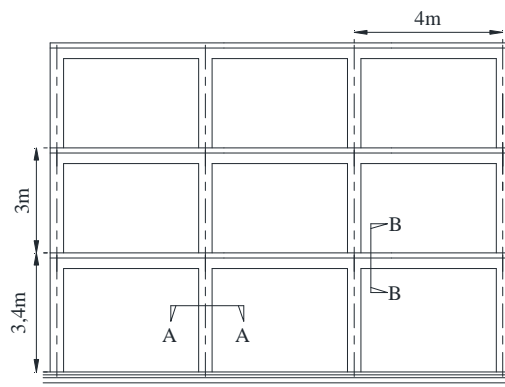


Figure 3-2 Elevation of the RC frame that is used as a reference structure.

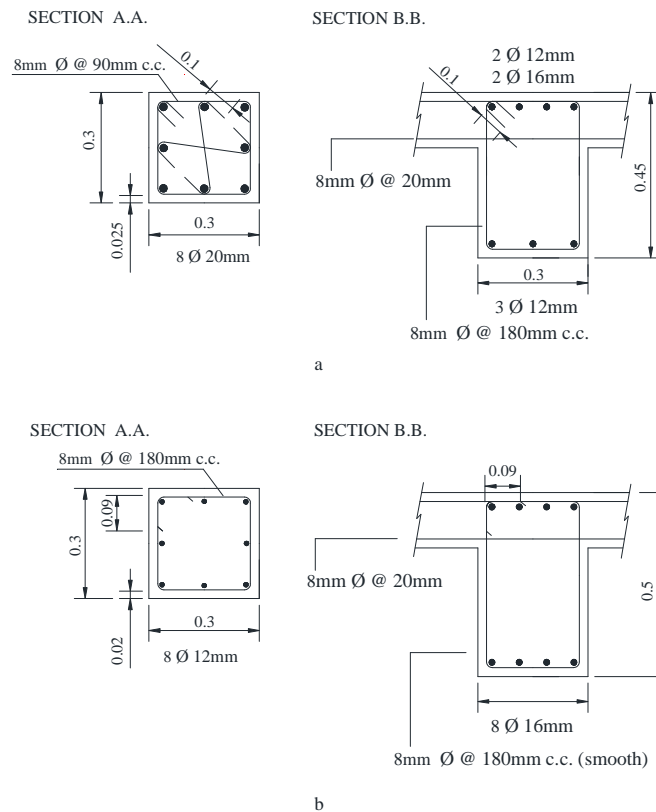


Figure 3-3. Design details of column (section A.A.) and beam (section B.B.) for the reference RC frame designed according to: a) EN1998-1 (CEN, 2005), b) BS8110 (British Standards, 1985).

3.2.4 Experimental setup for the experimental campaign

The tests were to be conducted at the structural laboratories at the University of Aveiro in Portugal. One of the first decisions that had to be taken was whether scaled tests or full scaled tests had to be conducted. Scaled tests are cheaper and faster, and hence give the opportunity to do more tests for the same financial budget. Although scaling relationships for structural components in terms of geometry and mechanical properties are available in literature (Harris *et al.*, 1999), there are no relationships that scale the quantification of damage that relate the damage in a model with that of a prototype (Borg *et al.*, 2008). Moreover, damage quantification of un-scaled prototypes alone is already a difficult and unclear task which is often debated in literature, and is one of the aims of this research to account for as discussed in Chapter 1. The facilities and apparatus available at the University of Aveiro were large enough to allow full scale testing of components and elements and sub-systems, and hence scaling of specimens was not considered. Within these facilities it was also possible to propose setups where specimens and corresponding results, comparison with tests from other databases such as Rossetto (1999) and Berry (2003) could be made.

The experimental setup for columns selected for this research (Figure 3-4) consist in a modification of the setup for internal beam-column connections for the experimental campaign of Fernandes (2012). The setup consists in a horizontal layout which is common in the absence of strong walls and the presence and availability of strong floors (Sasmal *et al.*, 2010). In the proposed setup, the specimens are supported horizontally on universal ball bearings which are fixed at the centre of mass of each element. The horizontal supports consist in high-strength concrete block that elevate the column a distance above the strong floor.

Lateral restraints, fixities and hinges consist in steel frames that are expected to transfer the reaction to the strong floor. In vertical setups, the foundation of column test specimens is directly fixed with the strong floor through post-tensioned bolts (Harris *et al.*, 1999). However in our horizontal setup, the foundation of the column specimens was fixed by two rectangular parallel steel frames through screw-clamps (3-4). The restraint of the foundation in a vertical setup is much more rigid and rotation of the foundation is very small (Harris *et al.*, 1999). In order to increase the stiffness in the horizontal layout of the testing campaign, an extended longer foundation was proposed, and the parallel frames were set at a distance of 1m from each other (Figure 3-5, 3-6). In addition pre-stress force by external jack was suggested while screw clamping the foundation with the restraining frames. These measures offer an increased resistance restricting rotation of the foundation. However, rotation of the foundation could not be eliminated, and was accounted for as described in section 3.4.

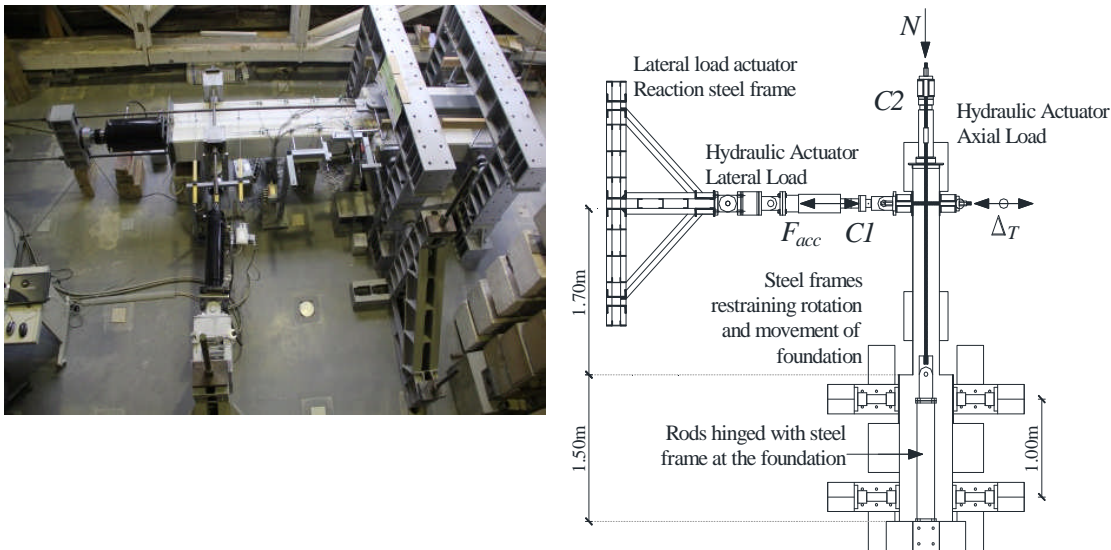


Figure 3-4 Test setup for column specimens.



Figure 3-5 Detail of the restraint of the foundation and hinging of the rods: a) from the front; b) from behind.

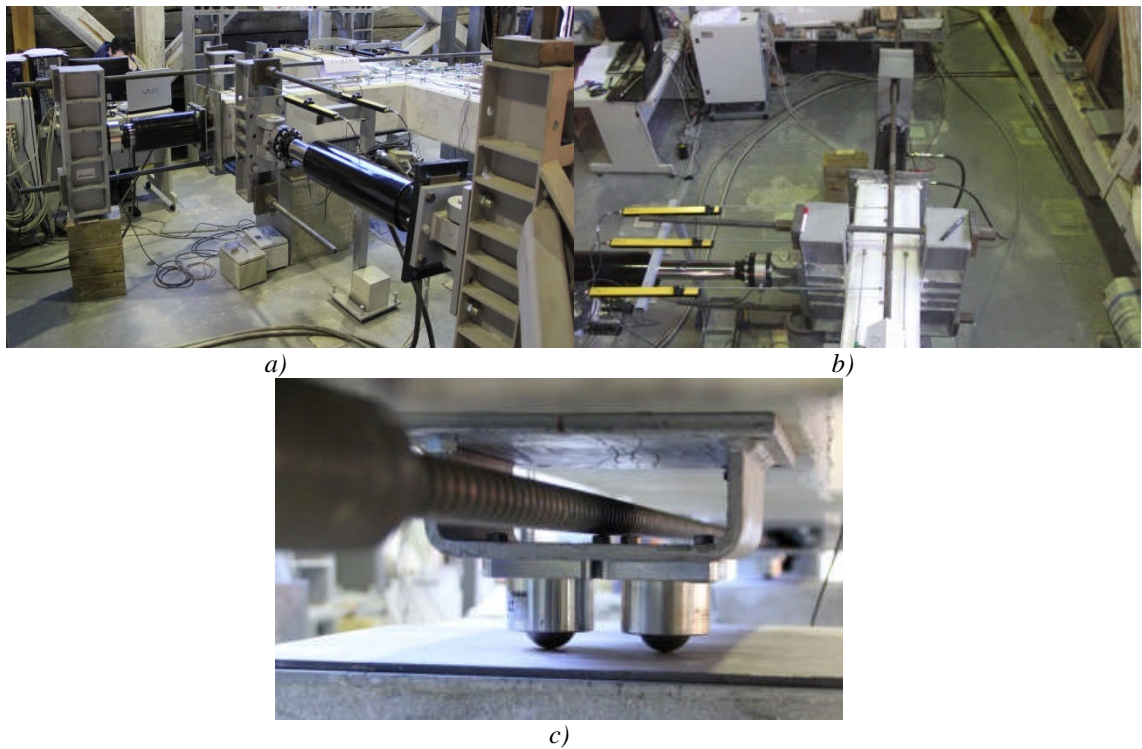


Figure 3-6 a) the axial load actuator and lateral load actuator setup; b) Frame with applied pre-stress connecting the column with lateral load actuator; c) Specimens are supported on universal ball bearings.

For the column specimens the lateral load is applied by a hydraulic actuator, acting on the upper column at its upper tip. The available actuator had a capacity of 200kN. At the end of the piston, the actuator is connected with the column through a linear steel bearing and a small steel frame that engages the upper tip of the section with applied pre-stress from a hydraulic jack in order to avoid or reduce possible errors due to relative displacements between the column and the stroke action. The other end of the actuator is connected with a linear steel bearing with a reaction frame.

Two axial load actuators were available. One had a capacity of 500kN and the other had a capacity of 1000kN. For column tests, there are four ways on how the axial load can be applied. The main

significant difference lies in accounting for P- Δ (Berry *et al.*, 2003). The four ways of axial load application for columns. The mechanics of the four types are described and discussed in section 3.4.2. The type that could be setup at the structural laboratories at the Univeristy of Aveiro was Type IV where, the actuator is connected and fixed in all directions with the upper tip of the column and above the point of application of the lateral load such that it moves as a rigid body with the upper tip of the column. The axial load is applied through the rods as post tensioning. The rods are hinged at the upper tip of the actuator and level or below the column foundation interface.

The main disadvantage of this typology is that it creates partial P- Δ effects which are difficult to justify and account. However, the setup is quite simple and one can control the axial load more easily than it can be done for Type I and Type III. In addition, the axial load setup for type I and III is more complex. In some tests (Pasulo *et al.*, 2001), the rods are passed through an internal hollow core along the element. This is more popular for scaled pier models simulating large cross-section prototypes, where the contribution of the centre part of the section does not contribute much to the flexural stiffness of the system. This possibility does not simulate adequately RC columns in buildings and was therefore ignored.

The axial load system is required to be in hyper-static equilibrium, where the load actuator exerts axial load on the column, which is counteracted by post tension force in steel rods. The rods are hinged with the other end of the axial load actuator and hinged with a steel frame at the bottom of the foundation. As shown in figure 3-4 the rods are hinged with the steel frame at the column foundation interface level, in order to limit P- Δ effects by the rod on the column. Since the foundation is very deep, the frame is consequently long, and hence rotation of the frame supporting the rods at the foundation may result. This has an adverse effect on P-D effects and is accounted for in subsequent sections.

The setup for the column specimens allows the foundation section to be particularly larger in the plane of application of the lateral load. In the transverse out of plane direction, the setup is such that the depth of the foundation and the column have to be equal for all the specimens. In practical cases, the section and stiffness of the foundation are bigger in both orthogonal directions. It is possible that this difference between the specimen and the prototype to be reflected in the response and damage development, resulting in a slightly inaccurate simulation. Although a uniform symmetrical column with unidirectional loading is considered as a 2D case, in practice, the column consists in a 3D element being applied with lateral load in a 2D plane. Consequently, the stress-strain distribution of a section in a column is not uniform along the orthogonal direction with the plane of lateral load application (Almeida, 2010). The lack of not having an unrealistic foundation that offers realistic change in stiffness at the column-foundation interface in the orthogonal direction may result in a slightly unrealistic simulation. For non-standardised tests

such as low cycle fatigue tests, Harris *et al.*, (1999) suggest the conduction of similar tests in different setups. However, access to other laboratories where tests could be done with uniform foundations in both directions was not available. Hence, it was not possible to check for reproducibility aspects that may be affected by the issue of the simulation of the foundation in the orthogonal direction.

3.3 Experimental schedule and testing requirements

3.3.1 Scheme of RC Column Experiments

The internal columns at the base of the two frame structures described in section 3.2.3, one designed according to EN1998-1(2004) and the other designed to gravity loads only according to old design codes were considered as reference columns for reference specimen of the testing campaign. The detailing aspect of these two specimens is shown in Table 3-4 and 3-5 as T12 and T14 respectively. These elements were selected because they consist in columns being connected with foundations and therefore can be adequately simulated by the experimental setup and apparatus available. Moreover, columns at the base are more important to the stability of structures, and their performance has a large influence on the overall performance of the RC frame.

The confinement ratio (α), the axial force ratio (ν), the reinforcement ratio (ρ), and the aspect ratio of the column were main parameters that were identified as design variables for the column benchmark tests. These are also the main parameters that were identified to correlate with chord rotation in existing equations for yield and ultimate limit states, and which were discussed in chapter 2. If the distribution of data of the columns in the data set compiled by Berry *et al.*, 2003 is considered, the characteristics of the two selected reference columns can be classified on approximately opposite ends of the range of interest.

Detailing aspects and material properties that characterise these main parameters distinguish T14 from T12. The properties of the seismically under-designed specimen T14 were varied gradually and in turn for different specimens until the properties of T12 are matched. This was done in order to obtain a set of column-foundation specimens that reflect the range of interest of the properties determined from the database. The range of interest is defined by the columns in the database that have realistic significance and which represent seismically designed and non-seismically designed columns. From the outcome of the tests a spectrum of EDPs could be obtained and which corresponds to different properties obtained from the correlating column specimens. The process is illustrated schematically in figure 3-7.

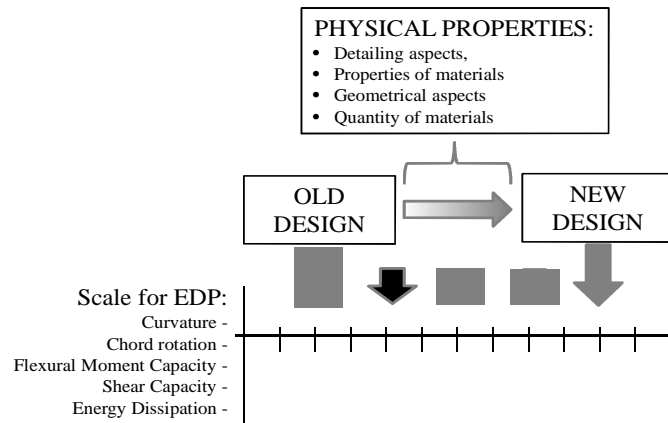


Figure 3-7 Schematic representation for the determination of the experimental schedule for columns.

In total, 19 column specimens were proposed for the column experimental campaign. The variation in geometry, reinforcement detailing and physical parameters for each specimen are shown in Table 4-8. The cross section of both reference columns T12 and T14 was 300x300mm and refer to the base column of the reference structures with a length of 3.4m. Since experiments were to be conducted at single curvature bending, contra-flexure was assumed at mid-height of the whole column. Hence the length of the column specimens T12 and T14 was 1.7m. This height was conserved for all other column specimens. The axial load force for these two specimens was assumed to be 450kN. This was based on the design load of the reference structures. The concrete grades for T12 and T14 were C16/20 and C.

The axial load ratio (v) range of interest in the database varies between 0.1 and 0.6%. T12 and T14 have a value of 0.13% and 0.26% respectively. Test on specimen T7 and T15 with an increased load of 750kN was proposed with $v = 0.44\%$ so that the range of the database is better represented. The confinement ratio of interest of the referred database varies between 0.05 and 0.65. The confinement ratio for T12 and T14 is 0.44 and 0.1 respectively. By introducing additional stirrups, and reducing the spacing the confinement ratio was varied in specimens T2, T3, T9 and T11 as shown in table 4-8 and 4-9. Apart from having a higher axial load ratio with respect to specimen T14, T7 has also a larger confinement ratio. The characteristics of T1-c are similar to T14. Specimen T14 had transverse reinforcement with 90° hooks. Other specimens with increased confinement had transverse reinforcement with 135° hooks. In order to avoid having to deal with specimens with more than two confining variables with respect to T14 and in order investigate the effect of incorporating 135° hooks with respect to 90° hooks, specimen T1-c was proposed with the same characteristics as T14 but having transverse reinforcement with 135° hooks.

The longitudinal reinforcement ratio of interest varies between 1% and 3%. The corresponding values for T12 and T14 are 2.7% and 1% respectively. Additional reinforcement ratio with intermediate values were not introduced. However, specimens with different confining

parameters were considered for these two axial load values in specimens T9, T10, T11 and T2 and T3. T9 and T10 have approximately the same characteristics and properties, yet the distribution of the longitudinal reinforcement in specimen T10 is unsymmetrical as shown in table 4-9. The aspect ratio of interest varies between 2 and 6. Both T12 and T14 have a value of 5.7 since the two specimens have the same shear length and cross-section. A larger cross section was proposed with dimensions 500x300m in order to have a lower aspect ratio for specimens T4, T5 and T8. The confinement ratio and the axial load ratio were also varied in turn with respect to characteristics of T12 and other specimens as shown in Table 3-4 and 3-5.

As described earlier, the setup consisted in a horizontal layout. The specimens were also cast horizontally with the foundation and column being cast in a single cast. However, in practice, the foundation is generally cast days or weeks before the columns, such that when the column is cast, a cold joint forms between the foundation and the column. As result, in order to investigate the effect of having a cold joint on the development of damage, specimen T6 was proposed. This specimen has the same characteristics as T14, yet the foundation and the columns were cast at different times and weeks apart.

Table 3-4 Nominal properties for column specimens.

Element Type	Section	Concrete Grade	Load Ratio	Confinement	Reinforcement Ratio	Lateral Load pattern	Anchorage Detail	Aspect ratio of Element	Test
Column	Square: 300x300	C16/20	v=0.26	a=0.1	Reinf.=1%	LP 1	Continuous	L/h=5.7	T14
				a=0.1	Reinf.=1%	LP 1	Continuous	L/h=5.7	T6
				a=0.1	Reinf.=1%	LP 1	Continuous	L/h=5.7	T1-c
				a=0.22	Reinf.=1%	LP 1	Continuous	L/h=5.7	T2
				a=0.44	Reinf.=1%	LP 1	Continuous	L/h=5.7	T3
	Rectangle:300x500	C16/20	v=0.26	a=0.1	Reinf.=1%	LP 1	Continuous	L/h=3.4	T5
				a=0.22	Reinf.=1%	LP 1	Continuous	L/h=3.4	T8
	Square: 300x300	C16/20	v=0.44	a=0.1	Reinf.=1%	LP 1	Continuous	L/h=5.7	T15
				a=0.22	Reinf.=1%	LP 1	Continuous	L/h=5.7	T7
	Square: 300x300	C16/20	v=0.26	a=0.22	Reinf.= 2.7%	LP 1	Continuous	L/h=5.7	T9
					Reinf.= 2.7%	LP 1	Continuous	L/h=5.7	T10
	Square: 300x300	C16/20	v=0.26	a=0.44	Reinf.= 2.7%	LP 1	Continuous	L/h=5.7	T11
		C30/37			Reinf.= 2.7%	LP 1	Continuous	L/h=5.7	T12
	Square: 300x300	C16/20	v=0.26	a=0.1	Reinf. =1%	LP 2	Continuous	L/h=5.7	T13
					Reinf. =1%	LP 3	Continuous	L/h=5.7	T1-a
					Reinf. =1%	LP 4	Continuous	L/h=5.7	T1-b
	Rectangle:300x500	C16/20	v=0.158	a=0.22	Reinf.=1%	LP 5	Continuous	L/h=3.4	T4
	Square: 300x300	C16/20	v=0.26	a=0.1	Reinf. =1%	LP 1	LS: 35 x D	L/h=5.7	T16-D1
							LS: 75 x D	L/h=5.7	T17-D2


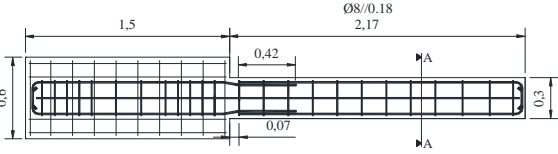
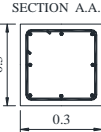
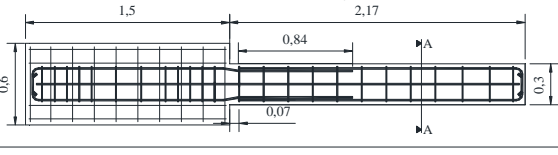
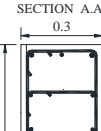

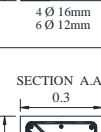
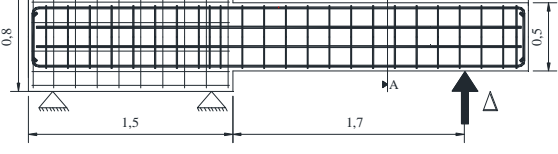
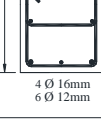

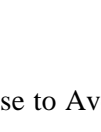
Two specimens with the same properties as T14 but with lap-splicing detailing were considered. T16-D1 incorporates lap-splicing equal to 35x diameter of the longitudinal reinforcement. This corresponds to the requirements of various European codes such as DM 26/03/80, before seismic detailing considerations were introduced. Specimen T17-D2 incorporates lap-splicing equal to 75xdiameter. This is above the minimum requirements according to Fardis (2009).

As described earlier, the tests in the described databases were conducted with different loading protocols. Chapter 2 has discussed how similar columns under different loading protocols or patterns can give different results in terms of EDPs. Three additional different loading patterns were therefore proposed for specimens T13, T1-a and T1-b, apart from a standard loading protocol that was used for all other tests. The characteristics of these three specimens are identical to those of the reference specimen T14. The loading patterns are determined and described in detail in Chapter 5.

Table 3-5 Detailing and nominal properties for the column specimens.

TEST	AXIAL FORCE	MECHANICAL PROPERTIES	LOAD PATTERN	LONGITUDINAL SECTION	CROSS SECTION
T15	750kN	Stirrups A235NL Longitudinal Reinforcement: A400NRSD Concrete: C16/20 Cover: 2cm			SECTION A.A.
T6	450kN				
T14					
T1-a					
T1-b					
T13					
T1-c					
T2					
T3					
T7			750kN		
T12	450kN	Stirrups A400NRSD Longitudinal Reinforcement: A400NRSD Concrete: C30/37 Cover: 2.5cm			SECTION A.A.
T11		Stirrups A400NRSD Longitudinal Reinforcement: A400NRSD Concrete: C16/20 Cover: 2.5cm			SECTION A.A.
T9		Stirrups A235NL Longitudinal Reinforcement: A400NRSD Concrete: C16/20 Cover: 2cm			SECTION A.A.
T10		Stirrups A235NL Longitudinal Reinforcement: A400NRSD Concrete: C16/20 Cover: 2cm			SECTION A.A.

...continued

T16 D1	450kN	Stirrups A235NL Longitudinal Reinforcement: A400NRSD Concrete: C16/20 Cover: 2cm			
T17 D2					
T4					
T8					
T5					

3.3.2 Construction of specimens and tests on the properties of materials

The specimens were constructed in the pre-fabrication plant Pavicentro in Eixo close to Aveiro (www.pavicentro.pt). The first steps in the specimen production process consisted in the selection of steel and the design of concrete mixes that could ensure actual capacity that corresponds with and very similar to the characteristic values of the materials specified for each specimen.

The steel utilised for the construction of the specimens referred to EN 10080 (2005). Since the experiments were carried out in Portugal, local materials were used and hence the steel utilised was also according to LDC41-10 (2010). As indicated earlier, seven different steel reinforcements had to be selected. These included 8mm, 12mm, 16mm, 20mm and 25 mm ribbed bars A400NRSD, 12mm ribbed bar A500NRSD and 8mm smooth bar A235NL and Tests for the yield and tensile strength of steel were conducted according to EN ISO 6892-1 (2009) and requirements by EN ISO 15630-1 (2010) on samples that were taken across batches of reinforcement. The reinforcement was selected from batches that showed uniform characteristics and similar to the nominal characteristics specified. For each reinforcement type, the number of samples tested was a function of the quantity of reinforcement required. The samples were selected at random and from over the whole length of each specific batch.

Figure 3-8a shows the general setup that was used for the tensile tests on steel, and figure 3-8b shows the instrumentation on a typical reinforcing bar. A 300kN actuator was used, and the tensile force was measured through 300kN or 100kN load cells depending on the diameter of the reinforcing bar and the associated sensitivity required.

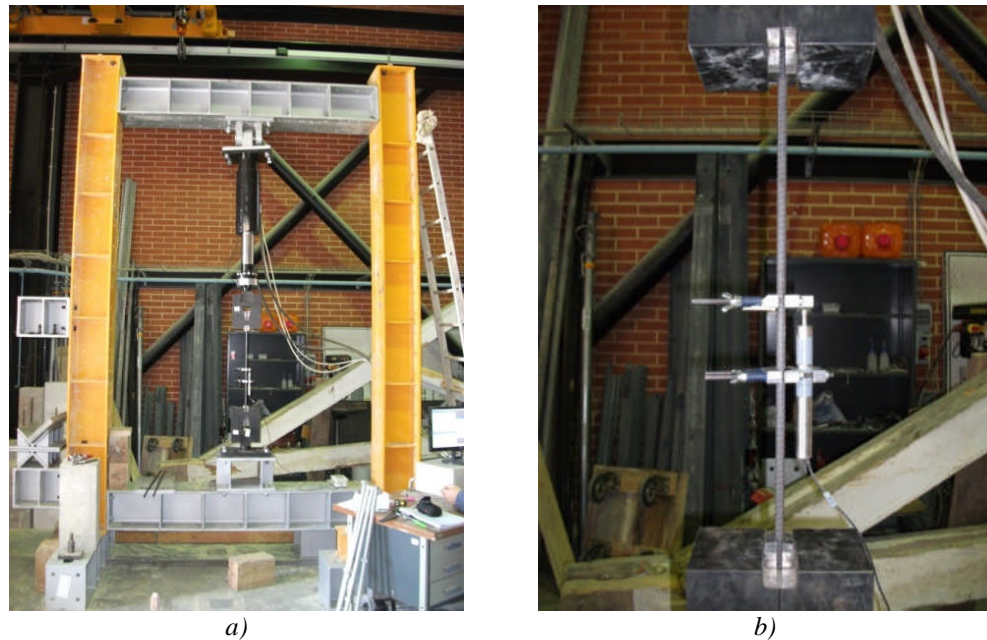


Figure 3-8 a) A general layout of the apparatus for the tensile test of steel reinforcement; b) Measurement of deformation by an LVDT on a 12mm A400NRSD reinforcing bar sample.

Deformation was measured by the controller over the whole length of the specimen and by 25mm LVDT over the central 5d of the bar according to EN ISO 6892-1(2009). Figure 3-9 shows tested reinforcing bars from each different typology required. The shape and spacing of the ribs is typical of the reinforcement used in Portugal and possibly also in Spain LDC41-10 (2010), and differs from other seismic European countries as discussed in Chapter 2. The grips of the testing facility could not take bar diameters larger than 20mm, and hence it was not possible to test 25mm bars. For this bar, characteristic values were assumed.

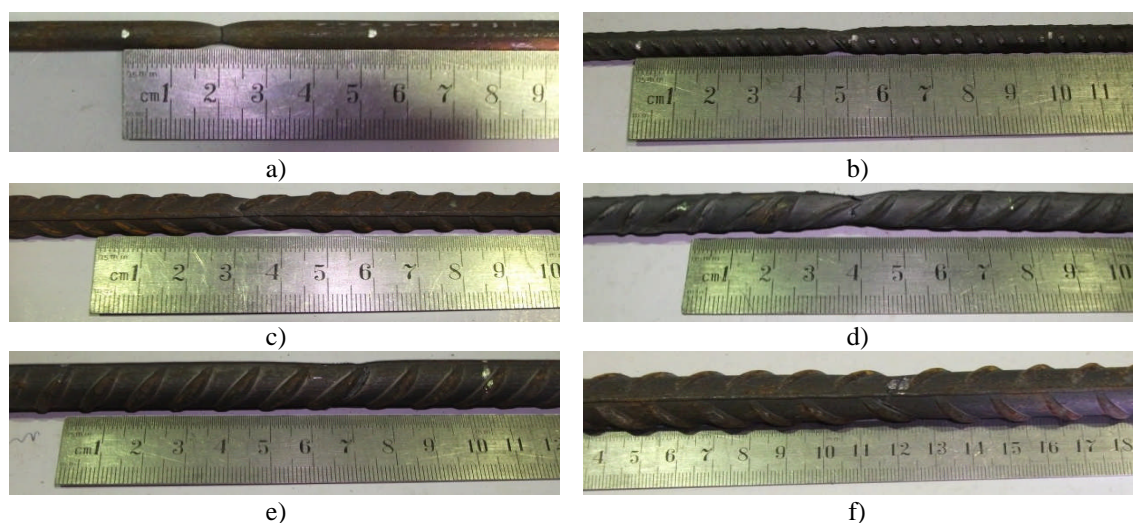


Figure 3-9 Reinforcement samples used for the construction of the specimens: a) 8mm A235NL; b) 8mm A400NRSD; c) 12mm A400NRSD; d) 12mm A500NRSD; e) 16mm A400NRSD; f) 20mm A400NRSD.

Table 3-6 Properties of the reinforcement that is used for the construction of the specimens.

		A235NL	A400NRSD	A400NRSD	A500NRSD	A400NRSD	A400NRSD	A400NRSD
		8mm Ø smooth	8mm Ø ribbed	12mm Ø ribbed	12mm Ø ribbed	16mm Ø ribbed	20mm Ø ribbed	25mm Ø ribbed
E_s	MPa	Max.	214170	235714	225908	232042	207314	235670
		Avg.	204850	208285	195233	192820	192357	196647
		Min.	190385	180043	165775	171762	178939	172294
		S.D.	8075	20837	20142	27760	12687	21221
	%	CoV	3.9	10.0	10.3	14.4	6.6	10.8
f_{ys}	MPa	Max.	433	489	459	536	484	478
		Avg.	397	457	426	532	471	474
		Min.	372	456	400	533	462	472
		S.D.	21	21	17	2	7.52	2.23
	%	CoV	5.3	4.6	3.9	0.4	1.6	0.5
f_{ts}	MPa	Max.	510	570	572	631	583	588
		Avg.	477	564	557	628	581	586
		Min.	450	553	547	627	579	584
		S.D.	22	7	7	2	2	1
	%	CoV	4.6	1.2	1.2	0.3	0.3	0.2
f_{ts} / f_{ys}	MPa	Max.	1.41	1.31	1.41	1.18	1.26	1.24
		Avg.	1.41	1.24	1.26	1.18	1.23	1.24
		Min.	1.15	1.16	1.18	1.18	1.20	1.23
		S.D.	0.09	0.06	0.08	0.00	0.02	0.01
	%	CoV	6.2	4.6	10.3	0.1	1.7	0.6
ε_{ys}	MPa	Max.	0.0025	0.0036	0.0035	0.0034	0.0026	0.0330
		Avg.	0.0022	0.0029	0.0025	0.0028	0.0023	0.0270
		Min.	0.0018	0.0026	0.0018	0.0024	0.0021	0.0330
		S.D.	0.0002	0.0004	0.0005	0.0004	0.0002	0.0023
	%	CoV	9.1	13.5	19.4	14.8	8.7	8.5
ε_{ps}	MPa	Max.	0.028	0.046	0.031	0.028	0.030	0.033
		Avg.	0.019	0.035	0.019	0.026	0.028	0.028
		Min.	0.015	0.013	0.011	0.025	0.024	0.027
		S.D.	0.005	0.013	0.007	0.001	0.002	0.002
	%	CoV	26.2	37.6	36.1	4.1	7.3	8.1
$\varepsilon_{ps} - \varepsilon_{ys}$	MPa	Max.	0.026	0.043	0.029	0.025	0.028	0.031
		Avg.	0.017	0.032	0.016	0.024	0.025	0.026
		Min.	0.013	0.009	0.009	0.022	0.022	0.024
		S.D.	0.005	0.013	0.007	0.001	0.002	0.003
	%	CoV	29.6	42.3	40.9	6.4	7.6	10.1
ε_{s-max}	MPa	Max.	0.16	0.17	0.17	0.12	0.15	0.16
		Avg.	0.13	0.15	0.13	0.12	0.14	0.15
		Min.	0.10	0.12	0.12	0.11	0.13	0.15
		S.D.	0.03	0.02	0.01	0.00	0.01	0.00
	%	CoV	21.5	11.7	9.2	3.8	3.6	2.0
ε_{us}	MPa	Max.	0.23	0.21	0.23	0.20	0.24	0.25
		Avg.	0.16	0.19	0.18	0.16	0.19	0.21
		Min.	0.12	0.17	0.13	0.13	0.16	0.18
		S.D.	0.05	0.01	0.03	0.03	0.03	0.03
	%	CoV	28.1	7.6	16.4	20.2	13.7	12.4

Max. = Maximum; Min. = Minimum; Avg.= Average; S.D.= Standard Deviation; CoV = Coefficient of Variation

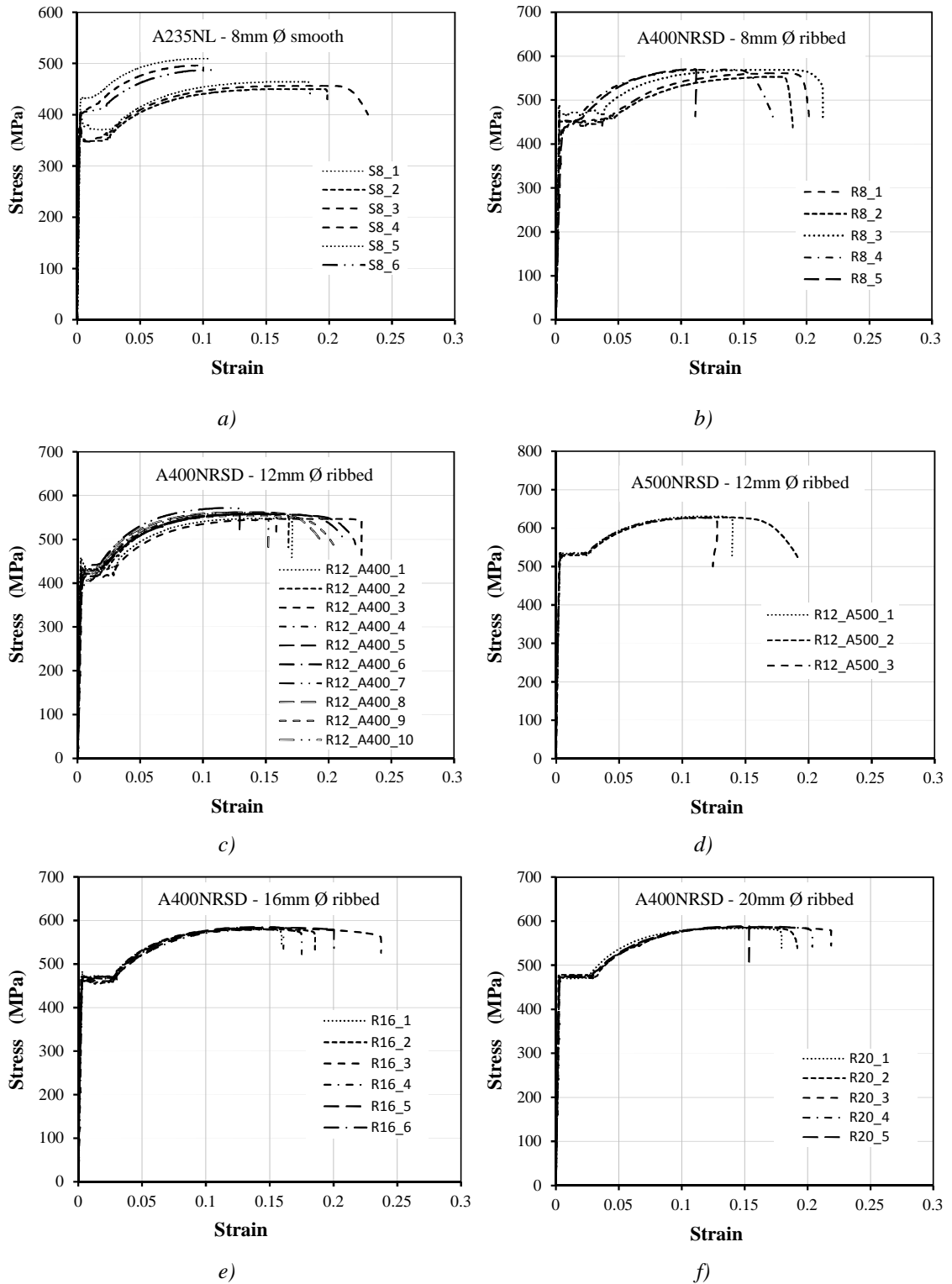


Figure 3-10 Stress strain relationship for: a) 8mm A235NL; b) 8mm A400NRSD; c) 12mm A400NRSD ; d) 12mm A500NRSD; e) 16mm A400NRSD; f) 20mm A400NRSD.

The comparison of the computed material properties for each bar typology is given in Table 3-6 and figure 3-10. These were derived from the stress-strain constitutive relationship of each tested sample for each corresponding reinforcement type. In general, the mean yield strength of the reinforcement that is used for the construction of specimens that are supposed to simulate old structures which are not seismically designed, are smaller than the typical values referring to the

era when seismic codes were introduced. The latter data compiled in Fardis (2009). For the larger diameter bar, 20mm, the mean yield strength is closer to the value given in the survey, and hence makes it an adequate representation for the reinforcement that is used in specimen T12 that is used to simulate a seismic design. For all the reinforcing types, with the exception of 8mm smooth bars, the tensile force and the associated f_t/f_y were found to be very large. This is due to the high carbon content that is used in current commercial steel. This was not characteristic of older unseismically designed structures where mild steel was generally used. The main issue in having a higher tensile strength is that this may affect the sequence of damage evolution where the occurrence of rupture is delayed.

Apart from controlling the consistency of reinforcing steel properties, it was also important to control the geometric schedule and mounting of the reinforcement in order to ensure that the mechanical properties and parameters with which each specimen was designed would be realistically represented. Figure 3-11 shows some details of the reinforcement cage for column-foundation specimens. The reinforcement close to and including the foundation-column interface is the most vital for the deformation behaviour of the specimens and hence was thoroughly checked, particularly the transverse reinforcement spacing, cover, and positioning of the longitudinal reinforcement. The reinforcement was adequately tied in order to avoid unnecessary movement or floatation during the concrete casting.

For the construction of the specimens, two grades of concrete were utilised, C16/20 and C30/37 (EN1992-1-1,2004). As indicated earlier, all the specimens with the exception of one were designed with low strength concrete. Low strength concrete was typical of old structures particularly before the introduction of seismic codes or structures which were or still are constructed with sub-standard materials as discussed in Chapter 2. Mix design for such concrete referred to mixtures possibly with low cement content, and with aggregate that did not conform with current code requirements provided by EN12620 (2013) and EN206-1(2000). It was not possible to obtain sub-standard aggregate and for the sub-standard concrete reference is only made to its strength. Hence for the simulation of concrete referring to old structures, the mix design was based on the low characteristic strength required equivalent to concrete grade C16/20 referring to current codes at the time of construction EN12620 (2009) and EN206-2 (2000). The mix design composition of grade concrete C16/20 is shown in table 3-7. The cement used was CEMII32.5/B-L N (EN 197-1-2000). It was not possible to go for CEMI where the evolution of strength with time could have been more controllable, and hence obtain samples with a more uniform strength. It was however possible to go for a 32.5N cement that ensures a slower development of strength and low actual concrete strength at the time of testing.



Figure 3-11 Details of the reinforcement layout and form work for various columns specimens: a) T14; b) T4; c) T6; d) T10; e) T12; f) T16-D1.

Table 3-7 Quantity of material required for the production of concrete C16/20.

Composition C16/20	Quantity (kg) / m ³ of concrete
Fines - 20/2	260
Sand - 30/2	600
Coarse Aggregate 1 - 8/12	460
Coarse Aggregate 2 - 12/20	700
Cement CEMII 32.5 N	240
Water	108

For the mix design, the geometric and granular properties of the aggregate were determined according to EN933-1(1997). Figure 3-12 shows the four granular classifications of aggregate used. The volumetric mass and the water absorption were determined according to EN 1097-6 (2000). The characteristics of the aggregate are shown in Table 3-8.

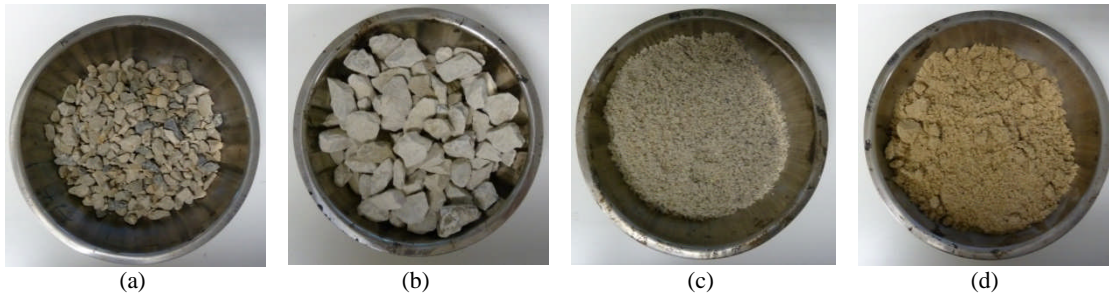


Figure 3-12 Aggregate for the concrete mixture: a) Coarse aggregate I; b) Coarse aggregate II; c) Sand; d) Fines.

For the concrete grade C30/37 referring to sample T12 a standard mixed design which was commonly used in the prefabrication plant was utilised. The proportions for the concrete mix are shown in table 3-9.

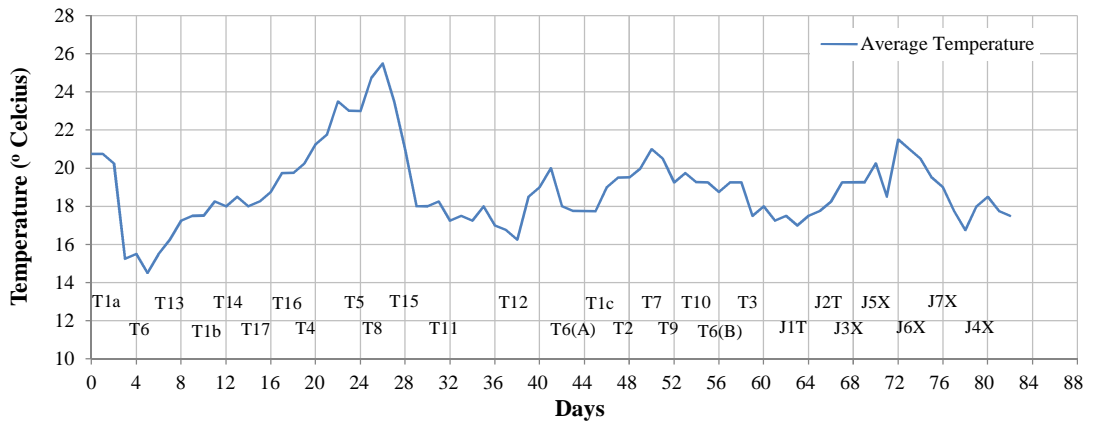
Table 3-8 Characteristics of aggregate that is used for C16/20 concrete.

Aggregate	Fines Modulus F.M.	Maximum Dimension D (mm)	Minimum Dimension d (mm)	Volumetric Mass ρ_{rd} (g/cm ³)
Fines	2.1	8	0.062	2.62
Sand	3.19	4	0.125	2.59
Coarse Aggregate 1	6.72	16	4	2.61
Coarse Aggregate 2	7.49	31.5	8	2.63

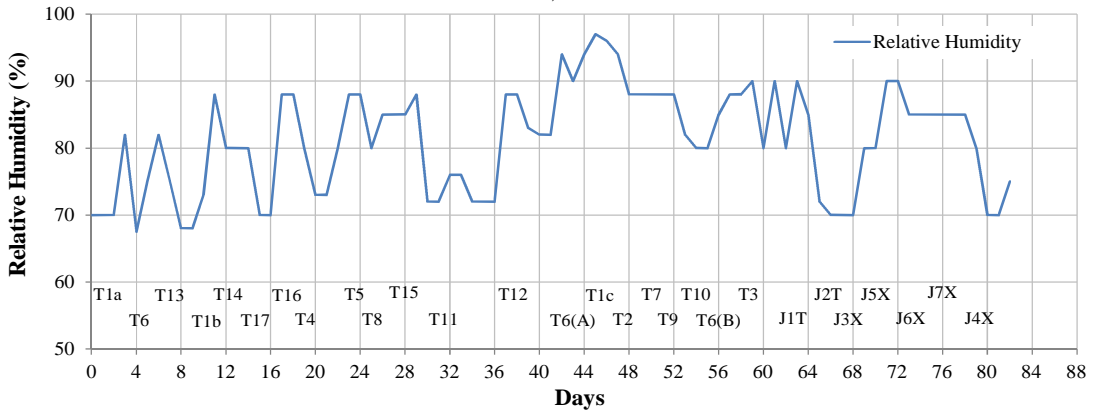
Table 3-9 Quantity of material required for the production of concrete C30/37.

Composition C30/37	Quantity / m ³ of concrete
Fines - 20/2	200 kg
Sand - 30/2	585 kg
Coarse Aggregate 1 - 8/12	305 kg
Coarse Aggregate 2 - 12/20	830 kg
Cimento CEMI 42.5 N	310 kg
Sika Viscococrete 3002HE	2.3 lit.

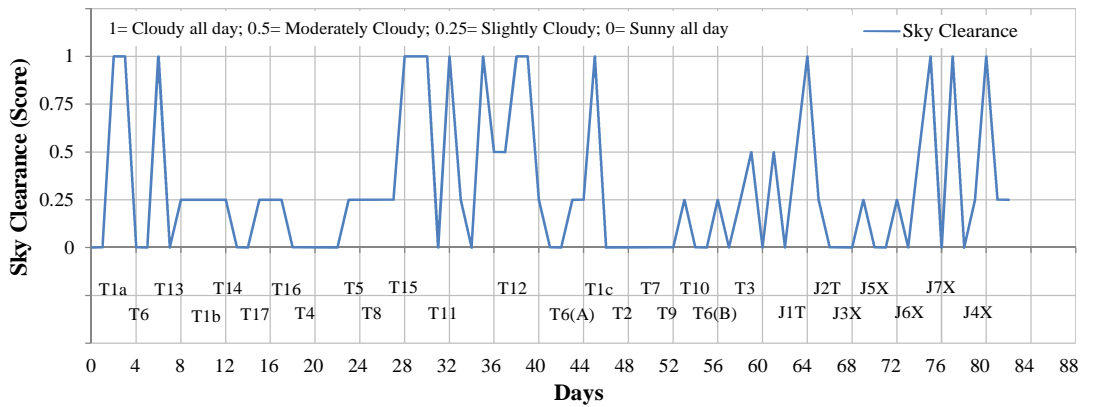
The specimens were not cast together but one at a time. One steel formwork was used for each different geometrical shape of specimen. This ensured geometrical uniformity between specimens of the same category. Since the specimens were cast in a prefabrication plant, the production and casting of concrete was done in a well-regulated environment.



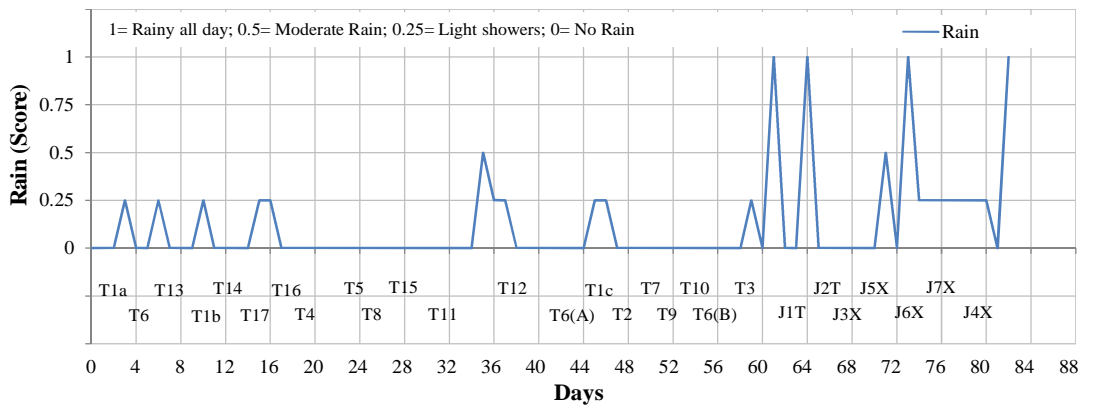
a)



b)



c)



d)

Figure 3-13 Monitoring of the climatic conditions with respect to casting and curing of the testing specimens: a) Average temperature; b) Average relative humidity; c) Sky clearance; d) rainfall.

However controllable the mixing plant was, variations in different batches from day to day are inevitable. Slump tests were performed following EN12350-1 (2009) in order to monitor the consistency of the concrete mix of each specimen. Samples from different batches of each specimen cast were collected following EN12350-1 (2009). Samples for ten 300x150mm and one 200x100mm concrete cylinders (EN12390-1:2000) were also collected for each specimen for splitting and compression tests. The casting process took about 3 months and hence different specimens were cast in different climatic conditions.

Concrete with cement 32.5N characteristics (EN 197-1-2000) develops strength at a slower rate compared to other classifications. Hence while ensuring approximately uniform time for all specimens between casting and testing having uniform curing conditions within reasonable control was also important. Track of the climatic condition was kept as shown in figure 3-13, and attention was paid to ensure that the specimens were on average exposed to the same climatic conditions. The cylinder samples were not cured in a climatic chamber, but were exposed to the same climatic conditions of their respective RC specimens. These measures were taken in order to reduce possible variability in the concrete properties of different samples having the same nominal properties. The reliability of the tests on the RC specimens as benchmark cases depends on this variability and the ability to assess it. Variability will have to be accounted statistically as shown in chapter 6, but the smaller it is, less is the uncertainty associated with it.

In order to further monitor and control the development of strength, compression tests on concrete cylinders at 7 days and 14 days curing were also performed. The compression test on the cylinders as a reference to the actual strength of the testing specimens were not performed after 28 days as normally required by the code (EN 1992-1-1: 2004) but closer to the date of the RC specimen test, which was always about 3 months from the casting date. This measure was taken so that the results of the compression strength of cylinders would be more representative of the state and strength of the concrete in the RC specimen during the low cycle fatigue test.

For each RC specimen six 300x150mm and one 200x100mm concrete cylinder samples were tested in compression. The compression tests were performed according to EN 12390-3 (2002). The deformation was also monitored by a compressometer having 3 LVDTs to measure deformation. Cyclic tests on some of the concrete cylinder samples were also performed (results in Appendix B). The scope and the results of the cyclic tests and corresponding computed stress-strain relationships are discussed in Chapter 2. Splitting tests were performed on three 300x150mm concrete cylinder samples following EN12390-6 (2009). Table 3-10 shows the collective compression and splitting test results for the column specimens, based on the 300x150mm concrete cylinder samples. In spite of the control measures taken, there is some variability in the strength of the concrete across the specimens with nominal concrete C16/20. The average compression strength across all the column specimens was 18MPa, while for beam-

column connection specimens this was 14MPa. Among the column specimens, T5 had the lowest mean compression strength at 13.5MPa while T3 had the highest value with 25.1MPa. The standard deviation for the mean of the compression strength of the column specimens with nominal concrete grade C16/20 was 3MPa and the coefficient of variation 16.6%. The standard deviation and coefficient of variation for all the means were 1.46 and 10.1% respectively. These values were much lower than the values for column specimens. The overall mean splitting test value for specimens with nominal concrete C16/20 was 2.0MPa for column specimens. The associated standard deviations was 0.23, while the coefficient of variations was 11.3%. The splitting test shows more consistent results, however, as discussed earlier, its significance for the purpose of this research is not as that of compression strength. The mean compression strength and splitting test values for specimen T12 were within characteristic expectations for concrete grade C30/37.

Table 3-10 Compression strength and splitting test results for column specimens.

Column Specimen	T1-a	T1-b	T1-c	T2	T3	T4	T5	T6	T7	T8	T9	T10	T11	T12	T13	T14	T15	T16-D1	T17-D2
<i>Compression Test: BS EN 12390-3 (2002)</i>																			
Max	19.5	19.0	18.3	25.8	26.9	17.0	14.5	18.3	20.0	15.7	19.6	22.0	16.9	40.7	19.5	16.7	18.4	21.9	16.9
Mean	17.9	17.0	17.9	24.2	25.1	15.4	13.5	16.7	19.4	14.8	18.8	20.6	15.6	37.2	17.6	15.7	17.1	20.4	15.6
Min	17.0	15.4	17.6	23.3	22.2	12.6	12.6	13.8	18.5	13.7	18.0	18.7	13.7	34.5	15.0	14.9	16.2	18.3	13.6
S.D.	1.0	1.3	0.2	0.8	1.7	1.3	0.6	1.7	0.5	0.7	0.6	0.9	1.3	1.8	1.6	0.7	0.8	1.5	1.1
CoV.	5.4	7.6	1.4	3.4	6.7	8.4	4.4	10.3	2.8	4.6	2.9	4.5	8.0	4.7	9.0	4.3	4.6	7.4	7.2
<i>Splitting Test: BS EN 12390-6 (2009)</i>																			
Mean	2.1	2.0	2.0	2.5	2.5	1.6	1.8	1.7	2.3	2.0	2.3	2.1	2.0	3.5	2.0	1.8	2.0	2.1	1.8

3.3.3 *Data acquisition and instrumentation*

The input load by the lateral actuator onto the RC specimen can be either force controlled or deformation controlled (Harris *et al.*, 1999). In the first approach the load is fed into the system as constant small increments of force until a target force value is reached, whereas in the latter, load is fed into the system as constant small increments of displacement until a target displacement is reached. In both cases, the direction, speed and load increment are controlled by servo-valves and hydraulic control valves. Whether force or displacement controlled, the increment should be small enough in order to have negligible dynamic effects (Sullivan *et al.*, 2002). Although full dynamic conditions are desirable, with partial dynamic effects it would not be possible to interpret the outcome of the results. The increment should also be low enough in order to avoid thermal effects and to be able to define damage states in terms of force if force controlled or in terms of displacement if displacement controlled (FEMA, 2007). However, the load increment should be large enough so that the test could be carried out in a reasonable timeframe. The load increment should be large enough to avoid creep effects, stiffness relaxation, and other effects of low cycle fatigue that are unlikely to be experienced by real components in buildings other than those referring to dynamic effects (FEMA, 2007).

The actuators did not have servo-valves and the controlling system did not have feedback control over the feeding signal and hence controlling in force would have been difficult.

Under force control, the hydraulic system would exert additional pressure in order to meet a higher incremental force value. After the maximum force capacity of the specimen is reached, the hydraulic pressure continues to increase, creating an unbalanced situation as the specimen's force capacity is exceeded and cannot offer higher resistance in terms of force to equilibrate the pressure. Hence, the specimen would have continued to deform until ultimate collapse or until the system is manually stopped. In case of deformation control, the specimen would be driven to the required deformation irrespective of its state and capacity. Control through deformation was therefore a more effective and practical approach and was adopted for all the tests of the campaign. The deformation velocities adopted varied between 0.1mm/s and 1.0mm/s depending on the level of target drift required for each cycle. With such deformation velocities the strain that could possibly develop in the specimens was estimated to be in the range of $0.00002s^{-1}$. As discussed in chapter 2, this value is within quasi-static behaviour. On considering control testing requirements, the expected rate of damage development and the variable sensitivity of the instrumentation, a data acquisition frequency of 20Hz was adopted for all the tests.

The parameters were identified earlier that had to be determined from the quasi-static tests. Force based parameters moment and shear distribution can be determined through data acquisition from load cells. Displacement based parameters lateral deformation, chord rotation, curvature and the plastic hinge length could be derived from data acquisition of potentiometers LVDTs and strain

gauges. Mixed parameters such as energy dissipation require data from both types of sets of instrumentation. Figure 3-14 shows the general deformation instrumentation layout for the column-foundation specimens. Load cells were used to monitor action by the axial load actuators and reaction forces by the specimens and the restraining steel frames. The position of the load cells is shown in the specimen layouts. Table 3-11 shows the instrumentation code and the type of instrument that is used for each type of specimen. Strain gauges were not adopted mainly for two reasons. The control and acquisition system was based in voltage while most affordable strain gauges are based in resistance and require additional device to convert from resistance to voltage. Strain gauges measure localised values and may not be representative of the deformation of the whole section. Deformation in concrete is mainly concentrated in cracks and unless the crack passes through a strain gauge, most of the deformation would not be recorded. To mount strain gauges on reinforcement, the surface requires smoothening. This would involve reducing the cross-sectional area of the reinforcement and removing ribs of reinforcement in critical sections which could have impact on bond and overall strength capacity. Moreover, mounting strain gauges is not an easy task and some may get damaged during concrete casting or even during the experiments (Harris *et al.*, 1999).

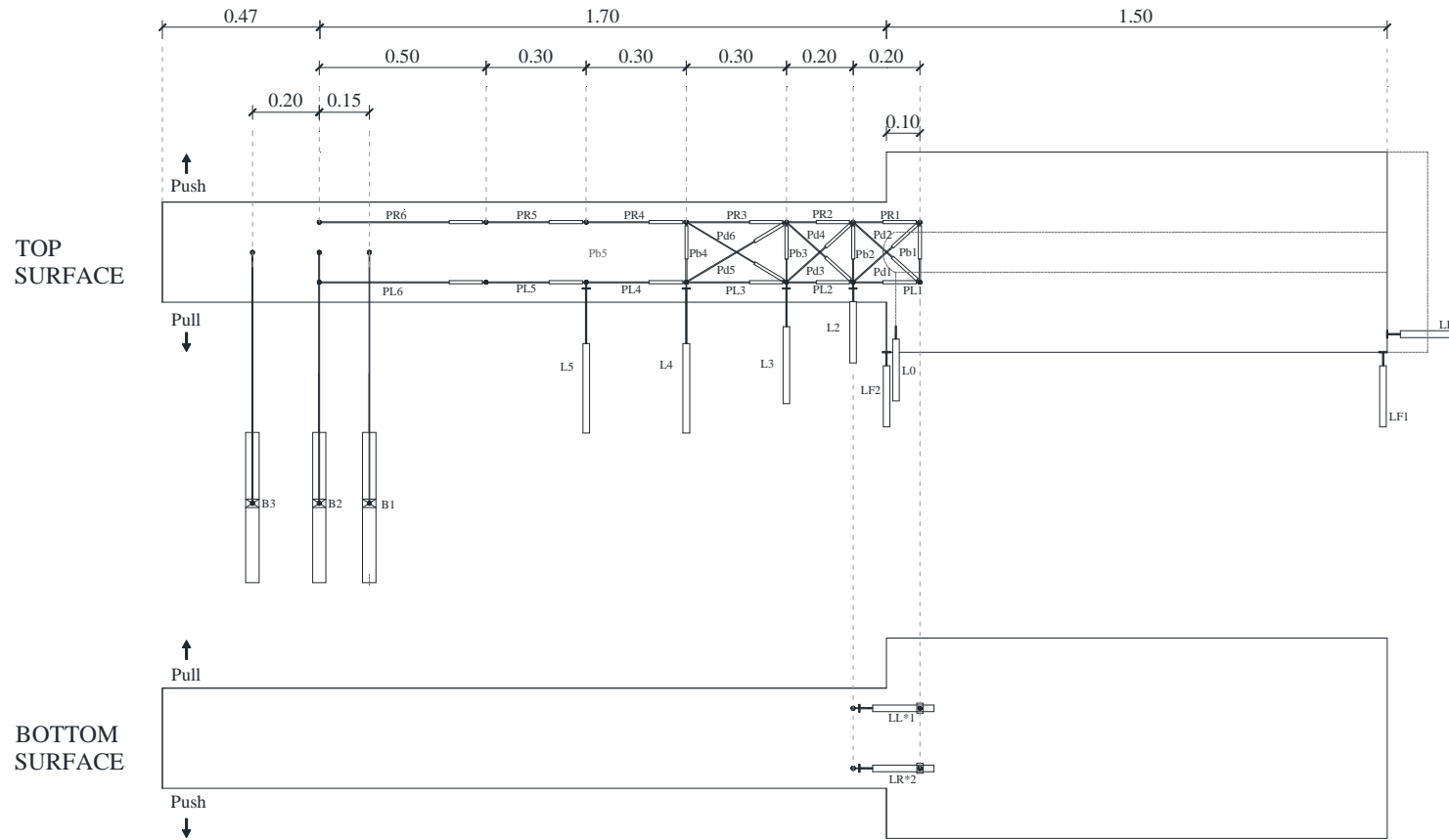


Figure 3-14 A general layout of the instrumentation that measures the deformation of column-foundation specimens.

Table 3-11 The instruments used to measure forces and deformation according to the column and beam-column connection schedules.

Column			
Instrument	Range	Units	T1-a; T1b; T1c; T2; T3; T4; T5; T6; T7 ^{note1} ; T8 ^{note1} ; T9; T10; T11; T12; T13; T14; T15 ^{note1} ; T16-D1; T17D2
Potentiometer	25	mm	Pb3; Pb4; Pd5; PD6; PL3; PL4; PL5; PL6; PR4; PR5; PR6
	50	mm	PR1; PR2; PL1; PL2; Pb1; Pb2; Pd1; Pd2; Pd3; Pd4
Bridge Potentiometer	400	mm	B1; B2; B3
String Potentiometer	750	mm	
Displacement Transducers (LVDT)	10	mm	
	25	mm	LF1; LF2; LF3; L2; LL*1; LR*2
	100	mm	L0; L3
	150	mm	L4; L5
	250	mm	
Load Cell	1000	kN	C2 ^{note1}
	500	kN	C2
	200 ^{note2}	kN	C1
	300	kN	
	100	kN	
Note:	^{note1} For T7, T8 and T15, since an axial load of 750kN was used		

Shear deformation, curvature, chord rotation and energy dissipation were required to be identified with the development of damage along the shear span of the elements. Hence, for each specimen, the shear span was divided in sub-elements and different types of LVDTs and potentiometers were used to measure deformation of these sub elements. The length of each sub-element was such that it is approximately a multiple of the depth of the cross section of the element being monitored. The larger the expected deformation within the sub-element, the shorter is the length of the sub-element, and the larger is the deformation capacity and sensitivity of the measuring LVDT or potentiometer.

Figure 3-15 show the mounting of the various displacement instruments used, and figure 3-16 shows details of the general layout for column-foundation specimens. Instrumentation was mounted on the upper surface only as it was quite difficult to work against gravity and install instrumentation on the lower surface. For sample T13, two LVDTs LL*1 and LR*1 were installed also at the lower surface of the column-foundation interface to investigate whether there are any

general losses or adverse effects in monitoring one surface only. The instruments measure deformation between two reference points at the boundaries of each sub-element, and at about 60mm from the edge of the element. This ensures that the measurements are taken inside the core, but close to the longitudinal reinforcement

Deformation was also measured externally relative to stationary absolute points. These are important to monitor the global deformation and displacement of the specimens. Moreover, monitoring of external deformation is relevant in accounting for undesired deformation that gives rise to experimental errors such as rotation of the foundation for column-foundation specimens, and rotation of the rod anchorage at the column foundation interface (figure 3-16 and 3-17).

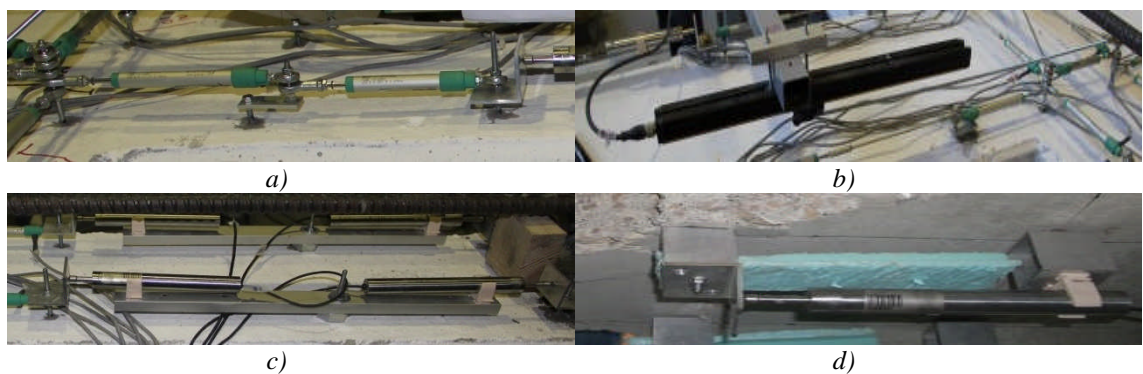


Figure 3-15 Instrumentation that was used to measure the deformation of the specimens during testing, and some of the corresponding mounting setups: a) Potentiometer (Gefran) measuring deformation in column, and deformation close to and including the node panel joint; b) Bridge potentiometer (Truck) measuring lateral movement of the specimens ; c) LVDTs on the upper surface of column specimens; d) LVDTs on the lower surface of column T13.

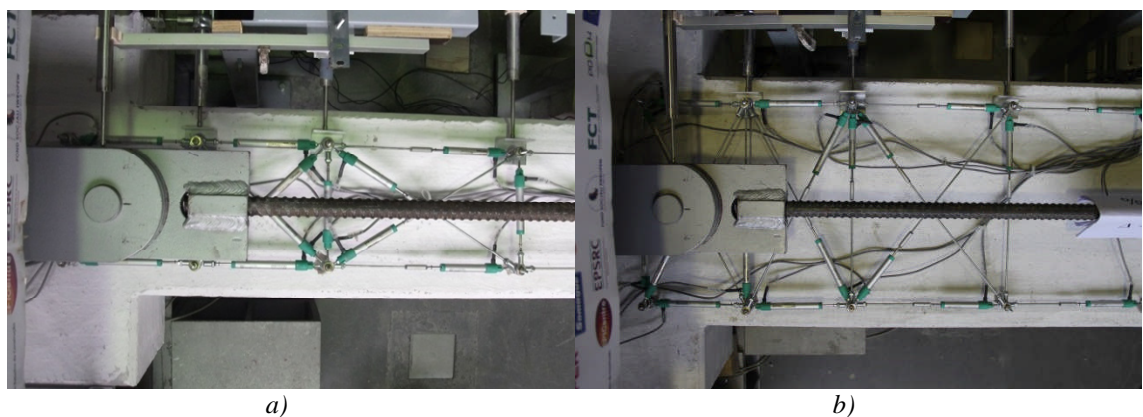


Figure 3-16 General overview of the deformation instrumentation in critical areas of: a) column-foundation specimens with 300x300mm sections; b) column-foundation specimens with 500x300mm sections.



Figure 3-17 Monitoring that can be a source of error: a) Rotation of the foundation in column specimens; b) Rotation of the rods and frame connection at the column-foundation interface.

3.4 Data processing requirements and diagnostics

3.4.1 Definition of General Parameters

There are various definitions in literature that define the state at which yielding occurs. A typical definition is given as the instance at which a second significant change in stiffness of concrete occurs at the onset of yield in the extreme tension reinforcement (Priestley et al., 2007).

In the derivation of empirical formulas of yield rotation, Biskinis *et al.*, (2010a) identifies section yielding with the yielding of the tension reinforcement. Together with steel yielding, Haselton et al., 2008 considers also the instant when concrete begins to crush significantly if it occurs before. Considering concrete crushing is very subjective and depends on the judgment by the individual since the concrete becomes non-linear much before the yielding of the longitudinal reinforcement and hence cycles occurring before yielding may have effect on the change in stiffness before yielding. On the consideration of yielding based on steel, Fardis (2007) highlights that on having members with high axial load ratio, apparent yielding is observed in the moment-curvature diagram as a distinct downward curving of the end section. This is due to the non-linearity of the concrete in compression, before the steel yields in tension.

Another definition of yielding is generally based on the plasticity model that is generally used for design purposes, and which refers to a bi-linear approximation of the capacity curve. In the definition by Priestley *et al.*, (1992), yielding is the point where the tangent from the maximum force intersects with the chord passing through the origin and the point where either concrete reaches a strain value of 0.002 or the longitudinal reinforcement yields. Alternatively, the elastic branch can be assumed to pass at a point $\gamma_y F_{max}$ on the pushover envelope. The fraction multiplier γ_y varies in the range of 0.7 (Petrini *et al.*, 2004). If the ultimate occurs before the first yield of the section such as in pure shear failure, γ_y is assumed to be 0.95 (Camarillo, 2003; Berry *et al.*, 2003). Another approach consists in having a minimum area between the elastic-plastic curve and the envelope of the response. The area above the elastic-plastic curve should also be equal to the

area below. Figure 3-18 shows various possibilities of how this can be computed, based on whether equilibrium of areas is considered until the maximum force or whether the ultimate point is considered.

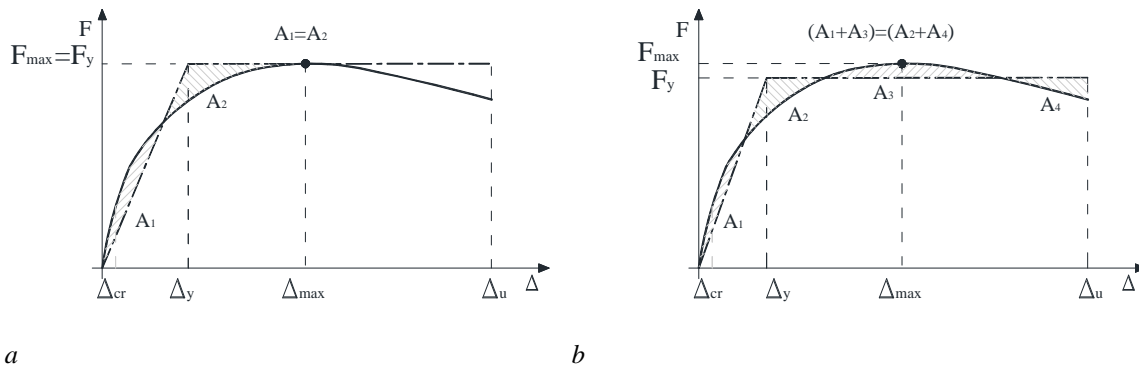


Figure 3-18 Determination of yielding based on equilibrium of minimum areas: a) until the maximum force, b) until the ultimate.

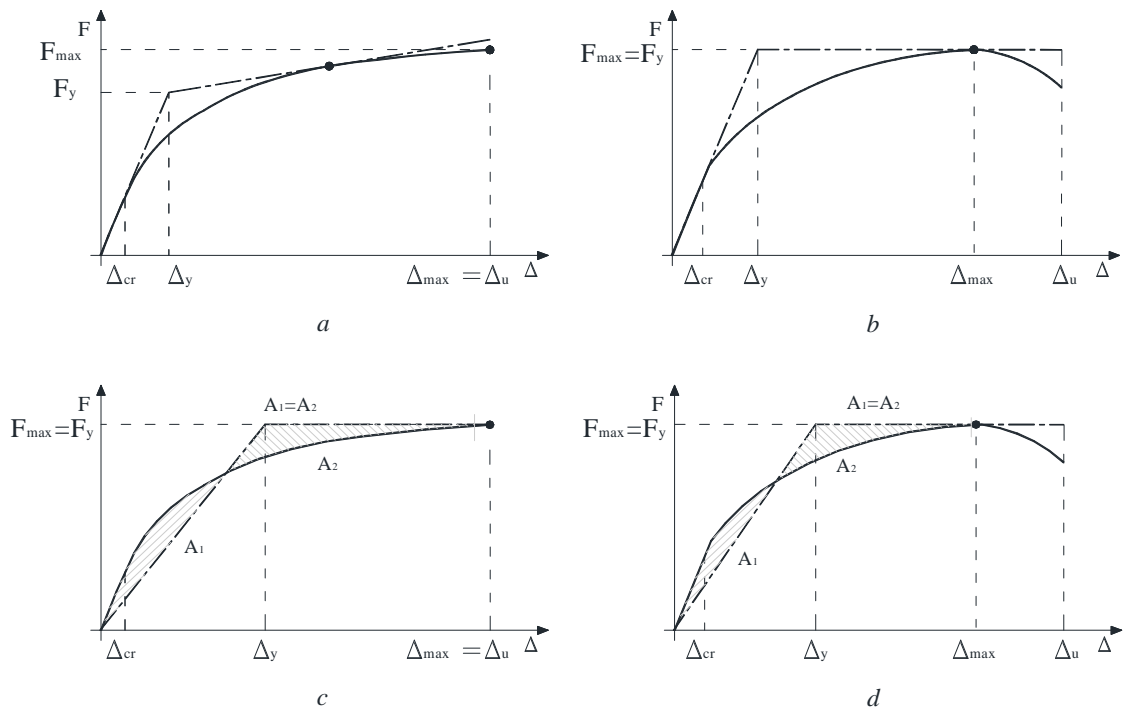


Figure 3-19. a) Determination of yielding based on equilibrium of minimum areas: a) until the maximum force, b) until the ultimate.

However, the interpretation of yielding can be problematic. Figure 3-19 shows two possible situations. In figure 3-19a and 3-19c, the maximum force coincides with the ultimate. In figure 3-19b and 3-19d the maximum is slightly away. While in figure 3-19a, the yield force is realistic, in the others it is overestimated. In figure c and d the position of the maximum has a direct influence on the definition of yielding, even though the initial part of the envelopes are similar.

The ultimate displacement can be expressed either based on the occurrence of a damage phenomenon or based as a percentage of strength reduction. The first is very difficult to define. The ultimate displacement is generally taken as the displacement beyond which strength decay exceeds 20% of the maximum recorded strength (Saatcioglu, 1991) shown in figure 3-20.

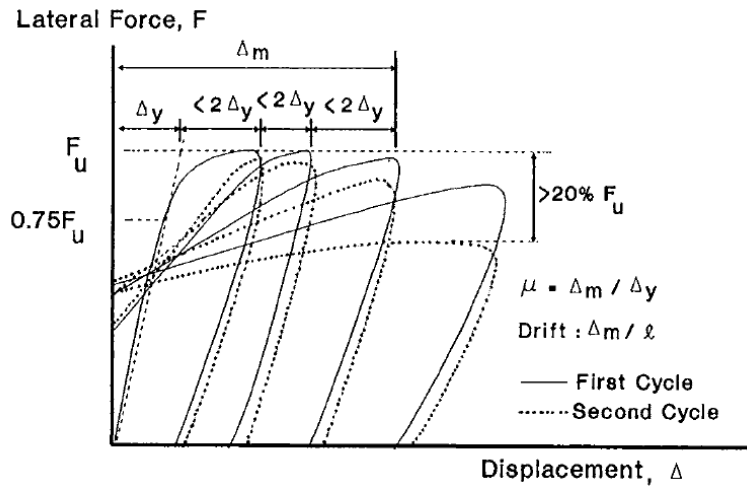


Figure 3-20 The interpretation of ultimate displacement as defined by Saatcioglu (1991) based on 20% maximum force reduction.

Prior to the definition by Saatcioglu (1991), there were interpretations defining the ultimate failure based on physical appearance of the specimens. However, according to Hwang *et al.* (1984) this is not acceptable as many specimens remain strong and stiff after spalling of the concrete cover. It is also very difficult to establish visually the exact moment when phenomena such as buckling starts or when the ultimate bond slip is reached. Rossetto (2002), Biskinis *et al.*, (2003, 2010) and Verderame *et al.*, (2012), Barry *et al.*, 2003 Hasleton *et al.*, 2007 all consider 20% maximum force reduction as the definition of ultimate displacement. Dhakal *et al.*, 2008 argues that in cases where P-Δ is present, adjustments have to be made to eliminate the P-Δ effect from the interpretation of the ultimate.

The reduction in maximum force is commonly assumed as a reduction of the envelope enclosing the cyclic deformation history. However, this brings various anomalies in the interpretation of the ultimate displacement. If figure 3-21 is considered, two possible scenarios are presented following tests on similar samples. In the first case resulting, the specimen is loaded with a pattern resulting in loops A, B, C, D, E, and F. Path 1 described its corresponding envelope and Δu_2 result in the ultimate displacement. However, at Δu_1 , the specimen has already reached a state where it cannot raise the force by more than 80% of the maximum. Moreover, if instead of continuing with cycles forming loops C, D, E and F, cycle B is extended then the ultimate displacement would be Δu_2 . However, the dissipated energy would be less.

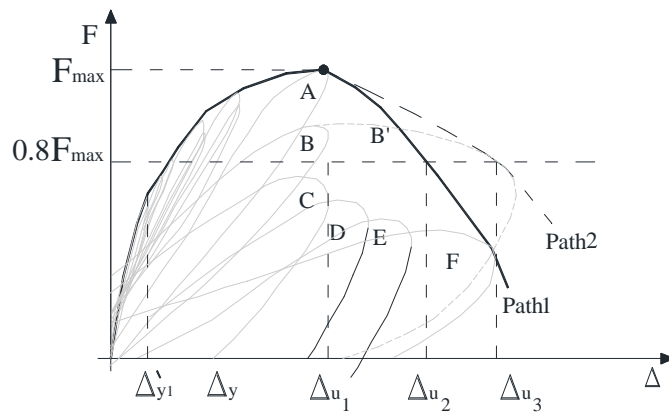


Figure 3-21 Anomalies in the definition of the ultimate.

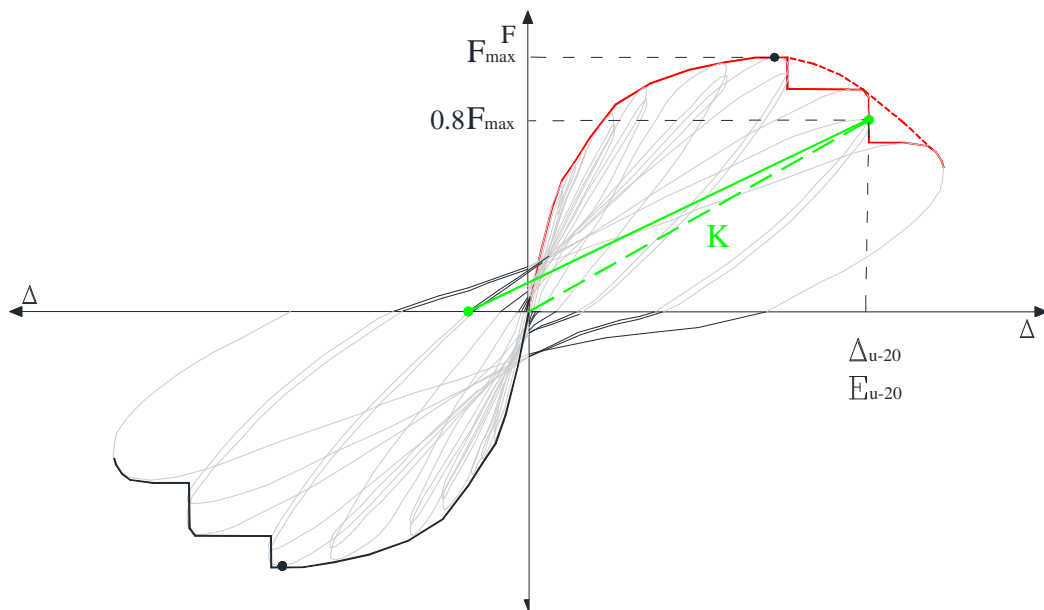


Figure 3-22 Interpretation of deformation, energy dissipation and residual stiffness at a particular % of maximum force reduction.

Following the above considerations about yield and ultimate, the interpretation of yielding for the purpose of this research is considered as the first yielding of a material or diverging point as it is conservatively associated with repair or retrofit actions (CEB, 2006). Beyond this point the equivalent hysteretic damping starts to be larger than 1.

Deformations defined at a percentage of force reduction are defined as shown in figure 3-22, and are reported with an associated dissipated energy that contributes to the strength decay. A definition for stiffness (K) at a damage level is also defined. In some cases, this is considered as the secant formed between the origin (Rodrigues *et al.*, 2011). However, this is not realistic, since in the inelastic range, the specimen will already have some residual displacement. Hence the

stiffness is suggested to be defined as the reduced force divided by the sum of displacement and the residual displacement.

3.4.2 Accounting of P-Δ and non-linear geometric effects

In the PEER database of cyclic tests on RC columns (Berry *et al.*, 2004), Axial load application and associated P-Δ effects can be categorised in four typologies, depending on the set-up arrangement. Various authors in literature present their force-displacement results in terms of the force of the actuator and the relative displacement of the column and do not take into account eccentricities, and components of the axial force, which make the effective force, and hence the shear distribution on the column, different from the force of the actuator. In order to compare results from different experiments, using different set-ups, it is essential that the same force component is used. For each set-up typology shown in Figure 3-23a-d, Berry *et al.*, 2004 suggests an approach accounting for P- Δ effects associated with the application of axial loads in order to estimate the effective force. This effective force is equivalent to the effective shear at the column-foundation interface. In *Type I*, the axial load is applied through external pre-stress rods, which are pin-jointed at the level of the actuator applying the lateral load and the column-foundation interface. The estimated shear at this latter cross-section is given by equation 3.2.

$$V_{eff} = F_{acc} - N_{acc} \frac{\Delta_{acc}}{L_s} \quad [3.2]$$

In *Type II*, the axial load is applied vertically and parallel to the stationary vertical axis of the column. The generated P- Δ effects are equivalent to those generated by gravity loads, and the effective shear at the column-column foundation interface is given by equation 3.3.

$$V_{eff} = F_{acc} \quad [3.3]$$

In *Type III*, the axial load actuator is fixed from moving horizontally at its upper end, and hence the axial load is applied diagonally, creating a horizontal component acting in the same direction of the lateral load application. The effective shear at the column-foundation interface is given by equation 3.4.

$$V_{eff} = F_{acc} + N_{acc} \frac{L_N}{\Delta_N} \quad [3.4]$$

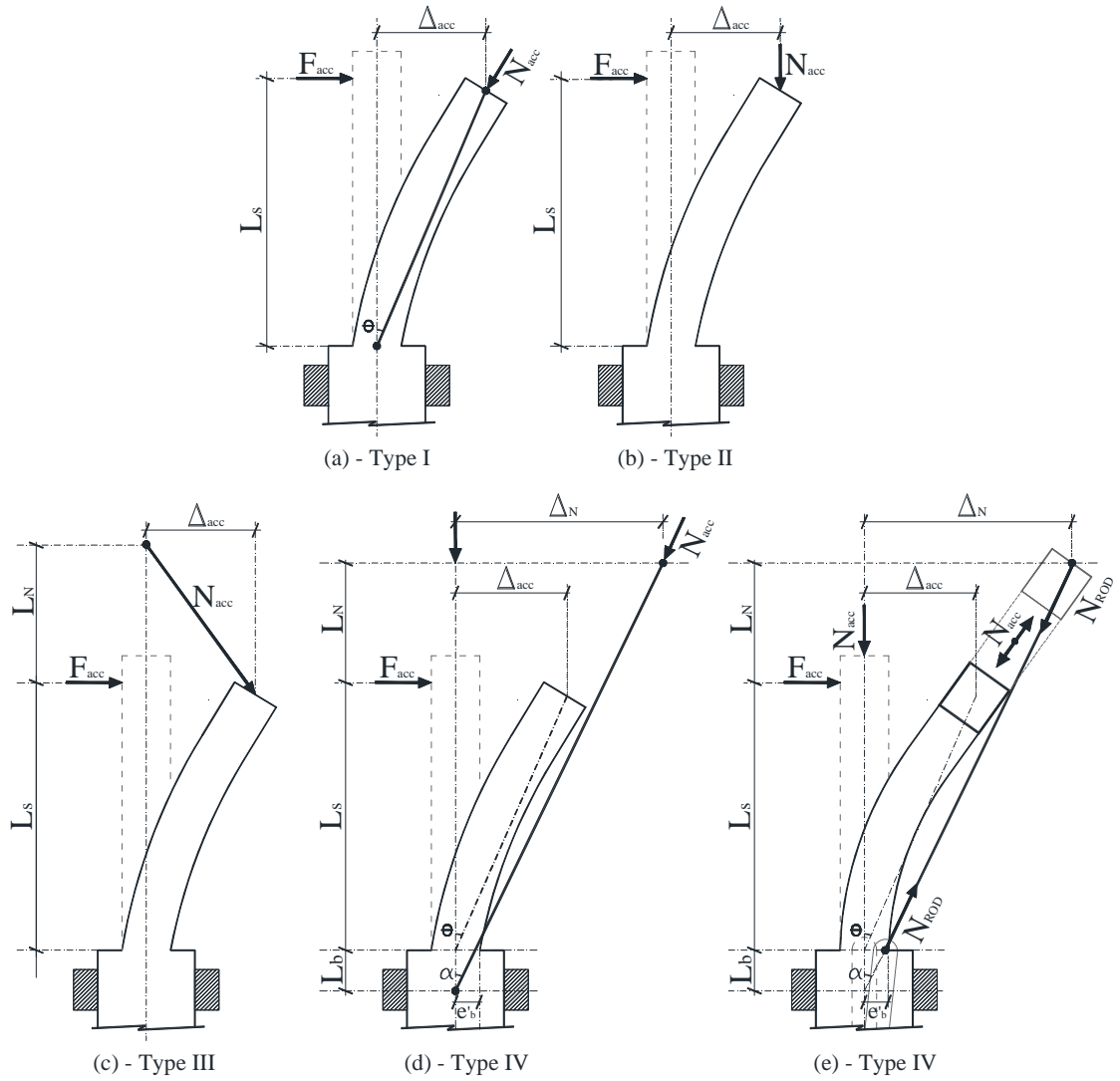


Figure 3-23 *P-A corrections for column tests with different axial load application set-ups.*

The tests on columns conducted under this research fall under the *Type IV* category (Figure 3-23 d-e). This is similar to Type I, but the hinges of the pre-stress rod are at a distance L_N above the point of application of the lateral load on the column, and a distance L_b below the column-foundation interface. The effective shear (V_{eff}) and moment at the column-foundation interface (M_{base}) are given by equation 3.5 and 3.6

$$V_{eff} = F_{acc} - N_{acc} \sin \left[\tan^{-1} \left(\frac{\Delta_N}{L_S + L_b + L_N} \right) \right] \quad [3.5]$$

$$M_{base} = F_{acc} L_S - N_{acc} L_S \sin \alpha + N_{acc} \Delta_N \quad [3.6]$$

The angle α made by the rod and the stationary vertical axis is given by equation 3.7.

$$\alpha = \tan^{-1} \left[\frac{\Delta_{acc} \left(\frac{L_S + L_N}{L_S} \right)}{L_S + L_b + L_N} \right] \quad [3.7]$$

In a similar computation for V_{eff} and M_{base} Verderame *et al.*, 2008 assume that the angles are very small and can be represented by the ratio of the lengths and displacements (equation 3.8).

$$\alpha = \left[\frac{\Delta_{acc} \left(\frac{L_S + L_N}{L_S} \right)}{L_S + L_b + L_N} \right] \quad [3.8]$$

The effective shear V_{eff} and moment at the base M_{base} according to Verderame *et al.*, 2008 are therefore given by equations 3.9 and 3.10.

$$V_{eff} = F_{acc} - N_{acc} \frac{\Delta_N}{L_S + L_b + L_N} \quad [3.9]$$

$$M_{base} = F_{acc} L_S + N_{acc} \Delta_N - N_{acc} \frac{\Delta_N (L_S + L_N)}{L_S + L_b + L_N} \quad [3.10]$$

In both correction approaches, the vertical force is assumed to be equal to the force in the rods. Both approaches ignore the bottom length L_b in the computation of Δ_N , and only consider the shear span (L_S) and height above the point of application of the lateral load (L_N), given by equation 3.11.

$$\Delta_N \cong \Delta_{acc} \left(\frac{L_S + L_N}{L_S} \right) \quad [3.11]$$

The corrections by Berry *et al.*, 2004 and Verderame *et al.*, 2008 rely on the consideration that the shear force on a cantilever is uniform, and the corresponding moment increases from zero at the point of lateral load application to maximum at the beam-column interface. V_{eff} and M_{base} refer to respective corrected values at the column foundation interface, due to P- Δ effects exerted by the axial force through the rods. Berry *et al.*, 2004 and Verderame *et al.*, 2008 consider these

values to be as either maximum values, or values associated to the section where most damage is concentrated, and can be assumed to represent the overall behaviour of the column.

The perpendicular distance between the rods and the axis of the column under lateral load is not uniform and is largest at a distance above the column base. The maximum effective moment and shear along the column can therefore be at a section in the column above the column-foundation interface. In addition, the column-foundation interface is associated with higher confining restraints than nearby sections, and hence larger damage may be expected at sections slightly higher than the column-foundation section. This means that the interpretation of the representation of the behaviour of the column through V_{eff} and M_{base} as proposed by Berry *et al.*, 2004 and Verderame *et al.*, 2008 may be very limited, particularly as the lateral deflection of the cantilever column becomes larger.

Due to the limitations discussed above, a more detailed and different correction approach is utilised for the column experiments carried out in this research. This approach is based on a similar approach used in the correction of forces in RC element tests carried out by Borg *et al.*, 2008. Figure 3-24 shows a more detailed representation of the forces and displacements for the consideration of the approach utilised for the corrections when compared to Figure 3-23e showing a generalised representation had the corrections been made according to Berry *et al.*, 2004 or Verderame *et al.*, 2008. The distribution of the flexural moment and shear along the column consist in two components; the distribution due to the lateral load and the distribution due to the rods counteracting the actuator responsible for the axial load.

In order to obtain the distribution of flexural moment and shear, various assumptions has to be made, and further corrections to readings other than those stated have to be made. The hinges connecting the rods and the column-axial-actuator-foundation system are assumed to allow the rods to rotate freely. The connection to the foundation system described in section 3.2.4 may be expected to rotate, resulting in an eccentricity e_{r0} at the column-foundation interface. Extrapolation of the parallel axis of the rods, make an angle α with the vertical axis of the undeformed column. The depth L_b is assumed to be the effective shear span inside the foundation, where the rods are assumed to hinge with the column-foundation.

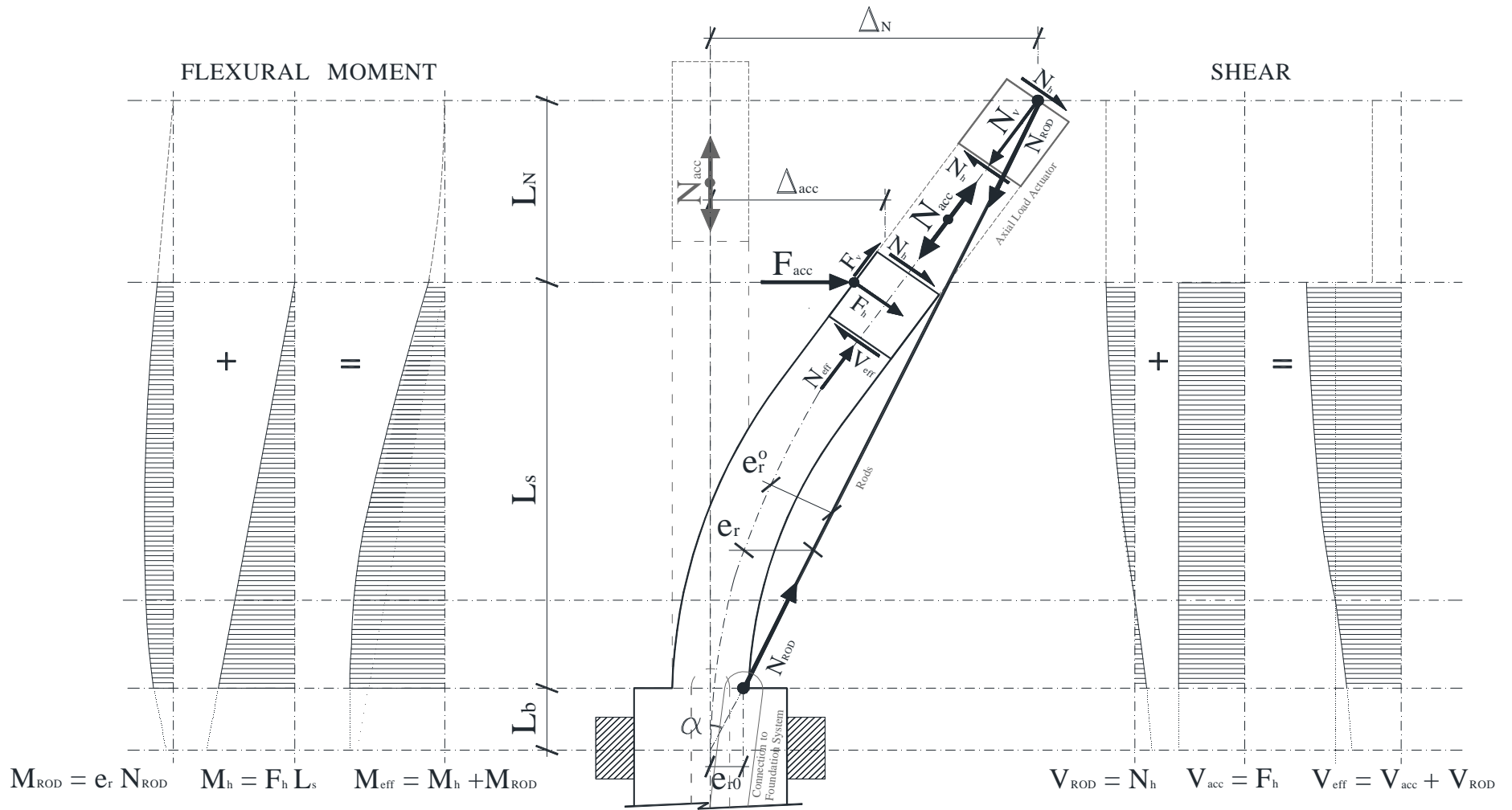


Figure 3-24 Schematic diagram for P-Δ corrections for the column test setup carried out in this research and described in section 4.2.2.

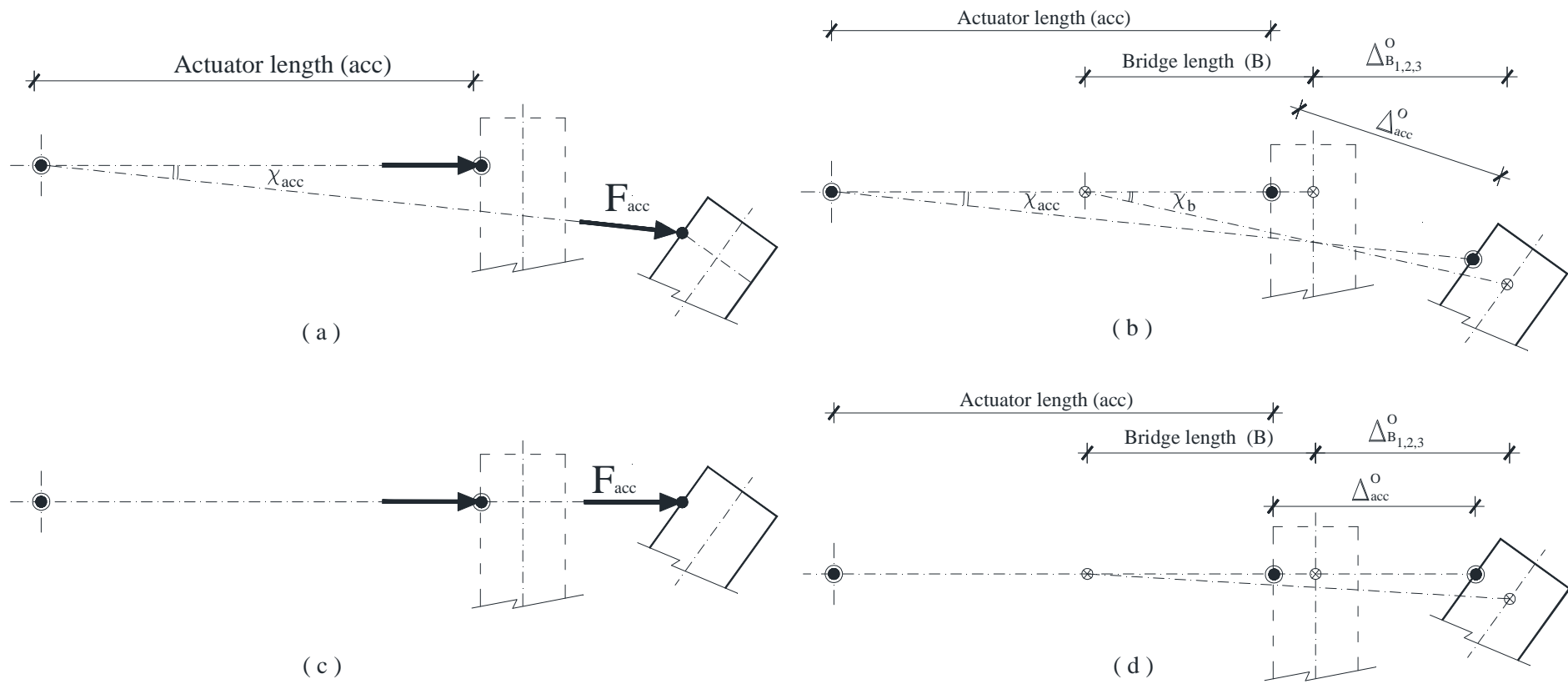


Figure 3-25 Schematic representation for the assumptions of the actuator load vector and the maximum lateral displacement obtained from the bridge potentiometers.

As the actuator pushes the column, the length of the actuator increases, and the tip of the column rotates downwards, such that an angle χ_{acc} is formed. Between the original position of the actuator and its new position as shown in Figure 3-25 a and c. Considering that the actuator is relatively long, and the rotation and displacement of the column relatively small, this angle is assumed to be negligible and the force from the actuator (F_{acc}) to always act in the horizontal direction. The actuator measures displacement relative to the surface of the column, whereas the bridge potentiometer measure displacement relative to the central axis of the column. Moreover, the bridge potentiometer measures the horizontal vector of the displacement of the column. These differences between the actuator displacement and the bridge potentiometer displacement are considered to have negligible effects on the interpretation of lateral displacement.

However, further to the assumptions by Berry *et al.*, 2004 and Verderame *et al.*, 2008 the lateral force (F_{acc}) and the axial force (N_{acc}) both obtained from their respective actuators were resolved as action and reaction forces acting on the surfaces of the system as shown in figure 3-26. The effective axial load (N_{eff}) acting on the column as a function of time (t) is given as the sum of the force from the axial load actuator (N_{acc}) and the load component (F_v) from the lateral load actuator parallel to the neutral axis of the column in equation 3.12.

$$N_{eff}(t) = N_{acc}(t) - F_v(t) \quad [3.12]$$

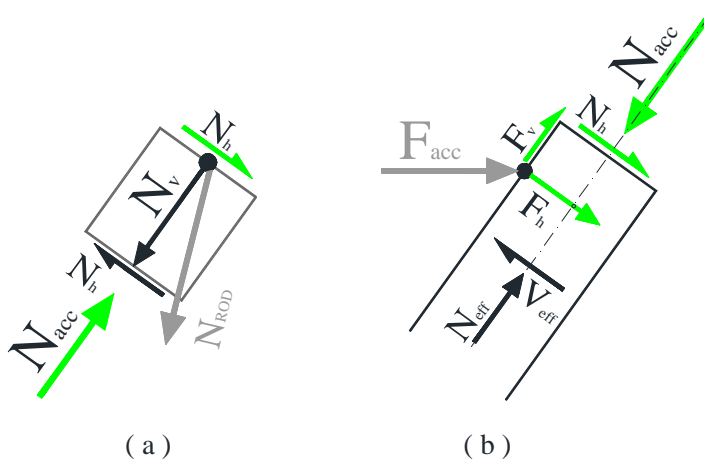


Figure 3-26 Details of the action (a) by the axial load actuator on the column, (b) by the lateral load actuator on the column, resolved in components about the axis of the column.

Although the frames restraining the foundation are very stiff, rotation of the foundation may still result. The displacement component due to the rotation of the foundation, resulting in full body rotation of the specimen, is reduced from the displacement measured by the external LVDTs along the column B1-3 and L2-5 and the displacement of the actuator as illustrated in figure 3-28.

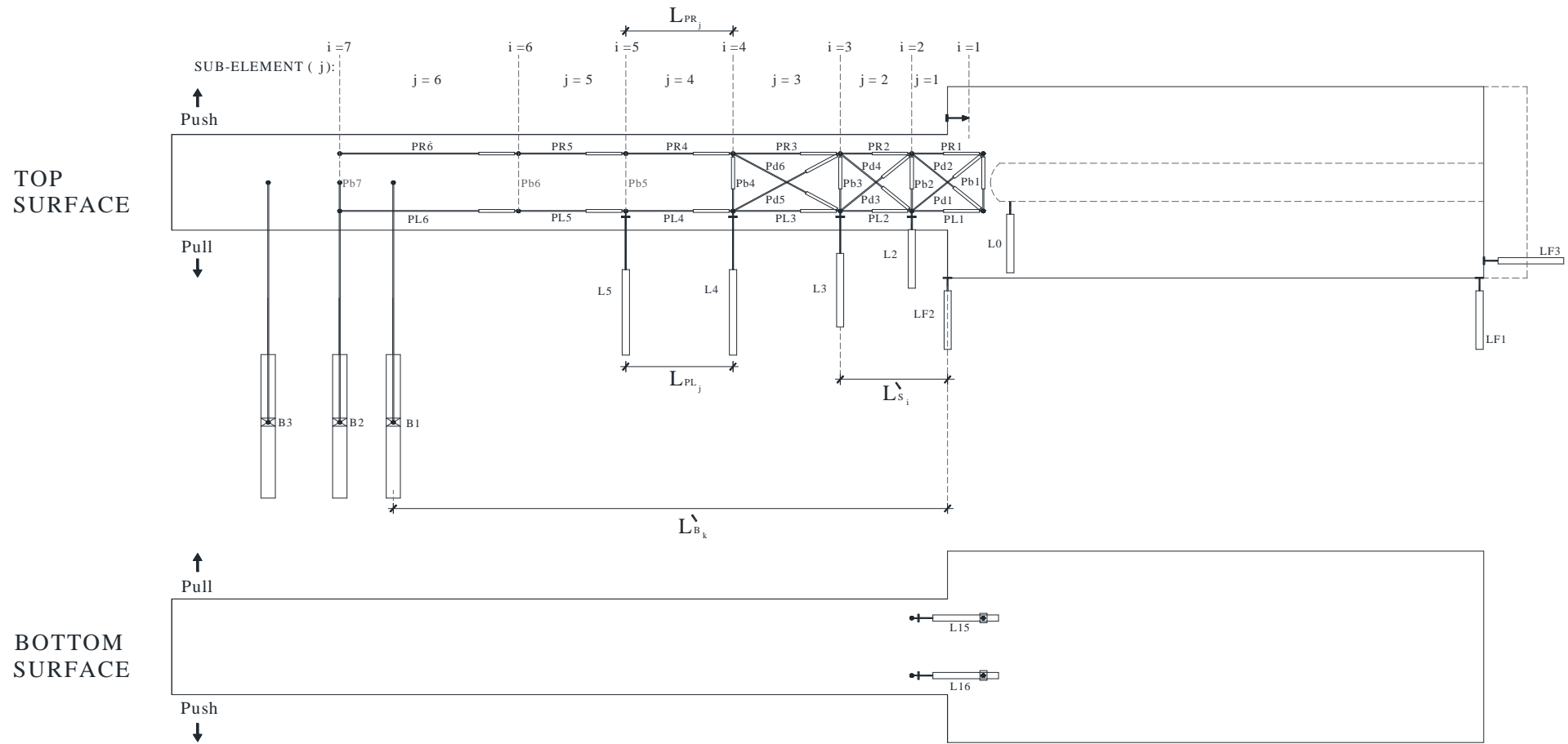


Figure 3-27 The set-up of the column specimen and instrumentation, indicating the position of each “i” section and “j” sub-element.

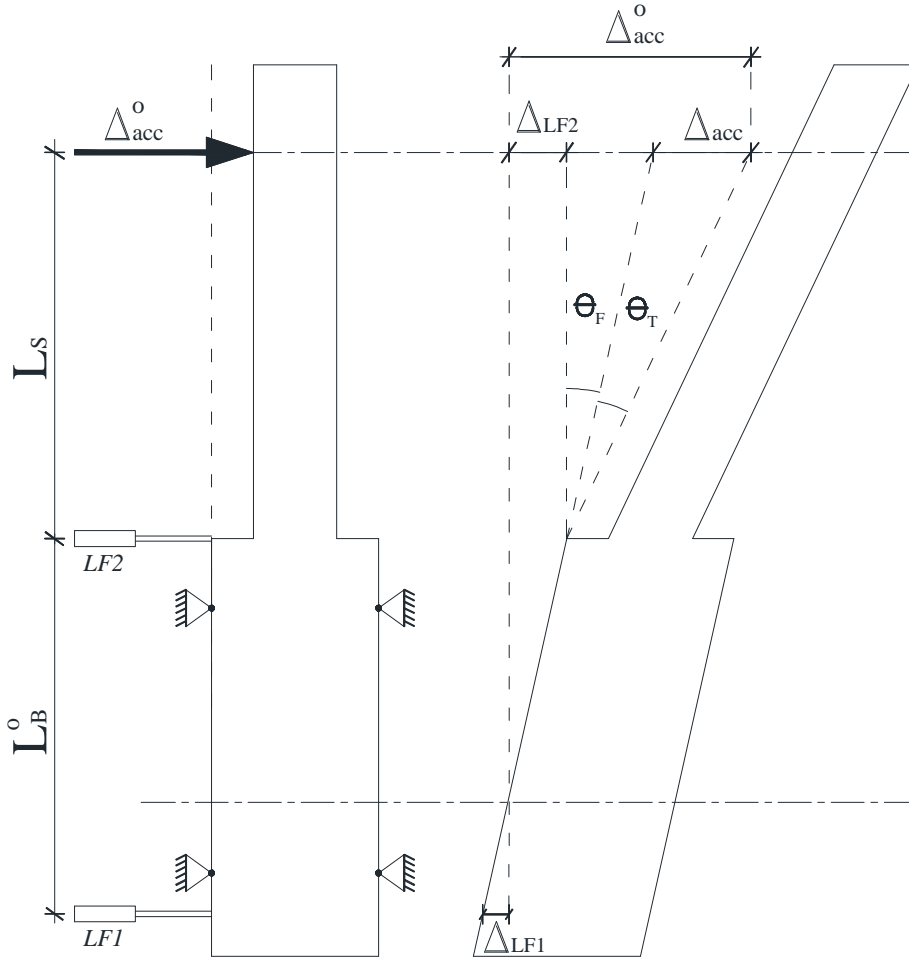


Figure 3-28 The rotation of the foundation.

The LVDTs LF2 and LF1 are used to find the rotation of the foundation (θ_F) which is given as a function of time (t) by equation 3.13.

$$\theta_F(t) = \frac{\Delta_{LF2}(t) - \Delta_{LF1}(t)}{L_B^0} \quad [3.13]$$

With reference to figures 3-25 and 3-28, effective displacements Δ_{B_k} , Δ_{L_i} and Δ_{acc} as a function of time (t) are obtained from the lateral displacements measured by the bridge potentiometers $\Delta_{B_k}^0$ where k=1-3, the lateral displacement measured by the LVDTs $\Delta_{L_i}^0$ where i=2-5 and the displacement measured by the actuator are given by equations 3.14, 3.15 and 3.16.

$$\Delta_{B_k}(t) = \Delta_{B_k}^0(t) - [L'_{B_k}\theta_F(t) + \Delta_{LF2}(t)] \quad [3.14]$$

$$\Delta_{L_i}(t) = \Delta_{L_i}^0(t) - [L'_{s_i}\theta_F(t) + \Delta_{LF2}(t)] \quad [3.15]$$

$$\Delta_{acc}(t) = \Delta_{acc}^o(t) - [L_s \theta_F(t) + \Delta_{LF2}(t)] \quad [3.16]$$

In order to find the rotations of the column specimen, the column is divided into sub-elements $j=1-6$ by sections $i=1-7$. Figure 3-29a zooms at one un-deformed sub-element (j) while figure 3-29b zooms at its corresponding deformed sub-element. The deformed potentiometers PL_j and PR_j are not parallel, nevertheless the angle with the vertical is assumed to be very small such that:

$$\left[L_{PL_j}(t) + \Delta_{PL_j}^o(t) \right] \approx \left[L_{PL_j}(t) + \Delta_{PL_j}(t) \right] \quad [3.17]$$

$$[3.18]$$

$$\left[L_{PR_j}(t) + \Delta_{PR_j}^o(t) \right] \approx \left[L_{PR_j}(t) + \Delta_{PR_j}(t) \right]$$

The width between parallel potentiometers is considered as the projection on the horizontal of the Pb LVDTs as illustrated in figure 3-29c. The rotation contribution (θ'_s) by each successive sub-element as shown in figure 3-29d is given by equation 3.19.

$$\theta'_s(t) = 2 \left(\frac{\Delta_{PR_j}(t) - \Delta_{PL_j}(t)}{L_{Pb_{i+1}} + L_{Pb_i} + \Delta_{Pb_{i+1}}(t) + \Delta_{Pb_i}(t)} \right) \quad [3.19]$$

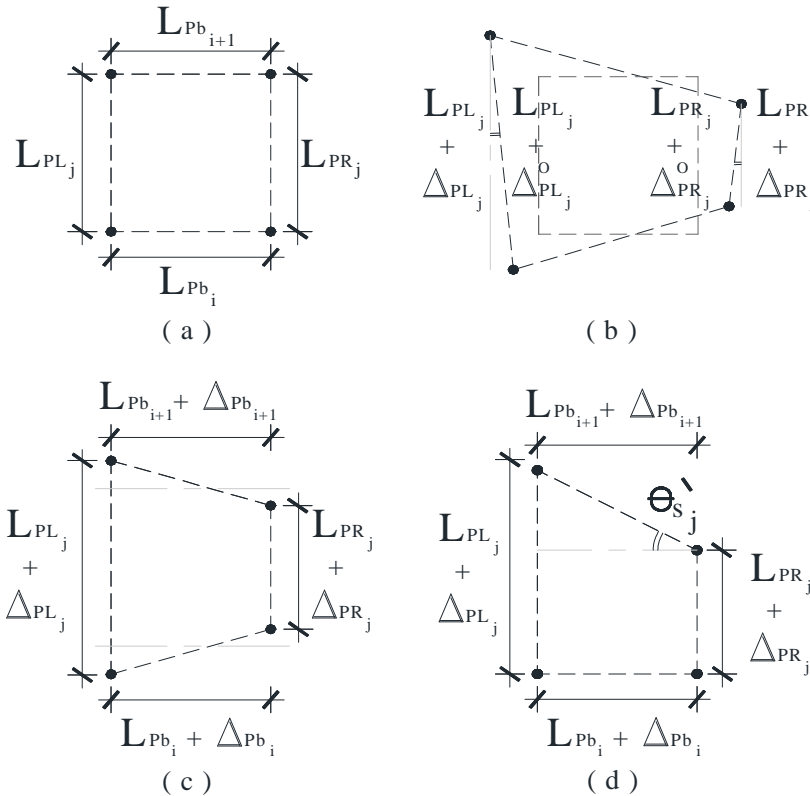


Figure 3-29 Considerations of potentiometer deformations for the determination of the rotation of a general sub-element.

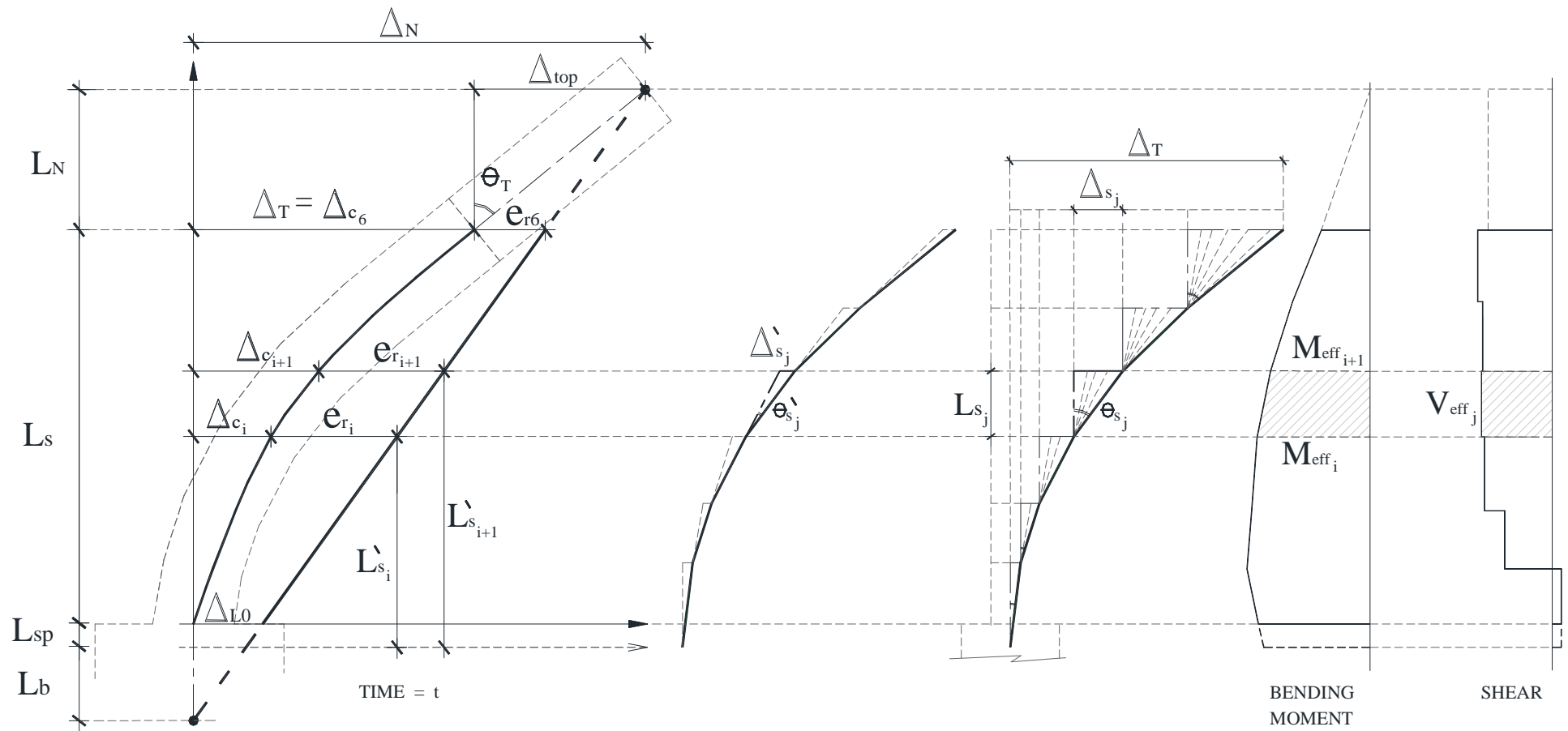


Figure 3-30 Displacement and rotation considerations at corresponding sections and sub-elements for the determination of shear and flexural moment distribution.

It is possible to obtain more precise computations if measurements from the diagonal potentiometers (Pd) are considered. For the purpose of this research, these potentiometers were however ignored, as the proposed corrections were accurate enough. It is also possible to estimate the rotation from the LVDTs and bridge potentiometers measuring the lateral displacement that are shown in figure 3-30 using equation 3.20.

$$\theta'_{L_j}(t) = \frac{\Delta_{L_{i+1}}(t) - \Delta_{L_i}(t)}{L'_{S_{i+1}}(t) - L'_{S_i}(t)} \quad [3.20]$$

Since these measurements are taken from one side of the specimen only, it is not expected to have reliable results. The average estimate rotation of each sub-element with respect to the original neutral axis (θ_{s_j}) is given as the summation of each rotation contribution (θ'_{s_j}) of each successive sub-element up to the relevant sub-element “j” as indicated in figure 3-30. The computation for θ_{s_j} is given by equation 3.21.

$$\theta_{s_j}(t) = \sum_{j=1}^6 \theta'_{s_j}(t) \quad [3.21]$$

Similarly, if reference is made to the rotation angles (θ'_{L_j}) defined using LVDT readings that measure external deformation, the average estimate rotation of each sub-element with respect to the original neutral axis (θ_{L_j}) is given by equation 3.22.

$$\theta_{L_j}(t) = \sum_{j=1}^6 \theta'_{L_j}(t) \quad [3.22]$$

On using this relationship, the inaccuracies discussed in the computation of θ_{L_j} are carried forward also in the determination of θ_{L_j} .

The angle at the top of the column can be defined in various ways. Considering the average estimate rotation of each sub-element with respect to the original neutral axis, the angle at the top can be defined by the rotation at the top θ_{s_6} using equation 3.23.

$$\theta_T^*(t) = \tan^{-1}[\theta_{s_6}(t)] \quad [3.23]$$

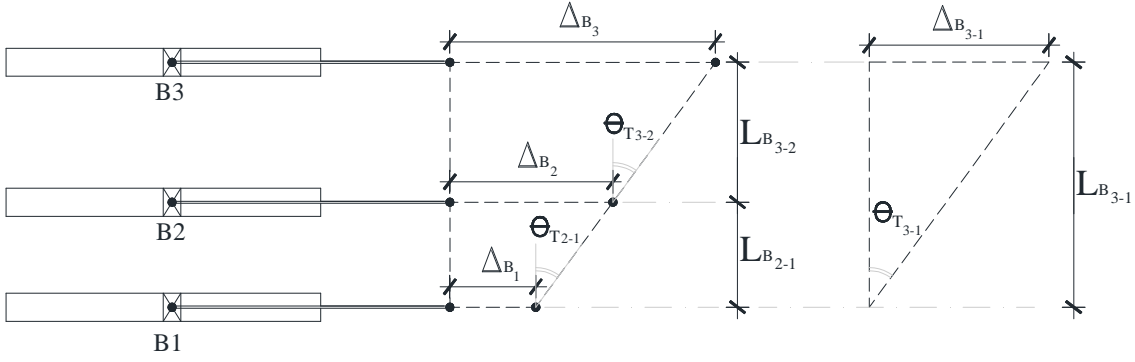


Figure 3-31 Determination of the angle of rotation at the top of the column by considering displacements of the bridge potentiometers B1, B2 and B3.

The rotation at the top of the column can also be obtained from the displacement measured by the bridge potentiometers. With reference to figure 3-31, three angles are defined using equations 3.24, 3.25 and 3.26. An average of all three angles is also a possible consideration in equation 3.27.

$$\theta_{T1}(t) = \tan^{-1} \left(\frac{\Delta_{B2}(t) - \Delta_{B1}(t)}{L_{B_{2-1}}} \right) \quad [3.24]$$

$$\theta_{T2}(t) = \tan^{-1} \left(\frac{\Delta_{B3}(t) - \Delta_{B2}(t)}{L_{B_{3-2}}} \right) \quad [3.25]$$

$$\theta_{T3}(t) = \tan^{-1} \left(\frac{\Delta_{B3}(t) - \Delta_{B1}(t)}{L_{B_{3-1}}} \right) \quad [3.26]$$

$$\overline{\theta_{T1,2,3}}(t) = \frac{[\theta_{T1}(t) + \theta_{T2}(t) + \theta_{T3}(t)]}{3} \quad [3.27]$$

The values of θ_{T1} , θ_{T2} , θ_{T3} , $\overline{\theta_{T1,2,3}}$ and θ_T^* are expected to be very similar. A decision on which parameter of θ_T to take for further computations is taken in Chapter 6, after comparing the test results.

An estimate of the effective bending moment (M_{eff}) at section $i=1-7$, combining components due to the lateral load, and partial P- Δ effects arising from the load inside the rods is given by equation 3.28.

$$M_{eff_i}(t) = N_{eff}(t)e_{r_i}(t) + F_h(t)[L_s + L_{sp}(t) - L'_{s_i}(t)] \quad [3.28]$$

Since in the inelastic range, considerable rotation is possible to take place also inside the foundation, due to strain penetration effects, a distance L_{sp} inside the foundation is considered, and the column is assumed to rotate about this level, beyond which no further rotation is considered. With reference to figure 3-32a and figure 3-32b, L_{sp} is assumed to be the distance inside the foundation at which tensile cracking is observed. It is not excluded that yielding of the reinforcing bars and bond-slipping occur at a distance further down than this distance. However, the cracks inside the foundation are an adequate representation of the surface about which the column can be assumed to rotate. The distance (L_{s_j}) over which deformation is assumed in the first sub-element ($j=1$) is considered as the distance between the column-foundation interface and section at level $i=2$. On the formation of tensile cracks inside the foundation, L_{sp} is also included as shown in figure 3-33.b.

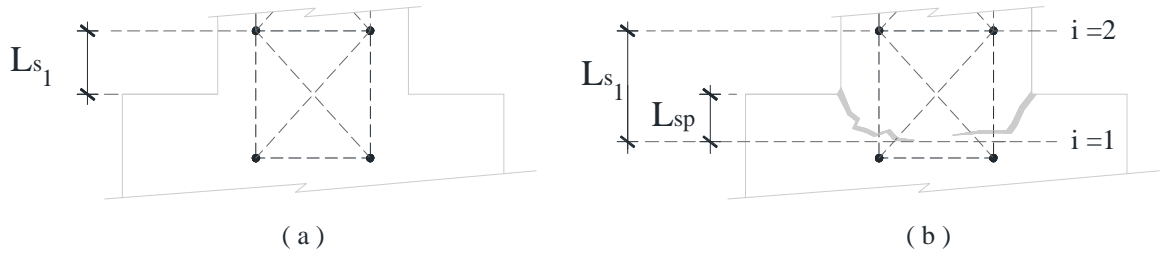


Figure 3-32 Definition of the length of the sub-element at the base: a) before considerable flexural cracking in the foundation, b) after considerable flexural cracking in the foundation.

With reference to figure 3-24, e_{r_i} is defined as the horizontal distance between the rod and the representative neutral axis at the corresponding level “i”. The actual lever arm is $e_{r_i}^o$. Nevertheless due to the expected small values of this parameter compared to the chord distance made by the rod $e_{r_i}^o \approx e_{r_i}$ can be assumed. The lever arm of the rods (e_{r_i}) is obtained from equation 3.29:

$$e_{r_i}(t) = \frac{\Delta_N(t)[L'_{s_i} + L_b(t)]}{(L_b + L_s + L_{sp}(t) + L_N)} - \Delta_{c_i}(t) \quad [3.29]$$

The distance (Δ_{c_i}) from the original neutral axis to the estimated neutral axis of the deformed shape is defined by equation 3.30,

$$\Delta_{c_i} = \sum_{j=1}^{i-1} \Delta_{s_j} \quad [3.30]$$

where Δ_{s_j} is defined by equation 3.31.

$$\Delta_{s_j} = L_{s_j} \tan \theta_{s_j} \quad [3.31]$$

The estimated neutral axis of the deformed shape could be such assumed, since measurements are computed as an average over a large length, and not based on section or stress-block analysis as discussed in Chapter 2. The depth L_b defined earlier is given by equation 3.32.

$$L_b(t) = \Delta_N(t) \left[\frac{L_N(t) + L_s}{\Delta_N(t) - \Delta_{L0}} \right] - [L_s + L_{sp}(t) + L_N] \quad [3.32]$$

The distance (Δ_N) between the original neutral axis of the column and the top of the centre of the axial load actuator is given by equation 3.33.

$$\Delta_N(t) = \Delta_T(t) + \tan[\theta_T(t)]L_N \quad [3.33]$$

The maximum displacement of the column at the top Δ_T is determined either from the lateral load actuator or bridge potentiometer B2. On obtaining the effective moment at each level “i”, with reference to figure 3-30, the effective shear at each level “j” can be obtained from equation 3.34.

$$V_{eff_j}(t) = \frac{M_{eff_{i+1}}(t) - M_{eff_i}(t)}{L_{s_{i+1}} - L_{s_i}} \quad [3.34]$$

The energy dissipation of the column is derived from the work done in deforming the column. This can be defined either as a function of bending moment and rotation, or shear and lateral deformation. The rotation is generally defined as the integration of the curvature of each section along the shear span of the column, for which the corresponding energy dissipation can be obtained for small changes in moment. In these experiments the rotation refers to deformations measured on a sub-element rather than sections where the corresponding variation in bending moment is also large. It is therefore possible that the corresponding estimated dissipated energy obtained may be inaccurate. Deriving energy dissipation from shear and lateral deformation is a more stable consideration. Although the lateral displacement changes considerably along the sub-element, its variation is more linear than rotation and the shear is uniform along the sub-element.

As shown in figure 3-33, the rotation of a sub-element “j” is responsible for a displacement $\Delta_s^T_j$ at the top of the column for the sub-elements above it. The maximum lateral displacement by the lateral actuator ($\Delta_s^T_j$) can be defined as the sum of all these individual displacements.

$$\Delta_T(t) = \sum_{j=1}^6 \Delta_s^T_j \quad [3.35]$$

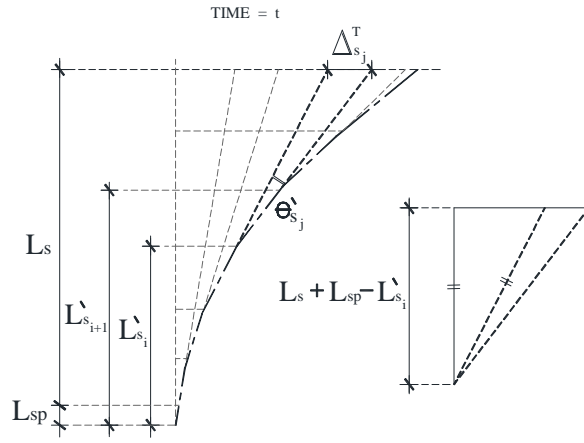


Figure 3-33 Definition of top displacement contribution by each section.

The displacement $\Delta_{s_j}^T$ can be determined in equation 3.36, as a function of rotation ($\theta'_{s_j}(t)$) contribution by the respective sub element and the distance to the top of the column ($L_s + L_{sp}(t) - L_{s_i}(t)$).

$$\Delta_{s_j}^T(t) = [L_s + L_{sp}(t) - L_{s_i}(t)] \tan [\theta'_{s_j}(t)] \quad [3.36]$$

For the lower sub-elements, the rotation is large but the tangential length is approximately equal to the vertical length ($L_s + L_{sp}(t) - L_{s_i}(t)$). For the upper sub-sections, these lengths may not be close to equal, however the angle θ'_{s_j} is relatively very small. In both situations, $\tan [\theta'_{s_j}(t)]$ could therefore be assumed.

The energy released due to change in displacement ($\delta\Delta_{s_j}$) in a time interval (δt) by a particular sub-element “j” is caused by a force equivalent to the effective shear at the respective times ($V_{eff_{j,t}}; V_{eff_{j,t-1}}$). This energy is defined by equation 3.37.

$$E_{S_j}(t) = \frac{1}{2} \frac{\delta\Delta_{s_j}^T}{\delta t} [V_{eff_{j,t}} + V_{eff_{j,t-1}}] \quad [3.37]$$

The cumulative energy for each subsection $j=1-6$ in turn, for the whole duration of the test ($t=1-n$) is given by equation 3.38.

$$E_{S_j} = \int_{t=0}^n E_{S_j}(t) \cdot \delta t \quad [3.38]$$

The dimensions of the sub-elements are large compared to a section. This means that the cumulative energy of the whole element cannot be defined as the integration over the whole shear

span of the column. The cumulative energy (equation 3.39) for the whole column can however be defined as the sum of the cumulative energy of each sub-element.

$$E_s = \sum_{j=1}^6 E_{S_j} \quad [3.39]$$

The cumulative energy of the whole column can also be obtained from the lateral deformation Δ_T , and the effective lateral force F_h or the average V_{eff} . The energy released due to change in lateral displacement ($\delta\Delta_T$) in a time interval (δt) is obtained from equation 3.40.

$$E_c(t) = \frac{1}{2} \frac{\delta\Delta_T}{\delta t} [F_{h_t} + F_{h_{t-1}}] \quad [3.40]$$

The cumulative energy for the whole duration of the test (t=1-n) is given by equation 3.41.

$$E_c = \int_{t=1}^n E_c(t) \cdot \delta t \quad [3.41]$$

The two global dissipated energies should be expected to be approximately equal ($E_s \approx E_c$) This is assessed in Chapter 4. If this approximation is true, since nearly all the parameters are indirectly incorporated in the computation of energy using the individual sub-elements, then it would mean that the assumptions made would be reasonably valid.

3.5 General Conclusions and Requirements

Before a low cycle fatigue experimental campaign on RC columns could be designed, boundary conditions in terms of range of geometric and material properties, detailing aspects and parameters that are required to be varied between different specimens which are beneficiary for the development of EDP relationships had to be defined.

The list of material and geometric properties from Chapter 2 that describe physical phenomena responsible for the deformation of RC elements is quite extensive. Many variables such as the carbon content in steel reinforcement, or parameters describing the adhesion between steel and concrete, apart from being difficult to quantify, are assumed to be secondary variables. Variables such as v , a , ω_T and L_s/h are already defined in Chapter 2 as important, they contribute significantly to the deformation capacity of RC elements and feature in many existing EDP relationships. Hence, these are selected as the main variables for the experimental campaign presented here.

The range of the variables that characterise the experimental campaign is based upon the properties and detailing aspects of typical structures from the European building stock, as identified in Chapter 2. Reference is also made to the distribution of variables in the existing

databases available. It is observed that the number of records in the databases with $f_{tl}/f_{yl} \approx 1.25$, $\rho_T < 2$, $a < 0.35$, $s/d_{bl} > 10$, $v > 0.2$ or $f'_c < 20$ is very low. These ranges are however very common in existing RC buildings, particularly those designed according to older codes where seismic detailing is generally not considered. Hence the test specimens are designed to cover these ranges. Since seismic assessment is required for both seismically designed and non-seismically designed structures, two reference structures are considered: one designed according to old design codes excluding seismic detailing, and the other following EN1998-1 (2004). Variables that separate the two reference structures are varied in turn; one for each of the 19 column specimens.

The experimental setup is a modification of an existing setup having a horizontal layout. This poses some problems in accounting for friction between the specimens and the support. This is monitored through load-cells, and LVDTs. The effects have to be checked when presenting the results in Chapter 4. Moreover, unlike in real situations, the specimens are also cast horizontally and with the same batch eliminating cold joints that in real structures characterise the column foundation interface. This phenomenon is however simulated by one specimen, in order to assess the importance of this detail.

It was not possible to find such steel in the market for the construction of the specimens. This difference in the steel affects the simulation of expected reinforcement rupture. Since the specimens are cast on different days from different concrete batches, and since, specimens are tested on different days, an attempt is made to ensure uniform curing conditions, particularly for specimens with the same concrete grade. Nevertheless, as observed in the concrete compressive strength tests, there remains a significant variation in strength across specimens of the same grade.

The system that provides the axial load in the RC specimens, induces P- Δ effects which differ from those in a real structure. While Verderame *et al.*, 2008 and Berry *et al.*, 2003 indicate that this reduces the maximum shear. This assumption is based on considerations of the column foundation interface only. However, following an understanding of the shear distribution along the column, it is observed that the maximum shear is still obtained slightly above the column foundation interface inside the column. The shear force along the shear span is not uniform, and hence in the results discussed in Chapter 4 the appropriate shear or lateral force has to be accounted for. The main variables that need to be measured, in order to have appropriate data that can be used in the development of EDP models are force, chord rotation and energy dissipation. Hence, LVDTs, potentiometers and load cells are used to monitor these variables. While the experiments could have benefitted from the inclusion of strain gauges on reinforcement, these were not included as the test specimen construction was sub-contracted to a company off-site.

In real structures, the width of the foundation is generally larger than the width of the columns. However, due to technical reasons in mounting the specimens, the width of the column is equal to the width of the foundation. In order to check whether this adversely affects the initial stiffness of the element, analytical checks on stiffness are required to be carried out before evaluating the experimental results.

In order to have a rational in defining EDP variables to be determined in Chapter 4, approaches on how to define energy dissipation, chord rotation and residual stiffness are identified. Since the mutual influence of EDPs is investigated, the definition is not entirely based on the envelope, as is generally done for analytical investigations.

In the next chapter, the results of this experimental campaign are presented and discussed in terms of dependent and explanatory variables that are required for the development of empirical models. The development of damage is analysed. The response of the specimens is also compared and verified with section analysis.

Chapter 4. RESULTS OF EXPERIMENTS: COMPARISONS AND INTERPRETATIONS

4.1 Introduction

The results and outcome of the experimental campaign presented in Chapter 4 are discussed and compared in this Chapter. One of the aims of the research is to determine engineering demand parameter (EDP) relationships in terms of material and physical properties at different damage levels. Hence, particular reference to different properties and detailing aspects including confinement configurations, reinforcement ratio and its distribution in the cross-section, span-to-depth ratios and detailing aspects is made. The effects of different loading patterns are also discussed. This is done with respect to the EDPs that are identified to quantify damage in Chapter 2. These include chord rotation, energy dissipation and residual stiffness. The damage levels considered are those identified in Chapter 2 and include Y (yielding), m (maximum force capacity), $u-10$ (10% maximum force reduction), $u-20$ (20% maximum force reduction) and $u-50$ (50% maximum force reduction). The occurrence of damage phenomena is also discussed. The magnitude of the variables are determined according to the diagnostics discussed in section 4.4.

The determination of EDP relationships is based on column tests only. The interpretation of results of columns is considered at sectional level, in order to evaluate the evolution of damage and the damage phenomena vis-à-vis the relevant properties. For the purpose of this research, the interpretation of results of beam-column connections are limited to force-displacement. The aim is to generally highlight response that is either not observed or is different than that observed by the experiments on columns only. The outcome is a possible limitation of such EDP relationships based on column tests.

The chord rotation is considered as the angle between the tangent to the axis at the yielding end and the chord connecting that end with the end of the shear span at the point of contraflexure. The drift ratio is the deflection at end of the shear span with the respect to the tangent to the axis at the yielding end, divided by the shear span. Since in principle the rotation of the column specimens is separated from the rotation of the foundation as discussed in section 4.4, chord rotation is used when interpreting the results of column specimens. However, since the overall rotation of the beam-column sub-element is considered, drift ratio is used when interpreting the results of this type of specimen.

Any interpretations from the observations are kept contextual and are specific to the experimental campaign. This is particularly relevant for two main reasons. Some observations of damage phenomena discussed are based on visual inspection during the tests and of visual recordings. Hence, the process involves human error that may possibly involve delay in the observation of

damage. In addition, any general or specific observations in the comparisons may be limited to the experimental campaign or tests involved and may not reproduce under other circumstances.

During the course of the experiments some possible errors are identified. By considering all the external load cells, a difference of 3% is generally observed. This is possibly the result of losses due to friction between the specimen and the reaction floor that supports the specimen. Moreover, the damage occurring on the upper surface of the specimens tested horizontally, is sometimes slightly different or occurs at a slightly different deformation than the damage on the lower part. This is mainly due to the self-weight of the specimen and friction. As the deformation increases, the axial load oscillates slightly around the target value by $\pm 1.5\%$.

4.2 General Observations on the Behaviour of RC Columns

Table 4-1 shows the maximum drift ratio of the cycle during which various damage phenomena are observed on the tested column specimens. The legend of the damage phenomena is found in table D-1. It is observed that in most cases flexural cracking occurs in the first five sections S1-S5 that are defined in Chapter 3. However, in specimens T2, T3, T4, T5, T6, T7, T8, T14 and T15 flexural cracking is observed in the first four sections only. With the exception of T13, T1a, T1b and T1c, the specimens where flexural cracking is also observed in S5 have a larger reinforcement ratio than the specimens where flexural cracking is only observed till S4. The sequence of the occurrence of flexural cracking is not necessarily proportional to the order of the sections S1-S6. The flexural cracks in S1, are generally first observed to form in the column and then in the foundation. The first flexural crack in a column specimen is observed during a cycle with a drift ratio magnitude of 0.003. All flexural cracks are formed before a drift ratio of 0.04 is reached.

The first spalling observed in section S1 of a column occurs during a cycle with a drift ratio of 0.01. Complete spalling of the cover in S1 is formed before a drift ratio of 0.055 is reached. In nearly all columns, with the exception of T6, spalling is also observed in S2. In this section, the first spalling observed occurs during a cycle having a drift ratio of 0.015. In samples T1a, T1b, T4, T5, T7, T8, T9, T11, T12, T13, T14, T15 and T16-D1 the cover of section S2 is observed to spall entirely. Diagonal cracks are observed to form in many specimens. These cracks form in any location between S1 and S3. They are observed to start forming on initial cycles with a drift ratio of 0.01, and are observed to form a complete diagonal crack before 0.055. Buckling is observed in most specimens, with the exception of T11 and T13. The earliest buckling observed in a column occurs during a cycle with a drift ratio of 0.025. Buckling in T12 which is the reference specimen designed to Eurocode 8 (CEN, 1998) occurs during a cycle with a drift ratio of 0.105. Most buckling occurs in S1 only. However, in T4, T5 and T7, buckling is also observed in S2. In some specimens, the transverse reinforcement is observed to fail. This is observed to occur on early cycles having a drift ratio of 0.03. A few specimens are also observed to suffer axial load loss. In T15, this is even observed during a cycle with a drift ratio equal to 0.03.

As a result of the steel rods (Chapter 3) responsible for the axial load in the column specimens, figure D-40a to figure D-58a indicate how the shear force is not uniform along the shear span of all column specimens. The shear-force demand is lowest in the sections closer to the foundation for all levels of damage in most columns. The lowest reduction in the shear force is generally in S1. Specimen T12 which has an axial load to maximum force capacity ratio of 0.24, and specimens T4, T5 and T8 which have a ratio of 0.17 have a lower shear force reduction in S1, than other specimens which have a ratio approximately equal to 0.1. However, in spite of T12 having a ratio larger than T4, T5 and T8 the force reduction in the latter specimens is less prominent. This is so, since these three have a cross section of 300x500mm which is larger than the cross-section measuring 300x300mm corresponding to T12. The eccentricity of the rod with respect to the effective depth of the section is therefore lower in T4, T5 and T8, than in T12. As a result, the shear force demand due to the induced $P-\Delta$ effect is also lower. Moreover, it is also observed that in the specimens with 300x500mm sections, the major reduction is in S2 is similar to that in S1. Figure D-40b to figure D-58b, indicate the corresponding flexural moments of each column specimen. The eccentricity of the rods induces a small moment at the end of the columns, such that the shear span is either slightly bigger than 1.7m or slightly smaller than 1.7m. Nevertheless, in the computation and interpretation of data, this effect is ignored.

Figure D-40c to figure D-58c show the cumulative energy dissipation of each section of each column. In many specimens, it is observed that the lowest section does not always dissipate the most energy. It is already observed earlier that the occurrence of damage phenomena does not always follow the order of the sections. This contrasts with the philosophy behind fibre models and its theory based on the plastic hinge model. The fibre sections of the column are generally assumed to be uniform, and the lower fibres in a cantilever are the first to fail, and subsequent fibres follow forming the plastic hinge (Petrini *et al.*, 2004). This behaviour can simulate the behaviour of T12 since the closely spaced transverse reinforcement ensures a uniformly confined section, and damage is observed to increment from the foundation interface upwards. However, in non-seismically designed specimens such as T14, most damage concentrates at a distance above the foundation. Due to the large spacing between the stirrups, the cross-section of the column cannot be assumed to be uniform. The evolution of damage and the mechanisms involved are more regional rather than cross-sectional (Figure D-2 to figure D-20).

As discussed in Chapter 4 Berry *et al.*, 2003 suggest the reduction of the lateral force at the base of the column due to the $P-\Delta$ effects induced by the rods. This strategy is also adopted by Verderame *et al.*, 2008 in the interpretation of column test results. However, as discussed above other sections above the bottom are subject to higher demands. The effective force at the bottom is therefore a demand that is lower than the true capacity of the section. Figure D-21a to figure D-39a show the force-chord rotation history of each column with and without force reduction. The average effective shear force on the sections that sustain damage is included. This is very

similar to the shear force without reduction. Further consideration of the lateral shear force is based on this average.

Figure D-21b to figure D39-b, figure D-21c to figure D-39c and figure D-21d to figure D-39d show the shear force-chord rotation, cumulative energy dissipation-chord rotation and residual stiffness-chord rotation envelopes. A better value of chord rotation of the occurrence of damage is determined using recorded visual imaging of the experiments, and is followed by the diagnostic corrections in section 3.4. Corresponding residual stiffness, shear force and cumulative energy dissipation are then interpolated. The legend of the damage phenomena is found in table D-1.

Further comparisons on the occurrence and sequence of damage for the different properties that distinguish the different columns specimen are then discussed in section 4.4.2 to section 4.4.9.

Table 4-1 The drift ratio of the cycle at which various damage phenomena are observed in each column specimen.

Test	SR	S1	S2	S3	S4	S5	S1				S2			S1-S3		S2	S1-S6
	CR	CR	CR	CR	CR	CR	SP-I	SP-C	SP-F	BK	SP-I	AL	BK	DC-I	DC-F	OS	AL
T1a	0.0075	0.003	0.004	0.005	0.0075	0.02	0.01	0.025	0.025	0.025	0.02	0.03	/	2	2.5	0.0298	/
T1b	0.01	0.005	0.005	0.01	0.015	0.02	0.02	0.025	0.03	0.03	0.035	0.035	/	0.02	0.03	0.0355	/
T1c	0.01	0.003	0.005	0.01	0.01	0.02	0.02	0.03	0.03	0.03	0.04	/	/	0.03	0.04	/	/
T2	0.005	0.003	0.003	0.005	0.01	/	0.02	0.03	0.04	0.04	0.055	/	/	0.03	0.04	/	/
T3	0.005	/	0.003	0.003	0.01	/	0.02	0.03	0.04	0.04	0.04	/	/	0.02	0.055	/	0.09
T4	0.01	0.005	0.005	0.005	0.01	/	0.015	0.02	0.025	0.025	0.02	0.025	0.025	0.015	/	0.03	/
T5	0.005	0.005	0.005	0.01	0.01	/	0.02	0.03	0.03	0.03	0.03	0.04	0.04	0.015	0.02	0.035	/
T6	0.003	0.01	0.005	0.005	0.01	/	0.02	0.03	0.03	0.03	/	/	/	0.02	0.04	0.055	0.07
T7	0.01	0.005	0.005	0.005	0.015	/	0.015	0.02	0.03	0.03	0.04	0.04	0.04	0.015	0.04	0.045	0.045
T8	0.01	0.005	0.005	0.005	0.01	/	0.015	0.02	0.03	0.03	0.04	0.04	/	0.01	0.03	0.04	/
T9	0.01	0.005	0.003	0.005	0.01	0.015	0.03	0.04	0.04	0.04	0.075	0.075	/	0.01	0.04	/	0.08
T10-R	0.005	0.005	0.005	0.005	0.005	0.015	0.02	0.03	0.04	0.04	0.075	/	/	0.02	0.04	/	
T10-L	0.005	0.003	0.005	0.005	0.005	0.015	0.03	0.075	0.09	/	0.055	/	/	0.02	0.04		0.09**r
T11	0.005	0.005	0.005	0.01	0.01	0.03	0.02	0.04	0.04		0.055	0.07	/	0.02	0.075	0.11	0.11
T12	0.005	0.005	0.005	0.005	0.01	0.015	0.03	0.04	0.055	0.105	0.07	0.105	/	0.025	0.09	/	0.12
T13	0.01	0.003	0.005	0.01	0.01	0.04	0.03	0.03	0.055	/	0.02	0.03	/	/	/	/	/
T14	0.01	0.005	0.005	0.005	0.01	/	0.02	0.03	0.04	0.04	0.04	0.055	/	0.02	0.03	0.055	/
T15	0.01	0.005	0.005	0.01	0.01	/	0.015	0.02	0.03	0.03	0.015	0.03	/	0.02	0.03	0.03	0.03
T16-D1	0.003	0.001	0.003	0.005	0.01	0.015	0.02	0.03	0.04	0.055	0.04	0.055	/	0.03	0.04	0.055	/
T17-D2	0.01	0.005	0.005	0.005	0.01	0.03	0.02	0.03	0.04	0.055	0.075	/	/	0.04	0.055	0.075	/

**r = Also includes rupture of longitudinal reinforcement

4.3 Comparison of Experimental results with Analytical Considerations

The numerical and analytical analysis is used to check and compare the analytical validity of some of the experimental results. Push-over analysis was performed in the fibre-based, finite element package Seismostruct (Seismosoft, 2011) on a model simulating a reference sample T13. A damping factor of 2% was applied. The modified model proposed by Menegotto and Pinto (1973) was adopted for steel, while the model for confined concrete was based on Mander et al. (1988). The ultimate strength of concrete (f_{cm}) was taken as 19MPa, the tensile strength (f_{ct}) 2MPa, and the yield strength of 12mm steel bars (f_{yk}) 416MPa. These values were based on specific tests carried out on the materials (Chapter 3).

Element T13 in Chapter 4 shows the geometry and the cross-sectional details of the reference element used in the analysis. Fibre-based inelasticity modelling is based on recommendations and calibrations by Almeida *et al.* 2010. A force-based element is used as shown in figure 4-1a. Fernandes *et al.* 2010 recommends not to use P- Δ for this type of setup. However, if ignored the initial stiffness and maximum force are overestimated as shown in figure 4-1b. If P- Δ effects are simulated, the maximum force will be underestimated, while the strength decay will be overestimated.

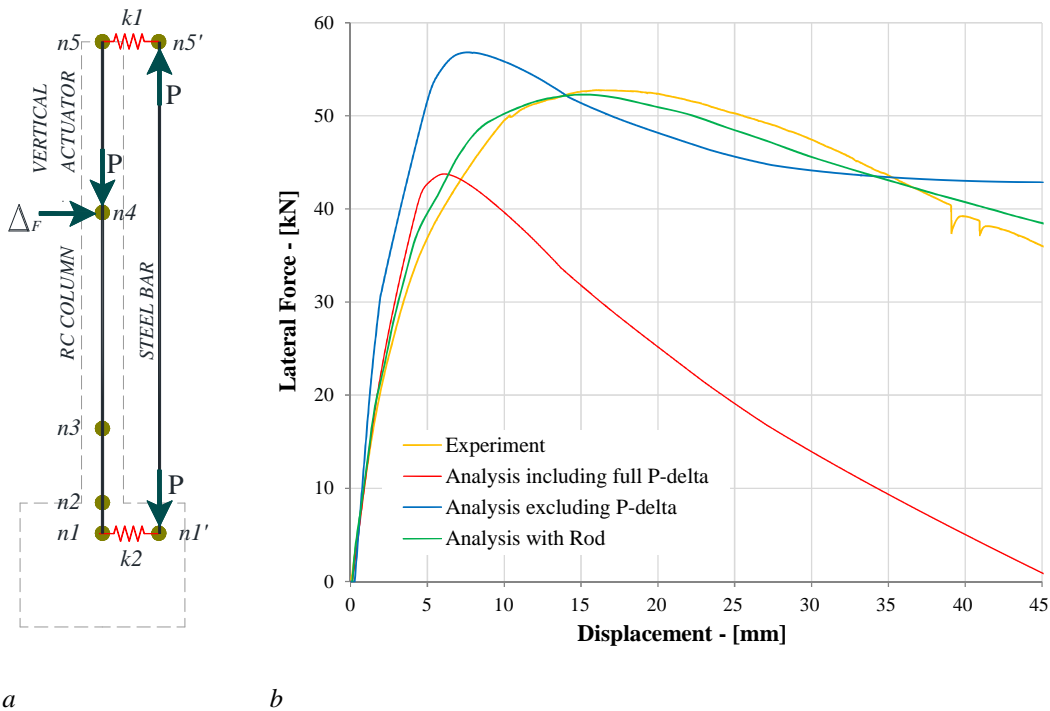


Figure 4-1 a) Model of the column specimen (T13) under monotonic loading, used in the numeric analysis. b) Comparison of the force-displacement response from the monotonic experiment and analysis.

The force deformation response of the experimental tests is used to verify and compare analytical quantities such as initial stiffness ($K_{initial}$), and force and deformation at initial cracking

(θ_{CR-I} ; F_{CR-I}), first yield (θ_Y ; F_Y) and ultimate capacity (θ_{u-20} ; F_{u-20}) determined through sectional analysis. Account for the effects of eccentricity discussed above is made. USC-RC (Esmaleley et al., 2006) and Seismostruct (Seismosoft, 2011) are used for the analysis and the results of the analytical analysis are provided in table 4-2. Table 4-2 also indicates the % difference between the analytical and the experimental values. The analytical values for T1a, and T1b are not indicated, since the analytical procedure was not sensitive to different loading regimes and hence provided similar results as to T14.

Table 4-2 Analytical quantities of initial stiffness, and chord rotation and force at first cracking, first yielding and ultimate capacity for each specimen, compared with experimental results.

Test	θ_{CR-I}	F_{CR-I} kN	θ_Y	F_Y kN	θ_{u-20}	$K_{initial}$ kN/m
T1c	0.0025	25.2	0.0051	40.0	0.038	5760
	<i>0.0</i>	<i>-10.0</i>	<i>-11.8</i>	<i>-3.7</i>	<i>5.6</i>	<i>2.4</i>
T2	0.0025	26.2	0.0052	40.8	0.044	6790
	<i>-7.4</i>	<i>-9.7</i>	<i>-10.8</i>	<i>-6.8</i>	<i>12.8</i>	<i>9.5</i>
T3	0.0027	26.2	0.0056	49.0	0.049	7206
	<i>-3.6</i>	<i>-9.7</i>	<i>-3.7</i>	<i>10.1</i>	<i>8.9</i>	<i>-9.9</i>
T4	0.0036	80.2	0.0052	123.9	0.034	28524
	<i>5.9</i>	<i>-4.5</i>	<i>-3.7</i>	<i>7.7</i>	<i>21.4</i>	<i>9.9</i>
T5	0.0036	80.2	0.0052	120.0	0.037	28524
	<i>-7.7</i>	<i>-8.9</i>	<i>-8.8</i>	<i>9.1</i>	<i>12.3</i>	<i>8.7</i>
T6	0.0024	25.2	0.0051	40.0	0.051	5760
	<i>-4.0</i>	<i>0.8</i>	<i>-13.3</i>	<i>-4.8</i>	<i>9.0</i>	<i>4.7</i>
T7	0.0032	29.2	0.0054	47.0	0.022	8263
	<i>-8.6</i>	<i>-14.1</i>	<i>9.5</i>	<i>11.9</i>	<i>14.7</i>	<i>7.3</i>
T8	0.0036	80.2	0.0052	123.9	0.031	28524
	<i>-10.0</i>	<i>-8.9</i>	<i>-11.9</i>	<i>10.6</i>	<i>13.6</i>	<i>7.2</i>
T9	0.0025	35.2	0.0072	74.7	0.067	8085
	<i>-10.7</i>	<i>-12.0</i>	<i>-12.2</i>	<i>-5.1</i>	<i>15.5</i>	<i>-10.2</i>
T11	0.0032	39.2	0.0074	75.3	0.105	8167
	<i>-8.6</i>	<i>-8.8</i>	<i>-11.9</i>	<i>1.6</i>	<i>13.5</i>	<i>8.2</i>
T12	0.0042	44.2	0.0076	97.0	0.125	8200
	<i>-12.5</i>	<i>-9.8</i>	<i>-11.6</i>	<i>9.0</i>	<i>13.6</i>	<i>8.9</i>
T13	0.0037	25.2	0.0063	40.0	0.055	5760
	<i>-9.8</i>	<i>-10.0</i>	<i>-13.7</i>	<i>-2.5</i>	<i>-1.7</i>	<i>4.7</i>
T14	0.0026	25.2	0.0052	40.0	0.038	5760
	<i>-7.1</i>	<i>-10.0</i>	<i>-5.5</i>	<i>6.0</i>	<i>13.4</i>	<i>4.3</i>
T15	0.0032	28.2	0.0065	47.0	0.021	7900
	<i>-8.6</i>	<i>-9.0</i>	<i>10.2</i>	<i>7.3</i>	<i>10.5</i>	<i>5.3</i>
T16	0.0026	25.2	0.0072	51.3	0.041	6615
	<i>36.8</i>	<i>68.0</i>	<i>-7.7</i>	<i>16.6</i>	<i>28.1</i>	<i>10.2</i>
T17	0.0026	25.1	0.0072	51.3	0.041	6615
	<i>-39.5</i>	<i>-19.0</i>	<i>-11.1</i>	<i>6.9</i>	<i>-24.8</i>	<i>6.7</i>

Note: The number in italics is the % difference between the analytical values and the experimental values. “-” indicates that analytical value is smaller than experimental value, and “+ve” indicates that analytical value is larger than experimental value.

It is observed that the initial analytical stiffness is consistently larger than the corresponding experimental values for all experiments. As a result, cracking is also observed to occur in the analytical analysis at lower values. Most values fall within 10% error. However, this is not the case in some cases. The error for the analytical quantities associated with T16-D1 and T17-D2 which are associated with lap-splicing is quite large. This is so since it was not possible to incorporate and model all aspects that affect deformation as a result of combined bond-slip and buckling of the lap-spliced elements.

4.4 Observations and Comparisons of the Results of Column Tests

4.4.1 Comparison of the Behaviour of RC Columns with Different Span-Depth Ratio

In this section the results of specimen T8 are compared with the results of T2. Most physical properties of both specimens are similar with the exception that T8 has a span-to-depth ratio of 3.6 while T2 has a ratio of 5.7. The confinement ratio, reinforcement ratio and the load ratio are similar however, the reinforcement diameters, spacing and number of legs of stirrups and the axial force are different in order to keep the ratios constant as shown in Chapter 3. Other specimens including T4 and T5 have a span-to-depth ratio of 3.6 as well. However the comparison of T4 and T5 specimens with corresponding specimens having a ratio of 5.7 are respectively discussed in section 4.4.3 and section 4.4.4, since they have other variables related to the loading pattern and confinement aspects.

There is a considerable variation between T2 and T8 in terms of damage development, strength degradation, energy dissipation and residual stiffness with respect to chord rotation which is a function of the different characteristics of the two specimens. Figure D-43 and figure D-49 indicate that the quantity of cumulative energy dissipation decreases from S1 to S6 along all range of chord rotation. Nevertheless, beyond $u-50$, the cumulative energy dissipation for T8 is equal in S2 and S1. Variation between T2 and T8 is also observed in figure 4-2 and figure 4-3. The shear force-chord rotation envelope, the cumulative energy dissipation – chord rotation envelope and the residual stiffness – chord rotation envelope of T8 enclose the corresponding envelopes of T2. However, the latter extends over a wider range of chord rotation to experience the same level of damage.

Initial flexural cracks in T8 are observed to occur at a chord rotation 33% larger than the corresponding value of T2, while indication of initial spalling and diagonal cracking in T8 respectively occur at a chord rotation 11% and 55% lower than values corresponding to specimen T2. The dissipated energy of T8 at the initial observation of flexural cracks and spalling are significantly larger than corresponding values of T2, while the dissipated energy of T8 at diagonal cracking is approximately 58% lower than the corresponding value of T2. The residual stiffness at initial flexural cracking, spalling and diagonal cracking for T8, are significantly larger than

values corresponding to T2. On comparing the occurrence of initial flexural cracks, spalling and diagonal cracking of T8 with the reference specimen T14, the former consistently has larger chord rotation, significantly lower dissipated energy and significantly larger residual stiffness.

Flexural cracks are observed before yielding in both T2 and T8. However, the number of cracks in T8 is small compared with the number of cracks in T2. Before the maximum force capacity is reached, both specimens start developing cover spalling. The specimen with the lower aspect ratio starts also to develop diagonal cracking at this stage. Beyond this point, no new flexural cracks are observed to form along the sides of both specimens T2 and T8. Moreover, cracks are observed to propagate in both foundations. More cracks are however observed in the foundation of specimen T8. In T2 initiation of diagonal cracks are observed just before u-10. During this stage, only further development of existing damage is observed in T8. Before u-20 is reached, buckling is observed in T8. Complete diagonal cracks are formed in T2 at this stage. Complete diagonal cracks are observed in T8 before u-50 is reached. Beyond u-50, no further extension of spalling is observed in T2, however further spalling is observed in T8 after u-50 which occurs simultaneously with the failure of the transverse reinforcement. The concrete core of both samples suffer considerable damage.

All damage levels of T8, including Y, m, u-10, u-20 and u-50 have a chord rotation which is lower than the corresponding values of T2. The variation increases gradually as the level of damage increases, and varies between 10% and 35%. The cumulative dissipated energy of T2 is larger than T8 for all damage levels. At yielding, the difference is more than double, however the difference decreases gradually as the damage level increases and at u-50 this is approximately 50%. Consequently, the residual stiffness at all damage levels of T8 is significantly larger than the residual stiffness of T2 at all damage levels. At yielding this is close to triple, while at u-50 this is close to four times. In spite of the large difference at the higher damage level, both values are low.

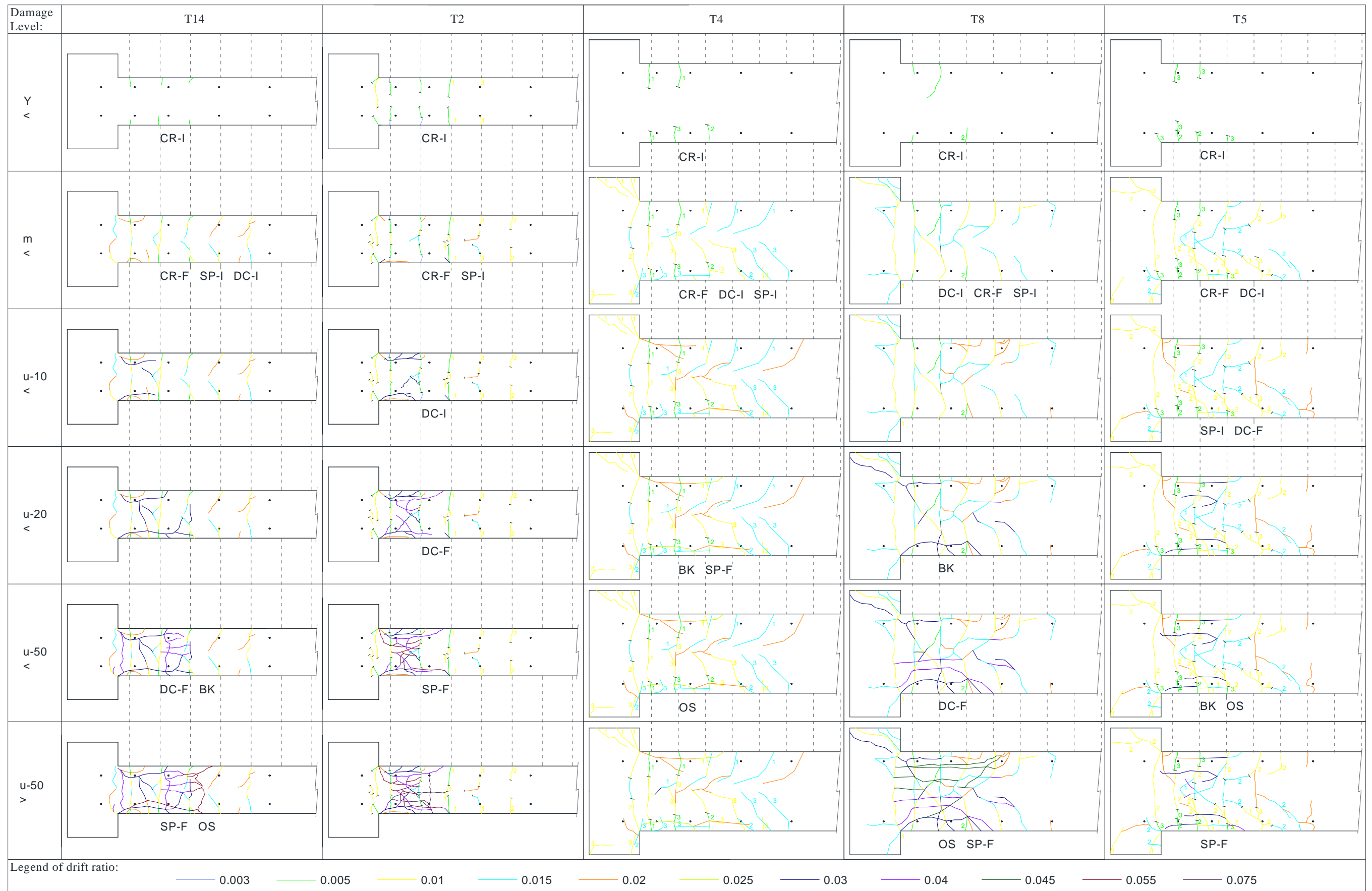
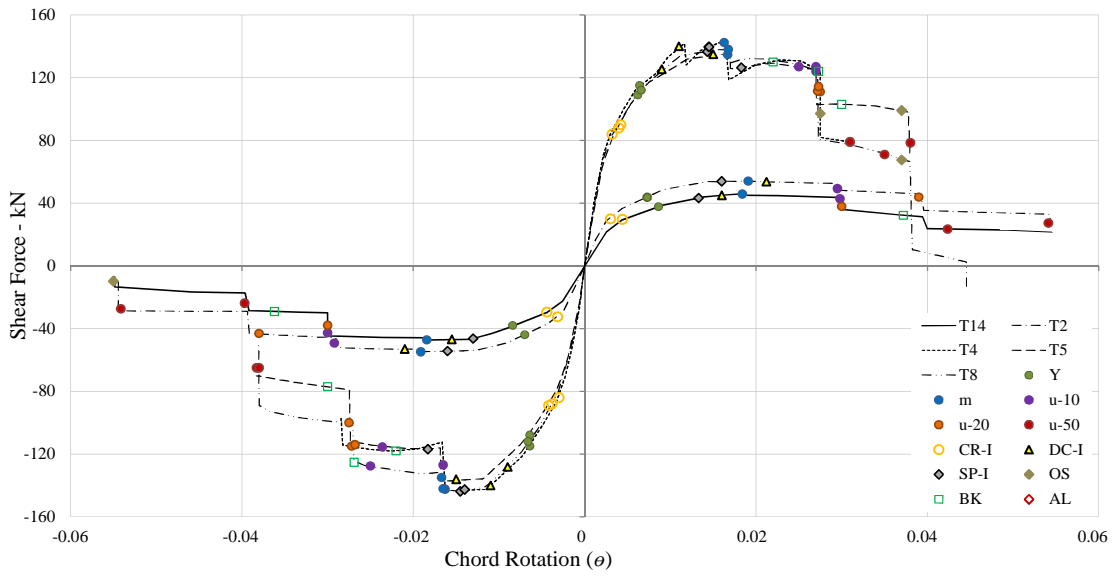
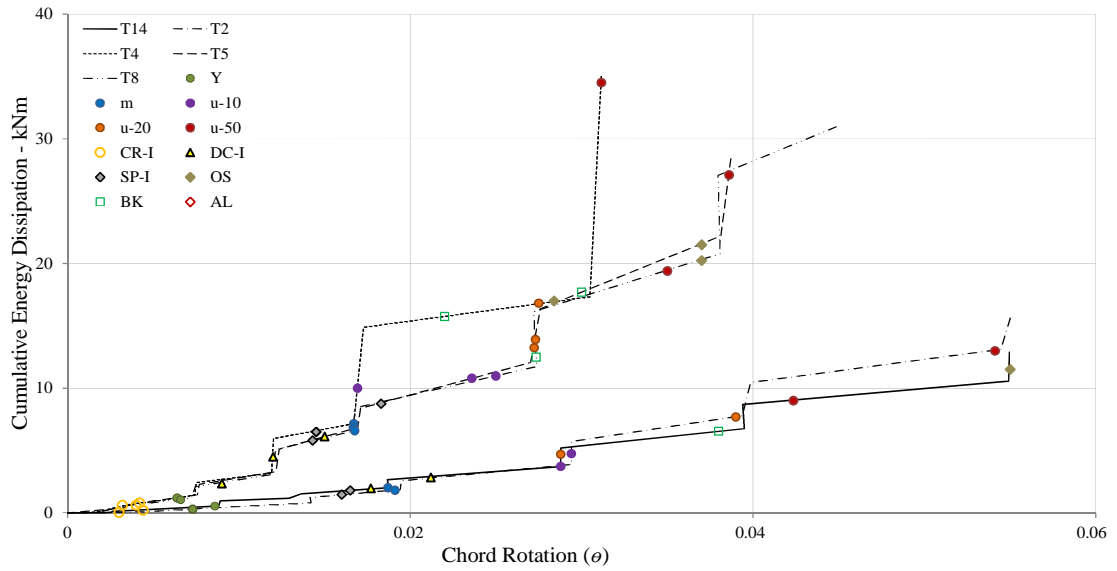


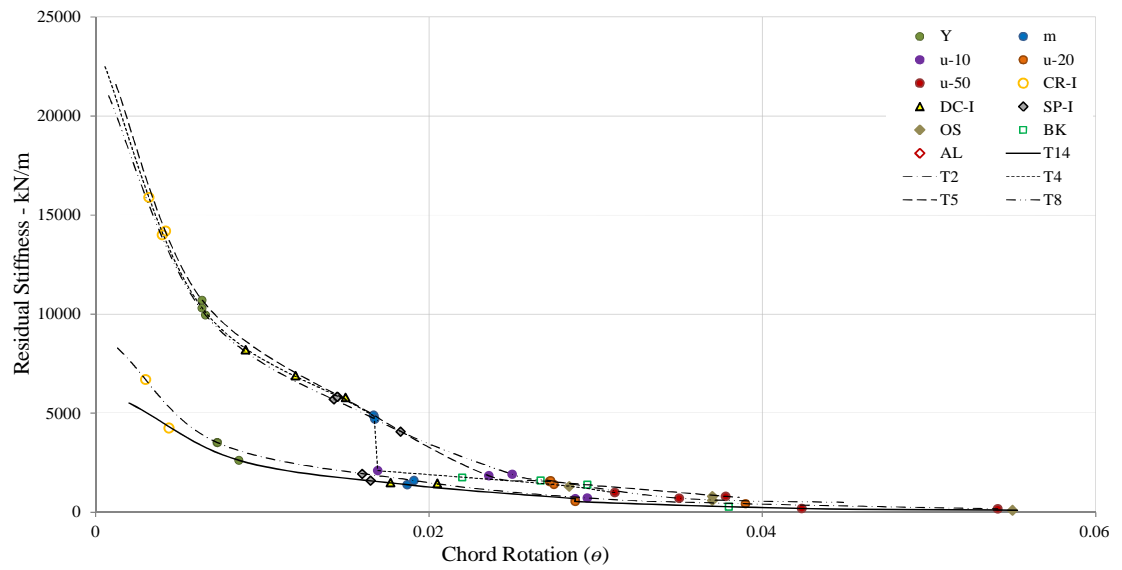
Figure 4-2 The development of damage as observed at the end of each damage level for column specimen T14, T2, T4, T5 and T8.



a



b



c

Figure 4-3 Comparison of T2, T14, T5, T4 and T8 in terms of: a) Shear force-chord rotation, b) Cumulative energy dissipation – chord rotation, c) Residual stiffness-chord rotation, envelopes.

4.4.2 Comparison of the Behaviour of RC Columns Subject to Different Loading Patterns

Comparisons of the effects of loading patterns are based on two sets of columns: T13, T14, T1b and T1a, and T8 and T4. The specimens in each set share similar detailing aspects, geometrical characteristics and material properties. The only major characteristic that distinguishes each column in each set is the different loading pattern and intensity in terms of number of cycles and displacement increment that each column is subject to during testing as presented in Chapter 3. Considerable differences are observed in the occurrence of damage sequence, and in the magnitude of chord rotation, cumulative energy dissipation and residual stiffness of columns within the same set. Both sets are discussed separately since the variability in the loading patterns is different across both sets.

In the first set, the difference in loading pattern consists in the magnitude of ascending displacement increments of each step and the number of cycles in each step. Specimen T13 is subject to monotonic loading (LP1), while T1a is subject to the most intense loading pattern (LP4), characterised with the largest number of cycles per increment, and the magnitude of increments is very small. T1b is subject to a less intense cyclic pattern, which is traditionally recommended by Krawlinker *et al.*, (1997), and the reference specimen T14 is subject to an even less intense cyclic pattern, based on the response analysis discussed in Borg *et al.*, 2012 and which is also used in the other column specimens. The intensity of the loading pattern therefore increases from LP1 to LP4. Figure 4-4 shows the comparison of damage development inside the columns, while figure 4-5 shows the comparison of strength degradation, energy dissipation and residual stiffness with chord rotation in all the specimens.

Flexural cracking is observed in all four specimens before yielding. The extent of this damage decreases gradually with specimens subject to less intense loading patterns. At this state of damage specimen T1a, which is subject to more loading cycles has more extensive cracks, while specimen T13, which is subject to monotonic loading has the least extensive cracks which occur on one side of the specimen only. The chord rotation on the initiation of flexural cracking decreases with respect to the chord rotation of T13 by 6%, 9% and 28% for specimens T14, T1b and T1a respectively. This indicates that as the intensity of the loading pattern increases, the rotation at which initiation of flexural cracking is observed decreases. Consequently, the residual stiffness is however observed to increase. This is particularly so since the strength at which initiation of flexural cracking occurs is quite similar for all the four specimens.

No formation of new flexural cracks along the shear span is observed in T14 and T1b after the maximum force capacity is reached. For T13, no new flexural cracks are observed to form after u-10 is reached while for T1a, no new flexural cracks are observed beyond u-20. It is also observed that flexural cracks in T13, T1a and T1b are formed in sections S1 to S5. However for

T14 no flexural cracks are observed in S5. The chord rotations on the last observed flexural crack of the specimen with cyclic loading are consistently lower than the observed value corresponding with T13. However, contrary to what is observed on the occurrence of initial flexural cracking, specimen T14 with the least intense loading pattern has the lowest chord rotation, while T1a which has the most intense loading pattern has the highest chord rotation of the three specimens subject to cyclic loading on the observation of their last formation of flexural crack. The values are very close and fall within the margin of error. Hence these observations can also be coincidental. No particular trends are observed for cumulative energy dissipation or residual stiffness of T1a, T1b and T14 with respect to T13.

The initiation of spalling is observed in all specimens before the maximum force capacity is reached. On the occurrence of this damage phenomenon, the chord rotation of T14, T1b and T1a are respectively 31%, 38% and 59% lower than the value of the specimen subject to monotonic loading. The energy dissipation is respectively observed to increase by half for T14, by approximately double for T1b and close to three times for T1a. The residual stiffness on the initiation of spalling increases by 33% for T14, by 46% for T1b and more than double for T1a with respect to T13.

Continuation of cover spalling along the shear span is observed to occur beyond u-50 damage level in T14. However, this is not observed in T1a and T1b beyond u-50 and in T13 beyond u-20. A lack of trend is also confirmed in terms of chord rotation, and residual stiffness. Both properties for T14 are observed to be relatively lower than corresponding values for T13. Nevertheless, the value of the properties for T1a and T1b are both higher when compared with T13. The difference in cumulative energy dissipation of T14, T1b and T1a with T13 is significantly large in all three cases. It is however larger for T1a and lower for T14.

The first indication of diagonal cracking in T14, T1b and T1a is respectively observed at a chord rotation 11%, 20% and 28% lower than the corresponding chord rotation of T13. While for T13, T14 and T1b this damage phenomenon occurs before u-10 is reached, for T1a this occurs just afterwards. The energy dissipation of the specimens associated with cyclic loading is significantly larger than the value corresponding to T13. The discrepancy increases as a function of the cyclic intensity of the loading pattern. The residual stiffness at the initiation of buckling is similar for T13 and T14, however it is approximately 12% lower for T1b and 17% larger for T1a. On the complete formation of a diagonal crack, the chord rotation, cumulative energy dissipation and residual stiffness in T14, T1b and T1a with respect to T13 follows a similar trend as that observed on the initiation of diagonal cracking. However, the discrepancy in chord rotation is slightly lower, the discrepancy in residual stiffness is slightly larger and the discrepancy in cumulative energy dissipation is significantly larger.

Buckling in specimen T13 occurs before u-20 damage level is reached. However for the other specimens, which are subject to cyclic loading, buckling is only observed before u-50 damage level is reached. However, the chord rotation at which this phenomenon is observed is lower with respect to T13 for all the other three specimens. For T14, the chord rotation is 30% lower, for T1b this is 45% lower and for T1a, this is 50% lower. The dissipated energy of T14, T1b and T1a are all substantially larger than the value of T13. The residual stiffness of T14 at the observation of buckling is only 27% larger than T13. However for T1b this is more than double, and for T1a this is close to three times the value of T13.

The failure of stirrups is not observed in T13, however this damage phenomenon is observed in all the three other specimens subject to cyclic loading after the u-50 damage level is reached. The chord rotation of T1b at which this phenomenon occurs is 35% while for T1a, the value is lower by 46%. However, the cumulative energy dissipation is approximately 60% larger for T1b, and more than twice as large for T1a, when both values are compared to T14. The relative residual stiffness follows a similar trend. This is approximately 80% larger for T1b, and more than three times as large for T1a, when compared to T14.

Trends are also observed in terms of the damage levels considered. The chord rotation at any of the five damage levels is highest for specimen T13 which is associated with monotonic loading. It decreases with the specimen associated with a more intense loading cycle. Inversely, the relative residual stiffness and cumulative dissipated energy of T14, T1b and T1a with respect to T13, in general increases with the specimen associated with the more intense loading pattern at all damage levels considered.

The least difference in terms of chord rotation is observed at the yielding. At this damage level, the chord rotation of T13, T14 and T1b is very similar, while that of T1a is only about 15% larger. Nevertheless, considerable residual stiffness difference is observed at this damage level which is much higher than that exhibited at maximum force, but much lower than other subsequent damage levels. In general, the relative cumulative dissipated energy and the residual stiffness of T14, T1b and T1a with respect to T13 increases with the rank of the damage level after the maximum force is reached.

The envelopes in figure 4-5 indicate that T13, the sample subject to monotonic loading is characterised with the larger ductility, lower dissipated energy, and in general larger residual stiffness at any chord rotation. In general, T1a, the specimen subject to the most intense loading pattern is characterised with the lowest ductility, largest cumulative energy dissipation and largest residual stiffness at any chord rotation.

Based on the discussed trends above, power trend lines are fitted for each damage phenomenon and damage level, and relate chord rotation with cumulative dissipated energy, and chord rotation with residual stiffness. The magnitude of the negative power of the chord rotation-cumulative

energy dissipation relationships decreases from u-50 till the maximum force and then increases till yielding. While in general, the negative magnitude increases from yielding for the chord rotation-cumulative energy dissipation relationships of damage levels. The trend lines associated with the initiation of diagonal cracking and initiation of spalling cross each other, indicating a change in the sequence of damage as a function of the different loading pattern used. This is observed in both cumulative energy dissipation and residual stiffness relationships. It is also observed that while the cumulative dissipated energy of each column in general increases with the chord rotation, the residual stiffness decreases. Nevertheless, the equations of both types of relationships have a negative power. The decay with the progression of damage level is stronger in the residual stiffness fitted trends than in the cumulative energy dissipation, so much so, that while the envelopes of each column for cumulative energy dissipation are very distinct, the envelopes of each column for residual stiffness overlap.

Figure D-54, figure D-55, figure D-41 and figure D-40, correspond with specimens T13, T14 T1b and T1a, and indicate the flexural moment, shear force and energy dissipation along each section S1 to S6 of each column. It is observed that for each column, S1 is the section that dissipates most energy up to a chord-rotation value beyond which S2 is then the section that dissipates most energy. The chord rotation where this occurs is highest for T13, the column subject to monotonic loading. The chord rotation at which this phenomenon occurs, decreases for the column subject to a more intense loading pattern.

In the second set of specimens consisting of T8 and T4, the difference in loading pattern consists mainly in the order of the loading cycles. While T8 is subject to LP2 which is a uniformly incremental pattern, T4 is subject to LP5 which consists of a pattern with initial cycles of uniform increments up to maximum force which is similar to LP2. This is then followed by a cycle with a large amplitude, and then by a number of cycles of lower amplitude. Figure 4-2 shows the comparison of damage development inside the columns, while figure 4-3 shows the comparison of strength degradation, energy dissipation and residual stiffness with chord rotation in all the specimens. In general, although both specimens T4 and T8 are physically similar, T4 fails at lower chord rotations.

The damage development and the shear force, cumulative energy and residual stiffness with chord rotation envelopes of T8 and T4, are similar up to maximum force. Up to this damage level, both columns exhibit initial spalling and initial diagonal cracking. Moreover, no formation of new flexural cracks is observed to form along the shear span of both columns. The chord rotation on the initial observation of cracking in T4 is 20% lower than T8. However, the residual stiffness and the cumulative energy dissipation are also similar. On the initiation of spalling, the chord rotation and residual stiffness of both specimens are similar, however, the cumulative energy dissipation of T4 is 12% lower than T8.

After the maximum force, the differences between the two specimens increase. While in T8 buckling is observed before u-20 is reached, in T8 a complete diagonal crack is also observed. A complete diagonal crack is observed in T8 before u-50 is reached. However, at u-50 complete failure of the transverse reinforcement is already observed in T4. This damage phenomenon is observed in T8 after u-50 damage level is reached. From u-10 to u-50, the chord rotation of T4 varies between 11% and 32% lower than the corresponding chord rotation of T8. The cumulative dissipated energy of T4 at u-20 is 21% larger than the corresponding value of T8 at the same damage level, while at u-50 the difference increases to 77%. At u-50, the residual stiffness of T4 is 39% larger than T8. On the initiation of diagonal cracking, the chord rotation of T4 is 33% larger than T8, the cumulative energy dissipation is 90% larger and the residual stiffness is 40% larger. Buckling in T4 is observed at a chord rotation 20% lower than T8. However, the dissipated energy at this stage is 26% higher and the residual stiffness is only 10% larger. On the observation of transverse reinforcement failure, the chord rotation of T4 is 23% lower than T8. The cumulative energy dissipation and residual stiffness are respectively lower by 15%, and by more than double. As shown in figure D-49 and figure D-44, section S1 is the section that dissipated most energy at most damage levels. However, at the highest deformations, the energy dissipated by S2 is similar. While in T8, S2 and S1 dissipate similar amount of energy at a chord rotation of 0.038, in T4, S2 and S1 dissipate similar amount of energy at a chord rotation of 0.03.

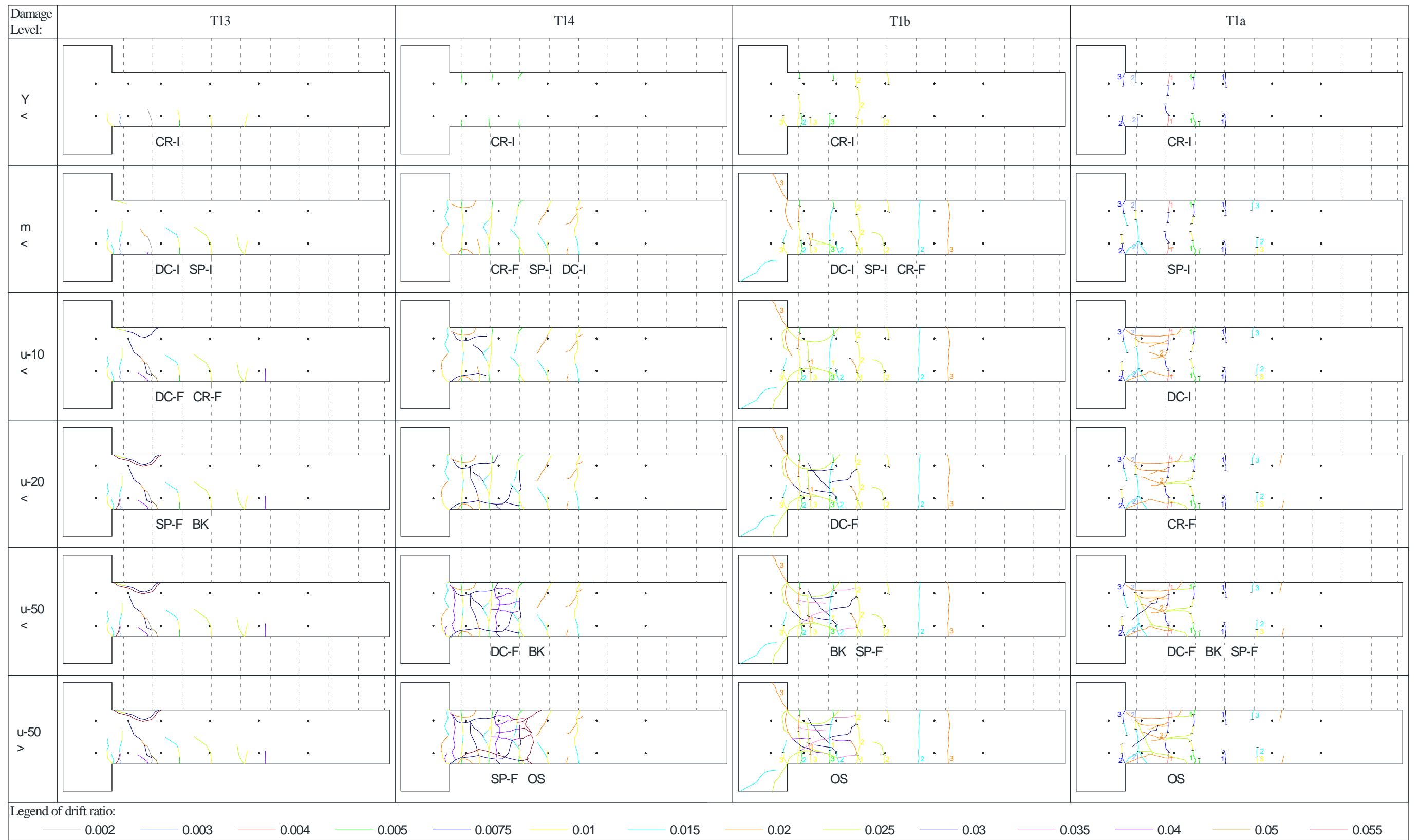
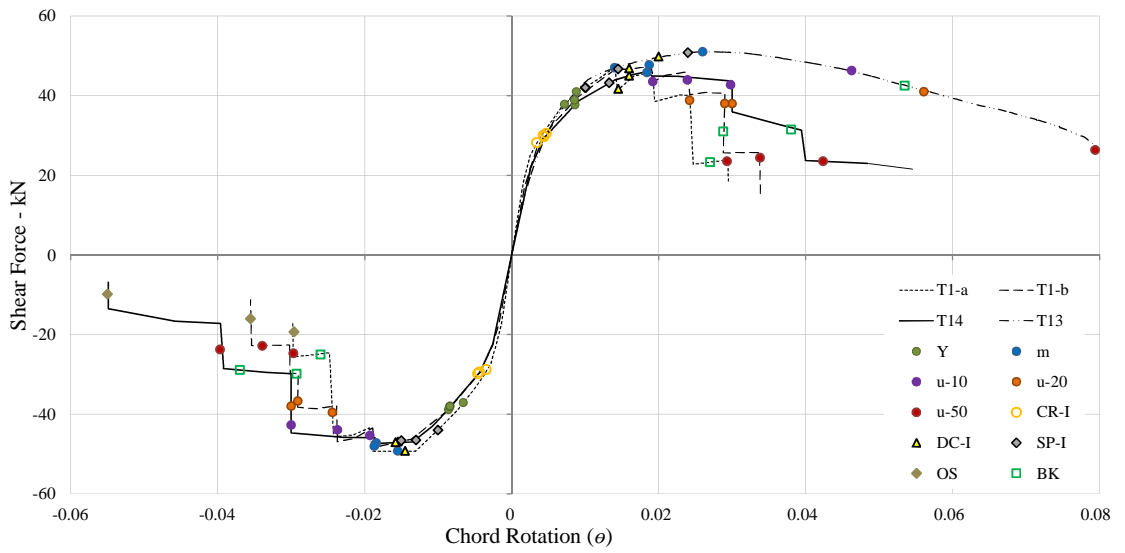
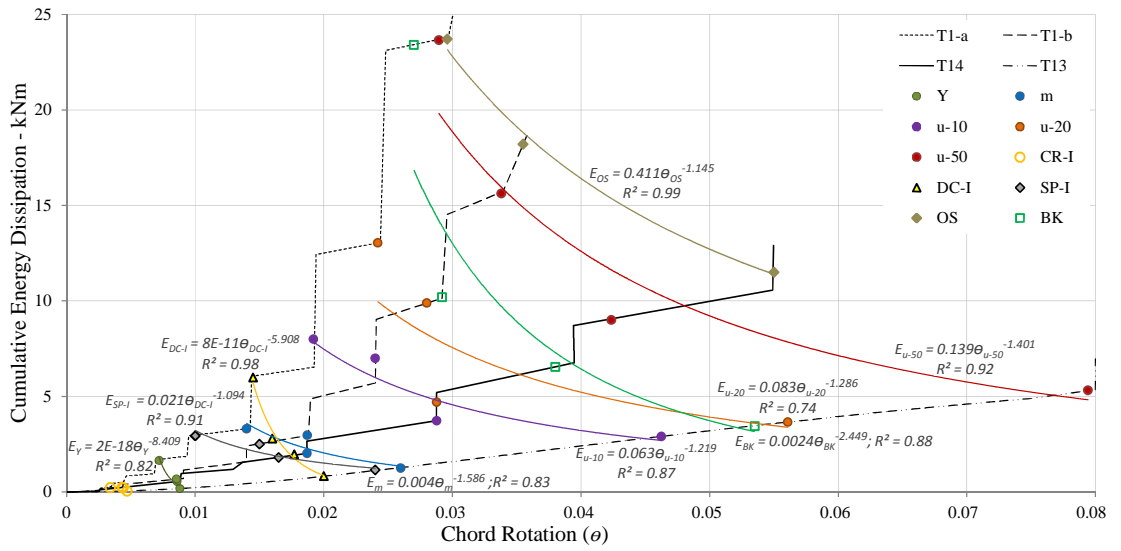


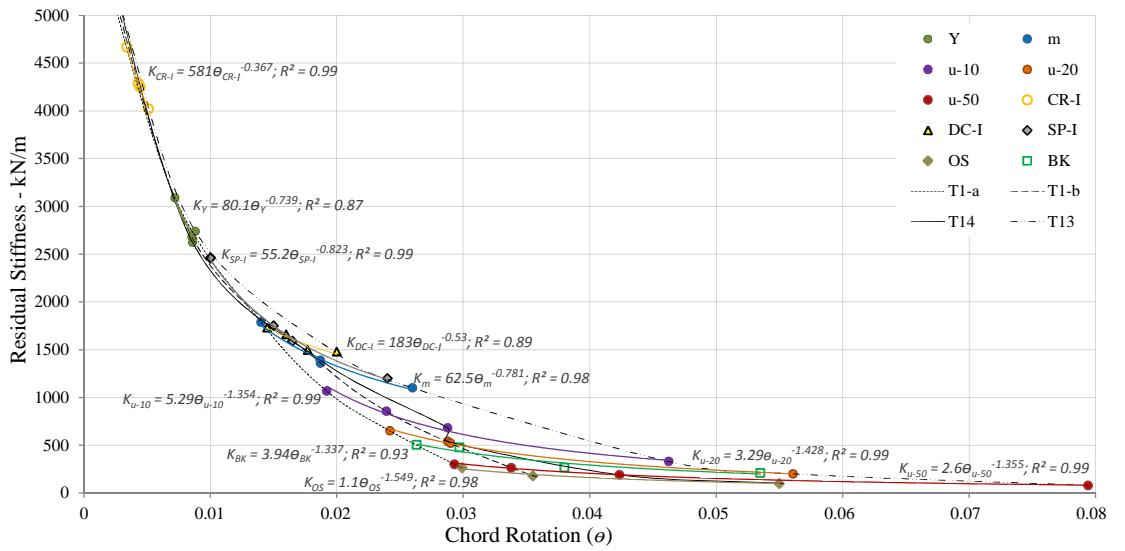
Figure 4-4 The development of damage as observed at the end of each damage level for column specimen T13, T14, T1a and T1b.



a



b



c

Figure 4-5 Comparison of T1a, T1b, T13 and T14 in terms of: a) Shear force-chord rotation, b) Cumulative energy dissipation – chord rotation, c) Residual stiffness-chord rotation, envelopes.

4.4.3 Comparison of the Behaviour of RC Columns with Transverse Reinforcement Having 90° or 135° Hooks

As shown in Chapter 3, specimens T1c, T2, T3, T5, T7, T9, T10, T11 and T12 are constructed with transverse reinforcement having 135° hooks, while specimens T1a, T1b, T4, T6, T8, T13, T14, T15, T16-D1 and T17-D2 are constructed with transverse reinforcement having 90° hooks. This characteristic is the only difference between specimens T14 and T1c, and between T8 and T5, while the confinement ratio and the aspect ratio are the major differences between these pair. The comparison of damage development between T14 and T1c is observed in Figure 4-6, while the corresponding comparison between T8 and T5 is shown in Figure 4-2. Comparison in terms of strength degradation-chord rotation, cumulative energy dissipation-chord rotation and residual stiffness-chord rotation is shown in figure 4-7 and figure 4-3 for T14 and T1c, and T8 and T5 respectively. Differences in damage development and capacity characteristics as a result of the differences are observed and confirm conclusions by Park *et al.*, 1975, Priestley *et al.*, 1992 and Fardis, 2009. The magnitude of the observed differences varies across the two pairs of compared test outcomes, as a result of the other different characteristics between the two pairs.

The shear force – chord rotation envelope of T1c encloses the envelope corresponding with T14 only until $u-10$. Beyond this damage level, the envelopes are very similar. Conversely, the envelope of T5 and T8 are similar until $u-20$ when the specimen is loaded in a particular direction. Subsequently the envelope corresponding with T5 encloses the envelope of T8. However, the negative part of the envelope corresponding to deformation is similar for T5 and T8 until the maximum force. Subsequently, the envelope corresponding with T8 encloses the envelope corresponding with T5. Hence, in this case the inclusion of 135° hooks does not clearly imply more ductility and larger capacity. The energy dissipation – chord rotation envelopes of T5 and T8 are very similar. Conversely, the envelope corresponding with T1c encloses the corresponding envelope of T14. The residual stiffness – chord rotation envelope of T1c indicates, that the residual stiffness is larger than T14 only until $u-10$, as then both envelopes follow similar paths. However, the envelopes of T5 and T8 are very similar throughout the deformation range. As indicated in figure D-49, S1 of T8 is the section that dissipates most energy at each damage level. However, a lot of energy is dissipated by S2 after $u-50$ is reached, and which is equal to the cumulative dissipated energy by S1. The cumulative energy dissipation until the maximum force is similar for both S2 and S3. In figure D-46, a similar trend is observed for T5. However, S1 dissipates more energy only until $u-20$. Beyond this level, S2 dissipates more energy. The envelopes of S2, S3 and S4 are also very similar until when the maximum force is reached. Figure D-42, and figure D-55 indicate that the energy dissipation patterns of the sections in T14 are similar to those in T1c. The shear force in T5 and T8 is more uniform on the columns than in T1c and T14.

The first flexural crack in T1c is observed at a chord rotation 32% lower than the same observation in T14. However, the first crack in T5 is observed at a chord rotation 6% larger than the same observation in T8. The residual stiffness of T1c is 21% larger than the value of T14, while the values of T5 and T8 are similar. The chord rotation at initial spalling in T1c, is observed to be approximately 12% larger, while for T5 is observed to be approximately 12% lower than the corresponding values of T14 and T8 respectively. The cumulative dissipated energy at the initiation of spalling in the columns with 135° hooks is larger than the corresponding columns with 90° hooks. For T1c, the cumulative dissipated energy is larger by 37% and for T5 this is even larger by 50%. Nevertheless, opposite trends are observed in residual stiffness. For T1c, the value is larger than that corresponding with T14 by 9%, while the value of T5 is lower than that of T8 by 29%. The difference in the observation of initiation of diagonal cracking is substantial. The chord rotation of T1c is larger than the value of T14 by 46%, and the chord rotation of T5 is larger than the value of T8 by 66%. The energy dissipation of both T1c and T5 is respectively larger than the values of T14 and T8 by more than double, while the residual stiffness is approximately lower by 33%. The difference in chord rotation on the occurrence of buckling between T1c and T14 is very small. However, the chord rotation for T5 is 10% larger than the value of T8. While the cumulative dissipated energy of T1c is only 19% larger than that of T14, the value of T5 is 40% larger than the value for T8. The residual stiffness of T1c is 5% larger than the corresponding value of T14. An opposite trend is observed in the other pair of specimens, as the residual stiffness of T5 is lower than that of T8 by 13%. Comparison in the failure of transverse reinforcement can only be made between T5 and T8 since this damage phenomenon is not observed in T1c. The chord rotation at which this transverse reinforcement failure occurs is similar for both T5 and T8, while the cumulative energy dissipation is 7% larger for the former. The residual stiffness at this stage is very low for both specimens.

Flexural cracking is observed to occur in T5 and T8, and T1c and T14 before yielding of the specimens. However more distributed cracks are observed on the two specimens with 135° hooks. Before the maximum force capacity is reached, initial spalling and initial diagonal cracks are observed on both specimens with 90° hooks. No new flexural cracks are observed in these two columns beyond this damage level. However in T1c, only initiation of spalling is observed, while in T5 the specimen with the larger cross-section and lower aspect ratio, the initiation of diagonal cracking is observed. No new flexural cracks are observed in this latter column beyond this damage level. Continuation of already occurring damage is observed in T14 and T8 until u-10 is reached. However in T1c initial diagonal cracking is observed. No development of new flexural cracks is observed in T1c beyond this damage level. A complete diagonal crack and initial spalling is observed in T5. Continuation of already occurring damage is observed in T14 and T1c before u-20 is reached. However, no further extension of spalling is observed along the shear span of T1c. Before u-20 is reached, buckling is observed in T8, while only extension of already occurring damage is observed in T5. In T14 and T1c, buckling and a complete diagonal crack are observed

before $u-50$ is reached, while buckling is observed in T5 and a complete diagonal crack in T8. Opening of the hooks in T5 are also observed at this stage and hence at a maximum force reduction lower than that in T8 which only has 90° hooks. Similar failure of the transverse reinforcement is also observed in T14 and T8 after $u-50$. This failure phenomenon is not observed in T1c. For all the four specimens, failure of the transverse reinforcement was further accompanied by further buckling and extension of cover spalling.

The chord rotation of T1c at yielding is 10% lower than the corresponding value of T14, while the chord rotations at yielding of T8 and T5 are similar. The cumulative energy dissipation of T1c at this damage level is however 36% larger than that of T14, while the value of T5 is 14% larger than that of T8. The residual stiffness of T1c is 26% larger than the corresponding value of specimen T14, while the value of T5 is only 8% larger than the value of T8. For the damage levels at maximum shear force, $u-10$ and $u-20$, the difference between the chord rotation of T1c and T14, and the difference between the chord rotation, cumulative energy dissipation and residual stiffness of T5 and T8, is less than 4%. The cumulative energy dissipation of T1c is 29% larger than the value of T14 when the shear force is at maximum. The difference is reduced to only 14% at $u-20$. The residual stiffness of T1c at maximum shear force is 19% larger than the value of T14, and this is reduced such that the residual stiffness of T1c is 12% lower than the corresponding value of T1, at $u-20$. At $u-50$ the difference between the pairs of specimens is more distinct. The chord rotation of T1c is 7% larger than the corresponding value of T14, while the value of T5 is 10% larger than the value of T8. The cumulative dissipated energy of T1c is 19% larger than the value of T14, while the value of T5 is 40% larger than the value of T8. The residual stiffness of T1c is 10% larger than the value of T14, while the residual stiffness of T5 is 13% larger than T8.

In general it is observed, that the difference between the specimens with 90° hooks and 135° hooks is more prominent in the pair with the larger aspect ratio and lower confinement ratio up to $u-20$. However, beyond this damage level this difference is more prominent in the pair of specimens with the lower aspect ratio and larger confinement ratio.

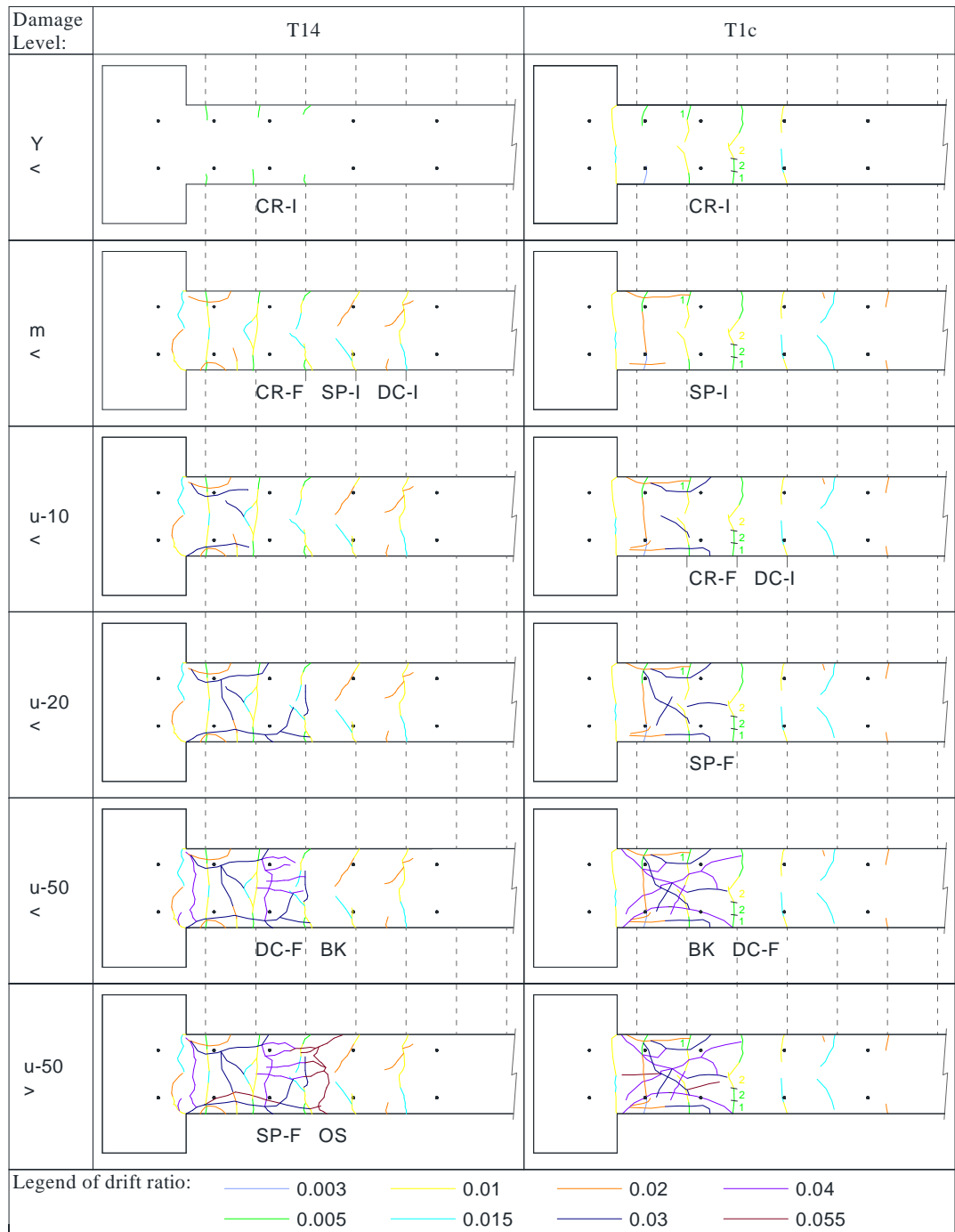
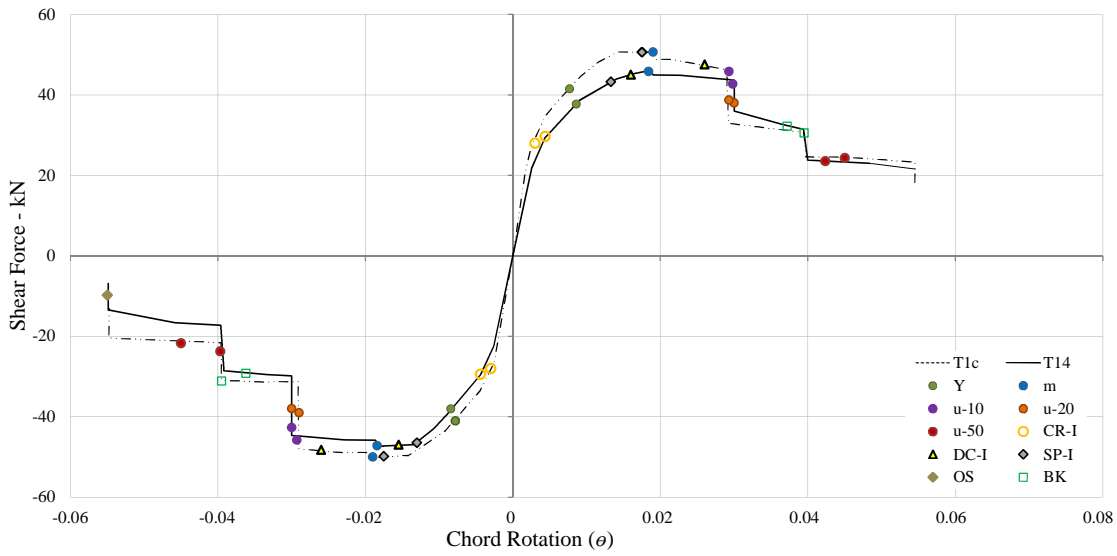
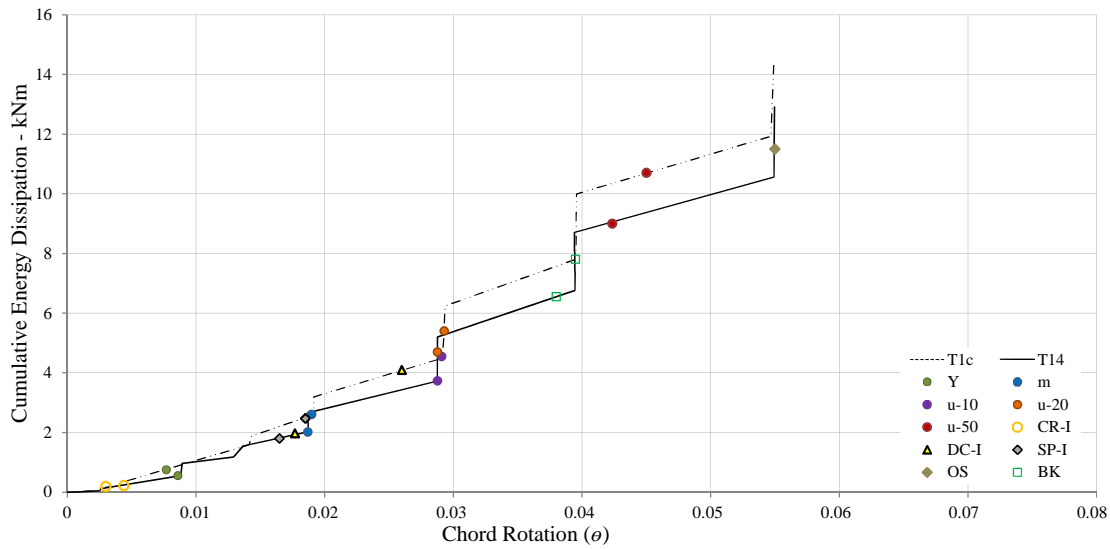


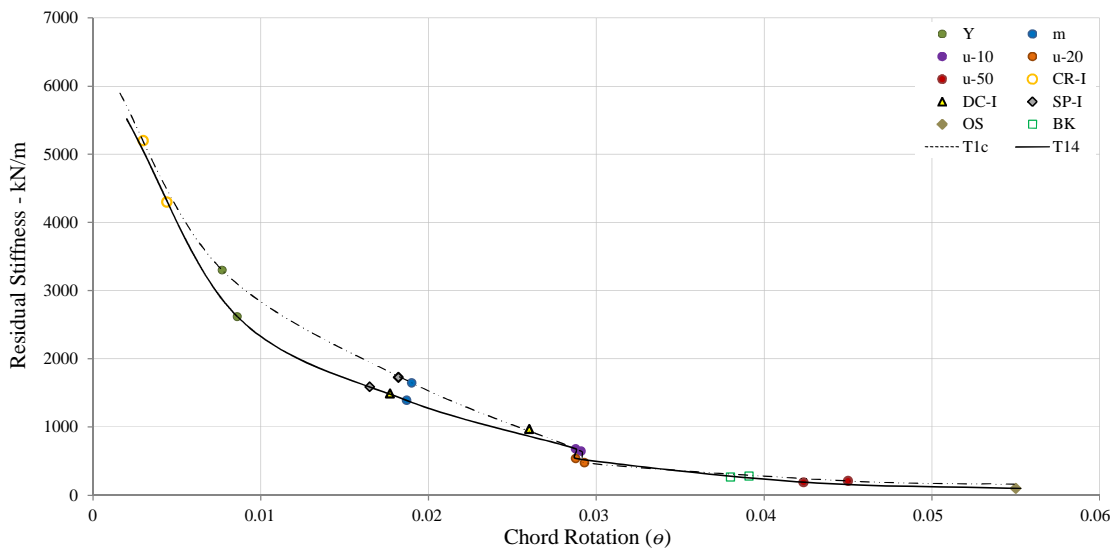
Figure 4-6 The development of damage as observed at the end of each damage level for column specimen T14 and T1c.



a



b



c

Figure 4-7 Comparison of T1c and T14 in terms of: a) Shear force-chord rotation, b) Cumulative energy dissipation – chord rotation, c) Residual stiffness-chord rotation, envelopes.

4.4.4 Comparison of the Behaviour of RC Columns with Different Reinforcement Ratio and Confinement Considerations

The response of T14 which is designed to gravity loads only, is compared with the response of T12 which is designed to Eurocode 8 (CEN,1998). The design parameters, reinforcement detailing aspects and material properties that separate the two specimens are various. Specimens T2, T3, T9 and T11 have intermediate properties between T14 and T12 which are gradually varied in turn. Reference to the response of these column specimens is also made in order to better understand gradually the difference in response between T14 and T12 as function of the different properties that distinguish the two. T2 has a higher confinement ratio than T14. The pattern is similar to T12, however, the spacing of the transverse reinforcement is similar to T14. T3 has an even higher confinement ratio, similar to T12 since apart from having a pattern similar to T12, the spacing is also similar. However, the reinforcement ratio of T2 and T3 is similar to T14 and less than T12. T9 has confinement characteristics similar to T2 but with a reinforcement ratio similar to T12. T11 has both confinement characteristics and reinforcement ratio similar to T12. The difference between T11 and T12 is that, like T14, T2, T3 and T9, the former has a high axial force ratio due to a lower concrete grade. T12 has a higher axial force ratio due to a higher concrete grade. Figure 4-8 shows the comparison of damage development, while figure 4-9 shows the envelopes of strength degradation, cumulative energy dissipation and residual stiffness with chord rotation. Considerable differences are observed in the occurrence of damage in terms of sequence, magnitude of chord rotation, energy dissipation and residual stiffness.

The shear force-chord rotation envelopes of the specimens T9, T11 and T12 which have a higher reinforcement ratio indicate a larger initial stiffness than T14, T2 and T3 which have a lower reinforcement ratio. The specimens T2 and T3, have a similar initial stiffness, but higher than T14 which also has lower confinement characteristics. T12 reaches the highest maximum force capacity while T14 reaches the lowest. In general the three specimens with the higher reinforcement ratio have a higher maximum force than the other three specimens. The rate of strength degradation of T12 is the slowest, and is followed by T11. The rate of strength degradation of T9 is the fastest and the envelope crosses the envelope of T3 at the highest deformation. The degradation of T2 is faster than the more confined specimen T3, but slower than the less confined specimen T14.

The cumulative energy dissipation – chord rotation envelope of T9 indicates that the specimen dissipates the most energy until it reaches a chord rotation of 0.05. As shown in figure 4-9, at this stage, the specimen has already reached $u-20$ and developed most of the damage phenomena that characterise its failure. Beyond a chord rotation of 0.05, T12 is the specimen that dissipates most energy followed by T11. The envelopes of T14, T2 and T3 follow a similar path, however, the envelope of T2 extend over a wider range of chord rotation and dissipated energy than T14, and the envelope of T3 extends over a wider range of chord rotation and dissipated energy than T2.

In general, the residual stiffness-chord rotation envelope of T12, T11 and T9 is very similar until yielding. Beyond this point, the residual stiffness decay occurs more gradually slower in T12 than in T11 and T9. As a result, the envelope of the former is above the latter for the remaining chord rotation range. The envelopes of T11 and T9 are similar until the maximum force is reached. Then the gradual degradation in residual stiffness of T9 is more rapid. The envelopes of the two specimens with lower reinforcement ratio T2 and T3 indicate a lower residual stiffness at any chord rotation when respectively compared with the corresponding specimens with a higher reinforcement ratio T9 and T11. The residual stiffness of T14 is the lowest at any chord rotation.

Flexural cracks are observed in all the six specimens before yielding is reached. T14 is characterised with few but wide cracks, while T12 is characterised with more but thinner cracks. Similarly, T3 and T11 have more but thinner flexural cracks at this damage level compared with corresponding specimens T2 and T9 which have a lower confinement ratio. Before the maximum force capacity is reached, initiation of spalling is observed in T14, T2, T3 and T9, while for T11 and T12, initiation of spalling is observed before $u-10$ is reached. Initiation of diagonal cracking in T14 is observed before the maximum force is reached, however in T2 and T3, the other two specimens with similar reinforcement ratio but better confinement, this damage phenomenon is observed before $u-10$ is reached. However, in T9, this phenomenon is already observed before yielding, and in T11 and T12 before maximum force capacity is reached. No new flexural cracks are observed to form in T14, T2, T3, T9 and T12 after the maximum force capacity is reached. However, the formation of new flexural cracks in T11 is not observed after $u-10$ is reached. A complete diagonal crack is observed to form in T2, T11 and T12 before $u-20$ is reached. Nevertheless, in T9 this is already observed before $u-10$ is reached while in T14 and T3 this is not observed until $u-50$ is reached. Buckling in T9 is observed to occur before $u-10$ is reached. The phenomenon in the better confined specimen T11 is only observed just before $u-20$ is reached. In T12, the specimen with a higher concrete strength, buckling is observed just before $u-50$ is reached. Buckling in T14 is also observed before $u-50$ is reached, however, no buckling is observed in T2 and T3. Failure of the transverse reinforcement is observed in T14 and T11 after $u-50$ damage level is reached. This phenomenon is not observed to occur in the other specimens until the termination of the experiment. Axial force loss is also observed after $u-50$ is reached in T3, T9, T11 and T12. However this is not observed in the specimens T14 and T2 until the termination of the experiments. In general, damage in T14 is observed to concentrate in the lower end of the specimen, however damage was observed to be more distributed for the other specimens with a higher reinforcement ratio and confinement. The damage in the foundation corresponding with specimens having the higher reinforcement ratio is in general more than the damage in the foundation corresponding with specimens having a lower reinforcement ratio.

The chord rotation on the observation of the first flexural cracks in T2 and T3 is approximately 32% lower than T14 which is the specimen with the lowest confinement ratio. However, the chord

rotation of T12 and T11 is 79% and 43% higher than T9. This indicates that an increase in confinement resulted in a premature chord rotation on the occurrence of flexural cracking, which is then delayed if the increase in confinement is accompanied by an increase in the reinforcement ratio, and then a further decrease in the axial force ratio. The chord rotation of T12 is then 14% larger than T14. On the occurrence of this damage phenomenon the residual stiffness of T2 is larger than T14 by 58%, while the stiffness of the even better confined T3 is larger by 65%. The residual stiffness of T9 is more than double the value of T14. However, the values of T11 and T12 are lower than T9 by 4% and 8% respectively. In spite of this reduction, the residual stiffness of T12 is still larger than T14 by 90%.

On the initiation of spalling, the chord rotation of T2 is slightly less than T14. However, the better confined specimen T3 has a chord rotation which is 9% higher than T14. T9 and T11 have initiation of spalling at a chord rotation which is relatively 18% and 53% more than T14. The value of T12 is then 90% larger than T14. The cumulative energy dissipation of T2 is 18% lower than T14, while T3 is 44% larger than T14. The cumulative energy dissipation of T9 is nearly 2.5 times more than the cumulative energy dissipation of T2, but the value of T11 is 13% lower than the corresponding specimen with a lower reinforcement ratio T3. The value of T11 is also 37% lower than the specimen with lower confinement T9. Nevertheless, the cumulative energy dissipation of T11 is still larger than T14 by approximately 30%. Due to its lower axial force ratio, T12 has a cumulative energy dissipation on the initiation of spalling which is more than double T9 and excessively higher than T14. The residual stiffness of T2 is 22% larger than T14, while the residual stiffness of T3 is only 13% larger than T14. The residual stiffness is further increased by 24% for T9 over T2, and by 7% for T11 over T3 as a result of a higher axial force ratio. However, the residual stiffness of T11 and T12 are approximately 19% lower than T9. As a result, the residual stiffness of T12 is only 23% larger than the corresponding value of T14 on the initiation of spalling.

Initiation of diagonal cracking in T2 is observed to occur at a chord rotation which is 19% larger than T14. However, the value of T3 is only larger by 13%. Moreover, specimens T9 and T11 have a chord rotation which is much lower than the values of the corresponding specimens with lower reinforcement ratio. The value of T9 is lower than T2 by 53%, however T11 is lower than T3 by only 10%. The chord rotation of T11 and T14 is therefore similar, but the chord rotation of T12 is larger than T14 by approximately 18%. The cumulative dissipated energy of T2 is 45% larger than T14, and the value of T3 is even larger by 96%. However, the value of T9 is 61% lower than T2 and the value of T11 is 66% lower than T3. The increase in cumulative dissipated energy at the occurrence of this damage phenomenon associated with specimen T11 over the specimen with lower confinement T9, is less than the increase between the corresponding specimens T3 and T2 characterised with a lower reinforcement ratio. The cumulative dissipated energy of T9 is therefore 43% lower than T14, but the value of T12 is more than twice the value corresponding

with T14. The difference in residual stiffness on the initial observation of diagonal cracking between T2 and T14, and between T3 and T14 is negligible. Nevertheless, the difference between the specimens with higher axial force ratio is not negligible. The value of T11 is in fact 40% lower than T9. The residual stiffness of T9 is more than 3 times larger than the value of the corresponding specimen with a lower axial force ratio. However, the residual stiffness difference between T11 and T3 characterised with better confinement is only 74%. The residual stiffness of T12 is 79% larger than T14.

The comparison on the occurrence of buckling, failure of the transverse reinforcement and axial force is limited to the specimens where the phenomena are observed. The chord rotation of T9 on the observation of buckling is very similar to T14. However, the value corresponding with T11 and T12 is more than twice the chord rotation of the less confined specimen T9. The chord rotation of T12 is then more than three times the chord rotation of T14. The cumulative energy dissipation of both T11 and T12 are both excessively more than T14 and T9. However, while the residual stiffness of T9 on the observation of buckling is excessively more than T14, the residual stiffness of T11 and T12 is excessively lower than T9. The residual stiffness of T12 is then 29% lower than the value of T14.

The chord rotation on the initiation of axial force loss in T11, is 15% larger than the corresponding value for the pair specimen T3 with lower reinforcement ratio, while it is 18% larger than the pair specimen T9 with lower confinement ratio. The value of T12 is even 30% larger than T9. The dissipated energy of T11 on the observation of this damage phenomenon is significantly larger than T3. While the value of T11 is also double the value of T9, the value of T12 is 3 times as large. The residual stiffness of T11 is 28% larger than T3, however it is 21% lower than T9. The residual stiffness of T12 is even 30% lower than T9. In spite of these differences on the observation of axial force loss, the residual stiffness values of T3, T9, T11 and T12 are very small compared to the residual stiffness of the specimens on the observation of other damage phenomena.

The chord rotation at yielding of T2 and T3 are similar and approximately 16% lower than the less confined specimen T14. However, the specimen with better reinforcement ratio T11 has a chord rotation 6% larger than the corresponding specimen T9 with lower confinement. The value of T12 is a further 5% larger. The chord rotation of T9 and T11 are 55 and 71% larger than the corresponding specimens T2 and T3 with lower reinforcement ratio. The value of T12 is then 49% larger than T14. At maximum force capacity, in spite of the difference in confinement, the chord rotation of T14, T2 and T3 is very similar. However, the chord rotation of T11 is 7% lower than less confined specimen T9, while the chord rotation of T12 is 13% larger. While the value of T9 is 13% larger than T2, the difference between T11 and T3 is only 5%. The chord rotation at maximum force of T12 is then 41% larger than T14. The chord rotation of T14, T2 and T3 is also similar at u-10 damage level, but the chord rotation of T11 is this time 55% larger than T9.

The value of T12 is even double the value of T9. While the value of T9 is only 45% larger than T2, the chord rotation of T11 is more than double the corresponding value of T3. The chord rotation of T12 is then excessively larger than T14. At u-20 damage level, the chord rotation of T2 and T3 are this time not similar to the value of T14. The value of T2 is 28% larger than T14, while the value of T3 which is better confined is even 56% larger. The chord rotation of T11 is nearly double the value of T9, while T12 is nearly 3 times the value of T9. The chord rotation of T9 is even 20% larger than T2, while the difference between the specimens with better confinement T3 is close to double. The chord rotation of T9 is even 62% larger than T14. The value of T12 is then significantly larger than the value of T14. The difference in chord rotation between the different specimens at u-50 follows a similar trend to that observed at u-20. However, at this damage level, the magnitude of the discrepancies is different.

At maximum force, the cumulative dissipated energy of T2 is 10% lower than T14, but the value of T3 is 29% higher than T14. The cumulative dissipated energy of T11 is also 63% lower than T9. Then, while the cumulative energy dissipation of T9 is more than double the value of T2, the value of T11 is lower than T3 by 43%. The cumulative energy dissipation of T9 is twice the value of T14 and the value of T12 is even more than 3 times the value of T14. At u-10 damage level, the cumulative energy dissipation of T2 is 27% higher than the corresponding sample T14 with lower confinement ratio, while the value of T3 with the highest confinement ratio is even 56% larger than T14. The cumulative energy dissipation of T11 is 35% higher than the corresponding specimen with lower reinforcement T9. The values of T9 and T11 are significantly larger than the values of the corresponding specimens with lower reinforcement ratio T2 and T3. The value of T9 is also significantly larger than the corresponding value of T14. As a result, the cumulative dissipated energy of T12 is larger by an excessively bigger magnitude. The difference in cumulative energy dissipation between the different specimens at u-20 and u-50 follows a similar trend to that observed at u-10. However, at this damage level, the magnitude of the discrepancies is different.

It is therefore observed that after the maximum force is reached, the chord rotation and cumulative energy dissipation increase with improvement in confinement, or with an increase in the reinforcement ratio or with a decrease in the axial force ratio, or with any combination of the three. However, an increase in the reinforcement ratio is more effective than improvement in confinement.

The residual stiffness of T2 is 34% larger than the residual stiffness of T14 at yielding. However in general, this difference decreases with higher ranked damage levels. At u-50 the residual stiffness of T2 is then approximately 15% lower than T14. A similar trend is observed between the specimens with better confinement T3, and T14. While at yielding, the value of T3 is 41% larger than T14, at u-50 the value of T3 is 27% lower than T14. This indicates that the change in the difference of residual stiffness between T3 and T14, and between T2 and T14 is higher for the

former. However, the residual stiffness of T11 is higher than the corresponding specimen T9 with lower confinement at any damage level. Moreover, the difference increases with the rank of the damage level. However, no pattern is observed in the residual stiffness difference between T12 and T9 that is related to the rank of damage level. At yielding, the value of T12 is approximately 5% larger than T9, at maximum the values are similar, while at u-10, u-20 and u-50, the residual stiffness of T12 is respectively 40%, 66% and 33% lower than the corresponding values of T9. At most damage levels, the residual stiffness of T12 is larger than the values of T14. At yielding, T12 is 50% larger, at maximum force it is 62% larger, at u-10 it is 54% larger and at u-50 it is 10% larger. However, at u-20, the residual stiffness of T12 is 12% lower than T14.

Figure D-55, figure D-44, figure D-50 and figure D-52 indicate that in specimens T14, T3, T9 and T11, section S1 dissipates most energy only until a certain deformation. It is then section S2 that dissipates most energy. Figure D-43 and figure D-53 indicate that section S1 dissipates most energy throughout the course of the experiment of specimen T2 and T12. Section S2 is then the second section that dissipates most energy after S1.

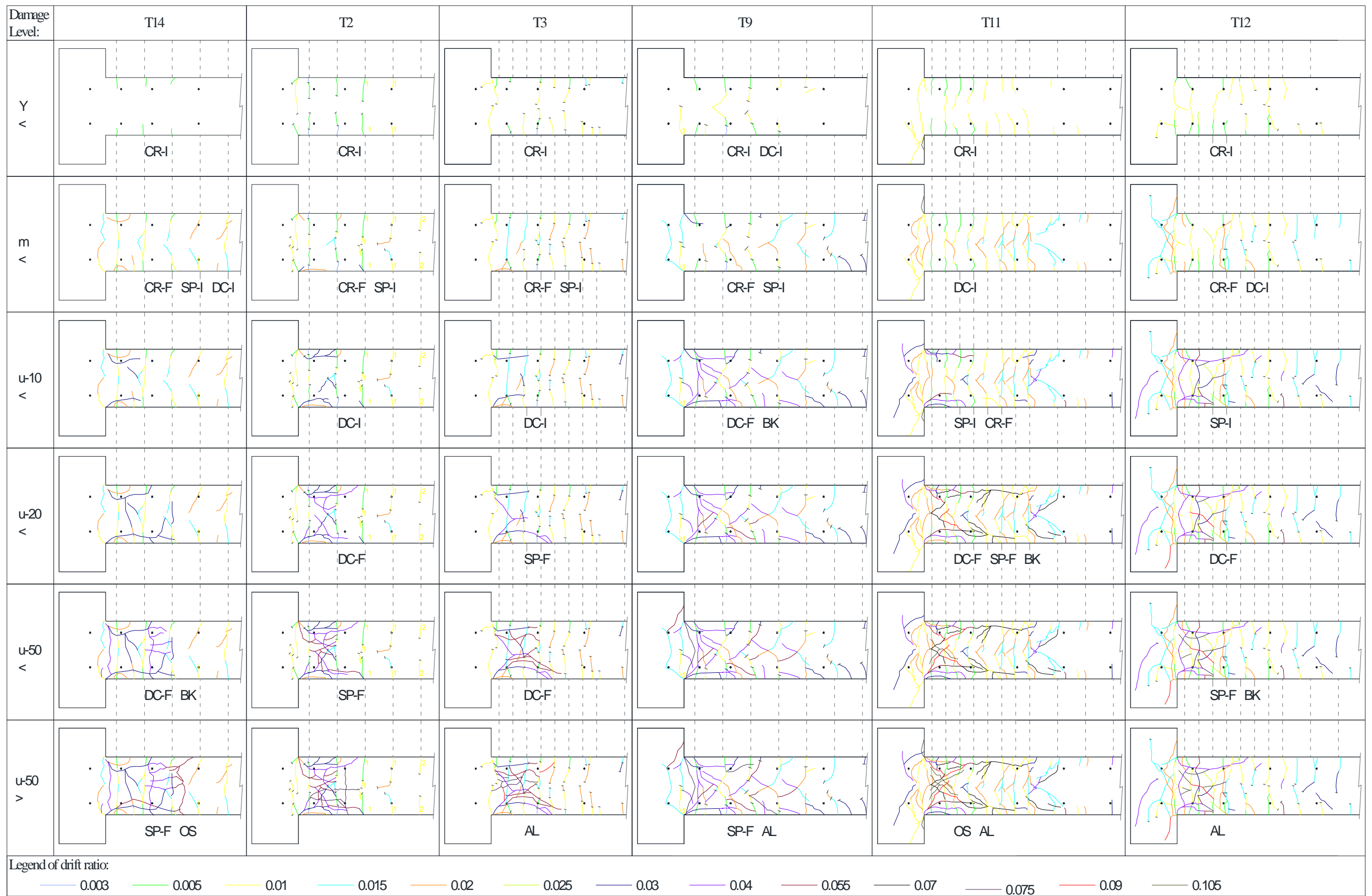
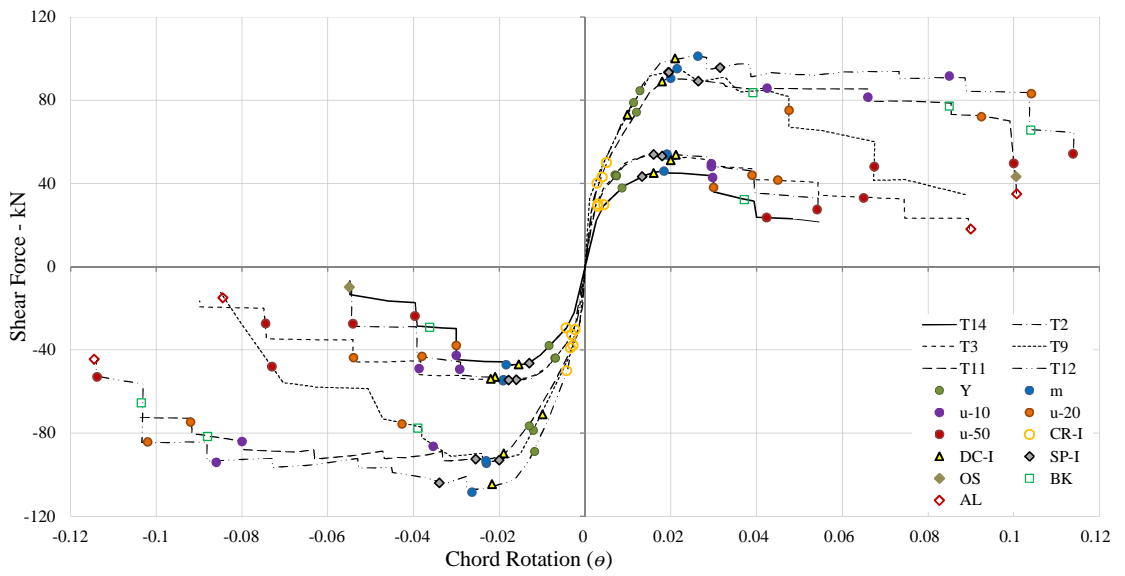
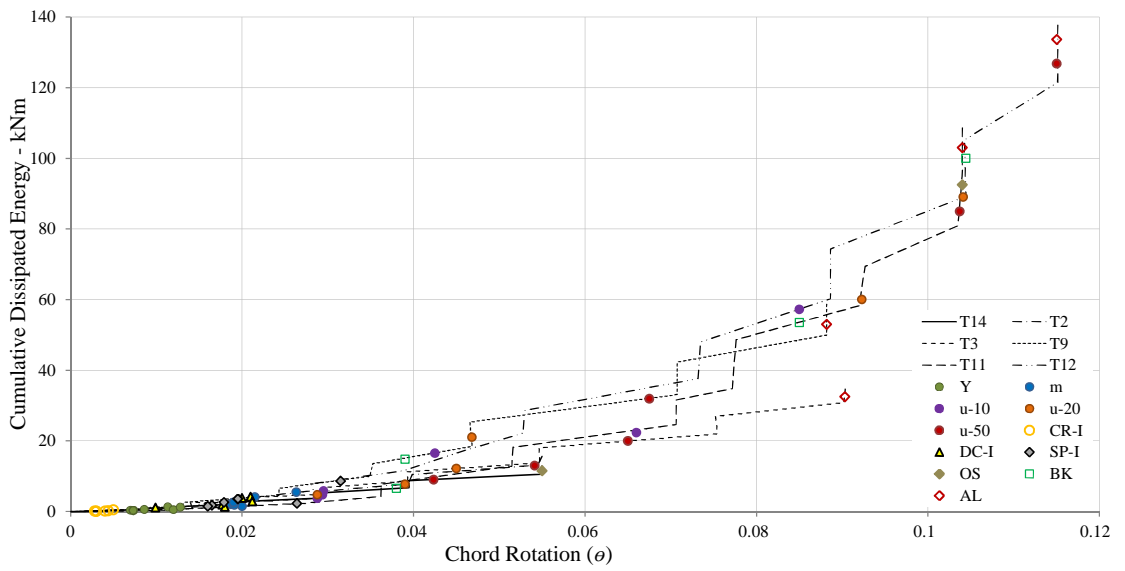


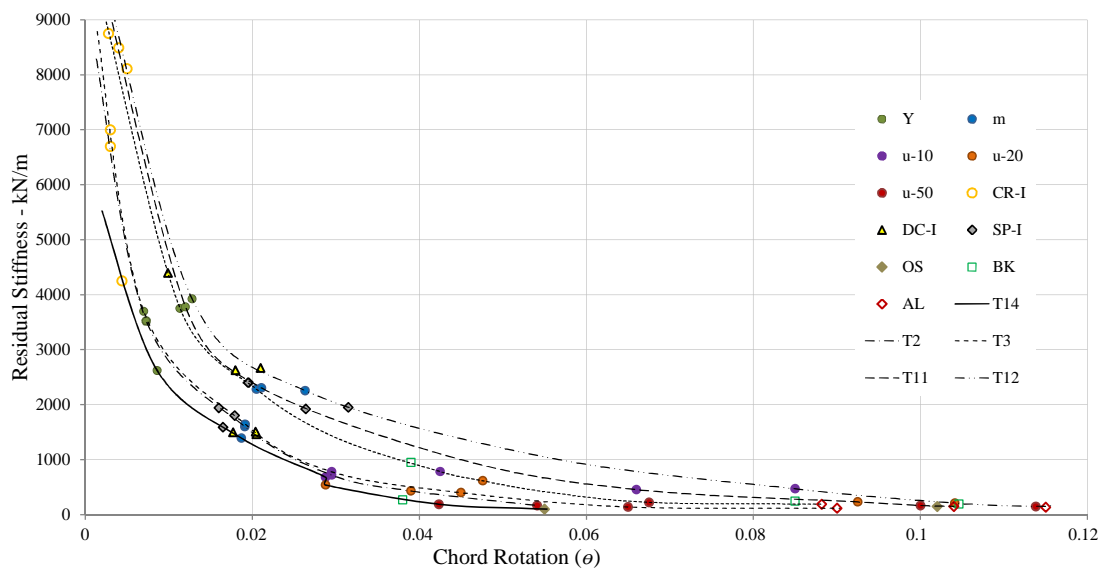
Figure 4-8 The development of damage as observed at the end of each damage level for column specimen T14, T2, T3, T9, T11 and T12.



a



b



c

Figure 4-9 Comparison of T2, T3, T9, T11, T12 and T14 in terms of: a) Shear force-chord rotation, b) Cumulative energy dissipation – chord rotation, c) Residual stiffness-chord rotation, envelopes.

4.4.5 Comparison of the Behaviour of RC Columns with Symmetric and Un-symmetric Distribution of Longitudinal Reinforcement

The experimental results of specimen T9 constructed with uniformly and symmetrically distributed reinforcement are compared with the results of specimen T10 constructed with un-symmetrically distributed reinforcement. All other major properties are approximately similar between the two specimens. Figure 4-10 shows the comparison of the damage development of the three columns, while figure 4-11 shows the comparison of strength degradation, energy dissipation and residual stiffness envelopes with chord rotation. Considerable differences are observed in these results.

In general, the development of cracking in T10 is similar to that in T9. However, since T10 consists in un-symmetric distribution of longitudinal reinforcement, damage development is un-symmetric. Moreover, shear force –chord rotation of T10 in figure 4-11 and figure D-32 is also un-symmetric. This implies that the residual stiffness capacity depends on the directionality of loading. Hence, in subsequent comparisons the lowest value of either side is considered also for other properties. The cumulative energy dissipation –chord rotation envelope corresponding with T9 is larger than the corresponding envelope for T10. On considering the direction of loading where 25mm diameter bars in T10 are in tension and 12mm bars are in compression, the shear force-chord rotation envelope is lower than that of T9 until the latter experiences buckling and reaches $u-20$. Subsequently the envelope of T9 falls below the corresponding envelope of T10. On considering the other direction, both envelopes are similar until the maximum force is reached, with the envelope corresponding to T10 being slightly lower. Nevertheless, after this point, the envelope corresponding to T9 encloses that of T10. The residual stiffness-chord rotation envelope of T10 is larger than the envelope corresponding with T10 mainly until $u-10$ is reached. Subsequently the envelope corresponding with T9 is larger. However, after $u-50$, both specimens have a similar residual stiffness. On comparing figure D-51 with figure D-50, it is observed that for T10, the lower column section (S1) dissipates the most energy followed by the subsequent section S2. Nevertheless, S1 dissipates most energy until $u-50$, as then S2 has a larger dissipated cumulative energy. By considering the shear force distribution, it is observed that this is more uniform in T10 than in T9.

The first flexural crack in T10 is observed to occur at a chord rotation 39% larger than the occurrence of the first flexural crack in T9. The residual stiffness is also 9% larger, but the cumulative energy dissipation is 33% lower. On the initiation of spalling, the residual stiffness and the chord rotation of T10 are 8% lower than the corresponding values of T9, while the cumulative energy dissipation is 11% lower. The occurrence of initial diagonal cracking in T10 is observed at a chord rotation and cumulative dissipated energy which are more than twice the values corresponding with specimen T9. However, the residual stiffness of T10 at the damage

occurrence is less than half the corresponding value for T9. The chord rotation on the occurrence of buckling is similar for both T9 and T10. However, the cumulative energy dissipation and the residual stiffness of T10 are respectively lower than the corresponding values of T9 by 30% and 42%. Loss in axial force in T10 is however observed to occur at a chord rotation which is 10% larger than that corresponding with T9. However the energy dissipation and the residual stiffness of T10 at this damage phenomenon is 37% and 21% lower than the values of T9. The occurrence of different damage phenomena at different damage levels, results in different distribution of energy dissipation by different sections of the columns.

Only flexural cracks are observed before yielding in T10, while in T9 both the initiation of diagonal cracking and flexural cracks are observed. Before the maximum force is reached, initiation of spalling is observed in both specimens. The last formation of a new flexural crack is observed in T9, while initiations of diagonal cracking in T10 are also observed at this level. Both specimens also suffer extensive cracking inside the foundation. Before u-10 is reached, buckling and a complete diagonal crack are also observed in T9. In T10 only extension of already occurring damage is observed at this until u-20 is reached, while for T9 extension of already occurring damage is observed until u-50 is reached. In T10, before u-50 is reached, the last new flexural crack is observed in section S5 together with the formation of a complete diagonal crack and buckling. No further extension of cover spalling is observed along the shear span beyond this level. As buckling occurs in the 12mm diameter bars, the column is observed to loose axial force resistance. No buckling is observed in the 25mm diameter bars. On the reverse cycle which brings the column beyond u-50, the buckled longitudinal reinforcement bars are observed to rupture as they are being straightened. Fardis, 2009 describes that such failure is due to deformation incompatibility, where part of the cross-section of the buckled reinforcement in compression is in the elastic stage while another part of the cross-section is in the plastic stage.

Yielding in T10 is observed to occur at a chord rotation 11% larger than yielding in T9. The residual stiffness is similar for both specimens. The chord rotation and cumulative dissipated energy of T10 at maximum force capacity is approximately 18% larger than the corresponding values of T9, while the residual stiffness is 11% lower. The chord rotation, the cumulative energy dissipation and the residual stiffness of T10 are all lower than the corresponding values of T9 at all subsequent damage levels which include u-10, u-20 and u-50.

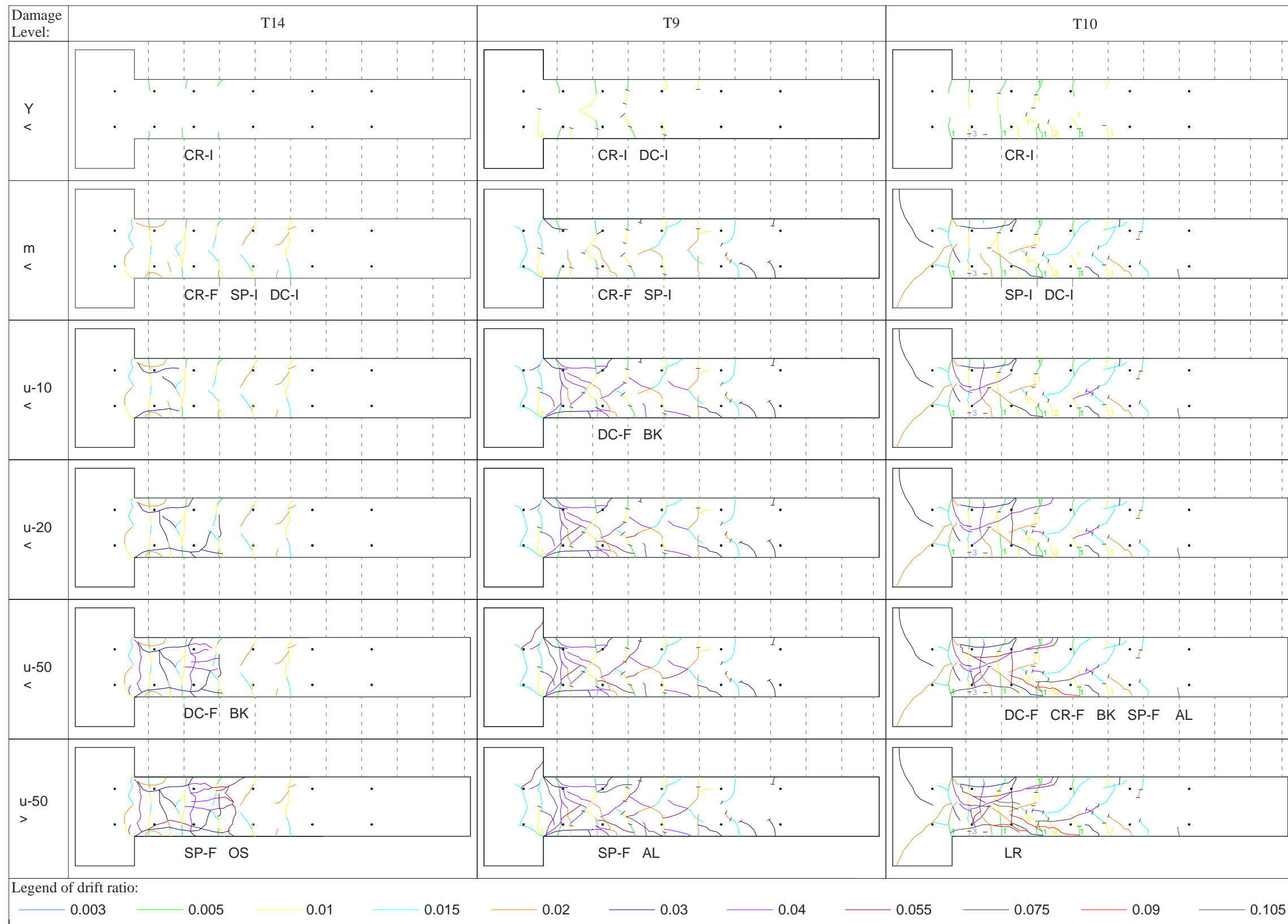
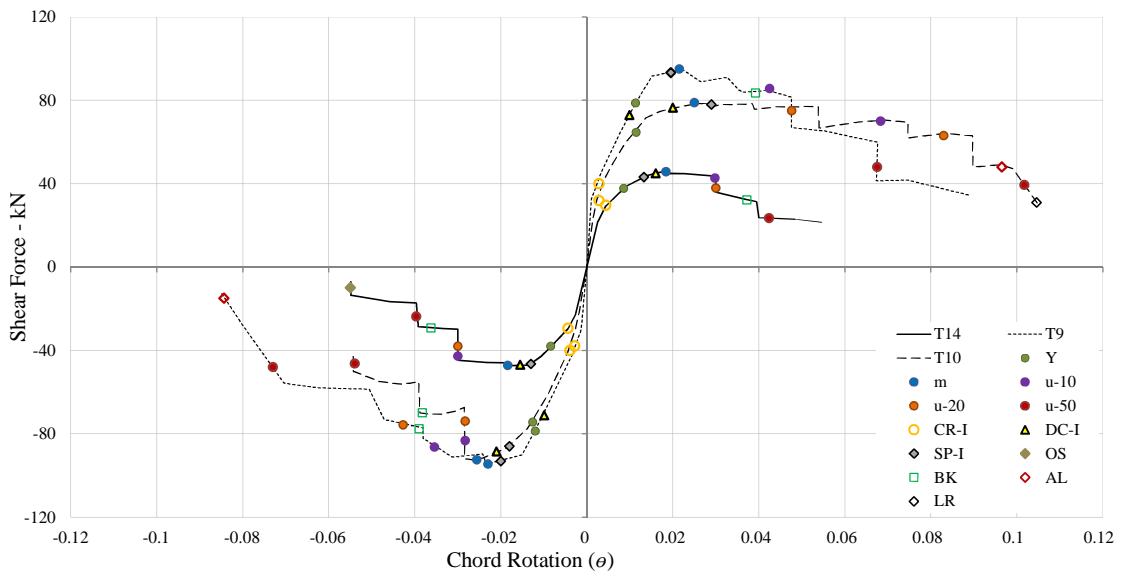
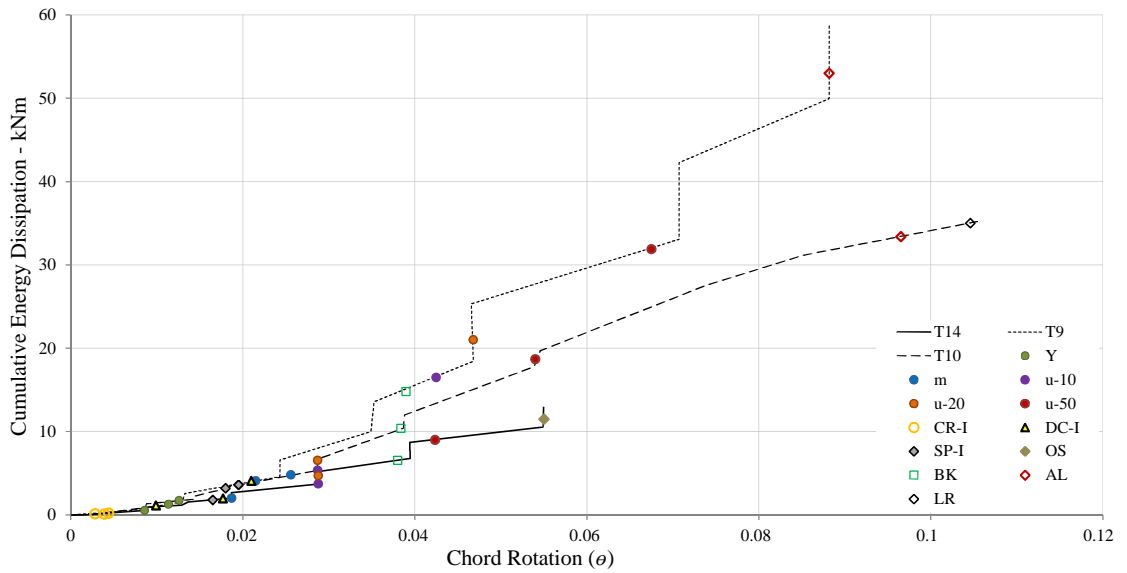


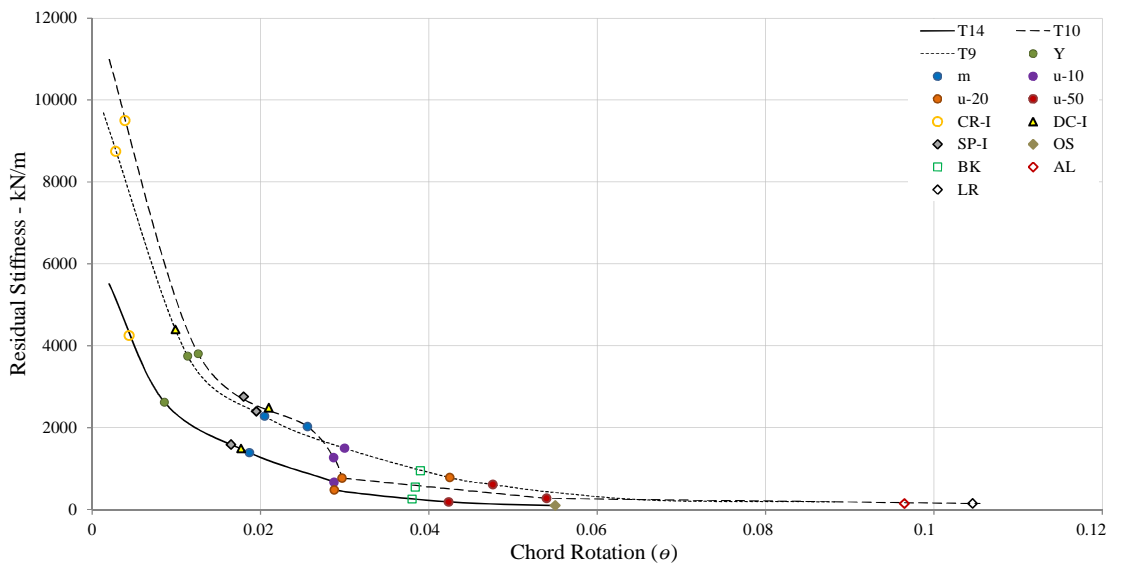
Figure 4-10 The development of damage as observed at the end of each damage level for column specimen T14, T9 and T10.



a



b



c

Figure 4-11 Comparison of T9, T10 and T14 in terms of: a) Shear force-chord rotation, b) Cumulative energy dissipation – chord rotation, c) Residual stiffness-chord rotation, envelopes.

4.4.6 Comparison of the Behaviour of RC Columns with Different Axial Load Ratio

Specimens T15 and T7, both with an applied axial force ratio of 0.44 are respectively compared with specimens T14 and T2 with a lower applied axial force ratio of 0.26. Specimens T14 and T15 have a confinement ratio of 0.1, while T2 and T7 have a higher confinement ratio of 0.22. Figure D-12 shows the comparison of damage development, while figure 5-12 shows the envelopes of strength degradation, cumulative energy dissipation and residual stiffness with chord rotation. Considerable differences are observed in the occurrence of damage in terms of sequence, magnitude of chord rotation, energy dissipation and residual stiffness.

The shear force-chord rotation envelopes of T15 and T7 are similar to T2 until their maximum shear force is reached. Subsequently, the force of T15 and T7 starts to decrease, while the force of T2 continues to increase until it reaches its maximum. Beyond this point the shear force-chord rotation envelope of T2 encloses all the other envelopes over the remaining chord rotation range. The envelope corresponding with T14 extends lower than the other three envelopes until the column specimen reaches its maximum shear force. It then extends with a higher capacity than T15 and T7 but with a lower capacity than T2. The strength decay with chord rotation of T15 occurs faster than T7. Similarly, the strength decay of T14 occurs faster than T2 over a shorter chord rotation range. The envelopes of T15 and T7 indicate more cumulative energy dissipation than the corresponding envelopes of T14 and T2 until their shorter chord rotation range. As the chord rotation of u-50 in T2 and transverse reinforcement failure in T14 extend further than the range covered by T7 or T2, the dissipated energy of the former two is more. The energy dissipation of T2 is lower than T14 until just after the maximum shear force since less damage is formed in the former. However, more energy is dissipated by the former beyond this damage level. The envelope of T7 is however constantly observed slightly lower than the envelope of T15. These observations are in general consistent with the theory and observations of Park *et al.*, (1975) and Priestley *et al.*, (1992) where the maximum lateral force capacity increases with the level of confinement and increased axial force that enhances the concrete strength. However, if the axial force is relatively too large, the force degradation occurs prematurely, even if it is better confined. The residual stiffness-chord rotation envelopes of T2, T7 and T15 indicate larger and similar paths before initial cracking, and higher residual stiffness than T14. However, initial cracking and yielding, T2 falls lower than T15 and T7. However, after the maximum force of T15 and T7 is reached, their strength decay is reflected also in their residual stiffness as the residual stiffness-chord rotation envelopes extend below the envelopes of T14 and T2.

On initial observation of flexural cracks, the chord rotation of T15 is 21% lower than that of T14. However, an opposite trend is observed between T7 and T2. Moreover, while the chord rotation of T2 is 32% lower than T14, the chord rotation of T7 is 9% higher than T15. An opposite trend observed in the relationship of chord rotation of each of the four columns, is observed the

relationship of residual stiffness. While T15 has cumulative energy dissipation 43% higher than T14, the value of T7 is 11% lower than T2, and while the value of T2 is 58% larger than T14, the value of T7 is 3% lower than T15.

The chord rotation of both specimens with higher axial force ratio is approximately 24% lower than the corresponding specimens with lower axial force ratio on the occurrence of spalling. On the occurrence of this damage phenomenon, the cumulative energy dissipation of T15 is 21% lower than T14. The difference between the other two specimens with better confinement is larger. The value of T2 is also 18% lower than T14, but the difference between the samples with larger axial force ratio is less. The residual stiffness of T15 is 61% larger than T14. However, the relative stiffness between T7 and T2 is only 40%. The value of T2 is 22% larger than T14, but the values of T7 and T15 are very similar to each other.

Initiation of diagonal cracking in T15 is observed to occur at a chord rotation 7% lower than the corresponding value of T14. The discrepancy between the values of T7 and T2 is about five times more. While the chord rotation of T2 is 20% more than T14, the value of T7 on the initiation of diagonal cracking is 13% lower than T15. The energy dissipation of T15 is more than double the value of T14. However, for T7 and T2, the cumulative energy dissipation is quite similar to each other. The value of T2 is approximately 45% larger than T14, however the value of T7 is 36% lower than T15. On the initial observation of diagonal cracking, the residual stiffness of T15 is only 5% larger than T14. However, the value of T7 is even 39% larger than T2. While the residual stiffness of T2 is 3% lower than T14, the value of T7 is 29% larger than T15.

Buckling in T15 is observed at a chord rotation 26% lower than T14. In specimen T7 which has the highest confinement factor and axial force ratio, buckling is observed at a further delayed chord rotation. The value of T7 is 4% larger than T15. The cumulative energy dissipation of T15 is 10% larger than T14. However, the corresponding value of T7 is 7% lower than T15. The residual stiffness of T15 is 9% lower than T14, while the residual stiffness of T7 is 33% larger than T15. No buckling is observed in T2.

Transverse reinforcement failure at the lower end of columns T14, T15 and T7 is observed as a result of the opening of hooks and following buckling. This damage phenomenon is not observed in T2. Failure of transverse reinforcement in T15 is observed at a chord rotation 46% lower than T14. However, the value of T7 is 28 Larger than T15. The cumulative energy dissipation of T15 is 35% lower than T14, but the value of T7 is 40% larger than T15. The residual stiffness of T15 is more than double the residual stiffness of T7, while the residual stiffness of T7 is approximately half that of T15.

Only flexural cracking is visually observed in all four specimens before yielding is reached. The extent of this damage is less in both specimens with the higher axial force ratio when compared with the corresponding specimens with a lower axial force ratio. In addition, the flexural cracking

before yielding in the specimens with the lower confinement ratio is less than in corresponding specimens with a larger confinement ratio. As the maximum force capacity is reached, the formation of all flexural cracks along the shear span and initiation of spalling are observed in all four column specimens. In addition, initiation of diagonal cracking is also observed in T14. For the other three specimens, initiation of diagonal cracking occurs before u-10 is reached. Progression of already occurring damage is observed in the four specimens until u-20 is reached. A complete formation of a diagonal crack is observed in T2 at this stage. Beyond this damage stage no particular trend is observed in the occurrence of damage, in relationship with the different design characteristics of the columns. Before u-50 is reached, a complete formation of a diagonal crack is formed in both specimens with the lower confinement. Buckling is observed in T14 and T7 and spalling of the cover is not observed to extend further along the shear span beyond this damage level in T2. After u-50 is reached, the specimens with the larger axial load ratio are observed to exhibit loss in axial force capacity. This is not observed in the other corresponding specimens. Failure of the transverse reinforcement and further extension of spalling along the shear span is observed in T14, T15 and T7. The complete formation of a diagonal crack in T7 is only observed at this stage.

At yielding, maximum force capacity, u-10, and u-50, the chord rotation of the two specimens with larger axial force ratio is approximately larger than the two specimens with a lower axial force ratio, by 34%, 24%, 33% and 40% respectively. At yielding and u-50, the chord rotation of the specimens with the larger confinement ratio is larger than the value of the specimens with the lower confinement ratio respectively by 13% and 27%. At u-10 and u-50, the difference is negligible. The chord rotation of T15 at u-20 is 32% lower than T14, while the value of T7 is even 50% lower than T2. The value of T2 is 36% larger than T14, while no significant difference is observed between the chord rotation of T7 and T15.

The cumulative energy dissipation of T15 is larger than T14 at yielding, maximum force capacity, u-10 and u-20 by 20%, 18%, 30% and 18% respectively. It is then 24% lower at u-50. The cumulative energy dissipation of T7 is relatively larger than T2 at yielding and maximum force capacity only by 75% and 15%. For u-10, u-20 and u-50, the cumulative energy dissipation is respectively lower by 8%, 33% and 26%. The values of T2 are lower than T14 at yielding and maximum force capacity by 46% and 10% respectively. However, cumulative energy dissipation is then larger at u-10, u-20 and u-50 by 27%, 63% and 44% respectively. In general, the relative cumulative dissipated energy of T7 over T15, is lower than that of T2 over T14.

At yielding, the residual stiffness of both T15 and T7 are larger than T14 and T2 respectively. T15 is larger by 79% while T7 is larger by 49%. The difference reduces to approximately 50% and 35%, when the maximum force is reached. However at u-20, while the difference between T15 and T14 is reduced to 48%, the difference between T7 and T2 increases also to 48%. At u-20, the difference between u-15 and u-14 further decreases to 37%, while between T7 and T2 the

difference increases again to more than double. At u-50, the residual stiffness of T15 is double the value of T14, however the chord rotation of T7 is only 21% larger than T2. The residual stiffness of T2 is larger than T14 by 34%, 15% and 6% at yielding maximum force and u-10 respectively. However, the residual stiffness is then lower by 20% and 13% at u-20 and u-50 respectively. The chord rotation of T7 is however larger than T15 at yielding, maximum force, u-10 and u-20 by 12%, 4%, 5% and 20% respectively, and is only lower by 46% at u-50.

Figure A-43 and figure A-48 indicate that section S1 in specimens T2 and T7 dissipates more energy, and is followed by S2 and S3. However, it is also observed that the contribution of dissipated energy by sections S2 and S3 in specimen T7 is much higher than the contribution by the corresponding sections in specimen T2. While the relative contribution of S2 and S3 to the overall dissipated energy in T15 is similar to that in T7, the contribution of S2 in T14 exceeds that of S1 after u-20 damage level is reached.

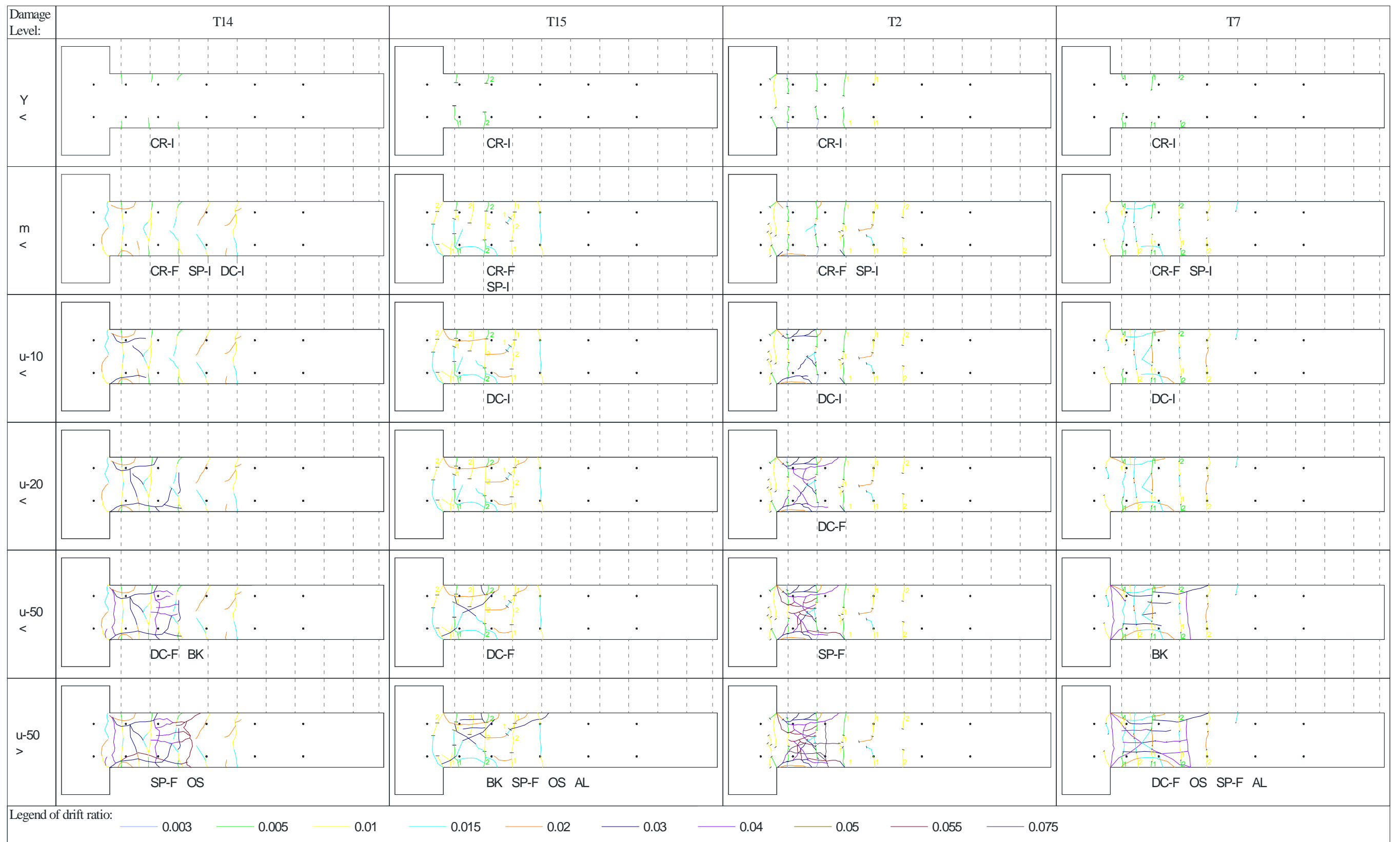
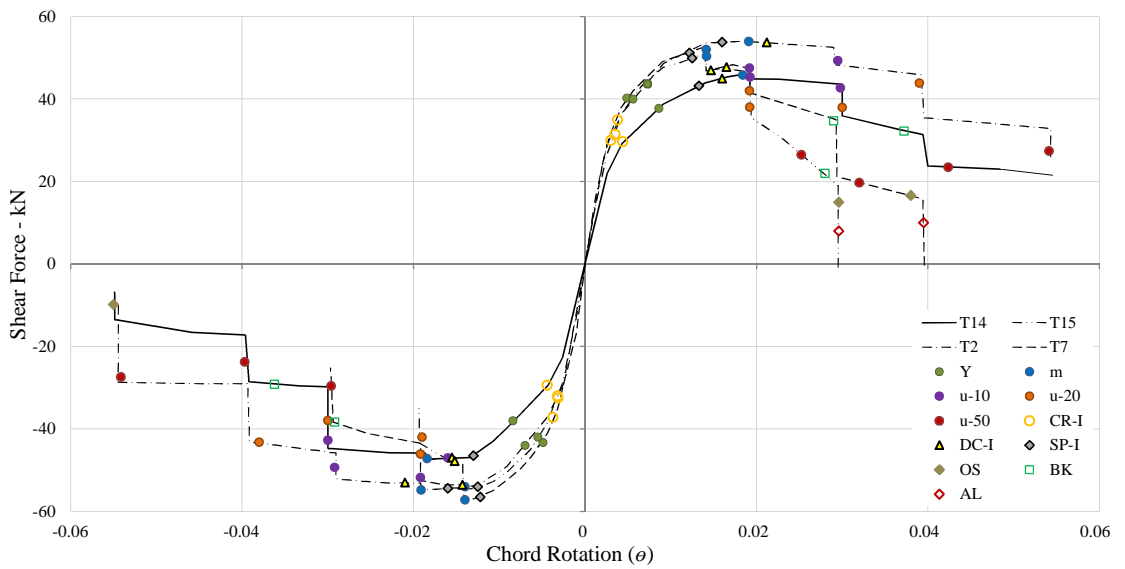
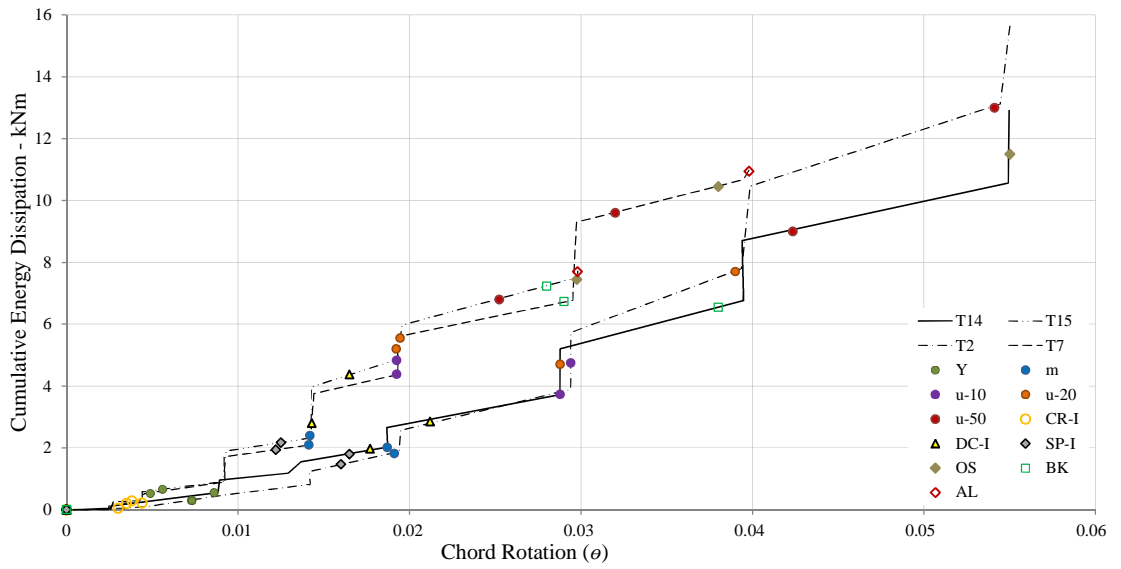


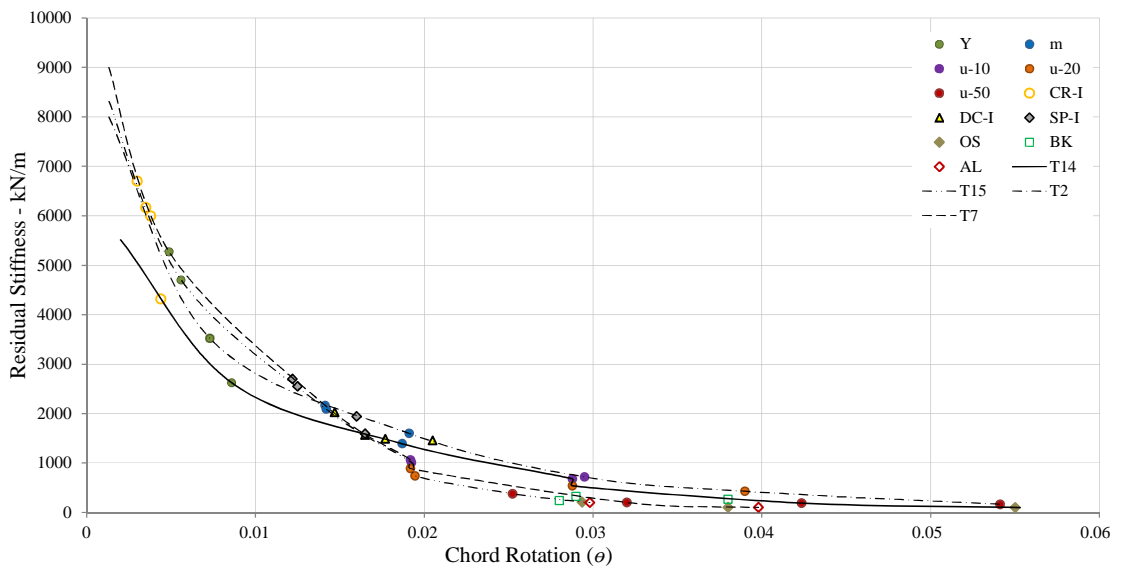
Figure 4-12 The development of damage as observed at the end of each damage level for column specimen T14, T14, T2 and T7.



a



b



c

Figure 4-13 Comparison of T7, T2, T15 and T14 in terms of: a) Shear force-chord rotation, b) Cumulative energy dissipation – chord rotation, c) Residual stiffness-chord rotation, envelopes.

4.4.7 Comparison of the Behaviour of RC Columns with Different Detailing Aspects at the Column –Foundation Interface

Specimen T6, constructed with a concrete cold joint at the foundation-column interface, is compared with specimen T14 having a continuous concrete foundation-column interface. Figure 5-13 shows the comparison of damage development, while figure 5-14 shows the comparison of strength degradation, energy dissipation and residual stiffness with chord rotation in both specimens. In spite of both specimens sharing the same design characteristics apart from the detailing at the foundation-column interface, considerable differences are observed in the occurrence of damage in terms of sequence, and magnitude of chord rotation, energy dissipation and residual stiffness. The envelopes for shear force- chord rotation, residual stiffness-chord rotation and energy dissipation-chord rotation corresponding with specimen T6 are bigger than the corresponding envelopes for T14.

The first flexural crack observed in T6 occurs at a chord rotation 43% lower than that occurring in T14. Consequently, the residual stiffness at initial cracking is 36% larger for T6. Although, the dissipated energy at this initial stage of damage is significantly higher for T14, both magnitudes are considered insignificant at this early stage of damage. These differences are the direct consequence of the detailing aspect at the foundation-column interface. The first crack in T6 occurs in the weakest cross-sectional plane at the cold joint. In T14 the continuity of concrete casting ensures a stronger cross-sectional interface between the two elements, and hence initial cracking occurs at a weaker plane, 0.07m away from the foundation-column interface inside the column and coinciding with the first stir-up.

Initial spalling and diagonal cracking in T6 occur respectively at a chord rotation 10% and 30% larger than the corresponding chord rotation for T14, but maintaining the same sequence. Resulting cumulative energy dissipation at these damage considerations are respectively 36% and 90% larger for T6 than T14. The residual stiffness of T6 at initial spalling is 7% more than the corresponding T14 value, while for initial diagonal cracking the residual stiffness of T6 is 16% less.

For specimen T6, a large share of the lateral deformation of the column is concentrated in the rotation of the region surrounding the cold joint, whereas for specimen T14, this is more spread over a region slightly away from the joint. As indicated in figure 4-14, while for T14 damage is spread inside a number of sections, substantial damage in T6 is concentrated in the first sections. Spalling in T6 is observed to extend in sections S1 and S2 only, while for T14, spalling is observed to extend in section S3. From Figure D-55c and Figure D-46c it is also observed that section S1 of specimen T6 dissipates more energy than any other section, while section S1 of specimen T14 dissipates the most energy only till a chord rotation of 0.04. Then, more cumulative energy is dissipated by S2.

Due to the concentration of damage in the lower regions of T6, buckling is observed to occur at a chord rotation 22% lower than T14. However this occurs at a lower maximum force reduction for T6, than for T14. The cumulative energy dissipation is similar at the observation of buckling for both specimens. However, the residual stiffness for T6 is double than that for T14. The hooks of the lower transverse reinforcement start to fail at the same chord rotation. The residual stiffness at this stage is very low for both columns but the magnitude is much larger for T6. The energy dissipation at this damage characteristic is 10% higher for T6 than T14.

Initial cracking is observed to occur before yielding for both specimens, while the initial spalling, initial diagonal crack and the last formation of a new flexural crack are observed to occur before the maximum force is reached. Only further extension of already occurring damage is observed in T14 before u-10 level. However, buckling and a complete formation of a diagonal crack is observed in T6. The formation of the last new flexural crack in T6 is also observed before this level is reached. Extension of the already occurring damage characteristics are further observed until u-20 is reached in both columns. Opening of the hooks of the lower transverse reinforcement is observed in T6 before u-50 is reached, while buckling and the complete formation of a diagonal crack in T14 is only observed at this damage level. Further damage is observed beyond u-50. The concrete core in the lower section of T6 is considerably cracked at this stage, and the specimen suffers considerable loss in its axial load capacity. This phenomenon is not observed in T14. However, unlike T6, further spalling is observed to extend in the third section at this stage, with the formation of new flexural cracks. Cracking of concrete is observed to propagate up to a distance of about 0.05m inside the foundation of column T14. Nevertheless, no cracking is observed inside the foundation of T6 at any damage state. This does not exclude the possibility of strain penetration of the longitudinal reinforcement.

The early occurrence of cracking in T6 and large concentration of rotation in the region of the cold joint results in having yielding occurring at a chord rotation slightly lower than yielding in T14. The residual stiffness at yielding in T6 is however 41% larger than the residual stiffness at yielding in T14. The chord rotation at maximum force is 50% larger for T6, while the cumulative dissipated energy at this state is more than double, and the residual stiffness is 38% lower than the values for T14. Both u-10 and u-20 occur at the same chord rotation for T14, and the chord rotation of these damage levels for T6 is approximately 37% larger. On having a larger deformation at these damage levels, the residual stiffness of T6 is smaller by approximately 30%, and the dissipated energy are larger by more than double the values of T14. A similar trend is observed at u-50. The chord rotation of T6 is larger by 30%, the dissipated energy is larger by 63% and the residual stiffness is lower by 15% compared to the values of T14.

In general, the cold joint affects the sequential occurrence of damage, and hence particular attention should be paid for minor detailing aspects that are conducted in real construction but are not reproduced in the laboratory. In general, the cold joint induces forced flexibility that results

in larger dissipated energies and lower residual stiffness, particularly after the maximum force is reached. While this is particularly true, as observed by the comparison of damage development in T6 and T14 where continuous ribbed longitudinal reinforcement is used, Melo *et al.*, 2015 observed an opposite trend on using smooth bars. The specimen with smooth bars and having a cold joint is observed to dissipate less energy, while the maximum force is observed to decline at lower chord rotations when compared to the specimen without cold joint. This is the result of considerable bond slip of smooth bars. These comparisons between the effects of cold joint when using ribbed or smooth bars must be kept in context that the cold joint in the specimen of the experimental campaign by Melo *et al.*, 2015 is formed after repairing the concrete at the lower end of the column. Moreover, while the cold joint in T6 is at the foundation-column interface, in the specimen by Melo *et al.*, 2015 this is formed at the first stirrup inside the column. While as observed in T6 and T14, the cold joint location is different than the location of the formation of the initial flexural cracks when the concrete cast is continuous, in the case of Melo *et al.*, 2015, the cold joint is located at the same position where the first flexural cracks form when the concrete cast is continuous.

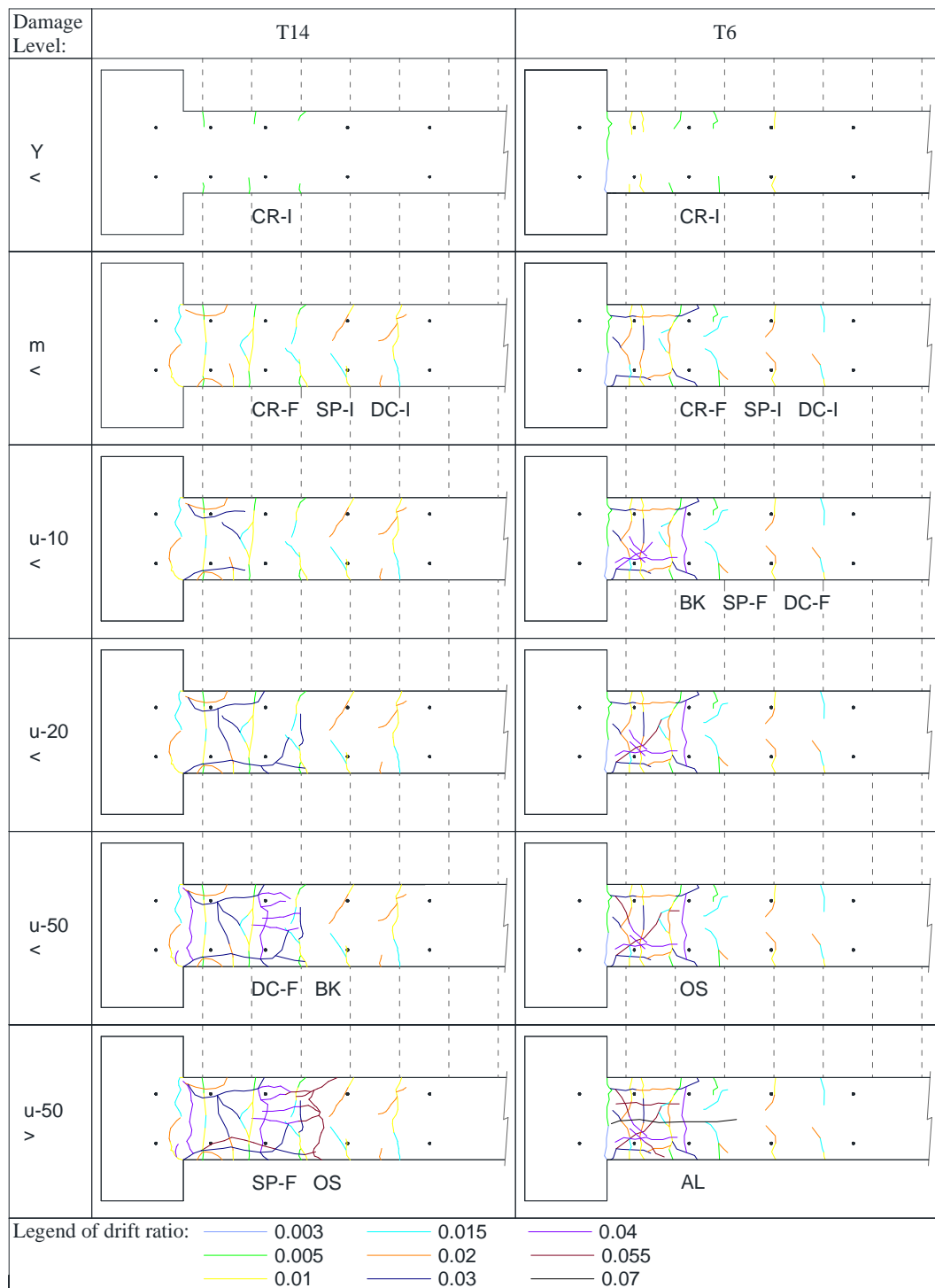
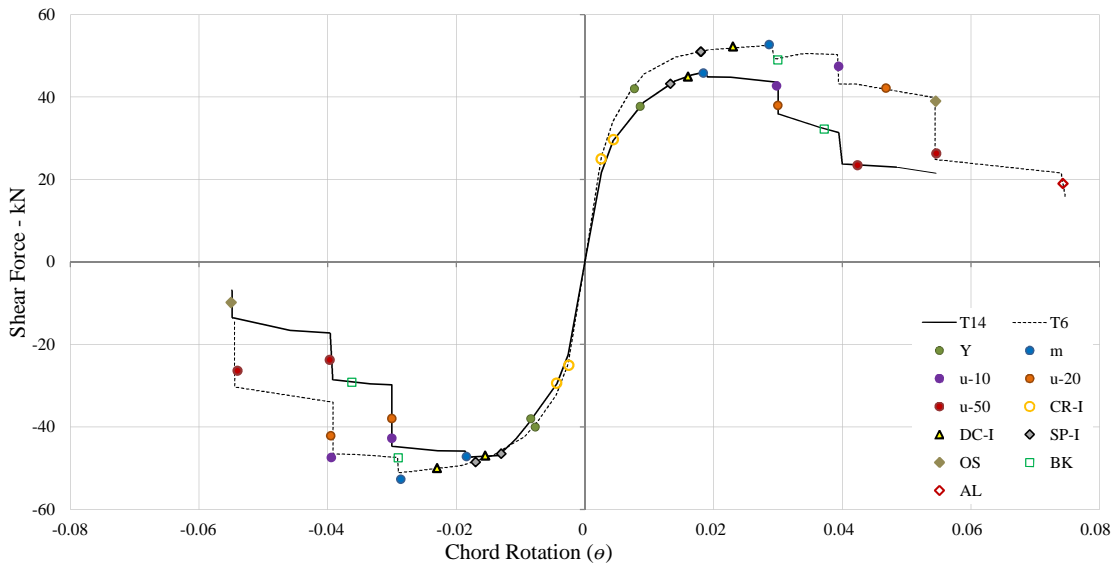
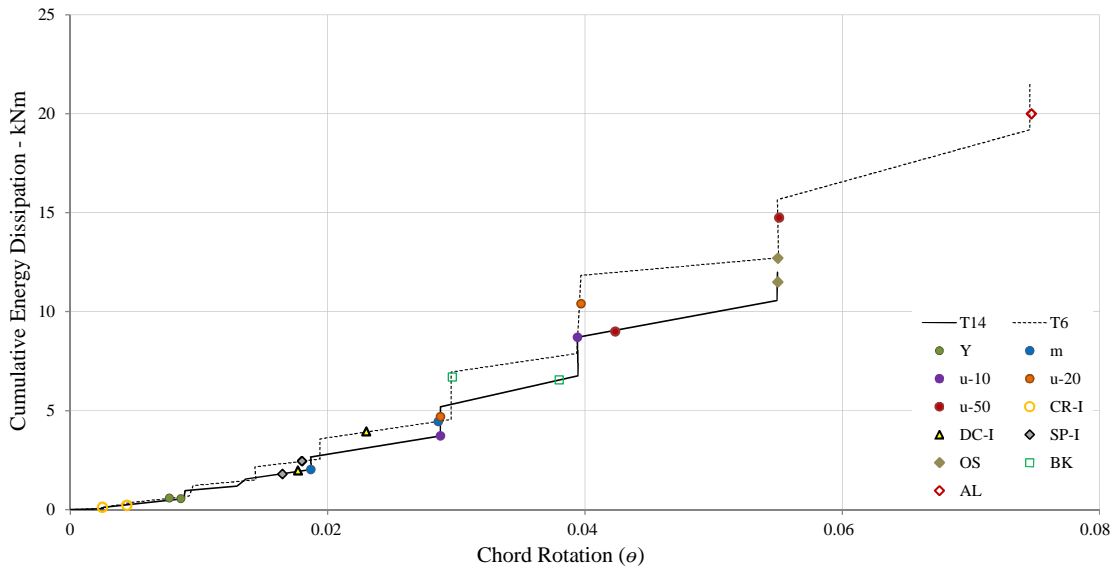


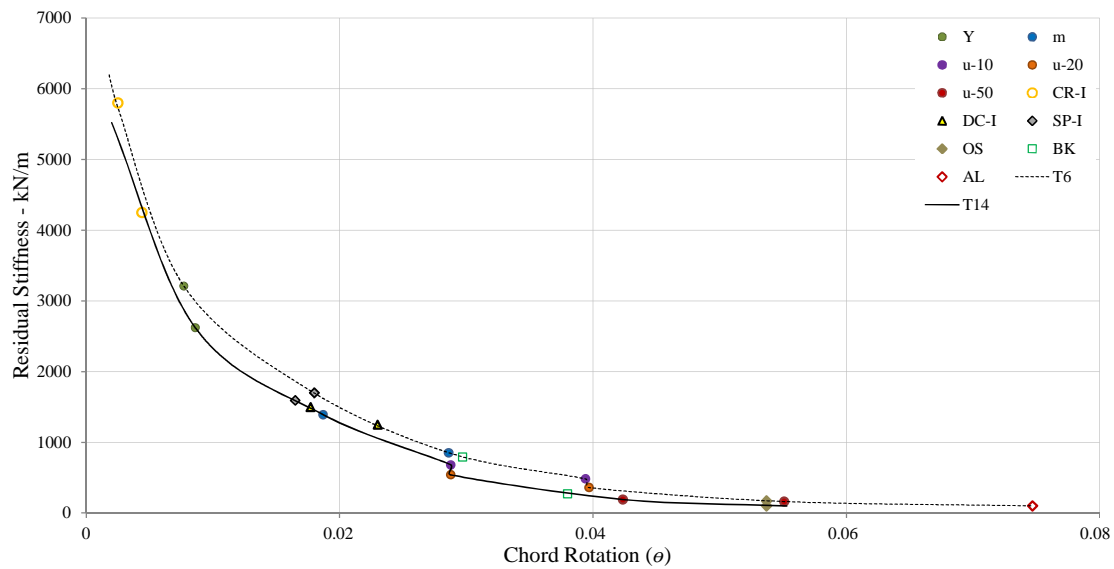
Figure 4-14 The development of damage as observed at the end of each damage level for column specimen T14 and T6.



a



b



c

Figure 4-15 Comparison of T6 and T14 in terms of: a) Shear force-chord rotation, b) Cumulative energy dissipation – chord rotation, c) Residual stiffness-chord rotation, envelopes.

4.4.8 Comparison of the Behaviour of RC Columns with and without Lap-splicing

The experimental results of reference specimen T14 constructed with continuous reinforcement, are compared with the results of T16-D1 and T16-D2, respectively constructed with reinforcement lap-splicing 35x diameter and 75x diameter of the longitudinal reinforcement. Figure 5-15 shows the comparison of the damage development of the three columns, while figure 5-16 shows the comparison of strength degradation, energy dissipation and residual stiffness envelopes with chord rotation. Specimen T14 has a longitudinal reinforcement ratio of 0.01 while T16-D1 and T17-D2 have a corresponding value equal to 0.02 since the lapped legs are considered twice in the computation as suggested by Fardis *et al.*, 2009. The difference in the reinforcement ratio and the different development lengths of reinforcement in the lap-splice, have a direct influence in the development of damage and its sequence.

The first flexural crack in T16-D1 occurs at a chord rotation 77% lower than the corresponding crack in T14. Nevertheless for T17-D1, this occurs at a value 14% larger than that in T14. In T16-D1, the first crack is 0.07m above the foundation coinciding with where lapping starts. However, this is not the case for both T14 and T17-D2 where initial cracking is observed to coincide with the position of the lower three transverse reinforcement. Moreover, at this damage level, T14 and T17-D2 share similar residual stiffness, while the corresponding residual stiffness at this damage state for T16-D1 is about 75% more.

Spalling in both T16-D1 and T17-D2 is observed to start at a chord rotation 21% larger than T14. However, the dissipated energy is larger by 58% for T16-D1 and only 51% for T17-D2. The residual stiffness of T17-D2 and T14 is very similar at the damage state, while the value of T16-D1 is 13% lower than the value of T14. Diagonal cracking of T17-D2 is observed to start at a chord rotation which is more than double the value of T14, while for T16-D1 diagonal cracking is observed to start at a value which is 60% more than T14. The cumulative dissipated energy of T17-D2 is more than three times, while that of T16-D1 is more than twice the value of T14. For both T16-D1 and T17-D2, the residual stiffness is approximately 55% lower than that of specimen T14.

While most flexural cracks along the shear span of T14 and T16-D1 are formed when a chord rotation of 0.015 is reached, the last flexural crack in T17-D2 forms on the loading cycle whose amplitude is equivalent to a drift demand of 0.03. On comparing Figure D-36, Figure D-38 and Figure D-39, and considering the damage development in Figure 5-15, spalling is observed to propagate inside S1, S2, S3 and S4 for T16-D1 and goes beyond the lap-spliced region. For T14 and T17-D2, spalling is observed to propagate only in the first three sections. A complete diagonal crack is formed in T14 at a chord rotation considerably lower than in T17-D2, and slightly lower than in T16-D1.

Buckling is not observed at any stage in specimens T16-D1 and T17-D2. Nevertheless, for T16-D1, when loaded with cycles of drift demand larger than 0.055, the lapped parallel reinforcement legs in compression are observed to divert at a small angle from each other in the region where spalling had occurred in the lower sections S1 and S2. The hooks of the lower transverse reinforcement of T16-D2 are observed to start failing at a chord rotation slightly lower than that of T14. The same failure phenomenon is observed in T17-D2 at a chord rotation 37% higher than that corresponding with T14. The cumulative dissipated energy at this failure phenomenon is 56% larger for T17-D2 and 16% lower for T16-D1 over the value of specimen T14. Nevertheless, the residual stiffness for all the three specimens is very low at this stage of damage, nevertheless it is largest for T16-D1, followed by T17-D2.

Only flexural cracking is observed until yielding is reached in all the specimens. In T17-D2 and T14 this is spread in S1 excluding the foundation, S2 and S3. In T16-D1, flexural cracks before yielding extend also in the foundation and section S4. Before the maximum force capacity is reached, all the new flexural cracks along the shear span of the columns in T14 and T16-D1 are formed. In T17-D2, a concentration of cracks is observed in S1, 0.07m inside the column just before the lap-splicing region. As indicated in Figure A-58b, this region is characterised by the largest flexural demands, while the reinforcement ratio is 0.01, which is half the value in the subsequent sections characterised with lap-splicing and having a lower flexural demand. In T16-D1, this concentration of flexural damage is less prominent. Having a shorter lap-spliced region, the considerable flexural damage is spread also in the region where the lapping ends which is also characterised by a lower capacity-demand ratio when compared to T17-D2. At this damage level, considerable spalling is observed in T14 and T17-D2, and initial diagonal cracking is only observed in T14. Before u-10, further development of already occurring damage is observed in T14. Initiation of spalling is observed in T16-D2, while the last formation of new flexural cracks is observed in T7-D2. While in T17-D2 and T14, spalling was previously observed to occur at the lower ends in the column, for T16-D1 spalling is observed to occur at both ends of the lap-splicing region at this damage level. Moreover, relative displacement of the lapped reinforcement bars is observed in these both ends in T16-D1, and at this damage level in T17-D2 at the lower end. Hence, the loss of cover at this stage might also be the result of splitting action in both columns due to considerable bond-slip as discussed in (CEB, 2000) under similar circumstances. Only further development of already occurring damage typology is observed before u-20 damage level is reached. In T17-D2, initial diagonal cracking is observed. A complete diagonal crack is observed in T16-d1 and T14 before u-50 is reached. Buckling is observed in T14 at this damage level. No further extension of spalling or splitting of the cover is observed beyond this damage level in T16-D1. The complete formation of a diagonal crack in T17-D2 is only observed beyond u-50. Moreover, further extension of spalling is observed in T14 and T17-D2. Failure of the stir-ups is observed in all columns beyond u-50, which is complemented by considerable cracks in the concrete core. This is more evident in T16-D2, and least in T17-D2.

Yielding in T17-D2 is observed to occur at a chord rotation which is only slightly higher than yielding in T14, while in T16-D1 this is lower than yielding in T14. At this damage level, the residual stiffness in T17-D2 and T16-D1 is approximately equal and about 10% higher than the corresponding value for T14. The chord rotation at maximum force for T16-D1 and T14 is approximately equal, while for T17-D2 this is 55% higher. The cumulative energy dissipation of T17-D2 is twice that of T14, while for T16-D1, this is only 15% more than that of T14. The residual stiffness of T17-D2 is 28% lower than the value of T14, while for T16-D the residual stiffness is slightly larger than the value of T14. Both u-10 and u-20 occur at the same chord rotation for T14. This is also true for T17-D2 and T16-D1. Nevertheless, for T17-D2, the chord rotation of both damage levels is larger than those corresponding to T14 by 33%, while for T16-D1 these are only larger by only 3%. The cumulative energy dissipation of T16-D1 and T14 is similar. Nevertheless, the cumulative energy dissipation of T17-D2 is approximately 80% larger than that of T14 for both damage levels. The residual stiffness for T16-D1 and T17-D2 is slightly higher than the values for T14. The chord rotation of T17-D2 at u-50, is larger than the corresponding value for T14 by 28%. However, the chord rotation at this damage level is similar for both T16-D1 and T14. The cumulative energy dissipation of T17-D2 is 41% larger than that of T14, while the value of T16-D1 is 10% lower than that of T14. The residual stiffness at u-50 of T17-D2 and T16-D1 are larger than the value corresponding to T14 by 51% and 41% respectively.

In general, the shear force-chord rotation envelope is larger for T17-D2 than the other two envelopes mainly beyond its maximum force limit. The envelope corresponding with T14, is slightly lower than the envelope corresponding with T16-D1 mainly beyond u-10. The cumulative energy dissipation against chord rotation envelope for T17-D2 is larger than the other two envelopes mainly after it reaches u-10. Beyond this level, the envelope corresponding with T14 is also larger than the envelope corresponding with T16-D1. The residual stiffness –chord rotation envelope corresponding with T17-D2 is the highest followed by the envelope corresponding to T16-D1. In Figure D-57-c, it is observed that for T16-D1, section S3 dissipates more energy just after yielding. This is the section where the upper side of the lap-splicing ends. However, section S1 is the section which dissipates more energy afterwards. S3 is then the second section that dissipates the most energy followed by S2 until u-20 is reached. Beyond this point, S2 then dissipates more energy than S3. In the case of T17-D2, figure D-58c indicates that section S1 is the section that dissipates most energy for all the range of deformation after yielding, and it is followed by section S3. In sample T14, S1 is the section that dissipates most energy only before u-50 is reached, as then section S2 dissipates the most energy. The energy dissipated by section S1 in both T16-D1 and T17-D2. However, the energy dissipated by S2 in T17-D2, is much more than that dissipated by the same section in T16-D1. However, the energy dissipated by S3 in T16-D1 is much more than the energy dissipated by S3 in T17-D2. These differences coincide in sections where lap splicing of bars begins or ends. These positions are different for T17-D2 and

T16-D1 due to different lap-length. It is observed that for T17-D2, flexural deformation gradually increases from the lower end of the column upwards. Nevertheless, for both T16-D1 and T14, flexural deformation starts at a distance from the bottom and further development is spread on either side. On comparing figure D-57a with figure D-58a, it is observed that the evolution of damage affects differently the distribution of resulting stiffness of both specimens T16-D1 and T17-D2 such that the shear distribution patterns after adjusting for the axial load rods are slightly different.

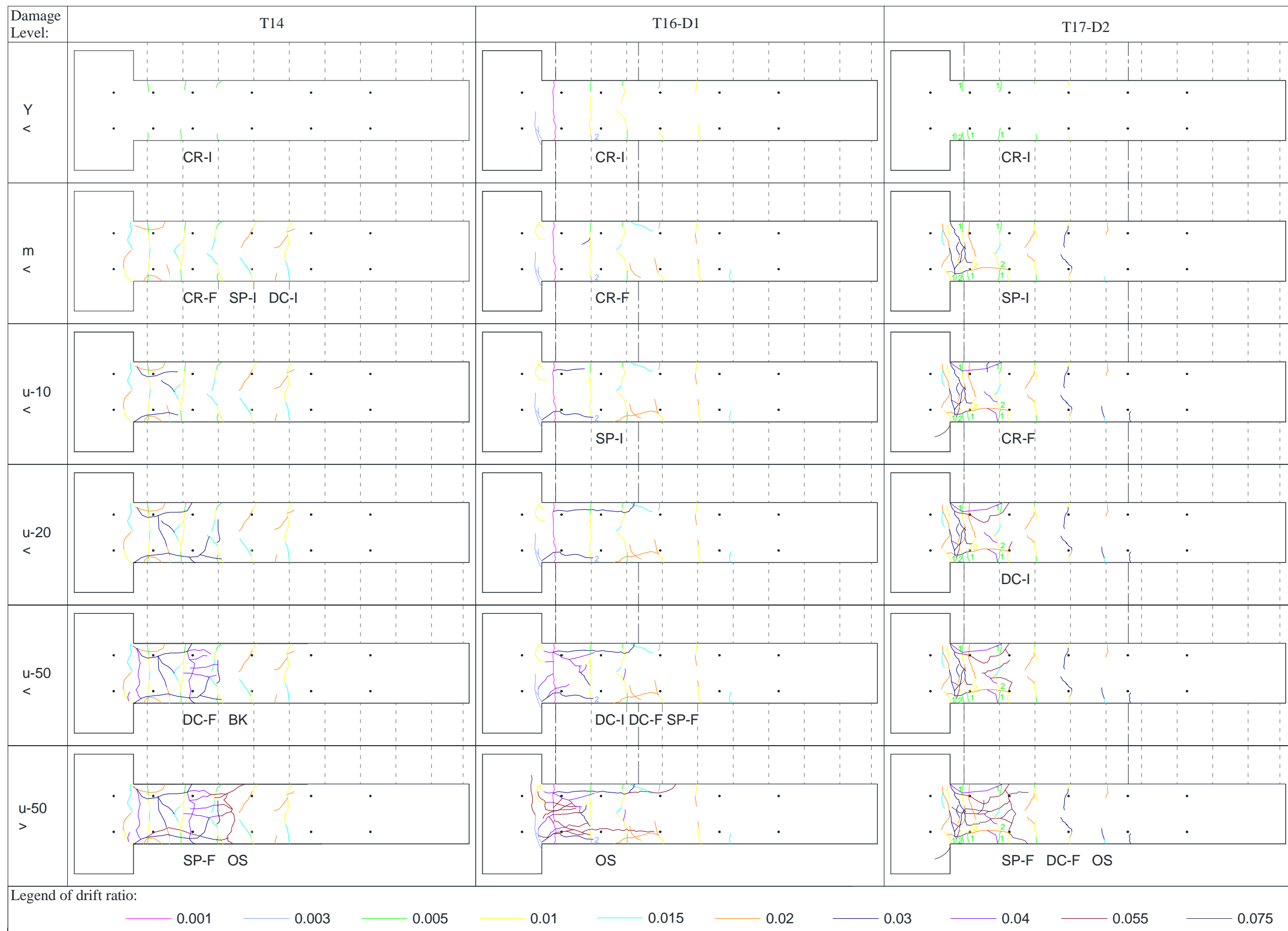
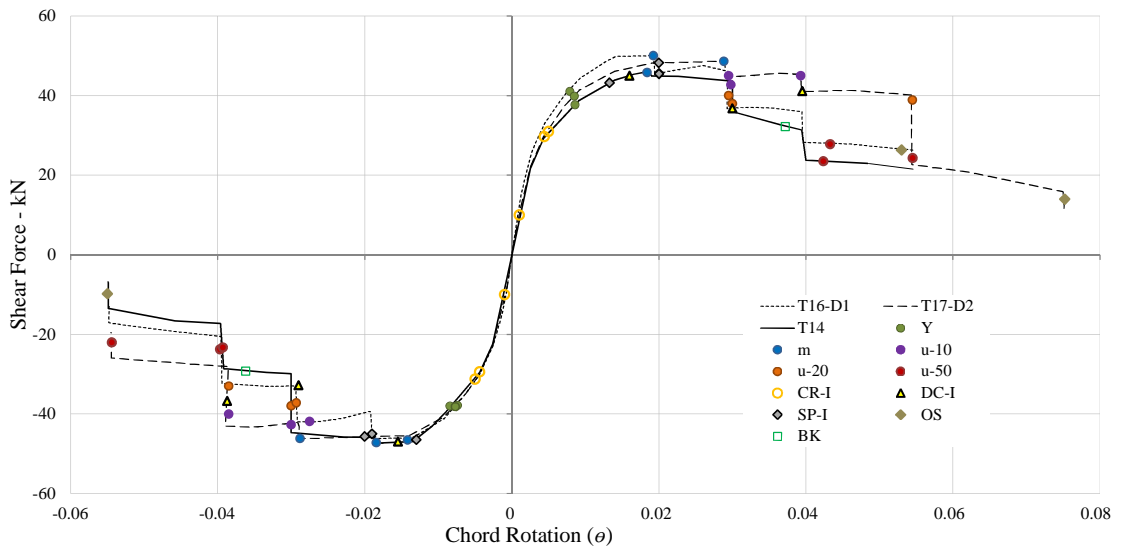
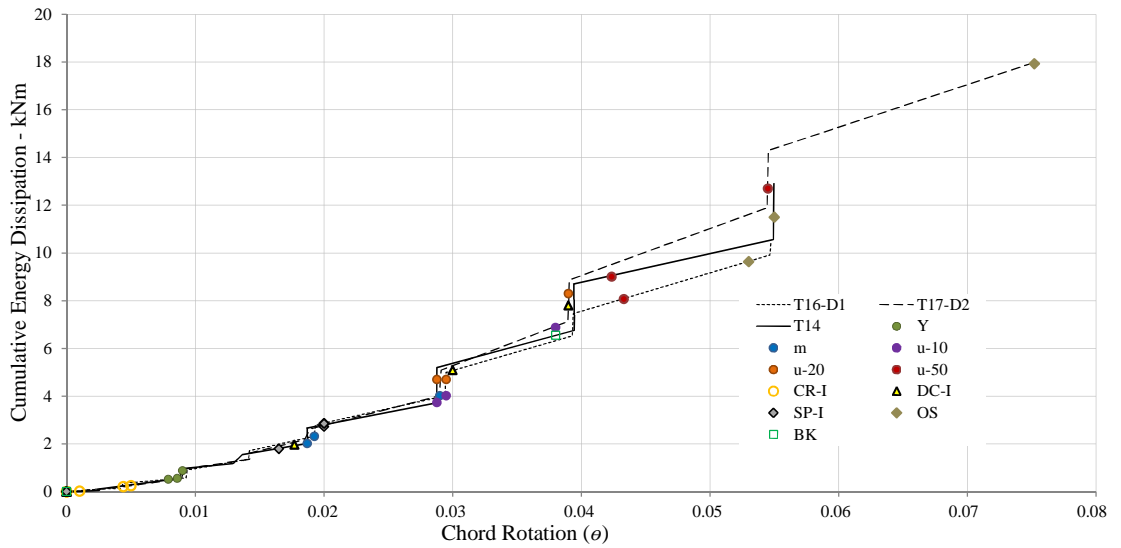


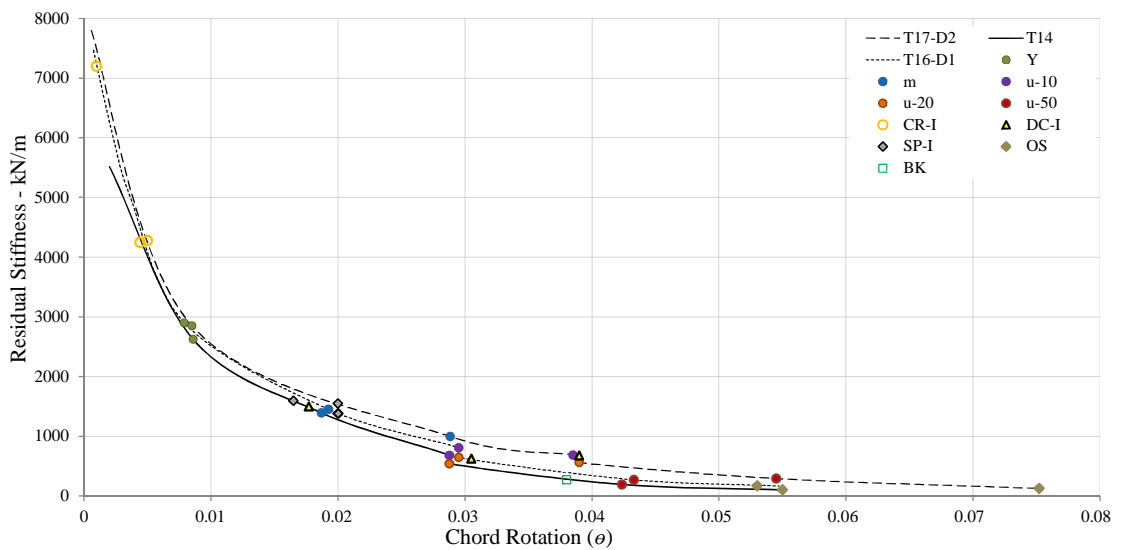
Figure 4-16 The development of damage as observed at the end of each damage level for column specimen T14, T16-D1 and T17-D2.



a



b



c

Figure 4-17 Comparison of T14, T16-D1 and T17-D2 in terms of: a) Shear force-chord rotation, b) Cumulative energy dissipation – chord rotation, c) Residual stiffness-Chord rotation, envelopes.

4.5 General Conclusions and Requirements

In this Chapter the results of the experimental campaign described in Chapter 3 are provided in terms of chord rotation, energy dissipation and residual stiffness. These tests are additions to those in the database compiled by Berry *et al.*, 2003 and discussed in Chapter 2 that is used for the development of EDP models in Chapter 5.

From the deformation history of the RC columns it is observed that all the considered variables v , α , ω_T and L_s/h contribute in the deformation capacity of RC elements and the sequence of damage development. In general, from the response of the specimens, it is observed that confinement affects more the deformation capacity, while the reinforcement ratio affects more the strength capacity. However, the extent of these effects depends on the axial force ratio. It is also observed that the loading pattern and associated energy input affects the deformation capacity and the sequence of damage occurrence in RC elements. It is observed that as the deformation capacity decreases, the rate of strength decay increases, and the residual stiffness increases if the intensity of the loading pattern increases. Hence, the development of models correlating these three parameters are essential to understand the contextual significance of each when determined independently through models based on material and geometric properties only.

It is observed that the inclusion of a cold joint affects only slightly the deformation of the RC specimen. Hence, although the exclusion of cold joints may be a source of error in simulating a real scenario, the differences are estimated to lie within tolerable limits of $\pm 10\%$. Many of the observations and conclusions discussed in this chapter follow theoretical conclusions described by Park *et al.*, 1976. However, these may only be assumed specific to this experimental campaign.

Analytical comparisons are made with the experimental results in order to investigate the validity of the latter. The initial stiffness of the experimental specimens was observed to be consistently lower than the computed analytical initial stiffness. This is possibly due to the reduced size of the section of the foundation which produces a relative stiffness between the column and the foundation which is lower than fixity simulated in an analytical model. Nevertheless, the difference in stiffness is consistently less than 10%, which is generally considered as an error limit (Harris *et al.*, 1999). Similarly, the difference between the analytical and experimental measurement of initial cracking and yielding fall within 10% of each other and hence, the deformation is validated analytically up to these damage considerations. Nevertheless, the difference at ultimate deformation exceeds 10% for most of the specimens. This is possibly due to the inability of simplified analytical models to model damage phenomena in the inelastic range.

Chapter 5. PROCEDURE FOR EMPIRICAL DETERMINATION OF ENGINEERING DEMAND PARAMETERS

5.1 Introduction

As explained in Chapter 1 and Chapter 2, the principal aim of this research is to develop tools that quantify damage in terms of engineering demand parameters (EDP) at various damage states. In this chapter, a methodology and requirements to determine empirical models relating chord rotation (θ_{dmg}), energy dissipation (E_{dmg}) and residual stiffness (K_{dmg}) at various damage states, and empirical models of chord rotation (θ_{dmg}) and stiffness ratio (EI_{dmg}/EI_g) at various damage states, in terms of combined physical and material is discussed. This is done in terms of the data requirements that are needed in addition to the experimental results discussed in Chapter 4 and Chapter 5, manipulation required on the data, identification of explanatory variables and trends between variables, identification of model characteristics, and identification of a regression procedure including statistical criteria required.

5.2 Methodology for the development of a new model

The methodology to obtain empirical relationships for engineering demand parameters at various damage states in terms of material and geometric properties of R.C columns that reflect seismic loading considerations, follows a general procedure. Figure 6-1 illustrates the steps of the procedure followed to determine empirical relationships for each EDP and corresponding damage state considered. A lot of uncertainty is associated with the determination of empirical relationships of EDPs. Consequently, some steps are iterative. The steps can be divided into 2 major parts. Part A consists in 11 steps where the data and variables for regression analysis are identified. Part B consists in 6 steps and describes the regression analysis process and the determination of ultimate models. The process for each EDP and damage level is considered separately for explanatory variables determined using dimensional analysis, or for explanatory variables determined otherwise.

Step 1. The combined variables and base variables from existing empirical equations of EDPs found in literature, material properties, constitutive models of materials and relationships describing physical phenomena of failure such as bond-slip and buckling are identified. The identified variables are listed and discussed in Chapter 2.

Step 2. The base variables sharing similar physical meaning are grouped together. The base variables are classified in terms of their physical representation or meaning. The categories refer to longitudinal steel reinforcement type, axial load considerations, confinement, buckling, bond-slip and geometrical aspects as identified in Chapter 2.

Step 3. a) Explanatory variables are determined as Π -groups using dimensional analysis in a series of compact solutions based on the classification of base variables in *Step 2*. This method is discussed in section 6.3.3.

b) Explanatory variables are identified as the combined variables determined in *Step 1*. For each of these combined variables, alternative possible substitute combinations with similar physical significance are identified using other base variables identified in *Step 2*. The alternative substitute variables are classified using the same classification strategy in *Step 2*. Variables within each group are considered dependent variables since they are alternative explanatory variable substitutes. Their simultaneous use in a model would mean that a physical property is represented more than once in a regression model. It will be an incorrectly parameterised model with a larger degree of over-fitting (Babyak, M.A., 2004). The classification is discussed in section 6.3.2.

Step 4. Databases containing data of capacity tests on R.C columns are considered. Experimental results from the experimental campaign discussed in section 6.4 are also considered. The data is organised rationally, in terms of the variables identified in *Step 3*.

Step 5. A database is selected for the regression analysis process. The resulting data of the experimental campaign discussed in Chapter 5 is added to the selected database. The selection is such that the identified database consists of data that is rationally presented, where the combined variables identified in *Step 3* can be computed, and without the need of further assumptions that could lead to increase the uncertainty associated with the value. Common test records across the considered databases in *Step 4* are identified. The values of the variables of common records are compared. Reference to the scatter is made in the selection process as discussed in section 6.4.3. For the identified database, missing values of variables are determined statistically as discussed in section 6.4.2. Data distribution is also used to identify the range of interest that is covered by the respective database.

Step 6. The experimental records and corresponding data constituting the selected database are categorized separately in terms of characteristics of loading patterns, sequence of damage development, failure mode and considerable presence of bond-slip.

Step 7. The data is used to identify the relationship between variables identified in *Step 3*, and between EDP and variables. The investigation is further discussed in section 6.6 and section 6.5, where data is analysed un-categorized and in terms of categories identified in *Step 6*. The approach consists in:

- a) Determination of correlation matrices of the variables identified in *Step 1* and *Step 3*.
- b) The determination of density distribution of the EDP and each variable in *Step 3*.
- c) Scatter plots of EDP against variables identified in *Step 3* or other EDPs using uncategorized and categorized data as defined in *Step 6*.

- d) Plots showing the effects of individual variables on EDP keeping the other variables constant. Each plot consists in a series of graphs. Each graph refers to a pair of single test series where the variable plotted against the EDP is the only variable changed for the pair of tests.

Step 8. The comparisons relationships in *Step 7* are evaluated and assessed to identify trends between EDP and variables, and between variables. The evaluation is done separately for:

- a) Combined variables (Π -groups) and associated compact solutions identified in *Step 3a*.
- b) Combined variables used in literature identified in *Step 3b*.

Step 9. a) The dimensional analysis process lead to various permutations of compact solutions. By referring to trends observed in *Step 8a*, compact solutions are revised as discussed in section 6.3.3 so that these are constituted by more relevant Π -groups. In this process, *Step 3a* to *Step 9* are revised.

- b) Alternative possible substitute combinations in *Step 3b* are revised by referring to trends or the lack of trends observed between EDP and combined variables in *Step 8b*. This is done by changing some of the base variables in the combination. The trends between combined variables are also used to check the categorization of variables in *Step 3b* as discussed in section 6.6. In this process, *Step 3a* to *Step 9* are revised.

Step 10. Once no further revision of Π -groups or combined variables is required, the relationships determined in *Step 7* identifying trends between EDP and combined variables using categorized data as defined in *Step 6*, are used to check whether such categories have an influence on the trend. If it does have a considerable effect, then the categorization is retained. However, if it is not the case, then data is either filtered, or the records constituting the category are discarded or the categorization is ignored. This is further discussed in section 6.5.

Step 11. a) Permutations of explanatory variables determined from dimensional analysis (*Step 3a*), are formed to possibly constitute EDP regression models. The Π -groups of each compact solution constitute such permutation.

- b) Permutations of explanatory variables determined in *Step 3b*, are formed to possibly constitute EDP regression models. Each permutation consists of a combined variable from each category defined in *Step 3b*. Combined variables from the same category cannot feature in the same permutation.

Step 12. A general form of a regression model for EDP which can be made up of the variables in each permutation identified in *Step 11* is identified as further discussed in section 6.8. This includes categorization selected in *Step 10*. The form and configuration of the model allows the effect of variables on each other to be expressed. The true and effective relationship between EDP and each independent variable will then be expressed in the model.

Step 13. Models of EDP for each permutation of variables identified in *Step 11* are formed in terms of the general model configuration identified in *Step 12*. Each model and associated data is logarithmically transformed. For each transformed model, backward-forward stepwise multi-variable regression is performed as discussed in section 6.7. For each model, the regression is

performed on two sets of data. The first set includes all data as ultimately defined in Step 10. In the second set of data, the same data is used with the exclusion of outliers and very extreme data-points.

Step 14. Models in logarithmic form are selected using statistical diagnostics and BIC criteria. Three sets of models are selected. Each set consists in two models referring to data where outliers and extreme data-points are either included or excluded. The three sets of models consist in:

- a) Models of EDP in terms of explanatory variables obtained from dimensional analysis.
- b) Models of EDP in terms of explanatory variables obtained from *Step 3b* and excluding an energy dissipation term.
- c) Models of EDP in terms of explanatory variables obtained from *Step 3b* and including an energy dissipation term.

Step 15. The models selected in *Step 14* are backward transformed in the non-logarithmic form, so that the EDP can be directly determined in terms of products or powers of explanatory variables and associated parameters.

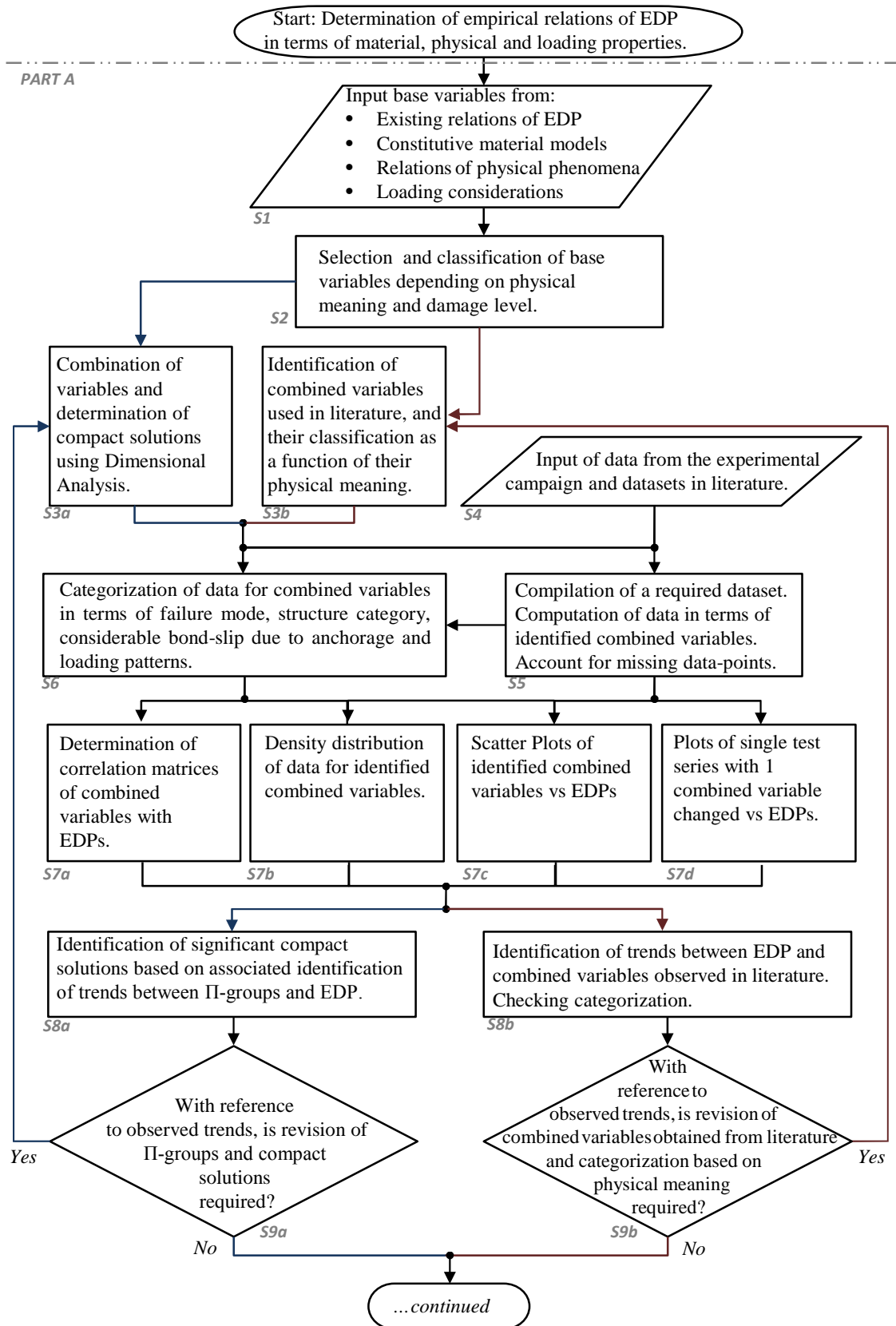
Step 16. Data distribution is plotted for each explanatory variable in the selected model. The range of application of the models is identified in terms of the range of the explanatory variables. The range is determined for the two set of models corresponding to data one including and the other excluding outliers and extreme data-points.

Step 17. a) Two models of EDP in terms of explanatory variables obtained from dimensional analysis. One model refers to data including extreme data-points and outliers, and the other based on data which excludes these points.

b) Two models for EDP in terms of explanatory variables obtained from *Step 3b* and excluding an energy dissipation term. One model refers to data including extreme data-points and outliers, and the other based on data which excludes these points.

c) Two models for EDP in terms of explanatory variables obtained from *Step 3b* and including an energy dissipation term. One model refers to data including extreme data-points and outliers, and the other based on data which excludes these points.

The methodology to obtain empirical equations relating EDPs at various damage states refers to regression analysis on models identified in section 6.8.1 and using data identified in *Step 5* previously discussed. The data is used both with the exclusion and inclusion of outliers and extreme data-points.



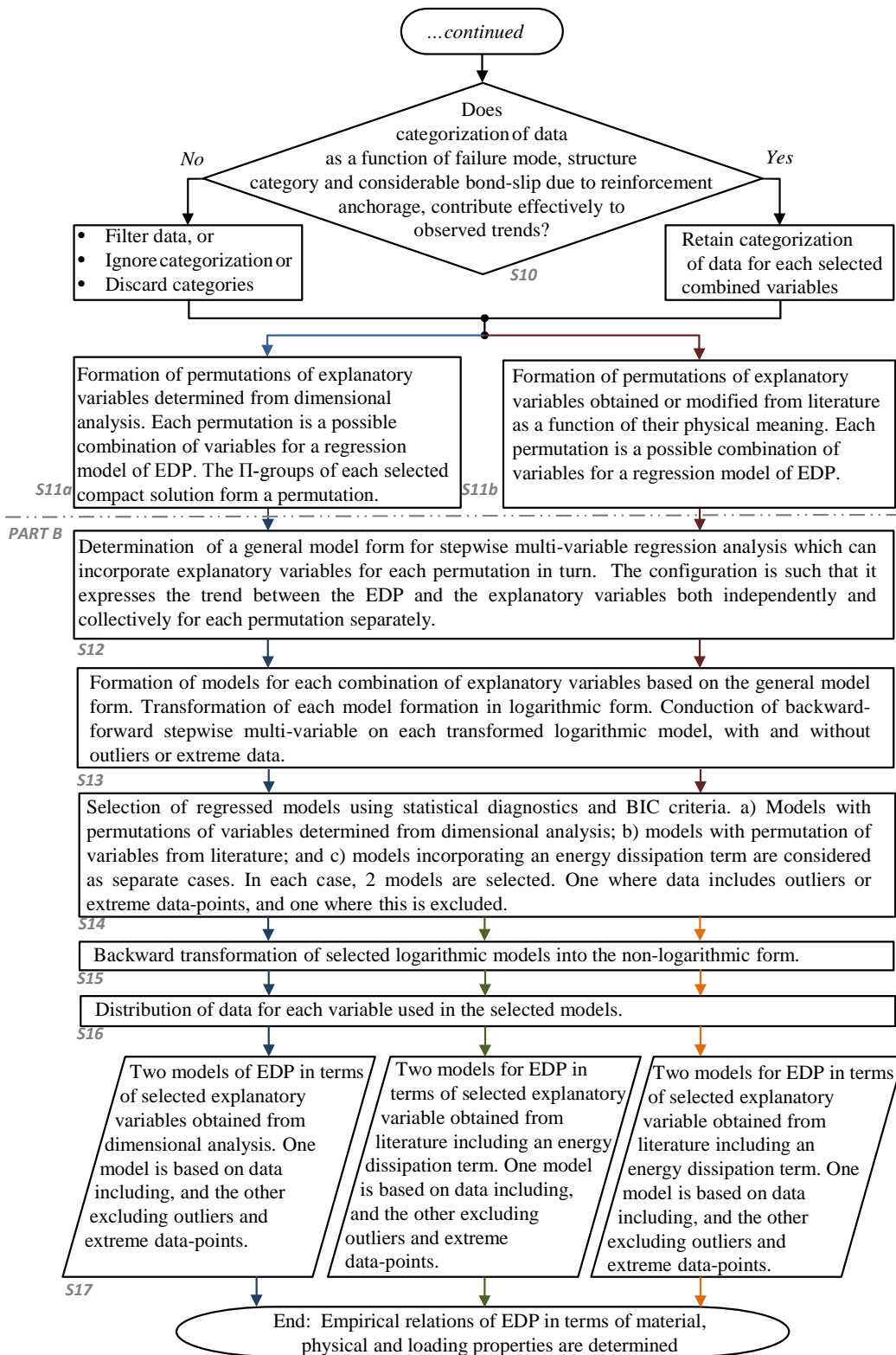


Figure 5-1 Schematic representation of the procedure that is followed to determine chord rotation and stiffness ratio empirical models at various damage states in terms of material and geometrical properties with loading considerations.

5.3 Consideration of variables for model development

5.3.1 Requirements for Explanatory Variables

Discovering the physical parameters connected with a phenomenon, and selecting between decisive variables and variables of subordinate importance is the very core of forming relationships that describe the phenomenon (Prandtl, 1935). A minimum of 5 points (r) are generally required to define a curve. For a number of variables (n), the number of required readings to proof an analytical solution is nr^{n-1} (Harris *et al.*, 1999). As observed in Chapter 2, EDPs can relate with about 16 un-combined material and geometric properties of RC columns. This means that 4×10^{11} experimental tests or records would therefore be required if un-combined variables are required to develop a model. To conduct an experimental campaign of this size, or collect experimental data on such a large number of tests is not possible. Whereas in section 6.6 trends between EDPs and explanatory variables are identified through statistical means, the main problem lies in identifying possible explanatory variables in terms of basic variables identified in Chapter 2 and Chapter 3.

Two approaches to the problem are used, and the process in developing empirical models is continued in subsequent sections separately for the two approaches. In the first approach discussed in section 6.3.2, the combined variables as possible explanatory variables are determined by using existing ones that are used in design equations, existing empirical or semi-empirical models of EDPs, or are included in models describing the development of a particular physical damage phenomenon. In this process, there is no formal analysis on whether each of the explanatory variables has an optimal structure in terms of the basic variables, or whether the structure of the explanatory variables is optimal with respect to the structure of the other variables in the same set forming the model. This can be problematic particularly when basic variables featuring in more than one combined variable can lead to overfitting in regression analysis processes (Harris *et al.*, 1999)

Dimensional analysis involves analysis of relationships between different physical quantities through the identification of their dimensions (Sonin, 2001), is the alternative solution used and discussed in section 5.3.3. The process produces relationships between parameters that are particularly useful when formal analysis is not available or not properly defined (Baker *et al.*, 1981). Dimensional analysis involves the grouping of non-dimensional parameters that result in a lower number of combined variables that describe the physical phenomenon. The combination of variables and determining non-dimensional terms through dimensional analysis would reduce the number of required tests.

Only one of the independent variables that make up the non-dimensional parameters would need to be changed in order to obtain a relationship for that variable (Baker *et al.*, 1981; Sonin, 2001;

Gibbings, 2011). However the number of tests required would still be excessively large for the determination of empirical solutions, as required in this research. The lack of data-points with respect to the number of variables would increase the uncertainty and reduce the accuracy of the results. However, Finney (1977), Davies (1980) and Gibbings (2011) account by giving practical examples that studying the physics of a phenomenon and further applying dimensional analysis before using statistical analysis to determine the form of the regression function offers a great advantage in increasing the accuracy and reducing the error of the solution describing the phenomenon.

The dimensional analysis process also helps in the identification of variables that affect the phenomenon, or relevant variables that have been omitted (Sonin, 2001; Gibbings, 2011). The definition of the physical phenomenon that is frequently used in dimensional analysis is mono-directional where it either increases or decreases monotonically in a negative or positive continuous dimension (Sonin, 2001). In our case, the physical phenomenon refers to a situation where cyclic response of R.C. columns is described or quantified by EDPs that are measured on monotonic continuous scales. The dimensional analysis is therefore carried out in terms of the latter continuous monotonic scenario, and inherits the deficiencies and errors of the mapping process which may affect the efficiency of the dimensional analysis process in identifying the appropriate variables and in making the appropriate decisions in the process.

5.3.2 *General Combined Variables*

The combined variables identified in Chapter 2 are categorized with respect to the damage level they have an influence on. For example, the maximum steel strength f_{yt} does not influence the yielding of an R.C. element, since it represents a subsequent state of damage. Similarly, the yield strength of stirrups f_{yw} is a characteristic associated with ultimate failure, after the maximum force is reached and hence does not occur during the yielding damage state. Only mostly relevant combined variables for which consistent and reliable information can be obtained are considered. Each column n in Table 5-1 lists a selection of explanatory variables that are alternatively used to represent a physical property for models of θ_Y and EI_Y/EI_g . Similarly, each column n in Table 5-2 lists a selection of explanatory variables that are alternatively used to represent a physical property for models θ_{dmg} and EI_{dmg}/EI_g where $dmg = \{m, u - 10, u - 20, u - 50\}$.

Table 5-1 Combination of variables for θ_{dmg} and EI_{dmg}/EI_g where $dmg = \{Y\}$.

X_n								
Axial force	Longitudinal reinforcement Ratio	Span-depth ratio	Concrete and longitudinal reinforcement strength			Other aspect ratios		
X_a	X_b	X_c	X_d	X_e	X_f	X_g	X_h	X_i
v	ρ_T	$\frac{L_s + a_v z}{h}$	$\frac{f_{yl}}{E_s}$	$\frac{f_{yl}}{f'_c}$	$\frac{d_{bl}}{h}$	$\frac{s}{h}$	$\frac{c}{h}$	$\frac{b}{h}$
$\frac{N}{bh}$		$\frac{L_s}{s}$					$\frac{c}{s}$	$\frac{b}{s}$
		$\frac{f_{yl}(L_s + a_v z)}{E_s h}$		$\left(\frac{d_{bl} f_{yl}^2}{E_s h \sqrt{f'_c}}\right)^{**}$				

** The variable is only used with interaction term a_{sl}

Table 5-2 Combination of variables for θ_{dmg} and EI_{dmg}/EI_g where $dmg = \{m, u - 10, u - 20, u - 50\}$

X_n											
Axial Force	Concrete and longitudinal reinforcement strength		Longitudinal reinforcement Ratio	Aspect ratios				Confinement		Load	
X_a	X_b	X_c	X_d	X_e	X_f	X_g	X_h	X_i	X_j	X_k	X_l
v	$\frac{f_{tl}}{f_{yl}}$	$\frac{f_{yl}}{f'_c}$	ρ_T	$\frac{L_s}{h}$	$\frac{s}{h}$	$\frac{c}{h}$	$\frac{b}{h}$	$\frac{d_{bl}}{s}$	$a\rho_s$	$\frac{f_{yw}}{f'_c}$	n_{cy}
$\frac{N}{bh f_{yl}}$	$\frac{f_{tl}}{f'_c}$		$\frac{\rho_{1+v}}{\rho_2}$			$\frac{c}{s}$	$\frac{b}{s}$	s_n	ρ_s		
			$\rho_T \frac{f_{yl}}{f'_c}$						$a\rho_s \frac{f_{yw}}{f'_c}$		
			$\frac{\omega_{1+v}}{\omega_2}$						ρ_w		
									ω_w		

Although the physical meaning of d_{bl}/s is linked with that of confinement variables such as $a\rho_s \frac{f_{yw}}{f'_c}$, do not represent mutual deformation considerations and are not necessarily proportional. This observation is also made by Haselton *et al.*, 2008. As a result, confinement and buckling are considered separately.

5.3.3 Dimensional Analysis

Dimensional analysis as used in this research is based on the Buckingham (1914) Π -theorem and modifications by Bridgman (1931) as put forward by Sonin (2001) and Gibbins (2011). The theorem states that for n variables that describe a physical phenomenon, with m different dimensions, the equation relating all the variables can be reduced to about $n-m$ non-dimensional combined variables or Π -groups. There are three general major steps in the dimensional analysis process for the formation of these groups.

In the first step all independent variables that describe the physical phenomenon are identified as a function of the dependent variable Q_o given by the general equation 5.1.

$$Q_o = f(Q_1, Q_2, Q_3 \dots Q_n) \quad [5.1]$$

Buckingham (1914) implies that no variable should be omitted in order to have a complete general equation 6.1 that models the phenomenon. Bridgman (1931) however does not specify a general equation to be complete as a requirement, and links a complete equation with equality of dimensions where the algebraic form remains unchanged by changes of the size of the unit measure. However for a more efficient dimensional analysis, the set of independent variables should ideally be complete, presumably within limits of the precision required with which equation 5.1 is expected to model the phenomenon or affect Q_o (Gibbings, 2011).

Based on the these considerations, general equation 5.2a describing deformation at yielding of reinforced concrete columns are determined in terms of geometric and material properties. Similarly, general equation 5.2a and equation 5.2c describing deformation after yielding of reinforced concrete columns, are determined in terms of geometric and material properties, and loading considerations.

$$\theta_Y = f\left(\beta_o, \varepsilon_{sy}, f'_c, f_{yl}, N, A_T, A_{bh}, \frac{L_s + a_v z}{h}, \frac{d_{bl}}{h}\right) \quad [5.2a]$$

$$\theta_{dmg} = f\left(\beta_o, n_{cy}, a, f'_c, f_{tl}, f_{yl}, f_{yw}, N, A_{1+v}, A_2, A_{sw}, A_{bx}, \frac{W}{q_1}, \frac{L_s}{q_2}, \frac{d_{bl}}{q_2}, \frac{c}{q_2}, \frac{s}{q_3}\right) \quad [5.2b]$$

$$\theta_{dmg} = f\left(\beta_o, n_{cy}, f'_c, f_{tl}, f_{yl}, f_{yw}, N, A_{1+v}, A_2, \frac{V_{sw}}{s}, A_{bh}, \frac{W}{q_1}, \frac{L_s}{q_2}, \frac{d_{bl}}{q_2}, \frac{c}{q_2}, \frac{s}{q_3}\right) \quad [5.2c]$$

Corresponding relationships for stiffness ratio at yielding and subsequent damage states are defined by equations 5.3a and, equation 5.3b and equation 5.3c respectively. Variables for substituting parameters W , q_1 , q_2 and q_3 are defined in Table 5-3a and Table 5-3b.

$$\frac{EI_Y}{EI_g} = f\left(\varepsilon_{sy}, f'_c, f_{yl}, N, A_T, A_{bh}, \frac{L_s + a_v z}{h}, \frac{d_{bl}}{h}\right) \quad [5.3a]$$

$$\frac{EI_{dmg}}{EI_g} = f\left(n_{cy}, a, f'_c, f_{tl}, f_{yl}, f_{yw}, N, A_{1+v}, A_2, A_{sw}, A_{bx}, \frac{W}{q_1}, \frac{L_s}{q_2}, \frac{d_{bl}}{q_2}, \frac{c}{q_2}, \frac{s}{q_3}\right) \quad [5.3b]$$

$$\frac{EI_{dmg}}{EI_g} = f\left(n_{cy}, f'_c, f_{tl}, f_{yl}, f_{yw}, N, A_{1+v}, A_2, \frac{V_{sw}}{s}, A_{bh}, \frac{W}{q_1}, \frac{L_s}{q_2}, \frac{d_{bl}}{q_2}, \frac{c}{q_2}, \frac{s}{q_3}\right) \quad [5.3c]$$

General equation 5.4 gives deformation in terms of other engineering demand parameters, stiffness (K_{dmg}) and energy dissipation (E_{dmg}) which can be computed for various damage states after yielding of R.C. elements.

$$\delta_{dm,g} = f\left(\frac{E_{dm,g}}{K_{dm,g}}, L_s\right) \quad [5.4]$$

The combinations in Table 5-3, and variables in equation 5.2 to equation 5.4 are such that derived quantities and associated base quantities are not provided all simultaneously as separate variables within the same general equation. This ensures an independent set of variables as requested (Sonin, 2001; Gibbings, 2011). The selection of variables for each equation 5.2 to equation 5.4, are based on variables identified in Chapter 2, where variables describing EDPs are defined with reference to existing relationships in literature, variables that define failure mechanisms, and constitutive models of materials and loading considerations.

The variables constituting the general equations for dimensional analysis consist in quantitative continuous variables (Sonin, 2001) as defined in Chapter 2. Reference to either discrete quantitative variables or descriptive variables is made at subsequent stages in section 5.5 and section 5.8 where the regression formulation and the regression analysis are carried out. The selected continuous quantitative variables are then variants for each discrete or descriptive category.

Table 5-3a *Substituting variables for general equation 5.2b and equation 5.3b.*

Combination	Substituting Variables				
	x	W	q_1	q_2	q_3
1	h	/	/	h	h
2	h	/	/	b	b
3	h	h	s	s	/
4	h	b	s	s	/
5	s	/	/	h	h
6	s	/	/	b	b
7	s	h	s	s	/

Table 5-3b *Substituting variables for general equation 5.2c and equation 5.3c.*

Combination	Substituting Variables			
	W	q_1	q_2	q_3
1	/	/	h	h
2	/	/	b	b
3	h	s	s	/
4	b	s	s	/

In the second step, the dimensions of the dependent and independent variables are identified (Sonin, 2001, and Gibbings 2011). Each variable is then expressed in terms of the identified dimensions. In order to avoid any controversy related with units-conversion factors in the definition of dimensions, parameters having the same units are used.

In order to identify different dimensions, its concept has to be defined as a function of the quantitative variable it is describing (Sonin, 2001). The concept of a quantitative variable as

utilised in dimensional analysis can be classified in two. It can either be an absolute quantity such as the length of column L_s or it can be the difference of more than one quantity such as extension Δ_s . A quantity can be defined as the cumulative number of elementary entries in a system. In order to have different dimensions the definition of the concept must be independent. Both absolute quantities and associated difference of quantities have the same dimensions. This means that Δ_s and L_s both have the dimension of length (L). The concepts of mass (M) and time (T) have different dimensions than length (L) since they are both independent of the latter.

For general equation 5.2 to equation 6.4 the mass (M), length (L) and time (T) are identified as the independent dimensions. Ratios of variables with same dimensions such as L_s/h are already in a dimensionless form and hence the dimension is denoted by 1 . Variable θ_{dmg} is considered an angular dimension α . Angular measures require units-conversion factor β_o (Gibbins, 2011). This is included in the list of independent variables for general equation 5.2 to equation 5.3. However, since θ_{dmg} is approximately equivalent to dimensionless measure δ_{dmg}/L_s , which is denoted by 1 , the relevance of this factor and its associated dimension is computational rather than physical.

In the third step, the number of Π -groups is identified as $n-m$. A set of independent variables of the size m is selected from Q_1 to Q_n as repeating variables. The selection is such that all identified dimensions are represented, and the selection of repeating variables cannot combine to form a dimensionless group. Then, Π -groups of dimensionless terms are formed by dividing the remaining independent non-repeating variables, and the dependent variable (Q_o) in turn, by the product of powers of the selected repeating variables having the same dimensions. The equation 6.1 is then transformed in equation 6.5 as a compact solution in terms of dimensionless Π -groups.

$$\Pi_o = f(\Pi_1, \Pi_2, \Pi_3 \dots \Pi_{n-m}) \quad [5.5]$$

Transformation combinations of general equation 5.2 to equation 5.4 into compact solutions in terms of Π -groups are given in Tables 5-4 to Table 5-7. When transforming into Π -groups, there is nothing mandatory about the completion of this transformation process where prior stages of transformation give equally valid transformed equations. The order of the cancellation of dimensions is of arbitrary choice (Gibbins, 2011). If a dimension is observed in only one variable, the process is such that the dimension will be eliminated by not showing up in a Π -group. The corresponding variable will consequently also be eliminated (Sonin, 2001). This means that either the variable does not describe the phenomenon, or another variable containing similar dimensions is overlooked in the first step.

A lot of uncertainty is associated with these considerations. Consequently, it is very difficult to determine unique complete solutions. A trial and error, iterative process involving steps 1 and 3, based on educated guess about the physics of R.C. column deformation and damage development

is followed to determine complete solutions, and corresponding compact solutions. The educated guess is based on the support for the analysis that is obtained *a posteriori* (Sonin, 2001) by showing that the independent variables in the derived dimensionless form statistically correlate with the dependent dimensionless variables. Correlation matrices and scatter plots are given in Appendix B and Appendix C respectively. Due to the large permutations and combinations, the list supplied in the appendices is limited to variables which are actually utilized in the regression analysis. This process reduces the number of irrelevant variables and identifies missing variables by observing inconsistent patterns or consistent irregularities in the scatter plots or correlations. Wherever possible, variables in general equations 5.2 to equation 5.3 are defined in terms of base quantities or derived quantities in the simplest form, rather than more complex forms. For example, axial force N is considered rather than the more complex derived quantity axial force ratio ν . This reduces the possibility of bias and omission of a relevant Π -group, while satisfying the criteria of the dimensional analysis process. However, the educated guess in choosing base variables, is such that combined dimensionless variables that are widely used in literature such as $\nu = N/(bhf'_c)$ can possibly be derived as Π -groups by the process.

The number of variables identified in the first step is large compared with the number of dimensions identified in the second step, and hence the number of Π -groups constituting a compact solution is also large. Additionally, in spite of using derived quantities in the simplest form rather than base quantities, a lot of variables constituting general equations have the same dimension combination due to similar physical quantities involved. The similar quantities mainly refer to stress, area and length measures. Thus, the trial and error iterative process involving the first and third steps leads to the vast number of possible combinations of general equations and associated compact solutions that describe the same physical phenomenon.

In equations 5.2a and equation 5.2b defining θ_Y and EI_Y/EI_g respectively, ε_{sy} substitutes E_s since it is a direct measure of deformation. Since ε_{sy} is already dimensionless it forms a Π -group without further computations as indicated in Table 5.4a and Table 5.4b. However, the term can be substituted with f_{yl}/E_s as used in Biskinis *et al.*, 2010, at subsequent stages. The main difference between equation 5.2b and equation 5.2c, and between equation 5.3b and equation 5.3c lies in the definition of the confinement parameter. In equation 5.2b and equation 5.3b, confinement is defined mainly by confining factor a as used in Biskinis *et al.*, 2010b. In equation 5.2c and equation 5.3c, confinement is defined mainly by the volume of transverse reinforcement per unit length of column (V_{sw}/s) as used in Berry *et al.*, 2003. This transforms into volumetric transverse reinforcement ratio as a Π -group. The normalisation of concrete and reinforcement strengths is done by either dividing by f_{yl} or f'_c . If the former case, ν is not determined as a function of f'_c as known in literature, but as $N/(bhf_{yl})$. Similarly, f_{yw}/f_{yl} is obtained instead of f_{yw}/f'_c as used in Biskinis *et al.*, 2010. In case of normalizing by f'_c , ν is determined

as $N/(bhf'_c)$, but the over-strength ratio of steel is provided as f_{tl}/f'_c instead of f_{tl}/f_{yl} . For either of the discussed alternatives, the data expresses similar correlations with the EDPs. In the case of longitudinal reinforcement representation, the quantity is defined in terms of areas. In the general equations, separate variables were considered for compressive (A_2) and tension (A_{1+v}) reinforcement. However these can be substituted by the total reinforcement area (A_T). A large number of length variables mainly c , s , h , b , L_s and d_{bl} characterise the general equations. In order to reduce, the number of combinations of possible Π -groups and compact solutions, these length parameters are represented in general solutions as a ratio of either s , h or b as indicated in Table 5-5 and Table 5-6. The ratios particularly those in terms of h and s express similar correlations with EDPs. However, the correlation for variables as a function of b is less strong.

The variables representing displacement (δ_{dmg}), residual stiffness (K_{dmg}) and dissipated energy (E_{dmg}) are assumed to be dependent on each other. Hence, in general equation 6.4, δ_{dmg} is considered as the dependent variable, whereas, energy dissipation and residual stiffness are combined together (E_{dmg}/K_{dmg}). This combination refers to the physical interpretation described in Chapter 2. The column length (L_s) is the variable that transforms δ_{dmg} into dimensionless Π -group $\theta_{dmg}(\approx \delta_{dmg}/L_s)$, and completes E_{dmg}/K_{dmg} in the dimensionless form.

A lot of uncertainty is still left in selecting a unique model or compact solution which would describe the phenomenon best. For every superfluous independent quantity included, there will be a superfluous dimensionless Π -group resulting from the later steps. Similarly, for every missing variable there will possibly be relevant missing Π -groups or Π -groups with less relevant combinations (Gibbings, 2011). Further selection follows in the regression analysis process, where statistical criteria is used to assess the validity of the compact solutions in describing θ_{dmg} or EI_{dmg}/EI_g , as discussed in section 5.7.

Further uncertainty is associated with the collection of data for analysis, as required by the dimensional analysis methodology. In the design, the ordering, the performance, the analysis and the synthesis of resulting data from experiments for the development of physical relationships, dimensional analysis is required a priory (Baker *et al.*, 1981; Gibbings, 2011). However, for the purpose of this research, dimensional analysis followed the experimental process, since most of the data had to be based on experiments already conducted in the past which are available in literature. Experimental campaigns in literature are conducted with different aims and scopes other than those of this research. In most of the cases, the information was not provided directly in the form of terms determined for the purpose of this research. The information is manipulated and interpreted to obtain the required terms. In some cases, sets of experimental data could not be utilised since they do not include the necessary information to obtain the values of the required

terms. In cases when the missing data is small, this is determined statistically as discussed in section 5.4.1. However, the variables in the experimental campaign discussed in Chapter 3 and Chapter 4 are based on the variation of terms that were also determined by dimensional analysis above.

Table 5-4a Compact solutions for the chord rotation at yielding - θ_Y .

Compact solution	Variables:	Dependent			Independent						
		θ_Y	β_o	ε_{sy}	f'_c	f_{yl}	N	A_T	A_{bh}	$\frac{L_s + a_v z}{h}$	$\frac{d_{bl}}{h}$
	Dimensions:	α	$\frac{1}{\alpha}$	l	$\frac{M}{L T^2}$	$\frac{M}{L T^2}$	$\frac{M L}{T^2}$	L^2	L^2	1	1
1	Π –Groups:	θ_Y		ε_{sy}	$\frac{f'_{yl}}{f'_c}$	$\frac{N}{A_{bh} f'_c}$	$\frac{A_T}{A_{bh}}$			$\frac{L_s + a_v z}{h}$	$\frac{d_{bl}}{h}$
2											
3											
4											

Table 5-4b Compact solutions for the stiffness ratio at yielding - EI_Y/EI_g .

Compact solution	Variables:	Dependent			Independent						
		EI_Y/EI_g	ε_{sy}	f'_c	f_{yl}	N	A_T	A_{bh}	$\frac{L_s + a_v z}{h}$	$\frac{d_{bl}}{h}$	
	Dimensions:	1	l	$\frac{M}{L T^2}$	$\frac{M}{L T^2}$	$\frac{M L}{T^2}$	L^2	L^2	1	1	
5	Π –Groups:	EI_Y/EI_g	ε_{sy}	$\frac{f'_{yl}}{f'_c}$	$\frac{N}{A_{bh} f'_c}$	$\frac{A_T}{A_{bh}}$			$\frac{L_s + a_v z}{h}$	$\frac{d_{bl}}{h}$	
6											
7											
8											

Table 5-5a Compact solutions for the chord rotation θ_{dmg} at various damage states after yielding, using confinement factor (a).

	Dependent	Independent																
Variables:	θ_{dmg}	β_o	n_{cy}	a	f'_c	f_{tl}	f_{yl}	f_{yw}	N	A_{1+v}	A_2	A_{sw}	A_{bx} ($x=h$ or s)	W/q_1 ($=h$ or b)	$\frac{L_s}{q_2}$	$\frac{d_{bl}}{q_2}$	$\frac{c}{q_2}$	$\frac{s}{q_3}$
Dimensions:	α	$\frac{1}{\alpha}$	l	l	$\frac{M}{LT^2}$	$\frac{M}{LT^2}$	$\frac{M}{LT^2}$	$\frac{M}{LT^2}$	$\frac{ML}{T^2}$	L^2	L^2	L^2	L^2	1	1	1	1	1
Π –Groups:	θ_{dmg}	n_{cy}	a						$\frac{f_{tl}}{f'_c}$	$\frac{f_{yl}}{f'_c}$	$\frac{f_{yw}}{f'_c}$	$\frac{N}{A_{bx}f'_c}$			$\frac{L_s}{q_2}$	$\frac{d_{bl}}{q_2}$	$\frac{c}{q_2}$	$\frac{s}{q_3}$
									$\frac{A_{1+v}}{A_{bx}}$	$\frac{A_2}{A_{bx}}$	$\frac{A_{sw}}{A_{bx}}$			$\frac{W}{q_1}$	$\frac{L_s}{q_2}$	$\frac{d_{bl}}{q_2}$	$\frac{c}{q_2}$	$\frac{s}{q_3}$
									$\frac{f'_c}{f_{yl}}$	$\frac{f_{tl}}{f_{yl}}$	$\frac{f_{yw}}{f_{yl}}$	$\frac{N}{A_{bx}f_{yl}}$			$\frac{L_s}{q_2}$	$\frac{d_{bl}}{q_2}$	$\frac{c}{q_2}$	$\frac{s}{q_3}$
														$\frac{W}{q_1}$	$\frac{L_s}{q_2}$	$\frac{d_{bl}}{q_2}$	$\frac{c}{q_2}$	$\frac{s}{q_3}$

Table 5-5b Compact solutions for the chord rotation θ_{dmg} at various damage states after yielding, using confinement variable ω_w .

	Dependent	Independent															
Variables:	θ_{dmg}	β_o	n_{cy}	f'_c	f_{tl}	f_{yl}	f_{yw}	N	A_{1+v}	A_2	$\frac{V_{sw}}{s}$	A_{bh}	W/q_1 ($=h$ or b)	$\frac{L_s}{q_2}$	$\frac{d_{bl}}{q_2}$	$\frac{c}{q_2}$	$\frac{s}{q_3}$
Dimensions:	α	$\frac{1}{\alpha}$	l	$\frac{M}{LT^2}$	$\frac{M}{LT^2}$	$\frac{M}{LT^2}$	$\frac{M}{LT^2}$	$\frac{ML}{T^2}$	L^2	L^2	L^2	L^2	1	1	1	1	1
Π –Groups:	θ_{dmg}	n_{cy}						$\frac{f_{tl}}{f'_c}$	$\frac{f_{yl}}{f'_c}$	$\frac{f_{yw}}{f'_c}$	$\frac{N}{A_{bh}f'_c}$			$\frac{L_s}{q_2}$	$\frac{d_{bl}}{q_2}$	$\frac{c}{q_2}$	$\frac{s}{q_3}$
								$\frac{A_{1+v}}{A_{bh}}$	$\frac{A_2}{A_{bh}}$	$\frac{V_{sw}}{sA_{bh}}$			$\frac{W}{q_1}$	$\frac{L_s}{q_2}$	$\frac{d_{bl}}{q_2}$	$\frac{c}{q_2}$	$\frac{s}{q_3}$
								$\frac{f'_c}{f_{yl}}$	$\frac{f_{tl}}{f_{yl}}$	$\frac{f_{yw}}{f_{yl}}$	$\frac{N}{A_{bh}f_{yl}}$			$\frac{L_s}{q_2}$	$\frac{d_{bl}}{q_2}$	$\frac{c}{q_2}$	$\frac{s}{q_3}$
													$\frac{W}{q_1}$	$\frac{L_s}{q_2}$	$\frac{d_{bl}}{q_2}$	$\frac{c}{q_2}$	$\frac{s}{q_3}$

Table 5-6a Compact solutions for stiffness ratio EI_{dmg}/EI_g at various damage states after yielding, using confinement factor (a).

Variables:	Dependent	Independent																		
	EI_{dmg}/EI_g	n_{cy}	a	f'_c	f_{tl}	f_{yl}	f_{yw}	N	A_{1+v}	A_2	A_{sw}	A_{bx} ($x=h$ or s)	W/q_1 ($=h$ or b)	$\frac{L_s}{q_2}$	$\frac{d_{bl}}{q_2}$	$\frac{c}{q_2}$	$\frac{s}{q_3}$			
Dimensions:	l	l	l	$\frac{M}{LT^2}$	$\frac{M}{LT^2}$	$\frac{M}{LT^2}$	$\frac{M}{LT^2}$	$\frac{ML}{T^2}$	L^2	L^2	L^2	L^2	1	1	1	1	1			
Π –Groups:	EI_{dmg}/EI_g	n_{cy}	a					$\frac{f_{tl}}{f'_c}$	$\frac{f_{yl}}{f'_c}$	$\frac{f_{yw}}{f'_c}$	$\frac{N}{A_{bx}f'_c}$				$\frac{L_s}{q_2}$	$\frac{d_{bl}}{q_2}$	$\frac{c}{q_2}$	$\frac{s}{q_3}$		
												$\frac{A_{1+v}}{A_{bx}}$	$\frac{A_2}{A_{bx}}$	$\frac{A_{sw}}{A_{bx}}$	$\frac{W}{q_1}$	$\frac{L_s}{q_2}$	$\frac{d_{bl}}{q_2}$	$\frac{c}{q_2}$		
								$\frac{f'_c}{f_{yl}}$	$\frac{f_{tl}}{f_{yl}}$			$\frac{f_{yw}}{f_{yl}}$	$\frac{N}{A_{bx}f_{yl}}$				$\frac{L_s}{q_2}$	$\frac{d_{bl}}{q_2}$	$\frac{c}{q_2}$	$\frac{s}{q_3}$
															$\frac{W}{q_1}$	$\frac{L_s}{q_2}$	$\frac{d_{bl}}{q_2}$	$\frac{c}{q_2}$		

Table 5-6b Compact solutions for stiffness ratio EI_{dmg}/EI_g at various damage states after yielding, using confinement variable ω_w .

Variables:	Dependent	Independent																	
	EI_{dmg}/EI_g	n_{cy}	f'_c	f_{tl}	f_{yl}	f_{yw}	N	A_{1+v}	A_2	$\frac{V_{sw}}{s}$	A_{bh}	W/q_1 ($=h$ or b)	$\frac{L_s}{q_2}$	$\frac{d_{bl}}{q_2}$	$\frac{c}{q_2}$	$\frac{s}{q_3}$			
Dimensions:	l	l	$\frac{M}{LT^2}$	$\frac{M}{LT^2}$	$\frac{M}{LT^2}$	$\frac{M}{LT^2}$	$\frac{ML}{T^2}$	L^2	L^2	L^2	L^2	1	1	1	1	1			
Π –Groups:	EI_{dmg}/EI_g	n_{cy}					$\frac{f_{tl}}{f'_c}$	$\frac{f_{yl}}{f'_c}$	$\frac{f_{yw}}{f'_c}$	$\frac{N}{A_{bh}f'_c}$				$\frac{L_s}{q_2}$	$\frac{d_{bl}}{q_2}$	$\frac{c}{q_2}$	$\frac{s}{q_3}$		
											$\frac{A_{1+v}}{A_{bh}}$	$\frac{A_2}{A_{bh}}$	$\frac{V_{sw}}{sA_{bh}}$	$\frac{W}{q_1}$	$\frac{L_s}{q_2}$	$\frac{d_{bl}}{q_2}$	$\frac{c}{q_2}$		
							$\frac{f'_c}{f_{yl}}$	$\frac{f_{tl}}{f_{yl}}$			$\frac{f_{yw}}{f_{yl}}$	$\frac{N}{A_{bh}f_{yl}}$				$\frac{L_s}{q_2}$	$\frac{d_{bl}}{q_2}$	$\frac{c}{q_2}$	$\frac{s}{q_3}$
														$\frac{W}{q_1}$	$\frac{L_s}{q_2}$	$\frac{d_{bl}}{q_2}$	$\frac{c}{q_2}$		

Table 5-7 Compact solution for the relationship between θ_{dmg} , E_{dmg} and K_{dmg} .

Compact solution	Variables:	Dependent	Independent	
		δ_{dmg}	E_{dmg}/K_{dmg}	L_s
	Dimensions:	L	L^2	L
	Π –Groups:	$\frac{\delta_{dmg}}{L_s}$	$\frac{E_{dmg}}{K_{dmg} L_s^2}$	

5.4 Database Considerations for EDP Model Development

5.4.1 Treatment of missing data

The available databases presented in Chapter 2 are characterised with two categories of missing data. The first category refers to missing data of EDPs at the required damage level. In databases provided by Rossetto et al., 2002 and Panagiotakos *et al.*, 2001, the information provided refers to chord rotation and stiffness ratio at yielding and chord rotation at 20% maximum force reduction.

The dependent variables or the EDPs presented in the databases by Rossetto et al., 2002 and Panagiotakos *et al.*, 2001 are flexural moment (M_y, M_{u-20}), curvature (ϕ_y, ϕ_{u-20}) and chord rotation (θ_y, θ_{u-20}) at yielding and 20% maximum force reduction only. No reference is made to other states of damage. For these two databases, this information is mostly obtained by reading this data manually from graphs in the literature papers. Hence, more data at other damage states is not possible unless this same procedure is followed.

Berry *et al.*, 2003 provides the force-displacement history for each test in the database accounting for the different test-setups and associated variations. Hence, all the EDPs discussed in Chapter 2 including chord rotation, stiffness, energy dissipation and cyclic pattern information associated with the required damage could be computed for each test in a rational format as discussed in 3.5 and Chapter 5. The accuracy in determining this data of the EDPs, which are the explanatory variables, is assumed to provide better accuracy and hence less bias and a less statistical uncertainty compared to the other two databases. In addition, the EDPs in question could be determined at all the damage states required which defined in Chapter 2. These two criteria provide major advantage of this database over the other two.

The other category of missing data consists in values of particular material and geometrical variables. No reference is found in Rossetto et al., 2002, Panagiotakos *et al.*, 1999, Panagiotakos *et al.*, 2001, Berry *et al.*, 2003, Haselton *et al.*, 2008 and Biskinis *et al.*, 2010a,b, on how this type of missing data is dealt with in the development of respective EDP models. In the database available from Panagiotakos *et al.*, 2001, the data is provided in terms of combined geometric and material properties, instead of basic terms. It is very difficult to determine the basic variables

without any form of subjective interpretation, and hence comparisons are only made between databases provided by Rossetto et al., 2002 and Berry *et al.*, 2003.

For the database provided by Rossetto *et al.* 1999, the missing data is associated with a number of un-combined variables mainly referring to reinforcement properties. This is an important component in the development of EDP relationships as discussed in Chapter 2. A summary of the missing data is provided in Table 6-9. While the actual percentage of missing values is only 5.2% for the beams and columns combined, the percentage of test records that have some kind of missing data is 68%.

Table 5-8 Missing data in the database from Rossetto *et al.*, 2002.

R.C. Element:	Columns	Beams	Columns and Beams
Number of Tests:	399	216	615
Number of missing data ^{1,2} :	289	127	416
Percentage of tests with missing data (%):	72	59	68
Percentage of values missing (%) ³ :	5.6	4.5	5.2

¹ Missing data refers to f_{tl} , f_{yw} , L_s , f_{yl} ; ² Data considered refers to 13 un-combined physical and geometrical parameters; ³ Total number of values considered for each R.C. element is equal to the number of parameters (13) multiplied by the number of test records.

In the database provided by Berry *et al.* 2003, the missing data refers mainly to the tensile strength of the longitudinal steel (f_{tl}). Out of the 275 rectangular column tests, this property is missing in 50 records. Out of these 50 records, the property is different in only 16 records. This means that 18% of the records have missing data, however if records with missing data are considered based the property being different, this drops to 7.1%.

As indicated in Chapter 2 the explanatory variables as used in the regression models are a combination of the basic variables. Hence the missing data has a recurrent multiple effect on other combined variables. The threshold of missing data allowed depends on the type of data and statistical approach used to retrieve the data, however under particular conditions Martin-Fernandez *et al.*, 2003 consider 10%

The missing data can either be missing completely at random (MCAR), missing at random (MCR) and missing not completely at random (MNAR) (Rubin, 1976). The statistical solution to find missing data must ensure precision by considering a large sample, and avoid bias by considering random selection from the population. These criteria are satisfied differently on whether the nature of the missing data is MCAR, MCR or MNCR (Rubin 1976). There are various statistical ways on how to deal with missing data (Howell, 2007), including list-wise and pair-wise deletion, simple imputation methods, mean imputation methods and principled imputation methods. Deletion techniques involve the removal of records from the dataset. Hence, since the number of records available is already limited, these procedures are not considered as a solution.

Random imputation, which is a principled method, limits bias and ensures precision for MCAR and MAR missing data (Howell, 2007). Since the missing data in the dataset provided by Berry *et al.*, 2003 can be classified as a mixture of MCAR and MAR, then random imputation is adopted. Simple or mean imputation approaches do not always satisfy un-bias and precision criteria for MCAR or MAR type missing data (Little *et al.*, 1987).

To find the missing values of f_{tl} , random imputation is applied using the statistical software *R* (R Core Team, 2013) and the package R-MICE (Van Buuren, 2011). The unknown f_{tl} values in the database is predicted based on regression of the relationship between f_{tl} and f_{yl} . The values of the missing f_{tl} are determined iteratively ensuring that statistical information on the residuals is conserved when the predicted data is introduced to the regression model that is originally built based on the observed and known values. Figure 6-2a shows the random distribution of the imputed tests with the observed tests, while Figure 6-2b shows the quasi superimposed distributions of the residuals for both the observed and, and the observed with the imputed.

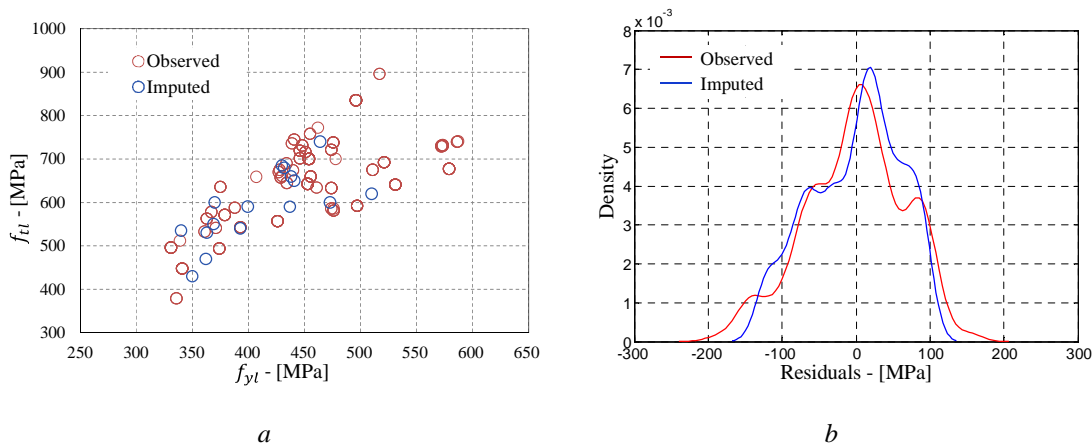


Figure 5-2 a) Scatter plot of $f_{tl} - f_{yl}$ showing complete observed data, and data with the imputation of f_{tl} b) Distribution of the residuals of observed f_{tl} only, and observed f_{tl} with the addition of missing values after imputation.

Missing data from Rossetto *et al.*, 2002 dataset is a mixture of MCAR, MAR and MNAR. The solution for MNAR data is very complex and consists in manipulation of maximum likelihood and multiple imputation methods, and sensitivity analysis (Howell, 2007). Considering the complexity of the method, the possible uncertainty associated in the imputation method due to the relatively large number of missing data, and considering that the database is not selected for regression analysis also due to other reasons discussed in section 2.4.2, then finding the missing values for this database is not considered.

5.4.2 Data variability between datasets

In the three databases utilised by Berry *et al.*, 2003, Rossetto *et al.*, 2002 and Panagiotakos *et al.*, 2001 discussed in section 6.4.2, there are 34 common test records. No variation on the data

referring to the independent variables is observed. However, differences are observed in the values defining the chord rotation at yielding (θ_Y) and at 20% maximum force reduction (θ_{u-20}).

Figure 6-3 shows the scatter plots of θ_Y for these records corresponding to each of the 3 databases, against the values determined following the interpretation provided in Chapter 2. Basic statistics on ratios of the different observations of θ_Y are provided in Table 6-10. As shown by the mean trend in the plots, the interpretation of yielding as provided in this research, provides lower values than the interpretation in other databases since in the latter a theoretical yielding of the component is utilised, while in the former, yielding refers to the material.

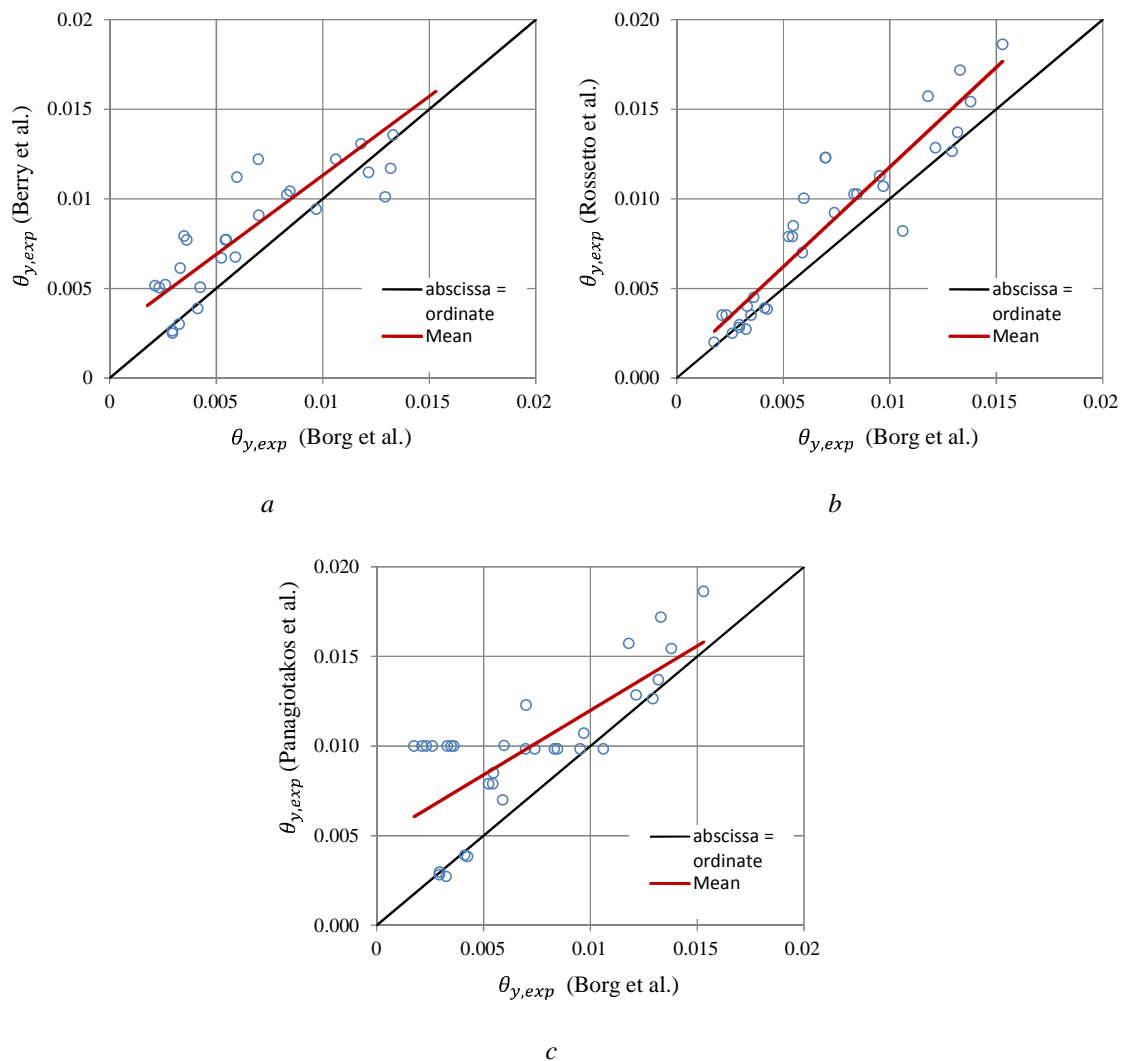


Figure 5-3 Scatter plots of experimental values of θ_Y for common records in different databases. The values measured in this research plotted against the values as reported in a) Berry et al., 2003, b) Rossetto et al., 2002 and c) Panagiotakos et al., 2001.

Table 5-9, shows that although on average, θ_Y are possibly characterised by lower values in this research, they are more consistent with the values provided by Rossetto et al., 2002. On average, the values by Berry et al., 2003 are lower than Rossetto et al., 2002, and higher than Panagiotakos et al., 2001. The scatter in terms of standard deviation (SD) and coefficient of variation (CoV) is

then similar for the ratios corresponding to Berry *et al.*, 2003/Panagiotakos *et al.*, 2001 and Rossetto *et al.*, 2002/Berry *et al.*, 2003. The interpretation by Panagiotakos *et al.*, 2001 is very different from that considered in this research both in terms of mean, SD, and CoV. This is unforeseen considering that the values provided by Rossetto *et al.*, 2002 which utilize the same data-source as Panagiotakos *et al.*, 2001, show consistent differences with the values provided by the interpretation as used in this research such that the θ_Y is characterised by the lowest CoV and SD. However, CoV and SD are also large for the θ_Y ratio that corresponds to the common values from Panagiotakos *et al.*, 2001 and Rossetto *et al.*, 2002. It is observed that for 12 tests Panagiotakos *et al.*, 2001 has considered $\theta_Y = 0.01$, while Rossetto, *et al.*, 1999 has considered yielding to vary $0.002 < \theta_Y < 0.011$. The values provided by this research, and those provided by Berry *et al.*, 2003 are also not constant at $\theta_Y = 0.01$.

Table 5-9. Summary of statistics on the ratio of values of θ_Y reported in common records of different databases.

$\theta_{Y,exp}$	Berry	Rossetto	Panagiotakos	Rossetto	Berry	Rossetto
$\theta_{Y,exp}$	Borg	Borg	Borg	Berry	Panagiotakos	Panagiotakos
Mean	1.38	1.22	1.79	1.18	1.18	1.49
Median	1.23	1.20	1.26	1.00	1.15	1.00
S.D.	0.48	0.26	1.23	0.39	0.32	0.99
CoV. (%)	34.5	21.6	68.6	33.2	27.0	66.4

Figure 6-4 shows the scatter plots of θ_{u-20} for the common records corresponding to each of the 3 databases, against the values determined following the interpretation provided in Chapter 2. Basic statistics on ratios of the different observations of θ_{u-20} are provided in Table 6-11. From the mean trend in the plots, it is observed that the values using the interpretation for this research are lower and more conservative particularly for lower values of θ_{u-20} . This is so since on having multiple cycles at the same deformation, 20% strength degradation is exceeded without any further increase in deformation, considerable posterior extrapolation of deformation is not considered for the purpose of this research as discussed in Chapter 2. The resulting discrepancy is observed by the large values of SD, CoV and mean in Table 6-11. However, on removing the 3 test records which are mostly affected by this interpretation, the CoV, SD, mean, and median are similar to all other ratios of θ_{u-20} corresponding to the different sources. On removing these 3 records, the interpretation of θ_{u-20} in this research is very similar to that of Berry *et al.*, 2003. The discrepancy between Rossetto *et al.*, 2002 and Panagiotakos *et al.*, 2001 in interpreting θ_Y are not repeated for θ_{u-20} .

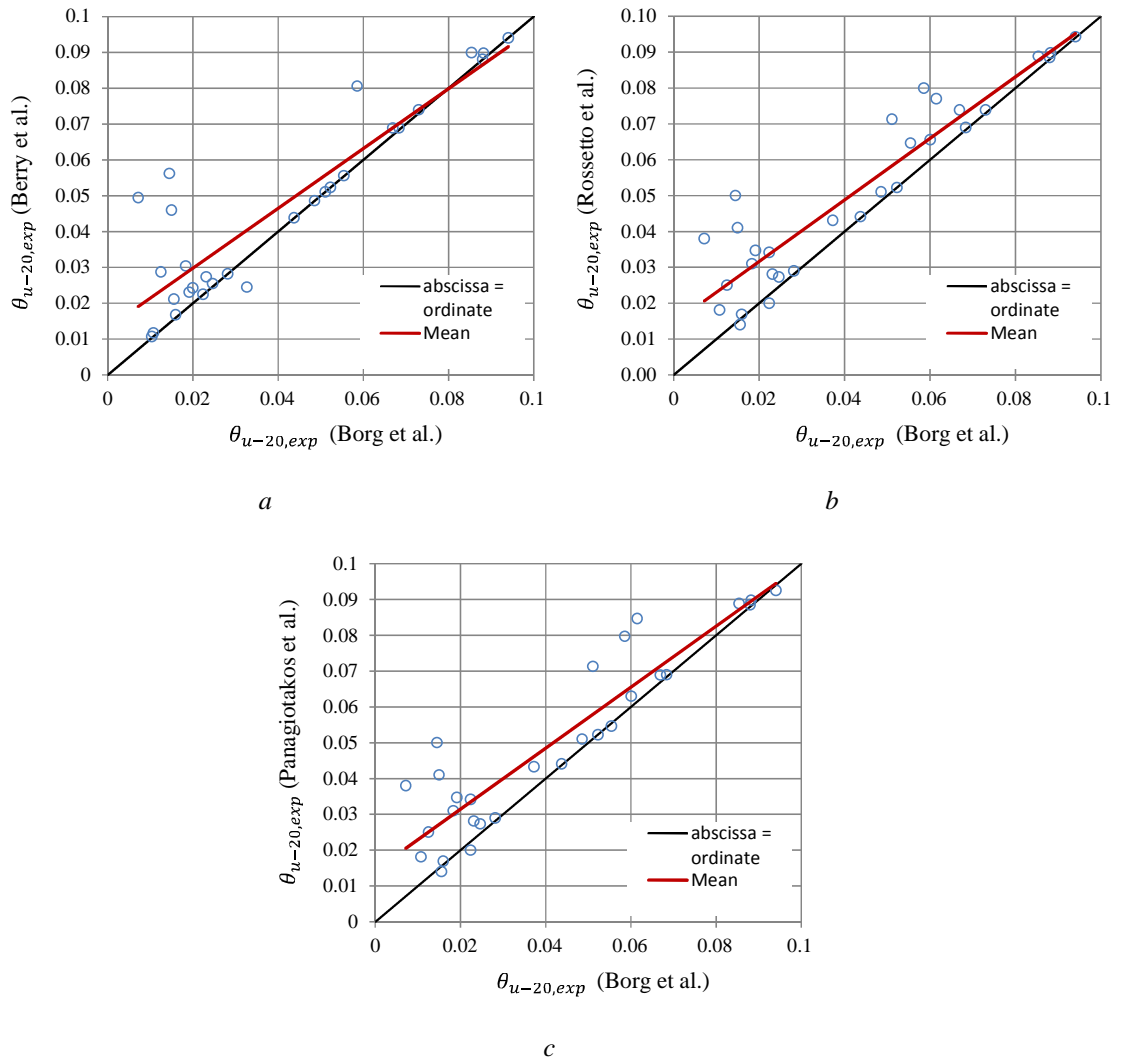


Figure 5-4 Scatter plots of experimental values of θ_{u-20} for common records in different databases. The values measured in this research plotted against the values as reported in a) Berry *et al.*, 2003, b) Rossetto *et al.*, 2002 and c) Panagiotakos *et al.*, 2001.

Table 5-10 Summary of statistics on the ratio of values of θ_{u-20} reported in common records of different databases.

$\frac{\theta_{u-20,exp}}{\theta_{u-20,exp}}$	Berry Borg	Rossetto Borg	Panagiotakos Borg	Rossetto Berry	Berry Panagiotakos	Rossetto Panagiotakos
Mean	1.47 (1.02)*	1.47 (1.05)*	1.48 (1.06)*	1.04	1.01	1.01
Median	1.03 (1.02)*	1.11 (1.07)*	1.06 (1.04)*	1.00	1.00	1.00
S.D.	1.25 (0.15)*	0.90 (0.23)*	0.92 (0.24)*	0.22	0.21	0.04
CoV. (%)	85.4 (14.5)*	61.3 (21.9)*	61.9 (22.6)*	21.3	21.2	3.9

* On the removal of 3 tests which give considerable low values with respect to values from Berry *et al.*, 2003, Rossetto *et al.*, 2002 and Panagiotakos *et al.*, 2001, since in the former, strength degradation at the same deformation due to internal cycles is taken into account.

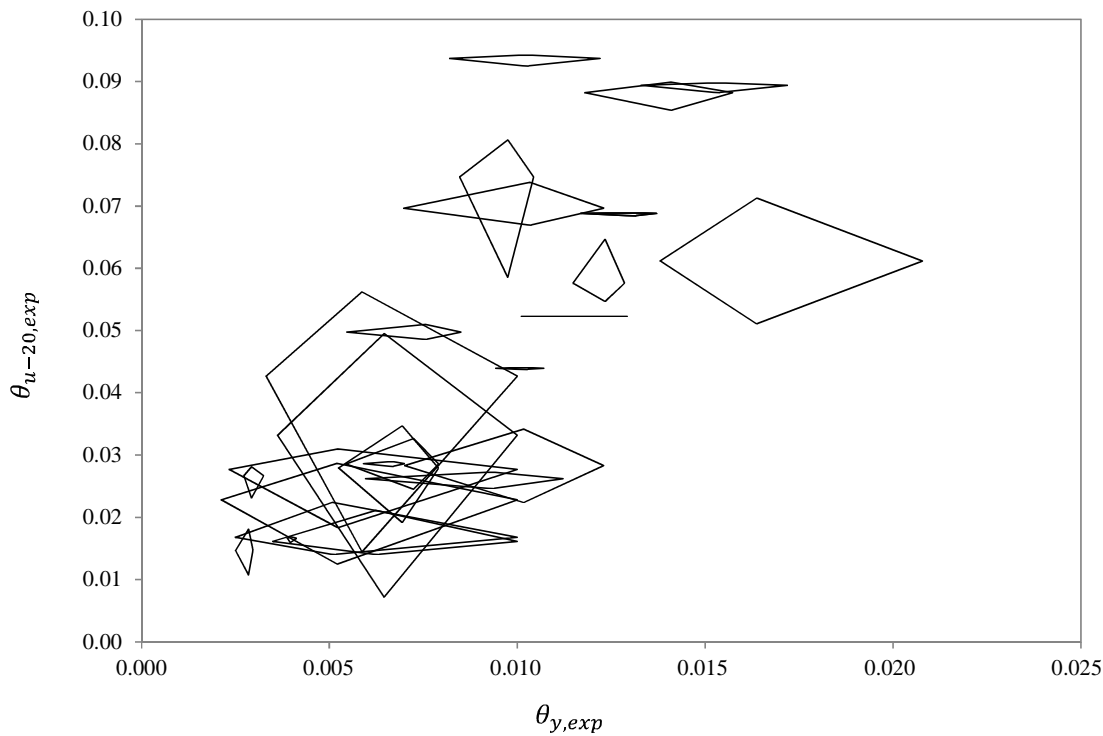


Figure 5-5 Scatter plots of $\theta_{u-20} - \theta_y$ from common records in different databases. Each record is represented by a quadrilateral enclosing the different values of chord rotation as used in this research, and as provided by Rossetto *et al.*, 2002, Panagiotakos *et al.*, 2001 and Berry *et al.*, 2003.

Figure 6-5 shows the scatter plot of $\theta_y - \theta_{u-20}$ of each test. Each test is represented by a quadrilateral enclosing the values corresponding to each of the 4 interpretations by different authors. The size of some points is evidence of the large discrepancy in interpreting the values that correspond to the same level damage. For most of the data the values are obtained by Panagiotakos *et al.*, 2001 and Rossetto *et al.*, 2002 by manual measurement from graphs, whereas the values for this research and those in Berry *et al.*, 2003 were obtained through computations on real data. This might have an impact on the accuracy. In addition, no rational approach that takes into account various aspects including P- Δ effects, and the role of internal cycles in damage development exist. Subjective interpretation is therefore unavoidable.

5.4.3 Corrections and filtering of data

Two major corrections and filtering processes are considered on the data in order to meet the scope of the research in taking a more rational approach in the regression analysis process. As observed in section 6.5.2, the number of records corresponding to specimens failing in shear is very small. However it is observed that clustering of EDPs occurs as a function of the failure mode. As a result, reference is only made to records whose specimens fail in flexure. The process discussed in Chapter 2 is utilised to filter-off the test specimens.

The other correction that is considered refers to the effect of P- Δ effect on the force deformation history and consequential effects on the damage criteria based on a limit that is a function of maximum force reduction. Table 5-11 shows the relative percentage of tests that is conducted by the different identified test setups for the selected database by Berry *et al.*, 2003. The table also indicates a summary of statistics on how the maximum force resulting in the force displacement history is affected by the nature of the test. No account on how P- Δ effects are accounted for in defining EDPs for the regression analysis of other relationships in literature is given, apart from those by Berry *et al.*, 2003 and Haselton *et al.*, 2008.

Table 5-11 Statistics on the correction of the maximum force of a force displacement history due to P- Δ effects due to different test setups.

Type of P- Δ correction:		Type I	Type II	Type III	Type IV
Number of tests (%):		20.5	52.4	2.6	24.5
Correction of F_{max} on original value (%)	Maximum:	26.8	/	0.8	20.0
	Minimum:	0.1	/	0.2	2.8
	Average:	7.2	/	0.5	7.9
	Median:	5.5	/	0.4	6.5
	S.D.:	6.2	/	0.2	4.6

As observed in Chapter 3 and Chapter 4, the force at the foundation column interface is assumed as the place where the maximum force (F_{max}) takes place. However it is observed that this is not effectively the case. The effective force contributing to the effective failure and deformation of the specimen may result at a different section. If reduction of forces is considered assuming that the effective force occurs at the interface, then the dissipated energy will only be a function of the interface, and would not reflect the global deformation of the column. In some occasions, this can be untrue for Type I setups. However, this can affect only part of the 20% of the setups, for which the median effect is less than 5.5% of F_{max} . This is very much within limits of tolerable error (Harris *et al.*, 1999). As a result, no account for P- Δ effects is considered, and true maximum shear forces resulting on the specimens are considered.

5.5 Categorization and classification of data

5.5.1 Loading pattern

The empirical models in literature referring to yield and ultimate chord rotation discussed in Chapter 2 are characterised with a large scatter and coefficient of variation. In this section, the data considered for the model development is classified in terms of loading patterns, building class, failure modes, and damage development sequences, in order to investigate the possibility of building the regression models about these classifications as one of the means to address this uncertainty. If the classification of an element is known, then predicting its EDPs based on a model that refers to data of a similar category is expected to be more reliable (Harris *et al.*, 1999). Although in this research an investigation on various damage levels is made, this section refers

only to the damage level at 20% maximum force reduction, since it is the most damage level referred to in literature in the development of empirical models and most resources and data available are limited to it. Considerations to expand on other damage levels are made in the end based on the outcome of this damage level.

Borg *et al.*, 2012 indicates that the development of damage and its magnitude depend on the loading pattern and the associated number of cycles. There are two definitions of loading patterns that can be considered. These are the Input Loading Pattern (ILP) which is the whole load history that is applied during the test and the Effective Loading Pattern (ELP) which is the loading pattern associated with the response and damage development of the test specimen. This is quantitatively defined as the loading pattern that ranges between the occurrence of considerable cracking or yielding, and a damage level being investigated. Cycles occurring before (Krawlinker *et al.*, 1997) and after the damage level are considered to have negligible or no effect on damage development up to the level considered.

The ELP may represent different loading history characteristics than those intended by the originally selected ILP. For example on considering the loading history patterns of the selected database, tests with random and decreasing amplitude ILP have an ELP which can be categorized as quasi-monotonic. Tests with nearly constant amplitude have an incremental or a quasi-monotonic ELP. Similarly some tests with an incremental ILP with more than one cycle per step, have an ELP consisting in either constant amplitude or constant amplitude with one relatively larger cycle that drives the specimen to the damage limit considered. The ELP covers a small range of the ILP and the similarity between the two increases if this superposition is larger. This highlights the importance of adopting a loading protocol that is based on a system suggested in Chapter 3. Classification of the tests in the selected database by loading protocol or in defining the number of cycles (n_{cy}) is specifically based on ELP.

Figure 5-6a and Table 5-12a show the statistics and the distribution of tests from the selected database with respect to the number of cycles (n_{cy}) at 20% maximum force reduction, and the ELP. Figure 5-6b, Figure 5-6c and Table 5-12b refer to the ultimate chord rotation and energy dissipation at the same damage state. An incremental loading pattern with 2 cycles per increment (ELP-2), is the ELP most frequently used. The number of tests with an incremental ELP with 4 or more cycles at each step are few (ELP-4,5). However, the number of tests with an ELP having a large number of cycles with constant amplitude is very large (ELP-8,9). The average energy dissipation and rotation increases, when the number of cycles per step is not more than 3 (ELP-1,2,3), however, the average is observed to drop when the number of cycles at each step is larger (ELP-4,5,8,9). It is difficult to assess or quantify the weighting of the number of cycles with constant amplitude to damage development, particularly if other cycles with different amplitudes are involved. It depends on whether the magnitude of the amplitude is close to the damage level

or not (Krawlinker *et al.*, 1997). Although, n_{cy} is considered as an explanatory variable upon which EDP are dependent, its significance may not be expected to be high due to this irrationality in the loading patterns for different tests. Hence the, energy dissipation (E) which is a function of both n_{cy} and the loading pattern may be expected to be a more successful representative parameter. Most of the tests have an ELP with a large n_{cy} , which can also be much larger than the response of an element in a structure during an earthquake. This is further discussed in Chapter 3.

On average, tests with incremental ELP increase the chord rotation and energy dissipation capacities as the number of cycles/step increases till 3 cycles/step (ELP-1,2,3). However this trend is not observed when the number of cycles/step gets larger (ELP4,5). Similarly, the average for ELP-8,9 is low as tests are characterised by a large number of intermediate cycles having an amplitude lower than the expected damage level. This decrease in the average may be due to the larger damage formation by more cycles at low amplitude as previously discussed. Tests with ELP-0 are characterised by few cycles with a large amplitude, hence the low n_{cy} , energy dissipation and chord rotation values. The magnitudes are therefore similar to the monotonic case ELP-7.

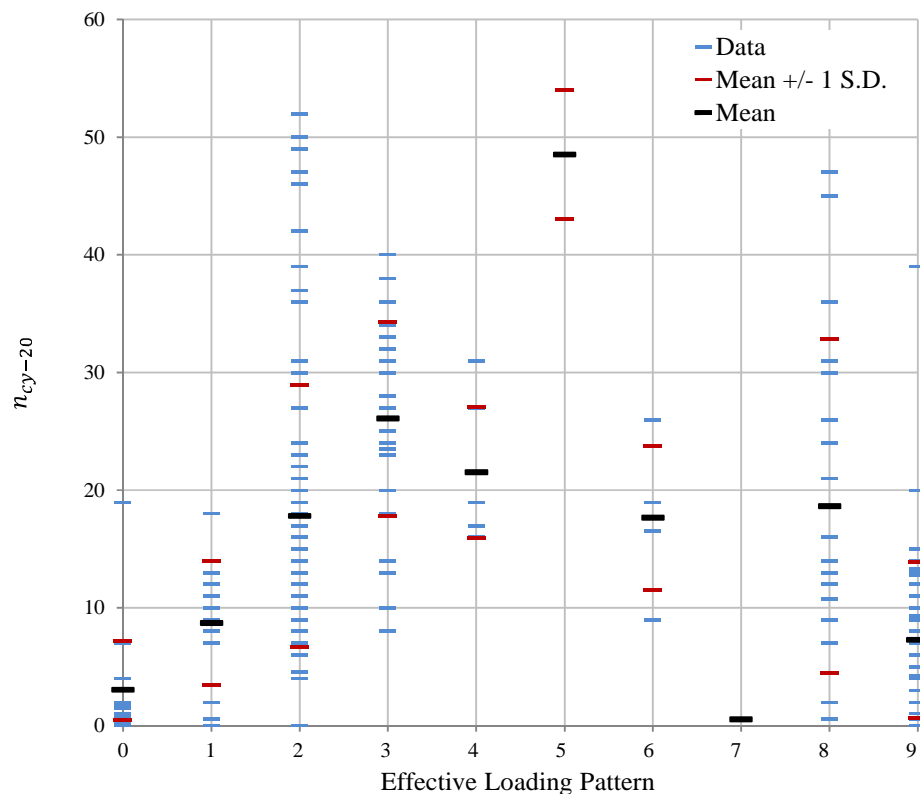


Figure 5-6a Distribution of effective inelastic cycles (n_{cy}) considering 20% maximum force reduction, for different effective load patterns.

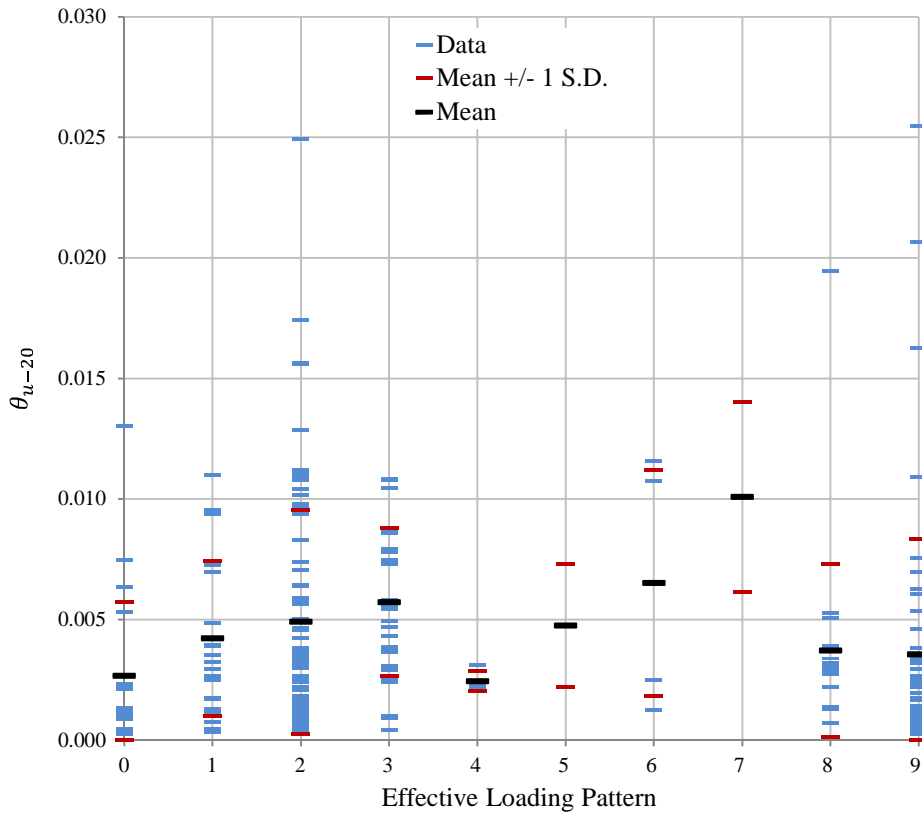


Figure 5-6b Distribution of chord rotation at 20% maximum force reduction (θ_{u-20}), for different effective load patterns.

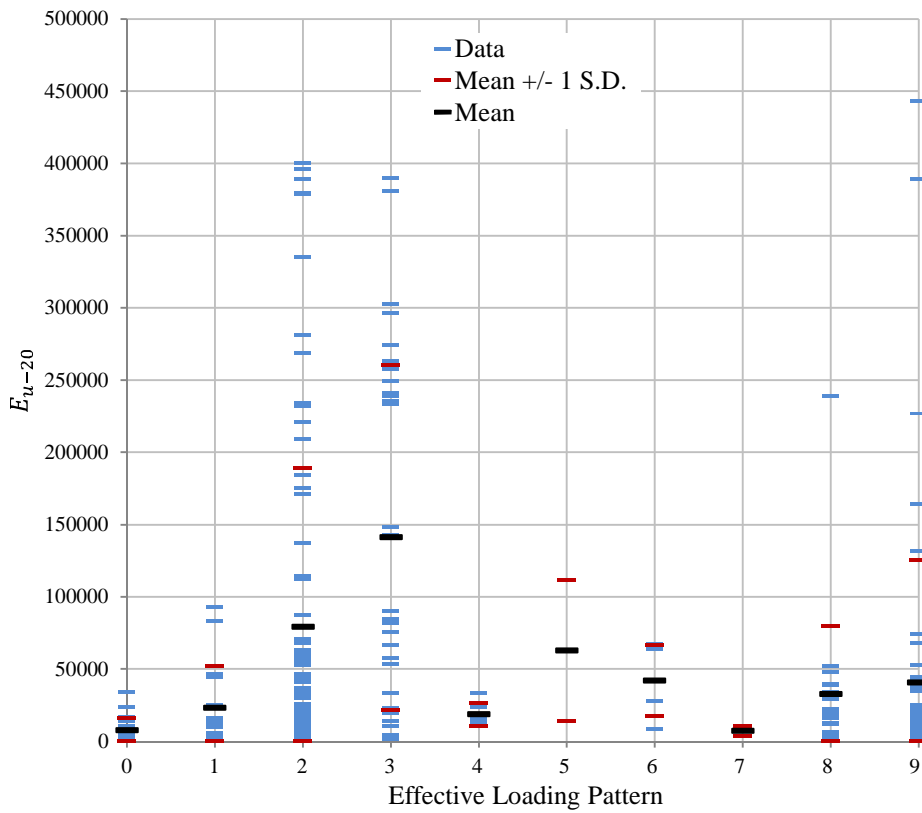


Figure 5-6c Distribution of energy dissipation at 20% maximum force reduction (E_{u-20}), for different effective load patterns.

Table 5-12a Summary of statistics for the distribution of the number of cycles at 20% maximum force reduction (n_{cy}), for different effective load patterns.

Effective Load Pattern	Description	Number of half-cycles between yield and 20% maximum force reduction [n_{cy-20}]				
		Max	Min	Mean	Median	SD
0	Incremental with large increments having 1 cycle/step.	19.0	0.5	3.0	2.0	4.1
1	Incremental with small increments having 1 cycle/step.	18.0	0.0	8.7	10.0	5.2
2	Incremental 2 cycles/step.	52.0	0.0	17.8	14.0	11.2
3	Incremental 3 cycles/step.	40.0	8.0	26.1	27.0	8.2
4	Incremental 4 cycles/step.	31.0	16.0	21.5	19.0	5.5
5	Incremental 5 cycles/step.	54.0	43.0	48.5	48.5	5.5
6	Incremental and unsymmetrical	26.0	9.0	17.6	17.8	6.1
7	Monotonic	0.5	0.5	0.5	0.5	0.5
8	Cycles with constant amplitude	47.0	0.5	18.6	14.5	14.2
9	Number of cycles with constant amplitude, and 1 cycle with larger amplitude to reach failure	39.0	0.5	7.3	7.0	6.6

Table 5-12b. Summary of statistics for the distribution of chord rotation (θ_{u-20}) and energy dissipation (E_{u-20}) at 20% maximum force reduction, for different effective load patterns.

Effective Load Pattern	Description	Chord Rotation at 20% maximum force reduction					Dissipated Energy at 20% maximum force reduction				
		[θ_{u-20}]					[E_{u-20} - kNm]				
		Max	Min	Mean	Median	SD	Max	Min	Mean	Median	SD
0	Incremental with large increments having 1 cycle/step.	0.0130	0.0003	0.0027	0.0013	0.0031	34096	183	7501	3636	8556
1	Incremental with small increments having 1 cycle/step.	0.0110	0.0003	0.0042	0.0034	0.0032	92673	418	23070	10751	28985
2	Incremental 2 cycles/step.	0.0249	0.0004	0.0049	0.0032	0.0047	400372	858	79213	32355	109781
3	Incremental 3 cycles/step.	0.0108	0.0004	0.0057	0.0054	0.0031	389422	1552	140937	90130	119523
4	Incremental 4 cycles/step.	0.0031	0.0021	0.0024	0.0022	0.0004	33345	10435	18586	15516	7791
5	Incremental 5 cycles/step.	0.0073	0.0022	0.0048	0.0048	0.0026	111549	13959	62754	62754	48795
6	Incremental and unsymmetrical	0.0116	0.0012	0.0065	0.0066	0.0047	67476	8511	41895	45796	24728
7	Monotonic	0.0140	0.0061	0.0101	0.0101	0.0039	10531	3676	7104	7104	3428
8	Cycles with constant amplitude	0.0195	0.0007	0.0037	0.0029	0.0036	238704	2262	32457	21313	47281
9	Number of cycles with constant amplitude, and 1 cycle with larger amplitude to reach failure.	0.0254	0.0003	0.0036	0.0022	0.0048	443205	343	40373	12546	85188

5.5.2 Failure mode

The data from the selected database is classified in terms of the three modes of failure as defined in Chapter 2. These include shear, shear-flexure and flexure. Figure 5-7 shows how the dissipated energy varies with chord rotation at 20% maximum force reduction. Trend lines representing failure modes show that the ratio is larger for specimens failing in flexure followed by shear-flexure and then shear. The number of test specimens where columns fail in shear and shear-flexure is very small to possibly develop regression models for each category. In order to reduce the bias in the regression process as a result of the classification due to failure mode, the categories referring to shear and shear-flexure failure are eliminated from the selected database.

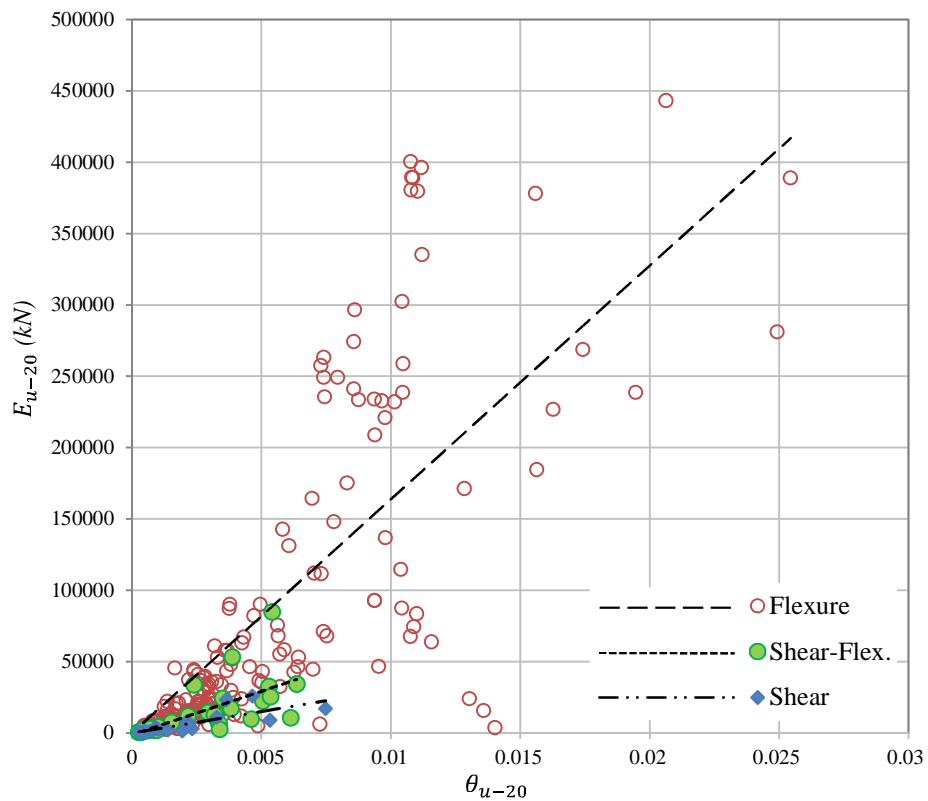
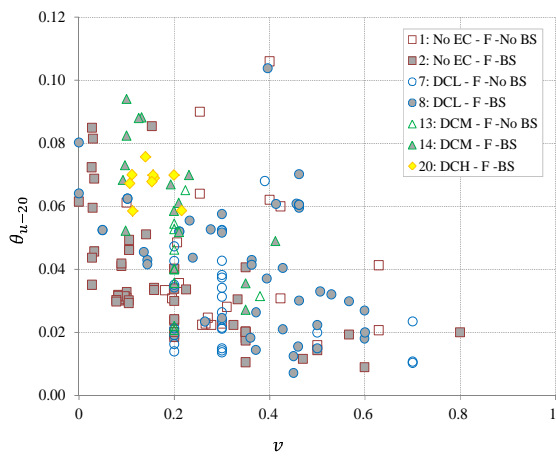


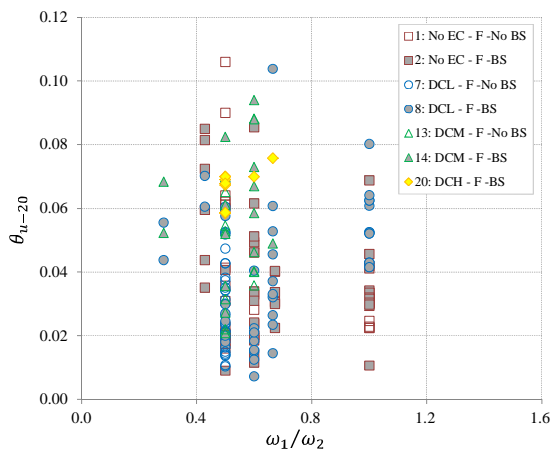
Figure 5-7 Scatter plot of dissipated energy against chord rotation at 20% maximum force reduction, distinguishing between failure in shear, shear-flexure and flexure.

5.5.3 Building Class

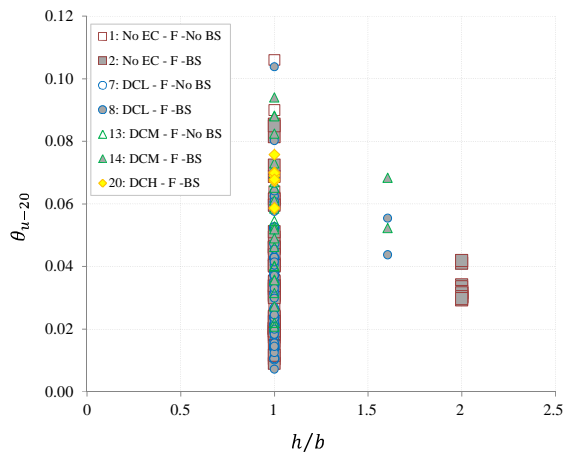
The data from the selected database, referring to flexural failure modes only, is classified in the building classes defined in EN1998-1-1(2004) and discussed in Chapter 2. The building classes include high ductility class (DCH), medium ductility class (DCM) and low ductility class (DCL). An additional class is added referring to elements whose properties fall below the lowest requirements for a DCL.



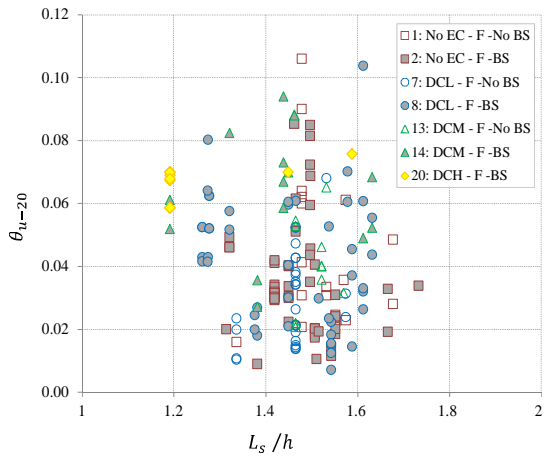
a



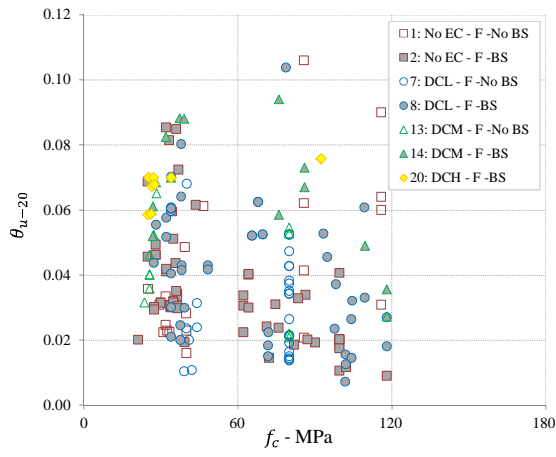
b



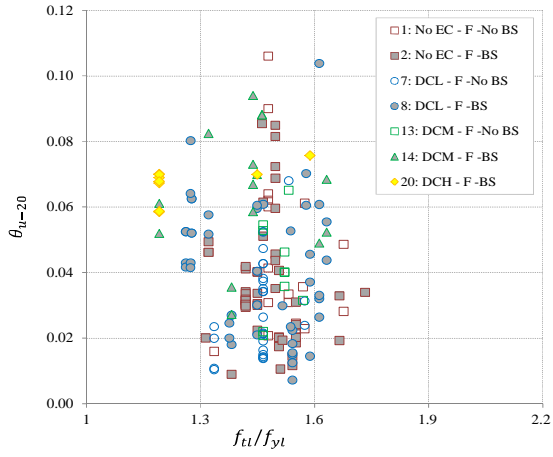
c



d



e



f

Continued...

...Continued

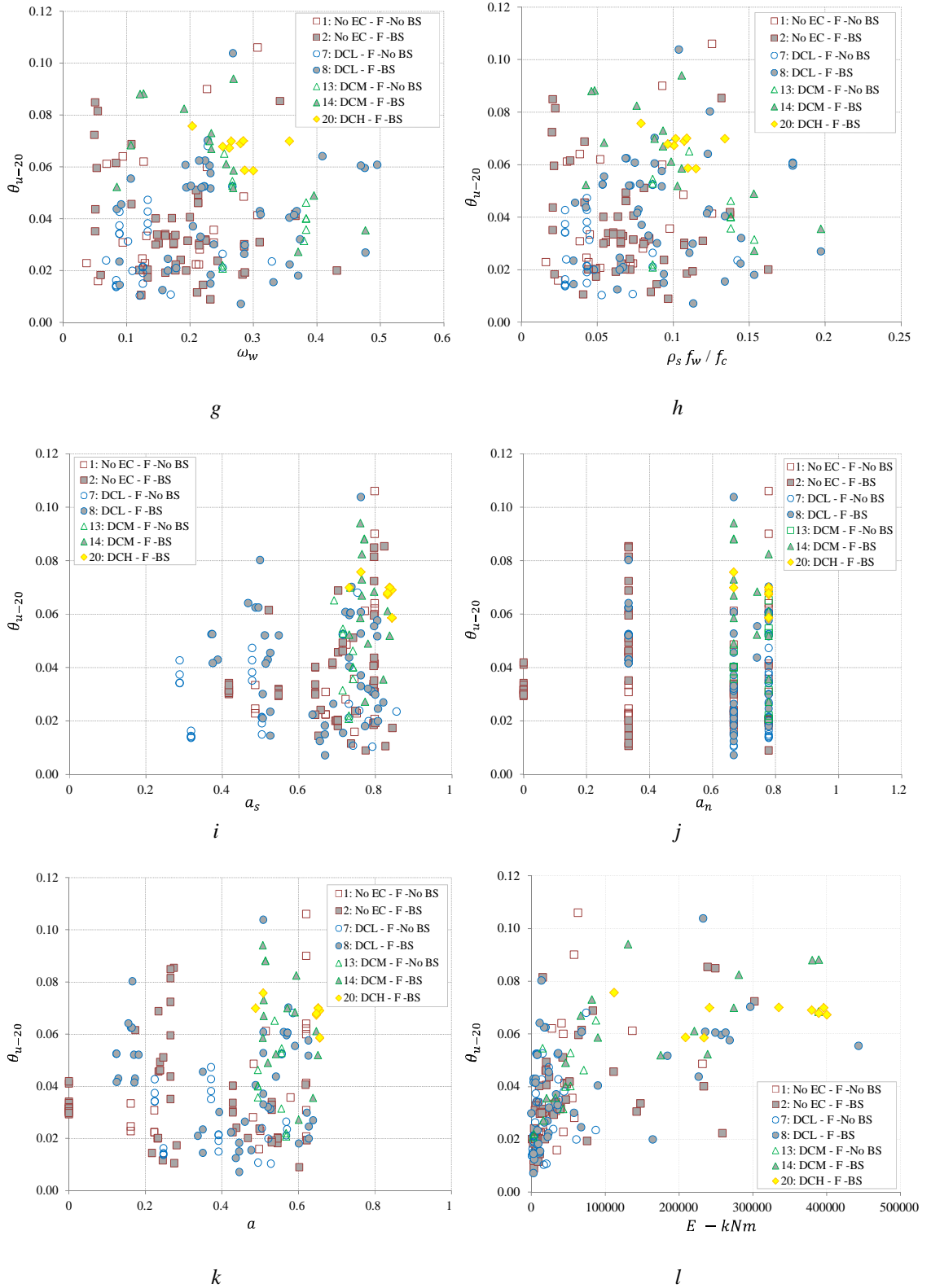


Figure 5-8 Scatter plots of chord rotation at 20% maximum force reduction against different explanatory variables. The data is separated in groups distinguishing between the different building class characteristics, and between the possibility of having considerable bond-slip.

The data was further classified on whether considerable bond-slip (BS) is expected or not (No BS). Figure 5-8 shows scatter plots of ultimate chord rotation at 20% maximum force reduction against explanatory variables in terms of geometric and material properties of the test specimens of the selected data base. Grouping and clustering of the data as a function of the four building classes is observed since building classes are defined in terms of the geometric and material properties.

The clusters are observed to overlap for all the properties investigated. This is so since each specimen is characterised by properties that fall within requirements of different building classes, and it is the lowest critical property that determines the class of the column specimen. For example, DCH specimen does not have the most conservative confinement properties. Other specimens with larger confinement properties are classified as DCM, DCL and even No EC since other properties mainly associated with longitudinal reinforcement ratio, concrete strength, and spacing of reinforcement are not characteristic with DCH. Similarly, specimens with the largest θ_{u-20} do not necessarily fall in the DCH class. Specimens may have a large θ_{u-20} but a lower ductility if the yield chord rotation (θ_y) is also relatively large (Fenwick *et al.*, 2007). For each building class considered with the exception of DCH where there is no bond-slip category, a trend was observed that the BS category has a larger θ_{u-20} than its corresponding No BS category within the same building class, on the same range of physical property. This is a case where a larger θ_{u-20} does not represent a larger capacity, but larger damage. For each building class, further segregation is also observed due to the inclusion or exclusion of considerable bond slip.

Segregation of data based on building class is also observed in scatter plots of dissipated energy against chord rotation at 20% maximum force reduction as shown in Figure 5-9. The mean trend lines representing each building category indicate that the E_{u-20}/θ_{u-20} ratio increases as the ductility class increases.

These clustering and grouping of data encourage the development of EDP models in terms of geometric and physical parameters that are specific for each building class. However, the size of the dataset available for most of the categories is too small to develop empirical models which are specific for different building classes. The grouping and clustering of data on building class, as a function of geometric and material properties, and EDPs is a source of error that will be reflected in the development of the regression models. The classifications on whether considerable bond-slip (BS) is expected or not (No BS) are considered to be included in the empirical models.

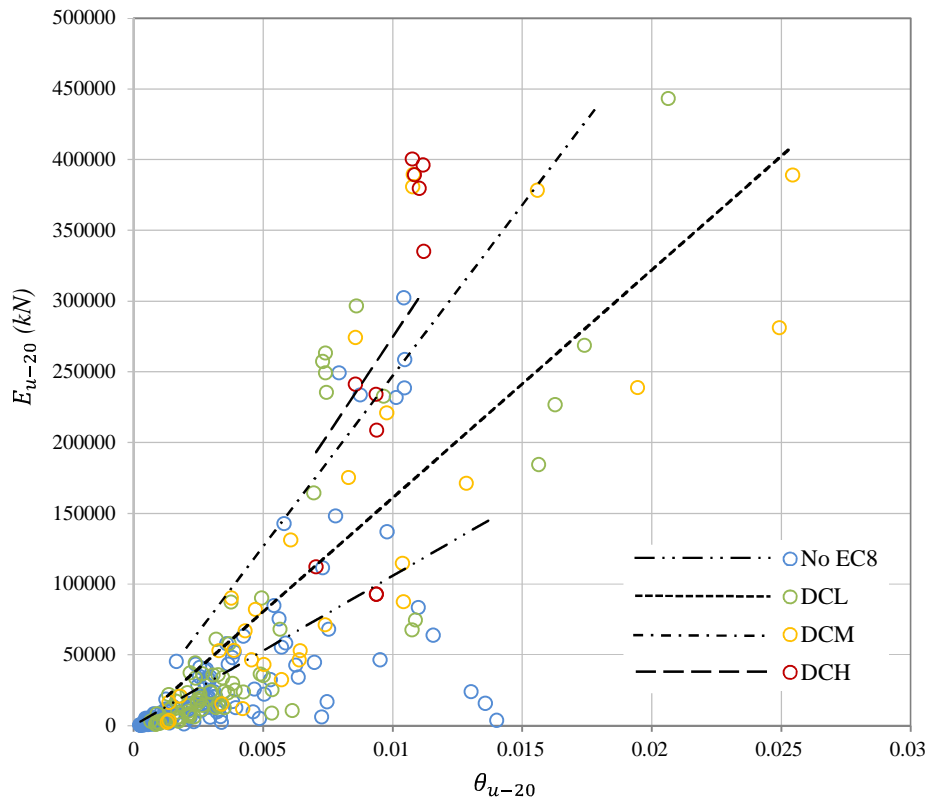


Figure 5-9 Scatter plot of dissipated energy against chord rotation at 20% maximum force reduction, distinguishing between different building classes.

5.6 Identification of trends

The variables considered in *Step 3* are based on trends that are reported by other authors in literature using data that is not necessarily similar to the data used in this research. The development of EDP models in terms of material, geometric and loading properties should be based on trends between EDPs and explanatory variables using the data available in the selected database (*Step 4-5*). As explained in *Steps 7-9* trends are identified by looking at scatter plots, data distribution, and correlation matrices. In order to understand the actual trend between an EDP and an explanatory variable, the influence of the other variables which are confounding has to be eliminated.

5.6.1 Correlation matrices

Spearman (1904) rank correlation coefficient (SRCC) is used to identify the correlation between EDP and explanatory variables, and among explanatory variables. Correlation matrices are computed in *R* (R Core Team, 2013) and *R Commander* (Fox, 2005). Observations are discussed in section 6.8. Since the data does not include missing values as this is accounted for in section 5.4.1, case-wise deletion is not required (R Core Team, 2013). Haselton, *et al.*, 2008, Biskinis *et al.*, 2010 and Berry *et al.*, 2003 observed that many EDPs have a non-linear relationship with various explanatory variables. Although more popular (Conover, 1999), Pearson (1895) correlation coefficient (PCC) was not considered to find the correlation between variables since

it is only sensitive to linear relationships. However, SRCC rank correlation coefficient has a reduced sensitivity towards extreme values compared with PCC since in the former outliers are limited to the value of the rank whereas in the latter, raw values are considered (Conover, 1999). The correlation between *log* transformation of the variables is also found in order to further reduce the possibility of overlooking of trends.

There are various rank correlation coefficients including Spearman (1904), Kendall (1970), and Goodman and Krustal (1972). The difference between each type of correlation lies in the computation of the statistic and the ranking system. The value of the rank may vary in magnitude depending on the type of correlation coefficient. This variation does not necessarily have any significance on the strength of the correlation. For example, SRCC tends to be larger than Kendall (1970) rank coefficient. However, as a test of significance, there is no strong reason to prefer one over the other (Conover, 1999). SRCC was preferred over other rank correlation coefficients since it is more convenient to implement in *R* (R Core Team, 2013) and *R Commander* (Fox, 2005) which are used to compute the correlation matrices.

Correlation coefficients vary between -1 and 1. A value of 1 or -1 is an indication of perfect correlation or perfect reverse correlation respectively. Correlation coefficients indicate the strength of a relationship between two variables, but its value does not necessarily characterize their relationship (Damghani *et al.*, 2013). The correlation coefficient for a very weak relationship is assumed to vary between absolute values 0-0.19, for a weak relationship between 0.2-0.39, for a moderate relationship between 0.40-0.59, for a strong relationship between 0.60-0.79 and for a very strong relationship between 0.8-1.00. This is based on rules of thumb followed in literature (Spiegel *et al.*, 2001; Damghani *et al.*, 2012). The limit in having an error by chance is assumed to be within 10% of the actual value (Harris *et al.*, 1999). A value larger than 10% is not considered by chance. A correlation is then assumed to be significant if the probability is less than 0.1 (Harris *et al.*, 1999).

The computation of SRCC is also used to indicate dependence based on the above categories if the value is larger than 0 (Spiegel *et al.*, 2001). However the dependence structure was not considered since this is not provided by SRCC (Damghani *et al.*, 2013). SRCC is used to check the classifications in *Step 3*, where the variables in the same group are expected to share high SRCC since they have similar physical meaning. However this information is used for indicative purposes since a correlation coefficient of 0 indicates that there is no definite correlation between the variables, but does not necessarily mean that the variables are independent (Damghani *et al.*, 2012; Dawid, 1979). For this reason, SRCC is also not used to select explanatory variables and is not used eliminate variables which are not observed to correlate with EDP.

SRCC is also considered with other limitations. Haselton *et al.*, 2008 shows how variables forming the regression model may have an influence on each other, and such influence can affect the resulting dependent EDP. Hence the obtained SRCC may underestimate the strength and significance of the correlation between the variables since SRCC does not eliminate the effect of the other variables (Conover, 1999). Partial correlation is a zero-order correlation measuring the degree of association between two variables with the effect of other controlling variables removed (Garson, 2012). Larger values of partial correlation coefficients between variables indicate that removing these variables results in a significant change in the relationship between the variables (Bailey, 1995). A lot of uncertainty is assumed with this process at this stage of analysis and model development. In practice, the determination of partial correlation coefficients involves fitting a regression model considering all the variables. The uncertainty is associated with the fact that at the stage the variables cannot be combined to form a correctly parameterised model. The estimated partial correlation coefficient may not necessarily represent realistic trends. Moreover, the reliability of partial correlation decreases as the number of variables increases (Bailey, (1995); Garson, 2012). Each of the models in literature provided by Rossetto *et al.*, 2002, Panagiotakos *et al.*, 2001, Berry *et al.*, 2003, and Haselton *et al.*, 2008 and Biskinis *et al.*, 2010 consisted in a large number of variables. The number of variable classifications in *Step 3* is also large and hence the expected reliability of partial correlation is expected to be low. Hence, for the purpose of this research, partial correlation is used in cases where the trend is not clear and Spearman (1904) correlation is interpreted with limited reservations.

5.6.2 Density distribution

The density distribution of variables is determined to indicate how the data is restricted within an interval. The size of the range of the interval affects the correlation and trend between random variables, and between the EDP and random variables (Nikolic *et al.*, 2012). Variables showing discontinuity or those which exhibit a considerable interval restriction are identified. The SRCC computed in section 5.6.1 involving these variables may be small not due to independence or lack of correlation, but due to insufficient representation of the population range. Such variables are therefore not eliminated at this stage and are marked for further evaluation at the regression analysis stage.

5.6.3 Scatter plots

The EDPs are plotted against variables identified in *Step 3* as scatter plots. These scatter plots are visually inspected to identify trends between the two. The major limitation of scatter plots is that they can obscure trends when multiple variables are changing between the different tests (Haselton *et al.*, 2008). The plot is characterized with a large scatter making it difficult to understand the direct trend between the EDP and the plotted variable. As a result, scatter plots show clear trends only when a few dominant variables affect the dependent variables. This is not the case when EDP is the dependent variable.

However, scatter plots are still useful. The determination of SRCC requires that trends follow a monotonic function (Damghani *et al.*, 2012). Whenever possible, scatter plots are used to inspect whether identified trends are monotonic or not. Anscombe *et al.*, 1973 shows that relationships between explanatory variables and dependent variables can have the same mean, variance, correlation coefficient and regression line and yet exhibit different distributions in the scatter plots that represent completely different trends. Hence, identified trends between EDPs and variables using SRCC are also checked that the trend is also represented visually in the scatter plot. In this way scatter plots are sometimes used to identify trends between EDP and variables that exhibit weak SRCC values.

Scatter plots of EDP and explanatory variables with data categorized as defined in *Step 6*, are used to investigate the effect of categorization on the trend. The segregation or grouping of categories of data forming independent trends is visually evaluated, and assessed to whether the incorporation of categories is required in the model build-up of the respective EDP.

5.6.4 Plots of single test series with only one variable changed

As discussed in section 5.6.1 and 5.6.3, both SRCC and scatter plots share the same limitation where in the direct investigation of a relationship between EDPs and variables, the effect of secondary variables is not eliminated. Except for the experimental campaign described in Chapter 3, it is very difficult to find experimental campaigns consisting in a large number of samples where a series of variables are varied in turn. Haselton *et al.*, 2008 suggests a procedure which eliminates the effect of secondary variables. This procedure is followed in order to check the trends already identified by SRCC and scatter plots, and identify direct trends between EDPs and variables that are overlooked by the other two processes. The advantage of this procedure over partial correlation is that trends can be visually inspected, and the trend does not depend on the parameterization of models at this stage which can be misleading.

The process is performed in *Matlab R2013* (Mathworks, 2013). In this process, for each variable X_n identified in Step 3, pairs of tests or test series where the only variable changed is X_n are defined. Plots of EDP against variable X_n are determined in turn, each plotting the graphs of the corresponding test series. Figure 6-11 shows an example of a possible plot, showing the trend between EDP and variable X_n . Further information on the relationship is obtained by looking at the rate of change of each test pair, which is equivalent to the slope of each line. For statistical significance of trends at 95% $p < 0.05$, hypothesis tests are computed to check whether the mean of the slope is non-zero (Haselton *et al.*, 2008). A non-zero second derivative indicates that the trend is variable, and does not reduce to a constant. This is checked using the same statistical criteria.

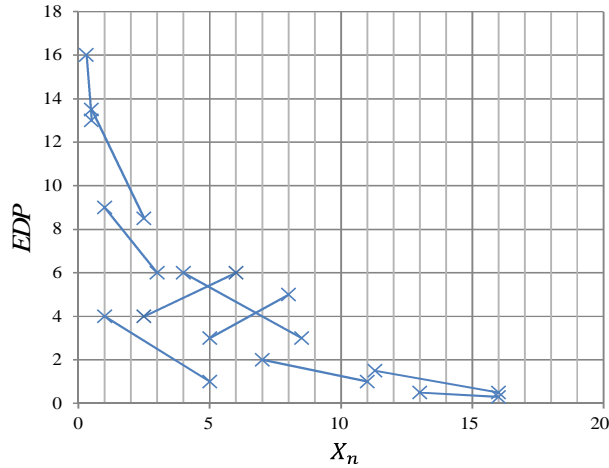


Figure 5-10 The plot shows the effects of variable X_n on EDP. Each line connects crosses corresponding to single test series in which X_n was the only variable changed.

5.7 The Regression Analysis Process and Associated Statistical Considerations

For the development of empirical models relating chord rotation, residual stiffness and dissipated energy, linear regression analysis is considered on logarithmic transformation of a general model discussed in section 5.8.1. The regression diagnostics and the procedure to remove outliers and extreme values of variables is discussed in this section. In order to develop empirical models relating chord rotation or stiffness ratio models in terms of material and geometric properties, a more rigorous procedure is followed.

5.7.1 General Requirements for the Regression Analysis Process

Regression analysis is required to quantify the best relationship between EDPs and the explanatory variables. Having the best relationship is quite subjective. Given a number of data, there will be an infinite number of models or hypothesis that fit the data equally well. Without making any further assumptions, there is no reason to prefer one hypothesis over the other (Sewell, 2008). Hence, one is forced to do assumptions providing an inductive bias. Box *et al.* (1987) consider that all models are wrong but some are useful, and the question is how wrong do they have to be in order not to be useful. The optimal model is determined by the best trade-off between the bias and the variance. This means trying to avoid high bias and low variance that would lead to under fitting, and avoid very low bias and high variance that would lead to overfitting (Alpaydin, 2010). Inducing the correct balance between bias and variance in order to have a reasonably useful model depends on various considerations.

Having a useful model depends on the type of regression analysis adopted which is associated with the nature of the dependent variable and type of data. The nature of the dependent variable then affects also the choice of the model form (Babyak, 2004). For a useful model, all the relevant

explanatory variables should be incorporated in the model, and the form should describe the relationship of the dependent and explanatory variables. The approach and form of model should account for the possibility that variables in isolation may behave differently with respect to the response variable when they are considered simultaneously (Babyak, 2004).

The form of the model is discussed in section 6.8.2 and various permutations and combinations of variables are identified in section 6.3 as possible alternatives that could form empirical models of EDPs at each damage state. The variables in each permutation are identified through their physical significance with respect to the EDP and by the support of identification of trends in section 6.6. The first consideration might be theoretically true but not represented as a trend by the data available. Little can be done to account for the effects of this consideration since the data is confined by what could be made available. In the second consideration, some of the trends identified are based on significance testing and do not ensure that the observed trend by the available data is not by chance as a result of data dredging (Alpaydin, 2010).

Each permutation consists in a considerable number of variables, and therefore involves a multivariable regression process. This can yield to a model which is characterised with overfitting. Overfitting is the result of having variables that describe the random error and noise instead of the relationship with the dependent variable. This is therefore further enhanced by variables which are included in the model as a result of data dredging. The possibility of overfitting is further enhanced since the ratio of variables in each permutation with respect to the number of records is very large. Overfitting results in a better goodness-of-fit, however it yields to overly optimistic model results that do not exist in the population and will therefore not replicate.

Various measures are therefore considered in order to reduce overfitting. The number of records per explanatory variable is kept above the threshold of 10-15 records per variables suggested by Green (1991). Apart from the selected database, the records for regression analysis are increased by conducting a relevant testing campaign. The testing specimens are designed to particularly cover ranges of variables which are underrepresented in literature. The testing campaign and corresponding results are further discussed in Chapter 4 and Chapter 5. Furthermore, regression analysis is performed on two sets of variables; one including all records of the selected but filtered database, and the other excluding extreme ranges where the variable is discontinuous or significantly underrepresented.

The use of combined variables also reduces overfitting (Babyak, 2004). Combined variables are therefore used by utilising variables that are already used in literature and describe a particular physical phenomenon significant to the EDP, and by using dimensional analysis (section 5.3.3) as an optimisation measure of the combination of variables. Moreover, the combined variables in each permutation are categorised as discussed in section 5.3.2, where each category represents a

particular phenomenon, and only one combined variable is selected from the category to feature in the model.

Overfitting is also controlled through the adoption of specific selection criteria. Model selection criterion has two main purposes. In the first, selection criteria is required so that the model includes only variables that are significant to the model for each respective permutation, and which is of optimal complexity for the given finite data (Sewell, 2008). Secondly the selection criteria is required to select a model, out of all the models corresponding to each permutation of possible variables. In both cases the selection criteria is required to keep balance between goodness-of-fit and parsimony such that overfitting is controlled. An adequate selection criterion also eliminates variables that are initially included in the model due to data dredging.

The multivariable selection process and the form of the model are therefore also required to allow the elimination or inclusion of suitable, conserving flexibility in having an optimal relationship representing the explanatory variables ultimately forming the model, and the EDP as the dependent variable. In order to develop a suitable regression procedure, different regression procedures and selection criteria are therefore considered.

Depending on the type of regression analysis chosen, regression assumptions are made. In order to have reliable and useful models, the diagnostics and the assumptions for the regression are required to be checked (Chatterjee, *et al.*, 2006).

5.7.2 Selection of Regression Analysis Process

There are various regression analysis processes in literature. Logistic regression considers that the dependent variable is a binary categorical variable. The model is built on the natural *log* of the odds by considering the probability of it being in a particular binary category (Chatterjee, *et al.*, 2006). Ordinal regression analysis is very similar to logistic regression, but considers the probability of odds in any particular category, rather than a particular one. Poisson's regression prevails when the dependent variable is discrete. Poisson's method assumes that the estimated mean and variances rates of the dependent variable are approximately equal. Negative binomial regression is a flexible extension of the Poisson regression allowing the mean and variance to differ (Chatterjee, *et al.*, 2006). These processes may not be optimal for the purpose of this research since the EDPs which are the dependent variables are continuous and not discrete variables, or binary categorical variables. However, they would have been more relevant if the damage level is based on the occurrence or not of damage phenomena discussed in Chapter 2.

Linear regression considers that the dependent variable is numerical, the explanatory variables are independent and the resulting residuals of the model are normally distributed with zero mean, standard deviation of 1 and constant variance (Chatterjee, *et al.*, 2006). In linear regression, the best estimates are determined when the sum of the squares of residuals e_i in equation 6.6, are

minimized. In equation 5.6, n refers to the number of records, y_i is an observed response corresponding to an input variable x_i and \hat{y}_i is the predicted response by the model.

$$e_i = (y_i - \hat{y}_i) \quad [5.6a]$$

$$SSE = \sum_{i=1}^n e_i^2 \quad [5.6b]$$

Non-linear regression is similar to linear regression, however considers that the relationship between the demand parameters and explanatory variables is non-linear with minimization of the residuals (Alpaydin, 2010). Generalised linear models (GLM) are an extension of linear models (McCullagh and Nelder, 1989). However, they are characterised by non-normal distribution and non-constant variance of the residuals. The regression process of GLM involves the internal transformation of the explanatory variables in exponential form in order to account for the non-linear relationship between the explanatory variables and the dependent variables.

These processes are widely used in determining empirical models of EDPs, and different authors in literature use different approaches. Panagiotakos *et al.*, 1999 and Haselton *et al.*, 2008 use linear regression on a logarithmically transformed general model. The explanatory variables originally composing the model are also preselected. Rossetto (1999) and Berry *et al.*, 2003 use non-linear regression analysis.

The regression process should also allow the selection process of the variables in each permutation through the chosen selection criterion in section 5.7.3. A more complete discussion on selection procedures is found in Alpaydin (2010), however, only possibly relevant procedures are discussed and presented here. Stepwise procedures are very popular in obtaining models by selecting the explanatory variables in the model by adding and removing them in turn. This can be done in various ways. In forward selection, regression analysis is performed on models by adding the variables in the permutation in turn until further addition does not decrease the error. The variable that reduces the error most is added each time (Efroymson, 1960). In backward selection, regression analysis is first performed on the model consisting in all the variables in the permutation. Then regression analysis is performed on models by removing each variable in turn until the error cannot substantially decrease any further. The variables that reduces the error most is removed each time (Efroymson, 1960). The backward-forward procedure is similar to the backward selection process. However, after the first variable exclusion, the variables are added and removed in turn. The variable that reduces the error most is added if it was previously removed, or removed if it is in the current iteration. Improvement on the error is checked through the selection criterion, or by satisfying hypothesis testing of p-value thresholds associated with the model or included variables.

In Haselton *et al.*, 2008, a stepwise procedure is used together with the linear regression process. Standard deviation is used to quantify the error. Explanatory variables that are statistically significant at 95% level using standard F-test are included in the final model in the stepwise selection process. However, Mark *et al.*, 2001 suggest that stepwise regression is not reliable when F-tests are used. In the EDP models by Panagiotakos *et al.*, 1999, Rossetto (1999), Berry *et al.*, 2003, Biskinis *et al.*, 2010a and Biskinis *et al.*, 2010b the model chosen a priori, is based on pilot models that refer to theory. However, once the general model is selected, no further elimination of variables is made.

Nevertheless, since various permutations of variables that can possibly describe EDPs are identified in section 5.3.2, relying on a priori model only is not ideal. EDP Backward selection is more conservative than forward selection (Alpaydin, 2010). Backward-forward selection has the advantage that it accounts for the possibilities that the model can still be improved by reinstatement of variables, and hence considers all true possibilities. A backward-forward stepwise procedure is therefore selected. Apart from reproducing the relationship of the variables in the model, the general model determined in section 5.8.1 is considered flexible to allow addition and removal of variables while conserving the true relationship between variables. Similar to Haselton *et al.*, 2008, linear regression is considered on the logarithmic transformation of the general model since it facilitates the stepwise process.

5.7.3 Criteria for Model Selection and Validation

There are various selection criteria in literature. The power of the criterion lies either in its ability to compare different models, or its ability to optimise the model (Babayak, 2003). A few popular methodologies will be discussed. Selection criteria can be divided into two main categories; empirical selection criteria and theoretical criteria (Sewell, 2008).

The most popular empirical criteria is the coefficient of determination R^2 which indicates the proportion of total variability in the response variable which is accounted for by the predictor variable (Chatterjee *et al.*, 2006; Moore *et al.*, 2009). The total sum of squares (SST) is given by equation 5.7a. The coefficient of determination is then given by equation 5.7b.

$$SST = \sum_{i=1}^n (y_i - \bar{y}_i)^2 \quad [5.7a]$$

$$R^2 = 1 - \frac{SSE}{SST} \quad [5.7b]$$

However, R^2 increases with the number of explanatory variables. The adjusted coefficient of determination R_a^2 after Wherry (1931) and given by equation 5.8 is generally preferred over R^2

since it weighs residuals as a function of the number of explanatory variables (k) and data-points (n) (Dziak *et al.*, 2012).

$$R_a^2 = 1 - (1 - R^2) \left(\frac{n - 1}{n - k - 1} \right) \quad [5.8]$$

The model with relatively largest R^2 or R_a^2 depending on which is being used, is supposed to have less uncertainty and better goodness-of-fit and is preferred over the other models. Although R_a^2 is more robust than R^2 , both measures of selection can yield to models characterised with overfitting since they don't employ parsimony characteristics (Alpaydin, 2010).

Cross validation methods are other empirical techniques. Models are evaluated by means of their forecasts where models are chosen with proper complexity (Hjorth, 1994). There are various cross validation methods and only few possible and relevant methods are discussed here. Test-set validation is generally conducted by either considering data from another database, or by first determine the models on most of the records, and then conduct the validation on the remaining records. In many cases in literature, as a rule-of-thumb 70% of the data is considered as the training set to develop the model and 30% of the data is left for the validation process (Geisser, 1975; Alpaydin, 2010). In K -fold cross-validation, the records are distributed at random into K partitions. Regression is performed on each partition. The validation is conducted by assessing the mean of the error of each regression corresponding to each partition (Stone, 1974). Leave-one-out cross-validation (LOOCV) in practice is similar to k -fold cross validation when the number of partitions is equivalent to the number of records. Shao, 1993 shows how LOOCV. In the process, each record is removed in turn from the dataset, and regression is conducted on the remaining records. The mean error can be used to compare the models (Moore *et al.*, 1994).

The test-set cross validation process is very simple. However, since the number of records in the selected database is particularly small, it can provide information on the variance that can be an unreliable estimate of future performance of the model (Alpaydin, 2010). In addition, it involves wasting a substantial amount of data from the regression analysis of the original model. In the LOOCV no records are wasted from the regression analysis process (Moore, 1994). However, it can lead to unclear observations (Alpaydin, 2010). In the K -fold process, the number of wasted records depends on the number of partitions. As the number of partitions increases, the number of training records increases, but the number of validation records decreases (Alpaydin, 2010). The computation of LOOCV and K -fold cross validation processes is not very quick, however various algorithms have been developed to optimise computation time with the error of the methodology (Moore *et al.*, 1994;). The success of the K -fold method lies in choosing an appropriate number of partitions. This is particularly relevant to cases where the number of records is small with respect to the number of variables as it could still lead to over-fitting.

Multiple runs of K -fold cross validation and use average over averages will lead to more reliable error estimates (Bouckaert, 2003).

Theoretical selection criteria include methods such as Akaike's Information Criterion (AIC) developed by Akaike (1973) and Bayesian Information Criteria (BIC) developed by Schwarz (1978) among others. A more exhaustive list is discussed in Burnham *et al.*, (2002). These approaches alternative to cross-validation, are based on regularization (Breiman, 1998). The error of the predicted dataset is considered to be made up of training error, and an optimization term which estimates the difference between the training and test error. AIC and BIC estimate the optimization which is added to the training error to give the test error without further need of validation (Alpaydin, 2010).

For the special case of least squares estimation with normally distributed errors Burnham *et al.*, (2002), AIC is expressed by equation 6.9. The first term is a measure of fit, while the second term is a penalty term. The parameter k refers to the number of explanatory variables in the model excluding the intercept, and n refers to the number of data. The lower the AIC the better the model. Burnham *et al.*, 2004 suggest that the AIC_c originally provided by Hurvich *et al.*, 1989, and reproduced here by equation 6.10 should be used instead of AIC as the penalty term is more rigorous when $n/k < 40$, but converges to AIC when the ratio increases. In the BIC reproduced here by equation 6.11, and originally derived by Schwarz (1978), the penalty term has a lognormal power and unlike AIC consists in both the number of variables k and the number of records n . In these selection criteria, optimization increases as the number of input variables, decreases as the number of records increases, and increases as the variance increases (Alpaydin, 2010).

$$AIC = n \ln \left(\frac{SSE}{n} \right) + 2(k + 1) \quad [5.9]$$

$$AIC_c = AIC + \frac{2 k (k + 1)}{n - k - 1} \quad [5.10]$$

$$BIC = n \ln \left(\frac{SSE}{n} \right) + (k + 1) \ln(n) \quad [5.11]$$

The Structural Risk Minimize (SRM) approach also forms part of the theoretical selection criteria methodologies, is based on Vapnik and Chervonenkis (1974). It describes a general model of capacity control and provides a trade-off between hypothesis space complexity known as the VC dimension of approximating functions, and the quality of fitting of the training data known as the empirical error (Alpaydin, 2010). In the process, based on a priori knowledge of the domain, a function is chosen together with neural network and splines having the same number of degrees, hidden layer neurons and rules respectively. The class of the function is increase into a hierarchy of nested subsets to increase the complexity. Parameters are selected when empirical risk

minimization is performed on each subset. The selected model has then the minimum sum of empirical risk and VC confidence dimension.

BIC is chosen as the selection criterion for the regression analysis process. There are big debates in literature on which is the better information criteria between AIC based and BIC in statistical theory. This goes beyond the scope of this research, however further discussion is found in Burnham *et al.*, 2004, Burnham *et al.*, 2002 and Dziak *et al.*, 2012. What is relevant is that BIC tends underfit the model, while AIC to overfit the model, particularly when the relative number of variables is low for the former, and high for the latter (Dziak *et al.*, 2012). It is difficult to identify where the cut-off number of variables lie. Stepwise regression as a procedure tends to overfit models (Mark *et al.*, 2001) and hence the criterion with stronger parsimony characteristics is preferred. Moreover, on conducting trial regressions on some permutations, it is observed that the ratio n/k is beyond the limits suggested by Green *et al.*, 1991 when AIC, while well within the limit when BIC is used. Selection criteria based on SRM is widely conservative (Alpaydin, 2010). Moreover, while AIC is considered asymptotically equivalent to LOOCV (Stone, 1977; Shao, 1993), K -Fold cross-validation is considered asymptotically equivalent to BIC, when an optimal value of K is considered (Shao, 1997).

5.7.4 Regression Diagnostics

Since linear regression analysis is used, the assumptions of having normally distributed residuals around zero and constant variance of the predicted values are checked for each model. Diagnostic plots are used to check these assumptions in various ways (Norusis, 2008). In scatter plots of residuals against fitted values and in square root of residuals against fitted values, data-points are checked to be randomly distributed around a horizontal line, with no distinct trend in the distribution of the points. In scatter plots of residuals against fitted values the line is checked to represent a residual mean of zero. Standardized residuals give a more meaningful representation than ordinary residuals since in the former, residuals are normalised by their standard deviation, and hence the residual is centred and scaled. Since the distribution of the residuals is normal and not uniform, then the distribution in scale-location and residual-fitted plots is also not uniform. The edges are characterised with a lower density distribution, and an offset of the mean residual trend, is possible by chance (Gibbon *et al.*, 2003). The line in a scale-location plot may not be perfectly horizontal but varies in a limited range of square-root standardized residual since this is very much more sensitive. Additionally, constant variance is checked by conducting the Breusch-Pagan test (Breusch *et al.* 1979) for each model. In the process, a linear model fits the residuals, and a null hypothesis H_0 : non-constant variance (heteroscedasticity) is rejected if $p > 0.05$.

Q-Q plots are used to evaluate the assumption of having normally distributed residuals in a least-squares regression linear regression. Q-Q plots are constructed from distributions, hence the shape of the Q-Q plot is a function of distributions (Gibbon *et al.*, 2003; Norusis, 2008). In Q-Q plots,

standardised residuals are used and for a linear model to hold their distribution is expected to have a 0 mean and standard deviation of 1. In order for this consideration to hold, 95% of the standardized residuals are checked to fall between ± 2 . If more residuals fall outside this range, then unusual circumstances are considered to govern the regression analysis, which are not desired. However, 5% of the residuals can be expected to fall outside this region by chance (Norusis, 2008). This is particularly so since Q-Q plots are very sensitive to differences in the tails (Gibbon *et al.*, 2003).

The type of divergence of the tails from a straight line in a Q-Q plot is used to further understand the nature of the distribution (Thode, 2002). The distribution of residuals is considered to be characterised with heavy tails (leptokurtosis) if tails of Q-Q plots are twisted anti-clockwise. If the tails of a Q-Q plot are twisted clockwise, then the distribution of residuals is characterised with very light tails. If the right tail of a Q-Q plot twists anti-clockwise and the left tail twists clockwise, then the distribution of the residuals is considered to be skewed to the right. If the left tail of a Q-Q plot twists anti-clockwise, and the right tail twists clockwise, then the distribution of the residuals is considered skewed to the left (Thode, 2002). If the divergence of tails of Q-Q plots is starts close to the ± 2 mark, then no further consideration is considered. However, if this starts before, then Shapiro-Wilk test for normality (Shapiro *et al.*, 1965) is performed on the distribution of the residuals to test the null hypothesis H_0 : the residuals are normally distributed if p-value > 0.05 .

5.7.5 Removal of outliers and Extreme Values of Variables

Outliers are observations that are considerably distant from other peers (Grubbs, 1969). Since the number of data-points in the sample is not large, the associated impact of each data-point on the outcome of the model is large. The removal of data-points as outliers is therefore done with caution. For the purpose of this analysis, outliers are considered for removal if they have a considerable effect on the outcome of the model, and after evaluating that its condition is not associated with inappropriate modelling aspects within the range of interest.

There is no exact definition of what determines and constitutes an outlier, and various authors use different approaches to identify outliers. In order to identify outliers, Haselton *et al.*, 2008 uses a t-test to statistically determine whether each residual had the same variance as the other residuals. Outliers are removed when the significance level is less than 5%. This means that the number of outliers removed is less than 10 or 4% of the data. Although errors of models are reported with and without outliers, no evidence is given on how the removal of the outliers affects the model, the actual selection of the explanatory variables through the stepwise regression technique, and the associated revised value of the coefficients.

Outliers are sometimes defined as data for which associated residuals are located more than m standard deviations away from their mean \bar{e} . Charvet *et al.*, 2013 considers $m = 2.5$. According to the empirical rule there will be a number of observations that differ by m standard deviations from the mean. The number of observations beyond the threshold m standard deviations increases with the number of observations and decreases as m increases (Ruan *et al.*, 2005). This procedure will therefore always identify outliers. However, these outliers may not necessarily have a considerable impact on the regression results, particularly if the leverage is very low. Their removal will then be undesirable since the uncertainty increases as the sample size decreases unnecessarily. The procedure based on the distribution of residuals overlooks outliers that have a moderate magnitude and large leverage. Such data-points may have a considerable impact on the outcome of the model.

For the purpose of this research, plots of standardised residuals against leverage are used to identify outliers. The criteria to identify outliers are then based on Cook's distance (Cook, 1977) which is defined by equation 5.12.

$$D_i = \frac{n \sum_{j=1}^n [\hat{y}_j - \hat{y}_j(i)]^2}{(k + 1)SSE} \quad [5.12]$$

Cook's distance (D_i) is a measure of influence of an observation on the regression model, and quantifies the effect of deleting each observation in turn from the dataset in the least-squares regression process. Using the Cook's distance to identify outliers does not involve any test. It involves a cut-off limit of D_i beyond which data-points are assumed to have particular impact on the accuracy of the regression. However this limit can be subjective. Cook *et al.*, 1982 consider $D_i \geq 1$, while Bollen *et al.*, 1990 suggest $D_i \geq 4/n$. The latter indicates that the cut-off limit is a function of the number of data-points n . The number of explanatory variables influences the goodness of fit. The cut-off limit is therefore considered as a function of k as $D_i \geq 4/[n - (k + 1)]$ (Fox, 1997). The latter is considered for the purpose of this analysis.

On conducting trial regression analysis of various models, it is observed that outliers referred to extreme variables of particular variables, particularly when the distribution of the variables is characterised by heavy tails. Moreover, some values are also observed to create discontinuity with the rest of the data as observed in Appendix A. Residuals of these extreme values are also observed to be extremes that have a large weight in satisfying limits of the regression criteria. The ranges covered by these extreme variables are underrepresented but pose a large influence the model outcome. Two sets of models are therefore considered for stiffness ratio, and for chord rotation in terms of residual stiffness and energy dissipation. One set of models is based on the database that includes all filtered data, and the other set of models is based on data that includes an interval where 47.5% of the data on either side of the mean of each relevant variable is

considered. Since various options of chord rotation are considered in terms of material and geometric properties, only the reduced set is considered.

5.7.6 Statistics for the Comparison of Models

Comparison of the selected empirical models is made through the statistical assessment of the relationship between experimental and corresponding predicted outcome of each model. Since models are used in the non-logarithmic transformation, the statistical comparisons are also made in the non-logarithmic format. The fitted mean, coefficient of variation (CoV), mean, median, standard deviation (SD) and 95% confidence intervals of ratio of the experimental EDP against predicted EDP are used to compare the models. These are based on the same statistical functions used by Rossetto *et al.*, 2002, Panagiotakos *et al.*, 1998, Berry *et al.*, 2003, Haselton *et al.*, 2008, Biskinis *et al.*, 2010a and Biskinis *et al.*, 2010b to compare the models determined in their respective research.

Biskinis *et al.*, 2010a and Biskinis *et al.*, 2010b identify 5% fractile factors as lower-bound limit that can be multiplied to the model. These factors indicate that 5% of the predicted EDP values corresponding with the experimental EDP values, do not fall below that limit. The 5% fractile is considered for all the models structure to estimate loading, then a lower stiffness may not necessarily produce a conservative estimate (Priestley *et al.*, 2003; Priestley, *et al.*, 2007). In this case, the application of the 5% fractile factor is not conservative. As a result for stiffness ratio models and models relating different EDPs including stiffness, a 95% fractile factor is also considered as an upper-bound. This indicates that 95% of the predicted EDP values that corresponds with the experimental EDP values do falls beyond that limit. This limit ensures that high stiffness is conservatively considered where necessary. The larger the 5% fractile factors, and the lower the 95% fractile values, the less is the scatter of the model.

The coefficients of the variables are rounded off to the nearest significant figure such that the mean, median, SD, 5% fractile factor and 95% fractile factor remain unchanged to the nearest ± 0.01 , and the CoV remains unchanged to the nearest $\pm 0.1\%$.

5.7.7 Summary of the Regression Analysis Procedure

The backward-forward stepwise linear regression procedure and the selection of the model is conducted in *R* (R Core Team, 2013), *R Commander* (Fox, 2005) and *Matlab R2013* (Mathworks, 2013) using in built routines and specifically developed algorithms. The algorithm to select an empirical model of chord rotation or stiffness ratio at any damage state in terms of material and geometric properties, is done on data that includes or excludes outliers and extreme values of variables separately. It consists in the following steps:

1. A multi-variable backward-forward stepwise regression is performed for each permutation consisting of possible explanatory variables identified in section 6.3 and corresponding with the EDP. The following steps are followed:
 - a. Assume a model that includes all the explanatory variables of the permutation, based on the general form discussed in section 6.8. The variables are considered in the logarithmic form that best describes the individual relationship between the EDP and each explanatory variable as discussed in section 6.8.
 - b. Multiple linear regression analysis is performed on the assumed model, and a model is fitted. The associated BIC value and the diagnostics of the residuals are identified.
 - c. The explanatory variables are then removed and added in turn, both individually or in groups. Until no further effective reduction of BIC results.
 - d. The model combination of variables that provide the least BIC value is selected as the model representing the permutation.
 - e. The diagnostics of the selected model are checked to satisfy linear regression criteria. The residuals are checked to be homoscedastic, and normally distributed around zero mean and standard deviation of 1. If these criteria are not satisfied, then steps (d) and (e) are repeated considering the model with the next least BIC value in (d).
2. The BIC of each model associated with each permutation of explanatory variables are compared. The model characterised with the lowest BIC criteria is selected as the ultimate empirical model that defines the particular EDP at the particular state of damage being investigated.
3. The model is back-transformed in the non-logarithmic format, and the mean, median, standard deviation, CoV and fractile quantities for the experiment-to-predicted ratio is identified.
4. The relationship of EDPs with explanatory variables featuring in the model is checked for consistency with the trends that are individually observed in section 6.6.

5.8 Form of the regression model

General model forms are considered separately for models relating EDPs, and EDP models in terms of material, geometric and loading properties.

5.8.1 Form of the model relating different EDPs

Two general model forms are considered for the regression analysis relating chord rotation, energy dissipation and residual stiffness. The first model in equation 5.13a is based on EDPs only, while the second model in equation 5.13b is based on dimensional analysis as discussed in section 5.3.3.

$$\theta_{u-dmg} = A \frac{E_{u-dmg}^B}{K_{u-dmg}^C} \quad [5.13a]$$

$$\theta_{u-dmg} = A \left(\frac{E_{u-dmg}}{K_{u-dmg} L_s^2} \right)^B \quad [5.13b]$$

Regression analysis is conducted on the corresponding logarithmically transformed models in linear format. Equation 5.13a and equation 5.13b are the corresponding transformed general equations of equation 5.14a and equation 5.14b.

$$\log[\theta_{u-dmg}] = \log[A] + B \cdot \log[E_{u-dmg}] - C \cdot \log[K_{u-dmg}] \quad [5.14a]$$

$$\log[\theta_{u-dmg}] = \log[A] + B \cdot \log \left[\frac{E_{u-dmg}}{K_{u-dmg} L_s^2} \right] \quad [5.14b]$$

Equation 5.15 denotes the set of damage states (dmg) for which the general models are considered.

$$dmg = \{ m, u - 10, u - 20, u - 50 \} \quad [5.15]$$

Backward transformation into the required original model forms is conducted after the regression analysis and correspondonding statistical considerations.

5.8.2 Form of the Model Relating Chord Rotation or Stiffness Ratio with Material and Physical Properties

The form of the general model used in the regression analysis relating EDPs as demand variables (Z_{dmg}) with material, geometric and loading properties as explanatory variables (X_n) is represented by equation 5.16.

$$Z_{dmg} = \left[\begin{pmatrix} X_a^{A_o} \\ or \\ A^{X_a} \end{pmatrix} \begin{pmatrix} X_b^{B_o} \\ or \\ B^{X_b} \end{pmatrix} \begin{pmatrix} X_c^{C_o} \\ or \\ C^{X_c} \end{pmatrix} \dots \begin{pmatrix} X_\psi^{\Psi_o} \\ or \\ \Psi^{X_\psi} \end{pmatrix} \right]^{a_{sl}} I \begin{pmatrix} X_1^{A_\omega} \\ or \\ A^{X_1} \end{pmatrix} \begin{pmatrix} X_2^{B_\omega} \\ or \\ B^{X_2} \end{pmatrix} \begin{pmatrix} X_3^{C_\omega} \\ or \\ C^{X_3} \end{pmatrix} \dots \begin{pmatrix} X_N^{\Psi_\omega} \\ or \\ \Psi^{X_N} \end{pmatrix} \quad [5.16]$$

Equation 5.17 denotes the set of corresponding EDPs as demand variables. I is the error term.

$$Z_{dmg} = \left\{ \theta_{dmg}, \frac{EI_{dmg}}{EI_g} \right\} \quad [5.17]$$

The form of the model is universal to the various damage states (dmg) identified in Chapter 2. Equation 5.18 represents the set of the considered damage states.

$$dmg = \{ Y, m, u - 10, u - 20, u - 50 \} \quad [5.18]$$

The model consists in ψ different physical properties that are represented by explanatory variables X_n each having a distinguished physical meaning. This set of explanatory variables is given by equation 5.19.

$$X_n = \{X_a, X_b, X_c, \dots, X_\psi\} \quad [5.19]$$

The explanatory variables are considered alone, and with interaction term a_{sl} as requested in section 5.5.3. This accounts for the possibility of considerable bond-slip due to detailing and anchorage configuration aspects, and the associated contribution of the other variables which also affect bond-slip. Equation 5.20 shows the binary representation of a_{sl} where 1 denotes the presence and 0 the absence of this phenomenon. This notation is similar to that utilised by Biskinis *et al.*, 2010, Panagiotakos *et al.*, 2001 and Haselton *et al.*, 2008.

$$a_{sl} = \{0,1\} \quad [5.20]$$

The set of corresponding regression coefficients is given by equation 5.21, where P_o denotes the set of coefficients for explanatory variables with the interaction of the general bond-slip parameter a_{sl} , while P_ω denotes the set of coefficients for explanatory variables without the interaction of terms.

$$P = \left\{ \begin{array}{l} P_o = \{A_o, B_o, C_o, \dots, \Psi_o\} \\ P_\omega = \{A_\omega, B_\omega, C_\omega, \dots, \Psi_\omega\} \end{array} \right\} \quad [5.21]$$

The form of the general model is such that it allows the representation of individual trends between EDPs (Z_{dmg}) and explanatory variables (X_n) observed in section 5.3, whilst their combination allows multiple regression analysis. Since equation 6.16 has a non-linear form, it is transformed into an equivalent linear form for multiple regression analysis using logarithmic transformation, as represented by equation 5.22. I' is the error term.

$$Z'_{dmg} = a_{sl}(A'_o X'_a + B'_o X'_b + \dots + \Psi'_o X'_\psi) + (A'_\omega X'_a + B'_\omega X'_b + \dots + \Psi'_\omega X'_\psi) + I' \quad [5.22]$$

Equation 5.23 represents the set of transformed explanatory variables that represent the ψ physical properties that characterise the dependent parameter.

$$X'_n = \{X'_a, X'_b, X'_c, \dots, X'_\psi\} \quad [5.23]$$

Equation 5.24 represents the corresponding coefficients. P'_o denotes the set of transformed coefficients for explanatory variables with the interaction of the general bond-slip parameter a_{sl} , while P'_ω denotes the set of transformed coefficients for explanatory variables without the interaction of terms.

$$P' = \left\{ \begin{array}{l} P'_o = \{A'_o, B'_o, C'_o, \dots, \Psi'_o\} \\ P'_\omega = \{A'_\omega, B'_\omega, C'_\omega, \dots, \Psi'_\omega\} \end{array} \right\} \quad [5.24]$$

Depending on the individual trend between the EDPs and explanatory variables, the latter can either be the base or the exponents of the coefficients. Figure 5-11 categorises the possible relationships between EDPs and explanatory variables and illustrates the corresponding individual transformations as used in equation 5.22. An initial guess of either position is based on the investigation on the trend between variables conducted in section 5.6 and Appendix G. Both positions are considered for initial trials of the model. However, the observed trend in the initial investigation and the ultimate trend of the variable in the model are checked for consistency according to the categories in Figure 5-11.

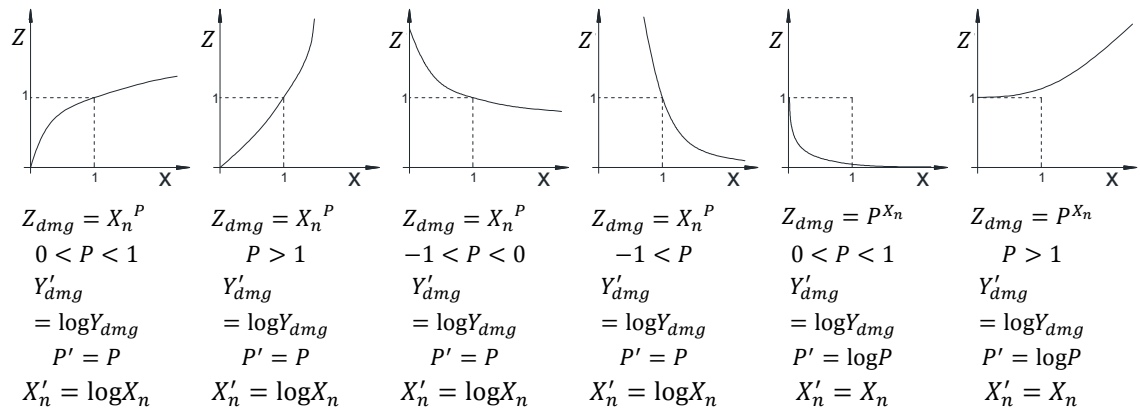


Figure 5-11. The permutations of possible non-linear trends between EDPs (Z_{dmg}) and explanatory variables (X_n) and corresponding linear conversion using logarithmic transformation.

As discussed in section 5.3 and Chapter 2, there are various combinations of individual base variables that form explanatory variables X_n that can describe the same physical property. These combinations vary differently for each of the three cases of regression relationships of EDPs highlighted in section 5.2, and hence are considered separately. The number of possible models for each case scenario is defined by equation 5.25.

$$m = \{1, 2, 3, \dots, \Gamma\} \quad [5.25]$$

In the first case where the determination of empirical relationships of EDPs is based on all types of explanatory variables excluding an energy dissipation term, the model combinations is based on Table 5-1 and Table 5-2. In the second case where the determination of EDPs is based on explanatory variables determined from dimensional analysis, reference to section 5.3.3 is made. The explanatory variables X_n that are used to form regression models are the row combinations of independent Π -groups of Table 5-3 to Table 5-5. In the third case the determination of empirical relationships of EDPs is based on dimensional analysis and includes an energy dissipation term refers to θ_{dmg} where $dmg = \{m, u - 10, u - 20, u - 50\}$. Permutations of models determined from Table 6-4 to Table 6-6 are combined with the explanatory variable ($X_m = \{[E/(bhsf'_c)], [E/(bhsf_{yl})]\}$) representing energy dissipation where either terms of X_m are considered in turn. For

the first and second case, explanatory variables from the same column do not feature in the same model. Table 6-13 provides different model configurations of Z'_{dmg} for each damage state.

Based on the possible permutations from Table 5-2, the number of models for the first case is $m=2240$ for $dmg = \{m, u - 10, u - 20, u - 50\}$. Based on the permutations of Table 5-1 the number of models for $dmg = \{Y\}$ is $m=48$ for $dmg = \{Y\}$. In the second case, $m=4$ for each of θ_Y and EI_Y/EI_g . For each EDP θ_{dmg} and EI_{dmg}/EI_g and for each damage state $dmg = \{m, u - 10, u - 20, u - 50\}$ the number of model permutations is $m=22$. The number of model permutations for the third case, is double that of the first case for each respective damage state.

Regression analysis is performed on the logarithmically transformed model combinations separately. Statistical criteria discussed in section 5.7.3 is used to select a single model in logarithmic form that best describes the EDP at each damage level, and for each case in turn. The selected models are then backward transformed into the model form of equation 5.16.

Table 5-13 Logarithmic transformation of for the m number of permutations of explanatory variables that can possibly form the empirical model of the EDP (Z_{dmg}) at the relevant damage state.

m	Model Configuration
1	$Z'_{dmg_1} = a_{sl} (A'_{o_1} X'_{a_1} + B'_{o_1} X'_{b_1} + \dots + \Psi'_{o_1} X'_{\psi_1}) + (A'_{\omega_1} X'_{a_1} + B'_{\omega_1} X'_{b_1} + \dots + \Psi'_{\omega_1} X'_{\psi_1}) + I'_1$
2	$Z'_{dmg_2} = a_{sl} (A'_{o_2} X'_{a_2} + B'_{o_2} X'_{b_2} + \dots + \Psi'_{o_2} X'_{\psi_2}) + (A'_{\omega_2} X'_{a_2} + B'_{\omega_2} X'_{b_2} + \dots + \Psi'_{\omega_2} X'_{\psi_2}) + I'_2$
3	$Z'_{dmg_3} = a_{sl} (A'_{o_3} X'_{a_3} + B'_{o_3} X'_{b_3} + \dots + \Psi'_{o_3} X'_{\psi_3}) + (A'_{\omega_3} X'_{a_3} + B'_{\omega_3} X'_{b_3} + \dots + \Psi'_{\omega_3} X'_{\psi_3}) + I'_3$
⋮	⋮
Γ	$Z'_{dmg_\Gamma} = a_{sl} (A'_{o_\Gamma} X'_{a_\Gamma} + B'_{o_\Gamma} X'_{b_\Gamma} + \dots + \Psi'_{o_\Gamma} X'_{\psi_\Gamma}) + (A'_{\omega_\Gamma} X'_{a_\Gamma} + B'_{\omega_\Gamma} X'_{b_\Gamma} + \dots + \Psi'_{\omega_\Gamma} X'_{\psi_\Gamma}) + I'_\Gamma$

5.9 General Conclusions and Requirement

In this chapter, a methodology to determine empirical relationships of EDPs is presented, taking into account requirements discussed mainly in Chapter 1 and Chapter 2. This is done through statistical techniques which account for models that define chord rotation and stiffness at various damage levels in terms of material and geometric properties, and models that relate the different EDPs.

Linear regression analysis on model formations transformed in log form are considered, but adhering with the assumption homoscedasticity and linear distribution of errors around 1 are observed. As observed in Chapter 2 and Chapter 3, a large number of variables are used to describe the deformation of RC elements, and some parameters describe deformation through different phenomena. Hence, variables are required to be categorised first in terms of phenomena that are responsible for deformation, then combined to form optimal explanatory variables that can be used in models through optimization approaches and selection criteria. Categorization is considered for confinement considerations, buckling, concrete and longitudinal reinforcement strength, geometric aspect ratios and axial force. From all the variables identified in Chapter 2 and 3, only those which are considered effective in literature and could actually be measured were considered. Variables such as carbon content in steel were ignored. Other aspects such as building class were considered. Although clustering of data is observed for each building class, the number of records available to develop models based on this consideration was not enough, and hence was not considered further. Energy dissipation is identified as a variable that is a function of the loading protocol and also affects the chord rotation. In existing EDP relationships discussed in Chapter 2 the variation of explanatory variables in the presence or absence of considerable bond-slip is expressed in terms of a constant. However, in section 2.2.4 it is observed that each explanatory variable have different effects on bond slip. Hence, the general model considered allows each variable to be considered independently in the presence or absence of bond-slip.

In order to determine an optimal form of combinations of variables that form explanatory variables within the same model, dimensional analysis of the variables is considered. Nevertheless, not all the explanatory variables could feature simultaneously in their form as found and popularly used in literature. For example L_s/h and ν could not feature in the same model in this form using dimensional analysis. In order to account for this, apart from developing models in terms of dimensional analysis only, a separate set of models based on explanatory variables as found in literature only is proposed. Then selection of the ultimate model could be based on the ability of each to fit data and is then discussed in the results in Chapter 6.

Both sets of models whether based on dimensional analysis or based on variables as found in literature involve various permutations and combinations of possible explanatory variables that can form a model. In most models discussed in Chapter 2, selection of the explanatory variables

is based on the significance of individual trends between the explanatory and the demand variables only. This ignores the mutual effect of each explanatory variables in the same model on the demand variable. As a result, criteria that selects between different models formed by the different permutations is considered, instead of using criteria that selects explanatory variables before forming the models only. A third set of models based on dimensional analysis but incorporating a term that includes dissipated energy is considered to evaluate that chord rotation varies also as a function of the loading pattern discussed in chapter 2.

Since the combination of variables in existing models in literature is not based on optimization, overfitting of the models is possible. Although overfitting due lack of optimization is reduced by considering dimensional analysis, this is still possible since the number of explanatory variables compared with the number of test records is quite large. As a result BIC selection criteria is considered in the selection process between explanatory variables to be included in the model and between models formed with different permutations. Selection using BIC is also equivalent to K-fold cross validation. The advantage of BIC is that no data is wasted in validation, and this is very important considering that the data available was very limited. However, the validation is a hidden within the statistical approach, and cannot be visually monitored like in K-fold cross validation.

With this process, the trend of the explanatory variables in the model is automatically defined by the statistical selection process considering best fit. For the selected models, the trend between the explanatory variables and the demand variables is required to be checked individually in order to identify that this is not a statistical coincidence. Scatter plots, plots of single test series and correlation are used. While scatter plots do not always provide clear trends, plots of single test series plot through variability between experiments with only one variation between them. Hence, clearer trends are observed with the latter considerations.

Together with the experimental results discussed in Chapter 4, the database presented by Berry *et al.*, 2003 is used to develop the models. It is not reported how models in literature discussed in Chapter 2 are accounted for missing data of dependent variables. However, a statistical approach is considered in the proposed method to reduce the uncertainty. It is observed that different authors give different values to EDPs of the same experiments. To further reduce uncertainty, rational interpretations and definitions that define how to determine EDP values are therefore considered. This was possible since the force-displacement history of the experiments in the database were available.

Although the dataset is enhanced by the data from the experimental campaign in Chapter 3 and Chapter 4, some gaps are still observed towards the tails of data distribution of individual parties. This can give rise to discontinuities leading to models which are defined by outliers that refer to these extreme and discontinuous data points. As a result, for most models, two regressions are recommended. One is based on all the data, and the other based on 95% of the significant data

eliminating data points with extreme values of explanatory variables which are not represented sufficiently. Assessment on which of the two models produces more reliable prediction is then required.

Chapter 6. NEW EMPIRICAL EDP MODELS

6.1 Introduction

In this chapter, three sets of empirical models are presented. These are determined according to the procedure discussed in Chapter 6. The first set of models consists in chord rotation models at various damage states with the exclusion of yielding damage state, in terms of residual stiffness and energy dissipation. The second set consists in chord rotation equations at various damage states. For each damage state with the exception of yielding, three models are provided. The first model is in terms of variables that are determined from dimensional analysis, the second model is in terms of combined variables that are obtained only from literature, and the third model incorporates an energy dissipation term. Due to the large computations required, only the models that are based on the dataset excluding outliers and extreme values of variables are presented, which also proved to be more consistent. The third set of empirical models consists in stiffness ratio models at various damage states. For each damage state, two models are presented. One is based on the dataset that includes outliers and extreme values of variables, and the other based on the dataset which excludes them. The empirical models are compared and assessed in terms of statistical criteria and diagnostics, and their range of application. The determined empirical models are also compared with other models in literature. However, this is only done for EI_Y/EI_g , θ_Y and θ_{u-20} , since no other models that describe the other defined states of damage are found.

6.2 Range of Application of the EDP Models

Appendix A shows the density distribution plots of each explanatory variable and EDP that are selected in the models corresponding to each damage level. In some distributions, a large density is concentrated around a few particular variables. For variable b/h a large concentration is around 1. Variables $E/(bhsf'_c)$, $a\rho_s$, s/d_{bl} , v , f_{yl}/f'_c , f_{tl}/f'_c , c/s , ω_w and ρ_w are observed to have a degree of skewness towards the minimum values. Some variables namely b/h , c/h , ω_w , ρ_T , $E/(bhsf'_c)$ and f_{yl}/E_s are observed to have discontinuity at either or both extremes. The discontinuities are eliminated and skewness reduced if not eliminated when 95% of the data is considered.

Table 6-1 to Table 6-7, show the range of application of the explanatory variables for each damage state that are determined from the plots in Appendix D. For the regression analysis of models based on all the filtered data but including outliers and extreme data-points, 100% of the range indicated is used. For regression analysis of models based on all filtered data and excluding outliers and extreme data-points, 95% of the range indicated is used. The same explanatory variables selected for different damage states have a similar range when 100% of the filtered data is considered. However, the range of the same explanatory variables for different damage states

varies when 95% of the data is considered since the number of data varies from damage level to another. The ranges of different EDP variables at particular damage states overlap with corresponding ranges at different damage states. Due to large densities at the extremes of K_m , K_{u-10} , K_{u-20} and K_{u-50} the range corresponding to 95% of the data is equivalent to the range when 100% of the data is considered.

The range of the variables utilised in the development of the new models of EI_Y/EI_g , θ_Y and θ_{u-20} in this research are more restricted than the ranges in the development of the corresponding models by Biskinis *et al.*, (2010a) and Biskinis *et al.*, (2010b). For the chord rotation at yielding (θ_Y) determined by Biskinis *et al.*, 2010a, the variables L_s/h , b/h , ρ_w , ρ_T and v vary between 1.0-13.0, 0.25-5, 0.002-0.0354, 0.0011-0.0855 and -0.05-0.9 respectively. For the development of the model in this research, these variables vary between 1.8-7.82, 0.5-1, 0.0022-0.072, 0.005-0.06 and 0-0.9 respectively when the data includes the outliers and the extreme variables. It is only the range of ρ_w that ranges beyond that specified in Biskinis *et al.*, 2010a. For the chord rotation at 20% maximum force reduction determined by Biskinis *et al.*, 2010b, the variables L_s/h , v and ρ_T vary between 1-13, -0.05-0.9 and 0.0021-0.0652 respectively. For the development of the model in this research, these variables vary between 1-7.81, 0.01-0.9, and 0.01-0.039 respectively when the data includes the outliers and the extreme variables.

Table 6-1 Range of explanatory variable values for empirical models at yielding damage state.

Minimum % of Data falling within range		Physical or material property						
		f_{yl}/E_s	f_{yl}/f'_c	v	$(L_s + a_v z)/h$	ρ_T	L_s/h	b/h
100%	Min.	0.0017	2.35	0.00	1.00	0.005	0.85	0.5
	Max.	0.0029	34.5	0.90	7.75	0.060	7.81	1.0
95%	Min.	0.0018	3.45	0.03	2.00	0.010	1.80	0.5
	Max.	0.0026	24.2	0.75	6.56	0.038	7.82	1.0

Table 6-2 Range of explanatory variable values for empirical models at maximum force.

Minimum % of Data falling within range		Physical or material property									
		f_{tl}/f'_c	f_{tl}/f_{yl}	v	L_s/h	ρ_T	s/d_{bl}	ρ_w	$a\rho_s$	c/s	$E/(bhsf'_c)$
100%	Min.	4.5	1.10	0.00	0.85	0.005	1.8	0.0022	0.0005	0.01	500
	Max.	43.0	1.73	0.90	7.81	0.060	18.0	0.0720	0.0142	1.07	350000
95%	Min.	4.7	1.19	0.03	1.55	0.010	2.5	0.0048	0.0005	0.13	660
	Max.	32.6	1.68	0.75	7.82	0.039	15.0	0.0550	0.0112	0.70	170476

Table 6-3 Range of explanatory variable values for empirical models at 10% maximum force reduction.

Minimum % of Data falling within range		Physical or material property												
		f_{tl}/f'_c	f_{tl}/f_{yl}	f_{yl}/f'_c	v	L_s/h	L_s/s	ρ_T	s/d_{bl}	ρ_w	ω_w	$a\rho_s$	c/s	$E/(bhsf'_c)$
100%	Min.	4.5	1.12	3.4	0.01	0.95	1.4	0.010	1.8	0.0022	0.025	0.0006	0.01	1100
	Max.	43.0	1.73	36.2	0.90	7.81	36.3	0.060	18.0	0.0720	0.720	0.0142	1.07	132057
95%	Min.	4.7	1.19	3.4	0.03	1.55	3.2	0.010	2.5	0.0049	0.045	0.0006	0.13	1200
	Max.	32.6	1.68	24.9	0.73	6.55	33.3	0.039	15.00	0.0550	0.480	0.0105	0.70	770064

Table 6-4 Range of explanatory variable values for empirical models at 20% maximum force reduction.

Minimum % of Data falling within range		Physical or material property													
		f_{tl}/f'_c	f_{tl}/f_{yl}	f_{yl}/f'_c	v	L_s/h	L_s/s	ρ_T	s/d_{bl}	ω_w	$a\rho_s$	$a\rho_s \frac{f_{yw}}{f'_c}$	c/s	c/h	$E/(bhsf'_c)$
100%	Min.	4.5	1.12	3.4	0.01	0.95	1.4	0.010	1.8	0.025	0.0006	0.001	0.01	0.01	2910
	Max.	43.0	1.73	36.2	0.90	7.81	36.3	0.060	18.0	0.720	0.0142	0.125	1.07	0.19	1820000
95%	Min.	4.7	1.19	3.4	0.03	1.55	3.2	0.010	1.58	0.045	0.0006	0.001	0.13	0.07	3392
	Max.	32.6	1.68	22.9	0.73	6.55	33.3	0.039	15.00	0.480	0.0105	0.090	0.70	0.14	1311180

Table 6-5 Range of explanatory variable values for empirical models at 50% maximum force reduction.

Minimum % of Data falling within range		Physical or material property															
		f_{tl}/f'_c	f_{tl}/f_{yl}	f_{yl}/f'_c	v	L_s/h	L_s/s	ρ_T	s/d_{bl}	ρ_w	ω_w	$a\rho_s \frac{f_{yw}}{f'_c}$	f_{yw}/f'_c	c/s	c/h	$E/(bhsf'_c)$	
100%	}	Min.	4.7	1.15	3.4	0.03	0.95	1.4	0.010	1.8	0.0022	0.025	0.002	3.5	0.01	0.01	3520
		Max.	43.0	1.73	36.2	0.90	7.81	36.3	0.060	18.0	0.0072	0.720	0.125	28.0	1.07	0.19	2413930
95%	}	Min.	4.8	1.19	3.4	0.05	1.50	3.2	0.010	2.36	0.0049	0.040	0.004	3.9	0.08	0.07	5214
		Max.	34.4	1.68	26.3	0.73	6.55	33.0	0.038	15.00	0.0550	0.480	0.100	24.4	0.68	0.14	2058242

Table 6-6 Range of chord rotation and stiffness ratio for all empirical models at each damage state.

Minimum % of Data falling within range		Engineering Demand Parameter (EDP)										
		Chord Rotation					Stiffness Ratio					
		θ_Y	θ_m	θ_{u-10}	θ_{u-20}	θ_{u-50}	$\frac{EI_Y}{EI_g}$	$\frac{EI_m}{EI_g}$	$\frac{EI_{u-10}}{EI_g}$	$\frac{EI_{u-20}}{EI_g}$	$\frac{EI_{u-50}}{EI_g}$	
100%	}	Min.	0.0021	0.003	0.004	0.0085	0.011	0.08	0.02	0.01	0.01	0.01
		Max.	0.0338	0.079	0.091	0.094	0.115	0.89	0.78	0.68	0.63	0.23
95%	}	Min.	0.0026	0.005	0.009	0.01	0.013	0.09	0.04	0.04	0.02	0.01
		Max.	0.0183	0.062	0.091	0.094	0.090	0.89	0.69	0.58	0.35	0.14

Table 6-7 Range of stiffness and energy dissipation for all empirical models at each damage state.

Minimum % of Data falling within range		Engineering Demand Parameter (EDP)							
		Stiffness $-[kN/m]$				Energy $-[kNm]$			
		K_m	K_{u-10}	K_{u-20}	K_{u-50}	E_m	E_{u-10}	E_{u-20}	E_{u-50}
100%	Min.	1083	591	307	136	133	350	835	2408
	Max.	156364	66257	46585	20098	191793	378302	443205	810669
95%	Min.	-	-	-	-	-	-	-	-
	Max.	132560	63521	-	-	148560	365208	400000	-

6.3 Relationship between Chord Rotation (θ_{dmg}), Residual Stiffness (K_{dmg}) and Energy Dissipation (E_{dmg}).

In this section, two sets of empirical models relating chord rotation (θ_{dmg}), residual stiffness (K_{dmg}), and energy dissipation (E_{dmg}), at various damage levels derived using linear regression analysis discussed in Chapter 5 are presented. The damage levels considered respectively refer to maximum force (m), 10% maximum force reduction ($u-10$), 20% maximum force reduction ($u-20$) and 50% maximum force reduction ($u-50$). A relationship at yielding was not considered since energy dissipation at this damage state is assumed to be negligible.

The first set of empirical models is given by equations 6.1 to 6.4, relate the EDPs in terms of their original form. In the second set of empirical models given by equations 6.5 to 6.8 relate EDPs using dimensionless terms by normalising E_{dmg}/K_{dmg} by the effective length of the specimen (L_s) as discussed in section 5.3.3. Two models are determined for each damage state a) referring to regression on all data and b) referring to regression on data excluding outliers and extreme variables.

$$\theta_{u-m} = 0.0635 \frac{E_{u-m}^{0.174}}{K_{u-m}^{0.304}} \quad \theta_{u-m} = 0.0576 \frac{E_{u-m}^{0.172}}{K_{u-m}^{0.304}} \quad [6.1]$$

a

b

$$\theta_{u-10} = 0.0375 \frac{E_{u-10}^{0.199}}{K_{u-10}^{0.264}} \quad \theta_{u-10} = 0.0331 \frac{E_{u-10}^{0.187}}{K_{u-10}^{0.234}} \quad [6.2]$$

a

b

$$\theta_{u-20} = 0.0307 \frac{E_{u-20}^{0.207}}{K_{u-20}^{0.25}} \quad \theta_{u-20} = 0.0291 \frac{E_{u-20}^{0.201}}{K_{u-20}^{0.234}} \quad [6.3]$$

a

b

$$\theta_{u-50} = 0.0315 \frac{E_{u-50}^{0.203}}{K_{u-50}^{0.258}} \quad \theta_{u-50} = 0.0336 \frac{E_{u-50}^{0.189}}{K_{u-50}^{0.243}} \quad [6.4]$$

a

b

$$\theta_{u-m} = \frac{0.0234}{L_s^{0.618}} \left(\frac{E_{u-m}}{K_{u-m}} \right)^{0.309} \quad \theta_{u-m} = \frac{0.0234}{L_s^{0.595}} \left(\frac{E_{u-m}}{K_{u-m}} \right)^{0.297} \quad [6.5]$$

a *b*

$$\theta_{u-10} = \frac{0.0212}{L_s^{0.55}} \left(\frac{E_{u-10}}{K_{u-10}} \right)^{0.275} \quad \theta_{u-10} = \frac{0.0212}{L_s^{0.538}} \left(\frac{E_{u-10}}{K_{u-10}} \right)^{0.269} \quad [6.6]$$

a *b*

$$\theta_{u-20} = \frac{0.0192}{L_s^{0.587}} \left(\frac{E_{u-20}}{K_{u-20}} \right)^{0.293} \quad \theta_{u-20} = \frac{0.0192}{L_s^{0.586}} \left(\frac{E_{u-20}}{K_{u-20}} \right)^{0.293} \quad [6.7]$$

a *b*

$$\theta_{u-50} = \frac{0.0161}{L_s^{0.614}} \left(\frac{E_{u-50}}{K_{u-50}} \right)^{0.307} \quad \theta_{u-50} = \frac{0.0159}{L_s^{0.621}} \left(\frac{E_{u-50}}{K_{u-50}} \right)^{0.31} \quad [6.8]$$

a *b*

Figure 6-1 to Figure 6-8 indicate the relationship between the experimental θ_{dmg} and predicted θ_{dmg} by the empirical models. A summary of the corresponding statistical data on the ratio of $\theta_{dmg,exp}/\theta_{dmg,pred}$ is given in Table 7-8. The median and mean for all the models are observed to be very close to 1. The fitted mean is however observed to be closer to the median than the total mean. In nearly all the cases, the standard deviation (SD) and coefficient of variation (CoV) for the models relating EDPs in terms of non-dimensional terms are lower than the corresponding models relating EDPs in terms of dimensional terms at the same level of damage. For the damage level at m , SD is lower by approximately 26% and CoV by 24%, for $u-10$ SD is approximately lower 21% and CoV by 19%, and for $u-50$, SD and CoV are approximately lower by 27%. SD is lower by 34% and CoV is lower by 32% for the damage level $u-20$. This latter case is however true for the model based on data excluding outliers and extreme data-points only. No difference is observed between the two models at damage level $u-20$ based on data including outliers and extreme data-points.

Similarly, no substantial difference was observed in the 5% and 95% fractile factors corresponding with these two models. However, in all the other cases, the 5% fractile and the 95% fractile are respectively higher and lower for the set of models composed of dimensionless

variables. This is true for both models based on data including outliers and extreme variables, and models which exclude them. For damage levels m , $u-10$ and $u-50$, the increase in the 5% fractile factor corresponding to models based on data including outliers and extreme variables is 14%, 14% and 40%. The decrease in the 95% factor is 7%, 11% and 10% respectively. For damage levels m , $u-10$, $u-20$ and $u-50$, the increase in the 5% fractile factor corresponding to models based on data excluding outliers and extreme variables is 7%, 9%, 12% and 16%. The decrease in the 95% factor is 7%, 11%, 22% and 10% respectively. The increase is more significant for the models based on data that includes outliers and extreme data-points.

Collectively these statistics indicate that the second set of equations 6.5 to 6.8 offer a better goodness-of fit over equations 6.1 to 6.4. However, this capability of the models has also to be evaluated in terms of their ability to satisfy the assumptions of the regression analysis. A summary of the statistical diagnostics of the regression analysis corresponding to each presented model is given in in Appendix J.

The trend line of the residuals in residual-fitted plots associated with equations 6.1a, 6.1b, 6.8a and 6.8b are relatively horizontal about zero. The trend line in corresponding scale location plots is also relatively horizontal. Moreover the Breusch-Pagan test confirms homoscedasticity. The trend lines in the residual-fitted plot and scale-location plot associated with equation 6.5 are not horizontal and the Breusch-Pagan test indicates heteroscedasticity. The residual-fitted plots and scale-location plots associated with 6.2a, 6.2b, 6.3a, 6.3b, 6.4a, 6.4b, 6.5b, 6.6a, 6.6b, 6.7a and 6.7b indicate that the trend lines have a slight twist at the edges. The trend line in the residual-fitted plots also varies close to zero. In the Breusch-Pagan test corresponding to equations 6.2a, 6.4a and 6.4b, the p -value=0.052. The hypothesis for homoscedasticity in the Breusch-Pagan tests is only just accepted. The Breusch-Pagan test confirms homoscedasticity for the models corresponding to equations 6.2b, 6.3a, 6.3b, 6.5b, 6.6a, 6.6b, 6.7a and 6.7b with a much higher p -value. Moreover, the resulting p -values from the Breusch-Pagan test corresponding with models of equations 6.2b, 6.5b and 6.6b that refer to regressions using data excluding outliers and extreme variables, are larger than p -values of the test corresponding with models of equations 6.2a, 6.5a and 6.6a that refer to regressions using data including outliers and extreme variables.

In many Q-Q plots in Appendix E.5, standardised residuals are observed to reach ± 3 . However, the 95% interval of standardised residuals corresponding to nearly all the equations 6.1 to 6.8, fall between ± 2 . Standardised residuals are observed to be characterised with a slight offset. However, this mainly occurs beyond ± 2 . As a result the normal distribution assumption is observed. However, considerable offset of standardised residuals in the Q-Q plot corresponding to equation 6.2a is observed. Moreover, the 95% interval of standardised residuals is not observed to fall between ± 2 . As a result, normal distribution of residuals cannot be assumed for the model consisting of dimensional variables at 10% maximum force reduction based on data that includes

outliers and extreme data-points. In general, the offset of the standardised residuals, is less for the group of models based on data excluding outliers and extreme variables, compared to the corresponding group of models based on data including outliers and extreme variables. Additionally, a wider interval of standardised residuals is also observed to fall within ± 2 for the former group.

In general, the diagnostics do not indicate any improvements in satisfying the regression analysis assumptions for the models consisting in dimensional variables over models consisting in non-dimensional variables, or vice-versa.

Table 6-8 Statistics of experiment-to-predicted chord rotation in terms of stiffness and energy dissipation.

Ref.	Chord rotations ($\theta_{dmg,exp}/\theta_{dmg,pred}$)	Variable Type	Outliers and extreme points	No. of Data	Mean	Median	S.D.	CoV - %	Fractile factor	
									5%	95%
Eq.7.1a	$\theta_{m,exp}/\theta_{m,pred}$	Dimensional	included	219	1.06	1.02	0.37	35.2	0.56	1.74
Eq.7.1b			excluded	214	1.06	1.03	0.36	33.8	0.61	1.73
Eq.7.5a		Non-dimensional	included	219	1.00	1.04	0.28	26.9	0.64	1.61
Eq.7.5b			excluded	214	1.03	1.00	0.27	25.7	0.65	1.50
Eq.7.2a	$\theta_{u-10,exp}/\theta_{u-10,pred}$	Dimensional	included	209	1.05	0.99	0.34	32.0	0.59	1.65
Eq.7.2b			excluded	206	1.05	0.98	0.31	29.5	0.62	1.63
Eq.7.6a		Non-dimensional	included	209	1.03	1.00	0.27	25.8	0.67	1.47
Eq.7.6b			excluded	206	1.03	1.01	0.24	23.6	0.68	1.46
Eq.7.3a	$\theta_{u-20,exp}/\theta_{u-20,pred}$	Dimensional	included	200	1.06	0.97	0.38	35.7	0.58	1.87
Eq.7.3b			excluded	196	1.05	0.97	0.35	33.5	0.60	1.85
Eq.7.7a		Non-dimensional	included	200	1.06	0.97	0.38	35.7	0.59	1.87
Eq.7.7b			excluded	196	1.02	0.98	0.23	22.7	0.67	1.44
Eq.7.4a	$\theta_{u-50,exp}/\theta_{u-50,pred}$	Dimensional	included	152	1.05	0.99	0.33	31.8	0.50	1.60
Eq.7.4b			excluded	150	1.04	0.99	0.30	29.4	0.60	1.57
Eq.7.8a		Non-dimensional	included	152	1.03	1.00	0.24	23.5	0.70	1.44
Eq.7.8b			excluded	150	1.02	1.00	0.22	21.5	0.70	1.43

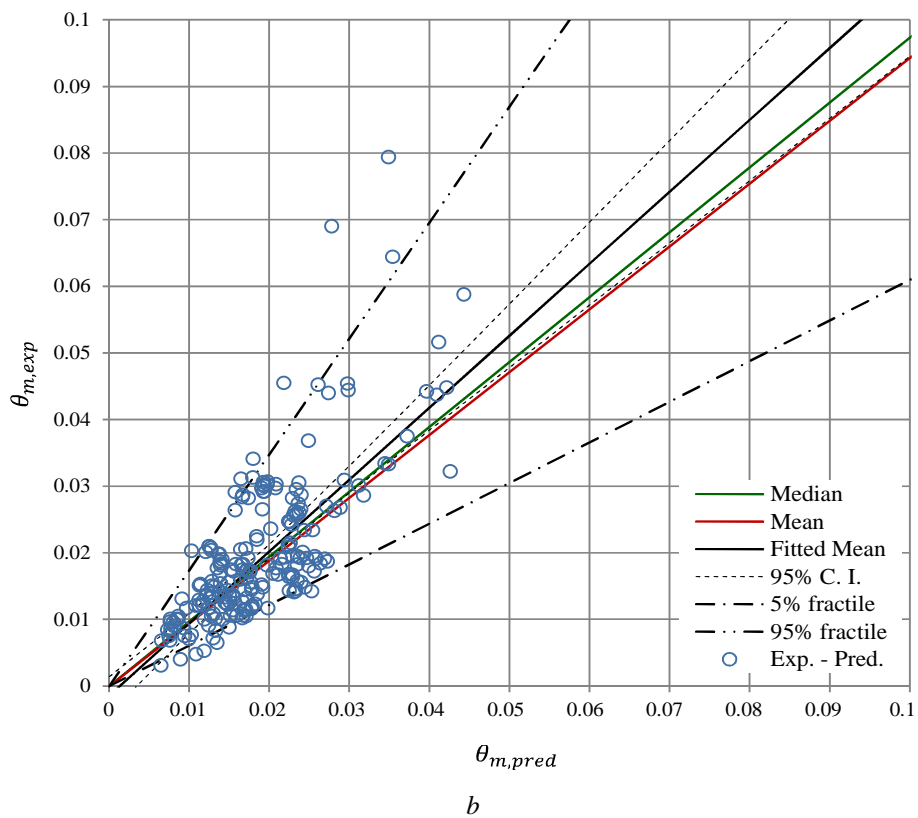
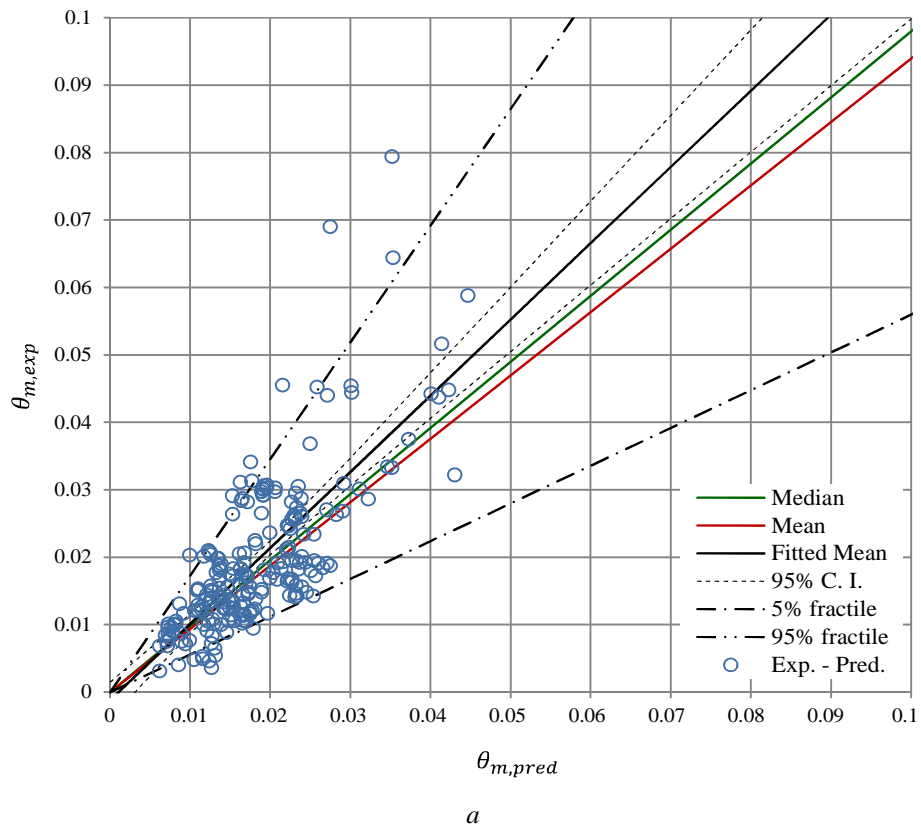


Figure 6-1 Experimental chord rotation at maximum force plotted against predictions from a) equation 7.1a and b) equation 7.1b, based on the inclusion and exclusion of extreme data-points respectively. The chord rotation is a function of dimensional terms of residual stiffness and energy dissipation.

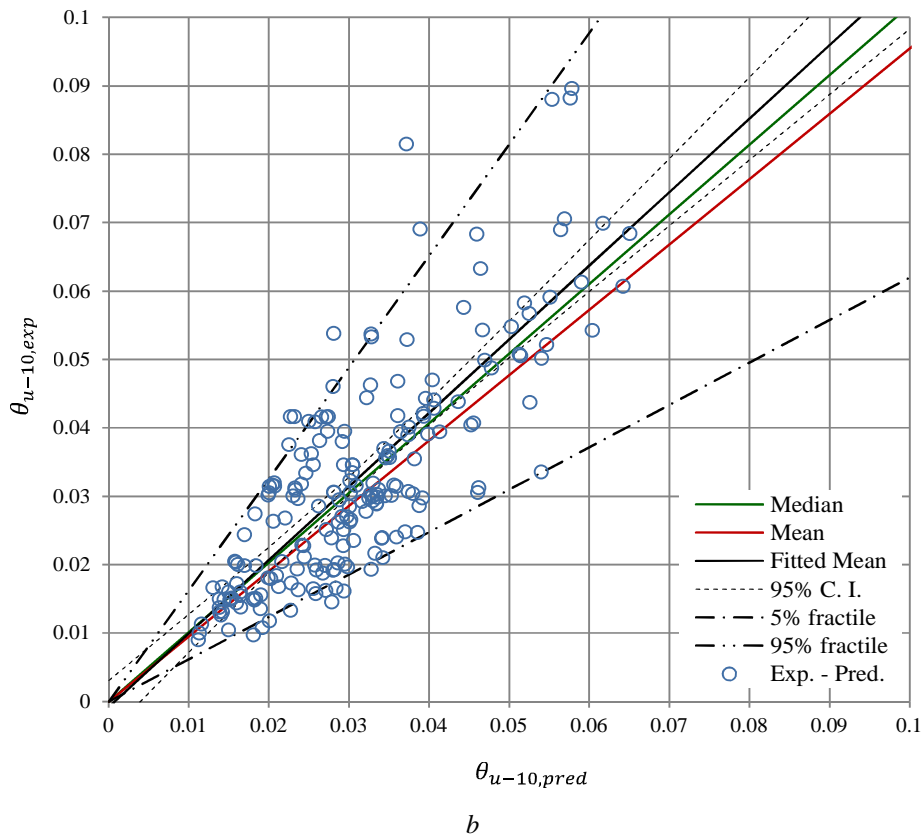
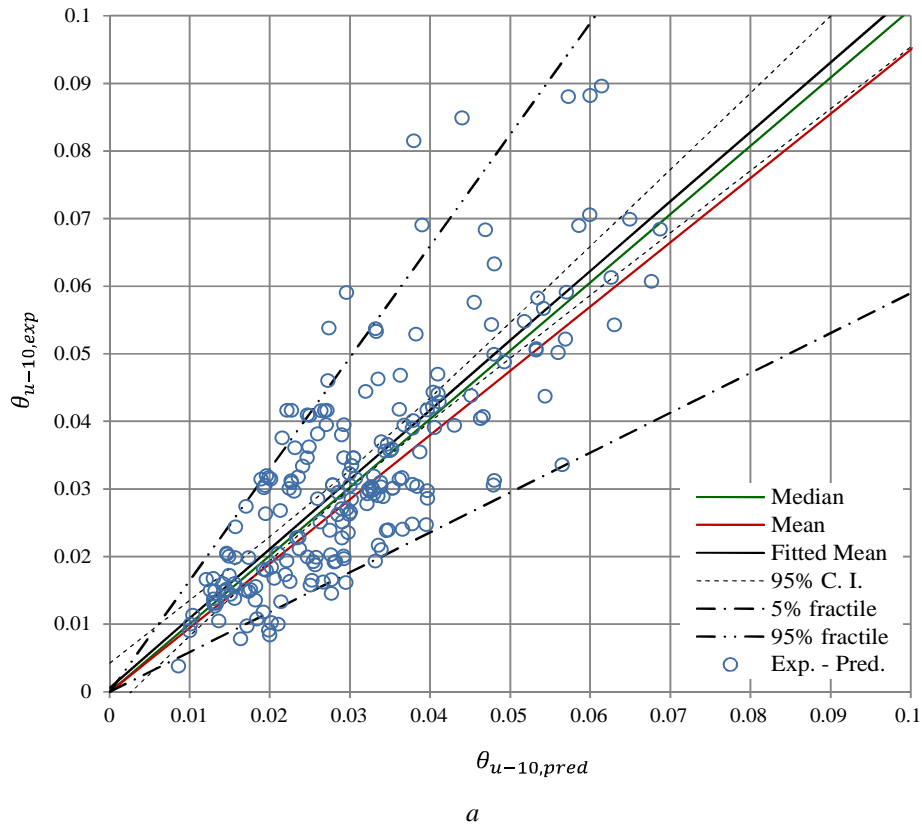
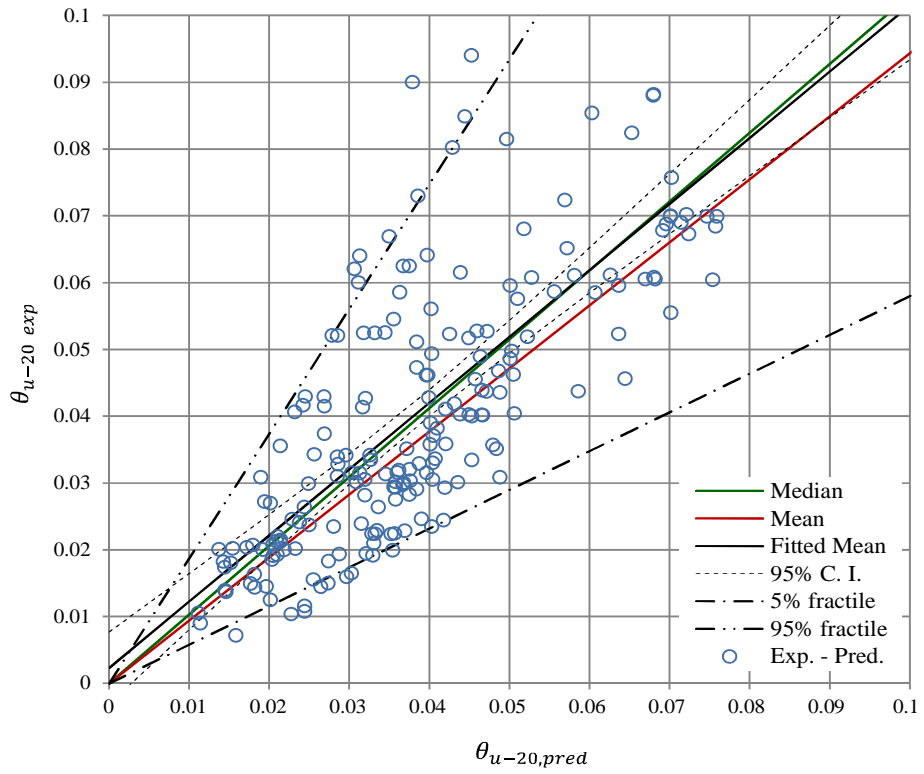
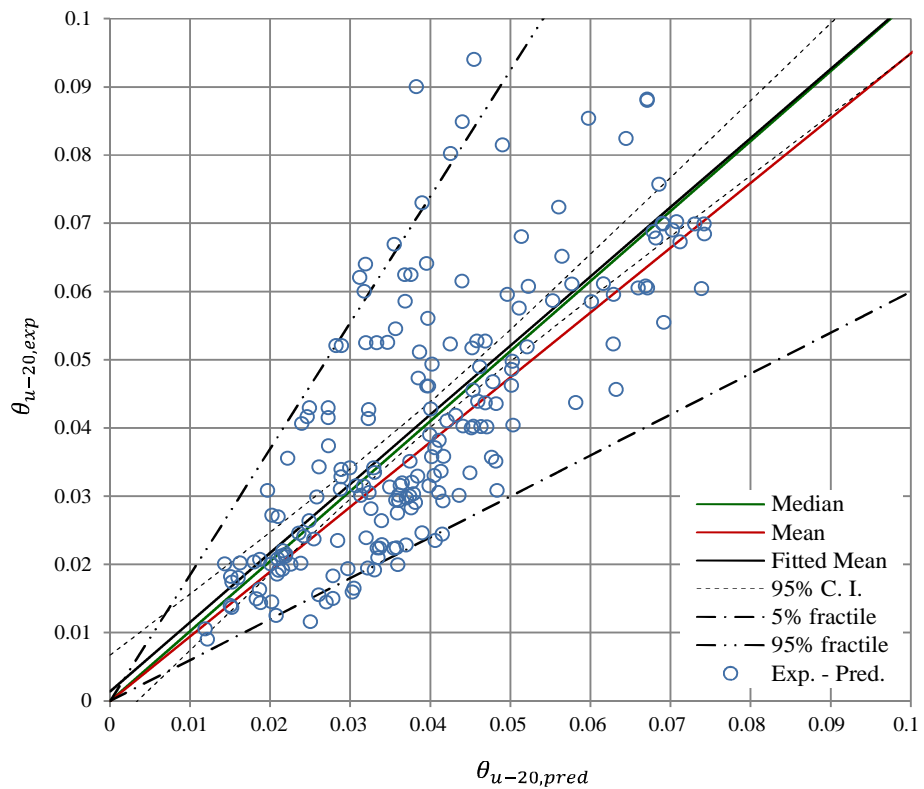


Figure 6-2 Experimental chord rotation at 10% maximum force reduction plotted against predictions from a) equation 7.2a and b) equation 7.2b, based on the inclusion and exclusion of extreme data-points respectively. The chord rotation is a function of dimensional terms of residual stiffness and energy dissipation.



a



b

Figure 6-3 Experimental chord rotation at 20% maximum force reduction plotted against predictions from a) equation 7.3a and b) equation 7.3b, based on the inclusion and exclusion of extreme data-points respectively. The chord rotation is a function of dimensional terms of residual stiffness and energy dissipation.

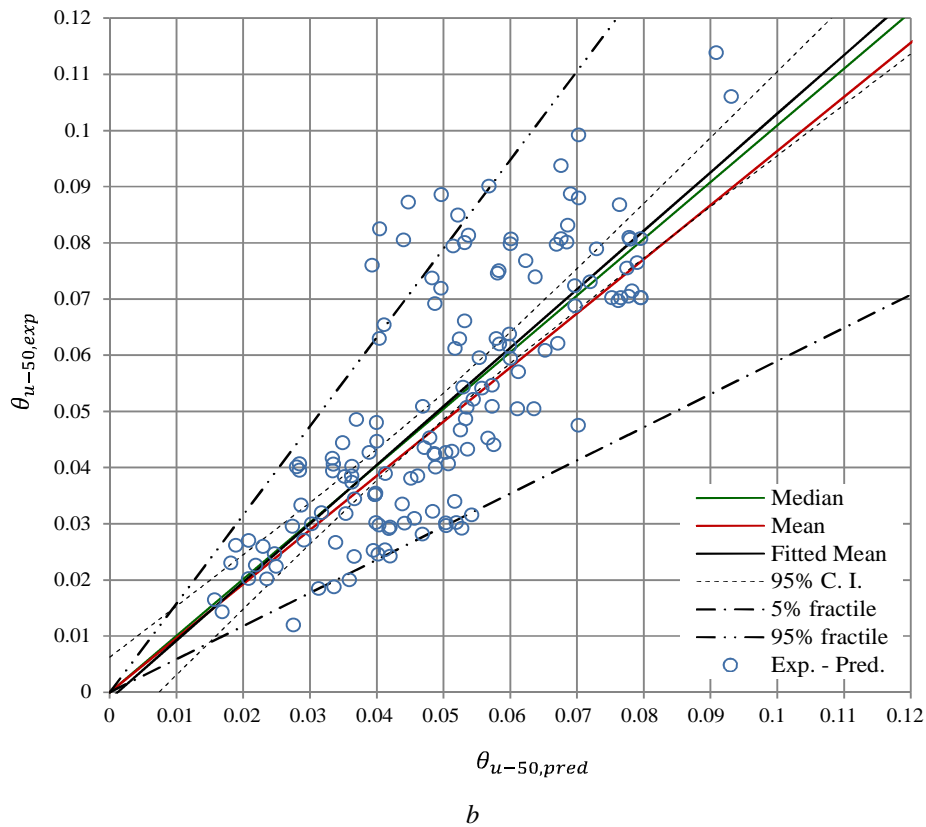
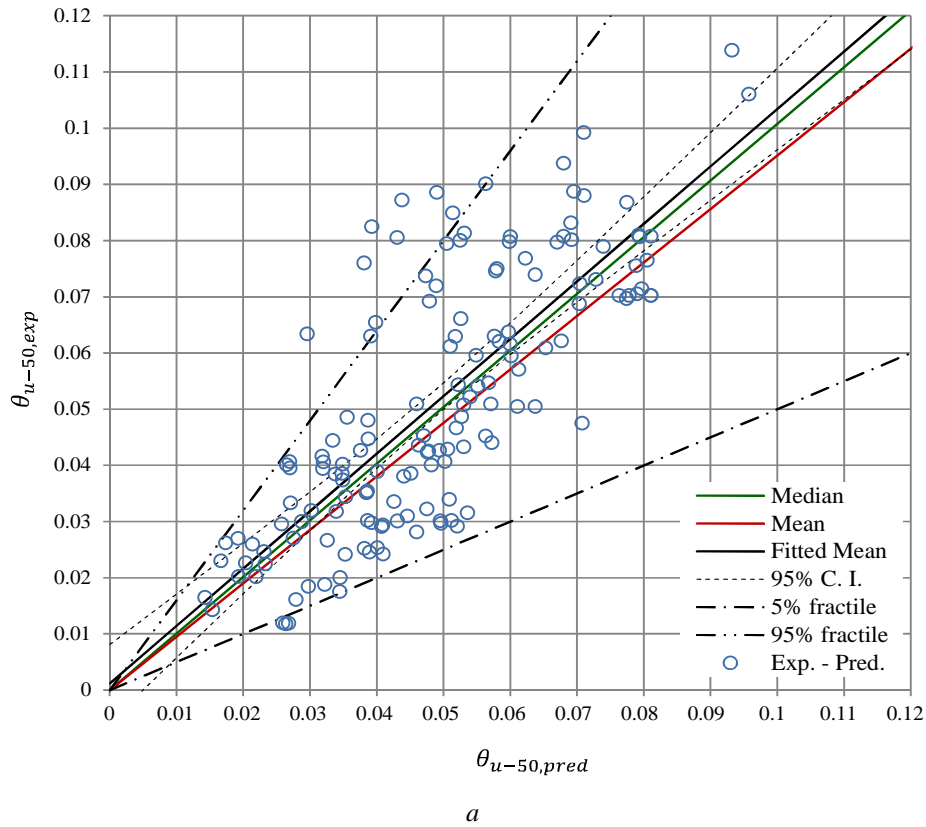


Figure 6-4 Experimental chord rotation at 50% maximum force reduction plotted against predictions from a) equation 7.4a and b) equation 7.4b, based on the inclusion and exclusion of extreme data-points respectively. The chord rotation is a function of dimensional terms of residual stiffness and energy dissipation.

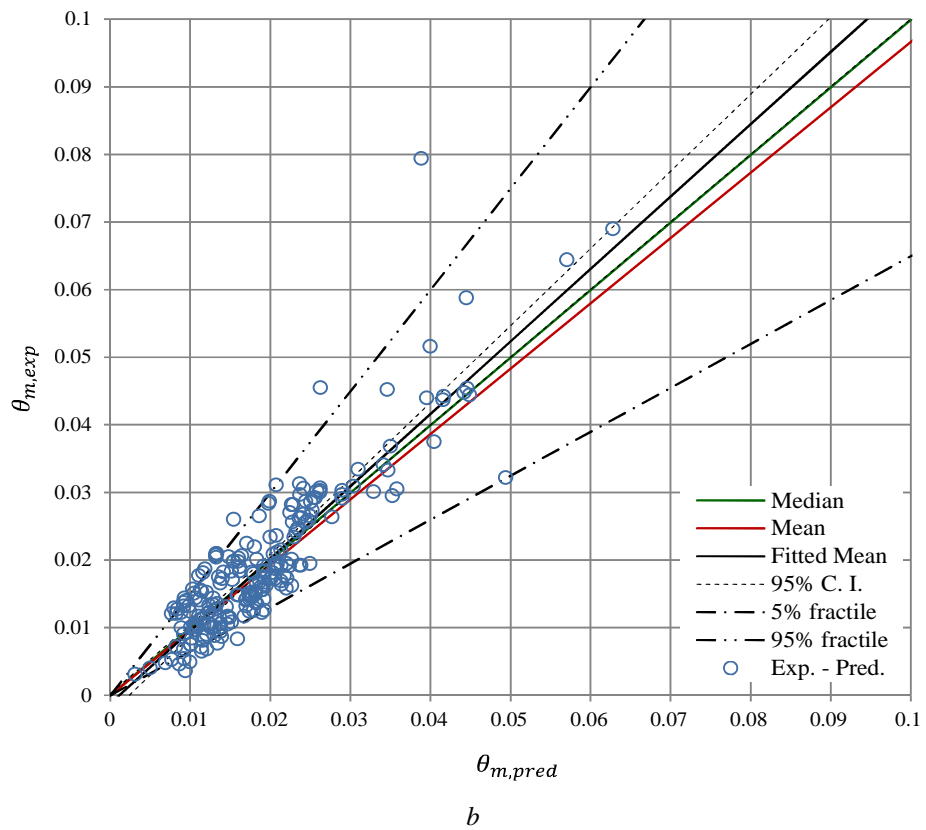
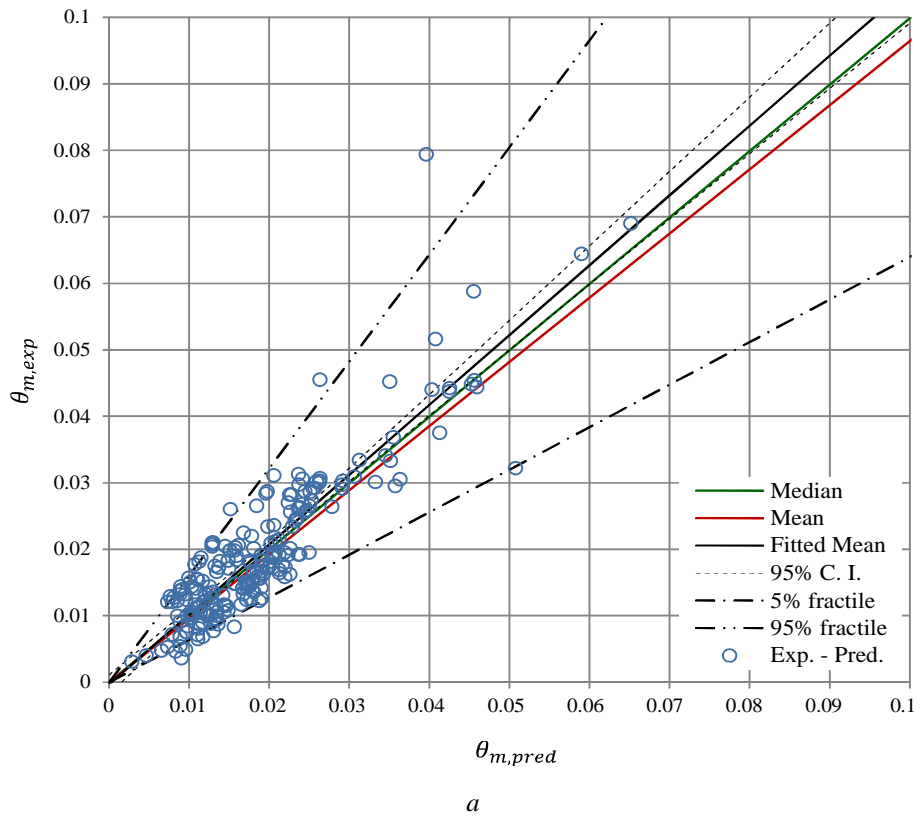


Figure 6-5 Experimental chord rotation at maximum force plotted against predictions from a) equation 7.5a and b) equation 7.5b, based on the inclusion and exclusion of extreme data-points respectively. The chord rotation is a function of non-dimensional terms of residual stiffness and energy dissipation.

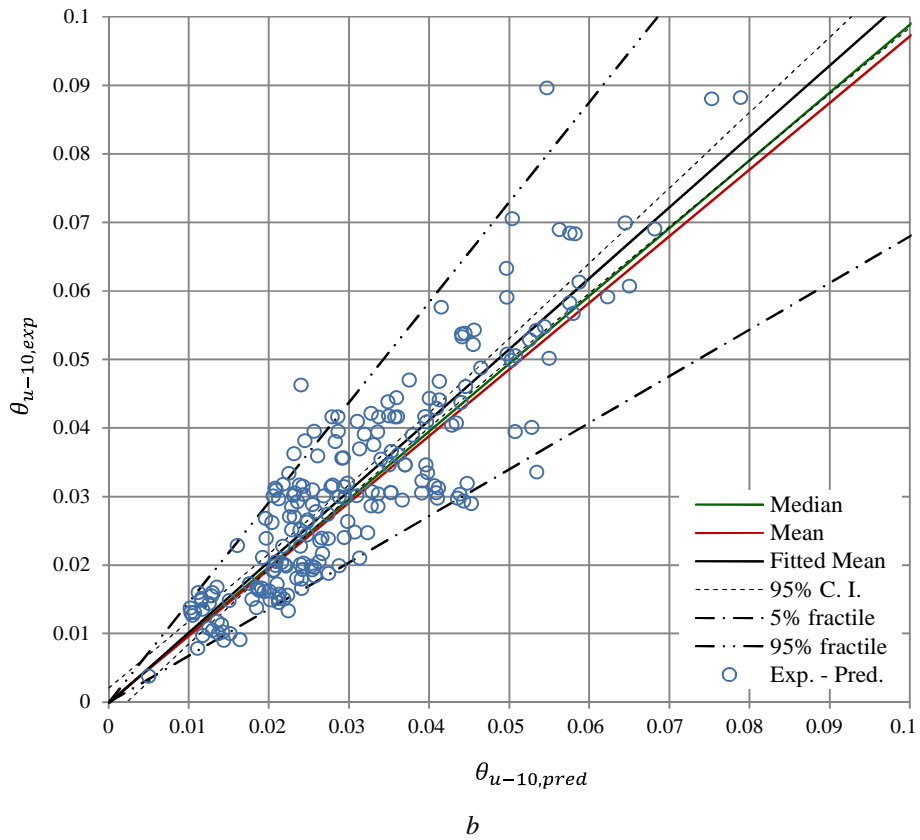
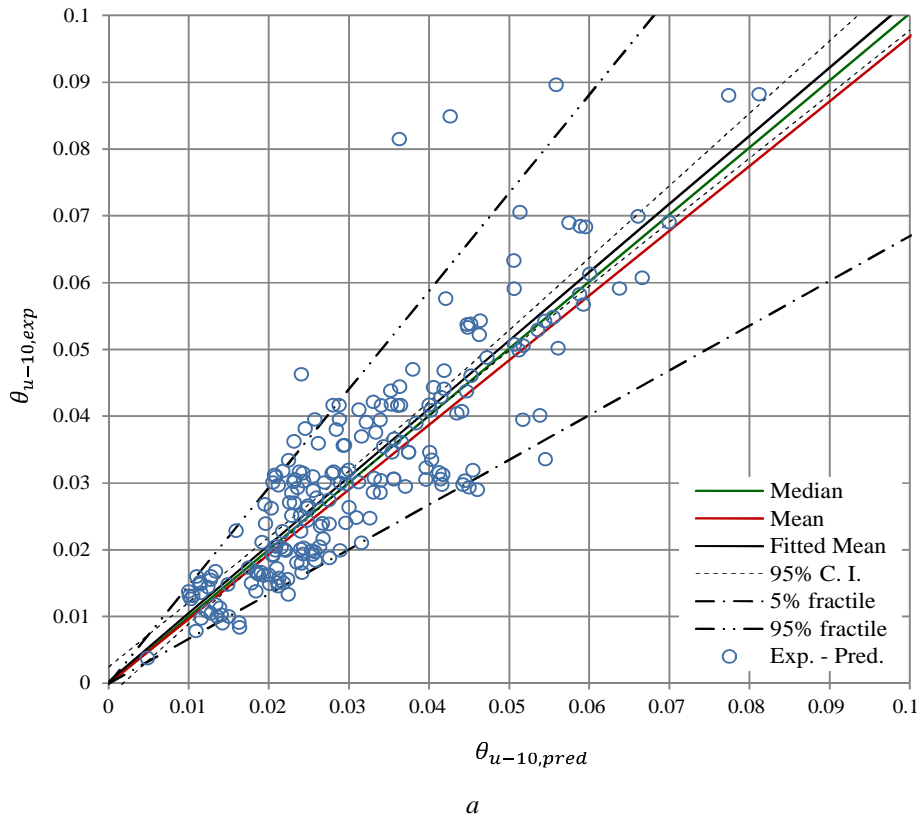


Figure 6-6 Experimental chord rotation at 10% maximum force reduction plotted against predictions from a) equation 7.6a and b) equation 7.6b, based on the inclusion and exclusion of extreme data-points respectively. The chord rotation is a function of non-dimensional terms of residual stiffness and energy dissipation.

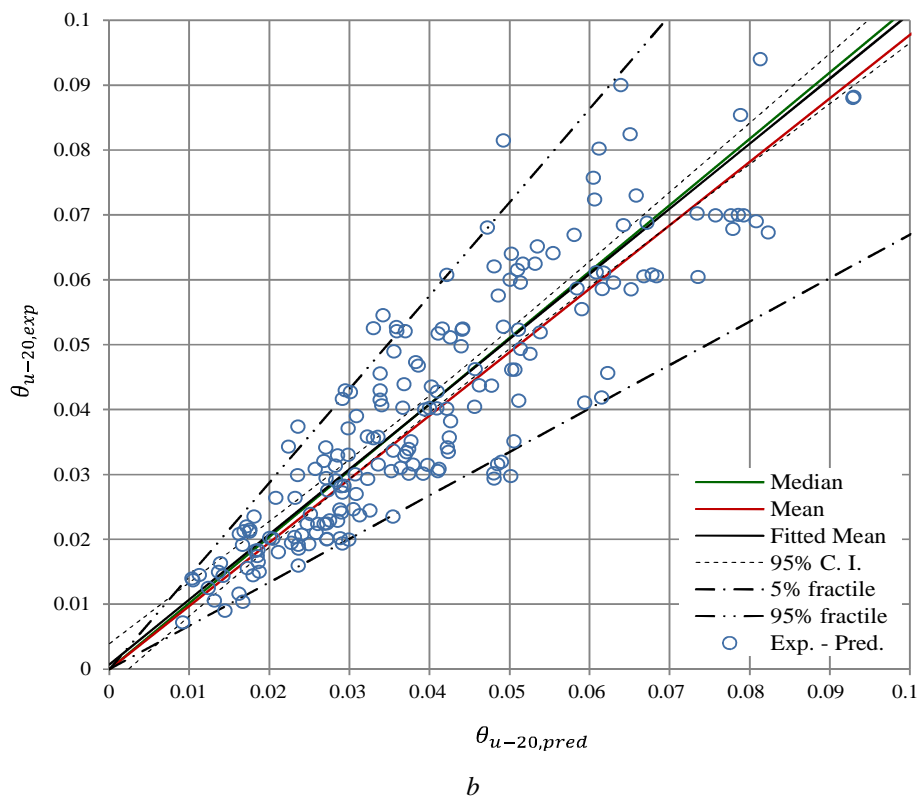
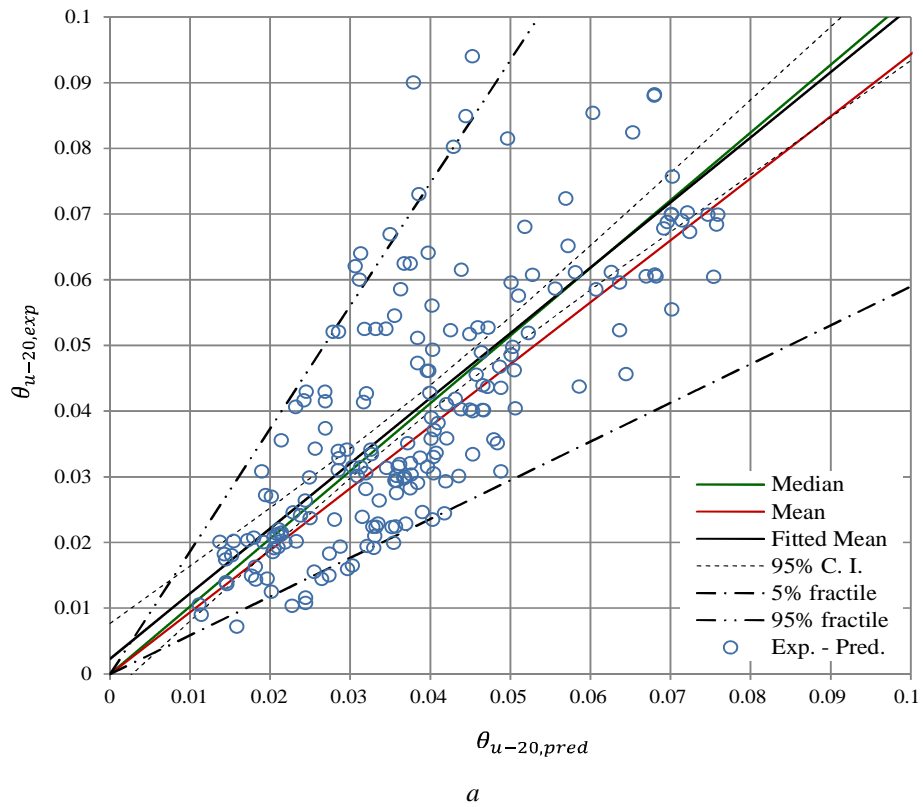
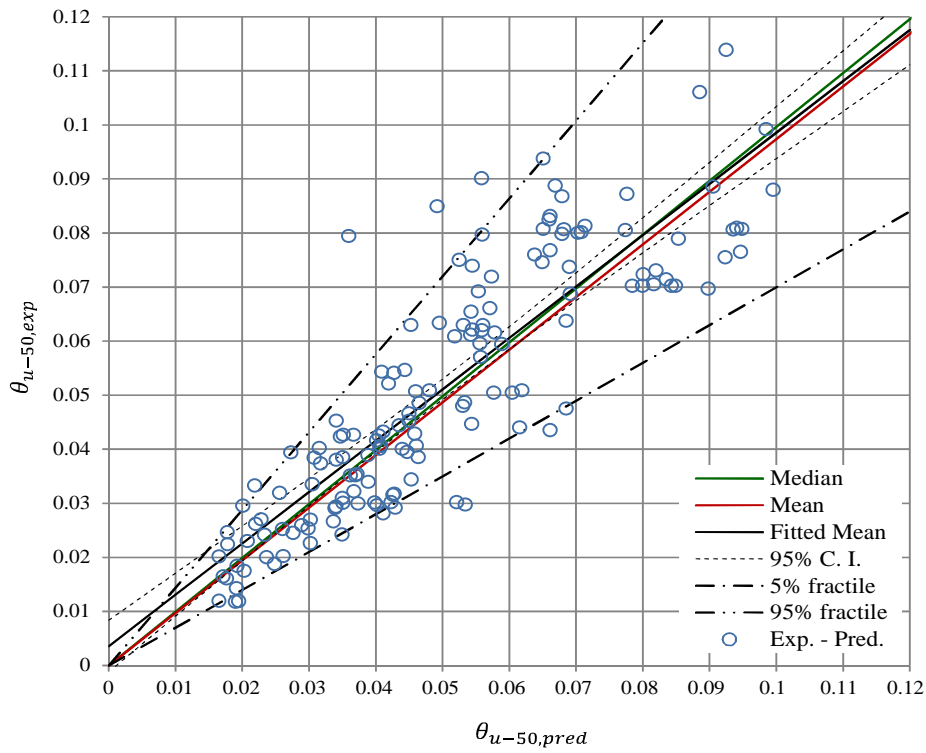
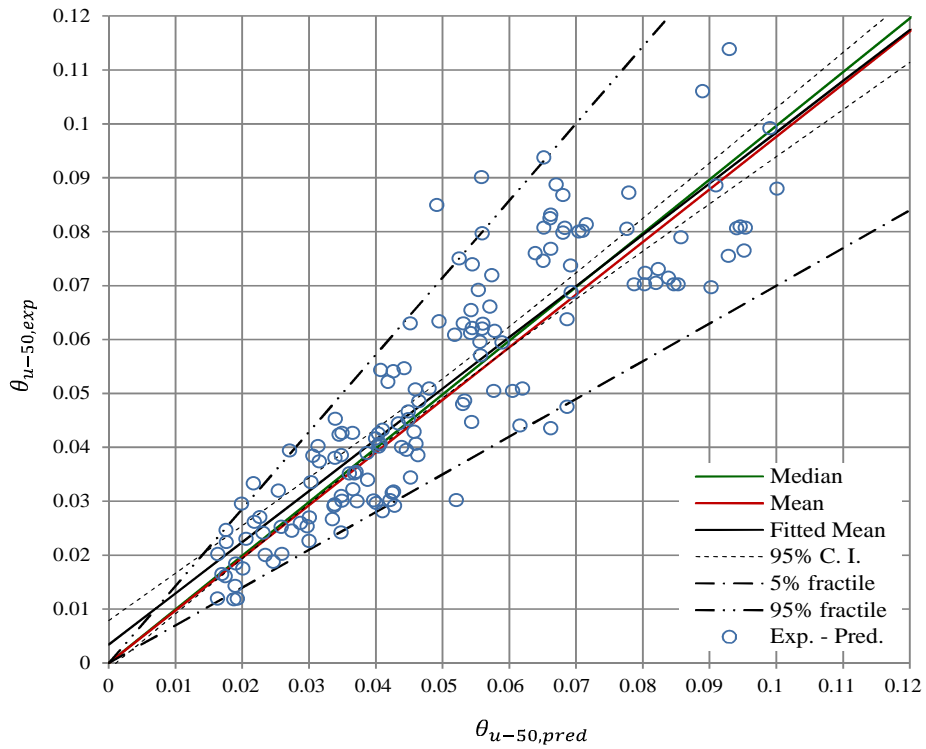


Figure 6-7 Experimental chord rotation at 20% maximum force reduction plotted against predictions from a) equation 7.7a and b) equation 7.7b, based on the inclusion and exclusion of extreme data-points respectively. The chord rotation is a function of non-dimensional terms of residual stiffness and energy dissipation.



a



b

Figure 6-8 Experimental chord rotation at 50% maximum force reduction plotted against predictions from a) equation 7.8a and b) equation 7.8b, based on the inclusion and exclusion of extreme data-points respectively. The chord rotation is a function of non-dimensional terms of residual stiffness and energy dissipation.

6.4 Chord Rotation Model

6.4.1 Chord Rotation at Yielding

Two empirical models that relate chord rotation at yielding θ_Y with explanatory variables describing material and geometrical properties selected based on the process discussed in section Chapter 5 are presented. In one model, the regression was based on data that included outliers and extreme variables, and in the other, based on data that excluded them. These models refer to equations 6.9a and 6.9b respectively. The variables f_{yl}/f'_c , f_{yl}/E_s , ρ_T and v are selected in both models based on data including and excluding outliers and extreme variables. The variable f_{yl}/E_s is also combined with a_{sl} as an interaction term. The variable $(L_s + a_v z)/h$ is also selected in the model based on data excluding outliers and extreme variables.

$$\theta_Y = \left(\frac{f_y}{E_s}\right)^{0.521} 1.015 \frac{f_y}{f'_c} \rho_T^{0.435} 0.366 v \quad [6.9a]$$

$$\theta_Y = \left(99.12 \cdot 5.61^{\log\left(\frac{f_y}{E_s}\right)}\right)^{a_{sl}} \left(\frac{f_y}{E_s}\right)^{0.554} 1.01 \frac{f_y}{f'_c} \rho_T^{0.457} 0.289 v^{1.105} \left(\frac{L_s + a_v z}{h}\right) \quad [6.9b]$$

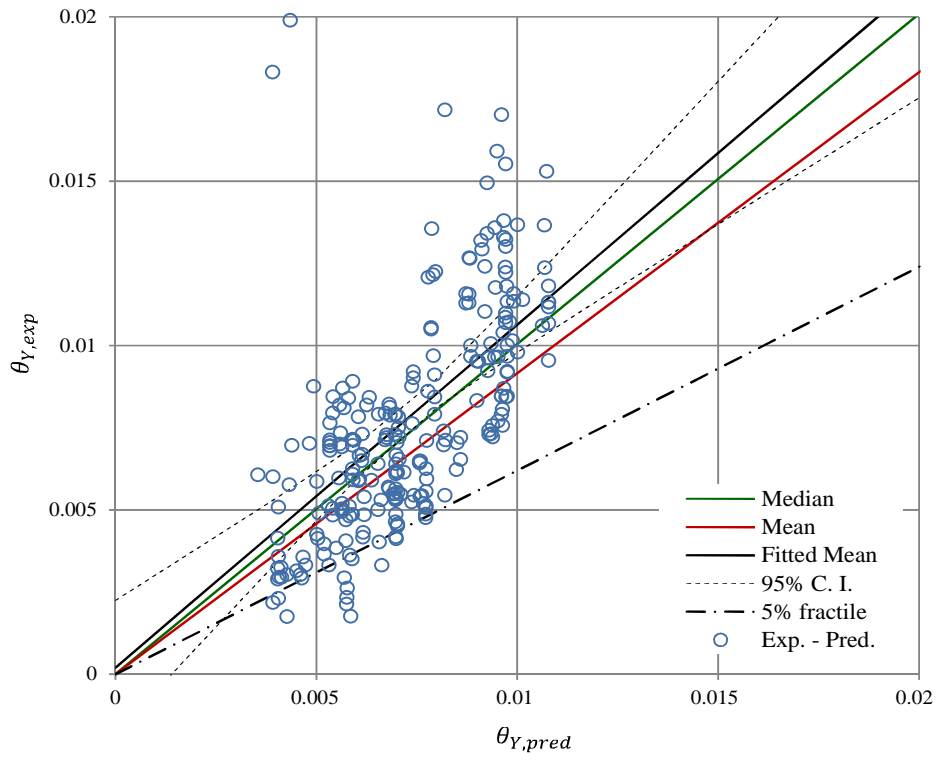
The indication on the relationship between θ_Y and explanatory variables in equations 6.9a and 6.9b, is also observed by separate investigation of trends or correlation discussed in section 5.6. As indicated in Appendix E Table E-1, the largest Spearman correlation of θ_Y is exhibited with v , followed by f_{yl}/E_s . The lowest correlations between θ_Y , and explanatory variables in the equations refers to f_{yl}/f'_c and $(L_s + a_v z)/h$. Scatter plots in Appendix F Figure F-1 indicate that θ_Y increases as f_{yl}/E_s increases, but decreases as v increases. The scatter in other plots is very wide to visually identify other trends. Trends are also observed by referring to plots of single test series where only one variable is changed with θ_Y . Appendix G, figure G-1 illustrates the plots for the explanatory variables selected in the equations 6.9a and 6.9b. The trends indicate that θ_Y increases with increasing f_{yl}/E_s , $(L_s + a_v z)/h$, ρ_T or f_{yl}/f'_c , and decreases with increasing v . When f_{yl}/E_s is combined with a_{sl} , θ_Y is observed to decrease. However, the latter is based on few but consistent observations.

The linear regression criteria for homoscedasticity and normal distribution of the residuals with zero mean are verified. A summary of some of the diagnostics is shown in Appendix H.1. The mean lines-of-fit in residual-fitted plots and scale-location plots of the residuals is also less dense. In residual-fitted plots, the line also oscillates about zero. Breusch-Pagan test for the model in equation 6.9a which is based on data that includes outliers and extreme data-points, indicates a p-value of 0.051. This just satisfies the criteria for homoscedasticity. However, the test for the corresponding model in equation 6.9b which is based on data that includes outliers and extreme

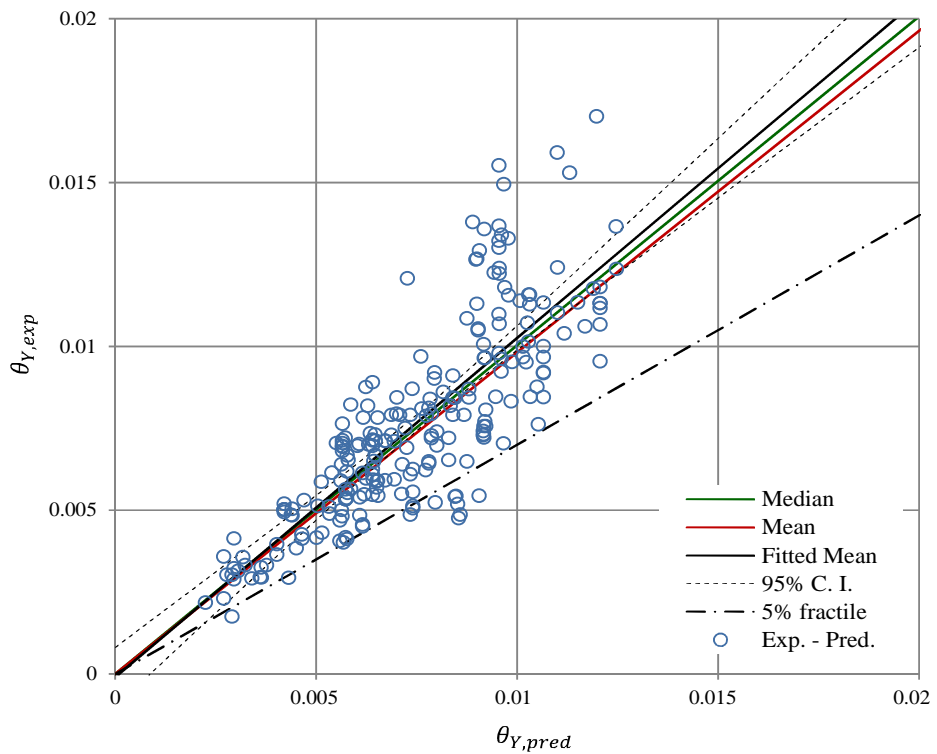
data-points indicates a p-value of 0.12, indicating that the hypothesis for homoscedasticity is not rejected.

In residual fitted plots, the line also oscillates about zero standardized residuals. In some plots, a slight twist is observed towards the ends, particularly where the data is less densely distributed. The Q-Q plot corresponding with the model in equation 6.9a indicates that the distribution of the residuals is characterised with heavy tails since the standardised residuals have an anti-clockwise twist. Moreover, less than 95% of the standardized residuals fall between ± 2 , and some residuals even reach 6. Hence the associated distribution of the residuals is not normally distributed. The value of some variables associated with these extreme residuals, fall beyond the 95% interval. The data-points are therefore excluded from the dataset for the regression analysis associated with equation 6.9b. The Q-Q plot corresponding with this model indicates negligible offset and 95% of the standardized residuals fall between ± 2 . Normal distribution is therefore assumed.

Statistics of test-to-predicted θ_Y are used to compare equations 6.9a and 6.9b. A summary of the statistics is given in Table 6-9. Plots of experimental θ_Y against predicted θ_Y , are shown in Figure 6-9. The model based on the exclusion of outliers and extreme data-points indicates improvement over the model based on the inclusion of outliers and extreme variables. In both cases, the fitted mean is closer to the median than the total mean. However, the dispersion between the three lines is larger in Figure 6-9.a corresponding with equation 6.9a, than in Figure 6-9.b corresponding with equation 6.9b. Similarly, the 95% confidence intervals are wider in the former than the latter. The mean, standard deviation and coefficient of variation associated with the model in equation 7.9b are 7%, 67% and 67% respectively lower than the corresponding values for the model in equation 7.9a. The 5% fractile factor is increased by 7%.



a



b

Figure 6-9. Experimental yield chord rotation of members plotted against predictions from a) equation 7.9a and b) equation 7.9b, based on the inclusion and exclusion of extreme data-points respectively. The chord rotation is a function of physical and material properties.

6.4.2 Chord Rotation at Maximum Force

Three empirical models that relate chord rotation at maximum force θ_m with explanatory variables describing material and geometrical properties are selected based on the process discussed in Chapter 5. Chord rotation at maximum force in terms of explanatory variables obtained from dimensional analysis is given by equation 6.10a. Chord rotation at maximum force in terms of explanatory variables used in literature is given by equation 6.10b. Chord rotation at maximum force in terms of explanatory variables obtained from dimensional analysis and include an energy dissipation term representing loading considerations is given by equation 6.10c.

$$\theta_m = \left(0.042 \cdot 0.359^{\log(\rho_T)} \cdot 0.365^{\log(\rho_w)} \cdot 0.526^{\log\left(\frac{s}{d_{bl}}\right)} \cdot 3.03^{\frac{c}{s}} \right)^{a_{sl}} \quad [6.10a]$$

$$\left(\frac{f_{tl}}{f'_c} \right)^{0.524} 0.153^v \rho_T^{0.565} \rho_w^{0.578} 0.136^{\frac{c}{s}}$$

$$\theta_m = \left(0.086 \cdot 4343^{\log\left(\frac{f_{tl}}{f_{yl}}\right)} \cdot 1.046^{\frac{f_{yl}}{f'_c}} \cdot 1.001^{\log(a\rho_s)} \cdot 2.777^{\log\left(\frac{L_s}{h}\right)} \right)^{a_{sl}} \quad [6.10b]$$

$$\left(\frac{f_{tl}}{f_{yl}} \right)^{-3.372} 0.122^v \rho_T^{0.332} \left(\frac{h}{L_s} \right)^{0.503} (a\rho_s)^{-0.0004} 0.963^{\frac{s}{d_{bl}}} 0.657^{\frac{c}{s}}$$

$$\theta_m = \left(0.011 \cdot 0.354^{\rho_T} \cdot 0.462^{\rho_w} \cdot 3.135^{\frac{c}{s}} \cdot 1.355^{\log\left(\frac{E}{bhsf'_c}\right)} \right)^{a_{sl}} \quad [6.10c]$$

$$\left(\frac{f_{tl}}{f'_c} \right)^{-0.415} 0.157^v \rho_T^{0.522} \rho_w^{0.572} 0.151^{\frac{c}{s}} \left(\frac{E}{bhsf'_c} \right)^{1.019}$$

Some explanatory variables, namely c/s and v are selected and feature in all three relationships. Equations 6.10a and 6.10c do not have a variable representing the aspect ratio of the column since this is not selected by stepwise regression approach. However, L_s/h is selected for equation 6.10b. Nevertheless, the latter does not incorporate a variable representing the longitudinal reinforcement whereas equations 6.10a and 6.10c include variable ρ_T . This variable is also included as an interaction term with bond-slip variable a_{sl} in both equations. A confinement variable in these two equations is represented by ρ_w , while in equation 6.10b confinement is represented by $a\rho_s$. Both variables are also included as interaction terms with a_{sl} for respective equations. The variable $a\rho_s$ does not feature with any normalised variable of confinement steel strength f_{yw} . Buckling effects are represented by s/d_{bl} in equations 6.10b and 6.10a. However, in the latter equation this variable features with the interaction term a_{sl} only. The strength of

longitudinal steel and concrete is represented by f_{tl}/f'_c in equation 6.10a and 6.10c. For these relationships, these properties are not represented with bond-slip interaction term a_{sl} . In equation 6.10b, f_{tl}/f_{yl} and f_{yl}/f'_c are used with interaction term a_{sl} , while the former is also incorporated alone. Equation 6.10c incorporates a normalised energy dissipation term $E/(bhsf'_c)$ representing loading considerations.

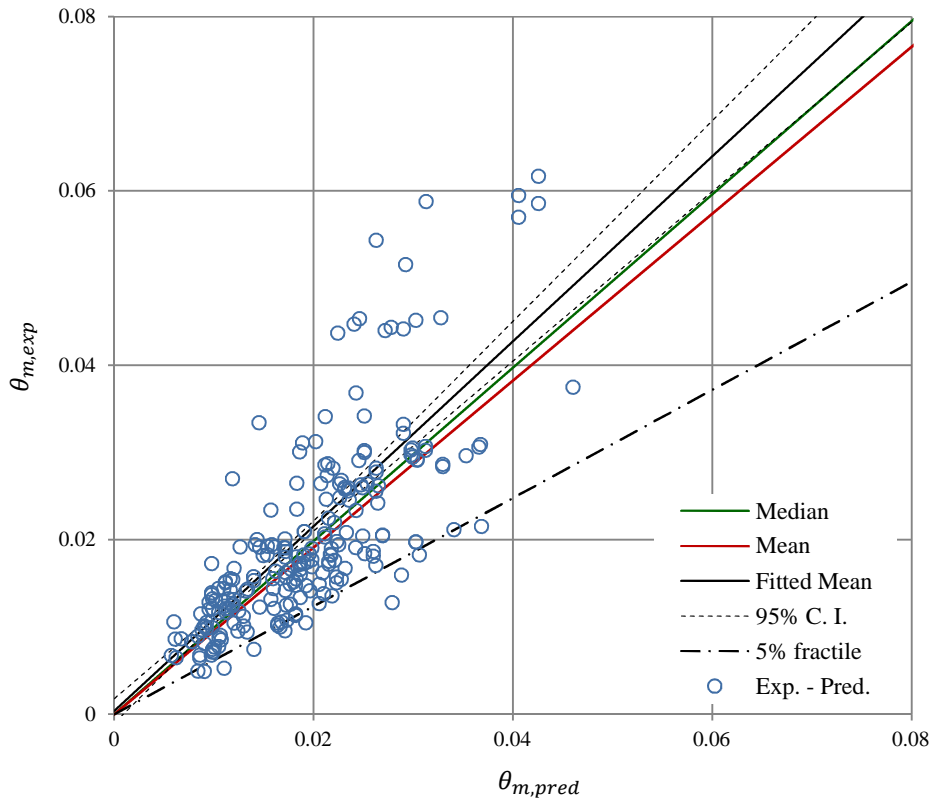
Trend in the relationship between explanatory variables constituting the equations, and rotation at maximum force are confirmed. As indicated in Appendix E Table E-2, the highest correlation with θ_m is exhibited by $E/(bhsf'_c)$ and v . The lowest correlations between θ_m , and explanatory variables in the equations refer to f_{tl}/f'_c , ρ_w , and c/s . The magnitude of the correlation between other variables with θ_m varies in between. In Appendix F, Figure F-2 scatter plots indicate that θ_m increases as ρ_w or $E/(bhsf'_c)$ increase, while θ_m decreases as v or s/d_{bl} increase.

Plots of single test series in Appendix G, Figure G-2 where only one variable is changed with θ_m further confirm trends of explanatory variables featuring in the empirical relationships. The statistical criteria are discussed in section 5.6. The trends indicate that θ_m increases with f_{tl}/f'_c , ρ_T or $E/(bhsf'_c)$ but decreases with v . An increase of θ_m is so observed with increasing ρ_w , however it is then observed to decrease as ρ_w increases when combined with the bond-slip interaction term a_{sl} . Similarly, θ_m decreases with increasing f_{tl}/f_{yl} , $a\rho_s$, c/s , s/d_{bl} or L_s/h , but increases with latter when they are combined with a_{sl} .

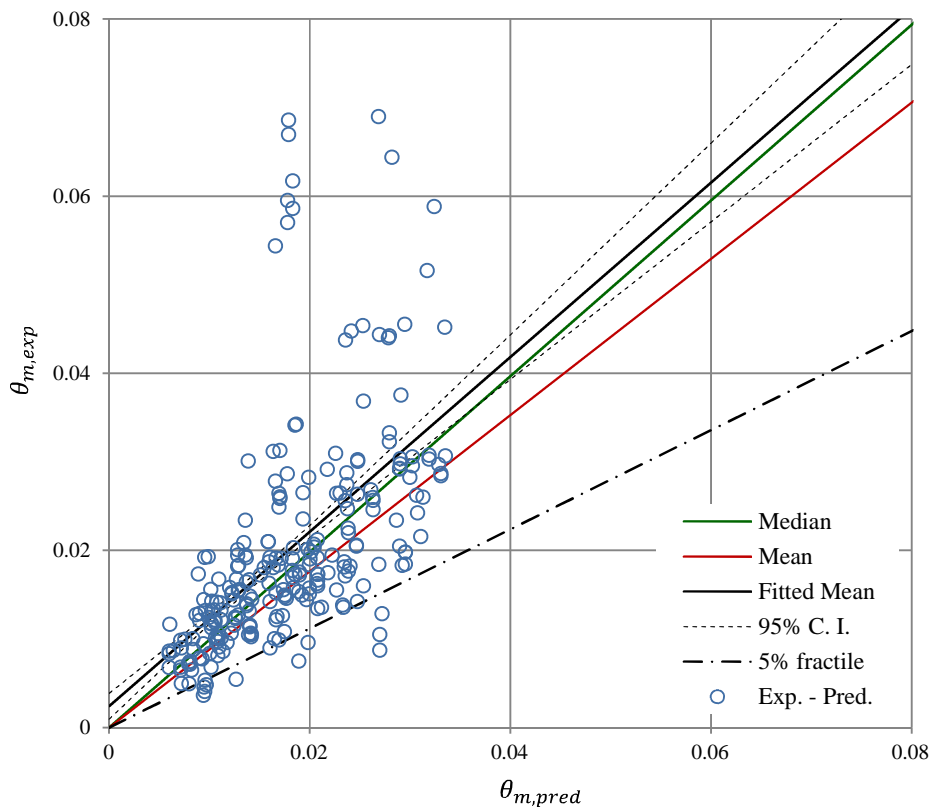
The residuals associated with the models are observed to satisfy criteria of normal distribution and homoscedasticity. A summary of diagnostics is shown in Appendix E.2. The mean line of the residuals is close to horizontal and oscillates around zero in residual-fitted plots. Similarly, the mean line is also relatively horizontal. However, in some plots, a slight twist is observed towards the ends, particularly where the data is less densely distributed. Normal distribution is considered since 95% of standardized residuals are observed to fall between ± 2 . A Breusch-Pagan test also further confirms homoscedasticity. However, the corresponding regression model for equation 6.10c satisfies the latter two criteria just within the limits.

Statistics of test-to-predicted θ_m are used to compare the corresponding three relationships. A summary of these statistics is given in Table 6-9. Corresponding plots of experimental θ_m against predicted θ_m are shown in Figure 6-10. In all the three cases, the median falls closer to the fitted mean than the total mean. Equation 6.10c has the lowest standard deviation (S.D.=0.26) while equation 7.10b has the highest standard deviation (S.D.=0.54) A similar trend is observed in the confidence interval. Equation 6.10c has the lowest value at CoV=26.4% while equation 6.10b has the largest value at CoV=47.5%. Equation 6.10a has the largest 5% fractile value possibly indicating less scatter. These statistical comparisons show that equation 7.10c provides the best

prediction followed by equation 6.10b. However, since the diagnostics of the former are just within limits, equation 6.10a is preferred.



a



b

Continued...

...Continued

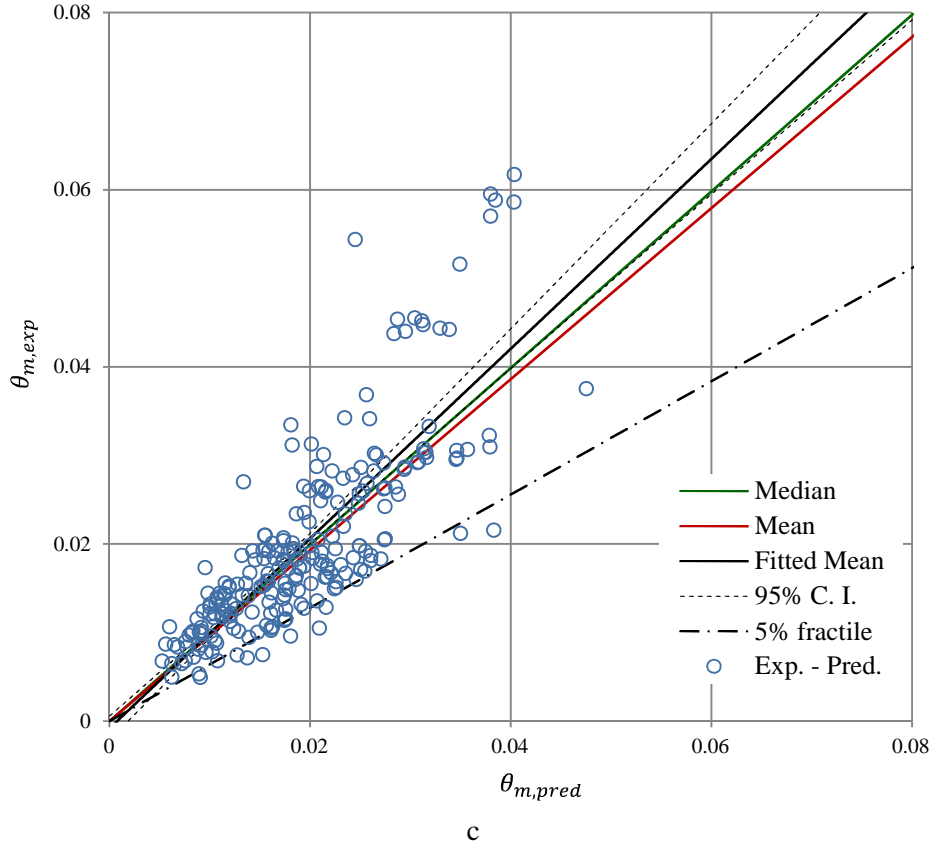


Figure 6-10 Experimental chord rotation at maximum force plotted against predictions from a) equation 7.10a – variables from dimension analysis b) equation 7.10b – variables as used in literature and c) equation 7.10c – includes an energy dissipation term.

6.4.3 Chord Rotation at 10% Maximum Force Reduction

Three empirical models that relate chord rotation at 10% maximum force reduction θ_{u-10} with explanatory variables describing material and geometrical properties are selected based on the process discussed in Chapter 5. Equation 6.11a describes the empirical relationship of θ_{u-10} in terms of explanatory variables obtained from dimensional analysis. Equation 6.11b describes the empirical relationship of θ_{u-10} in terms of explanatory variables used in literature. Chord rotation at maximum force in terms of explanatory variables obtained from dimensional analysis and include an energy dissipation term representing loading considerations is given by equation 6.11c.

$$\theta_{u-10} = \left(0.0593 \cdot 0.422^{\log(\rho_T)} \cdot 4.11^{\log\left(\frac{L_S}{s}\right)} \cdot 0.292^{\log(\omega_w)} \right)^{a_{sl}}$$

$$\left(\frac{f_t}{f'_c}\right)^{-1.364} \left(\frac{f_y}{f'_c}\right)^{1.634} 0.159^v \rho_T^{0.585} \left(\frac{L_S}{s}\right)^{-0.255} 4.366 \omega_w 0.96^{\frac{s}{d_{bl}}} 0.364^{\frac{c}{s}} \quad [6.11a]$$

$$\theta_{u-10} = \left(0.0848 \cdot 0.386^{\log(\rho_T)} \cdot 4.92^{\log\left(\frac{L_s}{h}\right)} \right)^{a_{sl}} \left(\frac{f_{tl}}{f_y} \right)^{-1.257} \left(\frac{f_{yl}}{f'_c} \right)^{0.357} 0.132^v \rho_T^{0.61} \left(\frac{L_s}{h} \right)^{-0.521} \times 10^{14})^a \rho_s 0.952^{\frac{s}{d_{bl}}} 0.522^{\frac{c}{s}} \quad (4.1) \quad [6.11b]$$

$$\theta_{u-10} = \left(0.043 \cdot 0.368^{\log(\rho_T)} \cdot 3.59^{\log\left(\frac{L_s}{s}\right)} \right)^{a_{sl}} \left(\frac{f_{tl}}{f'_c} \right)^{-0.455} 1.068^{\frac{f_{yl}}{f'_c}} 0.194^v \rho_T^{0.549} \left(\frac{L_s}{s} \right)^{-0.468} \rho_w^{0.235} 0.519^{\frac{c}{s}} \left(\frac{E}{bhsf'_c} \right)^{1.478} \quad [6.11c]$$

The variables f_{yl}/f'_c , v , ρ_T and c/s are selected and feature in all three empirical relationships. The variable ρ_T is also selected as an interaction term with bond-slip variable a_{sl} and features in all the three empirical relationships. An aspect ratio is also selected for each of the empirical relationships of θ_{u-10} . For equations 6.11a and 6.11c, L_s/s is selected both alone and as an interaction term with a_{sl} . The corresponding variable for equation 6.11b is L_s/h . For equations 6.11a and 6.11c, the maximum steel strength f_{tl} is normalised by f'_c , while for equation 6.11b, f_{tl} is normalised by f_{yl} . Confinement is represented by ω_w in equation 6.11a, by $a \rho_s$ in equation 6.11b and by ρ_w in equation 6.11c. The variable in equation 6.11a is also used as an interaction term with a_{sl} . The variable s/d_{bl} is also selected in equations 6.11a and 6.11b. None of the equations features a variable including the strength of the transverse reinforcement f_{yw} . In equation 6.11c, variable $E/(bhsf'_c)$ incorporates energy dissipation E and represents loading considerations.

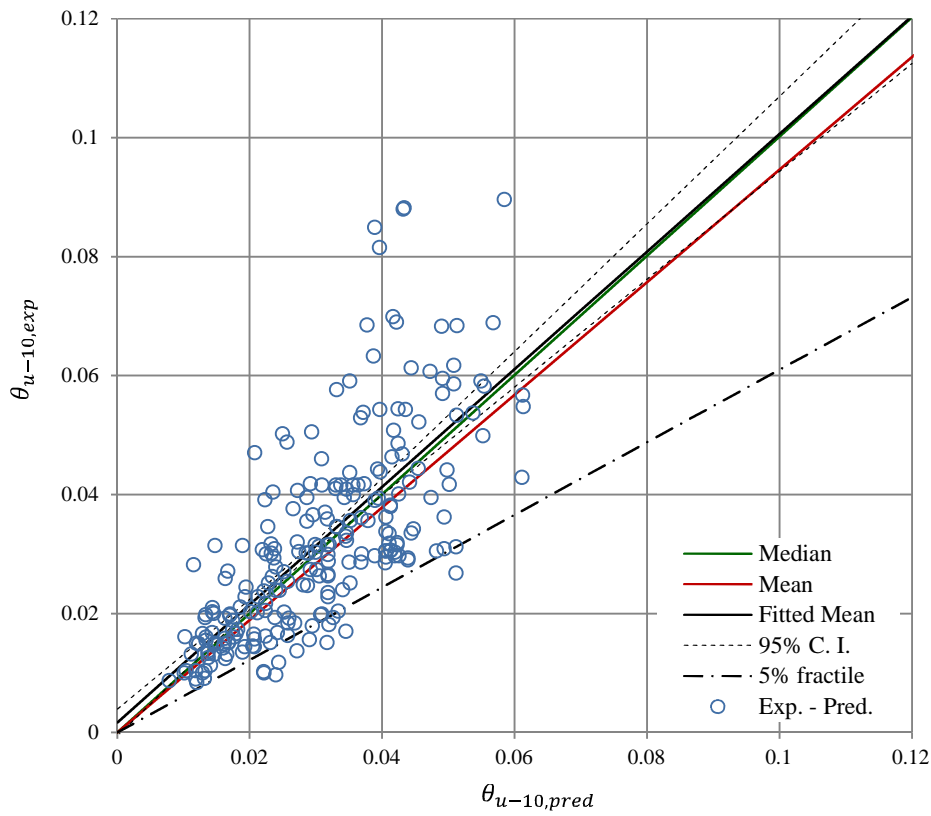
The trends in the relationship between explanatory variables constituting the equations, and θ_{u-10} are also observed through the process discussed in section 5.6. As indicated in Appendix E Table E-3, the largest Spearman correlation of θ_{u-10} is exhibited with $E/(bhsf'_c)$ and v respectively. The lowest correlations between θ_{u-20} , and explanatory variables in the equations refer to $a \rho_s$. In Appendix F, Figure F-3 scatter plots indicate that θ_{u-10} , increases as $E/(bhsf'_c)$ increases, while θ_{u-10} decreases as v or s/d_{bl} increase. The scatter in other plots is very wide to visually identify other trends.

The statistical criteria discussed in section 5.7.3 leads to the identification of trends by referring to plots of single test series where only one variable is changed with θ_{u-10} . Appendix G, Figure G-2 illustrates the plots for the explanatory variables selected in the equations. The trends indicate that θ_{u-10} increases with $E/(bhsf'_c)$, f_{yl}/f'_c , ω_w and $a \rho_s$, and decreases with increasing v , s/d_{bl} and f_{tl}/f'_c . A decreasing trend between θ_{u-10} and ω_w is observed when the latter is combined

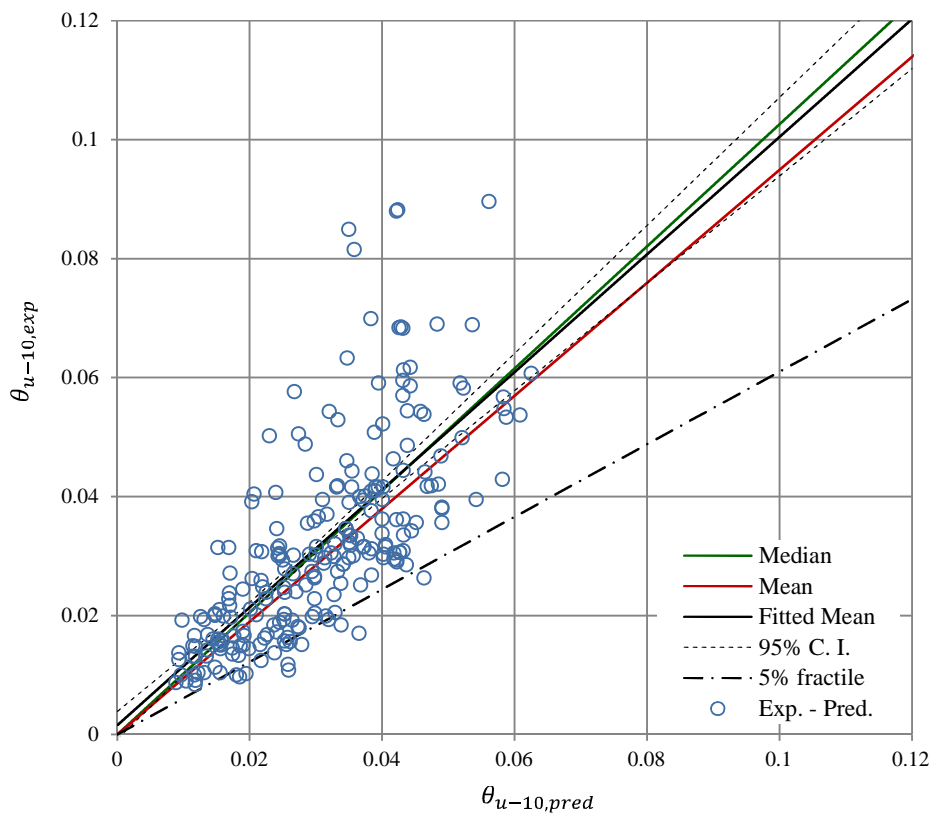
with the bond-slip interaction term a_{sl} . However, this trend was not confirmed using the specified statistical criteria due to the lack of identified pair of tests having only ω_w as a variable in common. The EDP θ_{u-10} is observed to decrease with c/s , L_s/s or L_s/h , however it is observed to increase when the aspect ratios are combined with a_{sl} . Although a trend is observed between θ_{u-10} and the interaction of c/s and a_{sl} the combination is not selected by the BIC in any of the regression models. The statistical significance of the observed trends of θ_{u-10} with ω_w and L_s/s are stronger than their corresponding trends of θ_{u-10} with a_{ρ_s} and L_s/h .

The linear regression criteria of homoscedasticity and normal distribution of the residuals with zero mean are verified. A summary of some of the diagnostics is shown in Appendix E.3. The trend line in residual-fitted plots and scale-location plots respectively is relatively horizontal. In residual fitted plots, the line also oscillates about zero standardized residuals. In some plots, a slight twist is observed towards the ends, particularly where the data is less densely distributed. However, the Breusch-Pagan test also confirms homoscedasticity. Normal distribution is considered since 95% of standardized residuals are observed to fall between ± 2 .

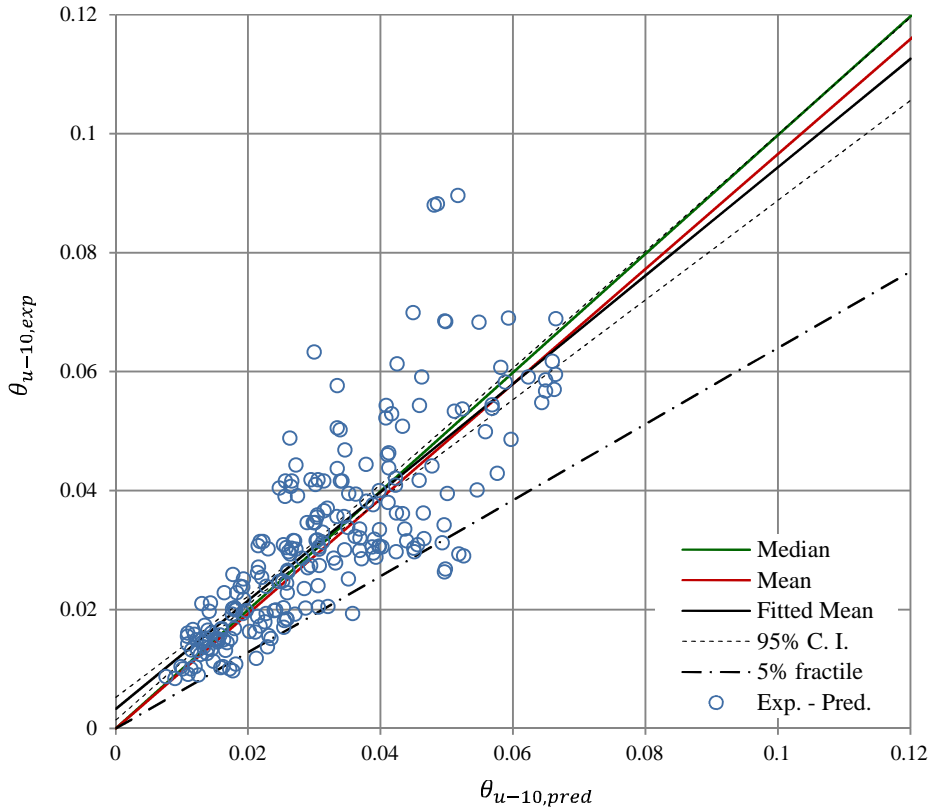
Statistics of test-to-predicted θ_{u-10} are used to compare the three empirical relationships. A summary of these statistics is given in Table 6-9. Plots of experimental θ_{u-10} against predicted θ_{u-10} are shown in Figure 6-11. The fitted mean is closer to the median than the total mean with the exception of the plot corresponding to equation 6.11c. In all three cases, the mean and median are very close to 1. The largest standard deviation is 0.37 and corresponds to equation 6.11b. The lowest standard deviation is 0.28 and corresponds to equation 6.11c. Similarly, the lowest CoV is 27.2% corresponding to equation 6.11a, while the highest is 35% corresponding to 6.11b. Equation 6.11a has the largest 5% fractile value possibly indicating less scatter, while equations 6.11a and 6.11b have similar values. These statistical comparisons show that equation 6.11c provides the best prediction, and equation 6.11a is slightly better than equation 6.11b.



a



b



c

Figure 6-11 Experimental chord rotation at 10% maximum force reduction plotted against predictions from a) equation 7.11a – variables from dimension analysis b) equation 7.11b – variables as used in literature and c) equation 7.11c – includes an energy dissipation term.

6.4.4 Chord Rotation at 20% Maximum Force Reduction

Three empirical models that relate chord rotation at 20% maximum force reduction θ_{u-20} with explanatory variables describing material and geometrical properties are selected based on the process discussed in Chapter 5. Equation 6.12a describes the empirical relationship of θ_{u-20} in terms of explanatory variables obtained from dimensional analysis. Equation 6.12b describes the empirical relationship of θ_{u-20} in terms of explanatory variables used in literature. Chord rotation at maximum force in terms of explanatory variables obtained from dimensional analysis and include an energy dissipation term representing loading considerations is given by equation 6.12c.

$$\theta_{u-20} = \left(0.0455 \cdot 0.264^{\log(\rho_T)} \cdot 2.31^{\log\left(\frac{L_S}{s}\right)} \right)^{a_{st}} \quad [6.12a]$$

$$\left(\frac{f_{tl}}{f'_c}\right)^{-1.129} \left(\frac{f_{yl}}{f'_c}\right)^{1.329} 0.166^v \rho_T^{0.569} \left(\frac{L_S}{s}\right)^{0.022} \omega_w^{0.165} 0.96^{\frac{s}{d_{bl}}} 0.446^{\frac{c}{s}} \quad [6.12b]$$

$$\theta_{u-20} = \left(0.0419 \cdot 0.367^{\log(\rho_T)} \cdot 12.2^{\log\left(\frac{L_S}{h}\right)} \cdot 0.965^{\frac{s}{d_{bl}}} \right)^{a_{st}}$$

$$\left(\frac{f_t}{f_y}\right)^{-0.942} \left(\frac{f_y}{f'_c}\right)^{0.209} 0.132^v \rho_T^{0.492} \left(\frac{L_s}{h}\right)^{-0.76} (1073)^{a \rho_s \frac{f_w}{f'_c}}$$

$$\theta_{u-20} = \left(0.012 \cdot 0.227^{\log(\rho_T)} \cdot 7.439^{\log\left(\frac{L_s}{s}\right)} \cdot 0.074^{\omega_w}\right)^{a_{sl}} \left(\frac{f_t}{f'_c}\right)^{-2.015} \left(\frac{f_y}{f'_c}\right)^{1.99}$$

$$0.183^v \rho_T^{0.508} \left(\frac{L_s}{s}\right)^{-0.601} 17.5^{\omega_w} 0.97^{\frac{s}{d_{bl}}} 0.305^{\frac{c}{s}} \left(\frac{E}{bhsf'_c}\right)^{0.138} \quad [6.12c]$$

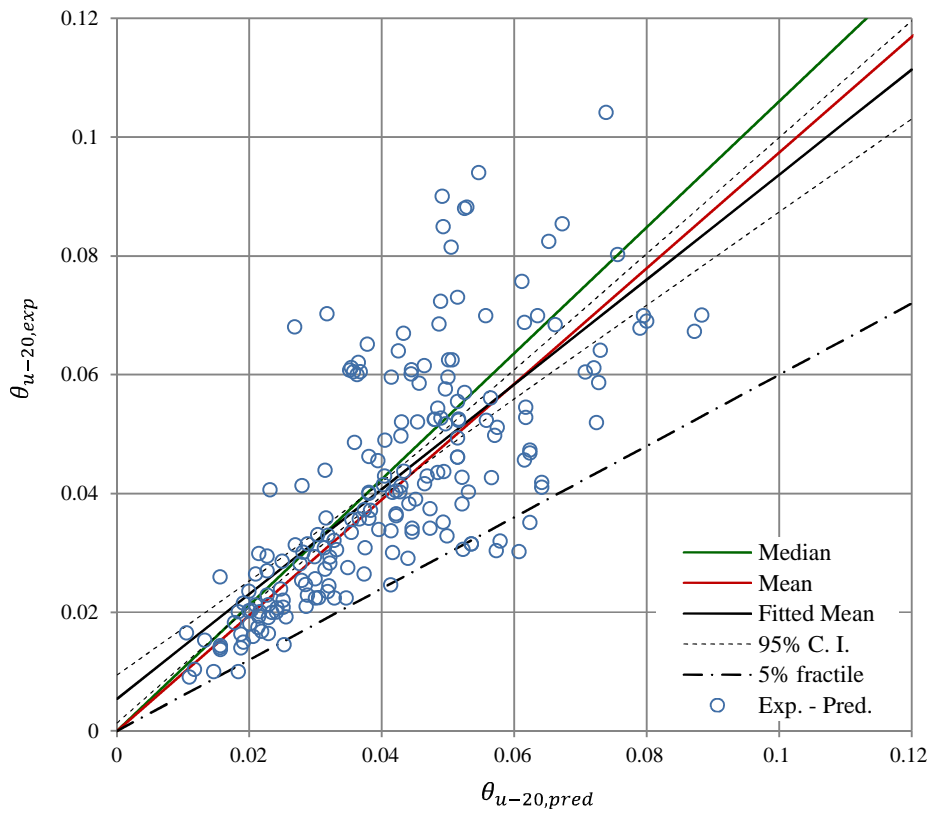
The variables f_{yl}/f'_c , v , and ρ_T are selected and feature in all three empirical relationships. The variable ρ_T is also selected as an interaction term with bond-slip variable a_{sl} . An aspect ratio is also selected for each of the empirical relationships of θ_{u-20} . For equations 6.12a and 6.12c, L_s/s is selected both alone and as an interaction term with a_{sl} . The corresponding variable for equation 6.12b is L_s/h . For equations 6.12a and 6.12c, the maximum steel strength f_{tl} is normalised by f'_c , while for equation 6.12b, f_{tl} is normalised by f_{yl} . Confinement is represented by ω_w in equation 6.12a and 6.12c, and by $a \rho_s f_{yw}/f'_c$ in equation 6.12b. The variable in equation 6.12c is also used as an interaction term with a_{sl} . The variable s/d_{bl} is also selected in equations 6.12a and 6.12b. The variables c/s and s/d_{bl} are selected in equations 6.12a and 6.12c. Variable s/d_{bl} is selected in equation 6.12b as an interaction term with a_{sl} . In equation 6.12c, variable $E/(bhsf'_c)$ incorporates energy dissipation E and represents loading considerations.

The trends in the relationship between explanatory variables constituting the equations, and θ_{u-20} are also observed through the process discussed in section 5.6. As indicated in Appendix E Table E-4, the largest Spearman correlation of θ_{u-20} is exhibited with $E/(bhsf'_c)$, v and s/d_{bl} respectively. The lowest correlation between θ_{u-20} , and explanatory variables in the equations refer to f_{tl}/f'_c , f_{tl}/f_{yl} , and f_{yl}/f'_c . In Appendix F, Figure F-4 scatter plots indicate that θ_{u-50} , increases as $E/(bhsf'_c)$ increases, while θ_{u-20} decreases as v or s/d_{bl} increase. The scatter in other plots is very wide to visually identify other trends.

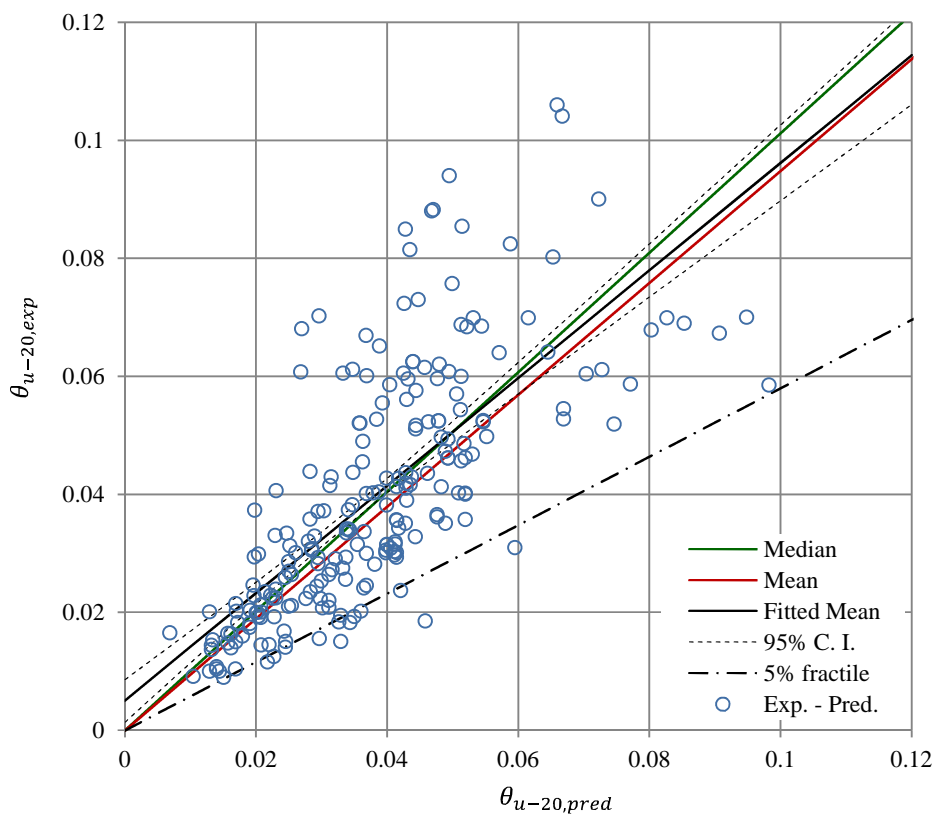
The statistical criteria discussed in section 5.7 leads to the identification of trends by referring to plots of single test series where only one variable is changed with θ_{u-20} . Appendix G, Figure G-4 illustrates the plots for the explanatory variables selected in the equations. The trends indicate that θ_{u-20} increases with $E/(bhsf'_c)$, f_{yl}/f'_c and $a \rho_s f_{yw}/f'_c$ and decreases with increasing v , s/d_{bl} and f_{tl}/f'_c . An increase of θ_{u-20} is also observed with increasing ω_w or ρ_T , however it is then observed to decrease as ω_w or ρ_T increase when combined with the bond-slip interaction term a_{sl} . Similarly, θ_{u-50} decreases with increasing L_s/s , L_s/h or c/s but increases with the latter when they are combined with a_{sl} . The statistical significance of the observed trends of θ_{u-20} with ω_w and L_s/s are stronger than their corresponding trends of θ_{u-20} with $a \rho_s f_{yw}/f'_c$ and L_s/h .

The linear regression criteria of homoscedasticity and normal distribution of the residuals with zero mean are verified. A summary of some of the diagnostics is shown in Appendix H.4. The trend line in residual-fitted plots and scale-location plots respectively is relatively horizontal for the regression models corresponding to equations 6.12a, 6.12b and 6.12c. In residual fitted plots corresponding with these models, the line also oscillates about zero standardized residuals. In some plots, a slight twist is observed towards the right ends. However, the Breusch-Pagan test also confirms homoscedasticity. Normal distribution is considered since 95% of standardized residuals are observed to fall between ± 2 .

Statistics of test-to-predicted θ_{u-20} are used to compare the three empirical relationships. A summary of these statistics is given in Table 6.9. Plots of experimental θ_{u-20} against predicted θ_{u-20} are shown in Figure 6-12. The fitted mean is closer to the total mean than the median. In most cases, the mean and median are very close to 1. However, the median corresponding with equation 6.12a is slightly lower with respect to the others. The largest standard deviation is 0.38 and corresponds to equation 6.12b. The lowest standard deviation is 0.32 and corresponds to equation 6.12a. Similarly, the lowest CoV is 31.6% corresponding to equation 6.12a, while the highest is 35% corresponding to 6.12b. The standard deviation and CoV corresponding to equation 6.12c are very close to equation 6.12a. Although equation 6.12a has the largest 5% fractile value where $\theta_{u-20,exp} = 0.6 \theta_{u-20,pred}$, the other two relationships have similar values. In spite of having the worst median, all the other statistical considerations of equation 6.12a are better than equations 6.12b and 6.12c. However, the statistics of equation 6.12c are very close to those of 6.12a.



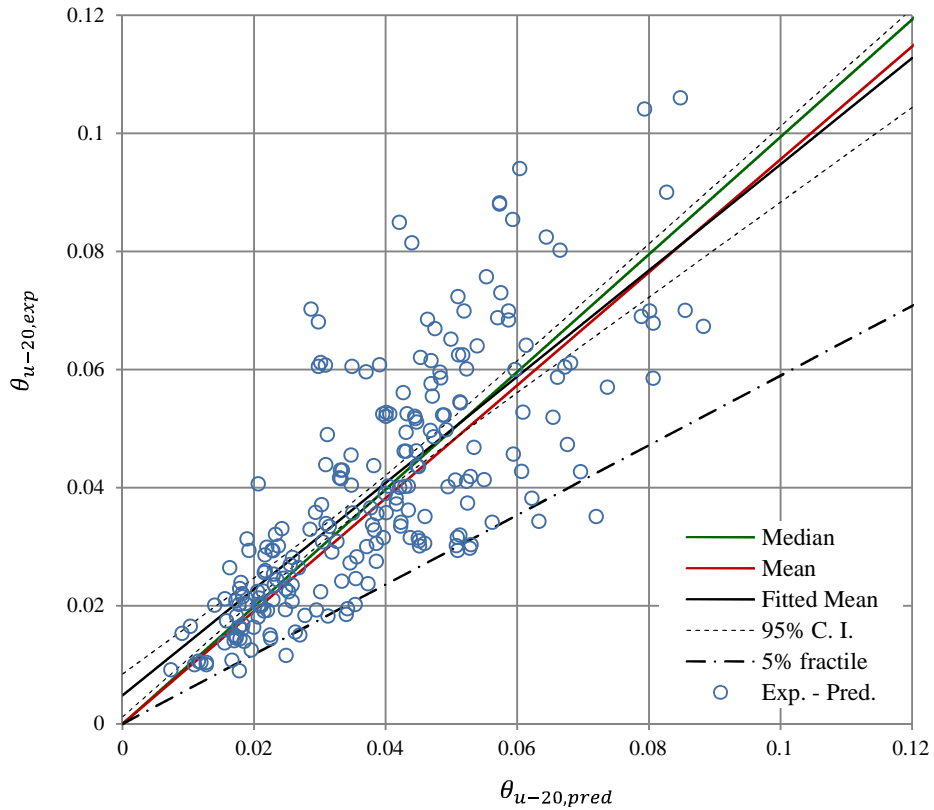
a



b

Continued...

...Continued



c

Figure 6-12 Experimental chord rotation at 20% maximum force reduction plotted against predictions from a) equation 7.12a – variables from dimension analysis b) equation 7.12b – variables as used in literature and c) equation 7.11c – includes an energy dissipation term.

6.4.5 Chord Rotation at 50% Maximum Force Reduction

Three empirical models that relate chord rotation at 50% maximum force reduction θ_{u-50} with explanatory variables describing material and geometrical properties are selected based on the process discussed in Chapter 5. Equation 6.13a. describes the empirical relationship of θ_{u-50} in terms of explanatory variables obtained from dimensional analysis. Equation 6.13b describes the empirical relationship of θ_{u-50} in terms of explanatory variables used in literature. Chord rotation at maximum force in terms of explanatory variables obtained from dimensional analysis and include an energy dissipation term representing loading considerations is given by equation 6.13c.

$$\theta_{u-50} = (0.0455 \cdot 0.372^{\log(\rho_T)})^{\alpha_{sl}}$$

$$\left(\frac{f_{tl}}{f'_c}\right)^{-1.056} \left(\frac{f_{yl}}{f'_c}\right)^{1.1} 0.102^v \rho_T^{0.562} \left(\frac{L_s}{s}\right)^{0.341} \omega_w^{0.376} 0.41^{\frac{c}{s}} \quad [6.13a]$$

$$\theta_{u-50} = \left(0.271 \cdot 9.662^{\log\left(\frac{L_s}{h}\right)} \right)^{a_{sl}} \quad [6.13b]$$

$$0.458^{\frac{f_{tl}}{f_y}} 0.115^v \rho_T^{0.215} (3227)^a \rho_s^{\frac{f_w}{f_c}} 0.977^{\frac{s}{d_{bl}}}$$

$$\theta_{u-50} = \left(0.0315 \cdot 0.341^{\log(\rho_T)} \cdot 6.697^{\log\left(\frac{L_s}{s}\right)} \cdot 0.044^{\omega_w} \right)^{a_{sl}} \quad [6.13c]$$

$$\left(\frac{f_t}{f_c}\right)^{-1.985} \left(\frac{f_y}{f_c}\right)^{1.88} 0.139^v \rho_T^{0.515} \left(\frac{L_s}{s}\right)^{-0.47} 52.29^{\omega_w} 0.338^{\frac{c}{s}} \left(\frac{E}{bhsf_c}\right)^{0.108}$$

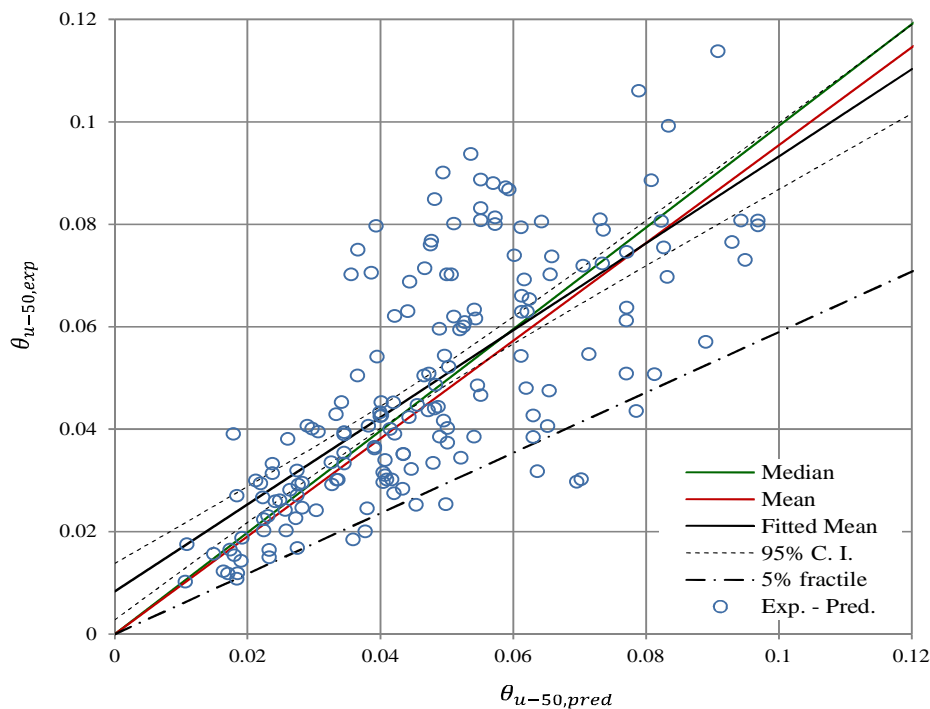
The variables f_{yl}/f_c' , v , and ρ_T are selected and feature in all three empirical relationships. For equations 6.13a and 6.13c, the aspect ratio selected is L_s/s . The corresponding variable for equation 6.13b is L_s/h . For equations 6.13a and 6.13c, the maximum steel strength f_{tl} is normalised by f_c' , while for equation 6.13b, f_{tl} is normalised by f_{yl} . Confinement is represented by ω_w in equation 6.13a and 6.13c, and by $a \rho_s f_{yw}/f_c'$ in equation 6.13b. The variable in equation 6.13c is also used as an interaction term with a_{sl} . The variable s/d_{bl} is also selected in equation 6.13b and variable c/s is selected in equations 6.13a and 6.13c. In equation 6.13c, variable $E/(bhsf_c')$ incorporates energy dissipation E and represents loading considerations.

The trends in the relationship between explanatory variables constituting the equations, and θ_{u-50} are also observed through the process discussed in section 5.6 As indicated in Appendix E Table E-5 with θ_{u-50} , the largest Spearman correlation is exhibited with $E/(bhsf_c')$ and v . The lowest correlations between θ_{u-50} , and explanatory variables in the equations refer to f_{tl}/f_c' , f_{tl}/f_{yl} , and f_{yl}/f_c' . In Appendix F, Figure C-5 scatter plots indicate that θ_{u-50} , increases as $E/(bhsf_c')$ increase, while θ_{u-50} , decreases as v or s/d_{bl} increase. The scatter in other plots is very wide to visually identify other trends.

The statistical criteria discussed in section 5.7 leads to the identification of trends by referring to plots of single test series where only one variable is changed with θ_{u-50} . Appendix G, Figure G-5 illustrates the plots for the explanatory variables selected in the equations. The trends indicate that θ_{u-50} increases with $E/(bhsf_c')$, f_{yl}/f_c' and $a \rho_s f_{yw}/f_c'$ and decreases with increasing v , s/d_{bl} and f_{tl}/f_c' . An increase of θ_{u-50} is also observed with increasing ω_w or ρ_T , however it is then observed to decrease as ω_w or ρ_T increase when combined with the bond-slip interaction term a_{sl} . Similarly, θ_{u-50} decreases with increasing L_s/s or L_s/h , but increases with latter when they are combined with a_{sl} . Variable $a \rho_s f_{yw}/f_c'$ is also observed to decrease when combined with interaction term a_{sl} . The statistical significance of the observed trends of θ_{u-50} with ω_w and L_s/s are stronger than their corresponding trends of θ_{u-50} with $a \rho_s f_{yw}/f_c'$ and L_s/h .

The linear regression criteria of homoscedasticity and normal distribution of the residuals with zero mean are verified. A summary of some of the diagnostics is shown in Appendix E.5. The trend line in residual-fitted plots and scale-location plots is relatively horizontal for the regression models corresponding to equations 6.13a, 6.13b and 6.13c. In residual fitted plots corresponding with these models, the line also oscillates about zero standardized residuals. In some plots, a slight twist is observed towards the left ends, particularly where the data is less dense. However, the Breusch-Pagan test also confirms homoscedasticity. Normal distribution is considered since 95% of standardized residuals are observed to fall between ± 2 . However, a slight clockwise twist is observed in the distribution on the QQ plot. As discussed in section 5.7.4, this indicates that the distribution has slightly short tails. This is not considered very significant since most of the twist occurs in the region beyond ± 2 where less than 5% of the standardised residuals fall.

Statistics of test-to-predicted θ_{u-50} are used to compare the three empirical relationships. A summary of these statistics is given in Table 6-9. Plots of experimental θ_{u-50} against predicted θ_{u-50} are shown in Figure 6-13. The fitted mean is closer to the total mean than the median. In most cases, the mean and median are very close to 1. The largest standard deviation is 0.34 and corresponds to equation 7.13a. The lowest standard deviation is 0.31 and corresponds to equations 6.13b and 6.13c. The lowest CoV is 29.7% corresponding to equation 6.13c, while the highest is 32.4% corresponding to 6.13a. Equation 6.13b has the largest 5% fractile value where $\theta_{u-50,exp} = 0.63 \theta_{u-50,pred}$. These statistics are very close and none is observed to be superior over another.



a

Continued...

...Continued

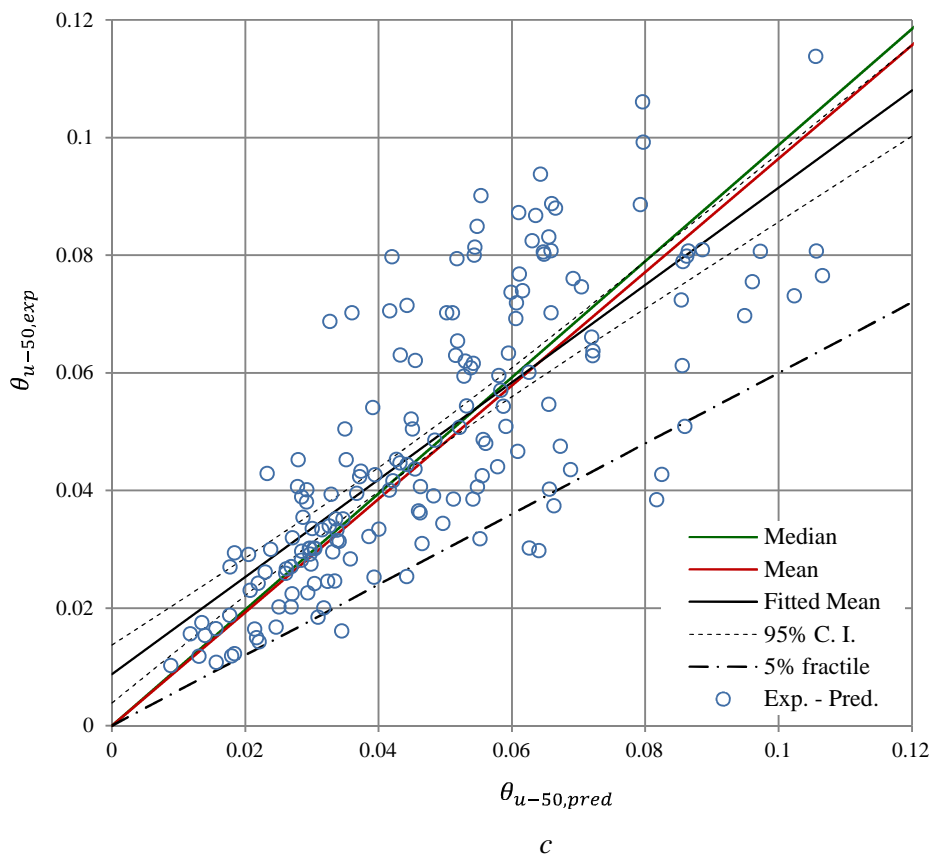
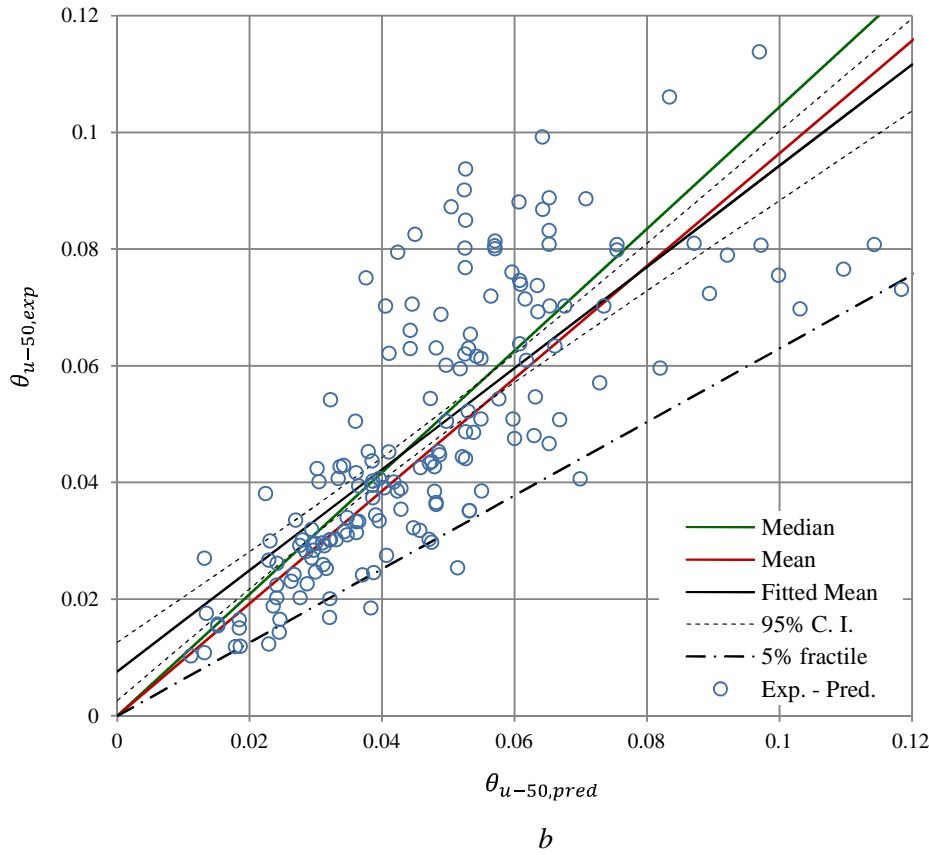


Figure 6-13 Experimental chord rotation at 50% maximum force reduction plotted against predictions from a) equation 7.13a – variables from dimension analysis b) equation 7.11b – variables as used in literature and c) equation 7.13c – includes an energy dissipation term.

6.5 Stiffness Ratio Model

6.5.1 Stiffness Ratio at Yielding

Two empirical models that relate the stiffness ratio rotation at yielding EI_Y/EI_g with explanatory variables describing material and geometrical properties selected based on the process discussed in Chapter 5. are presented. In one model, the regression was based on data that included outliers and extreme variables, and in the other, based on data that excluded them. These models refer to equations 6.14a and 6.14b respectively

$$\frac{EI_Y}{EI_g} = 0.256 \left[0.53^{\log \frac{f_y}{f'_c}} \cdot 1.256^{\log v} \cdot 3.21^{\log \frac{L_s}{h}} \cdot 0.02^{\log \frac{b}{h}} \right]^{a_{sl}} \quad [6.14a]$$

$$\left(\frac{f_y}{f'_c} \right)^{-0.207} 5.18^v \left(\frac{L_s}{h} \right)^{0.3} \left(\frac{b}{h} \right)^{1.52}$$

$$\frac{EI_Y}{EI_g} = 0.254 \left[0.6^{\log \frac{f_y}{f'_c}} \cdot 1.235^{\log v} \cdot 2.48^{\log \frac{L_s}{h}} \cdot 0.023^{\log \frac{b}{h}} \right]^{a_{sl}} \quad [6.14b]$$

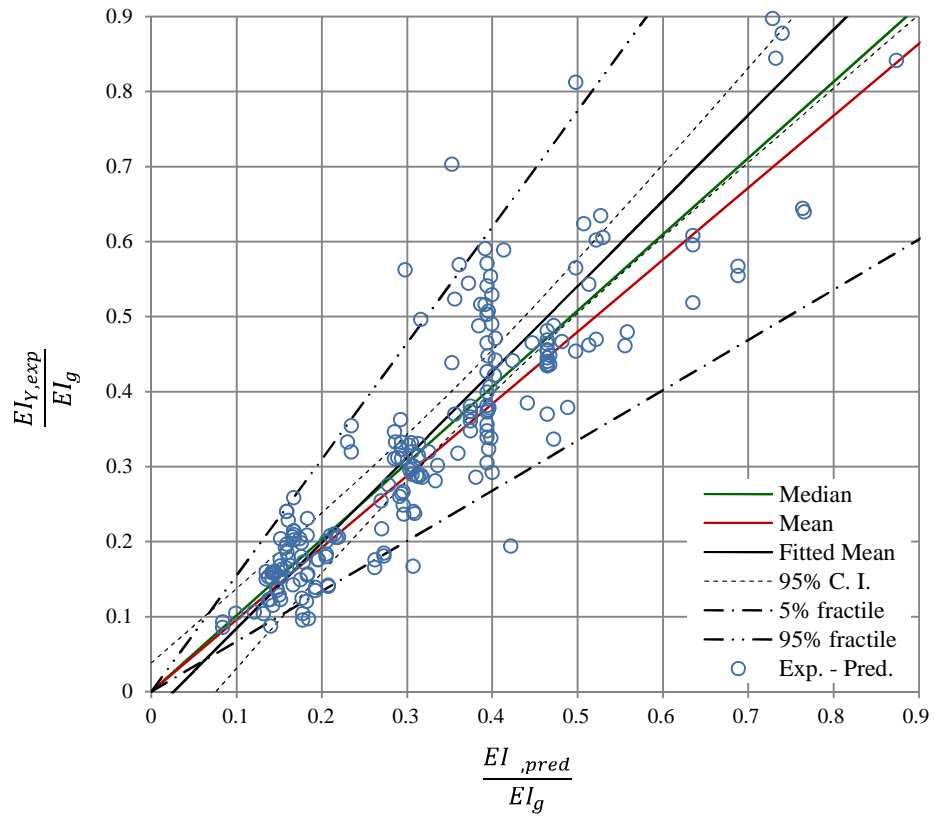
$$\left(\frac{f_y}{f'_c} \right)^{-0.203} 5.08^v \left(\frac{L_s}{h} \right)^{0.3} \left(\frac{b}{h} \right)^{1.5}$$

The trends in the relationship between explanatory variables constituting the equations, and EI_Y/EI_g are also observed through the process discussed in section 5.6. As indicated in Appendix E Table E-6, the largest Spearman correlation of EI_Y/EI_g is exhibited with v , while the lowest correlation is exhibited with $(L_s + a_v z)/h$. In Appendix I, Figure I-6 scatter plots indicate that EI_Y/EI_g , increases as L_s/h or v increases, while EI_Y/EI_g , decreases as f_{yl}/f'_c increases. The statistical criteria discussed in section leads to the identification of trends by referring to plots of single test series where only one variable is changed with EI_Y/EI_g . Appendix G, Figure G-6 illustrates the plots for the explanatory variables selected in the equations. The trends indicate that EI_Y/EI_g increases with increasing L_s/h or v and decreases with f_{yl}/f'_c . These trends are observed both when these variables are used alone or when combined separately as an interaction term with a_{sl} . The variable b/h increases with EI_Y/EI_g when considered alone. When b/h is combined with a_{sl} as an interaction term, the inverse of this trend is observed. This last trend is only based on a few but consistent observations since, only a few pair of tests in the database have b/h as the only common variable and $a_{sl} = 1$.

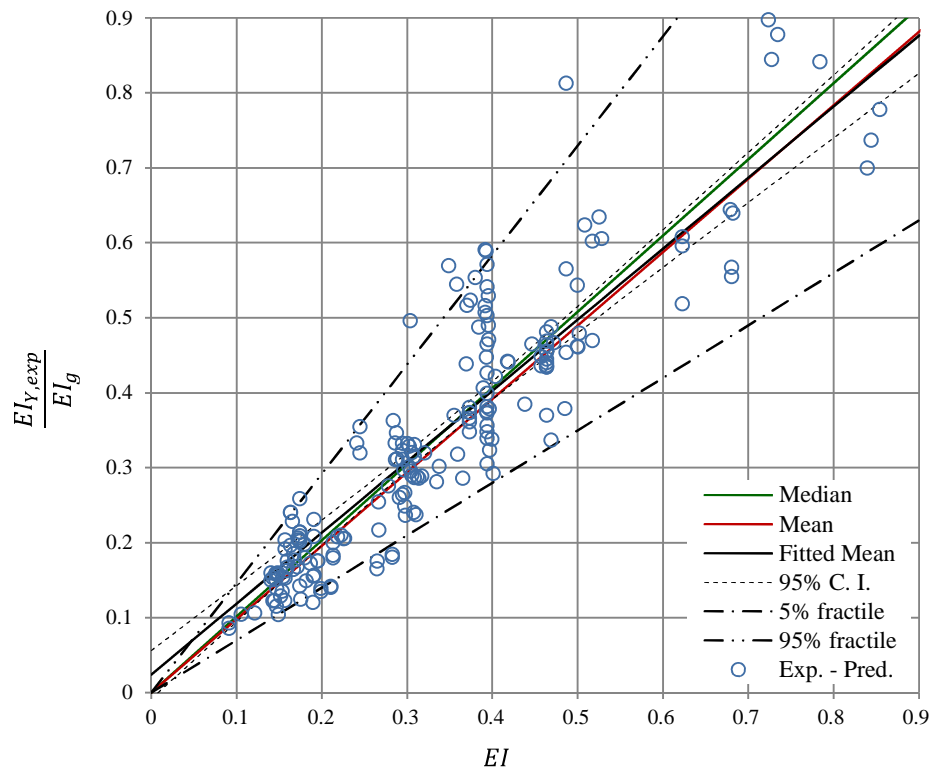
The linear regression criteria for homoscedasticity and normal distribution of the residuals with zero mean are checked. A summary of some of the diagnostics is shown in Appendix I.2. The trend lines in residual-fitted plots and scale-location plots corresponding with equation 6.14a is characterised with heavy twisting particularly on the right. Moreover, the p-value of the Breusch-Pagan test is 0.55 indicating that the model of EI_Y/EI_g , based on data that includes outliers and

extreme variables is characterised with heteroscedasticity. The degree of twisting is less in the in residual-fitted plots and scale-location plots corresponding with equation 6.14b. Moreover, the Breusch-Pagan test also confirms homoscedasticity in the latter. In the Q-Q plot corresponding with equation 6.14a. Moreover, less than 95% of the standardised residuals fall within ± 2 , and some even reach 6. As a result, the residuals associated with equation 6.14a are not normally distributed. A smaller degree of offset is observed in the Q-Q plot corresponding with equation 6.14b, and more than 95% of the standardised residuals fall within ± 2 .

Statistics of test-to-predicted EI_Y/EI_g are used to compare equations 6.14a and 6.14b. A summary of these statistics is given in Table 6-10. Plots of experimental EI_Y/EI_g against predicted EI_Y/EI_g are shown in Figure 6-14. The model based on the exclusion of outliers and extreme data-points indicates improvement over the model based on the inclusion of outliers and extreme variables. The dispersion between the three lines is larger in Figure 6-14a corresponding with equation 6.14a, than in Figure 6-14b corresponding with equation 6.14b. Similarly, the 95% confidence intervals are wider in the former than the latter. The standard deviation, coefficient of variation and the 95% fractile factor associated with the model in equation 6.14b are respectively 32%, 31% and 2% lower than the corresponding values for the model in equation 6.14a. The 5% fractile factor is increased by more than 4%. Hence, the model based on the exclusion of outliers and extreme data-points indicates improvement over the model based on the inclusion of outliers and extreme variables in terms of all these statistical considerations.



a



b

Figure 6-14. Experimental yield stiffness ratio plotted against predictions from a) equation 7.14a and b) equation 7.14b, based on the inclusion and exclusion of extreme data-points respectively. The stiffness ratio is a function of physical and material properties.

6.5.2 Stiffness Ratio at Maximum Force

Two empirical models that relate the stiffness ratio rotation at maximum force EI_m/EI_g with explanatory variables describing material and geometrical properties selected based on the process discussed in Chapter 5 are presented. In one model, the regression was based on data that included outliers and extreme variables, and in the other, based on data that excluded them. These models refer to equations 6.15a and 6.15b respectively.

$$\frac{EI_m}{EI_g} = 0.155 \cdot \left[0.98 \frac{f_{tl}}{f'_c} 1.375^{\log v} \cdot 1.09 \frac{L_s}{h} \right]^{a_{sl}} \quad [6.15a]$$

$$\left(\frac{f_{tl}}{f'_c} \right)^{-0.408} 6.19^v 1.23 \frac{L_s}{h}$$

$$\frac{EI_m}{EI_g} = 0.174 \cdot \left[0.98 \frac{f_{tl}}{f'_c} 1.401^{\log v} \cdot 1.11 \frac{L_s}{h} \right]^{a_{sl}} \quad [6.15b]$$

$$\left(\frac{f_{tl}}{f'_c} \right)^{-0.414} 5.18^v 1.22 \frac{L_s}{h}$$

The trends in the relationship between explanatory variables constituting the equations, and EI_m/EI_g are also observed through the process discussed in section 5.6. As indicated in Appendix B TableB-7, the largest Spearman correlation of EI_m/EI_g is exhibited with v . The correlation with L_s/h and f_{tl}/f'_c is however not much less. In Appendix F, Figure F-7 scatter plots indicate that EI_m/EI_g , increases as L_s/h or v increases, while EI_m/EI_g , decreases as f_{tl}/f'_c increases. The statistical criteria discussed in section 5.7 leads to the identification of trends by referring to plots of single test series where only one variable is changed with EI_m/EI_g . Appendix G, Figure G-7 illustrates the plots for the explanatory variables selected in the equations. The trends indicate that EI_m/EI_g increases with increasing L_s/h or v and decreases with f_{tl}/f'_c . These observations are valid for both situations where variables are considered alone or combined separately with a_{sl} .

The linear regression criteria for homoscedasticity and normal distribution of the residuals with zero mean are checked. A summary of some of the diagnostics is shown in Appendix I.2. The trend line is relatively horizontal in residual-fitted plots and scale location plots. In residual-fitted plots the line varies around zero. However, the trend line of the residuals and standardized residuals in fitted plots twists slightly at the edges where the data is less dense. Nevertheless, the Breusch-Pagan test also confirms homoscedasticity. In the Q-Q plot corresponding with equation 6.15a, a considerable offset is observed on the left side. Moreover, less than 95% of the standardised residuals fall within ± 2 , and some even reach ± 4 . As a result, the residuals associated with equation 6.15a are not normally distributed. Normal distribution of the residuals associated

with equation 6.15b is assumed. In spite of the twist observed on the right of the corresponding QQ plot, this is very small and occurs beyond ± 2 where less than 5% of the standardised residuals fall.

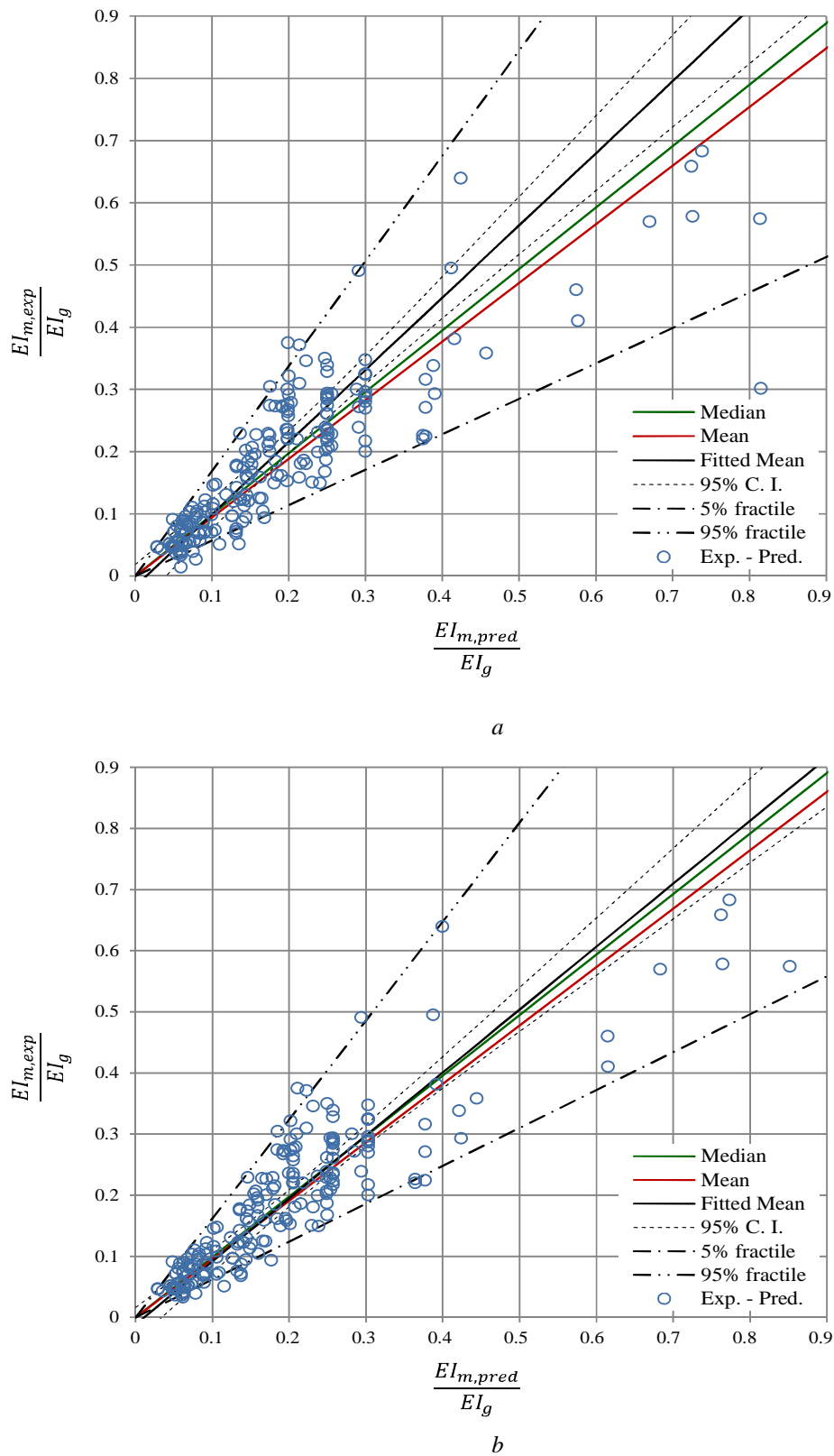


Figure 6-15 Experimental stiffness ratio at maximum force plotted against predictions from a) equation 7.15a and b) equation 7.15b, based on the inclusion and exclusion of extreme data-points respectively. The stiffness ratio is a function of physical and material properties.

Statistics of test-to-predicted EI_m/EI_g are used to compare equations 6.15a and 6.15b. A summary of these statistics is given in Table 6-10. Plots of experimental EI_m/EI_g against predicted EI_m/EI_g , are shown in Figure 6-15. In both cases, the fitted mean is closer to the median than the total mean. The median and total mean in Figure 6-10b corresponding with equation 6.15b are closer to the fitted mean than the median and total mean in Figure 6-10a corresponding with equation 6.15a. However, as shown in Table 6-10, the mean and median are very close to 1 in both cases. Equation 6.15b is based on 2.7% data-points less than equation 6.15a due to removed outliers and extreme variables. There is an improvement in the standard deviation and coefficient of variation associated with the model in equation 6.15b over the model in equation 6.15a, since these are lower by 14% and 12%. The model for equation 6.15b also provides a considerably lower BIC value. Moreover, the 5% fractile is increased by 9% and the 95% fractile reduced by 4% for the model associated with equation 6.15b. These statistical considerations are evidence of the improvement of the model in equation 6.15b over the model in equation 6.15a.

6.5.3 Stiffness Ratio at 10% Maximum Force Reduction

Two empirical models that relate the stiffness ratio rotation at 10% maximum force reduction EI_{u-10}/EI_g with explanatory variables describing material and geometrical properties selected based on the process discussed in Chapter 5. are presented. In one model, the regression was based on data that included outliers and extreme variables, and in the other, based on data that excluded them. These models refer to equations 6.16a and 6.16b respectively.

$$\frac{EI_{u-10}}{EI_g} = 0.0177 \cdot \left[0.945 \frac{L_s}{h} \right]^{a_{sl}} \quad [6.16a]$$

$$0.957 \frac{f_{tl}}{f'_c} 15.9^v 1.429 \frac{L_s}{h} \left(\frac{s}{d_{bl}} \right)^{0.183} (3.0 \times 10^{-15})^{a_{\rho_s}}$$

$$\frac{EI_{u-10}}{EI_g} = 0.02 \cdot \left[0.947 \frac{L_s}{h} \right]^{a_{sl}} \quad [6.16b]$$

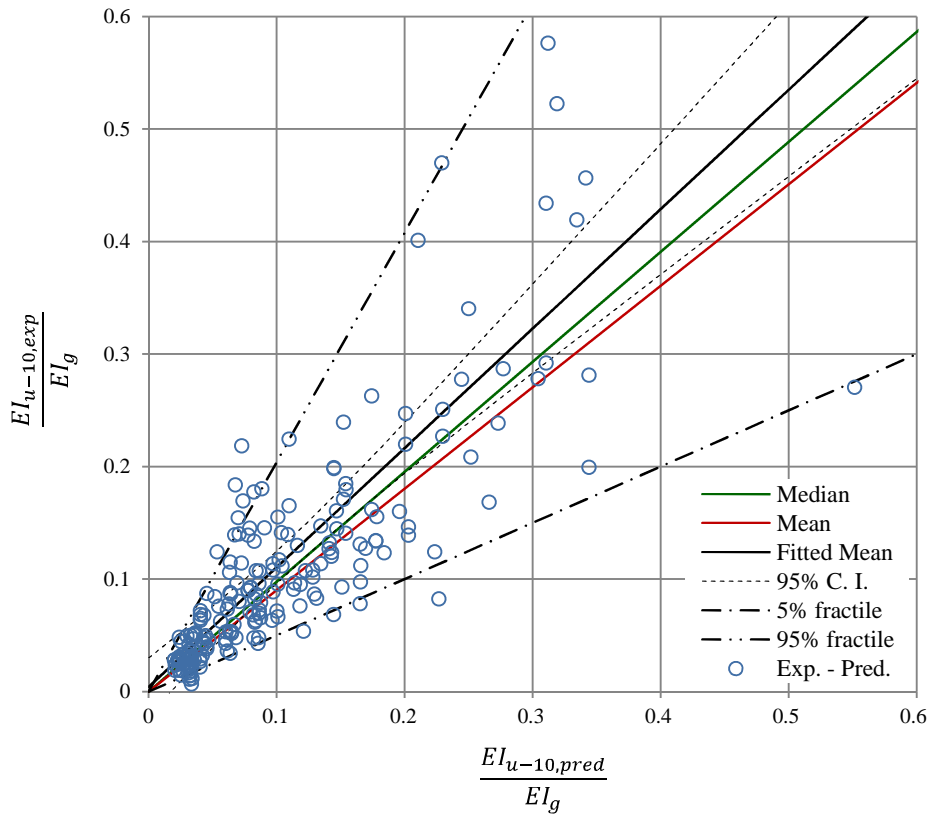
$$0.957 \frac{f_{tl}}{f'_c} 16.7^v 1.414 \frac{L_s}{h} \left(\frac{s}{d_{bl}} \right)^{0.139} (2.4 \times 10^{-18})^{a_{\rho_s}}$$

The trends in the relationship between explanatory variables constituting the equations, and EI_{u-10}/EI_g are also observed through the process discussed in section 5.6. As indicated in Appendix E Table E-8, the largest Spearman correlation of EI_{u-10}/EI_g is exhibited with v followed by L_s/h . The lowest correlation of EI_{u-10}/EI_g is exhibited with s/d_{bl} . In Appendix F, Figure F-8 scatter plots indicate that EI_{u-10}/EI_g , increases as L_s/h or v increases, while EI_{u-10}/EI_g , decreases as f_{tl}/f'_c or a_{ρ_s} increases.

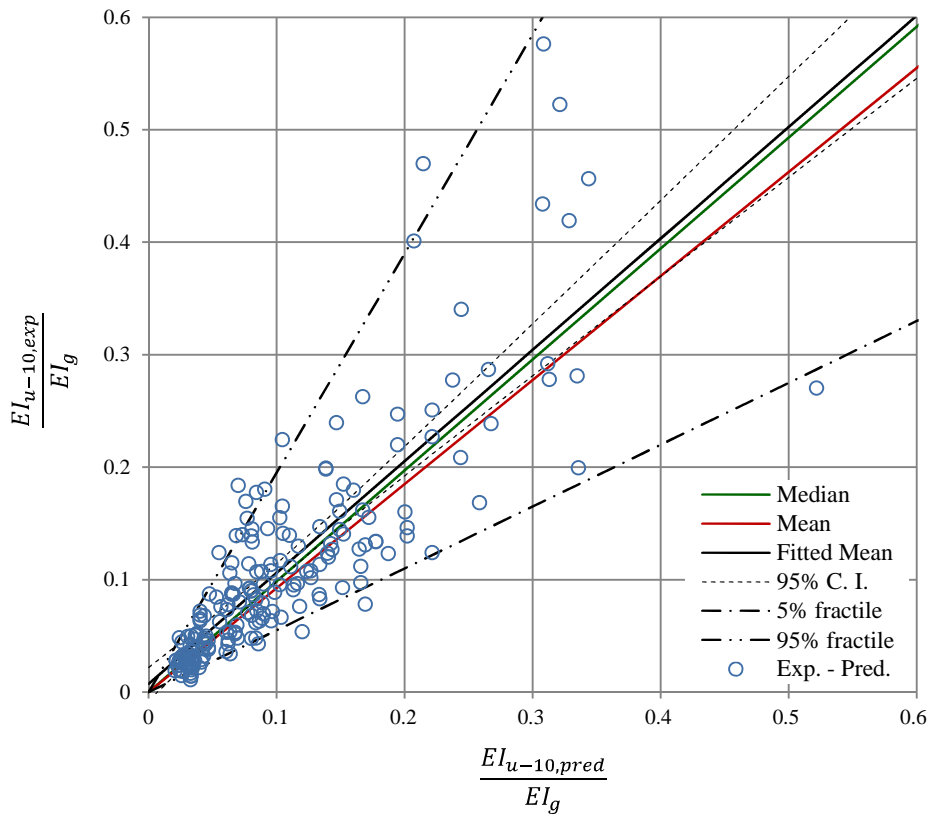
The statistical criteria discussed in section 5.7 leads to the identification of trends by referring to plots of single test series where only one variable is changed with EI_{u-10}/EI_g . Appendix G, Figure G-8 illustrates the plots for the explanatory variables selected in the equations. The trends indicate that EI_{u-10}/EI_g increases with increasing L_s/h , v or s/d_{bl} and decreases with $a \rho_s$ or f_{tl}/f'_c . When included as an interaction term combined with a_{sl} , the trend of EI_{u-10}/EI_g with L_s/h , s/d_{bl} or $a \rho_s$ is the opposite of that already specified. However, the interaction term of a_{sl} combined with s/d_{bl} and $a \rho_s$ was not selected to feature in the model.

The linear regression criteria for homoscedasticity and normal distribution of the residuals with zero mean are checked. A summary of some of the diagnostics is shown in Appendix I.3. The trend line is relatively horizontal in residual-fitted plots and scale location plots. In residual-fitted plots the line varies around zero. The Breusch-Pagan test also confirms homoscedasticity in both sets of residuals associated with equation 6.16a and 6.16b. More than 95% of the standardised residuals associated with both equations fall within ± 2 . However an offset is observed in the Q-Q plot associated with equation 6.16a, and one point reaches a value of +4. The data-point associated with this outlier, is eliminated from the dataset as an extreme data-point for the regression associated with equation 6.16b.

Statistics of test-to-predicted EI_{u-10}/EI_g are used to compare equations 6.16a and 6.16b. A summary of these statistics is given in Table 6-10. Plots of experimental EI_{u-10}/EI_g against predicted EI_{u-10}/EI_g are indicated in Figure 6-16. In both cases the fitted mean is closer to the median than the total mean. The median and total mean in Figure 6-16b corresponding with equation 6.16b are closer to the fitted mean than the median and total mean in Figure 6-16a corresponding with equation 6.16a. However, as shown in Table 6-10, the mean and median are very close to 1 in both cases. Equation 6.16b is based on 2.9% data-points less than equation 6.16a due to the removed outliers and extreme variables. There is an improvement in the standard deviation and coefficient of variation associated with the model in equation 6.16b over the model in equation 6.16a, since these are lower by 22% and 20% respectively. The model for equation 6.16b also provides a considerably lower BIC value. Moreover, the 5% fractile value is increased by 10% and the 95% fractile value reduced by 4% for the model associated with equation 6.16b. These statistical considerations are evidence of the improvement of the model in equation 6.16b over the model in equation 6.16a.



a



b

Figure 6-16 Experimental stiffness ratio at 10% maximum force reduction plotted against predictions from a) equation 7.16a and b) equation 7.16b, based on the inclusion and exclusion of extreme data-points respectively. The stiffness ratio is a function of physical and material properties.

6.5.4 Stiffness Ratio at 20% Maximum Force Reduction

Two empirical models that relate the stiffness ratio rotation at 10% maximum force reduction EI_{u-20}/EI_g with explanatory variables describing material and geometrical properties selected based on the process discussed in Chapter 5. are presented. In one model, the regression was based on data that included outliers and extreme variables, and in the other, based on data that excluded them. These models refer to equations 6.17a and 6.17b respectively.

$$\frac{EI_{u-20}}{EI_g} = 0.0345 \left[1.387^{\log v} \cdot (1.95 \times 10^{10})^{\rho_T} \cdot 9.35 \times 10^{-4} \frac{c}{h} \right]^{a_{sl}} \quad [6.17a]$$

$$\left(\frac{f_{tl}}{f'_c} \right)^{-0.704} 8.325^v 1.327^{\frac{L_s}{h}} (5.2 \times 10^{-7})^{\rho_T} (a\rho_s)^{-0.077} 498 \frac{c}{h}$$

$$\frac{EI_{u-20}}{EI_g} = 0.046 \left[2.252^{\log v} \cdot (2.2 \times 10^{10})^{\rho_T} \cdot 0.0128 \frac{c}{h} \right]^{a_{sl}} \quad [6.17b]$$

$$\left(\frac{f_{tl}}{f'_c} \right)^{-0.716} 4.716^v 1.32^{\frac{L_s}{h}} (2.23 \times 10^{-7})^{\rho_T} (a\rho_s)^{-0.089} 106 \frac{c}{h}$$

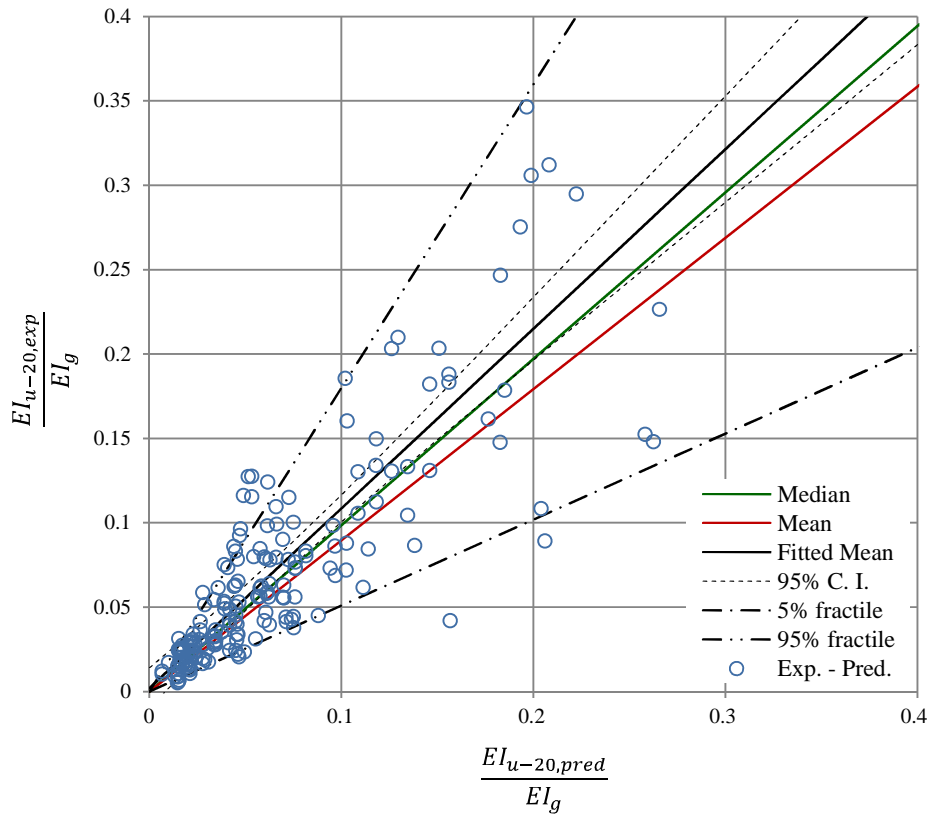
The trends in the relationship between explanatory variables constituting the equations, and EI_{u-20}/EI_g are also observed through the process discussed in section 5.6. As indicated in Appendix E Table E-9, the largest Spearman correlation of EI_{u-20}/EI_g is exhibited with v followed by L_s/h . The lowest correlation of EI_{u-20}/EI_g is exhibited with c/h and ρ_T . In Appendix F, Figure F-9 scatter plots indicate that EI_{u-20}/EI_g , increases as L_s/h or v increases, while EI_{u-20}/EI_g , decreases as f_{tl}/f'_c increases. However, scatter plots are not clear for c/h , ρ_T and $a\rho_s$.

The statistical criteria discussed in section 5.6 leads to the identification of trends by referring to plots of single test series where only one variable is changed with EI_{u-20}/EI_g . Appendix G, Figure G-9 illustrates the plots for the explanatory variables selected in the equations. The trends indicate that EI_{u-20}/EI_g increases with increasing L_s/h , v or c/h and decreases with ρ_T , $a\rho_s$ or f_{tl}/f'_c . When included as an interaction term combined with a_{sl} , the trend of EI_{u-20}/EI_g with c/h , L_s/h or ρ_T is the opposite of that already specified. The interaction term of a_{sl} combined with v is the same as that already specified when the explanatory variable is included in the model alone. The trends involving c/h alone, and ρ_T combined with a_{sl} are based on a number of consistent observations, however, the 95% significance criteria could not be applied due to a small number of identified pairs of tests with only the respective variable changed.

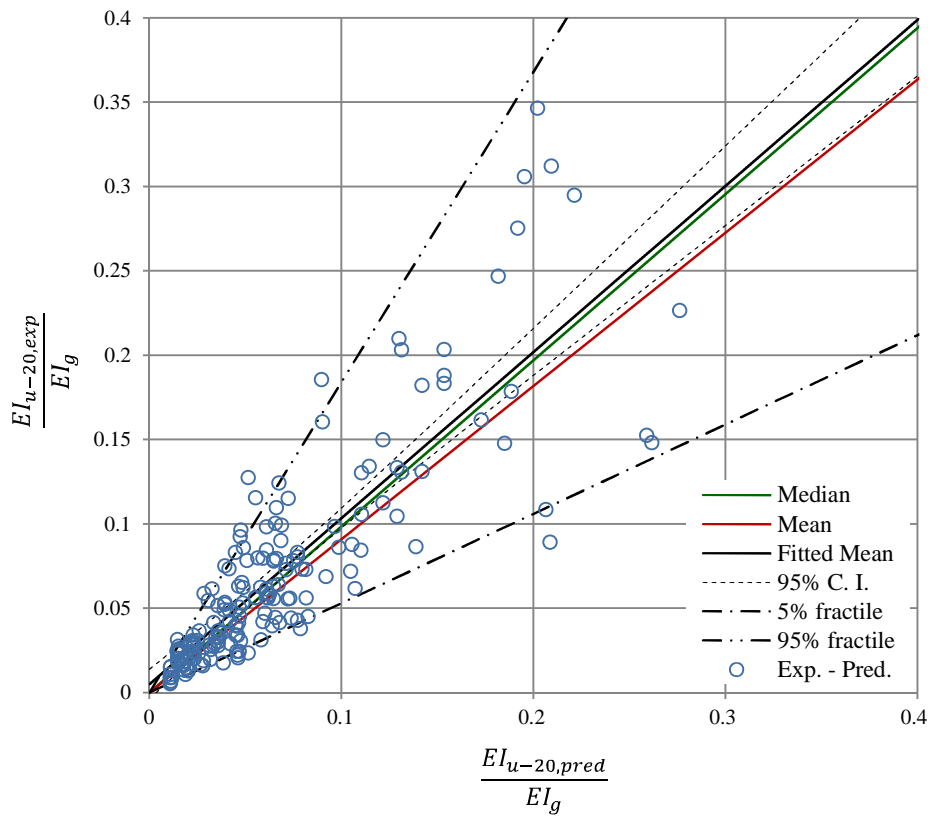
The linear regression criteria for homoscedasticity and normal distribution of the residuals with zero mean are checked. A summary of some of the diagnostics is shown in Appendix I.4. The trend line is relatively horizontal in residual-fitted plots and scale location plots. However, a slight

twist is observed particularly in the scale-location plots. In residual-fitted plots the line varies around zero. The Breusch-Pagan test also confirms homoscedasticity in both sets of residuals associated with equation 6.17a and 6.17b. Although 95% of the standardised residuals of the regression associated with equation 6.17a, fall between ± 2 , some points reach a value of 3 and are offset in the corresponding Q-Q plot. More than 95% of the standardized residuals of the regression associated with equation 7.17b fall between ± 2 . Although a slight twist is observed in the Q-Q plot, this only occurs beyond ± 2 for less than 5% of the data.

Statistics of test-to-predicted EI_{u-20}/EI_g are used to compare equations 6.17a and 6.17b. A summary of these statistics is given in Table 6-10. Plots of experimental EI_{u-20}/EI_g against predicted EI_{u-20}/EI_g are indicated in Figure 6-17. In both cases, the fitted mean is closer to the median than the total mean. The median and total mean in Figure 6-17b corresponding with equation 6.17b are closer to the fitted mean than the median and total mean in Figure 6-17a corresponding with equation 6.17a. However, as shown in Table 6-10, the mean and median are very close to 1 in both cases. Equation 6.17b is based on 3.5% data-points less than equation 6.17a due to the removed outliers and extreme variables. There is an improvement in the standard deviation and coefficient of variation associated with the model in equation 6.17b over the model in equation 6.17a, since these are lower by 11% and 9% respectively. The model for equation 6.17b also provides a considerably lower BIC value. Moreover, the 5% fractile value is increased by 4% and the 95% fractile value reduced by 12% for the model associated with equation 6.17b. These statistical considerations are evidence of the improvement of the model in equation 6.17b over the model in equation 6.17a.



a



b

Figure 6-17 Experimental stiffness ratio at 20% maximum force reduction plotted against predictions from a) equation 7.17a and b) equation 7.17b, based on the inclusion and exclusion of extreme data-points respectively. The stiffness ratio is a function of physical and material properties.

6.5.5 Stiffness Ratio at 50% Maximum Force Reduction

Two empirical models that relate the stiffness ratio rotation at 10% maximum force reduction EI_{u-20}/EI_g with explanatory variables describing material and geometrical properties selected based on the process discussed in Chapter 5. are presented. In one model, the regression was based on data that included outliers and extreme variables, and in the other, based on data that excluded them. These models refer to equations 6.18a and 6.18b respectively.

$$\frac{EI_{u-50}}{EI_g} = 0.00436 \cdot \left[1.666^{\log v} \cdot 0.805^{\frac{L_s}{h}} \cdot (8.86 \times 10^8)^{\rho_T} \cdot 0.55^{\log \frac{c}{h}} \right]^{a_{sl}} \cdot \left(\frac{f_{tl}}{f'_c} \right)^{-0.7} \cdot 9.325^v \cdot \left(\frac{L_s}{h} \right)^{1.77} \cdot (9.3 \times 10^{-5})^{\rho_T} \cdot \left(a \rho_s \frac{f_{yw}}{f'_c} \right)^{-0.186} \quad [6.18a]$$

$$\frac{EI_{u-50}}{EI_g} = 0.00631 \cdot \left[2.175^{\log v} \cdot 0.836^{\frac{L_s}{h}} \cdot (3.47 \times 10^7)^{\rho_T} \cdot 0.541^{\log \frac{c}{h}} \right]^{a_{sl}} \cdot \left(\frac{f_{tl}}{f'_c} \right)^{-0.67} \cdot 6.435^v \cdot \left(\frac{L_s}{h} \right)^{1.567} \cdot (3.9 \times 10^{-5})^{\rho_T} \cdot \left(a \rho_s \frac{f_{yw}}{f'_c} \right)^{-0.19} \quad [6.18b]$$

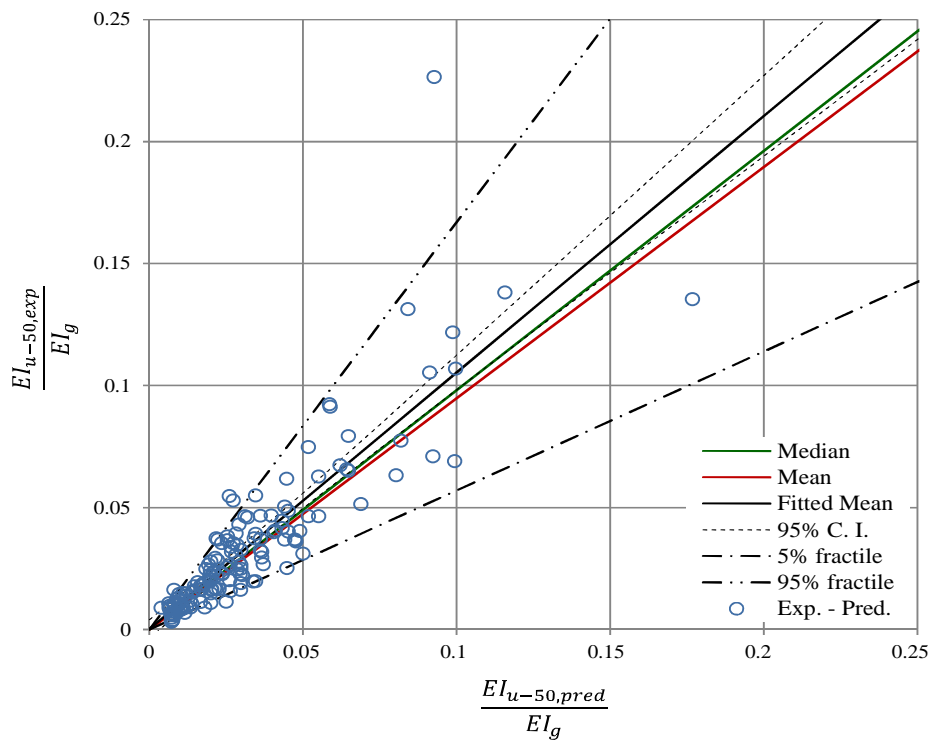
The trends in the relationship between explanatory variables constituting the equations, and EI_{u-50}/EI_g are also observed through the process discussed in section 5.6. As indicated in Appendix B Table B-10, the largest Spearman correlation of EI_{u-50}/EI_g is exhibited with v and the lowest correlation with ρ_T . In Appendix F, Figure F-10 scatter plots indicate that EI_{u-50}/EI_g , increases as L_s/h , $a \rho_s f_{yw}/f'_c$ or v increase, while EI_{u-50}/EI_g , decreases as f_{tl}/f'_c or ρ_T increase. The scatter plot for c/h does not indicate a clear trend.

The statistical criteria discussed in section 5.7 leads to the identification of trends by referring to plots of single test series where only one variable is changed with EI_{u-50}/EI_g . Appendix G, Figure G-10 illustrates the plots for the explanatory variables selected in the equations. The trends indicate that EI_{u-50}/EI_g increases with increasing L_s/h , v or c/h and decreases with ρ_T , $a \rho_s f_{yw}/f'_c$ or f_{tl}/f'_c . When included as an interaction term combined with a_{sl} , the trend of EI_{u-50}/EI_g with c/h , L_s/h or ρ_T is the opposite of that already specified. The interaction term of a_{sl} combined with v is the same as that already specified when the explanatory variable is included in the model alone. The trends involving ρ_T or L_s/h combined with a_{sl} are based on a number of consistent observations, however, the 95% significance criteria could not be applied due to a small number of identified pairs of tests with only the respective variable changed.

The linear regression criteria for homoscedasticity and normal distribution of the residuals with zero mean are checked. A summary of some of the diagnostics is shown in Appendix I.5. The trend line is relatively horizontal in residual-fitted plots and scale location plots. However, a slight twist is observed on the left in the plots associated with equation 7.18a. In residual-fitted plots the line varies around zero. The Breusch-Pagan test also confirms homoscedasticity in both sets of

residuals associated with equation 6.18a and 6.18b. More than 95% of the standardized residuals of the regression associated with equation 6.18b fall between ± 2 and residuals are assumed normally distributed. Although 95% of the standardised residuals of the regression associated with equation 6.18a fall between ± 2 , some points reach a value of 3.5 and are offset in the corresponding Q-Q plot. These residuals are associated with data-points that are considered outliers in the dataset for the regression analysis of equation 6.18b.

Statistics of test-to-predicted EI_{u-50}/EI_g are used to compare equations 6.18a and 6.18b. A summary of these statistics is given in Table 6-10. Plots of experimental EI_{u-50}/EI_g against predicted EI_{u-50}/EI_g are indicated in Figure 6-18. In both cases, the fitted mean is closer to the median than the total mean. The median and total mean in Figure 6-18b corresponding with equation 6.18b are closer to the fitted mean than the median and total mean in Figure 6-18a corresponding with equation 6.18a. However, as shown in Table 6-10, the mean and median are very close to 1 in both cases. Equation 6.18b is based on 4.1% data-points less than equation 6.18a due to the removed outliers and extreme variables. There is an improvement in the standard deviation and coefficient of variation associated with the model in equation 6.18b over the model in equation 6.18a, since these statistics are both lower by 11%. The model for equation 6.18b also provides a considerably lower BIC value. Moreover, the 5% fractile value is increased by 4% and the 95% fractile value reduced by 2% for the model associated with equation 6.18b. These statistical considerations are evidence of the improvement of the model in equation 6.18b over the model in equation 6.18a.



a
... Continued

Continued...

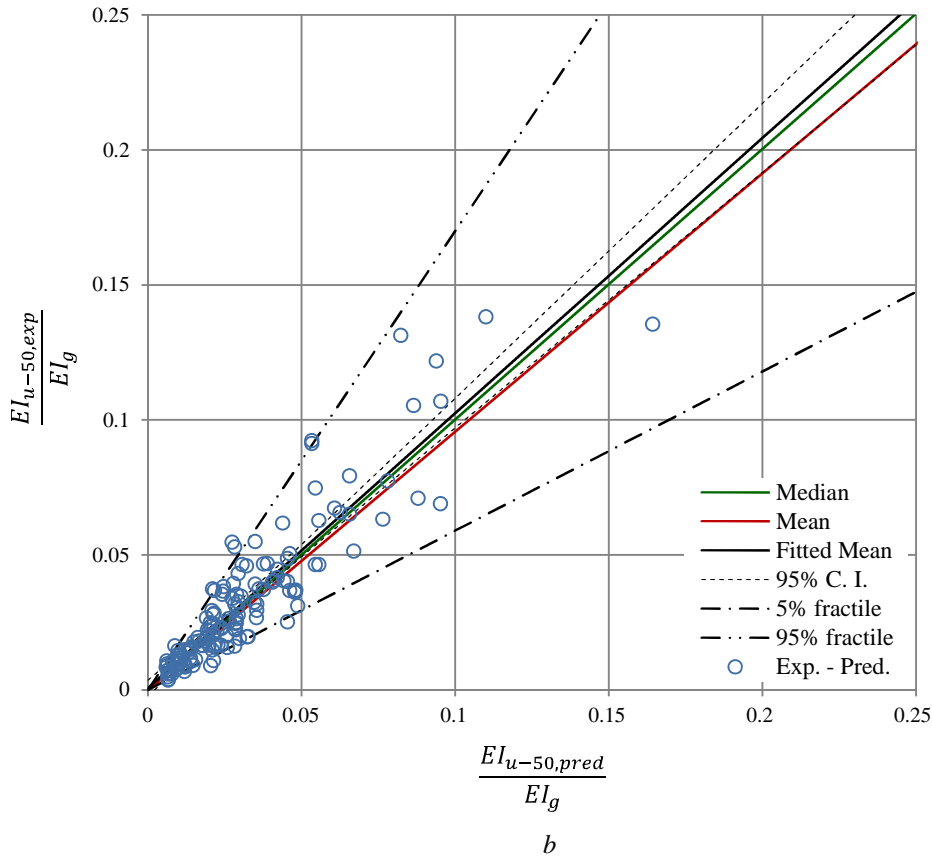


Figure 6-18 Experimental stiffness ratio at 50% maximum force reduction plotted against predictions from a) equation 7.18a and b) equation 7.18b, based on the inclusion and exclusion of extreme data-points respectively. The stiffness ratio is a function of physical and material properties.

6.6 Comparison of Different EDP Models at Various Damage States

Different explanatory variables are selected in the models of chord rotation or stiffness ratio at different damage states. If a variable does not feature in an equation, it does not necessarily mean that the variable has no physical relevance to the EDP at that particular damage state. It means that either other explanatory variables are selected in the model having a similar physical meaning, or it was not significantly represented by the available data to be selected in the model by the statistical criteria adopted, discussed in section 5.7.3.

The axial force ratio (v) is selected in all models of θ_{dmg} and EI_{dmg}/EI_g . For the stiffness ratio models at each damage state, EI_{dmg}/EI_g is observed to increase as v increases. However, θ_{dmg} decreases as v increases. The longitudinal steel ratio ρ_T is selected in most models with the exception of the models for EI_Y/EI_g , EI_m/EI_g and EI_{u-10}/EI_g . In the other stiffness ratio models, EI_{dmg}/EI_g is observed to decrease as ρ_T increases. However, θ_{dmg} increases with ρ_T for all the damage states. No variable representing confinement is selected for models at yielding damage stage, and for EI_m/EI_g . However, different explanatory variables representing

confinement are selected for different models at different damage states. The models for θ_m and θ_{u-10} in terms of combinations of variables from literature, and the models for EI_{u-10}/EI_g and EI_{u-20}/EI_g , include the confinement variable $a\rho_s$. However in models for θ_{u-20} and θ_{u-50} in terms of combinations of variables from literature, and the model for EI_{u-50}/EI_g , include the confinement variable $a\rho_s f_{yw}/f'_c$, which takes into account damage development due to stirrup failure which becomes more relevant in preceding damage states. Confinement in the model for θ_m in terms of explanatory variables obtained from dimensional analysis is represented by ρ_w . However, for similar models at subsequent damage states, confinement is represented by ω_w . The variable representing susceptibility for buckling (s/d_{bl}) is included in models for EI_{u-10}/EI_g , θ_{u-10} , θ_{u-20} and θ_{u-20} . Whereas the trend in the stiffness ratio model is that the EDP increases with s/d_{bl} , a consistently opposite trend is observed in the chord rotation models.

The aspect ratio L_s/h is selected for stiffness ratio models at all the considered damage states., where the EDP is observed to increase as L_s/h increases. However for θ_Y , the variable $(L_s + a_v z)/h$ is selected, and L_s/h is selected in subsequent damage states for chord rotation models based on combined explanatory variables from literature. For chord rotation models based on explanatory variables obtained from dimensional analysis, L_s/s is selected. For chord rotation models, θ_{dmg} is observed to decrease as the explanatory variable, whether L_s/s or L_s/h increase. The cover aspect ratios c/s or c/h are selected in random models after yielding damage state, and both are observed to increase with chord rotation and decrease as the stiffness ratio increases. The material property for longitudinal steel and concrete f_{tl}/f'_c is selected for all stiffness ratio models after yielding. For the model of EI_Y/EI_g , the explanatory variable f_{yl}/f'_c is selected. In all cases, the stiffness ratio is observed to decrease, as these material properties increase. For chord rotation models after yielding, either f_{tl}/f'_c and f_{yl}/f'_c , or f_{tl}/f_{yl} and f_{yl}/f'_c are selected. In all cases, θ_{dmg} is observed to increase with f_{yl}/f'_c , and decrease with f_{tl}/f'_c or f_{tl}/f_{yl} . At yielding the strain ratio f_{yl}/E_s is selected.

The number of explanatory variables which are also selected in combination with a_{sl} forming interaction terms are less than the number of explanatory variables which are selected alone. However, a few patterns can be observed. Steel and concrete properties which include either f_{tl}/f'_c , f_{yl}/f'_c or f_{tl}/f_{yl} , are consistently observed in models until the maximum damage state. The EDP is observed to decrease as the steel and concrete property increases. The steel ratio ρ_T is more frequently observed in higher damage states, and EI_{dmg}/EI_g increases as ρ_T increases, but θ_{dmg} decreases as ρ_T increases. The axial force ratio v is selected as an interaction term with a_{sl} , in stiffness ratio models, where EI_{dmg}/EI_g increases as v increases. Confinement explanatory variables are selected in only few random chord rotation models after yielding damage state. Similarly the cover aspect ratios c/s or c/h are selected in random models after

yielding damage state. On the other hand, L_s/s or L_s/h are selected for in most models for chord rotation or stiffness ratio at various damage states.

Although different models of different EDPs at different damage states are based on different explanatory variables and data, the differences in the statistical diagnostics are not many. Variability in the statistical diagnostics of the chord rotation models at different damage states is observed. However, no particular trend in the differences of the diagnostics can be observed across the different damage states for chord rotation models. Nevertheless, in case of stiffness ratio models the mean trend in residual-fitted plots tends to have larger offset at the edges as the level of the damage state increases. For stiffness ratio models, the interval of standardized residuals that falls between ± 2 is high at low damage states, and decreases at higher damage states. There are also differences in the diagnostics between models of EI_{dmg}/EI_g and θ_{dmg} at each damage state. However these differences are generally random. Differences in the outcome of the Breusch-Pagan tests are also random. The AIC is lower for lower damage states as shown in Table 6-9 and Table 6-10. This indicates that indicates that EDP models at low damage states fit data better than corresponding models at higher damage states.

The models at yielding indicate the lowest standard deviation and coefficient of variation and highest 5% fractile factor amongst all stiffness and chord rotation models. However, for subsequent damage states, no particular trend is observed. The lowest CoV and SD, and highest 5% fractile factor for chord rotation models after yielding based on combined explanatory variables as obtained from literature is associated with θ_{u-50} . The lowest CoV and SD for chord rotation models after yielding and based on explanatory variables determined from dimensional analysis is associated with θ_{u-20} . For the set of chord rotation models where an energy term is included, the lowest CoV and SD are provided by the model for θ_m . Amongst the stiffness ratio models after yielding, the model for EI_{u-50}/EI_g provides the lowest CoV and SD, while EI_{u-10}/EI_g provide the highest CoV and SD.

Table 6-9a Statistics of experiment-to-predicted chord rotation in terms of explanatory variables determined from dimensional analysis.

Equation	Description	No. of Data	Mean	Median	SD	CoV - %	BIC	AIC	5% Fractile
Eq. 6.10a	$\theta_{m,pred}/\theta_{m,exp}$	230	1.04	1.01	0.33	31.3	-876	-920	0.62
Eq. 7.11a	$\theta_{u-10,pred}/\theta_{u-10,exp}$	236	1.06	1.00	0.36	33.9	-858	-893	0.61
Eq. 7.12a	$\theta_{u-20,pred}/\theta_{u-20,exp}$	220	1.02	0.96	0.32	31.6	-770	-808	0.60
Eq. 7.13a	$\theta_{u-50,pred}/\theta_{u-50,exp}$	173	1.01	1.05	0.34	32.4	-627	-657	0.59

Table 6-9b Statistics of experiment-to-predicted chord rotation in terms of variables as combined and used in literature.

Equation	Description	No. of Data	Mean	Median	SD	CoV - %	BIC	AIC	5% Fractile
Eq. 6.10b	$\theta_{m,pred}/\theta_{m,exp}$	246	1.13	1.01	0.54	47.5	-860	-902	0.56
Eq. 6.11b	$\theta_{u-10,pred}/\theta_{u-10,exp}$	240	1.05	0.97	0.37	35.0	-849	-887	0.61
Eq. 6.12b	$\theta_{u-20,pred}/\theta_{u-20,exp}$	224	1.05	0.98	0.38	34.8	-821	-859	0.58
Eq. 6.13b	$\theta_{u-50,pred}/\theta_{u-50,exp}$	173	1.04	0.94	0.31	31.0	-662	-690	0.63

Table 6-9c Statistics of experiment-to-predicted chord rotation in terms of explanatory variables determined from dimensional analysis including an energy dissipation term.

Equation	Description	No. of Data	Mean	Median	SD	CoV - %	BIC	AIC	5% Fractile
Eq. 6.10c	$\theta_{m,pred}/\theta_{m,exp}$	246	1.00	0.98	0.26	26.4	-893	-921	0.64
Eq. 6.11c	$\theta_{u-10,pred}/\theta_{u-10,exp}$	229	1.03	1.00	0.28	27.2	-888	-920	0.64
Eq. 6.12c	$\theta_{u-20,pred}/\theta_{u-20,exp}$	224	1.05	1.01	0.34	32.4	-818	-862	0.59
Eq. 6.13c	$\theta_{u-50,pred}/\theta_{u-50,exp}$	173	1.03	1.01	0.31	29.7	-634	-672	0.60

Table 6-10a Statistics of experiment-to-predicted stiffness ratio. Database including outliers extreme variable values.

Equation		No. of Data	Mean	Median	SD	CoV - %	BIC	Fractile of mean	
								5%	95%
Eq. 6.14a	$(EI_{Y,exp}/EI_g)/(EI_{Y,pred}/EI_g)$	219	1.04	0.98	0.31	29.4	-857	0.67	1.55
Eq. 6.15a	$(EI_{m,exp}/EI_g)/(EI_{m,pred}/EI_g)$	219	1.05	1.01	0.36	33.8	-787	0.57	1.69
Eq. 6.16a	$(EI_{u-10,exp}/EI_g)/(EI_{u-10,pred}/EI_g)$	209	1.09	1.02	0.54	48.3	-677	0.50	2.03
Eq. 7.17a	$(EI_{u-20,exp}/EI_g)/(EI_{u-20,pred}/EI_g)$	200	1.09	1.01	0.46	40.9	-640	0.51	1.96
Eq. 7.18a	$(EI_{u-50,exp}/EI_g)/(EI_{u-50,pred}/EI_g)$	152	1.05	1.02	0.35	33.3	-512	0.57	1.67

Table 6-10b Statistics of experiment-to-predicted stiffness ratio. Database excluding outliers extreme variable values.

Equation		No. of Data	Mean	Median	SD	CoV - %	BIC	Fractile of mean	
								5%	95%
Eq. 6.14b	$(EI_{Y,exp}/EI_g)/(EI_{Y,pred}/EI_g)$	210	1.02	0.98	0.21	20.4	-950	0.70	1.46
Eq. 6.15b	$(EI_{m,exp}/EI_g)/(EI_{m,pred}/EI_g)$	213	1.04	1.01	0.31	29.9	-830	0.62	1.62
Eq. 6.16b	$(EI_{u-10,exp}/EI_g)/(EI_{u-10,pred}/EI_g)$	203	1.08	1.01	0.42	38.6	-706	0.55	1.95
Eq. 6.17b	$(EI_{u-20,exp}/EI_g)/(EI_{u-20,pred}/EI_g)$	193	1.09	1.01	0.41	37.3	-649	0.53	1.84
Eq. 6.18b	$(EI_{u-50,exp}/EI_g)/(EI_{u-50,pred}/EI_g)$	148	1.04	1.00	0.31	29.7	-555	0.59	1.70

6.7 Comparison of EDP Models with Other Models in Literature

6.7.1 Stiffness Ratio at Yielding

The model for stiffness ratio at yielding determined in equation 6.14a and 6.14b, are compared with the models determined by Biskinis *et al.*, 2010a and Haselton *et al.*, 2008, and rearranged in equation 6.19a and equation 6.20a respectively. In Biskinis *et al.*, 2010a, the axial force ratio is considered N/bh , while in the models corresponding with equations 6.19a, and 6.14, the variable v is selected. The model by Haselton *et al.*, 2008 does not account the variable for significant bond-slip a_{sl} . While this is included in the model in equation 6.14, the variables f_{yl}/f'_c and b/h are also selected. In the absence of a_{sl} , these two variables are not selected in the model.

Figure 6-19a and Figure 6-19b indicate experiment-to-predicted plots referring to data of the selected database computed by equation 6.19a. Figure 6-19a refers to the computation using data that includes outliers and extreme values of variables, while Figure 6-19b refers to the computation using data that excludes them. Figure 6-21a indicates experiment-to-predicted plots referring to data of the selected database computed by equation 6.20a. No substantial difference on the outcome is observed for this latter model as a result of using data that includes or excludes outliers and extreme values of variables.

As indicated in the plots and the statistics in Table 6-11, the predictions by equation 6.20a and equation 6.14a have similar CoV and SD, and are smaller than the values corresponding with equation 6.19a. However, equation 6.14a, has a better 5% and 95% fractile factor. When the used data does not include outliers and extreme values of variables, the CoV, mean, SD, and 5% and 95% fractile factor associated with the predictions of equation 6.14b are superior over corresponding values corresponding with equations 6.19a and 6.20a.

The regression by Biskinis *et al.*, 2010a is computed using a completely different data set. The regression by Haselton *et al.*, 2008 is computed using a similar dataset as utilised in this research since most data is obtained from Berry *et al.*, 2003. However, the databases utilised to determine equation 6.14 and 6.20 are still not exact. In order to account for discrepancies in the comparison of models that are the result of using different datasets, regression analysis is performed on the form of the models by Biskinis *et al.*, 2010a, and Haselton *et al.*, 2008 but using the data from the selected database which is available. Equation 6.19b represents the model determined on data that included outliers and extreme values of variables. Equation 6.19c represents the model determined on data that excluded them. Both these models are based on the original form of the model as used by Biskinis *et al.*, 2010a. Corresponding experiment-to predicted plots are shown in Figure 7-20. Equation 7.20b represents the model determined based on the original form of the model as used by Haselton *et al.*, 2008. No difference is again observed when using data that

included or excluded outliers and extreme values of variables. The corresponding experiment-to-predicted plots are shown in Figure 6-21b. As observed by considering Figure 6-20a, Figure 6-20b, Figure 6-21b and the statistics in terms of SD, CoV, and fractile factors, the equations 6.19c, and 6.20b are similar to equation 6.14a, however, they are still not superior to equation 6.14b.

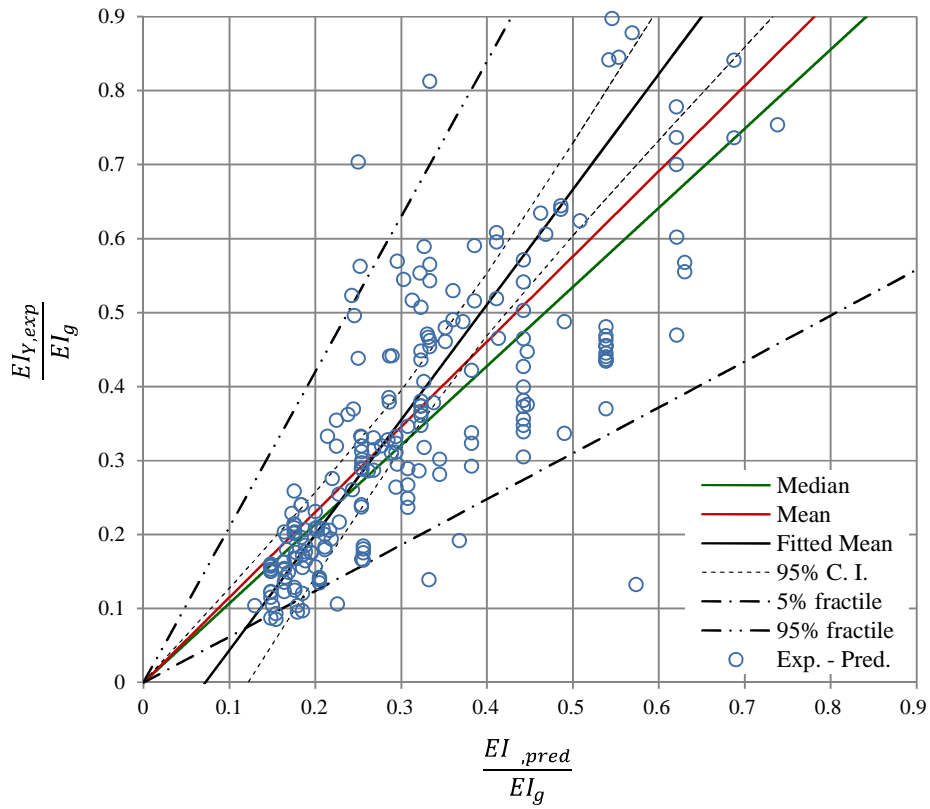
$$\begin{aligned} \frac{EI_Y}{EI_g} = 0.108 & \left[0.8 + \left(0.0384 \cdot \frac{N}{bh} \right) + \left(\ln \left(\frac{L_s}{h} \right) \right) + \left(0.048 \cdot \frac{N}{bh} \cdot \ln \left(\frac{L_s}{h} \right) \right) \right. \\ & - (0.2 \cdot a_{sl}) - \left(0.01 a_{sl} \frac{N}{bh} \right) - \left(0.25 a_{sl} \ln \left(\frac{L_s}{h} \right) \right) \\ & \left. - \left(0.012 a_{sl} \frac{N}{bh} \ln \left(\frac{L_s}{h} \right) \right) \right] \end{aligned} \quad [6.19a]$$

$$\begin{aligned} \frac{EI_Y}{EI_g} = 0.15 & \left[1.93 - \left(0.293 \frac{N}{bh} \right) - \left(0.267 \cdot \ln \left(\frac{L_s}{h} \right) \right) + \left(0.08 \frac{N}{bh} \ln \left(\frac{L_s}{h} \right) \right) \right. \\ & - (1.87 a_{sl}) + \left(0.047 a_{sl} \frac{N}{bh} \right) + \left(a_{sl} \ln \left(\frac{L_s}{h} \right) \right) \\ & \left. - \left(0.004 a_{sl} \frac{N}{bh} \ln \left(\frac{L_s}{h} \right) \right) \right] \end{aligned} \quad [6.19b]$$

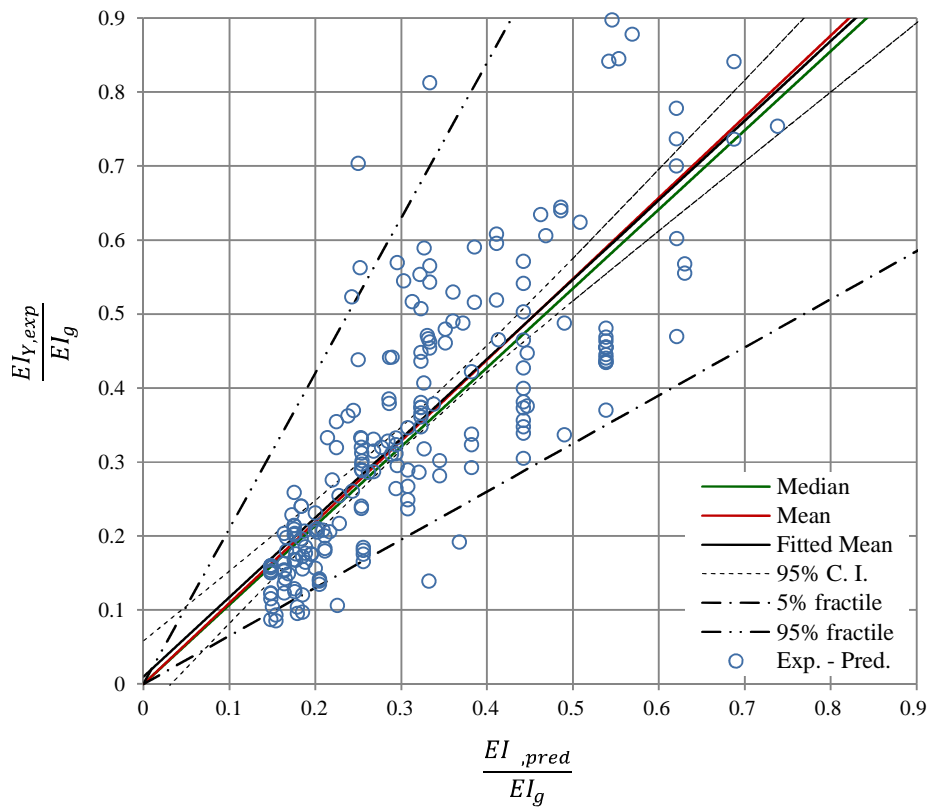
$$\begin{aligned} \frac{EI_Y}{EI_g} = 0.13 & \left[2.2 - \left(0.0341 \frac{N}{bh} \right) - \left(0.306 \cdot \ln \left(\frac{L_s}{h} \right) \right) + \left(0.09 \frac{N}{bh} \ln \left(\frac{L_s}{h} \right) \right) \right. \\ & - (2.75 a_{sl}) + \left(0.111 a_{sl} \frac{N}{bh} \right) + \left(1.85 a_{sl} \ln \left(\frac{L_s}{h} \right) \right) \\ & \left. - \left(0.081 a_{sl} \frac{N}{bh} \ln \left(\frac{L_s}{h} \right) \right) \right] \end{aligned} \quad [6.19c]$$

$$\frac{EI_Y}{EI_g} = -0.07 + 0.59v + 0.07 \frac{L_s}{h} \quad [6.20a]$$

$$\frac{EI_Y}{EI_g} = -0.059 + 0.86v + 0.05 \frac{L_s}{h} \quad [6.20b]$$

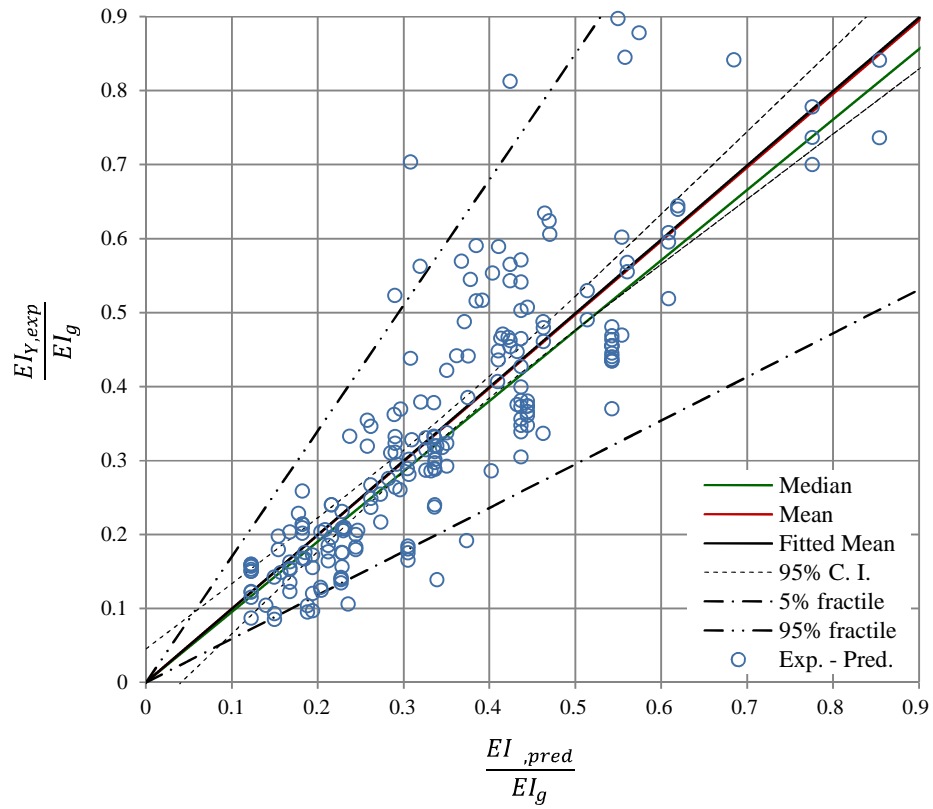


a

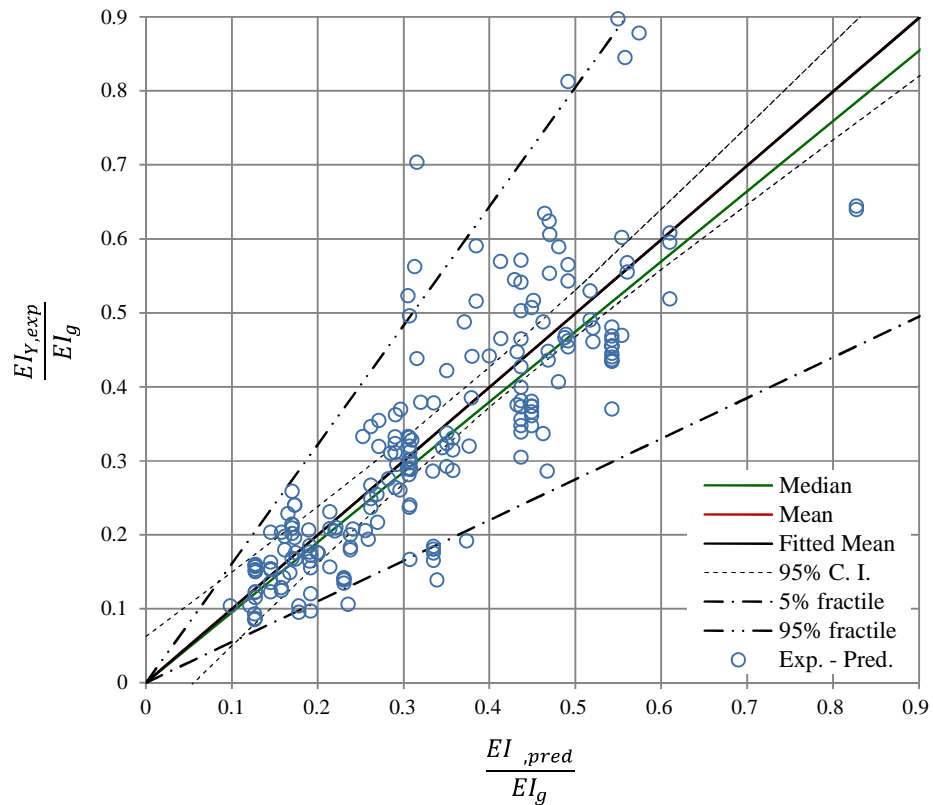


b

Figure 6-19 Experimental stiffness ratio at yield plotted against predictions from equation 7.19a determined by Biskinis et al., 2010a, using the selected database a) including and b) excluding extreme data-points.

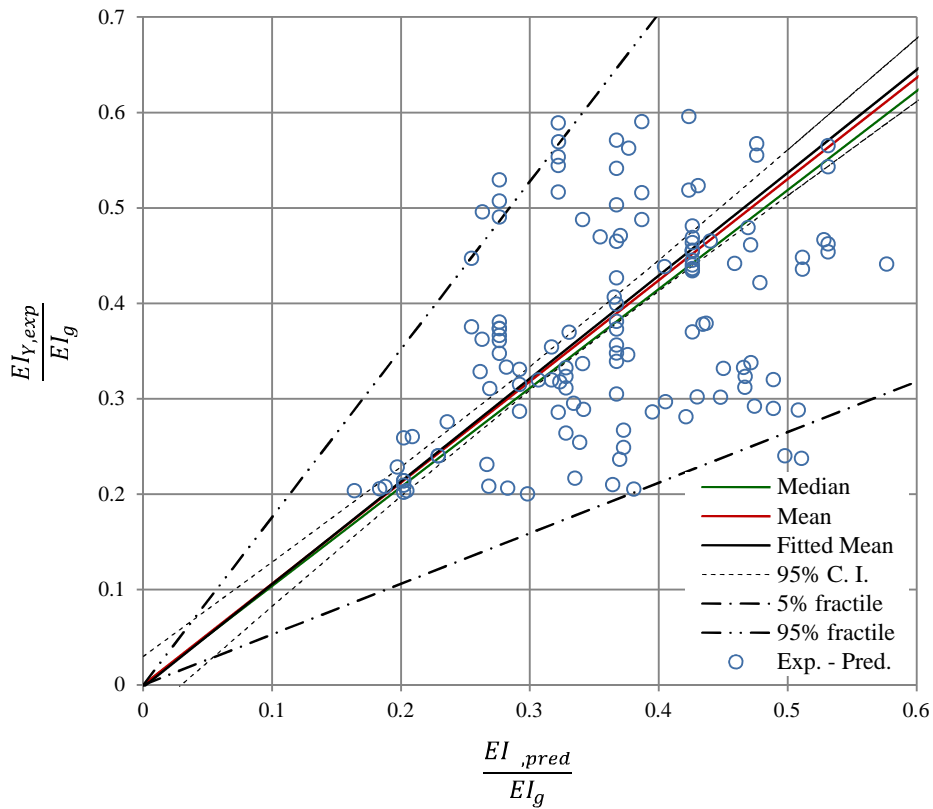


a

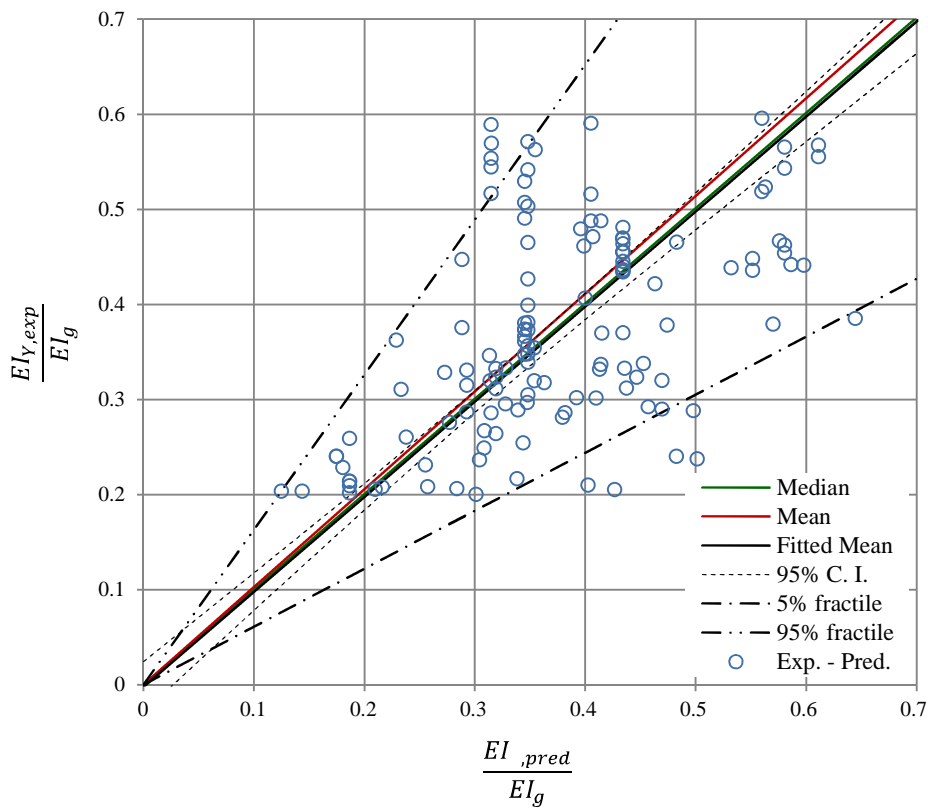


b

Figure 6-20 Experimental stiffness ratio at yield plotted against predictions from a) equation 7.19b – including outliers and extreme data-points, b) equation 7.19c – excluding outliers and extreme data-points. The form of model is based on Biskinis et al., 2010a, but coefficients are determined by regression analysis on the available data from the selected database.



a



b

Figure 6-21 Experimental stiffness ratio at yield plotted against predictions from a) equation 7.20a – model as determined by Haselton et al., 2008, b) equation 7.20b – model form as determined by Haselton et al.2008, but coefficients are obtained from regression analysis using the available data.

Table 6-11 Statistics of experiment-to-predicted stiffness ratio at yielding. Comparison of models in literature with the model provided by equation 7.14.

Equation Reference	$(EI_{Y,exp}/EI_g)/(EI_{Y,pred}/EI_g)$	No. of Data-points	Mean	Median	SD	CoV - %	5% Fractile	95% Fractile
Eq.7.19a	Equation form and regression coefficients from Biskinis <i>et al.</i> , 2010. Data from selected database. Extreme data-points and outliers included.	219	1.15	1.07	0.51	43.8	0.62	2.1
Eq.7.19a	Equation form and regression coefficients from Biskinis <i>et al.</i> , 2010. Data from selected database. Extreme data-points and outliers excluded.	210	1.08	1.07	0.34	31.4	0.65	2.1
Eq. 7.19b	Equation form based on Biskinis <i>et al.</i> , 2010. Regression on data from selected database. Extreme data-points and outliers included.	219	1.00	0.95	0.31	30.6	0.55	1.61
Eq. 7.19c	Equation form from Biskinis <i>et al.</i> , 2010. Regression on data from selected database. Extreme data-points and outliers excluded	210	1.00	0.96	0.27	27.2	0.62	1.65
Eq. 7.20a	Equation form and regression coefficients from Haselton <i>et al.</i> , 2008. Data from selected database.	219	1.06	1.06	0.31	29.5	0.53	1.76
Eq. 7.20b	Equation form based on Haselton <i>et al.</i> , 2008. Regression on data from selected database.	210	1.02	1.00	0.29	28.3	0.61	1.63
Eq. 7.14a	Equation explanatory variables based on dimensional analysis. Regression on data from selected database. Extreme data-points and outliers included.	219	1.04	0.98	0.31	29.4	0.70	1.55
Eq. 7.14b	Equation explanatory variables based on dimensional analysis. Regression on data from selected database. Extreme data-points and outliers included.	210	1.02	0.98	0.21	20.4	0.67	1.46

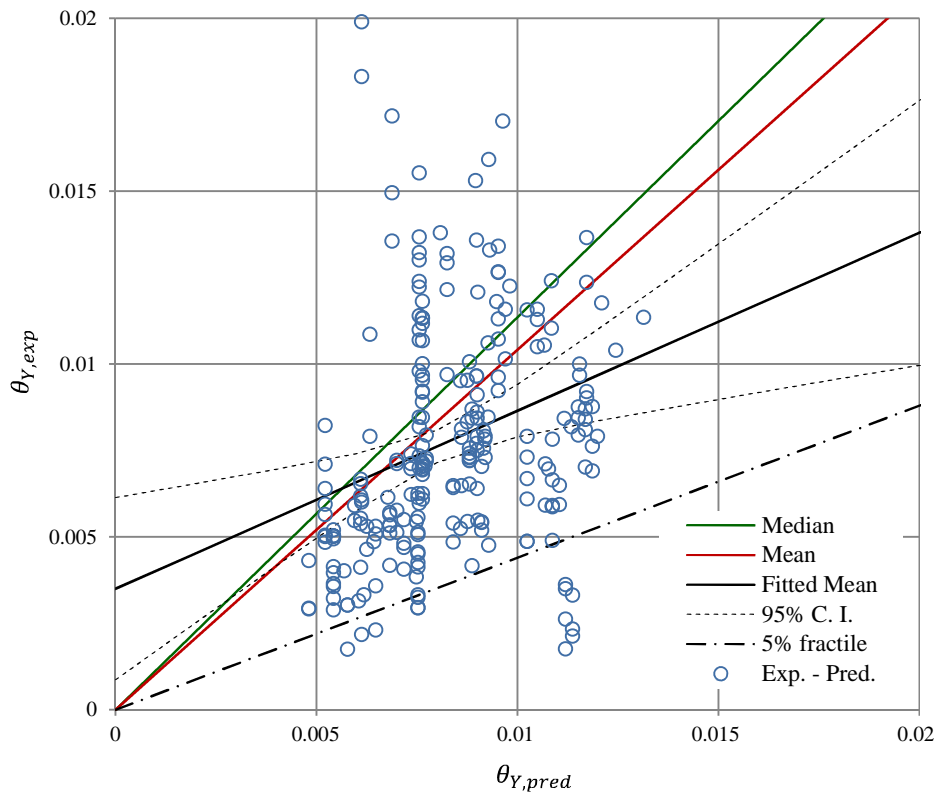
6.7.2 Chord Rotation at Yielding

The model for chord rotation at yielding determined in equation 6.9, is compared with the model determined by Biskinis *et al.*, 2010a, and rearranged in equation 6.21a. The form of the models is different since the model in equation 6.9 while the model in equation 6.21 is semi-empirical. However, most variables are represented in both models. However, the diameter of the longitudinal reinforcement does not feature in equation 6.9, while the aspect ratio b/h and reinforcement ratio ρ_T do not feature in 6.21a. Figure 6-22a and Figure 6-22b indicate experiment-to-predicted plots referring to data of the selected database computed by equation 6.21a. Figure 6-23a refers to the computation using data that includes outliers and extreme values of variables, while Figure 6-23b refers to computations using data that excludes them. As indicated in the plots and the statistics in Table 6-12, equation 6.21a has a better prediction in terms of CoV and SD over equation 6.9a, using data that includes outliers and extreme values of variables. However, this is not the case when data does not include outliers and extreme values of variables. The regression by Biskinis *et al.*, 2010a is computed using a completely different data set. Regression analysis is performed on the form of the model by Biskinis *et al.*, 2010a, but using the data from the selected database. This is done in order to account for discrepancies in the comparison of models that are the result of using different datasets. Equation 6.21b represents the model determined on data that included outliers and extreme values of variables. Equation 6.21c represents the model determined on that that excluded them. Figure 6.23 and Table 6-12 indicate corresponding experiment-predicted plots and statistics. The mean, median, SD and CoV resulting from equations 6.21b and 6.21c slightly improve over the corresponding properties corresponding to equation 6.21a. The 5% fractile factor are only improved for the case where the dataset used excluded outliers and extreme values of variables. In spite of the improvement of equation 6.21c, to model the experimental data of the selected data, the corresponding SD, CoV, median, and 5% fractile factor are not superior to those corresponding with equation 6.9b.

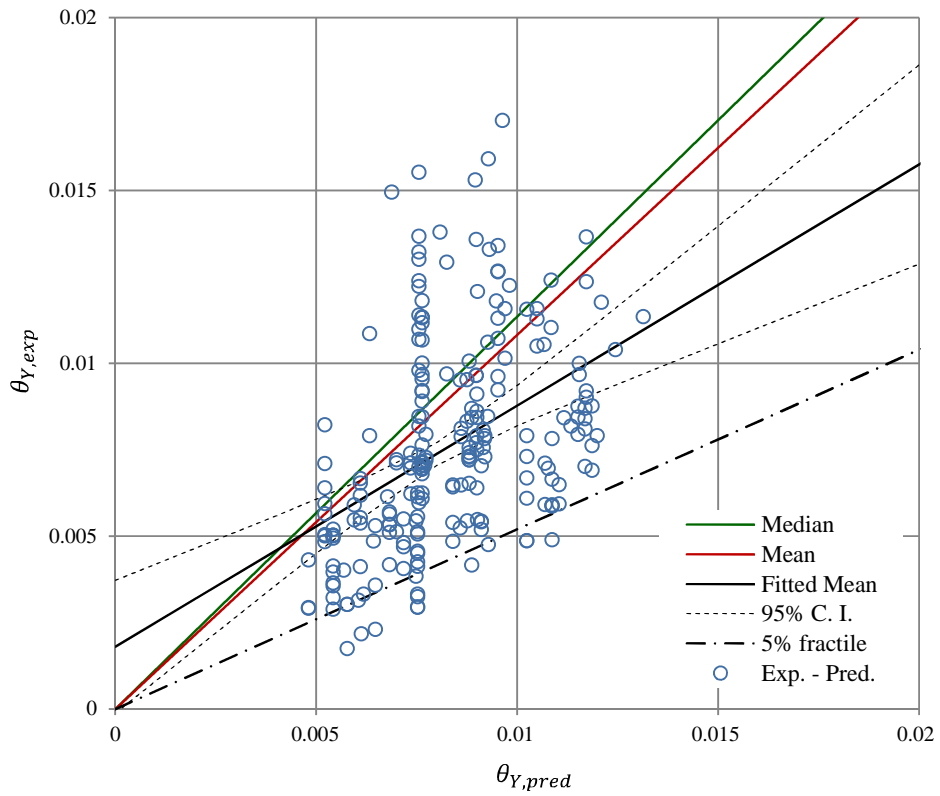
$$\theta_Y = 1.75 \frac{f_y}{E_s h} \cdot \left[\frac{L_s + a_v z}{3} + a_{sl} \frac{d_{bl} f_y}{8 \sqrt{f_c}} \right] + 0.0014 \left(1 + 1.5 \frac{h}{L_s} \right) \quad [6.21a]$$

$$\theta_Y = 0.95 \frac{f_y}{E_s h} \cdot \left[\frac{L_s + a_v z}{3} + a_{sl} \frac{d_{bl} f_y}{8 \sqrt{f_c}} \right] + 0.003 \left(1 + 1.5 \frac{h}{L_s} \right) \quad [6.21b]$$

$$\theta_Y = 1.33 \frac{f_y}{E_s h} \cdot \left[\frac{L_s + a_v z}{3} + a_{sl} \frac{d_{bl} f_y}{8 \sqrt{f_c}} \right] + 0.002 \left(1 + 1.5 \frac{h}{L_s} \right) \quad [6.21c]$$

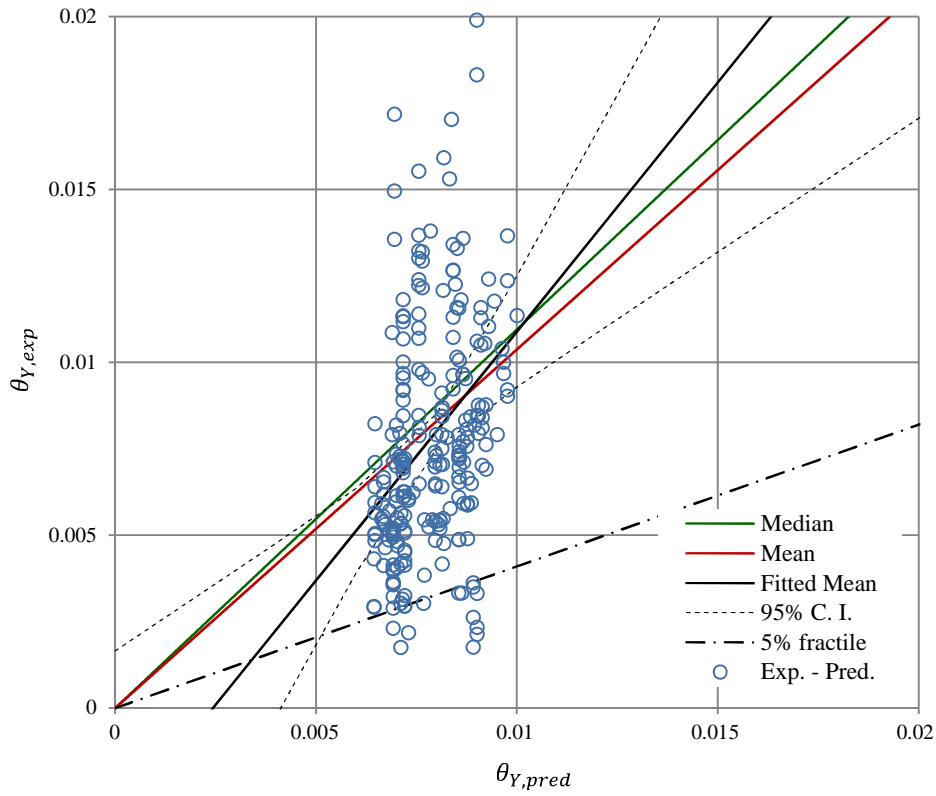


a

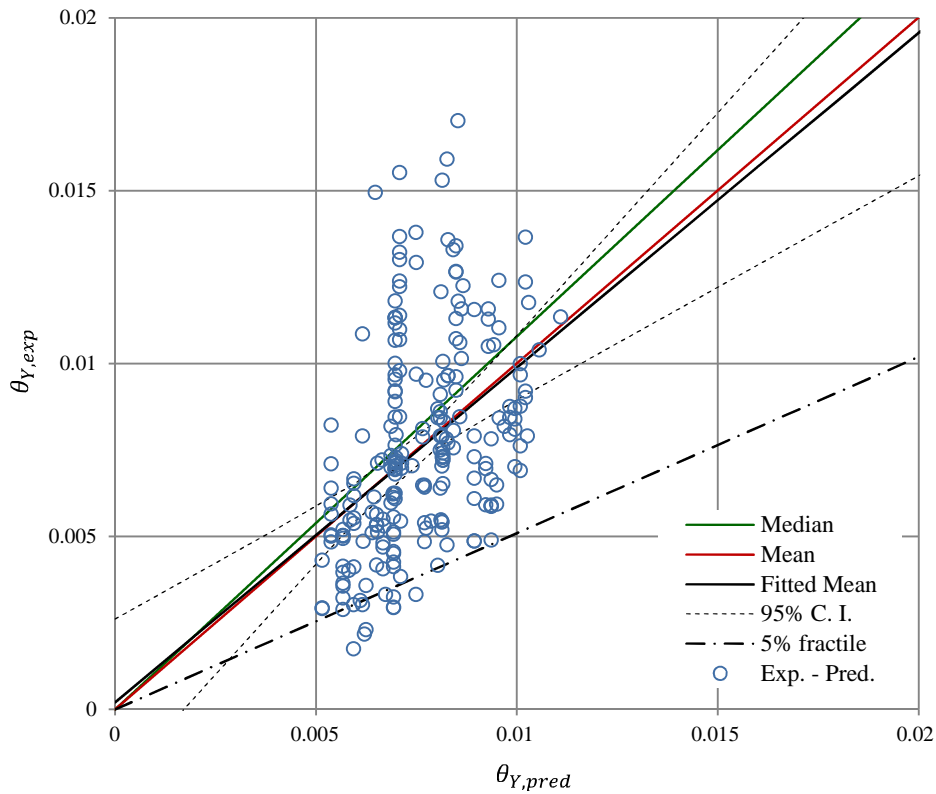


b

Figure 6-22 Experimental chord rotation at yield plotted against predictions from equation 7.21a. The model as determined by Haselton et al., 2008. The data a) includes, b) excludes outliers and extreme data-points.



a



b

Figure 6-23 Experimental chord rotation at yield plotted against predictions from: a) equation 7.21b – includes outliers and extreme data-points, b) equation 7.21c- data excludes outliers and extreme data-points. The form of the model is the same provided by Haselton et al., 2008, but the coefficients are determined from regression analysis using the available data.

Table 6-12 Statistics of experiment-to-predicted chord rotation at yielding. Comparison of models in literature with equation 7.9.

Equation Reference	$\theta_{Y,exp}/\theta_{Y,pred}$	No. of Data	Mean	Median	SD	CoV - %	5% Fractile
Eq. 7.21a	Equation form and regression parameters from Biskinis <i>et al.</i> , 2010. Data from selected database. Extreme data-points and outliers included.	255	0.96	0.88	0.47	49.3	0.44
Eq.7.21a	Equation form and regression parameters from Biskinis <i>et al.</i> , 2010 Data from selected database. Extreme data-points and outliers included.	232	0.92	0.88	0.33	36.0	0.52
Eq. 7.21b	Equation form from Biskinis <i>et al.</i> , 2010. Regression on data from selected database. Extreme data-points and outliers included.	255	0.99	0.89	0.45	45.7	0.41
Eq. 7.21c	Equation form from Biskinis <i>et al.</i> , 2010. Regression on data from selected database. Extreme data-points and outliers included.	232	1.00	0.93	0.36	36.1	0.52
Eq. 7.9a	Equation explanatory variables based on dimensional analysis. Regression on data from selected database. Extreme data-points and outliers included.	255	1.09	1.00	0.66	60.7	0.62
Eq. 7.9b	Equation explanatory variables based on dimensional analysis. Regression on data from selected database. Extreme data-points and outliers included.	232	1.02	1.00	0.21	20.5	0.70

6.7.3 Chord Rotation at 20% Maximum Force Reduction

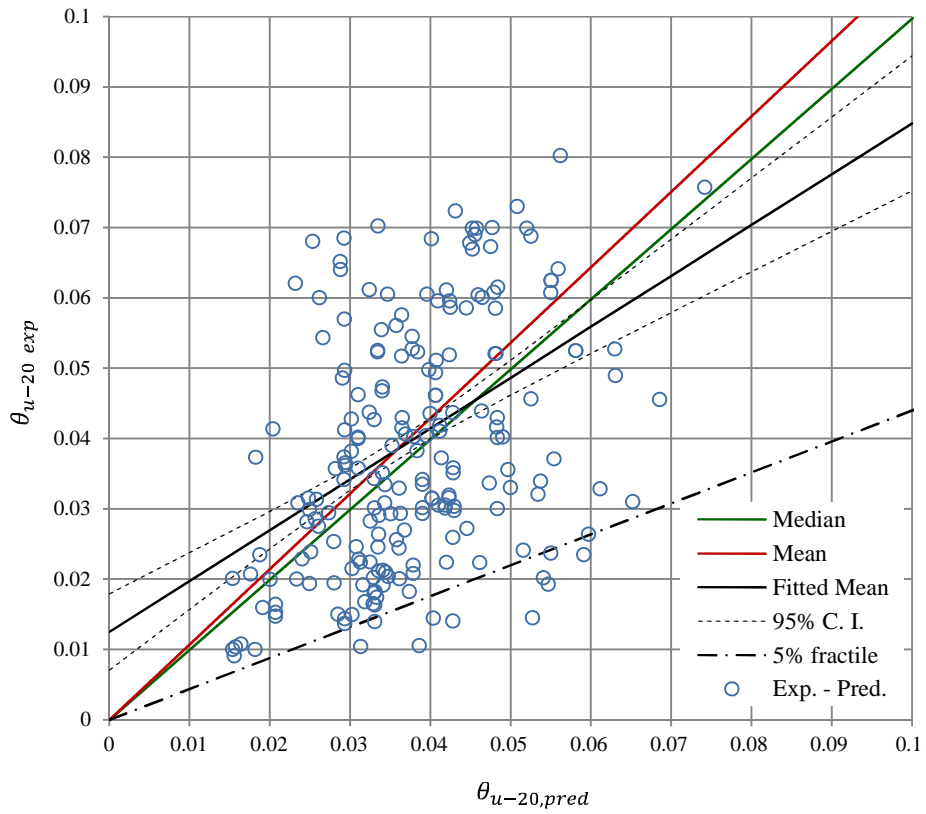
The model for chord rotation at 20% maximum force reduction given by equation 6.12, is compared with the model determined by Biskinis *et al.*, 2010b. The latter is reproduced in equation 6.22a. The form of the models is different. In equation 6.22a, all the variables are assumed to vary the same irrespective of whether substantial bond-slip occurs or not, the models in equation 6.12 account for the possibility that other variables represent different behaviour in the presence or absence of considerable bond-slip. In equation 6.22a, ω_2/ω_1 represents the quantity of longitudinal reinforcement. However, in the selected database, since most of the section of columns are symmetric, then ω_2/ω_1 is not very significant and is replaced with ρ_T . Other differences are the result of different regression analysis approaches.

Figure 6.24a indicate experiment-to-predicted plots referring to data of the selected database computed by equation 6.22a using data that excludes outliers and extreme values of variables. As indicated in this plot, and the statistics in Table 6-13, equations 6.12a, 6.12b and 6.12c have a better prediction over equation 6.22a. The regression by Biskinis *et al.*, 2010b is computed using a completely different data set. Regression analysis is performed on the form of the model by Biskinis *et al.*, 2010b, but using the data from the selected database. This is done in order to account for discrepancies in the comparison of models that are the result of using different datasets. Although an attempt is made to follow the same procedure utilised by Biskinis *et al.*, 2010b, in the regression analysis process, this might not be exact. Computations are very sensitive, and the outcome of the model may not be an exact similitude.

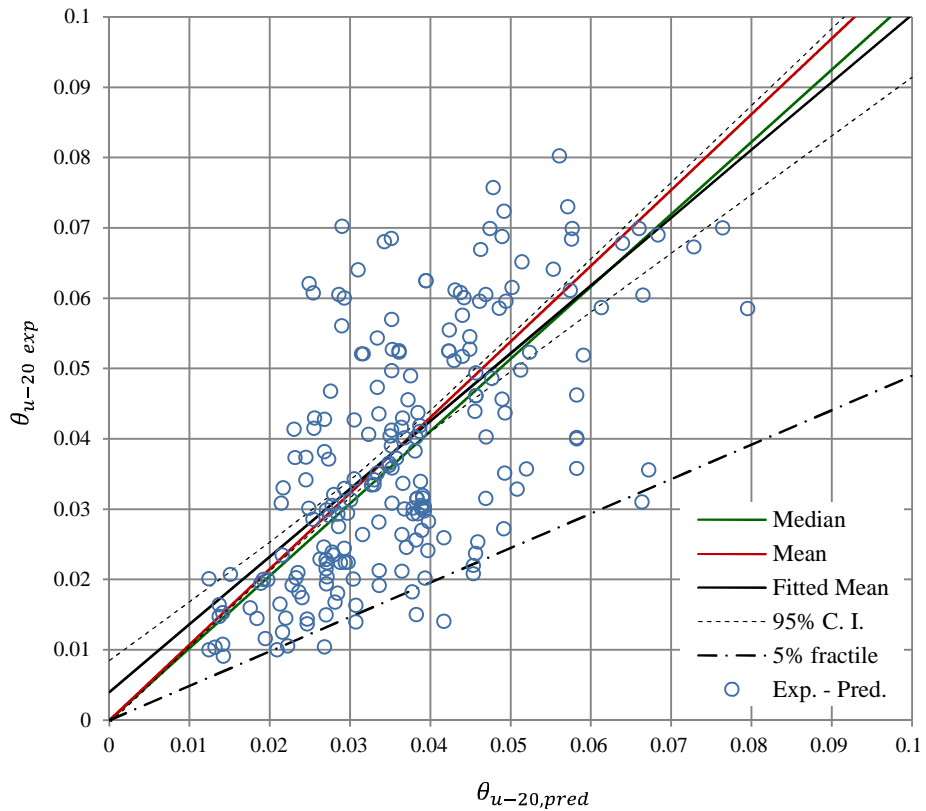
Equation 6.22b represents the determined model. Figure 6.24b and Table 6-13 indicate corresponding experiment-predicted plots and statistics. The new model indicates that it can better predict the experimental data when compared with equation 6.22a, however, it is not superior to the models provided by equation 6.12. The length to span ratio (L_s/h) is not selected in the model, since it does not show to be significant by the Wald test. This was also observed in comparisons by Haselton *et al.*, 2010.

$$\theta_{u-20} = 0.011 \cdot \left(1 + \frac{a_{sl}}{2}\right) \cdot 0.3^v \cdot \left[\frac{\max(0.01; \omega_2)}{\max(0.01; \omega_1)} f'_c\right]^{0.225} \left[\min\left(9; \frac{L_s}{h}\right)\right]^{0.35} 25^a \rho_s \frac{f_w}{f'_c} \quad [6.22a]$$

$$\theta_{u-20} = 0.062 \cdot \left(1 + \frac{a_{sl}}{25}\right) \cdot 0.158^v \cdot \left[\frac{\max(0.01; \omega_2)}{\max(0.01; \omega_1)} f'_c\right]^{0.8} 1580^a \rho_s \frac{f_w}{f'_c} \quad [7.22b]$$



a



b

Figure 6-24 Experimental chord rotation at 20% maximum force reduction plotted against predictions from a) equation 7.22a – model as determined by Biskinis et al., 2010b, b) equation 7.22b – model form as determined by Biskinis et al., 2010b, but coefficients are obtained from regression analysis using the available data.

Table 6-13 Statistics of experiment-to-predicted chord rotation at 20% maximum force reduction. Comparison of models in literature with equation 7.12.

Equation Reference	$\theta_{u-20,exp}/\theta_{u-20,pred}$	No. of Data	Mean	Median	SD	CoV - %	5% Fractile Factor
Eq. 7.22a	Equation form and regression parameters from Biskinis <i>et al.</i> , 2010b. Data from selected database. Extreme data-points and outliers excluded.	220	1.07	1.00	0.50	46.2	0.44
Eq. 7.22b	Equation form from Biskinis <i>et al.</i> , 2010b. Regression on data from selected database. Extreme data-points and outliers excluded.	220	1.07	1.03	0.42	39.0	0.49
Eq. 7.12a	Equation explanatory variables are based on dimensional analysis. Regression on data from selected database. Extreme data-points and outliers excluded.	220	1.02	0.96	0.32	31.6	0.60
Eq. 7.12b	Explanatory variables are based on combinations of variables in literature. Regression on data from selected database. Extreme data-points and outliers excluded.	224	1.05	0.98	0.38	34.8	0.58
Eq. 7.12c	Equation explanatory variables are based on dimensional analysis including an energy dissipation term. Regression on data from selected database. Extreme data-points and outliers excluded.	224	1.05	1.01	0.34	32.4	0.59

6.8 Validation of Proposed EDP Relationships

Statistical BIC criteria rather than K -fold validation is used in the selection process of the model in order to make the most of the data for the development of the models and reduce uncertainty as discussed in section 6.7. However, in order to investigate the application of the model to other data, proposed models are cross validated with a few experimental data that is not used for the development of the models themselves.

The experiments refer to specimen CD from Melo *et al.*, 2015, specimen SP2 from Nojavan *et al.*, 2015 and specimen BC from Ebead *et al.*, 2015. The first specimen refers to a non-seismically designed structure and is characterised with geometric and material properties that are in general average compared with the range of data used for the calibration of the models. The second specimen refers to a column which is designed to large loads, and whose properties fall at boundaries yet within limits of the range of application of the models. The third specimen refers to a beam where contrary to the other two, the axial force ratio is negligible. Hence, with these three specimens, the application of the models is being checked in various sections of their range of application.

Table 6-14 compares the values obtained from the experiments with the values predicted from the corresponding models. The experiment-to-predicted ratio is also determined. Experimental digital data was not available, and the associated experimental data was determined manually. Hence, human error might be associated in its determination.

In general, all relationships provide reasonable predictions which do not exceed 5% fractile values determined for each model. Stiffness ratio relationships are characterised with larger discrepancies between predicted and experimental values. In general relationships describing higher levels of damage, which are also determined on fewer specimen records are also characterised with larger discrepancies between predicted and experimental values. Among the three samples, sample SP2 (Nojovan *et al.*, 2015) shows the least agreement between the predicted and experiments. This is expected since the data values of the experimental model correspond to extremes of the application of the empirical models.

Table 6-14 Comparison of expected and predicted values of empirical models for records not utilized in the regression analysis.

Sample		θ_Y	θ_m	θ_{u-10}	θ_{u-20}	θ_{u-50}	EI_Y/EI_g	EI_m/EI_g	EI_{u-10}/EI_g	EI_{u-20}/EI_g	EI_{u-50}/EI_g
		Eq. 6.9b	Eq. 6.10b	Eq. 6.11b	Eq. 6.12b	Eq. 6.13b	Eq. 6.14b	Eq. 6.15b	Eq. 6.16b	Eq. 6.17b	Eq. 6.18b
CD	<i>Exp.:</i>	0.0087	0.017	0.022	0.037	0.032	0.219	0.172	0.110	0.032	0.016
	<i>Pred.:</i>	0.0085	0.014	0.031	0.041	0.046	0.237	0.177	0.114	0.046	0.025
	<i>Exp/pred.:</i>	1.02	1.22	0.71	0.90	0.70	0.93	0.97	0.97	0.70	0.64
SP2	<i>Exp.:</i>	0.0073	0.022	0.036	0.046	0.073	0.512	0.181	0.056	0.052	0.017
	<i>Pred.:</i>	0.0075	0.016	0.042	0.051	0.070	0.436	0.280	0.079	0.080	0.024
	<i>Exp/pred.:</i>	0.97	1.38	0.86	0.90	1.05	1.17	0.65	0.71	0.65	0.71
BC	<i>Exp.:</i>	0.0065	0.011	0.036	0.037	0.046	0.183	0.228	0.078	0.056	0.032
	<i>Pred.:</i>	0.0059	0.014	0.028	0.035	0.041	0.229	0.206	0.093	0.066	0.032
	<i>Exp/pred.:</i>	1.10	0.76	1.27	1.07	1.13	0.80	1.11	0.84	0.85	1.01

6.9 Application to Seismic Assessment

The chord rotation relationships determined in Eq 6.9b, Eq 6.10a, Eq 6.11a, Eq 6.12a and Eq 6.13a are used to check the response of the structure Building 1 in section 2.3.4 to earthquake loading 414, which represents a hazard with a return period of 2475 years, corresponding to a probability of exceedance of 2% in 50 years is considered. According to EN1998-3 (2005), for this hazard level the structure is expected to be associated with a response resulting in heavy damage to the structure. For this damage level, very low residual lateral strength and stiffness are expected and components should not exceed θ_{u-20} . Table 6-15 shows the chord rotation capacity requirements for each damage level, and figure 6-25 maps the corresponding exceeded level of damage from the response of each element in the column.

Table 6-15. Chord rotation capacity at Y , m , $u-10$, $u-20$, $u-50$.

Section	θ_Y	θ_m	θ_{u-10}	θ_{u-20}	θ_{u-50}
	<i>Eq. 6.9b</i>	<i>Eq. 6.10a</i>	<i>Eq. 6.11a</i>	<i>Eq. 6.12a</i>	<i>Eq. 6.13a</i>
A.A.; C.C.; E.E.	0.0064	0.010	0.029	0.033	0.059
H.H.	0.0072	0.017	0.033	0.040	0.061
I.I.	0.0076	0.019	0.030	0.035	0.065

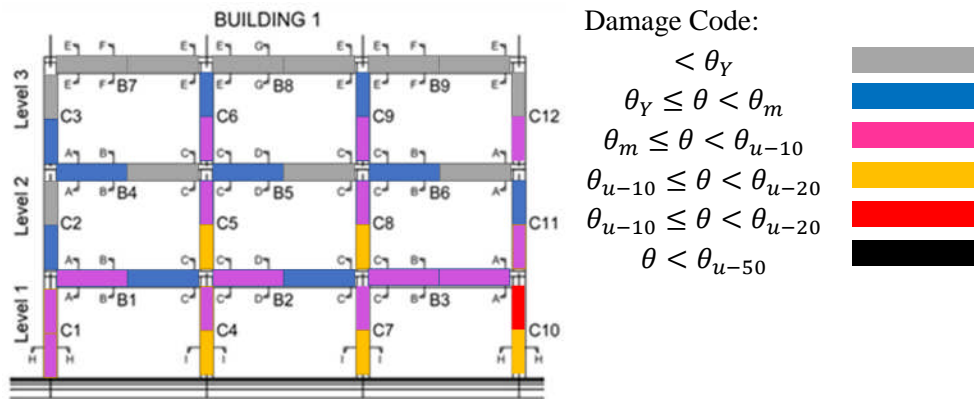


Figure 6-25. Damage distribution in Building 1 following response to earthquake 414, and capacity requirements according to EN1998-3(2005).

It is observed that the chord rotation of many elements distributed around the structure shows that the maximum strength capacity of the elements is exceeded, and hence characterised with significant damage. Many other elements that have not lost strength, have also yielded. However, a few columns at the lower level have also exceeded θ_{u-10} but not θ_{u-20} . One column has also exceeded θ_{u-20} . Hence the structure can be considered to suffer heavy damage in the event of an earthquake with characteristics similar to the hazard representing earthquake 414. This conclusion is similar to the one considered in the example in section 2.3.4 under criteria EN1998-3 (2005).

Nevertheless, with the criteria presented here, it is possible to differentiate more the extent of damage and hence allocate more efficiently the degree of retrofitting intervention that is required.

6.10 General Conclusions on the EDP Models Proposed

The process proposed in Chapter 5 allows for the consideration of many shortcomings in existing models identified in Chapter 1 and 2, for which models are proposed in this chapter. Three sets of EDP relationships are provided at each damage level considered. They refer to chord rotation and stiffness ratio in terms of material and geometric properties, and relationships that relate different EDPs including residual stiffness, chord rotation and energy dissipation as requested in Chapter 1 and Chapter 2.

The relationships that relate different EDPs and which are based on dimensional analysis, in general show better goodness of fit in terms of SD and CoV compared to the other models that are dimensional. Nevertheless, the diagnostics are similar for both sets. From the three models based on different types of explanatory variables referring to material and geometric properties as suggested in Chapter 5, only one is required to represent chord rotation at a particular damage level. From the models based on explanatory variables as found in literature, the models based on dimensional analysis excluding an energy dissipation term and models based on dimensional analysis but including an energy dissipation term, it is observed that in general, the latter provide the lower CoV and SD and hence are considered to provide a better fit out of the three. Nevertheless, this is not much lower than corresponding models based on explanatory variables determined from dimensional analysis and excluding an energy dissipation term. Considering that an energy dissipation term is not always possible to determine, the latter models are considered.

The models at yielding showed the lowest SD and CoV and highest 5% fractile factor, hence showing better goodness of fit compared to models at other damage levels. This is possibly so since the number of records at this damage level was the highest. The models based on 95% of the data nearly always show better fit compared to corresponding models based on all data. The models based on data that excludes the outliers and explanatory variables are therefore preferred.

As suggested in section 5.9, the trend of the explanatory variable in the model is checked with the trend between each explanatory variable and dependent variable individually. In general, these were similar for all explanatory variables. It is observed that the axial force ratio is the only variable that features in all models for chord rotation and stiffness ratio. For the data available the variable L_s/s was observed to show better statistical significance in the models than L_s/h at most damage levels. The presented models, also show the different variation of the explanatory variables with-respect-to the presence or absence of considerable bond slip. Depending on the

level of damage, the significance of explanatory variables varies if considerable bond slip is possible or not, and varies differently for each explanatory variable.

In spite of using BIC selection criteria, the validity of the selected models is still checked with data that was not used for the development of the models. The experiment-to-prediction ratio is within SD associated with the relations, however these statistics are at the limits for data that is at the limits of the range of applicability of the models. In general, the proposed models passed criteria for homoscedasticity and normal distribution of error around 1. The linear regression analysis associated with the models is therefore valid.

In order to check the improvement of the proposed models over existing models, comparison between the two is made. However, this was only possible on models for θ_Y , θ_{u-20} and EI_Y/EI_g since other models at other damage levels are not available as identified in section 2.3 the proposed models of θ_Y , EI_Y/EI_g and θ_{u-20} expressed in terms of material and geometrical properties based on data excluding outliers and extreme data points show a better CoV and SD statistics than corresponding models determined on the same data following forms proposed by Haselton *et al.*, 2008 and Biskinis *et al.*, 2010a. However, proposed models for EI_Y/EI_g and θ_Y based on all data points show similar CoV and SD to corresponding models from Haselton *et al.*, 2008 and Biskinis *et al.*, 2010 respectively, when models are derived on all data. As a result, the models determined on 95% of data are recommended. Nevertheless, the range of application of these models for most of the variables is less than the corresponding range for the models proposed by Biskinis *et al.*, 2010a and Biskinis *et al.*, 2010b.

Improvement is also observed in the applicability of the models as criteria to classify damage in an RC structure when compared with the outcome of the example in section 2.4.3 referring to criteria from EN1998-5 (2005). Although both criteria show coherency in the classification of the building, the classification of damage distribution using the proposed criteria is more refined and hence a more efficient intervention system could be proposed.

Chapter 7. CONCLUSIONS AND FUTURE RECOMMENDATIONS

7.1 General Conclusions

This research focuses on the prediction of RC element deformation capacity at different damage limit states for RC structures that fail in flexure and are characterised with ribbed reinforcement. A review of existing relationships, including recommendations by EN1998-3 (2005) show various restrictions in their definition, and in the application to structural performance based assessment. Existing relationships mainly only refer to yielding and ultimate damage states, including relationships defined in EN1998-3 (2005). Nevertheless, EDP relationships are proposed also at other intermediate states since damage scales show more sensitive division requirements between yield and ultimate. Comparison of the application of proposed models and models defined in EN1998-3 (2005) show similar and hence consistent overall damage classification of an analysed RC frame structure. Nevertheless, the damage distribution based on EN1998-3 (2005) relationships is variegated. Damage in some regions of the structure is considerably overestimated. The damage distribution based on the proposed models is more gradual.

Damage classification according to EN1998-3 (2005) refers to strength degradation and residual stiffness but no associated relationships are provided. However stiffness ratio models in terms of material and geometric properties are provided in order to assess the residual stiffness. By subtracting this from the required capacity of the element, the type, magnitude and size of the intervention required can be determined. Nevertheless, clearer descriptions of the stiffness and strength requirements at each damage level are required in EN1998-3 (2005) in order for stiffness ratio models to be effective.

The proposed models, address various issues that were lacking in existing models that are aimed to reduce uncertainty associated with the development of empirical models of EDPs. The explanatory variables in EDP models in terms of material and geometric properties found in literature, are assumed to vary constantly in the absence or presence of considerable bond slip. Literature discussed in Chapter 2 shows that this is not true, and in the proposed models, each explanatory variable varies differently in the presence or absence of considerable bond slip. Nevertheless, the models do not quantify between considerable and non-considerable bond slip other than the detailing aspects that are also used in EN1998-3 (2005).

In the development of existing models found in literature, an exhaustive approach is not used to define the optimal combination of explanatory variables. This is often determined using trial and error. The stepwise approach used allows for the combination that gives the best fit to be selected, based on BIC criteria which has parsimonious characteristics and hence accounts for overfitting.

In existing models, the explanatory variables consist of combinations that are generally used in other expressions in literature, and may not represent an optimal form when present together in the same model. The proposed models are therefore based on dimensional analysis, which allows for optimal combination of variables that form explanatory variables. It is observed that in general the models based on dimensional analysis provide better goodness-of-fit to the regression data, than corresponding models which are developed using explanatory variables as already used in literature. Nevertheless, explanatory variables which are standard in literature such as L_s/h and v cannot coexist in the same model and the former has to be replaced by L_s/s . This may not be popular.

Unlike existing models with the exception of models proposed by Berry *et al.*, 2004 and Haselton *et al.*, 2008, the proposed models in the research consider statistical treatment of missing data. The relationships in EN1998-3 (2005) are based on EDP data that is manually retrieved from journal articles where definitions are different. It is observed that human error associated with this approach is not small. Hence, to further decrease the uncertainty, the determination of EDP values for this research is based on a rational approach which is applied for all records where digital data is considered.

Experimental data shows that the chord rotation varies with loading characteristics of low cycle fatigue which is a function of the energy. Existing relationships do not account for these characteristics. A set of derived expressions, where loading characteristics are accounted through the incorporation of an energy dissipation term show that the goodness of fit in the models is improved over other models that exclude it. Nevertheless the extent of improvement is small compared to the effort required to determine accurate energy dissipation, and hence the relationships based on dimensional analysis excluding an energy dissipation term are still recommended.

An experimental campaign of low cycle fatigue tests was conducted on specimens that have characteristics associated with material properties and detailing aspects which are not common in literature and existing experimental campaigns, but are characteristic to a substantial number of European structures that generally require assessment, or are characterised with extensive damage in case of an earthquake. Apart from decreasing the uncertainty due to an increased number of records, the incorporation of data from the experimental campaign enhances the range of application of the models. Confinement properties, axial force ratio, span-depth ratio, reinforcement ratio and reinforcement detailing are confirmed as the properties that have a major affect on the deformation capacity and the sequence of damage development. This was useful in identifying the number of categories that constitute regression models for the development of the EDP models. The type of setup adopted provides limited simulation to P- Δ effects where the section with the maximum demand is at a distance from the column foundation interface. The

recommendations in literature by Berry et al., 2003 and Verderame et al., 2008 therefore provide underestimate values of force and associated deformation capacity. The results of the specimens referring to initial stiffness, yielding and ultimate capacity are also validated analytically through sectional analysis, where for most of the cases an error of not more than 10% is provided.

Since the models are calibrated on a limited number of experimental records, distribution of data is characterised with discontinuities which gave rise to outliers in the regression analysis to develop the models. As a result, 95% of the significant data was considered where records with very extreme variables were eliminated together with significant outliers. Models based on these data range provided better fit in terms of CoV and SD and are therefore preferred over models conducted on the complete set of data.

It is observed that the goodness-of-fit of the proposed models for θ_Y , θ_{u-20} and EI_Y/EI_g based on explanatory variables determined from dimensional analysis is better than corresponding models in literature when developed on the same data. It was not possible to compare with other models at other EDPs at different damage levels since, to the author's knowledge, such relationships are not available in literature. Cross validation on records that were not used for the calibration of the models proposed in this research also show fit within the SD.

7.2 Limitations and Future Research

In spite of the evident improvement of the proposed models over existing expressions for EDP estimation, there is still room for improvement. While chord rotation equations in EN1998-3 (2005) refer to damage development in a column element, they are used to describe the damage of the whole structure. Damage indices like Park and Ang (1985) indicate that the global damage is a function of a combination involving the damage in each element and not of one element only. Such assumption by EN1998-3 (2005) therefore limits the reliability of the models in their application.

The damage levels, intermediate between yielding and ultimate capacity are defined in terms of strength degradation. This is in line with the definition of ultimate capacity widely used in literature including EN1998-3 (2005). Nevertheless, definitions of DIs and associated DS, show that damage quantification is more reliable when descriptions are based on the occurrence of damage phenomena. Hence the proposed models can be extended to define EDPs at the occurrence of damage phenomena.

The existing and proposed models refer to columns and beams only. Nevertheless, the overall deformation of a structure is also attributed to beam-column connections, interaction with infills and soil structure interaction. Nevertheless, this is not accounted in either the existing or the proposed models. Hence, these should be extended to incorporate these contributors. However,

this requires further testing which is not available in literature. The auxiliary experimental campaign described in Appendix C and D is useful in this regard.

While the proposed models are valid for rectangular elements with ribbed reinforcement failing in flexure, models can be extended to circular sections, elements with smooth bars, and elements that fail in shear or flexure shear since these are also characteristics that are observed in elements that failed in recent historic earthquakes. Moreover, EDP models are based on low cycle fatigue tests, but they are used for the assessment of structures characterised with dynamic characteristics. The extent of this omission should therefore be quantified to assess the limitations of the existing and proposed models in this regard.

In both existing and proposed models, it is possible that some relevant explanatory variables are excluded not because they are not theoretically significant, but because they are not significant to the available data in the database. Hence, more tests are required considering variables not included in the models proposed. Moreover, more tests are required either to be found in literature or to be specifically conducted, in order to further calibrate the models and reduce uncertainty. Part of the solution also involves further development on semi-empirical approaches. The true variables that are responsible for deformation can be identified through mechanics. So far, such methods are based on many assumptions, that when put together and are associated in an EDP model, they produce worse fit to data than empirical models.

The models can also be improved from a statistical point of view. While BIC criteria is used to select the model and associated explanatory variables since it has parsimony characteristics, complex models are still obtained. This is so, since in dimensional analysis, optimal explanatory variables are defined, and which also result more statistically significant. The models can therefore be improved by further reduction of overfitting through robust regression analysis

REFERENCE LIST

- Abbott, G., McDuling, J., Parsons, S and Schoeman, J. (2007). Building condition assessment: A performance evaluation tool towards sustainable asset management. CIB World Building Congress.
- Akaike, H., (1973). Information Theory and an Extension of the Maximum Likelihood Principle. 2nd. *International Symposium on Information Theory*. Budapest: Akademia Kiado.
- Albarelo, D. (1999). New seismic hazard maps of the Italian territory. Available at <http://www.serviziosismico.it>
- Almeida, J.P., Das, S. and Pinho, R. (2010). Guidelines for Fibre-based Inelasticity Modelling of Reinforced Concrete Members. 14th. *European Conference on earthquake Engineering*, Ohrid, F.Y.R.Macedonia.
- Alpaydin, E., (2010). Introduction to Machine Learning, 2nd ed. MIT Press.
- Anscombe, Francis J., (1973). Graphs in statistical analysis. *The American Statistician* 27, pp. 17–21.
- Arakawa, T., (1970). Allowable unit shearing stress and design method of shear reinforcement for reinforced concrete beams. *Concrete Journal*, V8, No.7, (In Japanese), pp.11-20.
- Arede, A., Costa, A., Costa, A.A., Oliveira, C. and Neves, F., (2008). Experimental in-situ testing of typical masonry constructions of Faial Island-Azores. 14th *World Conference on earthquake Engineering*, Beijing, China.
- Babyak, A.B., (2004). What you see is what you get: A Brief Introduction to Overfitting in Regression-Type Models. *Statistical Psychosomatic Medicine*, 66:411-421.
- Babyak, M.A., (2004). A Brief Nontechnical Introduction to Overfitting in Regression-Type Models, *Psychosomatic Medicine* 66:411– 421
- Bae, S., Miseses, A. and Bayrak, O. (2005). Inelastic Buckling of Reinforcing Bars. *Journal of structural Engineering* 10.1061/(ASCE)0733-9445 131:2 (314)
- Bailey, N.T., (1995). *Statistical Methods in Biology*. 3rd ed., Cambridge University Press.
- Baker, W., Westine P., and Dodge, F. (1981). *Similarity Methods in engineering Dynamics: Theory and Practice of Scale Modeling*. Southwest Research Institute, San Antonio, Texas, USA.
- Biskinis, D. and Fardis, M. (2010). Deformations at flexural yielding of members with continuous or lap-spliced bars. *Structural Concrete*, **11**, no 3.
- Biskinis, D. and Fardis, M. (2010). Flexure-controlled ultimate deformations of members with continuous or lap-spliced bars. *Structural Concrete*, **11**, no 3.
- Blong R (2003a) A review of damage intensity scales. *Nat Haz* 29:57–76.
- Bollen, K.A. and Jackman, R.W. (1990). *Regression diagnostics: An expository treatment of outliers and influential cases*. *Modern Methods of Data Analysis*, pp. 257-91. Newbury Park, CA: Sage

- Bommer J, Spence R, Erdik M, Tabuchi S, Aydinoglu N, Booth E, Del Re D, Peterken O (2002) Development of an earthquake loss model for Turkish catastrophe insurance. *J Seismol* 6:431–436
- Borg, R.C., Rossetto, T. and Varum, H. (2012). “The Effect of the Number of Response Cycles on the Behaviour of Reinforced Concrete Elements Subject to Seismic Loading.” *15th. World Conference on Earthquake Engineering*, Lisbon, Portugal. (Oral)
- Bouckaert, R. R., (2003). Choosing between Two Learning Algorithms based Calibrated Tests, *Proceedings of the 11th. International Conference on machine Learning*, Menlo Park, CA: AAAI Press.
- Box, G.E.P. and Draper, N.R., (1987). *Empirical Model Building and Response Surfaces*. John Wiley & Sons, New York.
- Bozorgnia, Y. and Bertero, V.V. (2003). Damage spectra: characteristics and applications to seismic risk reduction. *Journal of Structural Engineering*, ASCE, **129:10**, 1330-1340.
- Bracci, J.M., Reinhorn, A.M., Mander, J.B. and Kunnath, S.K. (1989). Deterministic model for seismic damage evaluation of RC structures. *Technical Report NCEER-89-0033*, State University of New York, Buffalo N.Y.
- Bracci, J.M., Reinhorn, A.M., Mander, J.B. and Kunnath, S.K. (1989). Deterministic model for seismic damage evaluation of RC structures. *Technical Report NCEER-89-0033*, State University of New York, Buffalo N.Y.
- Breiman, L., (1998). Bias-Variance, Regularization, Instability and Stabilization in Neural networks and Machine Learning, ed. C.M. Bishop, Berlin: Springer, pp.27-56.
- Breusch, T. S. and Pagan, A. R., (1979). A Simple Test for Heteroscedasticity and Random Coefficient Variation. *Econometrica*, 47 (5), pp.1287–1294.
- Bridgman, P.W., (1931). *Dimensional Analysis*, 2nd ed., Yale University Press, New Haven, USA.
- BS8110:Part1 (1985). *Structural use of concrete. Part 1. Code of practice for design and construction*. British Standard Institution.
- Buckingham, E., (1914). On Physically Similar Systems: Illustrations of the Use of Dimensional Analysis. *Physical Review*. 4 pp. 345-376.
- Burnham, K. and Anderson, (2002). *Model Selection Criterion and Multimodel Inference: A Practical Information-Theoretic Approach*. 2nd ed., New York: Springer-Verlag.
- Burnham, K. P. and Anderson, D. R. (2002), *Model Selection and Multimodel Inference: A Practical Information-Theoretic Approach*. 2nd ed., New York: Springer-Verlag.
- Burnham, K. P. and Anderson, D. R., (2004). Multimodel Inference: Understanding AIC and BIC in Model Selection, *Sociological Methods and Research*, 33, pp: 261–304
- Calvi, G., Miranda, P., Pinho, R. and Priestley, M. (2005). Displacement-Based Assessment of RC Columns with Limited Shear Resistance. Research Report No. ROSE-2005/04.
- Calvi, G.M., Pavese, A., Dacarro, F., Lai., C.G. and Beltrami, C., (2001). Design of a Large Dynamic and Pseudo-dynamic Testing Facility. IUSS Press, Pavia, Italy.
- CEB (1993). CEB - Bulletin D'information n° 217 - Selected Justification Notes -Bond and Detailing Lausanne, CEB - Comite euro-international du beton.
- CEB (2000). FIB - BULLETIN 10: Bond of reinforcement in concrete – State-of-the-art report. Lausanne, CEB-FIP.

- CEN (2005). EN 10080 - Steel for the reinforcement of concrete - Weldable reinforcing steel - General, CEN.
- Charvet, I., Eames, E. and Rossetto, T., (2013). New Tsunami Runup Relationships Based on Long Wave Experiments. *Ocean Modelling* 69, pp.79-92.
- Chatterjee, S. and Hadi, A.S., (2006). Regression Analysis by Example, 4th. Ed. Wiley & Sons, Hoboken, New Jersey, USA.
- Chiauszi, L., Masi, A., Mucciarelli, M., Vona, M., Pacor, F., Cultrera, G., Gallovič, F. and Emolo, A. (2012) Building Damage Scenarios Based on Exploitation of Housner Intensity Derived from Finite Faults Ground Motion Simulations. *Bulletin of Earthquake Engineering*, 10, 517-545.
- Chopra A.K., (2001). Dynamics of Structures. Prentice-Hall, New Jearsey.
- Ciampi, V., Eligenhausen, R., Bertero, V. V., and Popov, E. V. (1982). Analytical model for deformed bar bond under generalized excitations. Rep. No., UCB/EERC-82/23, University of California Berkley, California.
- Collins, M.P., and Mitchell, D., (1980). Shear and Torsion design of prestressed and non-prestressed concrete beams. *Journal of the Prestressed Concrete Institute*. V.25, No.5, pp. 32-100.
- Colombo, A. and Negro, P. (2005). A damage index of generalised applicability. *Engineering Structures* 27, 1164-1174.
- Colombo, A. and Negro, P. (2005). A damage index of generalised applicability. *Engineering Structures* 27, 1164-1174.
- Concrete Structures*, Tokyo - ASCE, Special Publication, New York., 226-254.
- Cook, R.D. and Weisberg, S., (1982). *Residuals and influence in regression*, New York, NY: Chapman & Hall.
- Cook, R.D., (1977). "Detection of Influential Observations in Linear Regression". *Technometrics* (American Statistical Association), 19 (1), 15–18.
- Damghani Mahdavi, (2013). The Non-Misleading Value of Inferred Correlation: An Introduction to the Cointelation Model. *Wilmott Magazine*.
- Damghani, M. and, Babak (2012). The Misleading Value of Measured Correlation. *Wilmott* ,1, pp. 64–73.
- Davies P.T., (1980). Dimensions of statistics and physical quantities, *Journal of Applied Statistics*, Vol.29, No.1, pp. 96-97.
- Davies, P.T.. (1980). Dimensions of Statistics and Physical Quantities. *Journal of Applied Statistics*. Vol. 29, No.1, pp.96-97
- Dawid, A. P., (1979). Conditional Independence in Statistical Theory. *Journal of the Royal Statistical Society, Series B* 41 (1) pp. 1–31.
- DiPasquale, E. and Cakmak, A.S. (1987). Detection and assessment of seismic structural damage. *Technical Report NCEER-87-007*, State University of New York, Buffalo N.Y.
- Dolce, M., Kappos, A.J., Masi, A., Penelis, G. and Vona, M. (2006) Vulnerability Assessment and Earthquake Scenarios of the Building Stock of Potenza (Southern Italy) Using the Italian and Greek Methodologies. *Engineering Structures*, 28, 357-371.
- Donea, J. and Jones, P.M., (1991). Experimental and Numerical Methods in Earthquake Engineering. Kluwer Academic Publishers, Netherlands.

- Dymiotis, C., Kappos, A. and Chryssanthopoulos, M., (1999). Seismic Reliability of R/C Frames with Uncertain Drift and Member Capacity. *ASCE Journal of Structural Engineering*, **125:9**, 1038-1047. *Engineering and Structural Dynamics*. **21**: 837-848.
- Dziak, J.J., Coffman, D.L., Lanza, S.T. and Li, R., (2012). Sensitivity and Specificity of Information Criteria. Technical Report Series: 12-119, The Pennsylvania State University, USA.
- EEFIT (2009). The L'Aquila, Italy Earthquake of 6 April 2009: A Preliminary field report, Earthquake Engineering Field Investigation Team (EEFIT).
- EEFIT. (2003). The Bingol, Turkey Earthquake of the 1st of May 2003. Earthquake Engineering Field Investigation Team (EEFIT).
- EERI (1999). Structural Engineering Reconnaissance of the August 17, 1999 earthquake: Kocaeli (Izmit), Turkey. PEER Report 2000/09.
- Efroymson, M.A., (1960). Multiple regression analysis. In Ralston, A. and Wilf, HS, editors, *Mathematical Methods for Digital Computers*. Wiley.
- Eligenhausen, R., Popov, E. P., and Bertero, V. V., (1983). Local bond stress-slip relationships of deformed bars under generalized excitations. Rep. No., UCB/EERC-82/23, University of California Berkley, California.
- Elwood, K. and Eberhard, M. (2006). Effective Stiffness of Reinforced Concrete Columns. PEER Research Digest 2006-1.
- EN 1998-3 (2005). Eurocode 8: Design of structures for earthquake resistance – Part 3: Assessment and retrofitting. Committee for Standardization (CEN).
- EN 1998-3 (2009). Corrigendum for Eurocode 8: Design of structures for earthquake resistance – Part 3: Assessment and retrofitting. Committee for Standardization (CEN).
- EN ISO 6892-1 (2009). Metallic materials – Tensile testing Part 1: method of test at ambient temperature. Committee for Standardization (CEN).
- EN12390-3 (2009). Testing Hardened Concrete-Part3: Compressive strength of test specimens. European Committee for Standardization (CEN).
- EN1998-1 (2004). Eurocode 8: Design of structures for earthquake resistance – Part 1: general rules, seismic actions and rules for buildings. European Committee for Standardization (CEN).
- EN1998-1(2004). Eurocode 8: Design of structures for earthquake resistance – Part1: General rules, seismic actions and rules for buildings. European Committee for Standardization (CEN).
- Erduran E. and Yakut A. (2004). Drift based damage functions for reinforced concrete columns. *Computers and Structures* **82**, 121-130.
- Ernst, G.C., (1957). Plastic hinging at the intersection of beams and columns. *Journal of American Concrete Institute*, Vol. 28, No. 12, pp.1119-1144.
- Euler, L., (1759). Sur le forces des colonnes. *Memores de l'Academie Royale des Sciences et Belles Lettres*, 13, Berlin, (in French).
- Fajfar, P. (1992). Equivalent Ductility Factors, Taking into Account Low-Cycle Fatigue. *Earthquake*
- Fardis, M. (1995). Damage measure and failure criteria for reinforced concrete members. *Proceedings 10th. European Conference on earthquake Engineering*, Vienna. Rotterdam: Balkema 1377-1382.

- Fardis, M.N. (2009). Seismic Design, Assessment and Retrofitting of Concrete Buildings. *Geotechnical, Geological and earthquake Engineering-8*, Springer.
- Fattah, A.M.A. (2008). Eccentricity Based Analysis of Confined Reinforced Concrete Circular Columns. M.Sc. Thesis, Kansas State University.
- Ferreira, T., Vincente, R., Silva, J., Varum, U., and Costa A. (2013). Seismic vulnerability assessment of historical urban centres: case study of old city centre in Seixal, Portugal. *Bull Earthquake Eng* DOI 10. 1007/S10518-013-9447-2.
- Finney D.J., (1977). Dimensions of statistics, *Journal of Applied Statistics*, Vol 26. , pp. 285-289.
- Fox, J., (1997). Applied Regression Analysis, Linear Models, and Related Methods. SAGE Publications, Inc. Thousand Oaks, CA.
- Fox, J., (2005). The R Commander: A Basic Statistics Graphical User Interface to R. *Journal of Statistical Software*, 14(9), pp. 1-42.
- Garson, G.D. 2012. Partial Correlation. Statistical Associates Publishers
- Geisser, S., (1975). The Predictive Sample Reuse Method with Applications. *Journal of the American Statistical Association*, 70, (350), pp. 320-328.
- Ghobarah A., Abou-Elfath, H. and Biddah A. (1999). Response-Based damage Assessment of Structures. *Earthquake Engineering and Strcutural Dynamics* **28**, 79-104.
- Ghobarah A., Abou-Elfath, H. and Biddah A. (1999). Response-Based damage Assessment of Structures. *Earthquake Engineering and Strcutural Dynamics* **28**, 79-104.
- Ghobarah, A., Elfath H., and Biddah A. (1999). Response-based damage assessment of structures. *Earthquake Engineering and structural dynamics* **28**, 79-104.
- Gibbings, J.C., (2011). Dimensional Analysis, Springer, UK.
- Gibbons, J.D. and Chakraborti, S., (2003). Nonparametric Statistical Inference. 4th. Ed. Marcel Dekker.
- Gomes, A. and Appleton, J. (1997). Nonlinear cyclic stress-strain relationship of reinforcing bars including buckling. *Engineering Structures*, Vol. 19, No.10, pp.822-226.
- Goodman, L., and Krustal, W. H., (1972). Measures of Association for Cross Classifications, IV: Simplification of Asymptotic Variances. *Journal of the American Statistical Association* 67 (338): 415-421.
- Goretti, A., Brammerini, F., Di Pasquale, G., Dolce, M., Lagomarsino, S., Parodi, S., Iervolino, I., Verderame, G.M., Bernardini, A., Penna, A., Rota, M., Masi, A. and Vona, M. (2008) The Italian Contribution to the USGS PAGER Project. *Proc. of 14th World Conference on Earthquake Engineering*, Beijing, 2008.
- Green, S.B., (1991). How many subjects does it take to do a regression analysis? *Multivariate Behavioral Research*, Taylor & Francis, 26, pp. 499-510.
- Grubbs, F.E. (1969). Procedures for detecting outlying observations in samples, *Technometrics* 11 (1) pp. 1–21.
- Gulkan, p. and Akkar, S. (2002). A critical examination of near-field accelerograms from the sea of marmara region earthquakes. *Bulletin of the Seismological society of America*, 92, 1, pp. 428-447.
- Harajli, M. H. and Hamad, B. S., (1995). Effect of confinement on bond strength between steel bars and concrete. *ACI Structural Journal*.

- Harajli, M. H., (2009). Bond stress-slip Model for steel bars in unconfined or steel, FRC or FRP confined concrete under cyclic loading. *Journal of structural engineering*, ASCE, p.17
- Harajli, M. H., (2006). Effect of confinement using steel, FRC, or FRP on the bond stress-slip response of steel bars under cyclic loading. *Mater. Struct.*, 39, pp. 621-634.
- Harris, H.G. and Sabnis,, G., (1999). *Structural Modeling and Experimental Techniques*. 2nd. ed., CRC Press.
- Haselton, C., Leil, A., Lange, S., and Deierlein, G. (2008). Beam-Column Element Model Calibrated for Predicting Flexural Response Leading to global Collapse of RC Frame Buildings. PEER 2007/03.
- Hill, M. and Rossetto, T. (2008). Comparison of building damage scales and damage descriptions for use in earthquake loss modelling in Europe. *Bull Earthquake Engineering* 6:335-365.
- Hjorth, J.S., (1994). *Computer Insensitive Statistical Methods: Validation, Model selection and Bootstrap*. Chapman & Hall.
- Horiuchi, T., Inoue, M. and Konno, T., (2000). Development of a real-time hybrid experimental system using a shake table. 12th. *World Conference in Earthquake Engineering*, Auckland, New Zealand.
- Howell, D.C., (2007). The analysis of missing data. In Outwaite, W. & Turner S. *Handbook of Social Science Methodology*. London: Sage.
- Huang, Z. B. and Engstrom, C., (1996). Experimental and analytical studies of the bond behaviour of deformed bars in high strength concrete. 4th *International Symposium on Utilization of High-Strength High Performance Concrete*.
- Hurvich, C. and Tsai, C., (1989). Regression and Time Series Model Selection in Small Samples. *Biometrika*, 76(2), pp. 297-307.
- Ibarra, L., Medina, R. and Krawinkler, H. (2003). Hysteric models that incorporate strength and stiffness deterioration. *Earthquake Engng Struct. Dyn.* 34: 1489-1511.
- Ioannou, I., Borg R.C., Novelli, V., Melo, J., Alexander, D., Kongar, I., Verrucci, E., Cahill B. and Rossetto, T. (2012). "The 29th May 2012 Emilia Romagna Earthquake." EPICentre Field Observation Report No. EPI-FO-290512., UCL-EPICentre, www.epicentre.com
- Kendall, M. G., (1970). *Rank Correlation Methods*. London: Griffin.
- Kim, T., Lee, K. and Chung, Y. (2005). Seismic damage assessment of R.C. bridge columns. *Engineering Structures* 27, 576-592.
- Koutoumanou, E. and Wade, A., (2013). Introduction to dealing with missing Data. *Course Notes, Institute of Child Health*, University College London, U.K.
- Kunnath, S.K., Reinhorn, A.M. and Park, Y.J. (1990). Analytical modelling of inelastic seismic response of R/C structures. *Journal of Structural Engineering*, ASCE, 116:4, 996-1017.
- Kunnath, S.K., Reinhorn, A.M. and Park, Y.J. (1990). Analytical modelling of inelastic seismic response of R/C structures. *Journal of Structural Engineering*, ASCE, 116:4, 996-1017.
- Kwon, O., Elnashai, A.S., Spencer, B.F. and Park, K., (2007). UI-SIMCOR: A Global platform for hybrid distributed simulation. 9th. *Canadian Conference on Earthquake Engineering*, Ontario, Canada.
- Little, R.J.A. and Rubin, D.B., (1987). *Statistical analysis with missing data*. New York, Wiley.

- Lowes, L. and Moehle, J., (1996). Behaviour and rehabilitation of beam-column T-joints in older reinforced concrete bridge structures. 11WCEE, Paper No. 668.
- Mander, J. B., Priestley, M. J. N., and Park, R. (1988). "Theoretical stress-strain model for confined concrete." *J. Struct. Engrg.*, ASCE, 114(8), 1804-1826.
- Mander, J.B., Priestley, M.J.N., and Park, R. (1988). Theoretical Stress-Strain Model for Confined Concrete. *Journal of Structural Engineering*, ASCE, 114(8), 1804-1826.
- Mark, J. and Goldberg, M. A.. (2001). Multiple regression analysis and mass assessment: A review of the issues. *The Appraisal Journal*, January, pp. 89–109.
- Martin-Fernandez, J.A., Barcelo-Vidal, C. and Pawlowsky-Glahn, V., (2003). Dealing with Zeros and Missing Values in Compositional Data Sets Using Nonparametric Imputation. *Mathematical Geology* , 35:3 pp. 253-278.
- Masi, A., Chiauzzi, L., Samela, C., Tosco, L. and Vona, M. (2014) Survey of Dwelling Buildings for Seismic Loss Assessment at Urban Scale, the Case Study of 18 Villages in Val d’AgrI, Italy. *Environmental Engineering and Management Journal*.
- Mathworks, (2013). MATLAB R2013. Natick, Massachusetts: The MathWorks Inc.
- Mau, S.T. and El-Mabsout, M., (1989). Inelastic buckling of reinforcing bars. *Journal of Engineering Mechyanics*, 115(1), pp. 1-17.
- McGullagh, P. and Nelder, J.A., (1989). Generalised Linear Model. Chapman & Hall/CRC.
- Mehanny, S. and Deierlein, G. (2000). Modelling of assessment of seismic performance of composite frames with reinforced concrete columns and steel beams. Blume Earthquake Engineering Center, report No. 135.
- Milutinovic Z, Trendafiloski G (2003). An advanced approach to earthquake risk scenarios with applications to different European towns, RISK-UE Report WP4: vulnerability of current buildings. European Commission, Brussels.
- Miranda, E. and Akkar, S. (2005). Statistical evaluation of approximate methods for estimating maximum deformation demands on existing structures. *Journal of Structural Engineering* 10.1061/(ASCE) 0733-9445 131:1 (160).
- Moore, A.W. and Lee, M. S., (1994). Efficient Algorithms for Minimizing Cross Validation Error, *Proceedings of the 11th. International Conference on machine Learning*, Morgan Kaufmann.
- Moore, D.S., Mc Cabe, G.P. and Craig, B. (2009). Introduction to Practice of Statistics, 6th. ed. Freeman, New York, USA
- Mostafaei, H., and Kabeyasawa, T. (2007). Axial-shear-flexure interaction approach for reinforced concrete columns. *ACI Structural Journal* no. 104-S23.
- Nakashima, M., Hato, H. and Takaoka, E., (1992). Development of real-time pseudo dynamic testing. *Earthquake, Engineering & Structural Dynamics*, V21-Issue 1, pp. 79-92.
- Newland, D.E., (1975). An introduction to random vibrations and spectral analysis. Longman Group Limited, London.
- Nikolic D., Muresan R., Feng W., Singer W., (2012). Scaled correlation analysis: a better way to compute a cross-correlogram. *European Journal of Neuroscience*, pp. 1–21
- Nilsson, I.H.E. and Losberg, A., (1976). Reinforced concrete corners and joints subjected to bending moments. *Journal of the Structural Division*, Vol. 102. No. 6, June 1976, pp.1229-1254.
- Norusis, M.J., (2008). SPSS Guide to Data Analysis, Prentice Hall, USA.

- OPCM-3519. (2006). Criteri Generali per l'Individuazione Delle Zone Sismiche e per la Formazione e l'aggiornamento deglielenchi delle medesime zone. *Italian Government Gazette* (In Italian).
- Padilla D. and Rodriguez M.E., (2009). A damage index for the seismic analysis of reinforced concrete members. *Journal of earthquake engineering*, **13**:364-383.
- Panagiotakos, T., and Fardis M. (2001). Deformations of reinforced concrete members at yielding and ultimate. *ACI Structural Journal* **98**-S13.
- Park, R., Kent, D.C. and Sampson, R.A., (1972). Reinforced Concrete Members with Cyclic Loading. *Journal of the Structural Division, ASCE*, Vol. 98, ST7, pp. 1341-1360.
- Park, R., Scott, B., and Priestley M. (1982). Stress –Strain behavior of concrete confined by overlapping hoops at low and high stress rates. *ACI Journal* no. **79**-2.
- Park, Y. and Ang, A. (1985). Mechanistic Seismic Damage Model fpr Reinforced Concrete. *Journal of Structural Engineering* **11**:4, 722-739.
- Pearson, K. (1895) "Notes on regression and inheritance in the case of two parents," *Proceedings of the Royal Society of London*, 58: 240–242.
- Powanurson, S. (2003). Effect of Confinement on Shear Dominated Reinforced Concrete Elements. Ph.D. Thesis, Texas A&M University.
- Powell, G.H. and Allahabadi, R. (1988). *Earthquake Engineering and Structural Dynamics*, **16**, 719-734.
- Prandtl, L., (1935). The Mechanics of Viscous Fluids. (W. F. Durand, Ed.) *Aerodynamics Theory*, Vol. 3, Div. G, Sec 2.6, p189. Springer Berlin.
- R Core Team, (2013). R: A language and environment for statistical computing. *R Foundation for Statistical Computing*, Vienna, Austria. <http://www.R-project.org/>.
- Rahnama, M. and Krawinkler, H. (1993). Effects of soft soil and hysteresis model on seismic demands. *Blume Earthquake Engineering Center*, Report No. 108, Stanford University, CA, USA.
- Rodgers, J. and Nicewander, W., (1988). Thirteen ways to look at the correlation coefficient. *The American Statistician*, 42(1):59–66, February 1988.
- Rossetto T. (2004). Vulnerability Curves for the Seismic Assessment of Reinforced Concrete Building Populations, Ph.D. Thesis, Dept. of Civil and Environmental Engineering, Imperial College, University of London.
- Rossetto, T. and Elnashai, A. (2003). Derivation of vulnerability functions from European-type RC structures based on observational data. *Engineering Structures* **25**, 1241-1263.
- Ruan, D., Chen, G., Kerre, E.E. and Wets, G., (2005). Intelligent Data Mining: Techniques and Applications. *Studies in Computational Intelligence*, Vol. 5; Springer.
- Rubin, D.B., (1976). Multiple imputation for nonresponse in surveys. *Wiley series in Probability and Mathematical Statistics*.
- Sasmal, S., Ramanjaneyulu, K., Novak, B., Srinivas, V., Kumar, K. S., Korkowski, C., Roehm, C., Lakshmanan, N. and Lyer, N. R., (2010). Seismic retrofitting of nonductile beam-column sub-assembly using FRP wrapping and steel plate jacketing. *Construction and Building Materials* **25**, pp.175-182.
- Schwarz, G. E., (1978). Estimating the dimension of a model. *Annals of Statistics* 6(2): 461-464.

- Seismosoft (2010). SeismoStruct V5.03., Seismosoft, Available at <http://www.seismosoft.com>
- Sewell, M. (2008). Model Selection. Department of Computer Science, University College London.
- Shao, J., (1993). Linear Model Selection by Cross-Validation. *Journal of The American Statistical Association*, Taylor & Francis, Vol. 88, No.422: 486-494.
- Shao, J., (1997). An Asymptotic Theory for Linear Model Selection. *Statistica Sinica*, 7:221-264.
- Shapiro, S. S. and Wilk, M. B. (1965). An analysis of variance test for normality (complete samples). *Biometrika*, 52 (3-4): 591-611.
- Sonin, A.A. (2001). The Physical Basis of Dimensional Analysis. *Department of Mechanical Engineering*, MIT, USA.
- Spearman, C.E. (1904) The proof and measurement of association between two things. *American Journal of Psychology* 14: 72-101.
- Spiegel, M., Schiller, J. and Srinivasan, A., (2001). Probability and Statistics. McGraw-Hill.
- Stone, M. (1977). An Asymptotic Equivalence of Choice of Model by Cross-Validation and Akaike's Criterion, *Journal of the Royal Statistical Society. Series B (Methodological)* 39 (1): 44-47.
- Stone, M., (1974). Cross-Validatory Choice and Assessment of Statistical Predictions. *Journal of the Royal Statistical Society. Series B (Methodological)* 36(2), 111-147.
- Sullivan, T., Pinho, R. and Pavese, A., (2004). An Introduction to Structural Testing Techniques in Earthquake Engineering. *Educational Report No. ROSE-2004/1*, IUSS Press, Pavia, Italy.
- Takanashi, K., Udagawa, K., Seki, M., Okada, T. and Tanaka, H., (1975). Nonlinear earthquake response analysis of structures by a computer-actuator on-line system. *Bulletin of earthquake Resistant Structure Research Center*, No. 8, Institute of Industrial Science, University of Tokyo, Japan.
- Tassios, T. P., (1979). Properties of bond between concrete and steel under load cycles idealizing seismic actions. Bulletin d'Information N.o 131, CEB, Paris.
- Thewalt, C.R. and Mahin, S.A. Hybrid solution techniques for generalized pseudodynamic testing. *Earthquake Engineering Research Centre UCB/EERC-87/01*, University of California, Berkley.
- Thode, H.C., (2002). Testing For Normality. Statistics; Tesxtbooks and Monographs, Volume 164. Marcel Dekker.
- Urmson, C. and Mander, J. (2012). Local buckling analysis of longitudinal reinforcing bars. DOI: 10.1061/(ASCE)ST.1943-541X.0000414.
- Van Buuren, S. and Groothuis-Oudshoorn, K., (2011). MICE- Multivariate Imputation by Chained Equations in R. *Journal of Statistical Software*. December, 2011, V45 Issue 3.
- Van Mier, J.G.M. (1986). "Multiaxial Strain-Softening of Concrete." *Materials and Structures*, RILEM, 19(111), 179-200.
- Vapnik, V. N. and Chervonenkis, (1974). Teoriya Raspoznavaniya Obrazov: Statisticheskie Problemy Obucheniya. (Russian) [Theory of Pattern Recognition: Statistical Problems of Learning]. Moscow: Nauka.
- Varian, H., (2005). Bootstrap Tutorial. *Mathematica Journal*, 9, 768-775.
- Vecchio, F. J., (1989). Nonlinear Finite Element Analysis of Reinforced concrete members. *ACI Structural Journal*, V.86, No.1, pp.26-35.

Vecchio, F. J., and Collins, M. P. (1988), Predicting the Response of Reinforced Concrete Beams Subjected to Shear Using Modified Compression Field Theory. *ACI Structural Journal*, V.85, No.3pp. 258-268.

Vecchio, F.J., and Collins, M.P. (1982). "The Response of Reinforced Concrete to In-Plane Shear and Normal Stresses." *Publication No. 82-03*, Department of Civil Engineering, University of Toronto.

Vecchio, J. and Collins, M. (1986). The modified compression-field theory for reinforced concrete elements subjected to shear. *ACI Journal* no. 83-22.

Verderame, G.M., Fabbrocino, G. and Manfredi, G., (2008). Seismic response of r.c. columns with smooth reinforcement. Part 1: Monotonic tests. *Engineering Structures*, 30(2008)2277-2288.

Vererame, G., Ricci P., Manfredi G. and Cosenza E. (2010). Ultimate chord rotation of RC columns with smooth bars: some considerations about EC8 prescriptions. *Bull Earthquake Eng* **8**:1351-1373.

Wang, L., Zhou, X. and Yan, W., (2012). Damage detection of RC beams based on experiment and analysis of nonlinear dynamic characteristics. *Construction and Building Materials*. 29 (2012) 420-427.

Wherry, R., (1931). A new Formula for Predicting the Shrinkage of the Coefficient of Multiple Correlation. *The Annals of mathematical Statistics*, 2(4), 440-457.

Willam, K.J., Hurlbut, B., and Sture, S. (1986). "Experimental and Constitutive Aspects

Williams, M. and Sexsmith, R. (1995). Seismic Damage Indices for Concrete Structures: A State-of-the-Art Review. *Earthquake Spectra* **11:2**, 319-349.

Yabana, S. and Kanazawa, K., (1996). Shaking table tests of earthquake resisting walls. *11th World Conference on Earthquake Engineering*, Paper No. 456.

Yakut, A. (2004) Reinforced Concrete Frame Construction. *World Housing Encyclopedia—Summary Publication*.

Zhu, C., Chen, L., Lundgren, K. and Fang C. (2004). Corrosion influence on bond in reinforced concrete. *Cement and concrete Research* **34**. 2159-2167. Pg 44

Zovkic, J., Sigmund, V. and Guljas, I., (2012). Cyclic testing of a single bay reinforced concrete frames with various types of masonry infill. *Journal of the International Association for Earthquake Engineering*.

Appendix A Detailing Requirements by Different Guidelines

Table A-1. Detailing recommendations according to various past codes in Turkey.

1968	Turkey: Seismic Code
<ul style="list-style-type: none"> Minimum beam dimensions: 150x300mm; Minimum column dimensions: min(0.05h, 240mm); Minimum shear walls: min(0.04h, 200); To provide sufficient transverse reinforcement, without exact specifications. Column ties continued within the node section. 	
	For beam column joints: Spacing of stirrups/column ties in the confinement region should be half the spacing of the middle region. The confinement region is defined as having a length equal to the largest effective depth of any member framing in the joint.
1975	Turkey: Specification for Structures to be Built in Disaster Areas
<ul style="list-style-type: none"> Minimum beam dimensions: 200x300mm; Minimum column dimensions: min(0.05h, 150mm); Minimum stirrup/tie diameter: 8mm Minimum stirrup spacing: B or 0.5D 	
<ul style="list-style-type: none"> Minimum slab thickness: 100mm Maximum column width/depth ratio: 3 Minimum/maximum rebar ratios by area: 0.01/0.035 Region of confinement > max(0.167Column height; 450); Volumetric ratio of transverse reinforcement (ρ) 	
<ul style="list-style-type: none"> Angle of Hooks for ties in confinement regions: 135° S1 (Minimum/maximum tie spacing): 50mm/100mm S2: based on gravity and seismic forces requirements 	

Table A-2. Detailing recommendations according to various past codes in Turkey.

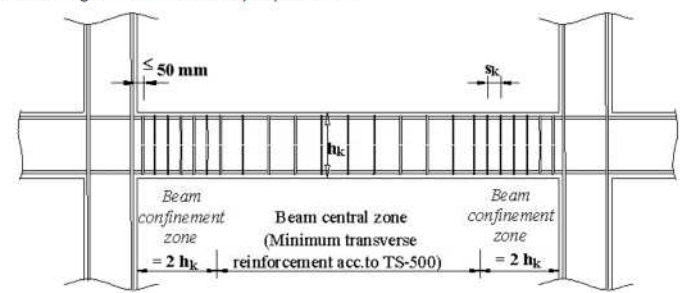
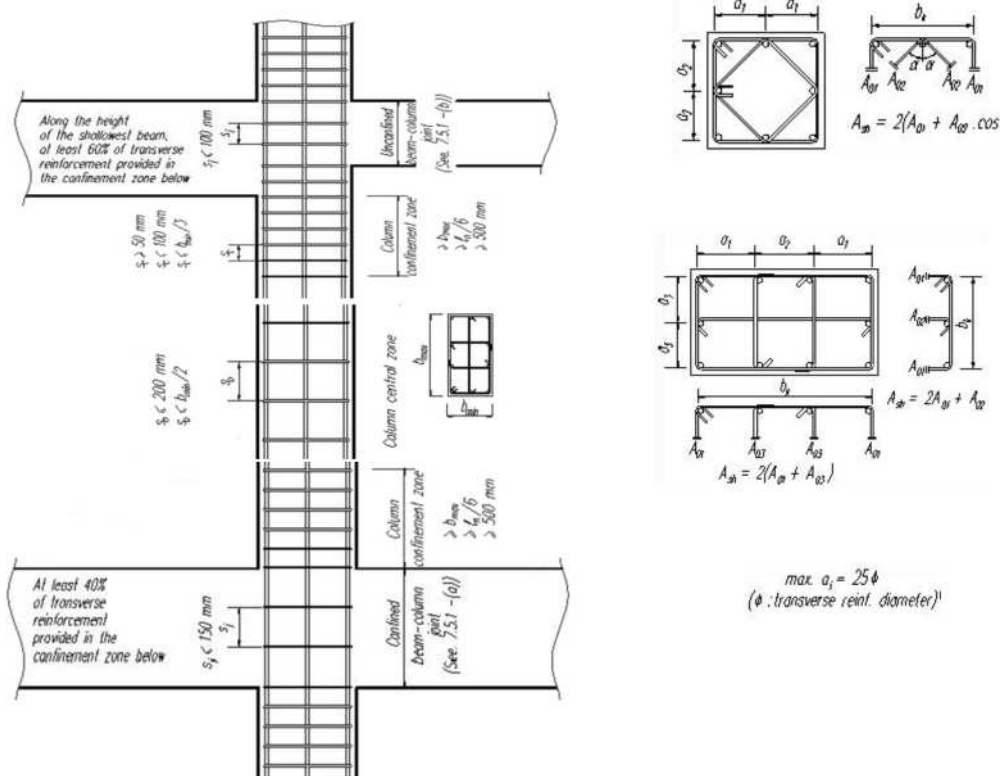
1997	<p align="center">Turkey: Specification for Structures to be Built in Disaster Areas</p>
	<ul style="list-style-type: none"> Classification of R.C., buildings into high or normal ductility, based on detailing of components Detailing for beams with high and normal ductility requirements:  <p align="center"> $s_k \leq h_k / 4$ $s_k \leq 8\phi$ (ϕ = min. longitudinal rebar dia.) $s_k \leq 150$ mm </p>
	<ul style="list-style-type: none"> Minimum column dimensions: 250x300mm. Angle of Hooks for ties in all regions: 135°; Cross ties may have 90° at ends;
	<p>Column Confinement:</p>  <p> $A_{sq} = 2(A_{o1} + A_{o2} \cdot \cos a)$ $A_{rec} = 2(A_{o1} + A_{o2})$ max. $a_1 = 25\phi$ (ϕ: transverse reinf. diameter) </p>
	<ul style="list-style-type: none"> Lap-splicing of longitudinal bars in middle third of column; If lap-splicing is at the lower part of column, splice length to increase by 125%-150% of the development length Transverse reinforcement in confinement region to be double that indicated in the figure. At joints: Column strength > 1.2 beam strength Shear forces associated with the plastic moments in the columns to be lower than the shear strength of the column

Table A-3 Detailing recommendations according to various past codes that affected various Commonwealth countries, and were an influence in other countries.

1957 UK; Commonwealth Countries; influences on Cyprus, Greece and Turkey: CP114	
•	No specifications for seismic considerations.
•	Size of aggregate for general use: 19mm
•	Type of reinforcement: Cold twisted steel bars (not as compression reinforcement); smooth rolled steel bars; hard drawn steel wire
•	Mix proportions of concrete prepared to be measured by weight: 41-31MPa - 1:1:2 / 50.8kg cement: 0.035m ³ fines: 0.071m ³ coarse; 26-34MPa - 1:1.5:3 / 50.8kg cement: 0.053m ³ fines: 0.106m ³ coarse; 21-28MPa - 1:2:4 / 50.8kg cement: 0.071m ³ fines: 0.142m ³ coarse.
•	Density of longitudinal reinforcement: 0.8% > (lapping 8.0%; no lapping 4.0%)
•	Minimum d _{bl} for columns: 13mm
•	Minimum d _{bl} for columns: >max(5mm; 0.25d _{bl})
•	Column transverse reinforcement pitch: min(b; h; 305mm; 12d _{bl})
•	General cover (c): >2.5cm, >d _{bl}
•	Concrete cover (c) for longitudinal bars in columns: > 3.8cm, > d _{bl} . For b,h< 19cm where d _{bl} <13mm, c=2.5cm
•	Concrete cover (c) for longitudinal bars in beams: >2.5cm, >d _{bl} .
•	Concrete cover (c) for corrosive environments on all steel including transverse reinforcement: >3.8cm
•	Distance between parallel bars: > max(d _{bl} of larger bar; nominal maximum size of coarse aggregate + 0.6mm)
•	Laps in members to be staggered. For deformed bars, assume 25% increase in the bond stresses.
<p>The diagrams illustrate four types of hook anchorage for reinforcement bars:</p> <ul style="list-style-type: none"> (a) Hook with radius $r = 2\phi$. The equivalent anchorage length is $8r = 16\phi$. The hook starts at the 'start of hook' and extends a distance of 4ϕ before curving. An 'additional length as required' is shown extending from the end of the hook. (b) Hook with radius $r = 2\phi$. The equivalent anchorage length is $4r = 8\phi$. Similar to (a), it starts at the 'start of hook' and extends 4ϕ before curving. (c) Hook with radius $r = 3\phi$. The equivalent anchorage length is $8r = 24\phi$. It starts at the 'start of hook' and extends 4ϕ before curving. (d) Hook with radius $r = 3\phi$. The equivalent anchorage length is $4r = 12\phi$. Similar to (c), it starts at the 'start of hook' and extends 4ϕ before curving. 	
1972 UK; Commonwealth Countries; influences on Cyprus, Greece and Turkey: CP110	
•	Bars are either smooth bars, square twisted bars and ribbed bars.
•	Distance between parallel bars: >dbl; bundled bars allowed if bond stress is not a problem.
•	Cover: depends on exposure and concrete grade. Cover measured from transverse steel edge.
•	Size of links for columns: >6mm, >d _{bl} /4
•	Spacing between links: <min(0.75d, 300mm, 12d _{bl})
•	Every corner bar and alternate bar is supported by a link passing round the bar with an included angle of less than 135°.
•	Spacing between longitudinal bars in compression: 150mm
•	Maximum tension, compression reinforcement: <4% in general, <6% for vertically cast columns, <8% for horizontally cast columns, <10% in lap splice areas.
•	Span /depth (L _v /h) ratio for continuous beams: 26
•	Maximum reinforcement length: 6m for 8mm ϕ bars, 12m for 32 mm ϕ bars
•	The bond stress of deformed bars is assumed 30% higher than that of smooth bars.
•	Anchorage may be provided mainly by means of hooks in mild steel or by lapping or anchorage in the case of deformed high yield steel bars.

Table A-4 Detailing recommendations according to various past codes in Italy.

1939	Italy: R.D. 2229 / 39
•	$f_u = 420-500$ [soft carbon steel]; 500-600 [semi hard carbon steel]; 600-700 [hard carbon steel] (MPa)
•	$f_y = >230$ [soft carbon steel]; >270 [semi hard carbon steel]; >310 [hard carbon steel] (MPa)
•	Column- Longitudinal reinforcement: 0.8% for sections 2000cm^2 ; 0.5% for sections $> 8000\text{cm}^2$.
•	Column- Transverse Reinforcement: $s_{\min} = \min(0.5D; 0.5H; 10d_{bl})$
•	Beam- Transverse Reinforcement: 50% shear reinforcement, 50% bent longitudinal reinforcement
•	Cover: 2cm; $\min(2\text{cm}; d_{bl})$
1972, 1974	Italy: D.M. 30 / 05 / 72,74
•	$f_u = 340-500$ [smooth reinforcement]; 460-550 [ribbed reinforcement] (MPa)
•	$f_y = 230-320$ [smooth reinforcement]; 380-440 [ribbed reinforcement] (MPa)
•	Beams and columns bar size: $d_{bl,\min} = 12\text{mm}$
•	Column - Longitudinal Reinforcement: $0.6-5\% A_{\text{conc}}; 0.3-5\% A_{\text{eff}}$.
•	Beam- Longitudinal Reinforcement: $>0.25\% A_{\text{sec}}$ [Smooth Bars]; $>0.15\% A_{\text{sec}}$ [Ribbed Reinforcement]
•	Column- Transverse Reinforcement: $s_{\min} = \min(25\text{cm}; 15d_{bl})$; $d_{bw,\min} = 6\text{mm}$
•	Cover: 2-4cm; $\min(2\text{cm}; d_{bl})$
1980	Italy: D.M. 26 / 03 / 80
•	$f_u = 340-500$ [smooth reinforcement]; 460-550 [ribbed reinforcement] (MPa)
•	$f_y = 230-320$ [smooth reinforcement]; 380-440 [ribbed reinforcement] (MPa)
•	Columns bar size: $12\text{mm} < d_{bl} < 30\text{mm}$
•	Beam bar size: $5\text{mm} < d_{bl} < 30\text{mm}$
•	Column - Longitudinal Reinforcement: $>0.8\% A_{\text{conc}}; 0.3-6\% A_{\text{eff}}$.
•	Beam- Longitudinal Reinforcement: $>0.25\% A_{\text{sec}}$ [Smooth Bars]; $>0.15\% A_{\text{sec}}$ [Ribbed Reinforcement]
•	Column- Transverse Reinforcement: $s_{\min} = \min(25\text{cm}; 15d_{bl})$; $d_{bw,\min} = 6\text{mm}$; For $B_{\text{web}}, D > 400\text{mm}$ -> 4 legs or more.
•	Beam - Transverse Reinforcement: $A_{sh,\min} = 3\text{cm}^2/\text{m}$; $s_{\text{general}} > \min(0.8d; 0.5B)$, >3 hoops/m; $s_{\text{near support}} > 12d_{bl}$; For $B_{\text{web}}, D > 400\text{mm}$ -> 4 legs or
•	Cover: 2-4cm; $\min(2\text{cm}; d_{bl})$
•	Spacing of parallel longitudinal bars : $s_{x,\min} = \max(d_{bl}, 2\text{cm})$
•	Minimum lap-splice length: $L_{sp} = 35d_{bl}$; Minimum inter lap-splice distance: $60d_{bl}$; Maximum reinforcement to be lap-spliced: $1/3 A_{sv}$
•	Effective flange width: $b_{\text{eff}} = B_{\text{web}} + 10t_{\text{slab}}$ [Internal beams]; $b_{\text{eff}} = B_{\text{web}} + 10t_{\text{slab}}$ [External beams]
1996	Italy: D.M. 09 / 01 / 96
•	$f_u = 340-500$ [smooth reinforcement]; 460-550 [ribbed reinforcement] (MPa)
•	$f_y = 230-320$ [smooth reinforcement]; 380-440 [ribbed reinforcement] (MPa)
•	Beams and columns bar size: $d_{bl,\min} = 12\text{mm}$
•	Column - Longitudinal Reinforcement: $>0.8\% A_{\text{conc}}; 0.3-6\% A_{\text{eff}}$.
•	Beam- Longitudinal Reinforcement: $>0.25\% A_{\text{sec}}$ [Smooth Bars]; $>0.15\% A_{\text{sec}}$ [Ribbed Reinforcement]
•	Cover: 2-4cm; $\min(2\text{cm}; d_{bl})$

Table A-5 Detailing recommendations to EN1998 following Fardis (2007).

Property	Building Class		
	DCH	DCM	DCL
Axial load ratio $v_d = \frac{N_{Ed}}{A_c f_{cd}}$	≤ 0.55	≤ 0.65	/
Cross-section sides, h_c , $b_c \geq$	0.25; $\frac{h_v}{10}$ if $\theta = \frac{N\delta}{v_h} > 0.1$	/	/
“critical region” length	1.5; $1.5b_c$; $0.6m$; $\frac{l_c}{5}$	h_c ; b_c ; $0.45m$; $\frac{l_c}{6}$	h_c , b_c
<i>Longitudinal bars:</i>			
ρ_{min}		1%	$0.1 \frac{N_d}{A_c f_{yd}}$; 0.2%
ρ_{max}			4%
$d_{bl} \geq$			8mm
Bars /side \geq		3	2
Spacing between restrained bars	$\leq 150mm$	$\leq 200mm$	/
Distance of unrestrained bar from nearest restrained bar		$\leq 150mm$	
<i>Transverse reinforcement outside critical regions:</i>			
$d_{bw} \geq$			$6mm$; $\frac{d_{bl}}{4}$
Spacing ($s \leq$)	$20d_{bl}$; h_c ; b_c ; $400mm$		$12d_{bl}$; $0.6h_c$; $0.6b_c$; $240mm$
<i>Transverse reinforcement within critical regions:</i>			
$d_{bw} \geq$	$6mm$; $0.4d_{bl} \sqrt{\frac{f_{yd}}{f_{ywd}}}$		$6mm$; $\frac{d_{bl}}{4}$
$s \leq$	$6d_{bl}$; $\frac{b_o}{3}$; $125mm$	$8d_{bl}$; $\frac{b_o}{2}$; $175mm$	/
$\omega_{wd} \geq$	0.08		/
$\alpha\omega_{wd} \geq$	$30\mu_\phi^* v_d \frac{b_c}{b_o} - 0.035$		/
<i>Transverse reinforcement in critical region at column base:</i>			
$\omega_{wd} \geq$	0.12	0.08	/
$\alpha\omega_{wd} \geq$	$30\mu_\phi v_d \frac{b_c}{b_o} - 0.035$		/
(0)	National determined parameter according to Eurocode 2.		
(1)	h_v is the distance of the inflection point to the column end further away, for bending within a plane parallel to the side of interest; l_c is the column clear length.		
(2)	For DCM: If a value of $q < 2$ is used for the design, the transverse reinforcement in critical regions of columns with axial load ratio v_d not greater than 0.2 may just follow the rules applying to DCL columns.		
(3)	For DCH: In the 2 lower storeys of the building, the requirements on d_w , s apply over a distance from the end section not less than 1.5 times the critical region length.		
(4)	Index c denotes the full concrete section and index o the confined core to the centreline of the perimeter hoop; b_o is the smaller side of this core.		
(5)	ω_{wd} is the ratio of the volume of confining hoops to that of the confined core to the centreline of the perimeter hoop multiplied by f_{yd}/f_{cd} .		
(6)	α is the “confinement effectiveness” factor, computed as $\alpha = \alpha_s \alpha_n$, where $\alpha_s = (1 - s/2b_o)(1 - s/2h_o)$ and $\alpha_n = 1 - \{[b_o/((n_h - 1)h_o)] + [h_o/((n_b - 1)b_o)]\}/3$ for rectangular hoops with n_b legs parallel to the side of the core length b_o , and n_h legs parallel to the side with length h_o .		
(7)	For DCH: at column ends protected from plastic hinging through the capacity design check at beam-column joints, μ_ϕ^* is the value of the curvature ductility factor that corresponds to 2/3 of the basic value, q_o , of the behaviour factor used in the design. At the ends of the columns where plastic hinging is not prevented by some exemptions $\mu_\phi^* = \mu_\phi$.		
(8)	The exemptions consist in a) beam-column joint is at the top floor, b) ground storey in a 2 storey structure with design axial load ratio $v_d < 0.3$, c) shear walls resist at least 50% of the base shear parallel to the plane of the frame, and d) in case of one-out-of four columns of plane frames with columns of similar size. $\varepsilon_{sy,d} = f_{yd}/E_s$		
(9)	μ_ϕ is the value of the curvature ductility factor that corresponds to the basic value, q_o , of the behaviour factor used in the design as: $\mu_\phi = 2q_o - 1$ if $T \geq T_c$ or $\mu_\phi = 1 + 2(q_o - 1)T_c/T$ if $T < T_c$.		
	For DCH: $q_o = 4.5\alpha_u/\alpha_1$ where $\alpha_u/\alpha_1 = 1.3$ for multi-frame systems according to EN1998-1-1-2004.		
	For DCM: $q_o = 3.0\alpha_u/\alpha_1$ where $\alpha_u/\alpha_1 = 1.3$ for multi-frame systems according to EN1998-1-1-2004.		

Appendix B Auxiliary Testing Campaigns

B.1 Cyclic Tests on Concrete Specimens

In an auxiliary testing campaign, uni-axial compression tests are conducted on 144 standard concrete cylinders measuring 150x300mm using three different loading patterns. The specimens refer to the concrete with grade C16/20 used in the experimental campaign discussed in Chapter 4. Nine cylindrical specimens are produced per concrete cast. Then, 3 specimens from each cast are used for each loading pattern. Out of the total number of specimens, 11 gave errors when recording the deformation, or failed.

The loading patterns consisted in a monotonic compression, a cyclic compression with 10 cycles at 80% of the maximum stress before this is reached, and a cyclic compression with 10 cycles after the maximum force is reached. Figure B-1 shows the typical normalised stress with strain response of each of the three compression patterns. The response indicates how the strain and strength decay is not much affected by cycles before the maximum. The same cannot be said when the cycles are applied after the maximum.

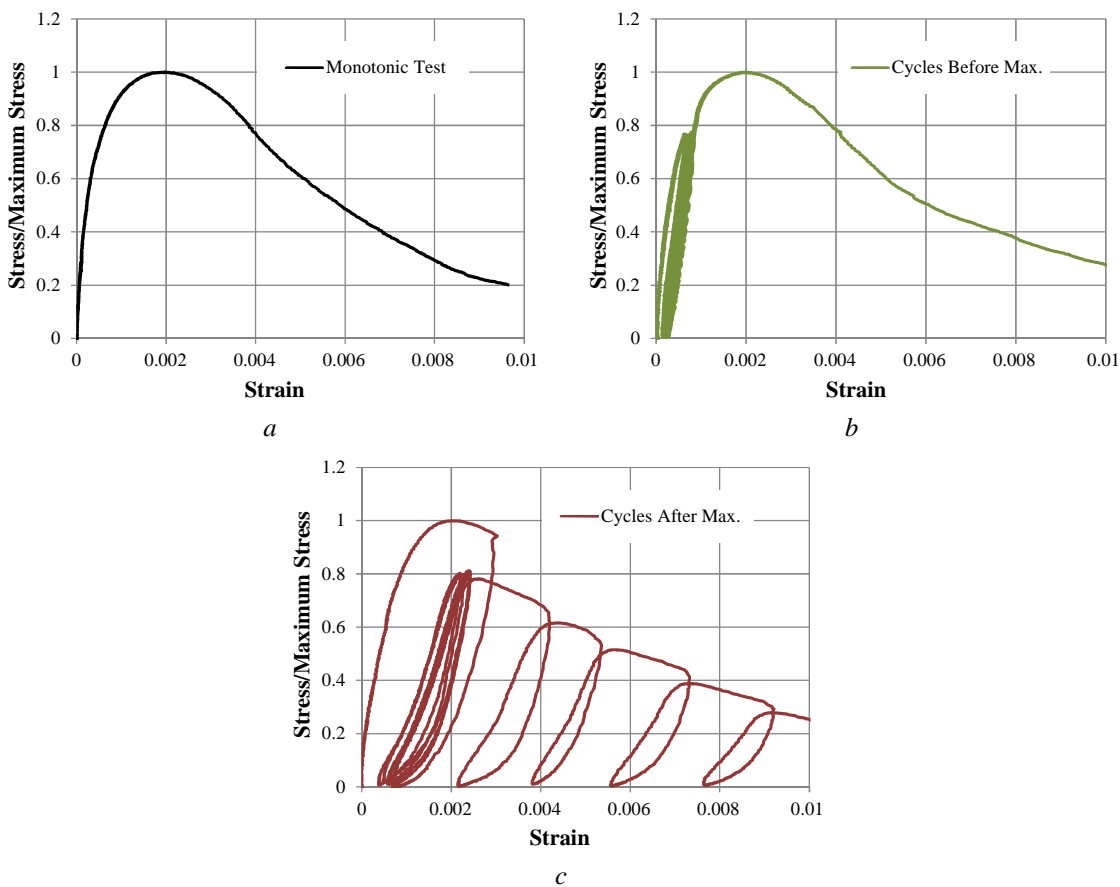


Figure B-1 Stress/maximum stress – strain response of: a) monotonic compression pattern, b) 10 cycles before maximum stress loading pattern, c) 10 cycles after maximum stress loading pattern.

Figure B-2 shows the distribution of strain at maximum stress, strain at 20% of maximum stress after this is reached, and strain at 50% of maximum stress after this is reached. The strain at maximum stress is confirmed as assumed in EN1992-1 (CEN,2004) to be around 0.02. Following Shapiro-Wilk tests for normality, t-tests are used to compare means in the statistical package *R* (R Core Team, 2013) and *R Commander* (Fox, 2005). For the strain at maximum stress, $p > 0.05$, and hence the mean strain is statistically affected by a different loading scenario. However, for strain at 20% and 50% maximum stress reduction, the hypothesis is accepted that corresponding means of after cycles distribution is different than means of the monotonic distribution, and cycles before distributions. However, the hypothesis between means of cycles before distribution and monotonic distribution is rejected. This means that cycles before maximum does not have large influence on the general behaviour of concrete in terms of strain, however cycles after the maximum have a large influence on the stain and failing concrete. This highlights the importance of how different cyclic effects, effect the behaviour of concrete differently, and the importance in seismic applications.

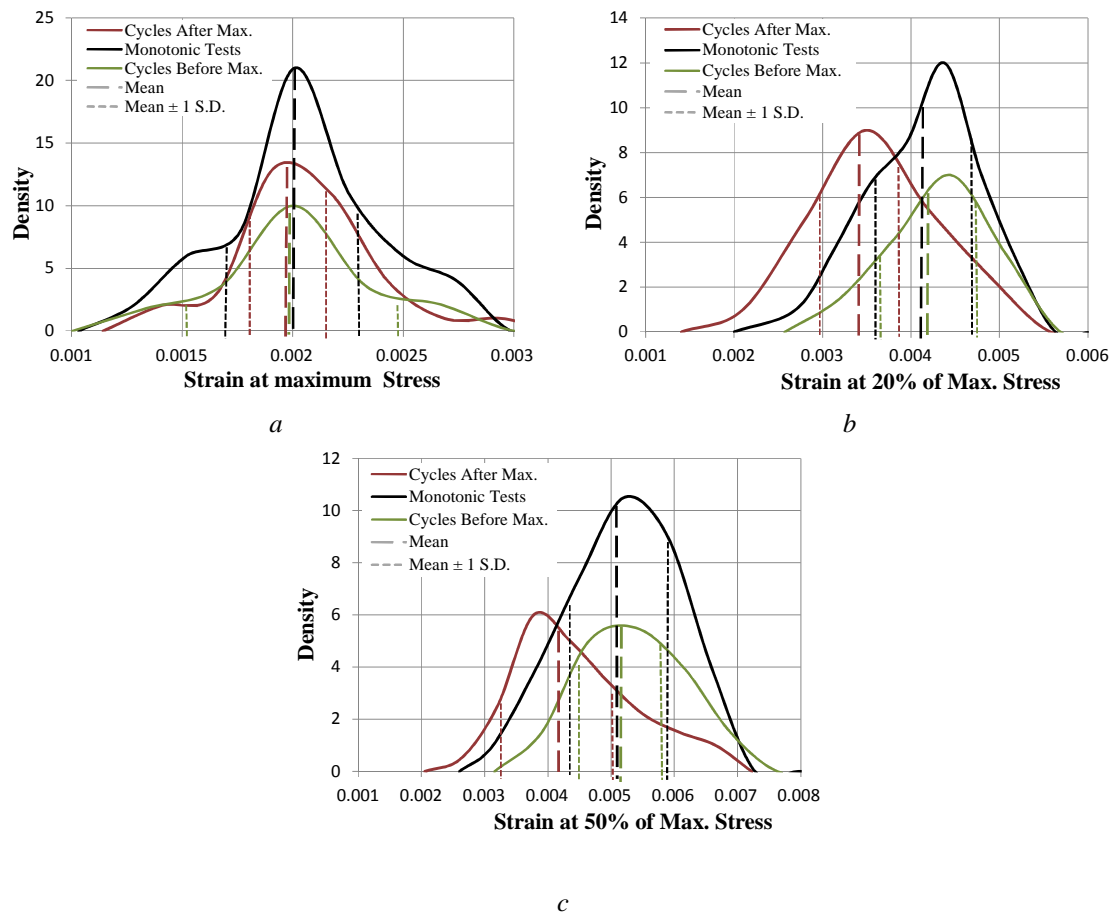


Figure B-2 Distribution of strain from compression tests using monotonic loading, 10 cycles after reaching the maximum stress, and 10 cycles before reaching the maximum stress. Strains are considered at: a) maximum stress, b)20% maximum stress reduction, c)50% maximum stress reduction.

B.2 Pull-out Tests

In an auxiliary testing campaign pull-out tests are conducted on 52 specimens. The tests carried out following CEB-217 (1993) and EN1008 (CEN, 2005) compliment the experimental campaign on columns and beam-column connections discussed in Chapter 3. Figure B-3 shows the test setup used. Three tests are conducted for each variable which included different bar diameter (8mm, 12mm, 16mm and 20mm), different concrete grade (C16/20 and C30/37), ribbed and smooth 8mm reinforcement bars, different reinforcement grade (A235NL, A400NRSD and A500NRSD), different compaction application (using vibrator and by hand simulating past practice) different hooks on 8mm bars used as stirrups (90° and 135°, ribbed and smooth) and different restraint on 12mm bars (without restraint and with restraint from an 8mm bar simulating a stirrup tied with a longitudinal bar). The outcome and detailed comparison of these test results is beyond the scope of this research, however as shown in figure B-4, all these variables affect the bond-slip relation development and agree with recommendations and observations by CEB (2000), and are therefore important to be included as explanatory variables in the determination of EDP models.



Figure B-3 Test setup for pull-out tests.

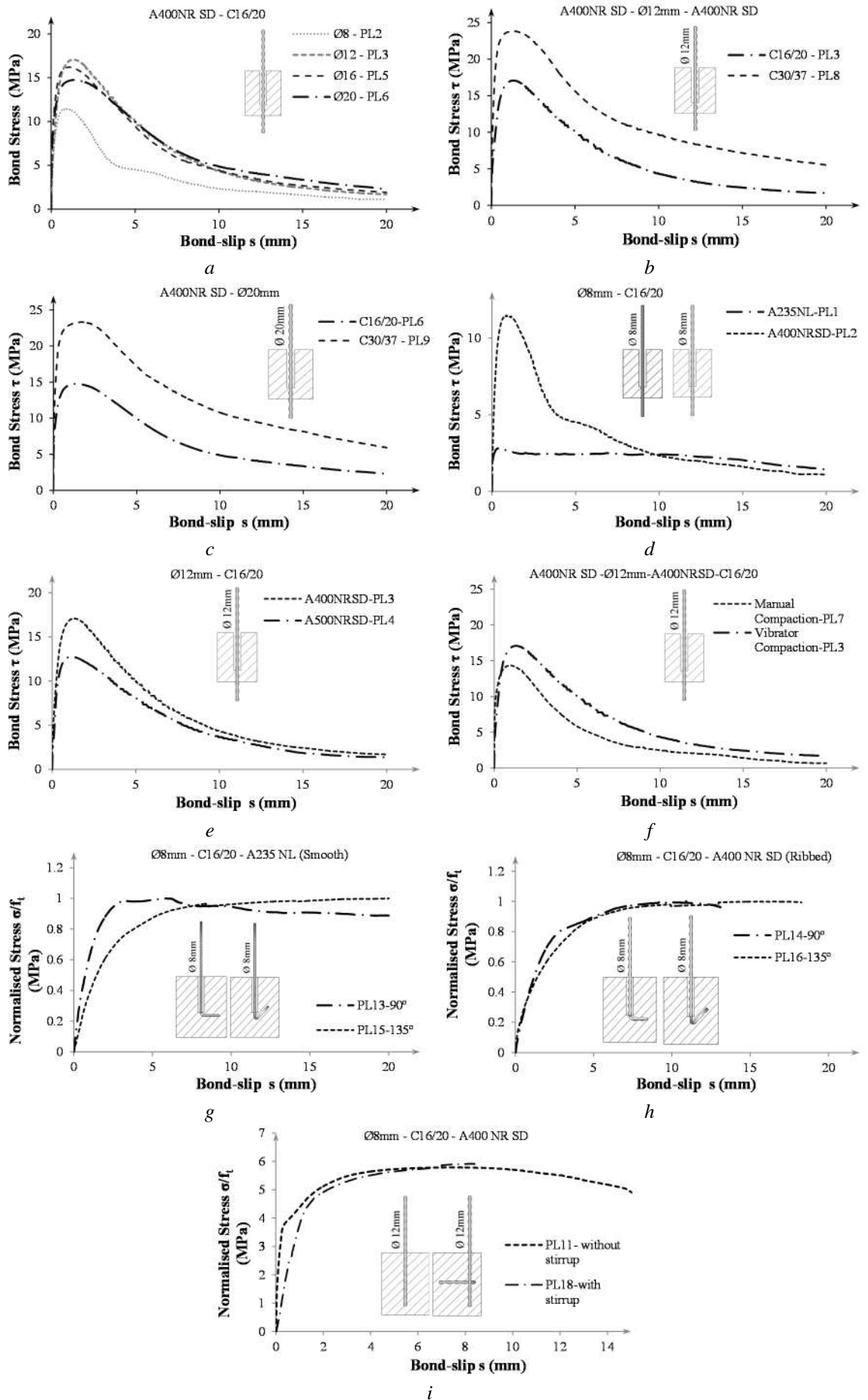


Figure B-4 Pull-out tests on specimen with varying: a) reinforcement diameter, b) concrete grade for 12mm diameter bars, c) concrete grade for 20mm diameter bars, d) smooth and ribbed 8mm

reinforcement, e) reinforcement grade, f)compaction method, g) hooks on smooth bars, h) hooks on ribbed bars, i) restraint on longitudinal bar.

Appendix C Low-cycle fatigue tests on Beam-Column Connections

C.1 Experimental setup for the experimental campaign

Similar to the low-cycle fatigue tests on column-foundation specimens, tests on beam-column connections were conducted at the structural laboratories at the University of Aveiro in Portugal. The setups of the beam-column connections (Figure C-1) consist in a modification of the setup for internal beam-column connections for the experimental campaign of Fernandes (2012). The setups consist in a horizontal layout which is common in the absence of strong walls and the presence and availability of strong floors (Sasmal *et al.*, 2010). In the proposed setups, the specimens are supported horizontally on universal ball bearings which are fixed at the centre of mass of each element. The horizontal supports consist in high-strength concrete block, that elevate the column a distance above the strong floor in order to allow the possibility of incorporating slabs with beam-column connection specimen.

Internal and external beam-connections (Figure C-2) are hinged by a linear bearing at the tip of the lower column allowing rotation of the specimen in the horizontal plane. The beams are allowed to move perpendicular to the axis of the columns and in the horizontal plane, and restrain movement in all other directions by a system of rectangular frames, linear bearings and screw-clamps for each beam.

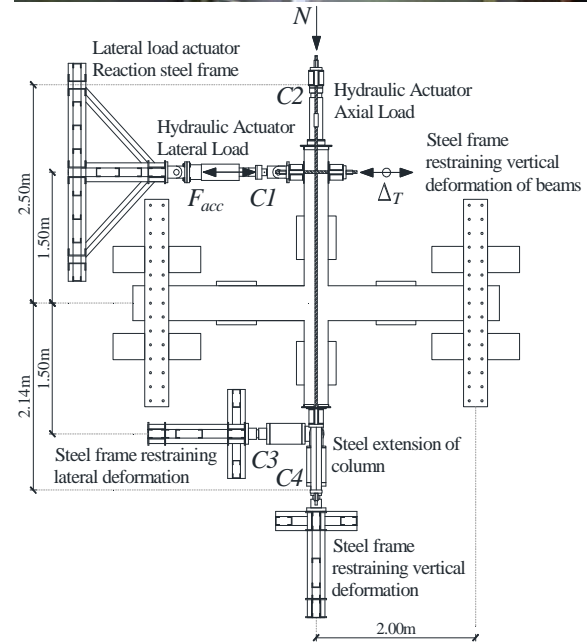
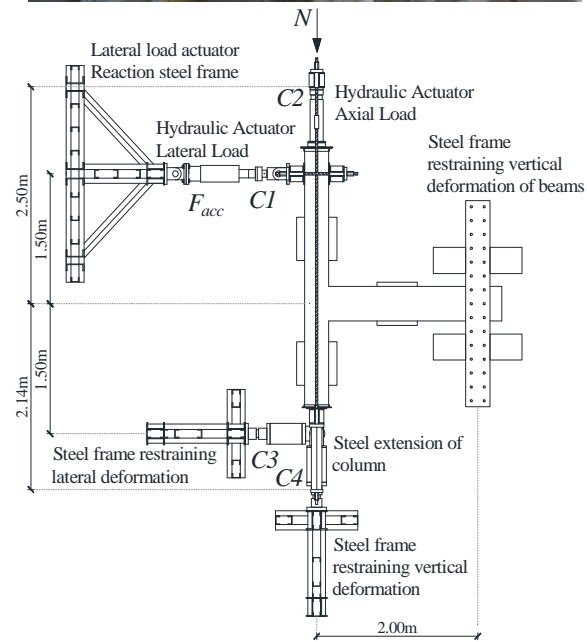
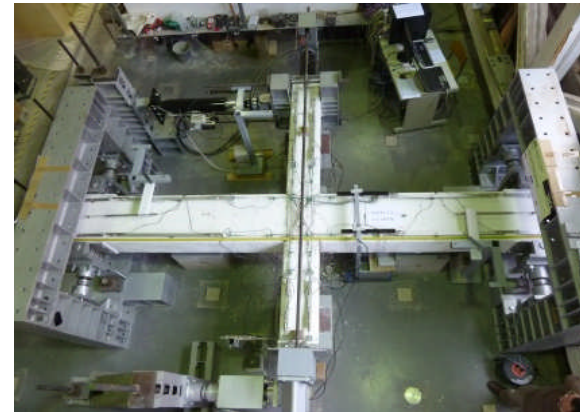


Figure C-1 Test setup for: (a) beam-column T-joints, (b) beam-column X-joints.

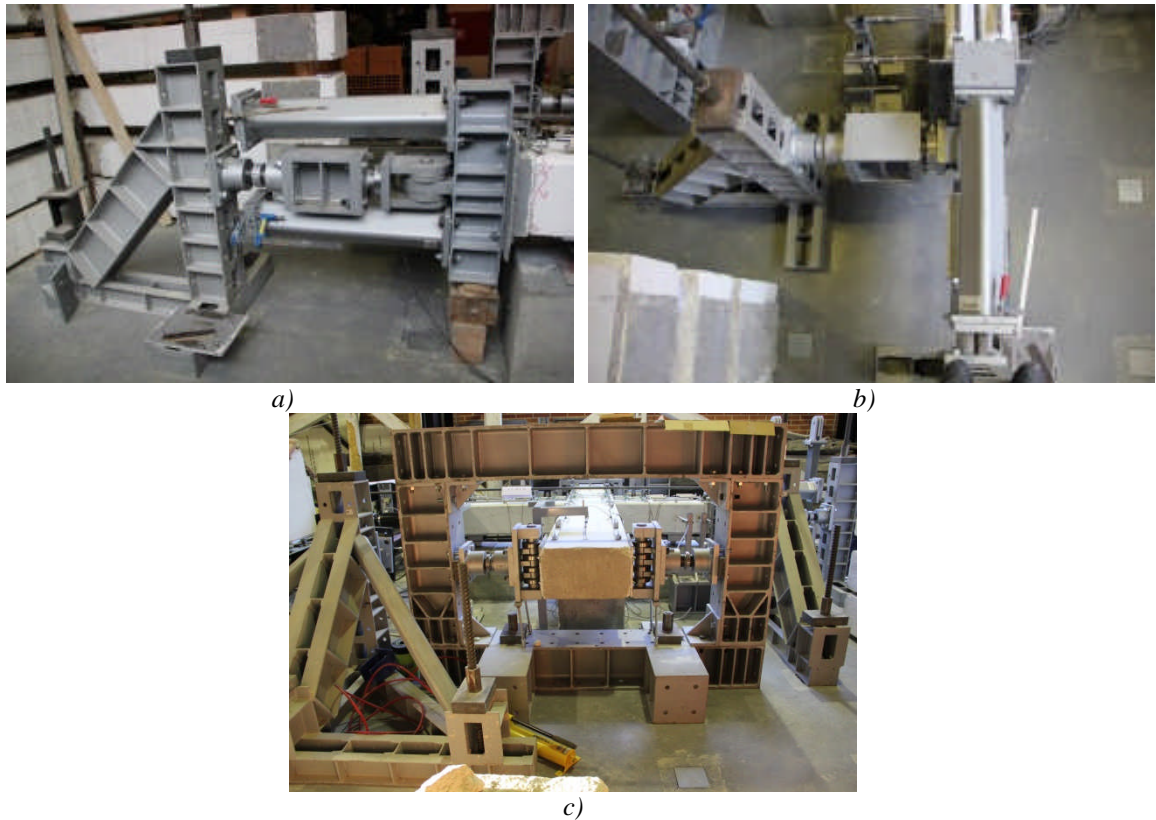


Figure C-2 a) side view of the steel frame extension with the lower column in a beam-column specimen; b) a plan view of the frame restraining lateral displacement in any direction except gravity of beam-column connection specimen; c) linear bearings and support frame restraining displacement of beams in the upper direction at the assumed point of contra-flexure.

The setup is a modification of the setup proposed by Fernandes (2012). In the setup proposed by the latter, the axial load actuator was an extension of the upper column and forming part of the upper columnar arch, as the specimen deformed under lateral loading. The lower column consisted in the specimen column and part of the length of the hinge, forming a shorter columnar arch. Consequently the post-tensioning rods which connected the top end of the axial load actuator and the lower end of the lower column, did not pass through the centroid of the node panel, creating differential $P-\Delta$ effects between the upper and lower columns that were difficult to account for. Consequently a stiff frame extension was fixed at the bottom of the lower column, such that a symmetrical system could be obtained resulting in the post-tensioning rods approximately passing from the centroid of the node panel (Figure C-2).

C.2 Experimental schedule and testing requirements

C.2.1 Scheme of Experiments: Beam-column connections

For the selection of the beam-column connection specimens, reference to the external and internal beam-column connections at the first level of the frame structures described in Chapter

3, designed to gravity loads only according to old design codes were considered as reference connections (figure C-3). For beam-column connections, there are two main important aspects that affect the behaviour of connections. These are the relative stiffness of the different parts that make up the connection, i.e. the beams, columns and the node panel, and the detailing and anchorage of the beams and columns at the intersection node panel. For the selection of the different specimens, the relative stiffness between the elements was varied by changing confinement properties or increasing the section by incorporating slabs.

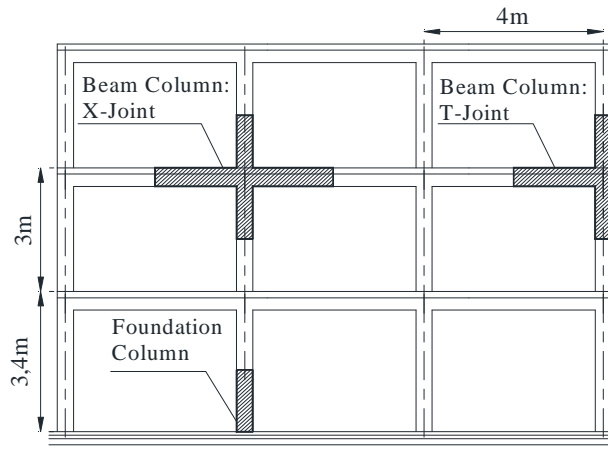


Figure C-3 General frame layout of the reference structure and sub elements selected for the experimental campaign.

The experimental campaign of the beam-column connections consisted in seven specimens, of which two were T-joints, representing the exterior column and beam of the frame, and five were X-joints, representing an internal column connected with beams on either side of the node panel. Table C-1 indicates the schematic variation of the physical properties of each test specimen. Table C-2 shows the geometry and the detailing aspects of the beam-column connections. All the beam-column connections were constructed without slab flanges, with the exception of J4-X where the effective length was based on the requirements of EN1998-1 (2004). A slab depth of 15mm was considered. For all specimens, the cross section of the beams was taken as 300x500mm, whereas for the columns this was taken as 300x300mm. On conducting a moment-curvature analysis at section level for the beam and the general column, the moment capacity of the former was found to be 130kNm, while the moment capacity of the column was found to be 47kNm. This is a typical strong-beam weak-column situation which characterised soft-storey failure mechanisms in past earthquakes (EERI, 1999).

The confinement in the beams was kept constant for all specimens, while the confinement in the column was only varied for J7-X. The confinement in the joint was introduced in J5-X and J7-X. Joint confinement was not a popular practice before the introduction and adoption of seismic codes. Nevertheless, this was incorporated in these specimens in order to investigate how the behaviour of the system evolves on such inclusion. Lap-splice effects were investigated in

exterior beam-column connection J2-T and interior beam-column connection J6-X. In both cases the lap-splice length was considered to be equal to 35x the bar diameter as suggested by the Italian design code DM 26/03/80. Although gravity loads on beams could not be incorporated due to the setup being in the horizontal plane, curtailment of reinforcement was still provided for all specimens, with the exception of J3-X where symmetric reinforcement was provided. The strength of materials and loading pattern are similar to those adopted for the column specimen campaign.

Table C-1 *Nominal properties for beam-column connection specimens*

Element Type	Section	Concrete	Load Ratio	Confinement	Reinforcement Ratio	Lateral Load pattern	Anchorage Detail	Aspect ratio of Element	Test
Inner T-Joint	Square: 300x300	C16/20	v=0.26	a=0.1	Reinf. =1%	LP 1	Continuous	L/h=5	J1-T
							LS: 35 x D	L/h=5	J2-T
Inner X-Joint	Square: 300x300	C16/20	v=0.26	a=0.1	Reinf. =1%	LP 1	Continuous	L/h=5	J3-X
							Conf. Node	L/h=5	J5-X
							Continuous	L/h=5	J4-X
							LS: 35 x D	L/h=5	J6-X
							Conf. Node	L/h=5	J7-X
			v=0.26	a=0.22	Reinf. =1%	LP 1	Conf. Node	L/h=5	

Table C-2 Detailing and nominal properties for the beam-column connection specimens

TEST	MECHANICAL PROPERTIES	LONGITUDINAL SECTION	CROSS SECTION
J1-T			<p>SECTION A.A. 0.3 0.3 8 Ø 12mm</p> <p>SECTION B.B. 0.3 0.09 0.5 0.02</p>
J2-T	<p>Stirrups A235NL</p> <p>Longitudinal Reinforcement: A400NRSD</p> <p>Concrete: C16/20</p>		<p>SECTION C.C. 0.3 0.09 0.5 0.02</p> <p>6 Ø 16mm</p>
J3-X	<p>Cover: 2cm</p> <p>Axial Force: 450kN</p> <p>Load Pattern:</p>		<p>SECTION A.A. 0.3 0.3 8 Ø 12mm</p> <p>SECTION B.B. 0.3 0.09 0.5</p>
J5-X			<p>SECTION A.A. 0.3 0.3 8 Ø 12mm</p> <p>SECTION B.B. 0.3 0.09 0.5</p> <p>SECTION C.C. 0.3 0.09 0.5 6 Ø 16mm</p>

... continued

TEST	MECHANICAL PROPERTIES	SECTIONS
J4-X	<p>Stirrups A235NL</p> <p>Longitudinal Reinforcement: A400NRSD</p> <p>Concrete: C16/20</p>	<p>SECTION B.B. 1.5 0.09 0.15 8 Ø 20mm (smooth) 0.3 0.5</p> <p>SECTION C.C. 0.8 0.09 0.3 0.5</p> <p>ALL REGIONS 8mm Ø @ 180mm c.c. (smooth) 6 Ø 16mm (ribbed)</p> <p>SECTION A.A. 0.3 0.3 8 Ø 12mm</p> <p>0.18 0.3 0.07 0.18 1.45 0.07 0.93 2.1 0.5</p>
J6-X	<p>Cover: 2cm</p> <p>Axial Force: 450kN</p> <p>Load Pattern:</p>	<p>SECTION A.A. 0.3 0.3 8 Ø 12mm</p> <p>SECTION B.B. 0.3 0.3 0.09 0.3</p> <p>SECTION C.C. 0.3 0.5 0.09 0.3</p> <p>1.7 0.18 0.75 0.42 1.45 0.07 0.45 0.93 2.1 0.5</p>
J7-X		<p>SECTION A.A. 0.3 0.3 8 Ø 12mm</p> <p>SECTION B.B. 6 Ø 16mm 0.3 0.5</p> <p>SECTION C.C. 6 Ø 16mm (ribbed) 0.3 0.5</p> <p>1.7 0.07 0.14 0.18 1.45 0.75 0.18 0.93 2.1 0.5</p>

Figure C-4 shows some details of the reinforcement cage for external beam-column internal beam-column specimens respectively. The reinforcement close to the beam-column joint panel is the most vital for the deformation behaviour of the specimens and hence was thoroughly checked, particularly the transverse reinforcement spacing, cover, and positioning of the longitudinal reinforcement. The reinforcement was adequately tied in order to avoid unnecessary movement or floatation during the concrete casting.

The same material grades of concrete and steel were utilised as those specified for column specimens discussed in Chapter 3. Table C-3 represents statistics of the concrete for the beam-column connection specimens.

C.2.2 Data acquisition and instrumentation

The same system and type of instruments that are used in the conduction of tests on column-foundation specimens, are also utilised for beam-column specimens. Table C-4 shows the instrumentation code and the type of instrument that is used for each type of specimen. Figure C-5, figure C-6 and figure C-7 shows the corresponding instrumentation layout.



a)



b)



Figure C-4 Details of the reinforcement layout and form work for the internal beam-column specimens: a) J3-X; b) J5-X; c) J6-X; d) J7-X; e) J4-X

Table C-3 Compression strength and splitting test results for beam-column connection specimens.

Beam-Column Connection	J1-T	J2-T	J3-X	J4-X	J5-X	J6-X	J7-X
<i>Compression Test: BS EN 12390-3 (2002)</i>							
Max	15.3	12.0	18.3	15.6	15.4	15.9	16.4
Mean	14.2	10.9	15.6	14.9	14.7	15.1	15.1
Min	13.5	9.8	11.5	14.2	13.5	13.3	13.9
S.D.	0.6	0.7	2.7	0.5	0.8	0.9	0.9
CoV.	4.5	6.6	17.1	3.3	5.7	6.0	6.2
<i>Splitting Test: BS EN 12390-6 (2009)</i>							
Mean	1.8	1.5	2.0	1.9	1.9	2.0	1.6

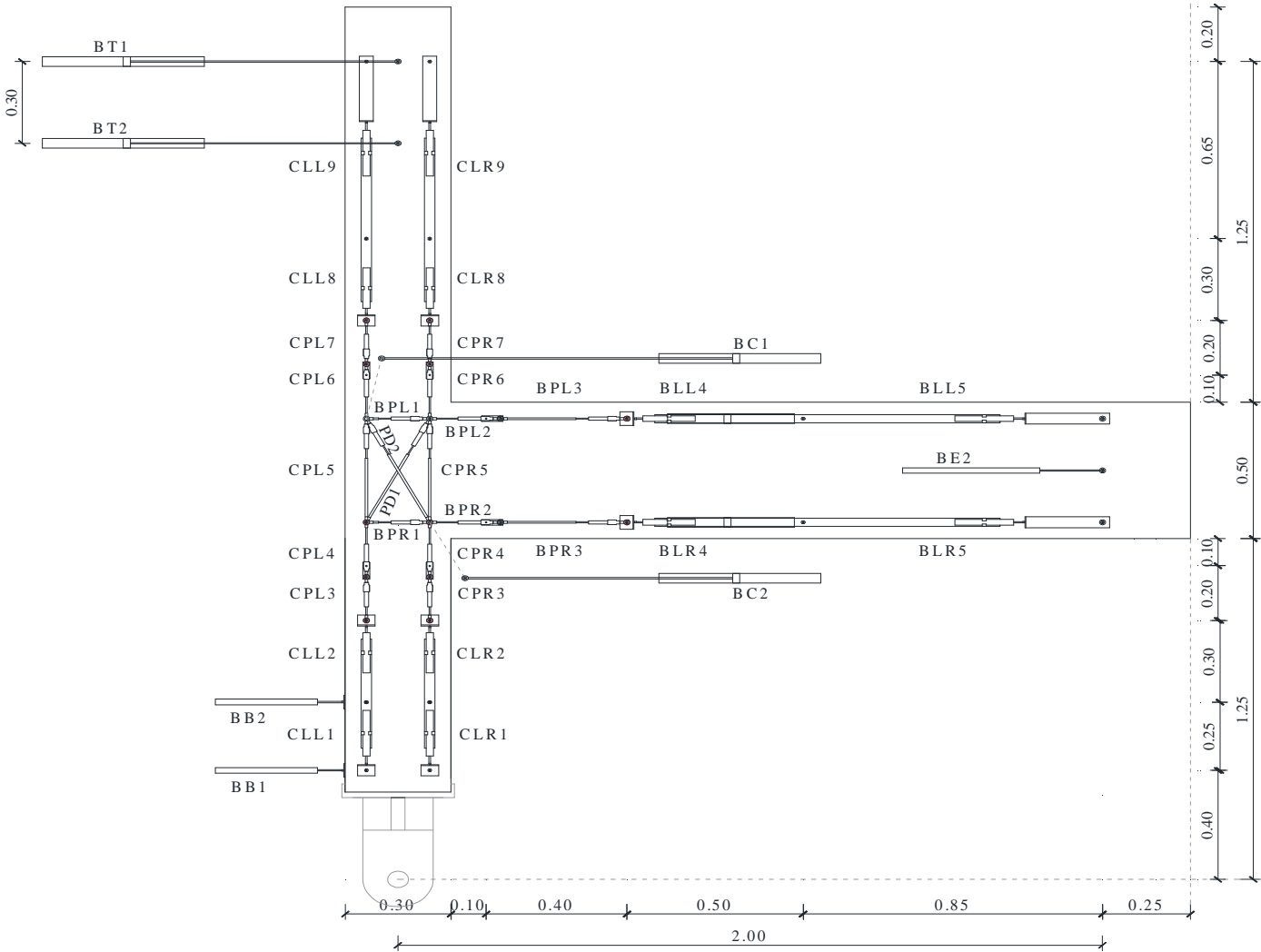
Table C-4 *The instruments used to measure forces and deformation according to the column and beam-column connection schedules.*

Instrument	Range	Units	External Beam-Column Connection		Internal Beam-Column connection	
			J1-T; J2-T	J3-X; J5-X; J6-X; J7-X	J4-X	
Potentiometer	25	mm	BPL1; BPL3; BPR1; BPR3; CPL3; CPL5; CPL7; CPR3; CPR5; CPR7	BPL3; BPR3; BPL5; BPR5; BPL7; BPR7; CPL3; CPR3; CPL5; CPR5; CPL7; CPR7; PD1; PD2	CPR5; CPL5; CPL7; BPL1; BPL2; BPL3; BPL5; BPL7; BPL8; BPL9; BPL*5; BPR5; PD1; PD2	
	50	mm	CPL4; CPL6; CPR4; CPR6; BPL2; BPR2	CPL6; CPR6; CPL4; CPR4; BPL4; BPR4; BPL6; BPR6	BPL4; BPL6; BPR4; BPR6; CPL4; CPL6; CPR4; CPR6	
Bridge Potentiometer	400	mm	BT1; BT2; BC1; BC2	BT1; BT2; BC1; BC2	BT1; BT2; BC1; BC3	
String Potentiometer	750	mm			BC2; SP1	
Displacement Transducers (LVDT)	10	mm	CLL8; CLR8; CLL2; CLR2; BLL4; BLR4; BLR5	BLL2; BLL8; BLR2; BLR8; CLL2; CLL8; CLR2; CLR8; BLR9	CLR8; CLR2; CLL2; BLR2; BLR3; BLR7; BLR8; BPL*4; BPL*6	
	25	mm	BLL5; CLL1; CLR1; CLL9; CLR9	CLL1; CLL9; CLR1; CLR9; BLL1; BLL9; BLR1	CLR1; CLR3; CLR7; CLL1; CLL3; CLL9	
	100	mm			CLR9	
	150	mm	BB1; BB2	BB1; BB2	BB1; BLR9	
	250	mm	BE2	BE1; BE2	BE1; BE2; BLR1	
Load Cell	1000	kN				
	500	kN	C2	C2	C2	
	200 ^{note2}	kN	C1	C1	C1	
	300	kN	C3	C3	C3	
	100	kN	C4	C4	c4	

Note: ^{note1} For T7, T8 a

the load cell for 1000kN was used instead of the one with 500kN; ^{note2} The load cell is the one used by the controller

Figure C-5 A general layout of the instrumentation that measures the deformation of external beam-column specimens.



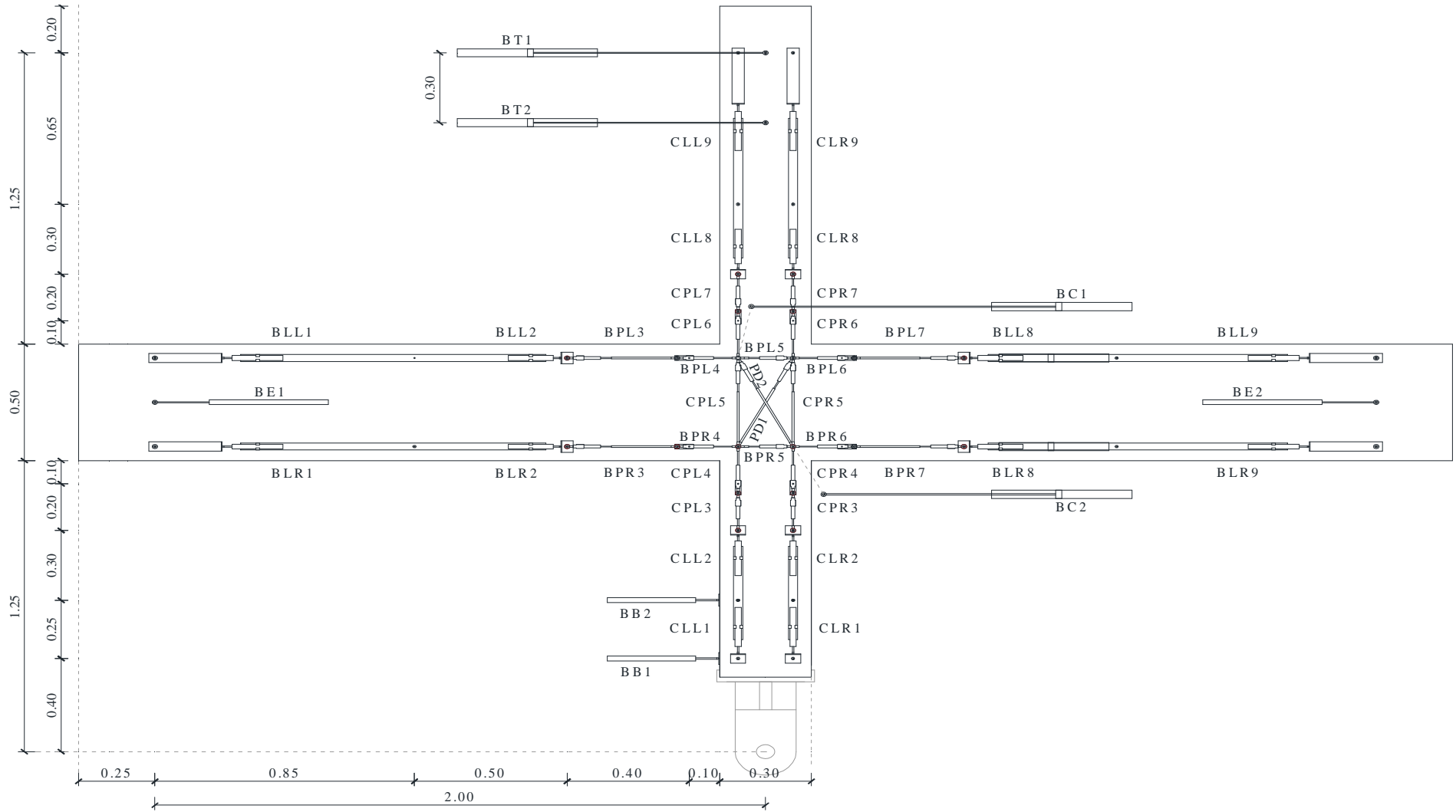


Figure C-6 A general layout of the instrumentation that measures the deformation of internal beam-column specimens.

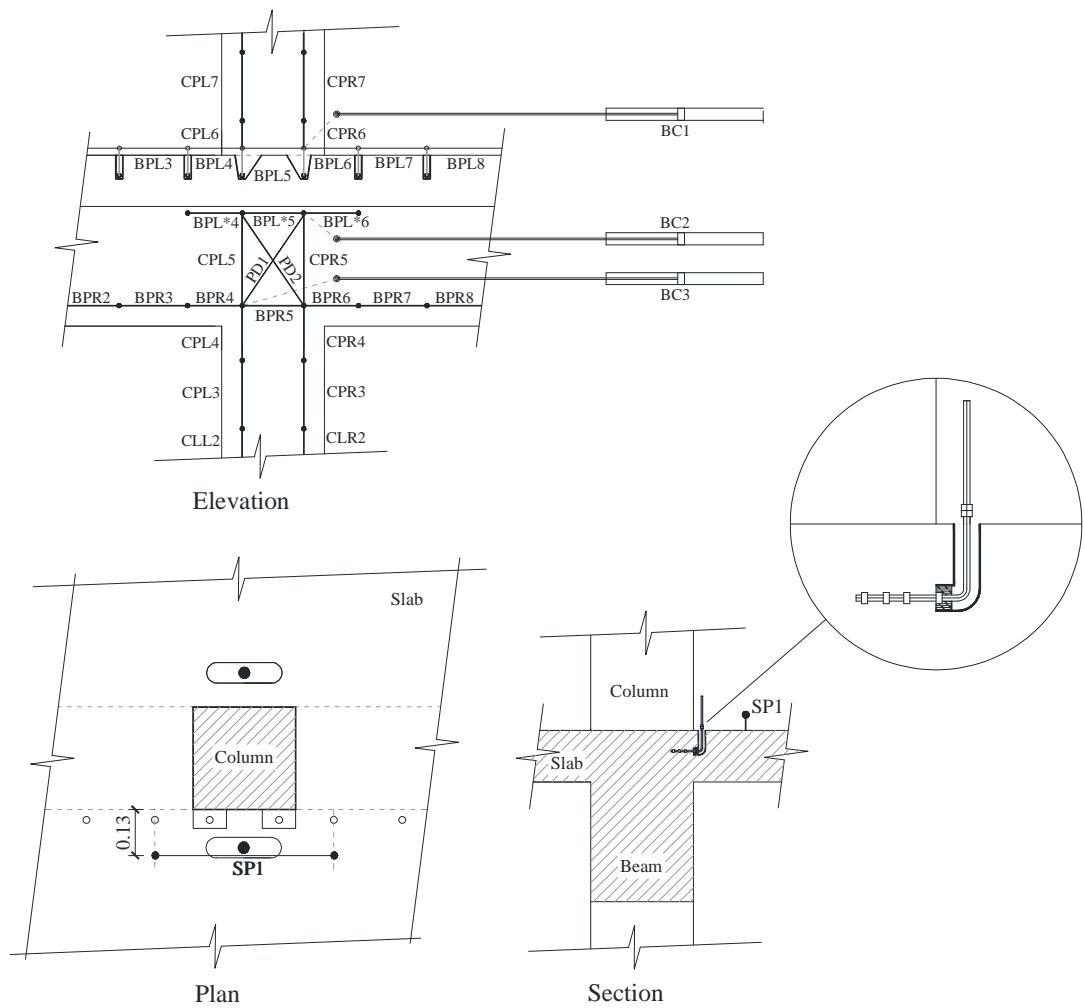


Figure C-7 A general layout of the instrumentation that measures the deformation of internal beam-column specimen J4-X.

Figure C-8 and C-9 show the mounting of the various displacement instruments used, and figure 4-21 shows details of the general layout for column-foundation specimens and beam-column connection specimens. Since J4-X had a slab and incorporated a different instrumentation layout, some of the mountings were different from the other specimens as shown in figure C-9. Instrumentation was mounted on the upper surface only as it was quite difficult to work against gravity and install instrumentation on the lower surface. Figure C-10 shows the mounting of an external LVDT to monitor the rotation at the end of the column with respect to the metal frame extension.

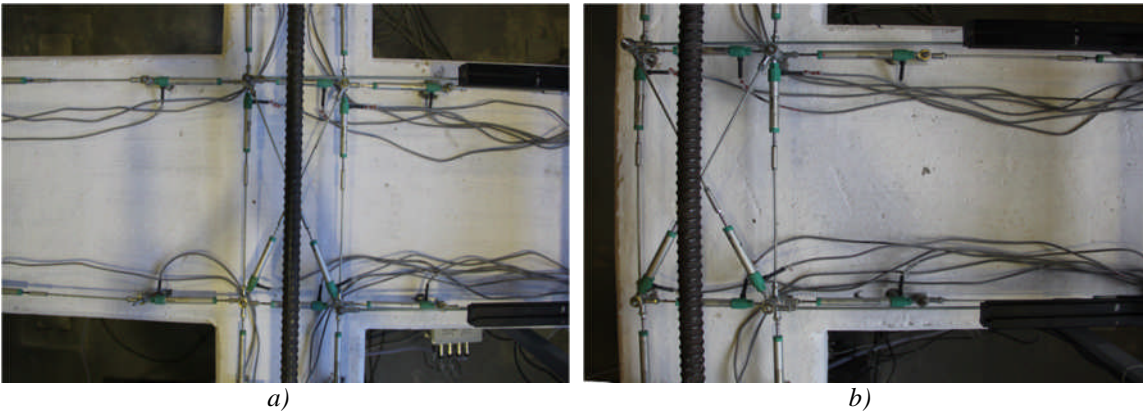


Figure C-8 General overview of the deformation instrumentation in critical areas of: a) column-foundation specimens with 300x300mm sections; b) column-foundation specimens with 500x300mm sections; c) external beam-column connections and d) internal beam-column connections.

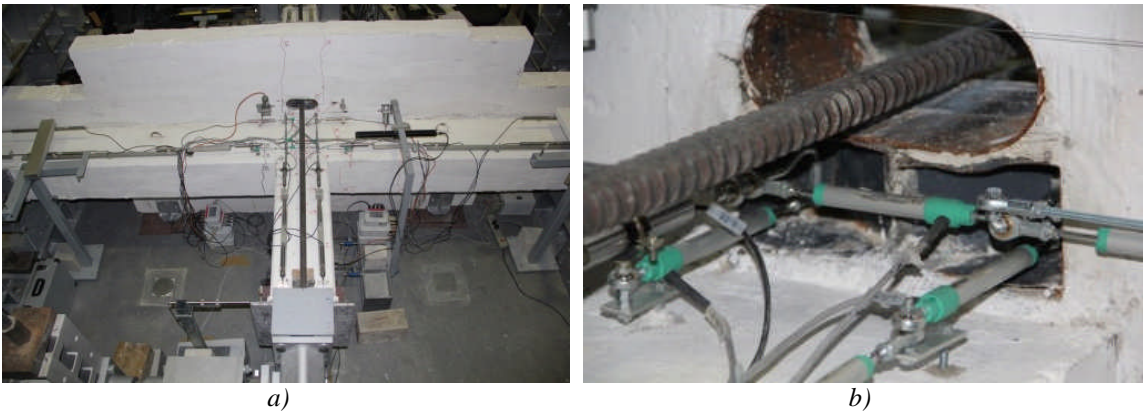


Figure C-9 a) general layout of the instrumentation of specimen J4-X; b) detail of the mounting of the potentiometers inside the slab-beam-column interface.

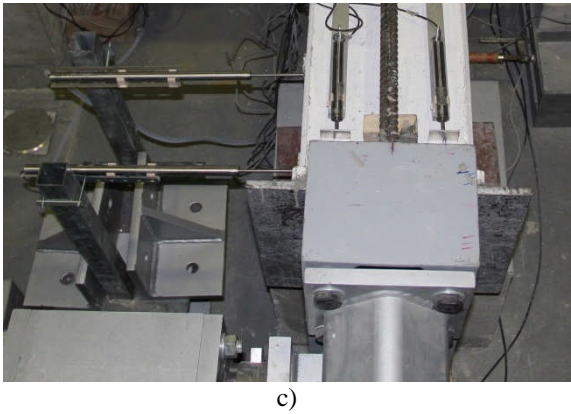


Figure C-10 Monitoring the rotation of the lower column with respect to the steel frame extension.

C.3 Observations and Comparisons of the Results of Beam-Column Connections

Joint J1-X is the reference specimen for the two external T-connections, whereas J3-X is the reference specimen of the internal X-connections. Both of them have continuous longitudinal reinforcement in the columns and no transverse reinforcement in the nodes. Specimens J2-X and J6-X are external and internal connections, respectively similar to J1-X and J3-X but have lap-splicing at the bottom of the upper column. As shown in figure C-11 and figure C-12 both J1-X and J3-X reach a maximum force which is bigger than their corresponding specimens with lap splicing. While the maximum force capacity of J2-X is 18% lower than J1-X, the difference between the internal joints is only 8%. The difference in the drift ratios between J1-X and J2-X and J3-X and J6-X at maximum force, u_{-10} and u_{-20} is lower than 6%. Experiment J6-X is terminated before u_{-50} damage limit is reached since the maximum deformation that could be sustained by the actuator is reached before. However, J3-X reaches u_{-50} at a much lower chord rotation which is at least 10% lower than J6-X. Nevertheless, the difference in chord rotation between the two external columns at u_{-50} is however less than 2%. At yielding the force of J2-X is only 4% lower than J1-X while the force of J6-X is 10% lower than J3-X. While the chord rotation of J2-X at this damage level is about 12% larger than J1-X, yielding of both internal connections occur at similar chord rotations.

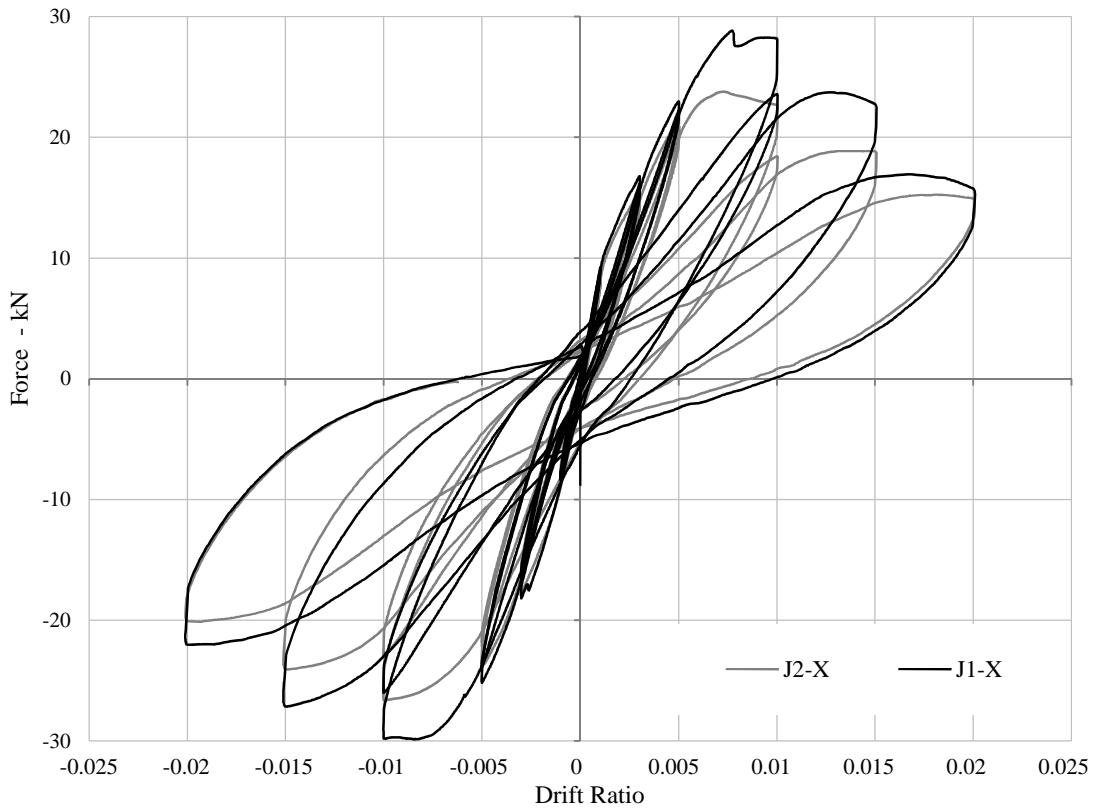
As discussed in Chapter 4, the columns with lap-splice T16-D1 exhibited the same maximum force capacity as the reference column specimen without lap-splice T14. In the case of the column specimens, both the column and the foundation are considered very stiff. If not the foundation is considered relatively stiffer than the column since it has a larger section, more longitudinal reinforcement and transverse reinforcement. However, in the case of the beam column connections, the column can be assumed to be stiffer than the node since the latter is not confined. As a result, for a particular drift demand, more deformation is absorbed by the node, and the maximum deformation capacity of the columns in the connection is not reached in the lap-splicing specimen. Most damage is observed to be concentrated in the node. However, the lap-spliced specimen J6-X has a higher ductility than T3-X, as the former delays the formation of buckling due to the dual action of the lapped reinforcement in the upper column.

Figure C-13 and figure C-14 indicate that the external columns J1-X and J2-X with and without lap-splicing have lower ductility and force capacity than corresponding specimens J3-X and J6-X with and without lap-splicing. Since the drift demand in an earthquake is generally the same for all columns within a particular level (Priestley *et al.*, 2003), lower ductile capacity may result in a possible soft storey failure. The differences in maximum force capacity and drift ratio between of J1-X and J3-X, are very similar to the differences between J2-X and J6-X at maximum force, u_{-10} and u_{-20} . The maximum force of J1-X is 50% lower than J3-X, while the maximum force of J2-X is 55% lower than J6-X. The drift ratios of J1-X and J2-X at maximum

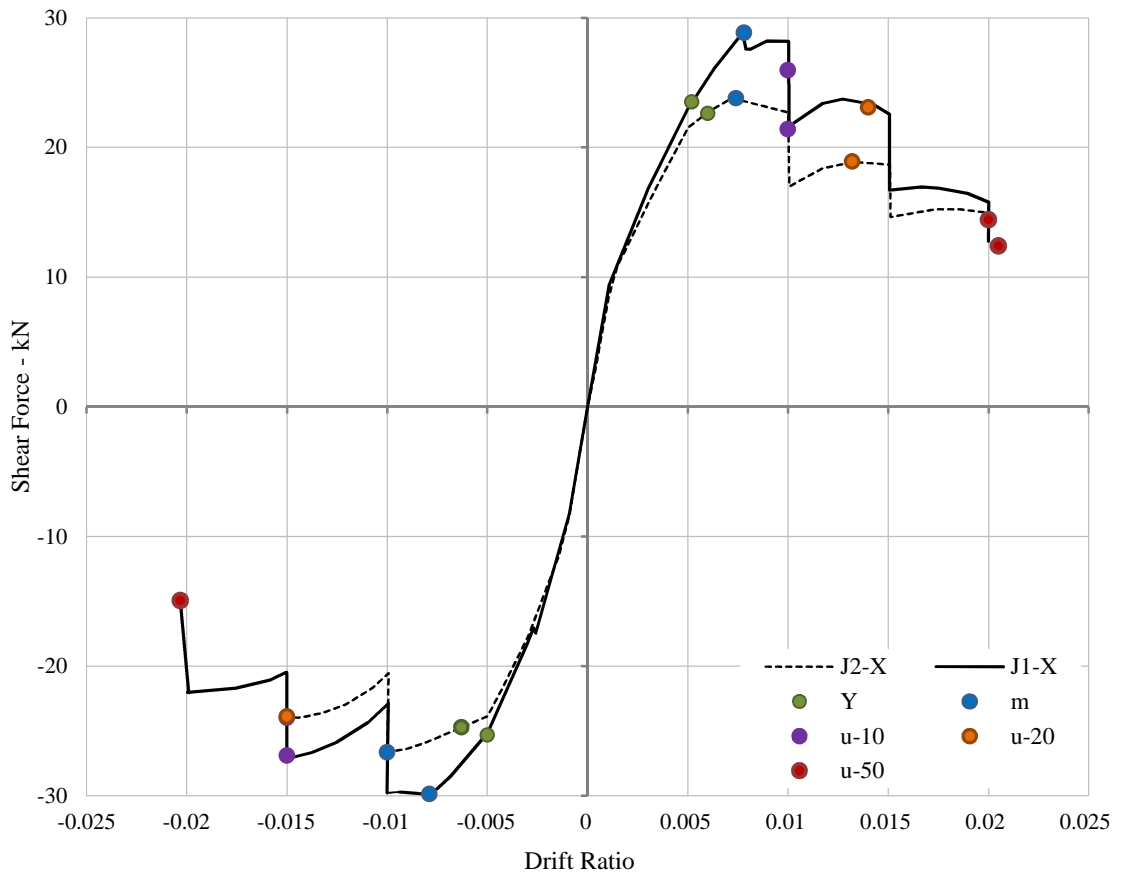
force, u-10 and u-20 are on average 63% lower than the drift ratios of the respective specimens J3-X and J6-X. The drift ratio of J1-X at u-50 is approximately 52% lower than the corresponding value at J3-X. Although, the drift ratio at u-50 of J6-X is not available, it is much higher than the corresponding drift ratio of J2-X. At yielding force of J1-X is 55% lower than J3-X, while the yielding force of J2-X is 49% lower J6-X. However while the drift ratio at yielding of J1-X is 48% lower than J3-X, the value of J2-X is only 37% lower than J6-X.

As discussed in Chapter 4, in spite of the similar reinforcement spacing of specimen T14 and T2, the latter has larger ductility and maximum force capacity as a result of an increase in confinement at cross-sectional level. However, this is not always true in beam-column connections. The pattern of T14 has 2 legs on each side with 90° hooks and T2 has 3 legs with 135° hooks. While the transverse reinforcement pattern and spacing in the columns of connections J3-X and J5-X is similar to T14, the transverse reinforcement pattern and spacing of J7-X is similar to T2. The transverse reinforcement of both J5-X and J7-X is continuous inside the node. As indicated in figure 5-21, the confinement inside the node of specimen J5-X induces larger ductility capacity than specimen J3-X. As shown in figure C-15, the damage in the node of specimen J3-X is more than the damage in the column, while the distribution of damage in the columns and node of specimen T5-X is very similar. However, although specimen J7-X has a higher confinement ratio in the column and the node, it exhibits lower ductility than both J3-X and J5-X. The damage of specimen J7-X is more concentrated in the columns. The higher confinement in specimen T7-X results in a transverse element consisting of the beam and node which is stronger and stiffer compared to its corresponding intersecting columns. This induces larger demands on the column elements and damage phenomena such as buckling are observed to occur in specimen J7-X at deformations which are lower than J3-X, and much lower than J5-X.

The maximum force capacity of J7-X, J5-X and J3-X is only within 7% of each other. Damage development in J3-X, J5-X and J7-X is compared in figure C-17. The maximum force of J7-X is slightly larger than J5-X, but slightly lower than J3-X. The force at yielding of J5-X is 11% lower than the force at yielding of J3-X, and the value of J7-X is only 7% lower than J3-X. The drift ratio of J7-X and J3-X is very similar at yielding, maximum force and u-10. At u-20 and u-50, the drift ratio of J7-X is 14% lower than the corresponding value of J3-X. The drift ratio of J5-X is only similar to the other two specimens until yielding. At maximum force, the drift ratio of J5-X is 50% larger than J3-X and 46% larger than J7-X. At u-10, the drift ratio of J5-X is then 33% larger than the values of both J3-X and J7-X. However, at u-20 the drift ratio of J5-X is then 53% larger than J3-X and 66% larger than J7-X.

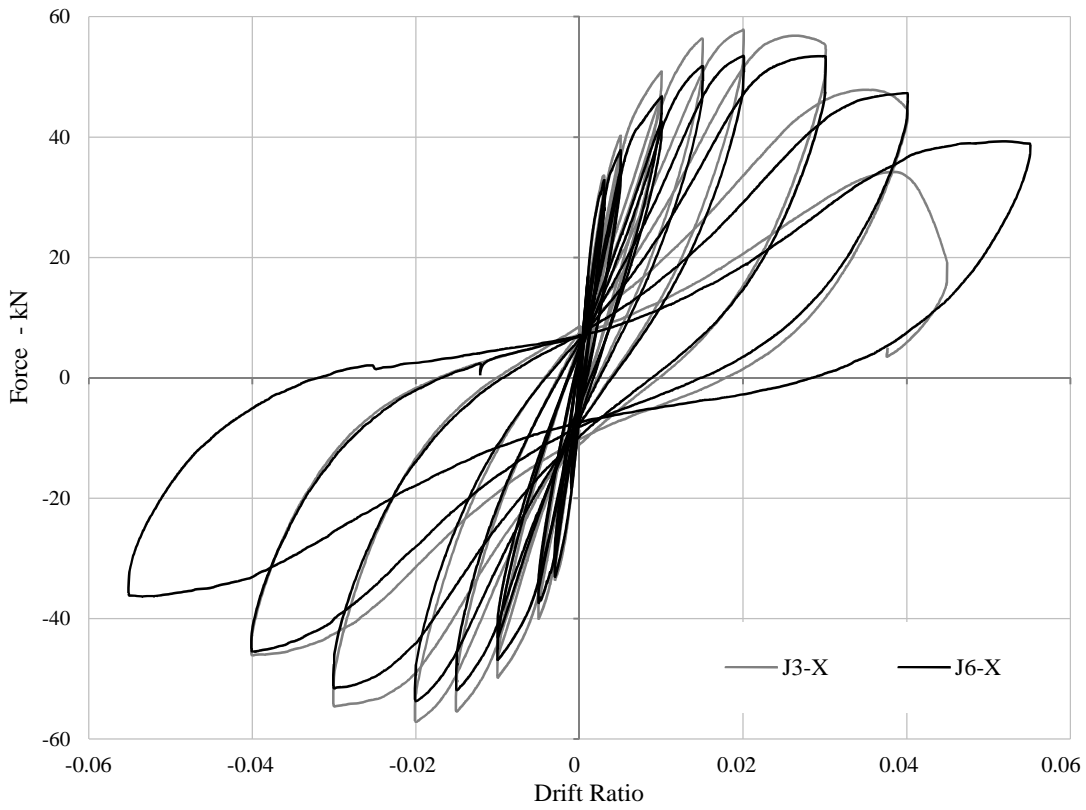


a

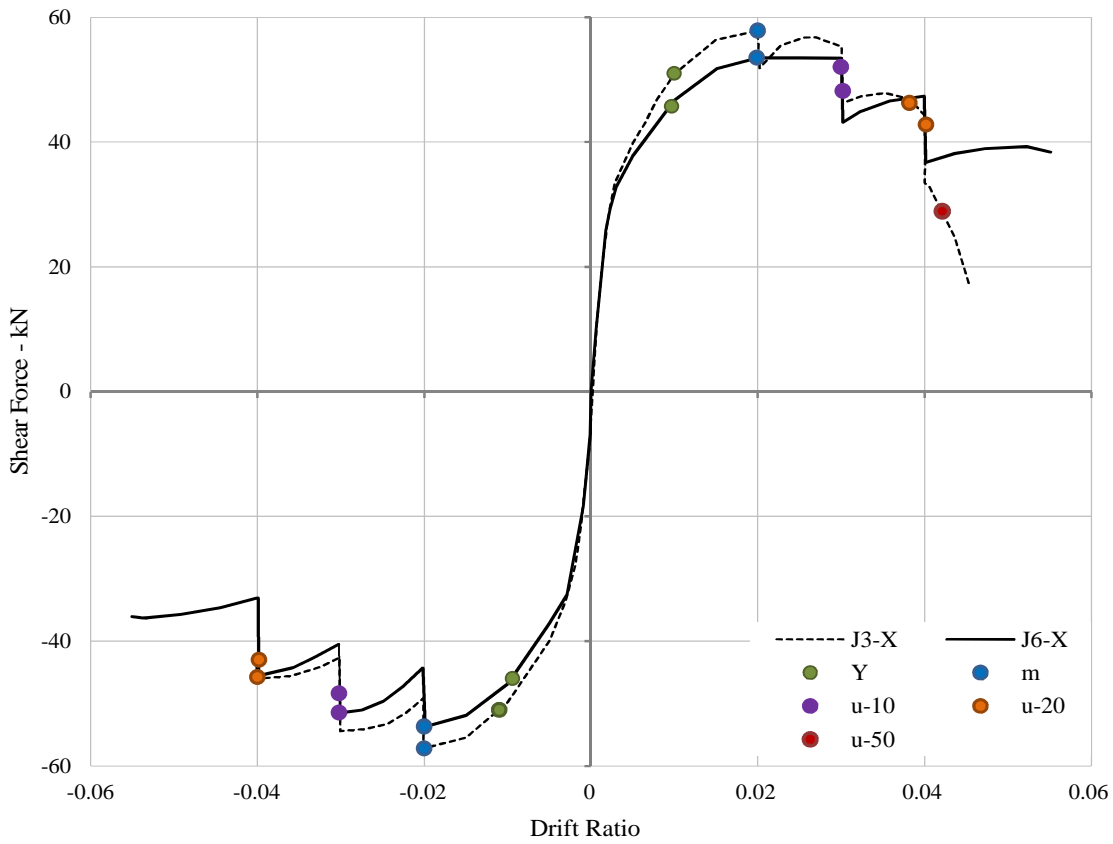


b

Figure C-11 Comparison of the response of specimens J1-X and J2-X: a) Force - Drift ratio history, b) Force - Drift ratio envelope.

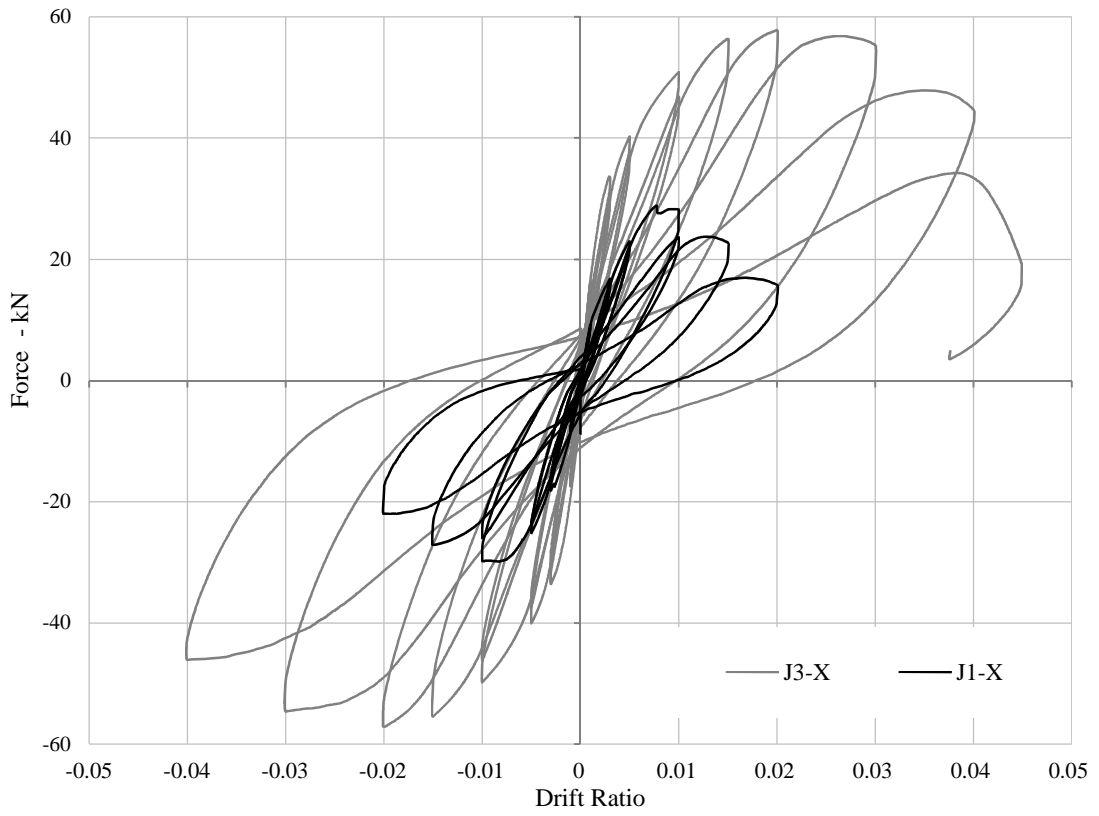


a

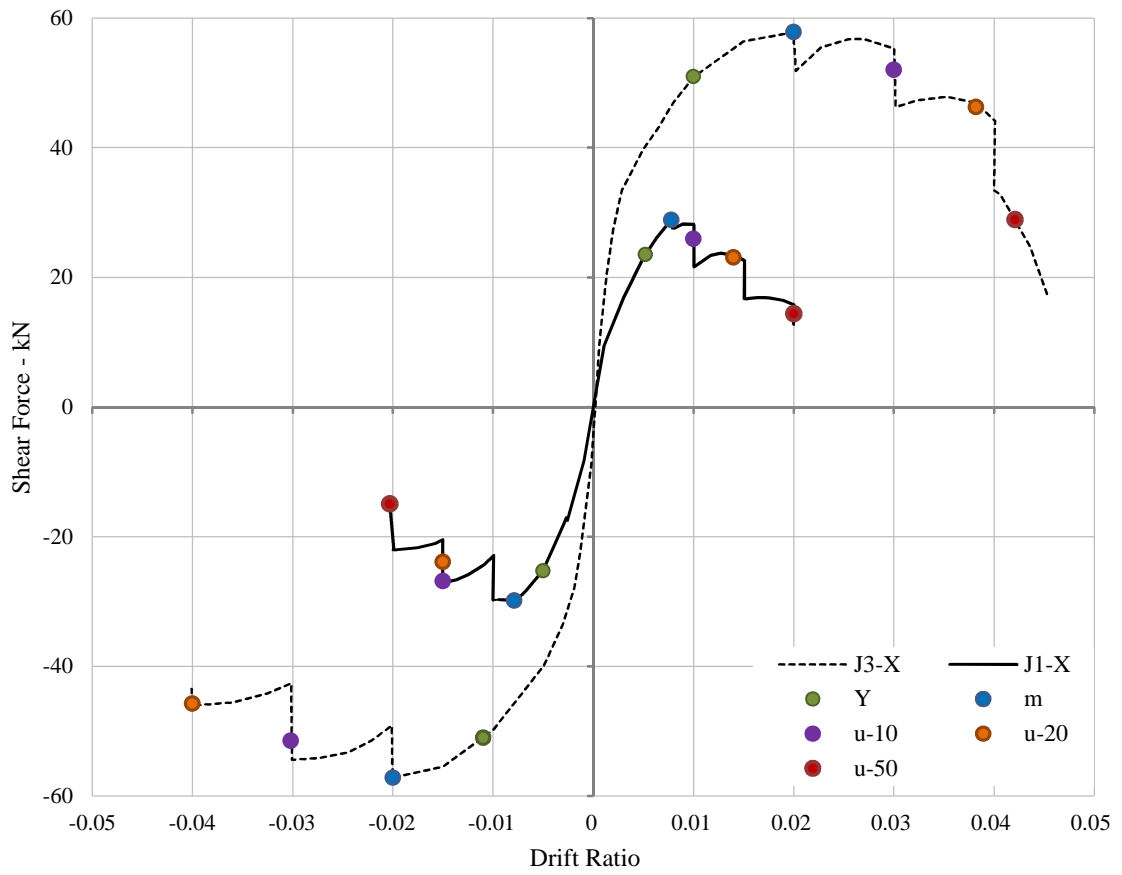


b

Figure C-12 Comparison of the response of specimens J3-X and J6-X: a) Force - Drift ratio history, b) Force - Drift ratio envelope.

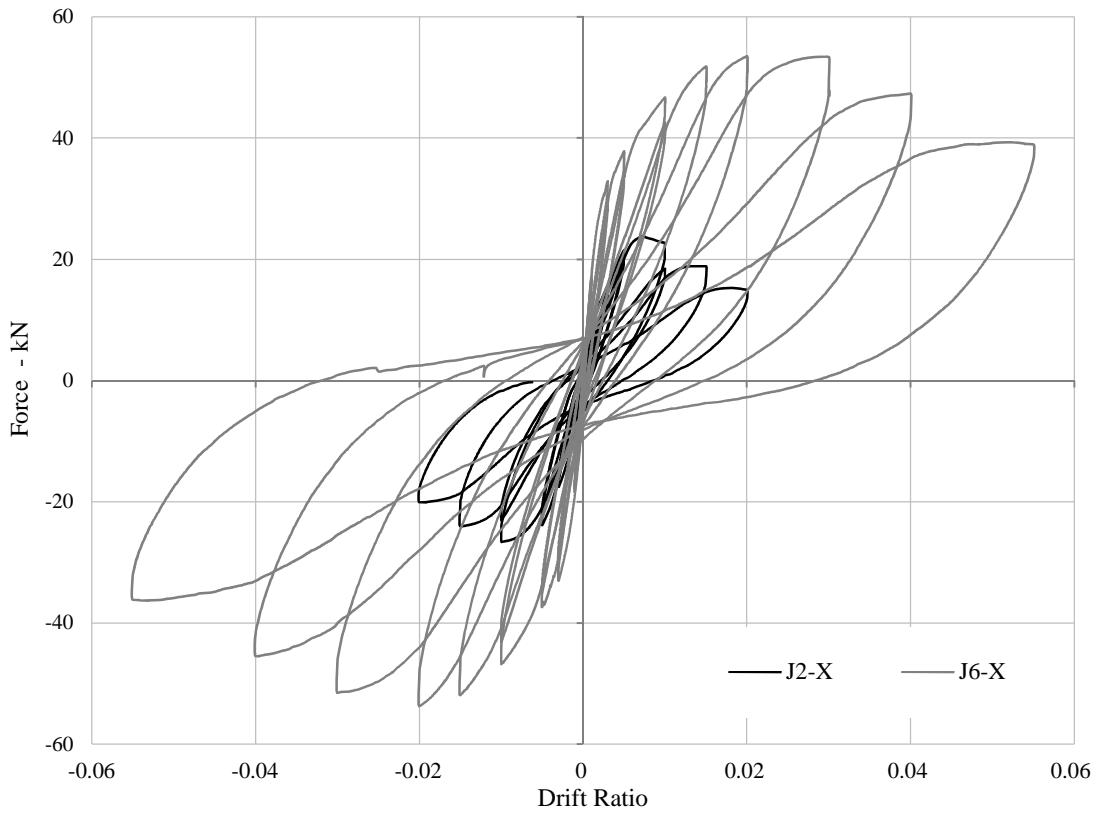


a

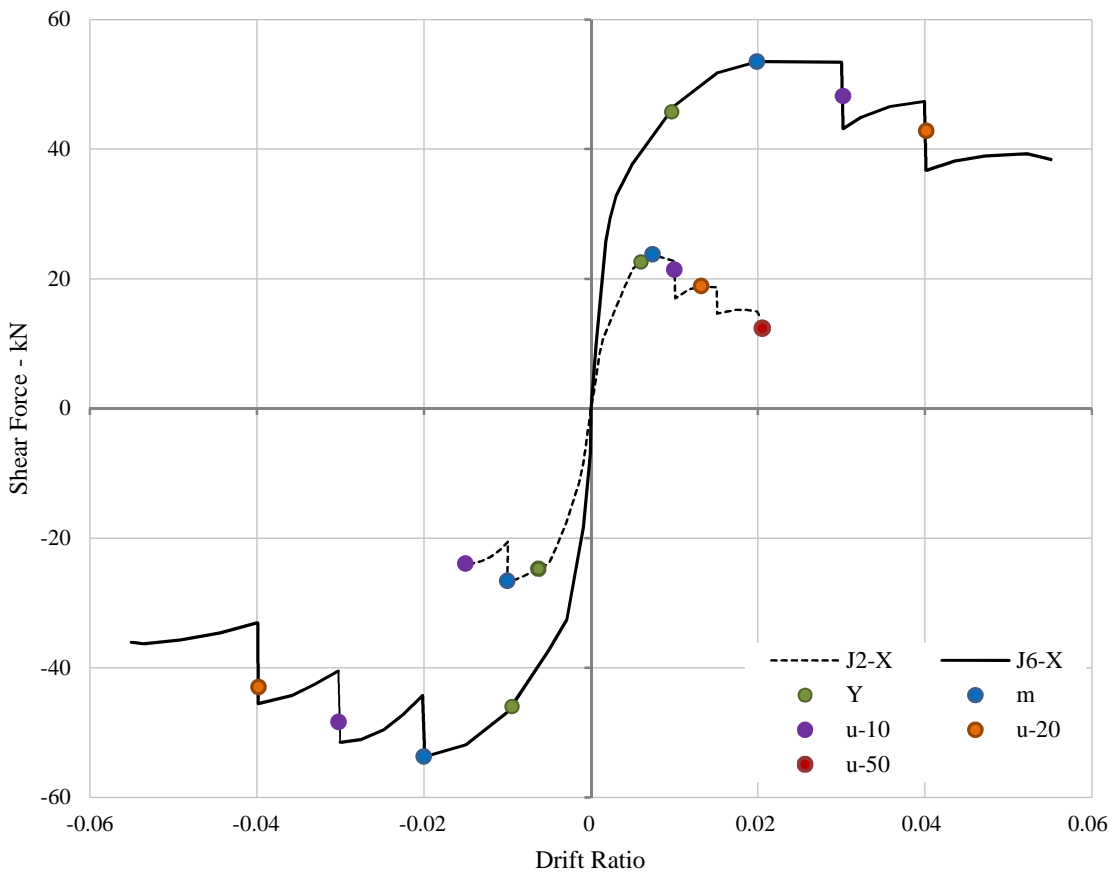


b

Figure C-13 Comparison of the response of specimens J3-X and J1-X: a) Force - Drift ratio history, b) Force - Drift ratio envelope.

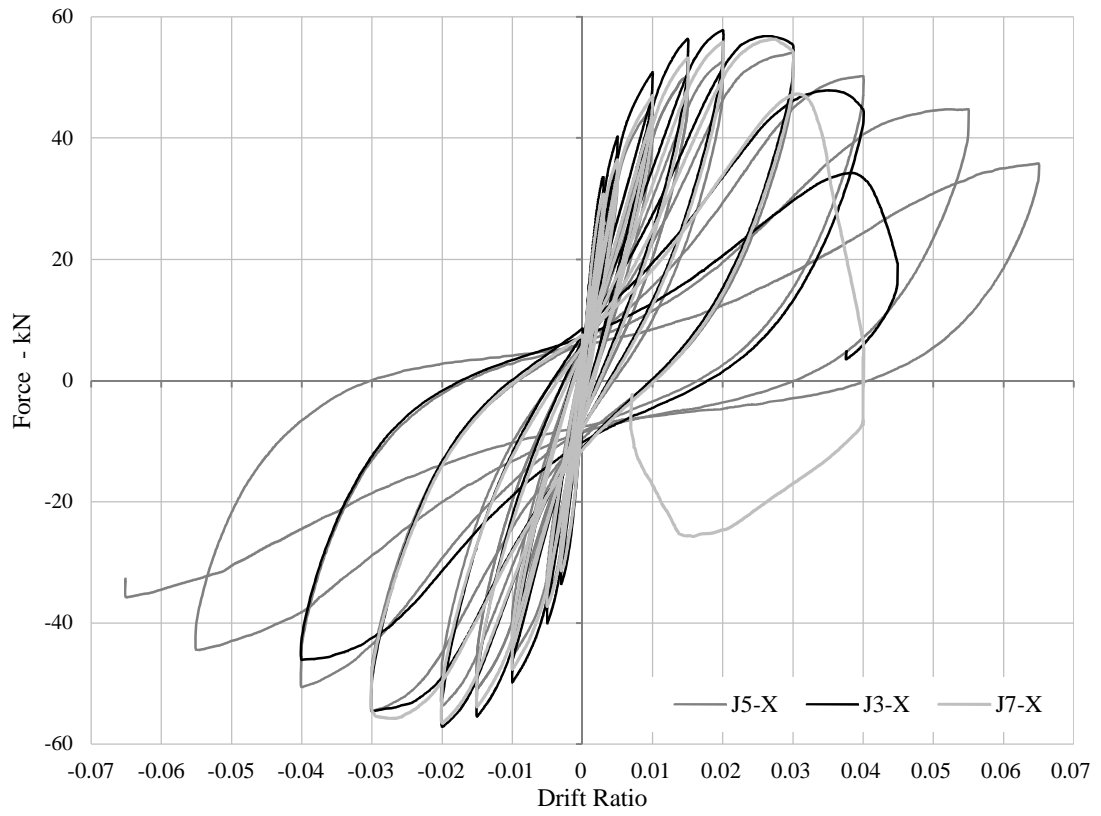


a

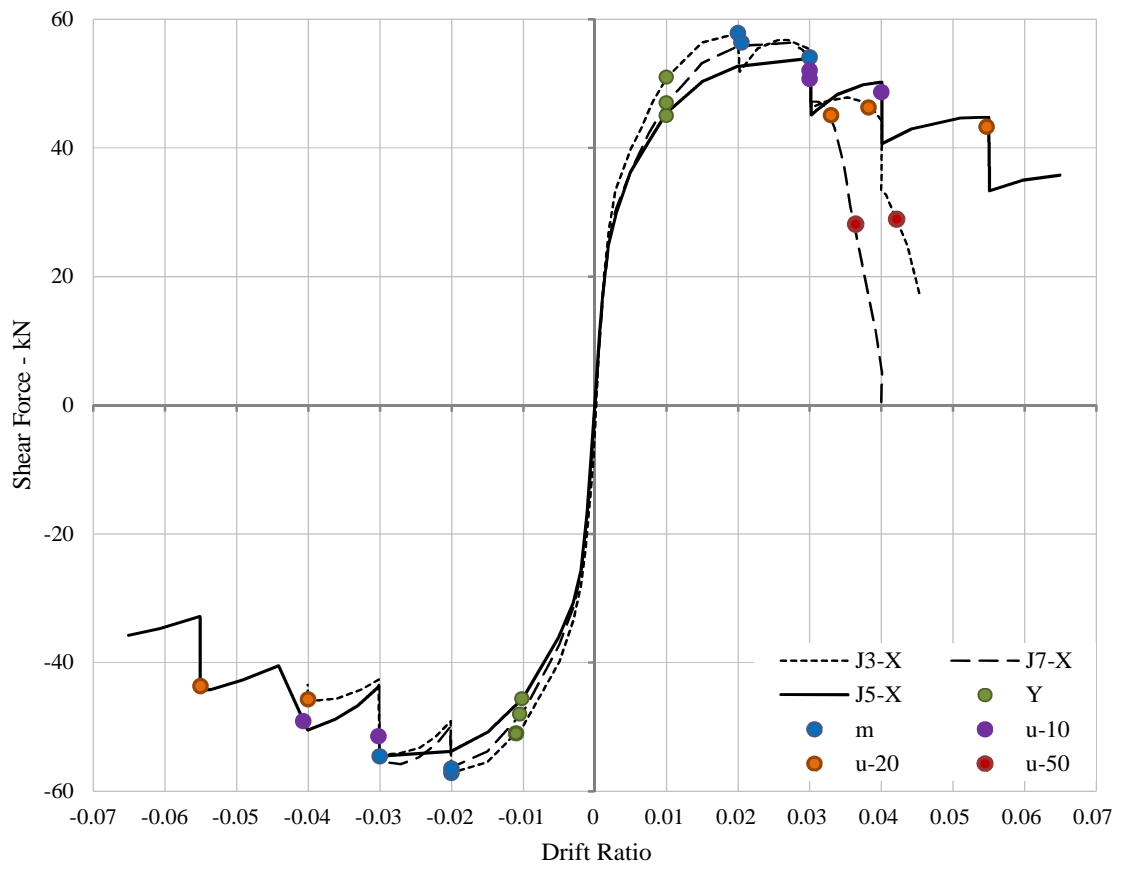


b

Figure C-14 Comparison of the response of specimens J2-X and J6-X: a) Force - Drift ratio history, b) Force - Drift ratio envelope.

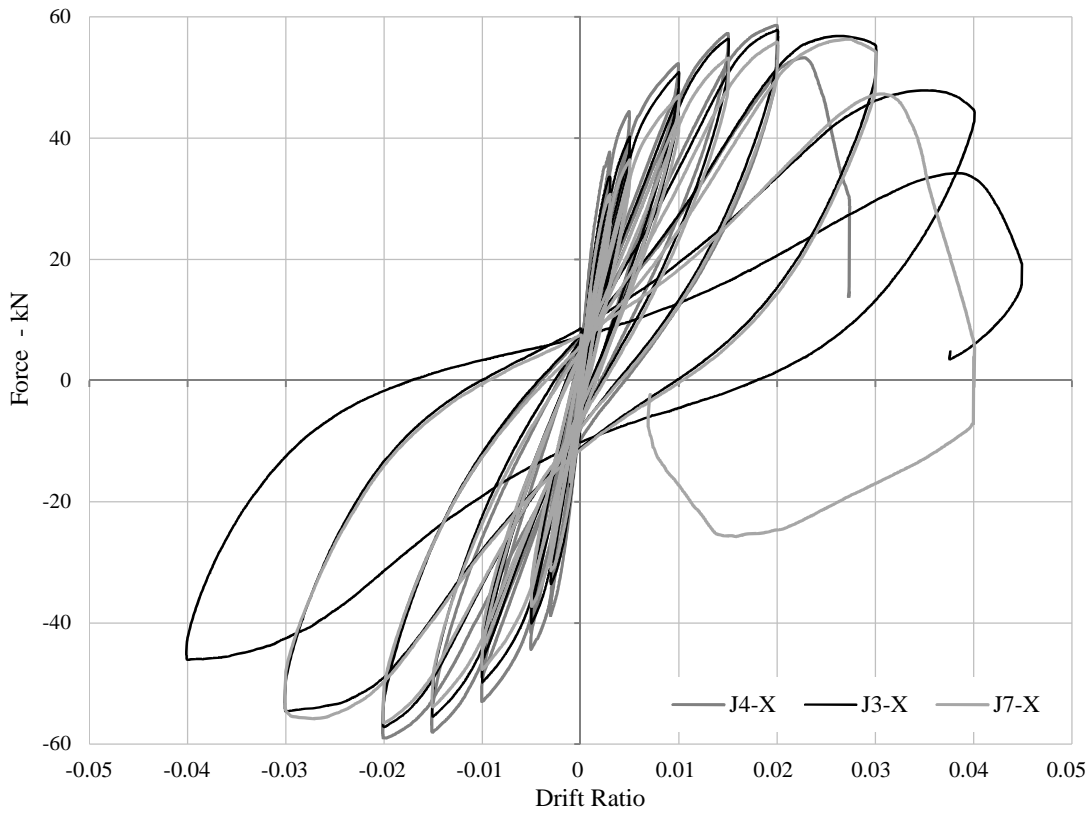


a

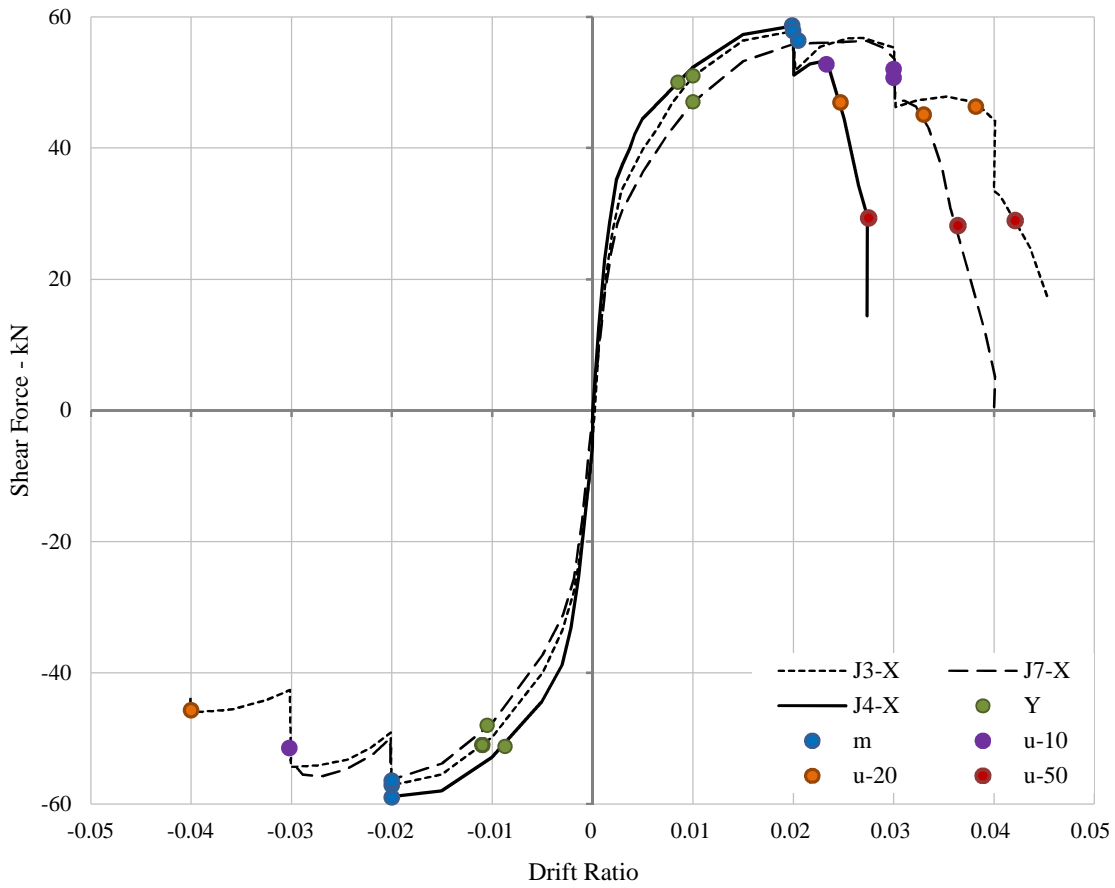


b

Figure C-15 Comparison of the response of specimens J3-X, J5-X and J7-X: a) Force - Drift ratio history, b) Force - Drift ratio envelope.



a



b

Figure C-16 Comparison of the response of specimens J3-X, J4-X and J7-X: a) Force - Drift ratio history, b) Force - Drift ratio envelope.

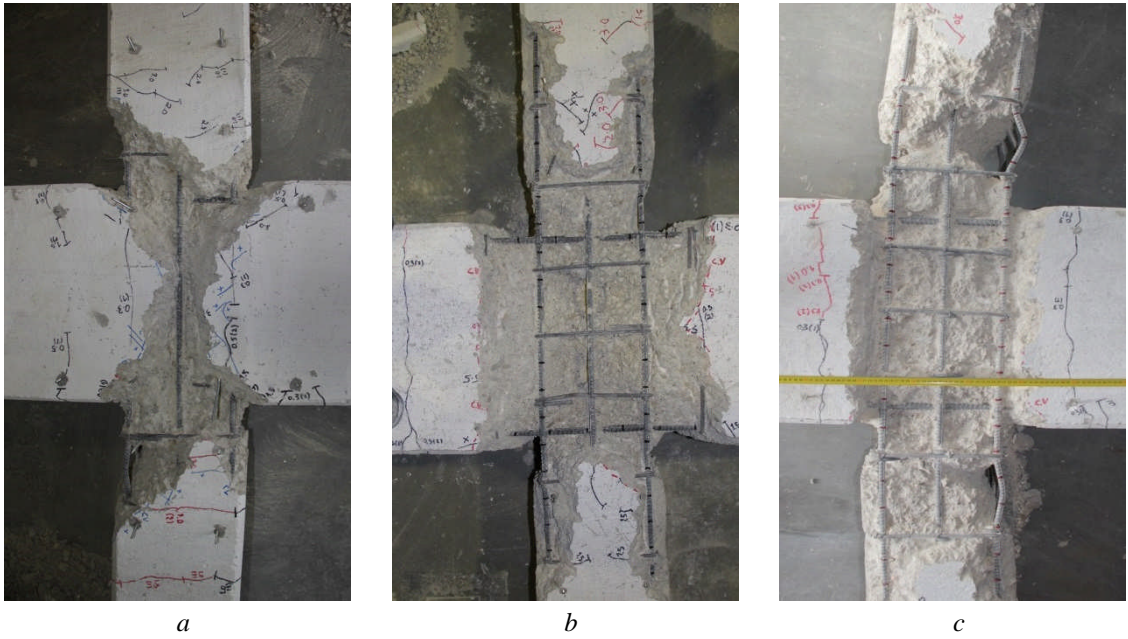


Figure C-17 Damage at the end of the experiment in specimens: a) J3-X, b) J5-X and c) J7-X.

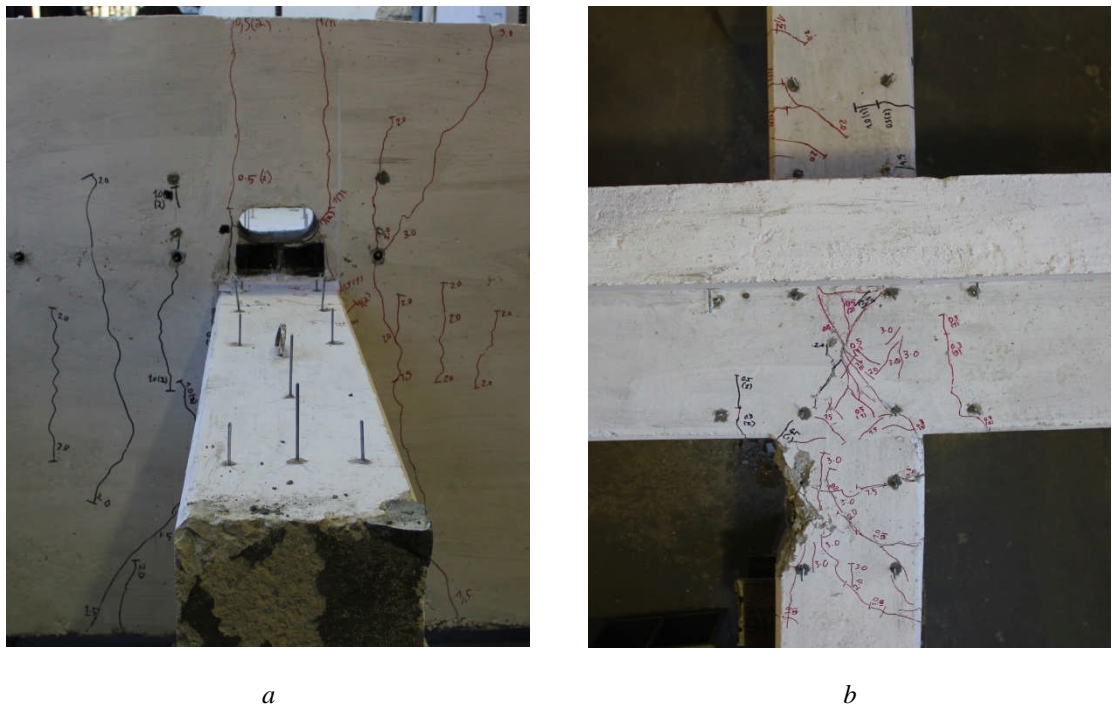


Figure C-18 Damage at the end of the experiment in specimen J4-X: a) View of the damage in the flanges, b) View of the damage in the columns and node.

As discussed in Chapter 4, most experimental campaigns in literature involve beam column connections that do not incorporate a slab. However, in real buildings slabs work with beams in the transfer of loads and contribute to the overall stiffness of the frame (Booth *et al.*, 2002). The response of specimen J3-X is compared with the response of specimen J4-X which has similar detailing aspects and material properties as the former, but incorporates a beam with flanges simulating a slab. Figure C-16 shows how the incorporation of a slab can affect the lateral force

capacity and ductility. The incorporation of the slab increases the overall stiffness of the beam and the joint in relationship to the stiffness of the columns. This results in a reduction in the system ductility which is even worse than the reduction in specimen J7-X. In this case, since the effective beam is un-symmetrical, more damage is observed to form in the upper column. Damage in the beams propagates also in the flanges as shown in figure C-18. The force at yielding and the maximum force capacity in J4-X are observed to be similar to J3-X and approximately 5% larger than J7-X. The drift ratio at yielding of J4-X is 15% lower than J3-X and J7-X. However, the drift ratio of the three is very similar at maximum force capacity. After the maximum force is reached in both directions of deformation, J4-X suffers complete collapse in the next half cycle. At u-10, the drift ratio of J4-X is 22% smaller than J3-X and J7-X. At u-20 and u-50, the drift ratio of J4-X is 35% smaller than J3-X and 25% smaller than J7-X.

Appendix D Experimental Results of Column and Beam-Column Specimens

D.1 Damage Development of the Column Specimens

Table D-1. Description of general damage that is observed to form on the columns.

Damage	Description of observed damage
CR-I	Initial observed flexural crack formation.
CR-F	Last observed flexural crack formation.
SP-I	Initial observed spalling or splitting.
SP-F	Last observed propagation of spalling or splitting cracks.
DC-I	Observed initial diagonal crack.
DC-F	Complete observed diagonal crack.
BK	Observed considerable buckling of longitudinal reinforcement.
OS	Observed considerable opening of stirrup hooks.
AL	Observed considerable loss of axial force capacity.
LR	Observed rupture of longitudinal reinforcement.

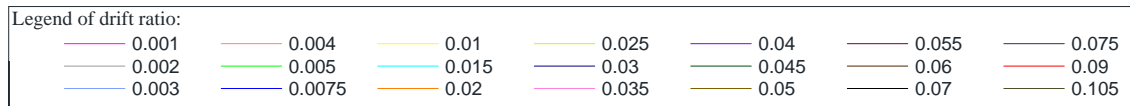


Figure D-1. The legend of drift ratios corresponding with the maximum value of the loading cycle in which cracking is observed.

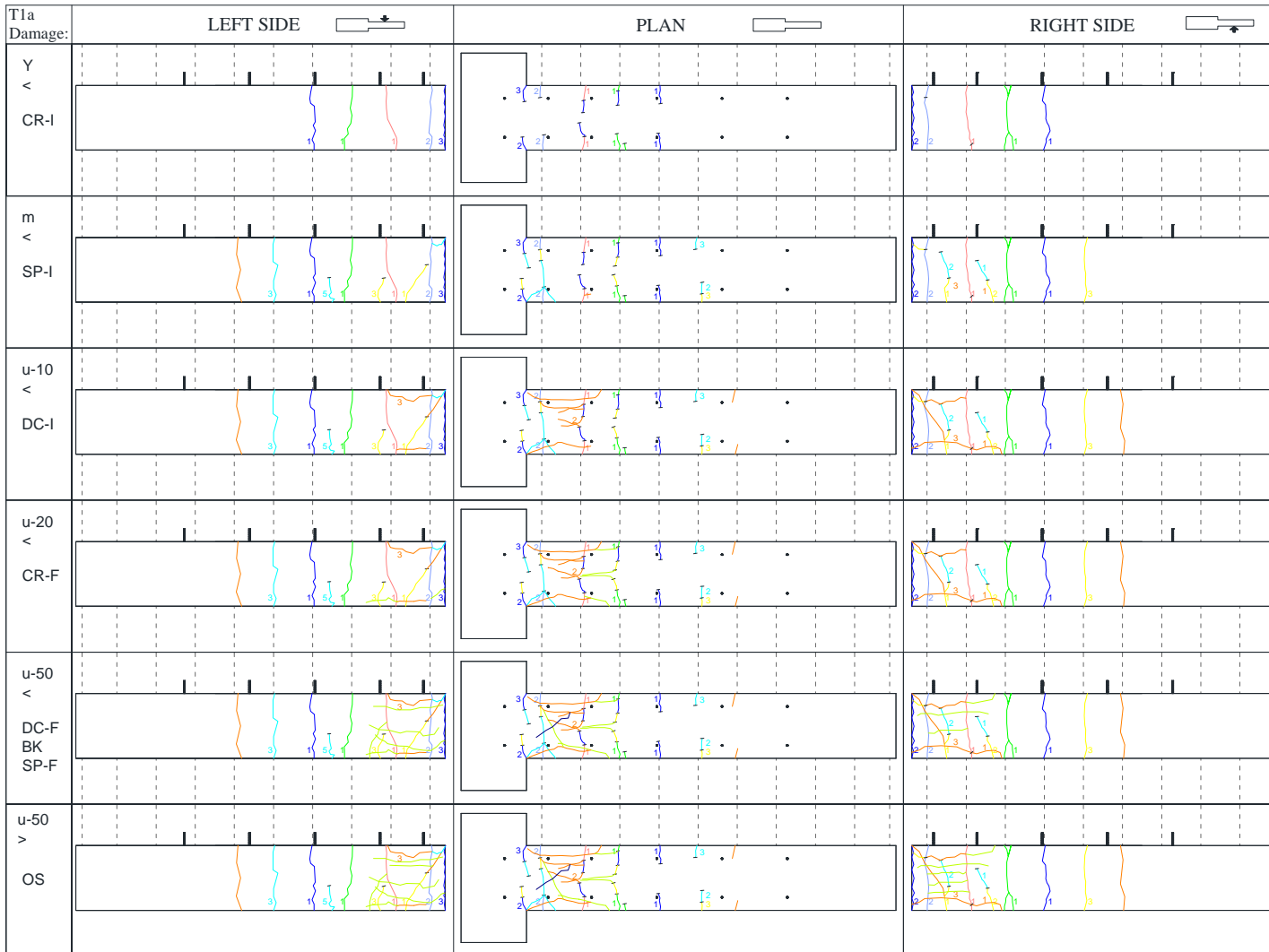


Figure D-2. Damage development on column specimen T1a at different damage levels.

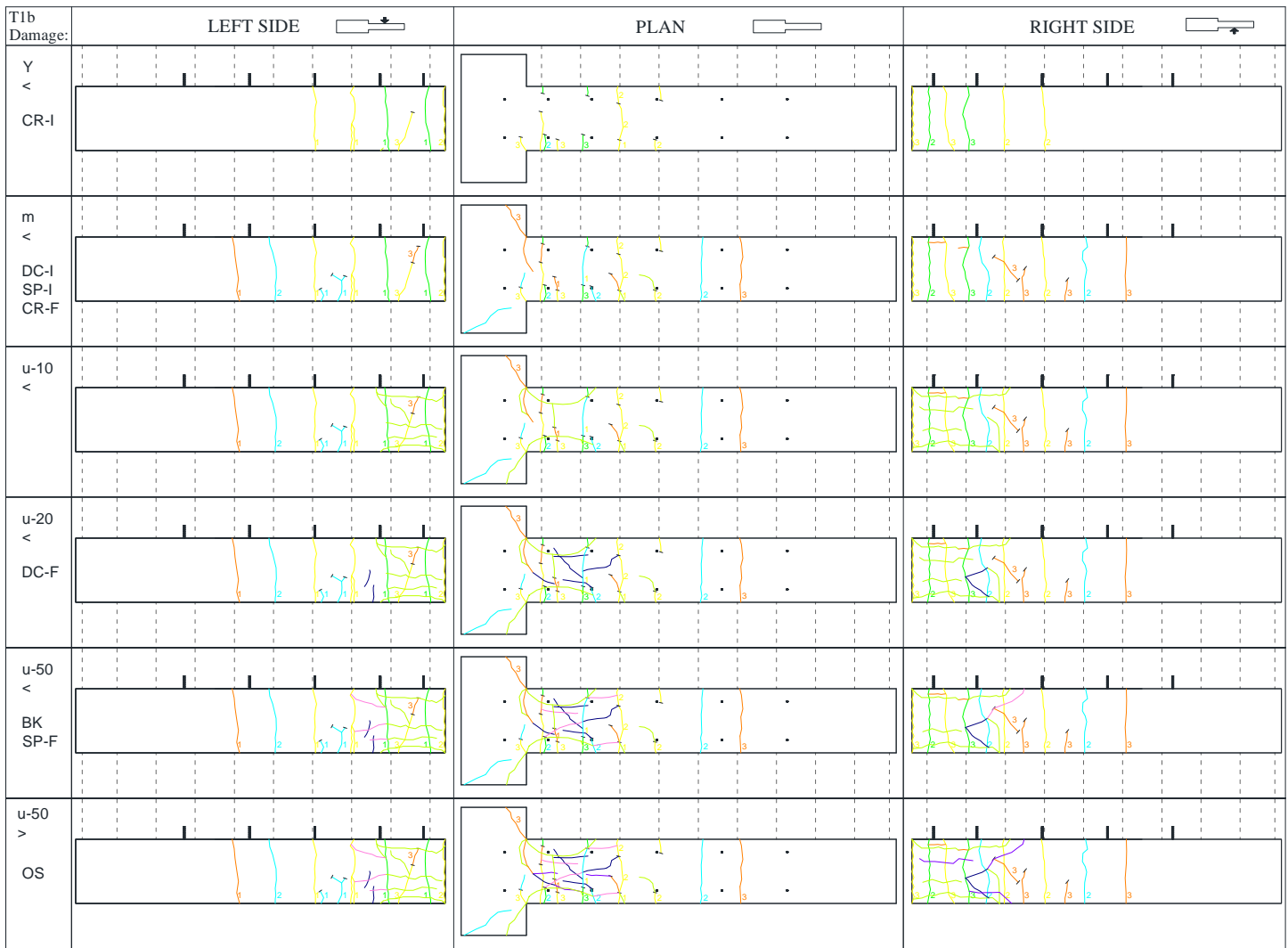


Figure D-3. Damage development on column specimen T1b at different damage levels.

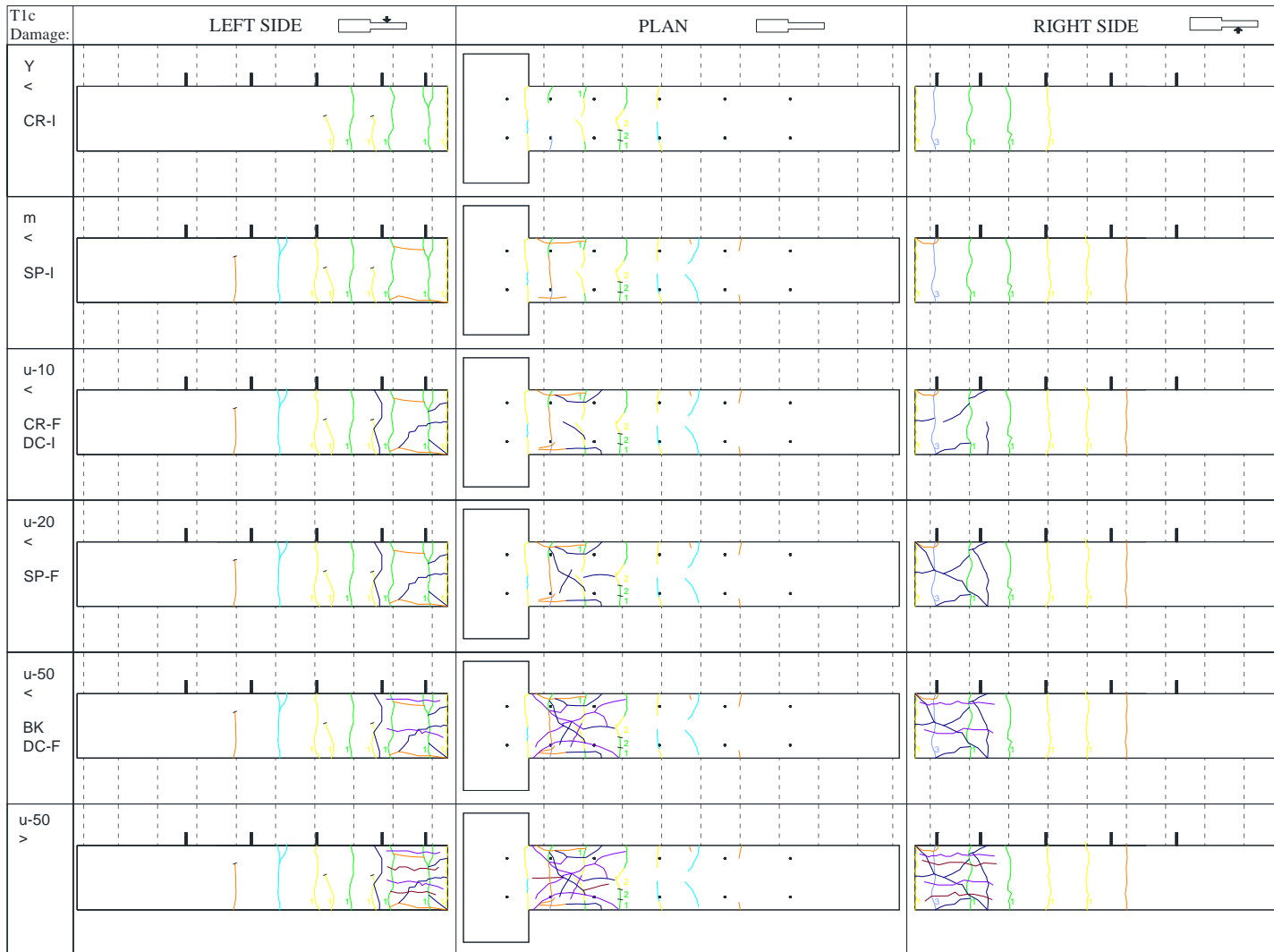


Figure D-4. Damage development on column specimen T1c at different damage levels.

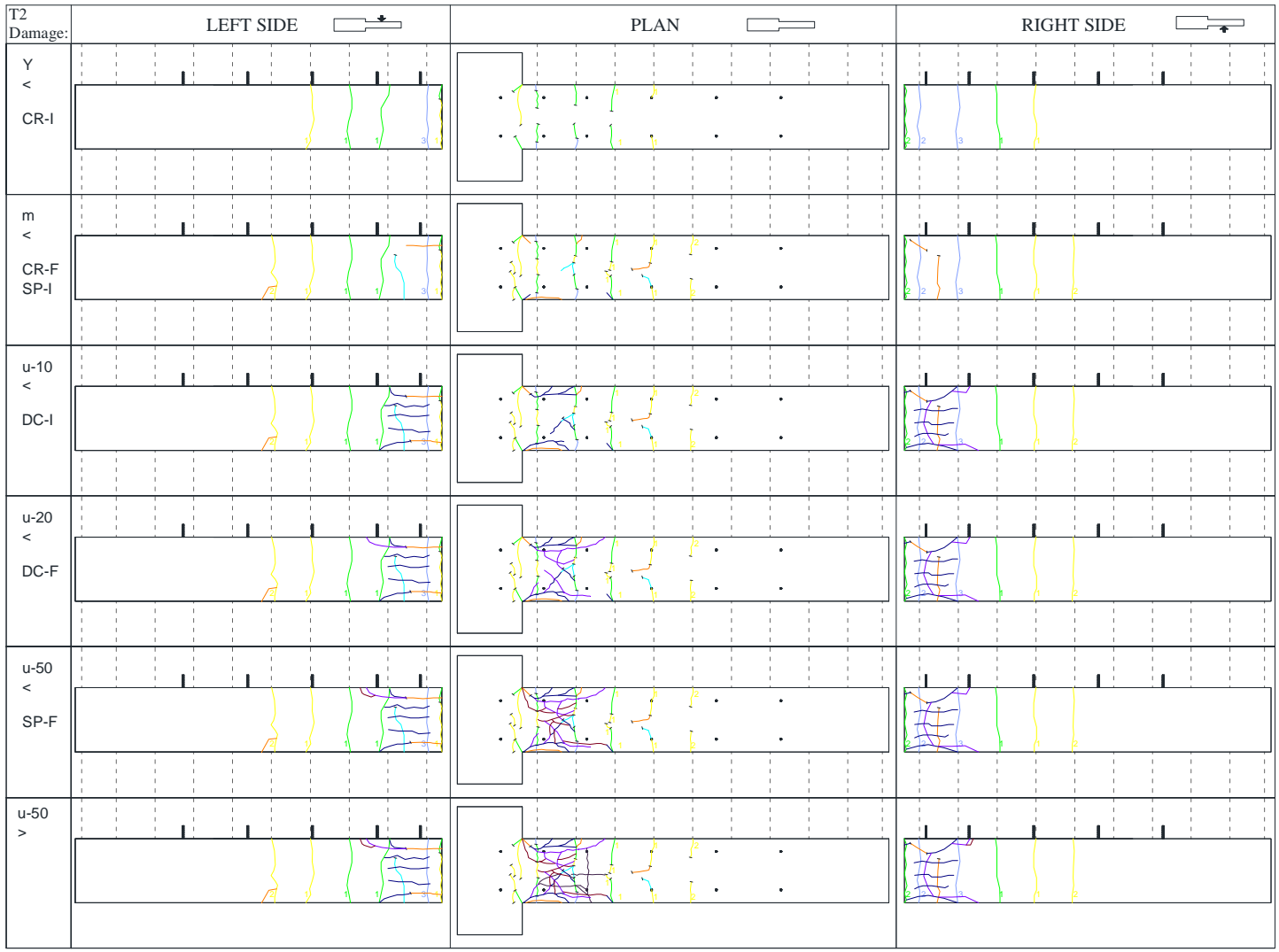


Figure D-5. Damage development on column specimen T2 at different damage levels.

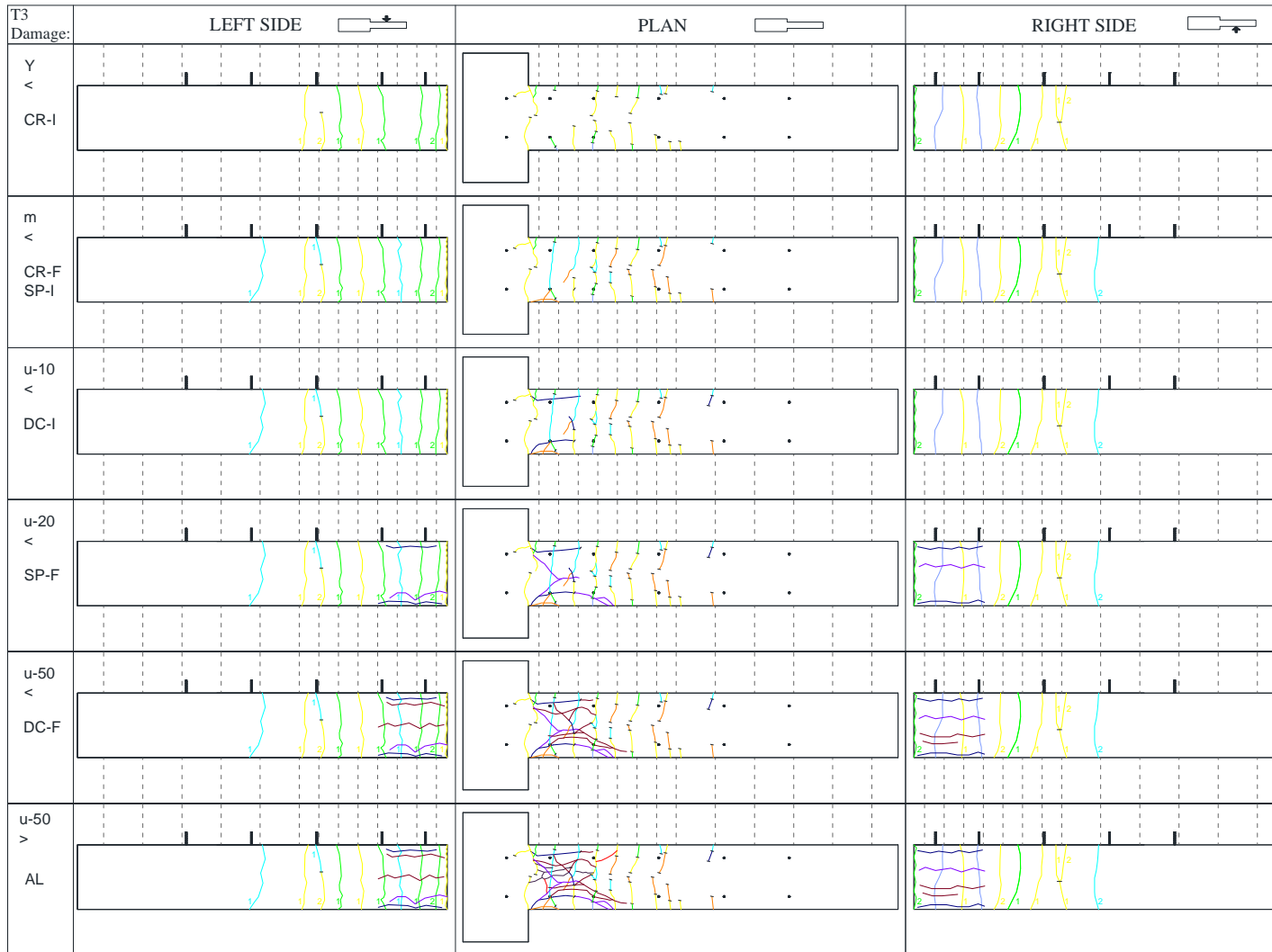


Figure D-6. Damage development on column specimen T3 at different damage levels.

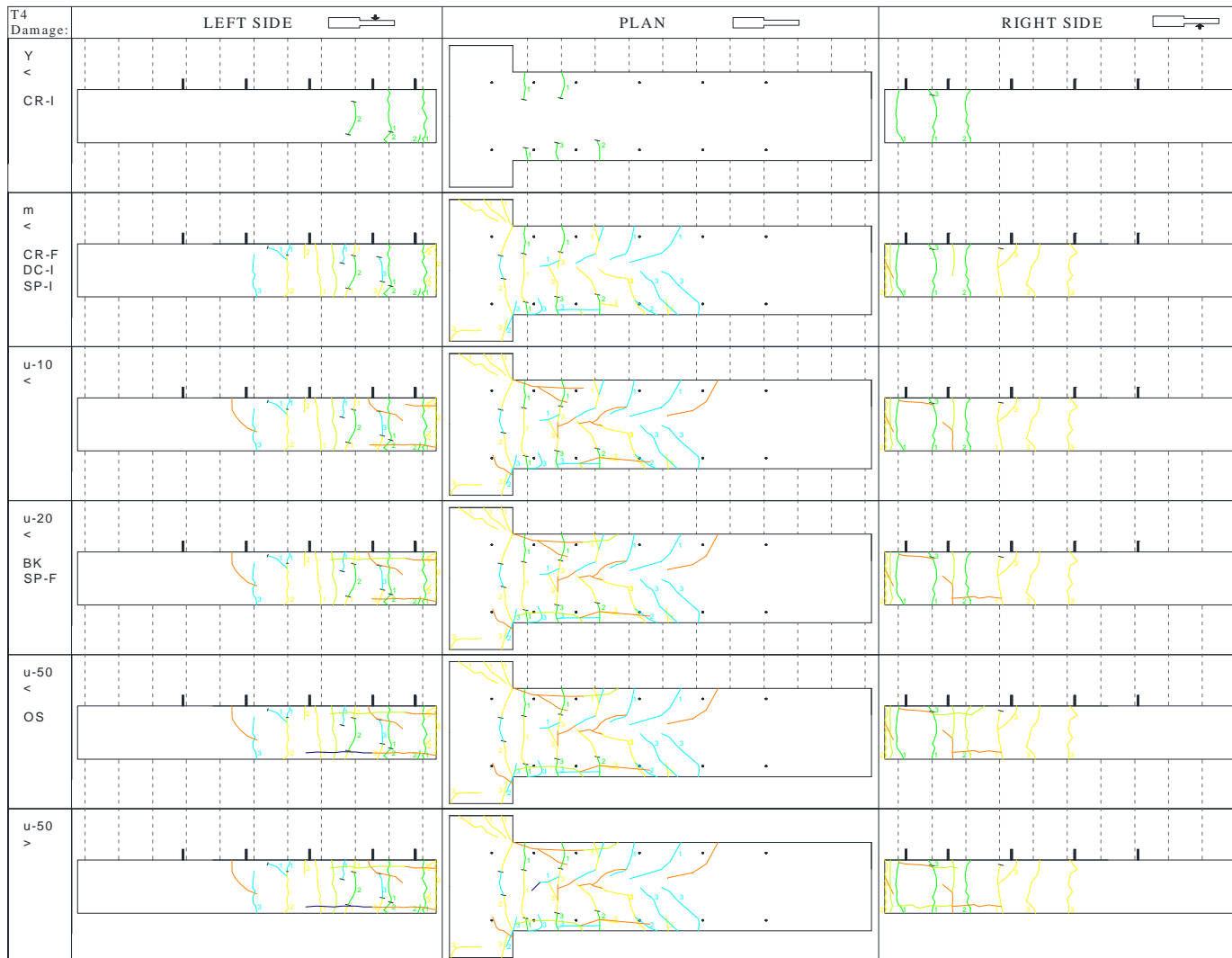


Figure D-7. Damage development on column specimen T4 at different damage levels.

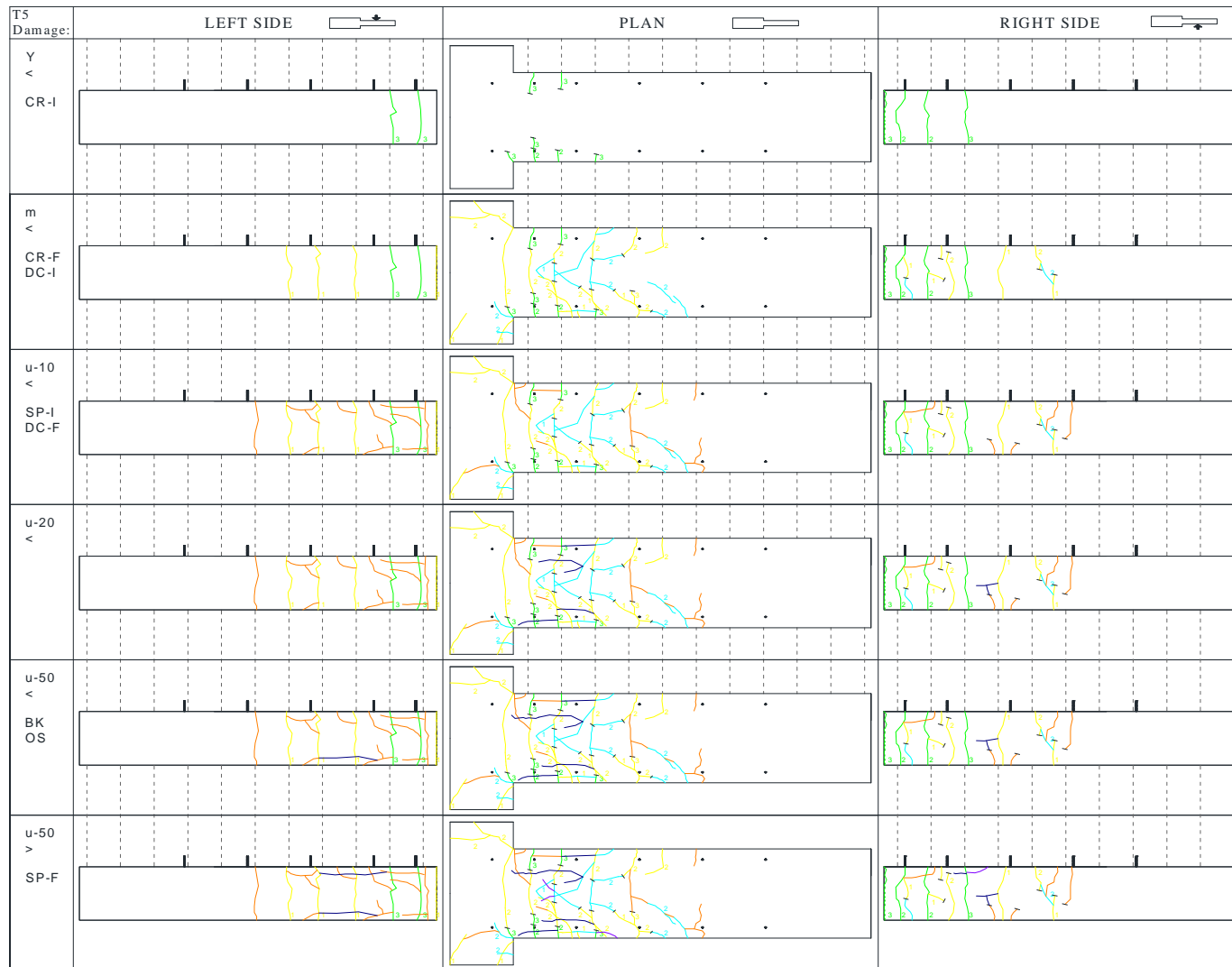


Figure D-8. Damage development on column specimen T5 at different damage levels.

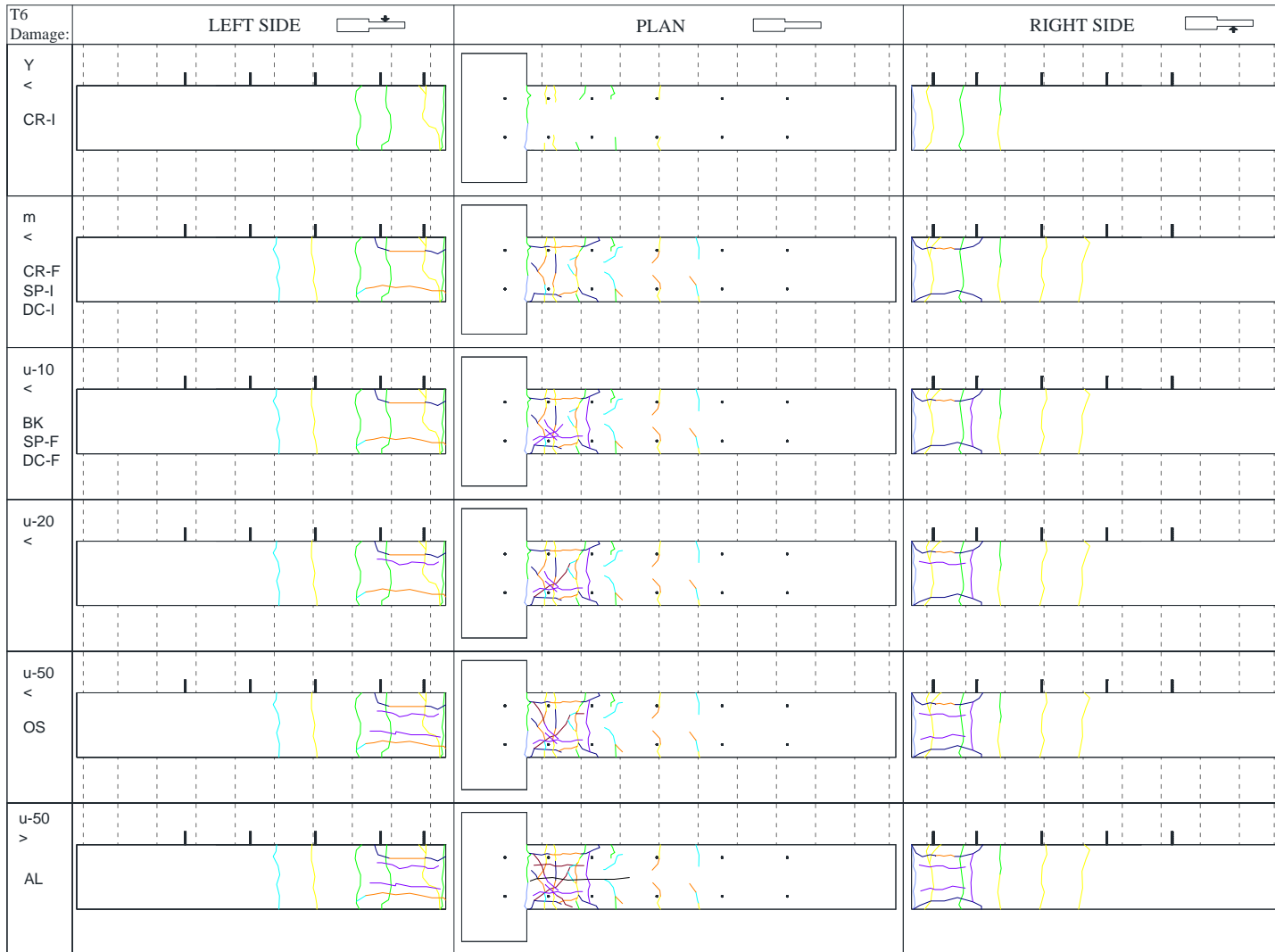


Figure D-9. Damage development on column specimen T6 at different damage levels.

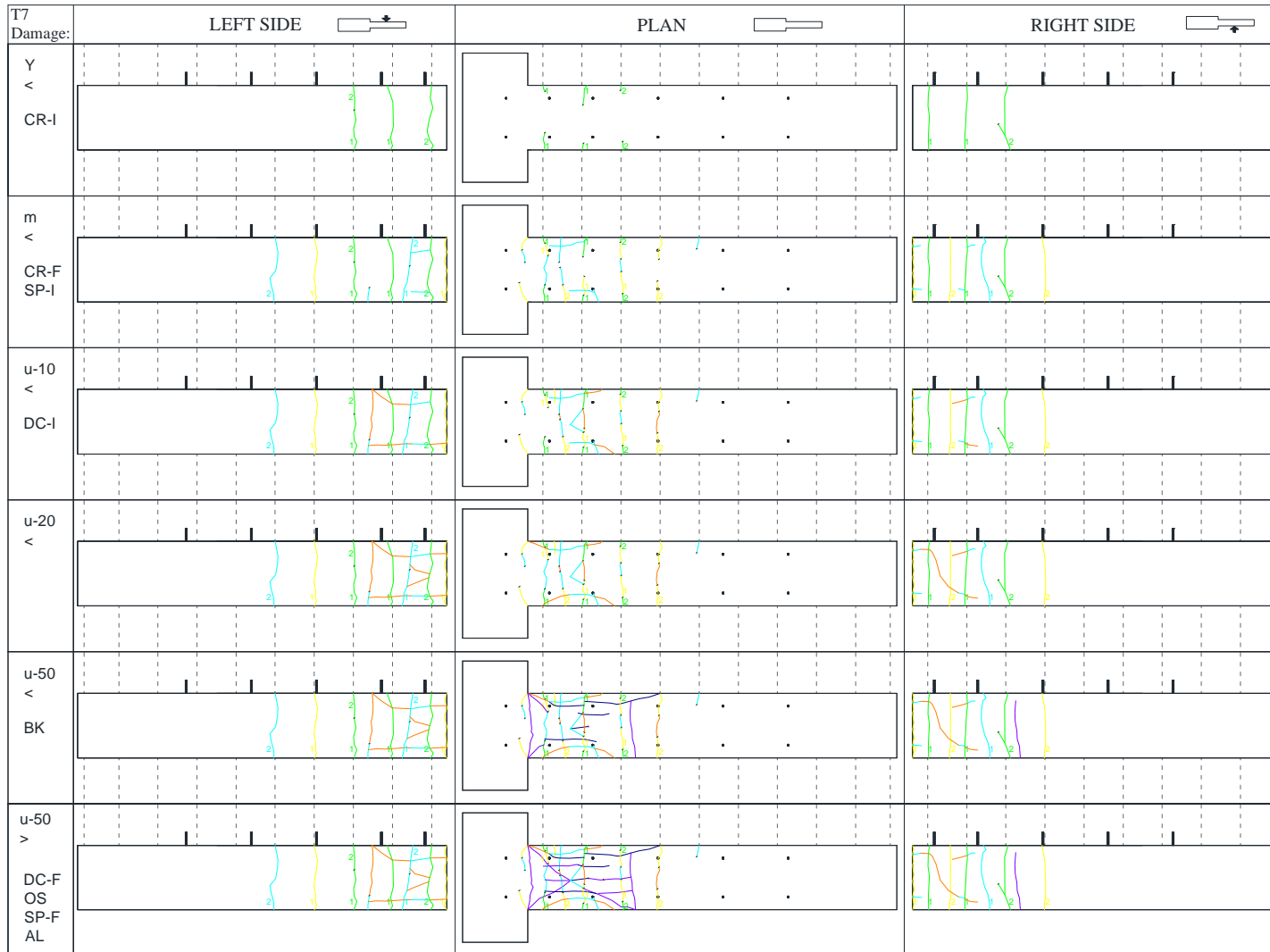


Figure D-10. Damage development on column specimen T7 at different damage levels.

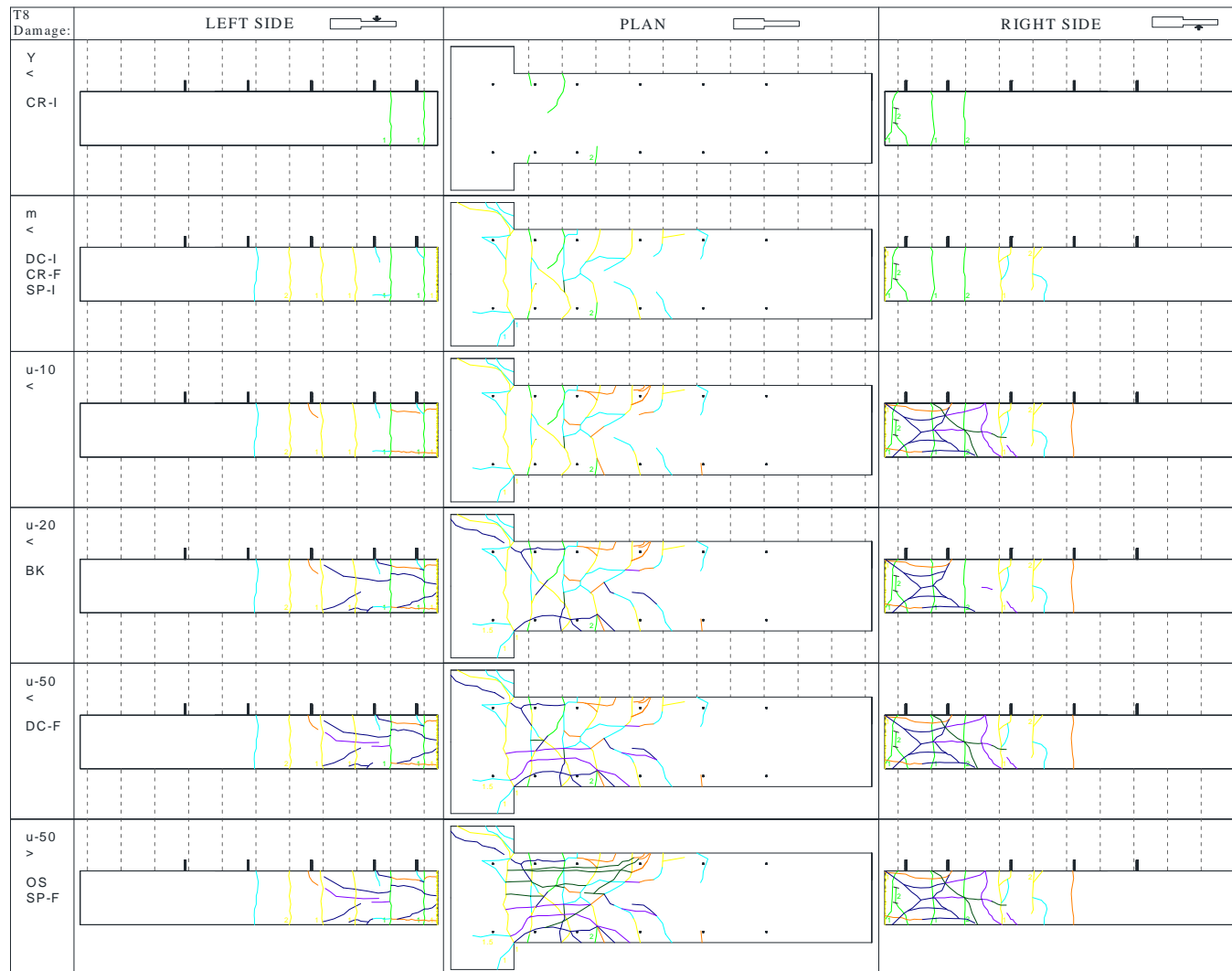


Figure D-11. Damage development on column specimen T8 at different damage levels.

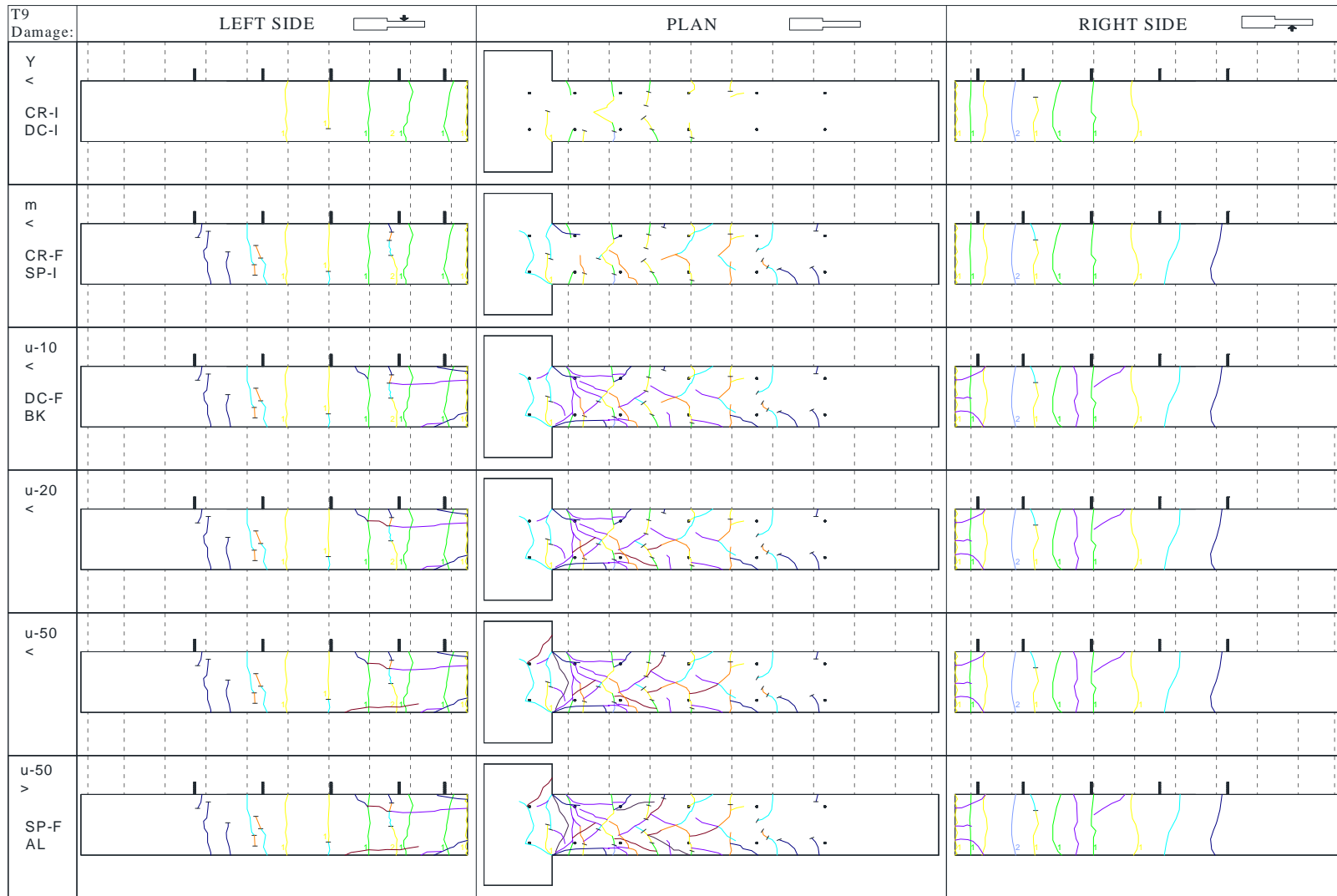


Figure D-12. Damage development on column specimen T9 at different damage levels.

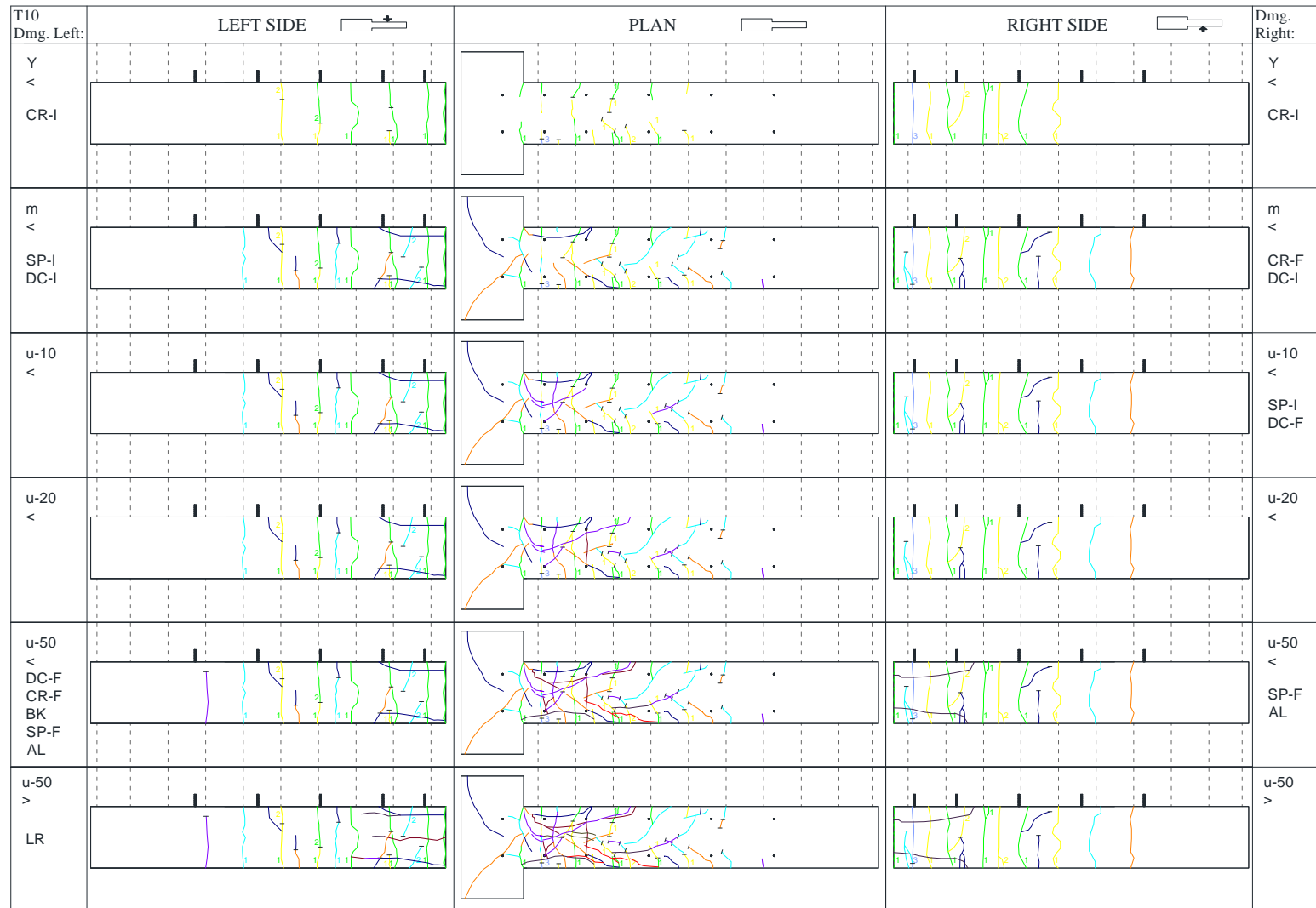


Figure D-13. Damage development on column specimen T10 at different damage levels.

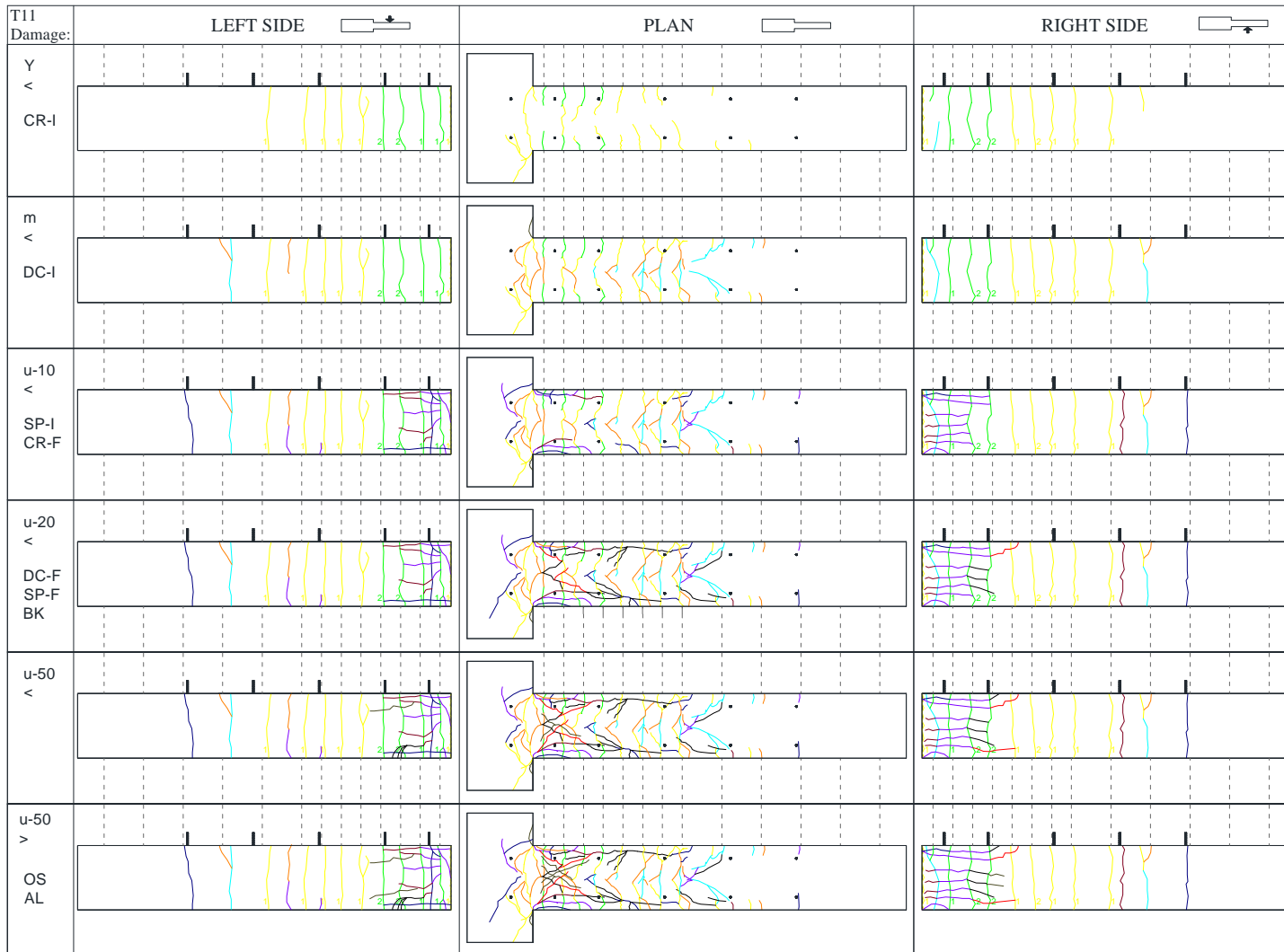


Figure D-14. Damage development on column specimen T11 at different damage levels.

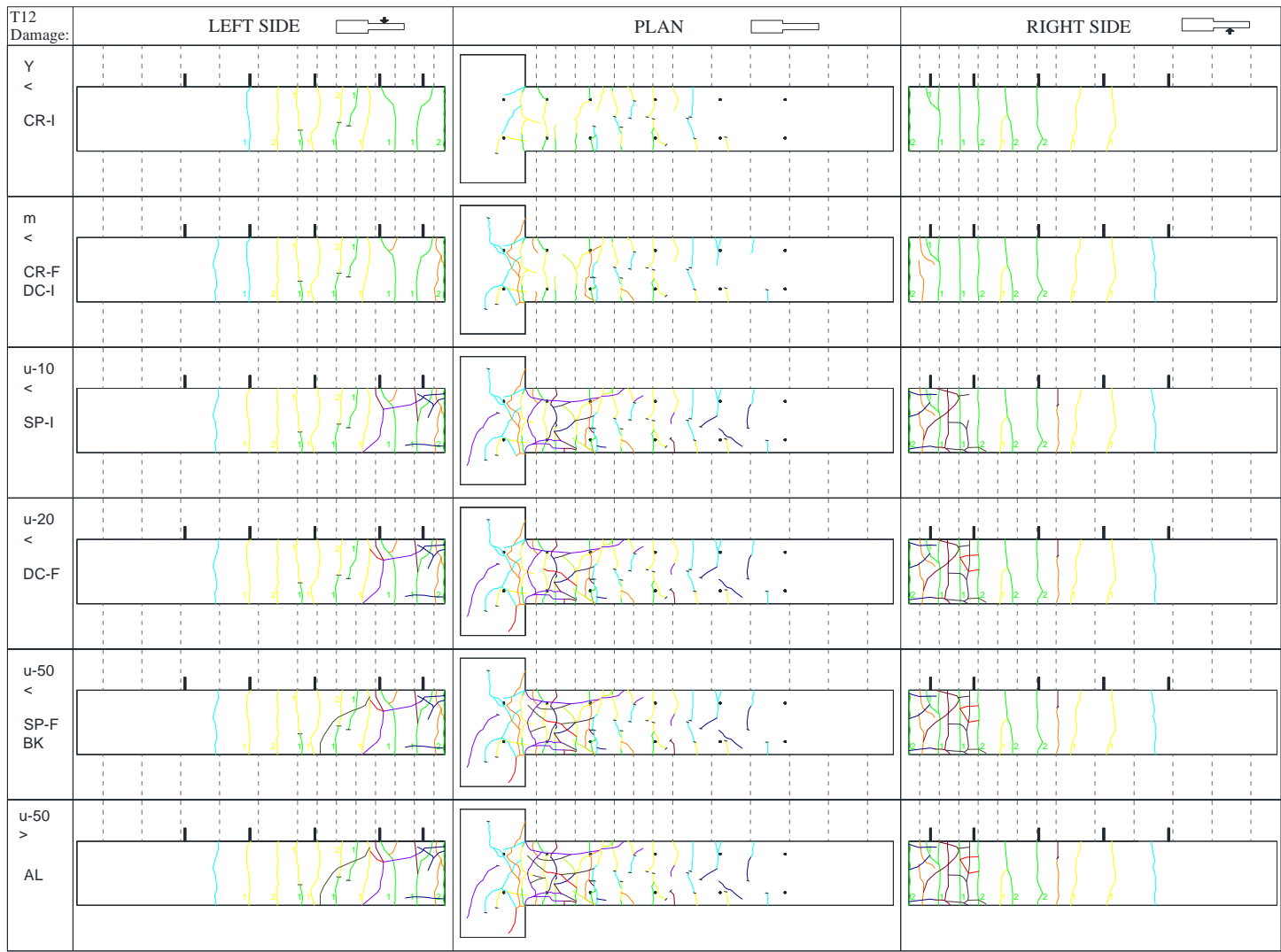


Figure D-15. Damage development on column specimen T12 at different damage levels.

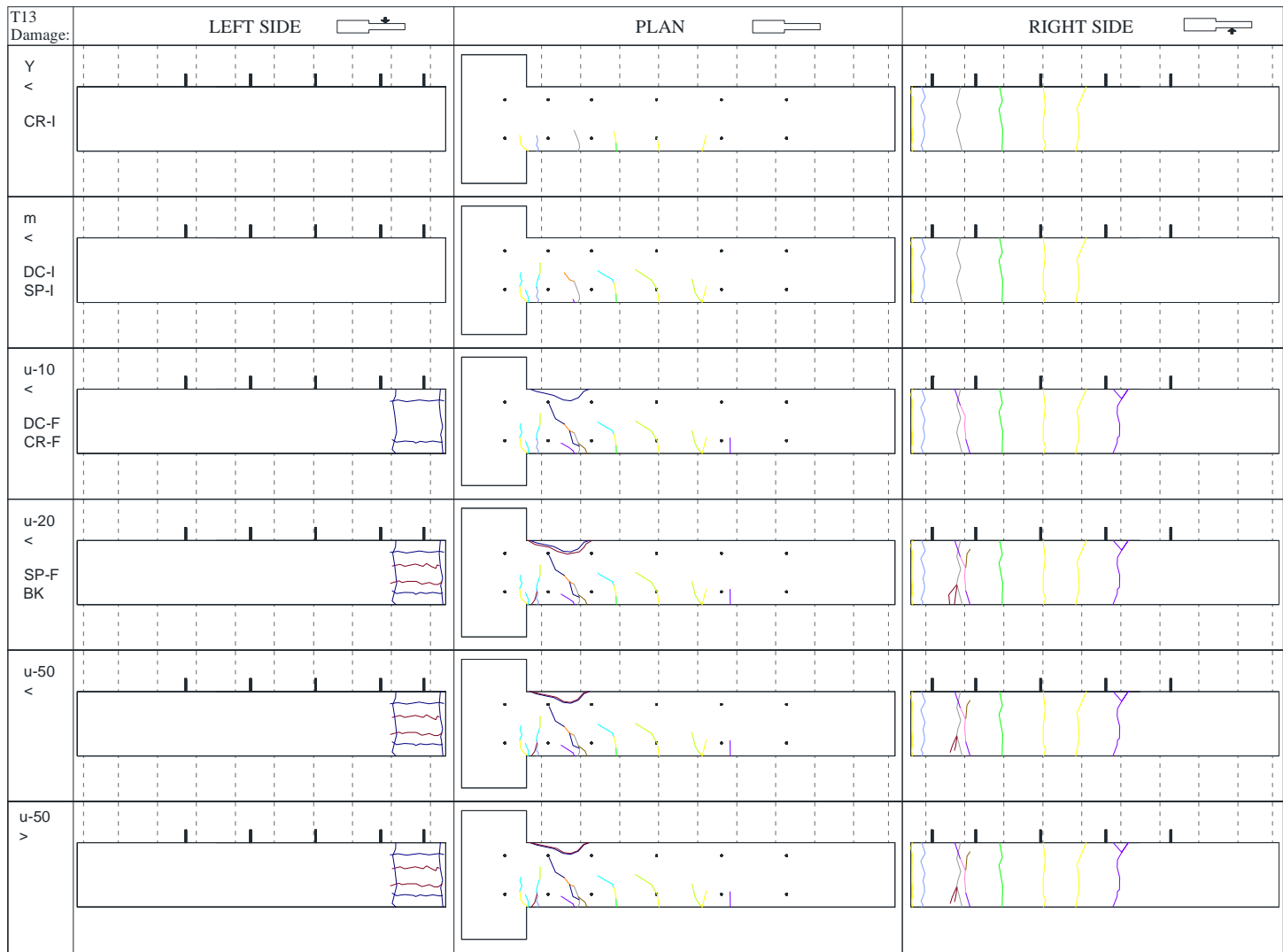


Figure D-16. Damage development on column specimen T13 at different damage levels.

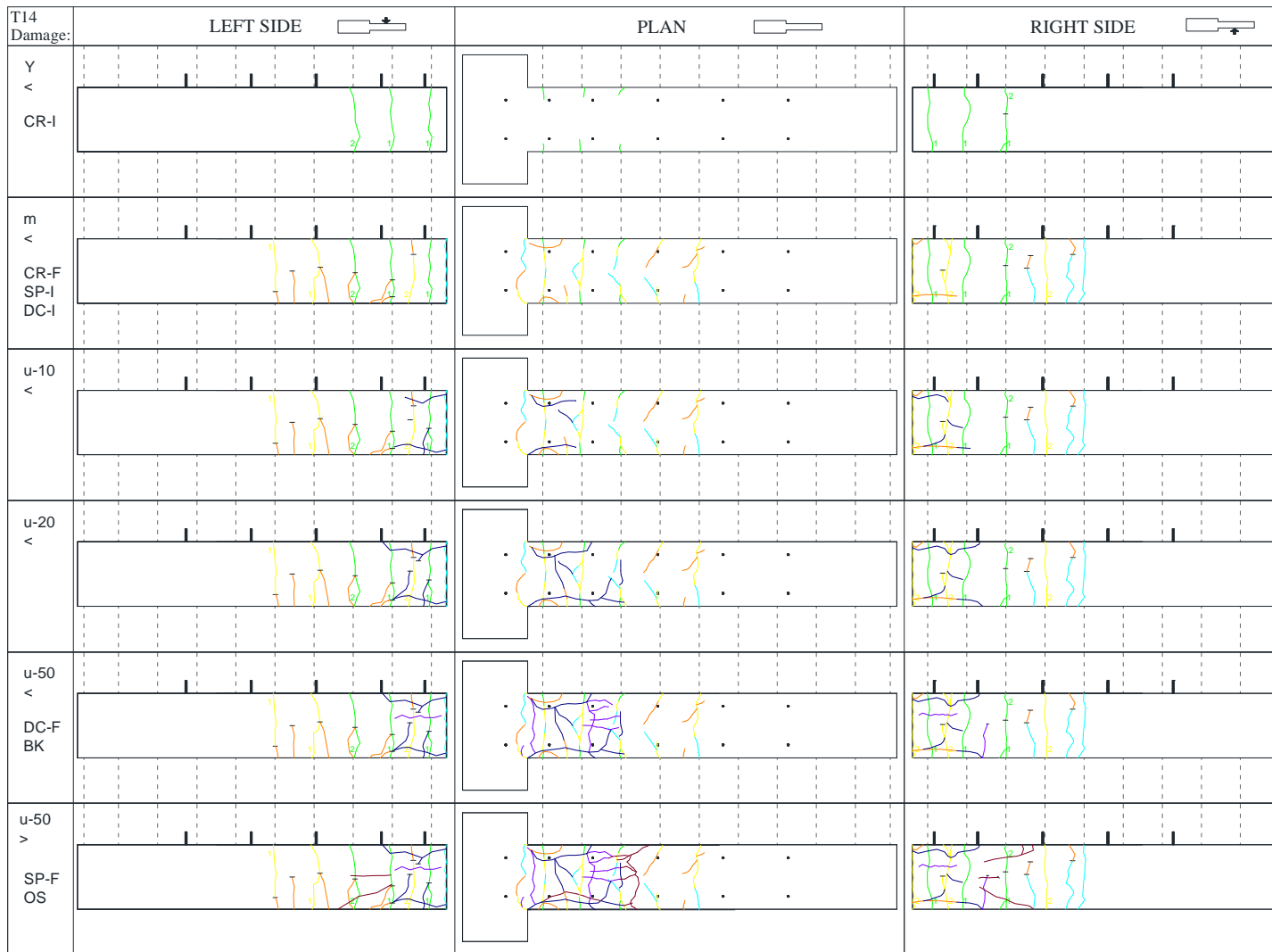


Figure D-17. Damage development on column specimen T14 at different damage levels.

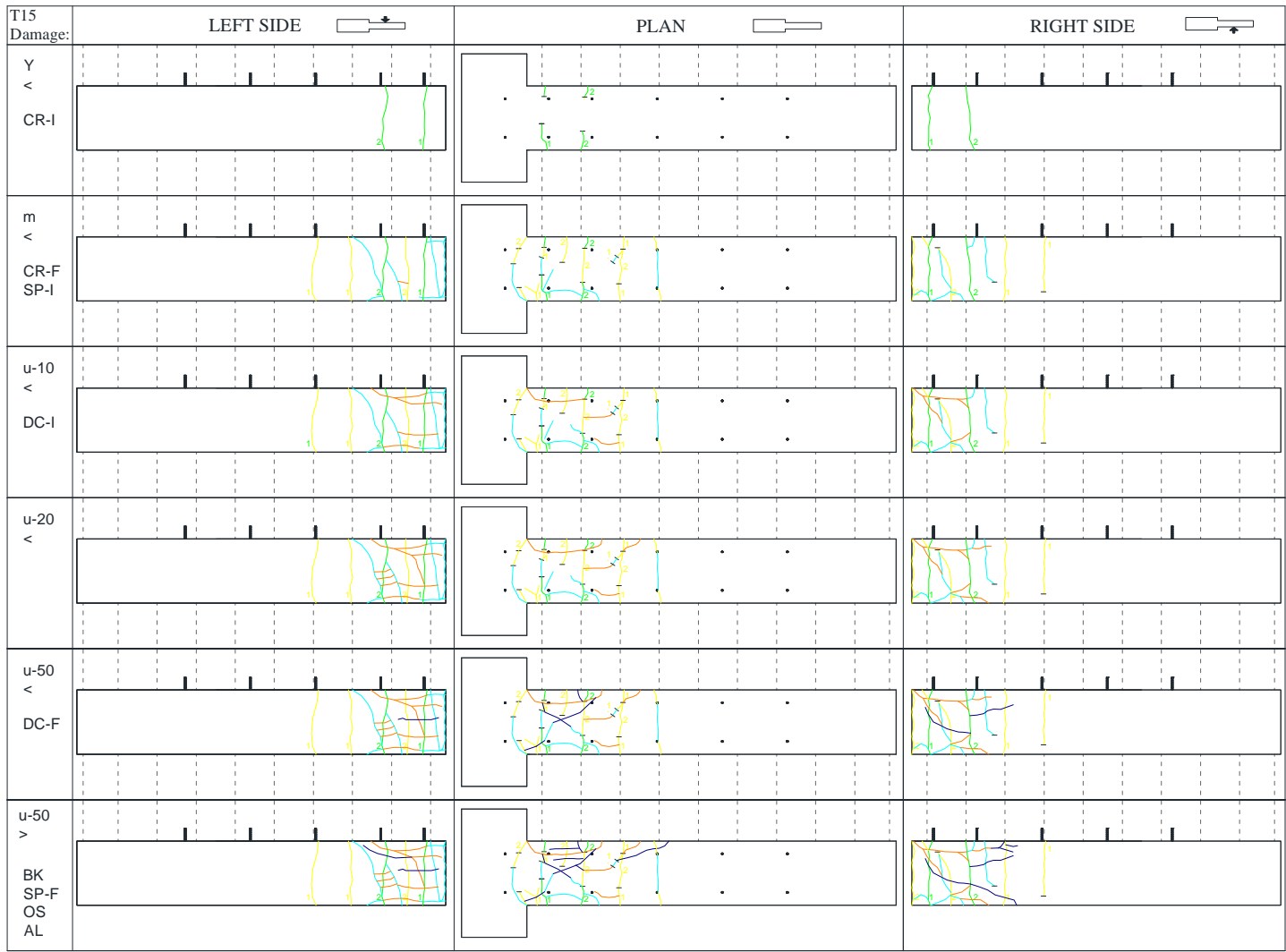


Figure D-18. Damage development on column specimen T15 at different damage levels.

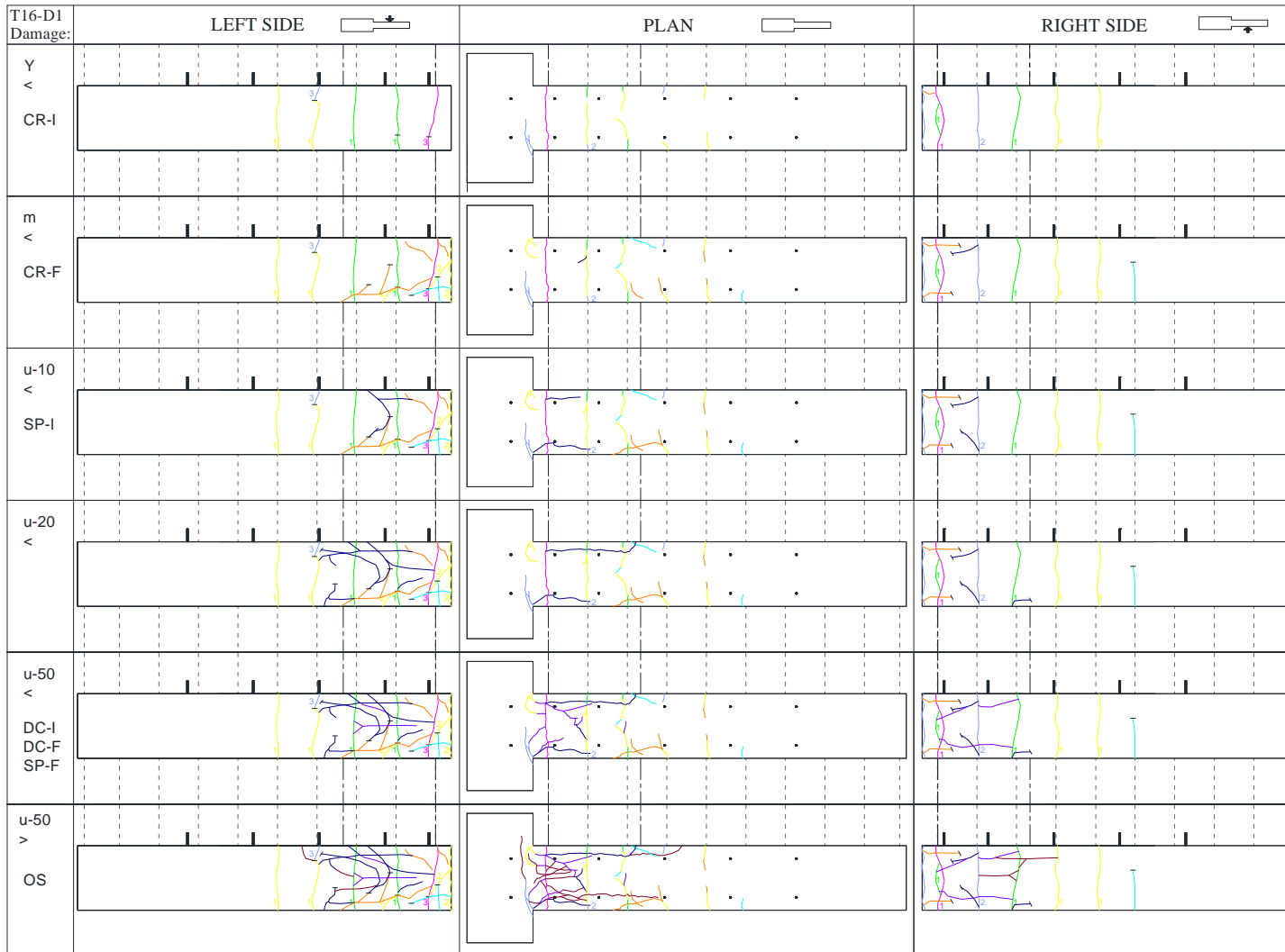


Figure D-19. Damage development on column specimen T16-D1 at different damage levels.

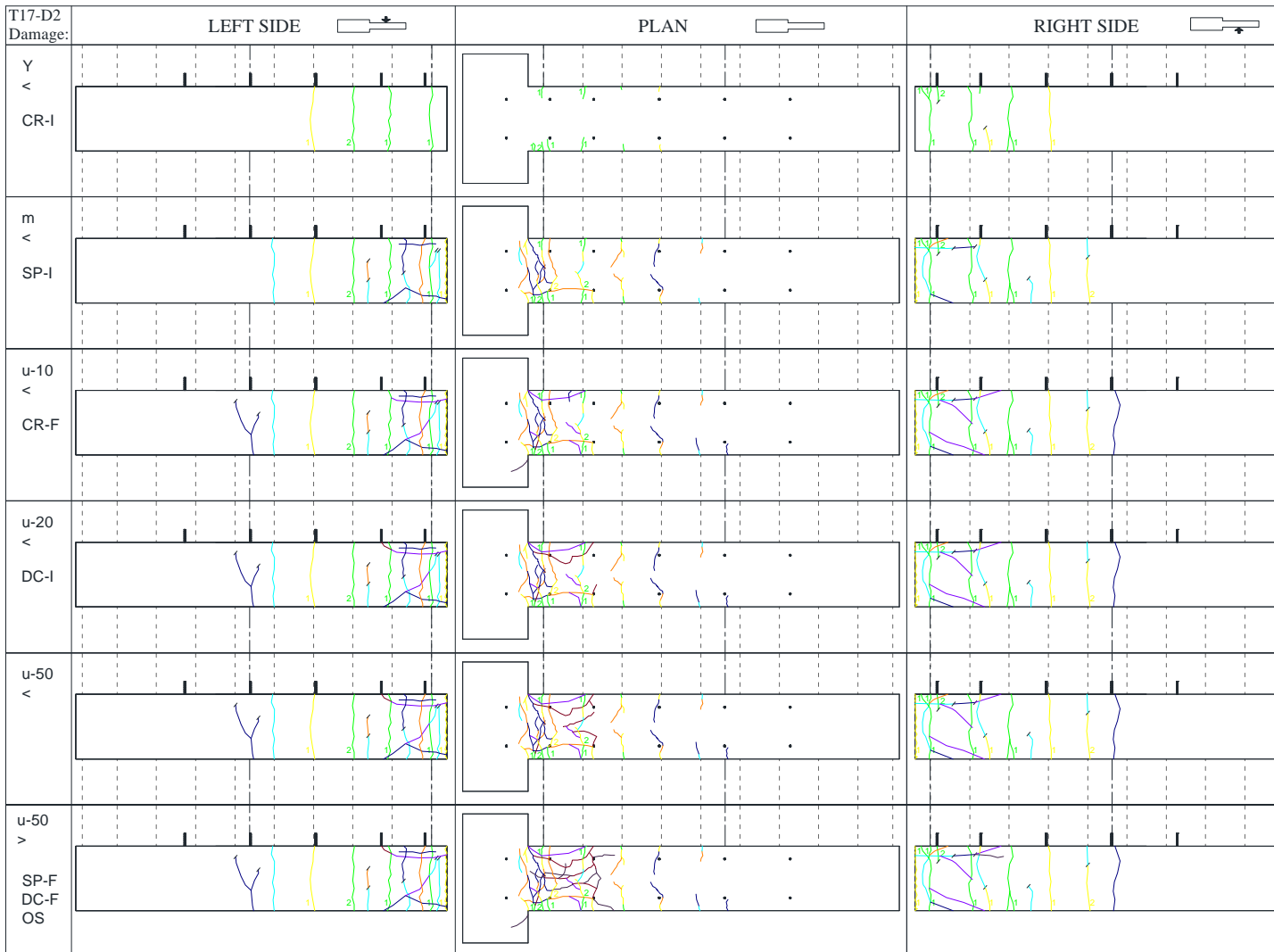


Figure D-20. Damage development on column specimen T17-D2 at different damage levels.

D.2 Global EDP Response of the Column Specimens

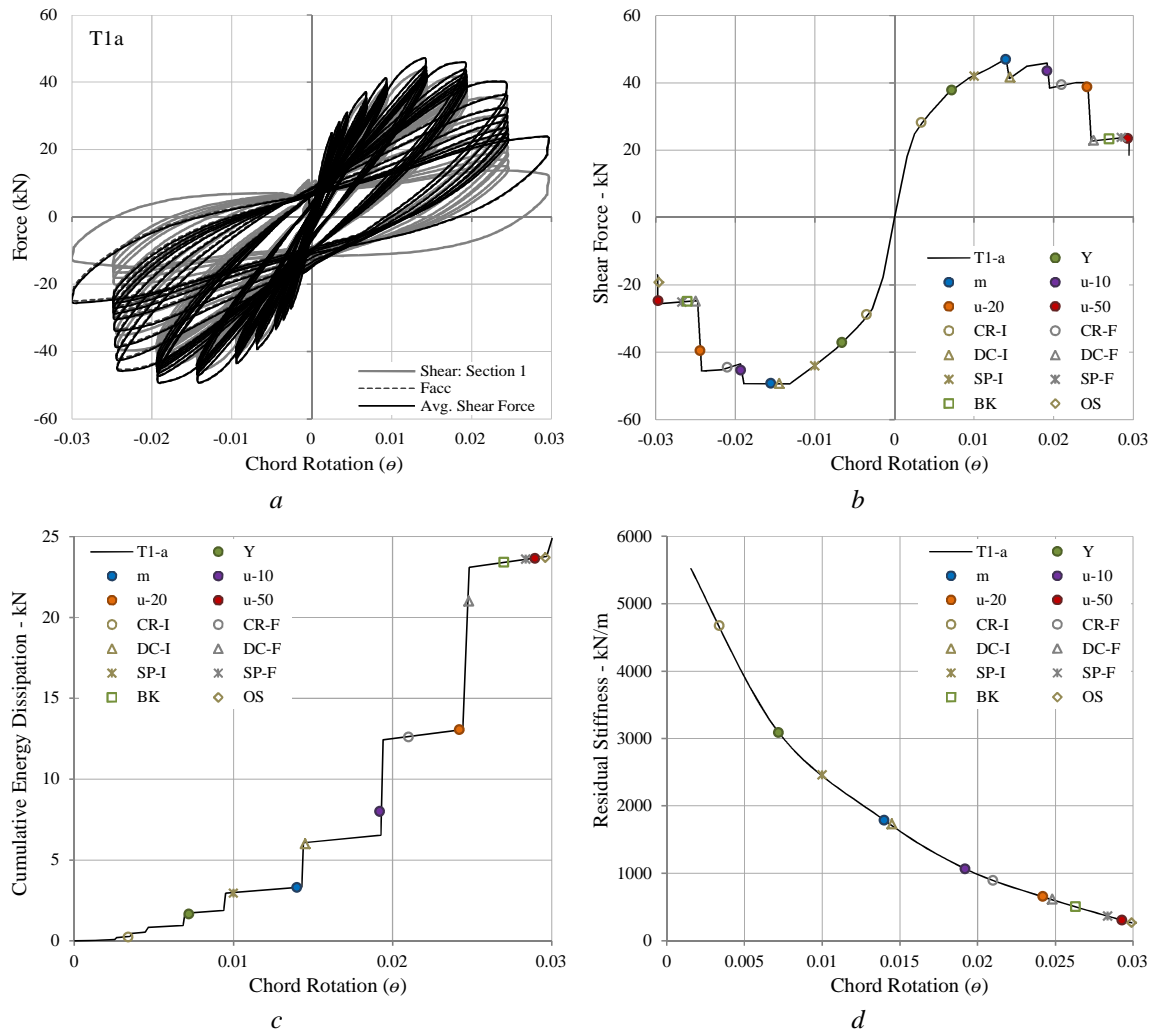


Figure D-21. Global EDP response of column T1a, indicating different failure modes and damage levels: a) Force-Chord Rotation hysteresis; b) Shear Force-Chord Rotation envelope; c) Cumulative energy dissipation – Chord rotation; d) Residual Stiffness - Chord Rotation.

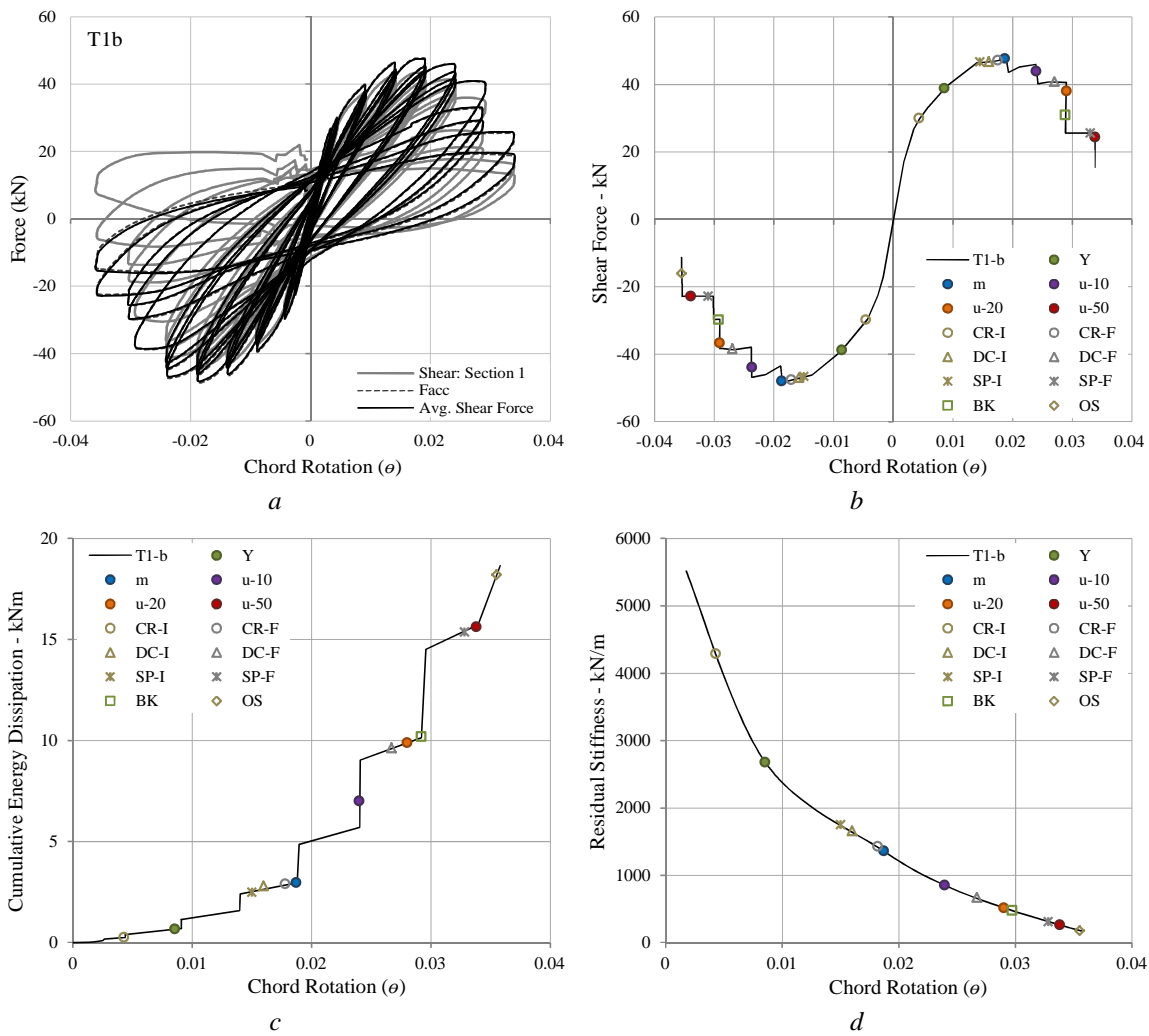


Figure D-22. Global EDP response of column T1b, indicating different failure modes and damage levels: a) Force-Chord Rotation hysteresis; b) Shear Force-Chord Rotation envelope; c) Cumulative energy dissipation – Chord rotation; d) Residual Stiffness - Chord Rotation.

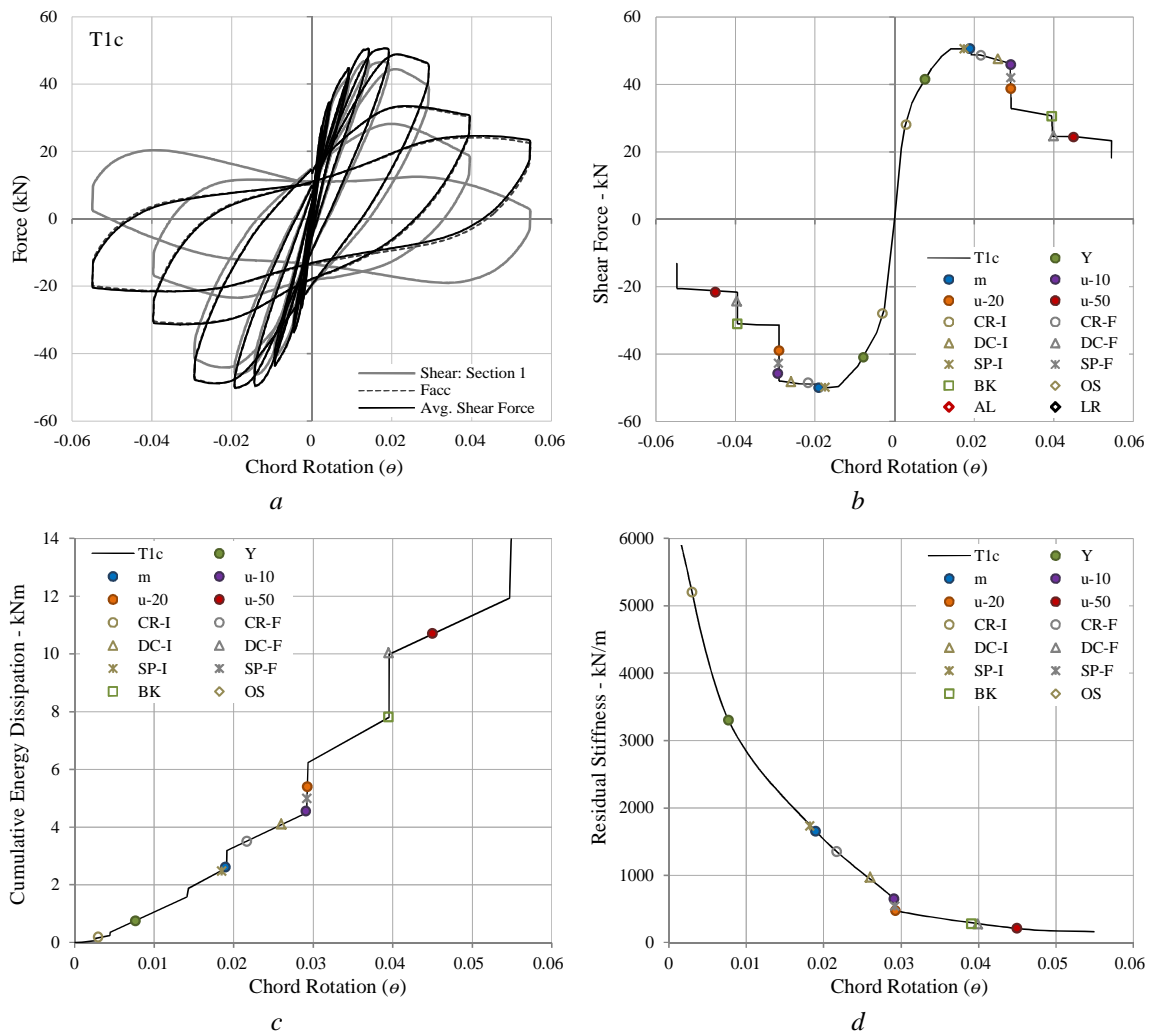


Figure D-23. Global EDP response of column T1c, indicating different failure modes and damage levels: a) Force-Chord Rotation hysteresis; b) Shear Force-Chord Rotation envelope; c) Cumulative energy dissipation – Chord rotation; d) Residual Stiffness - Chord Rotation.

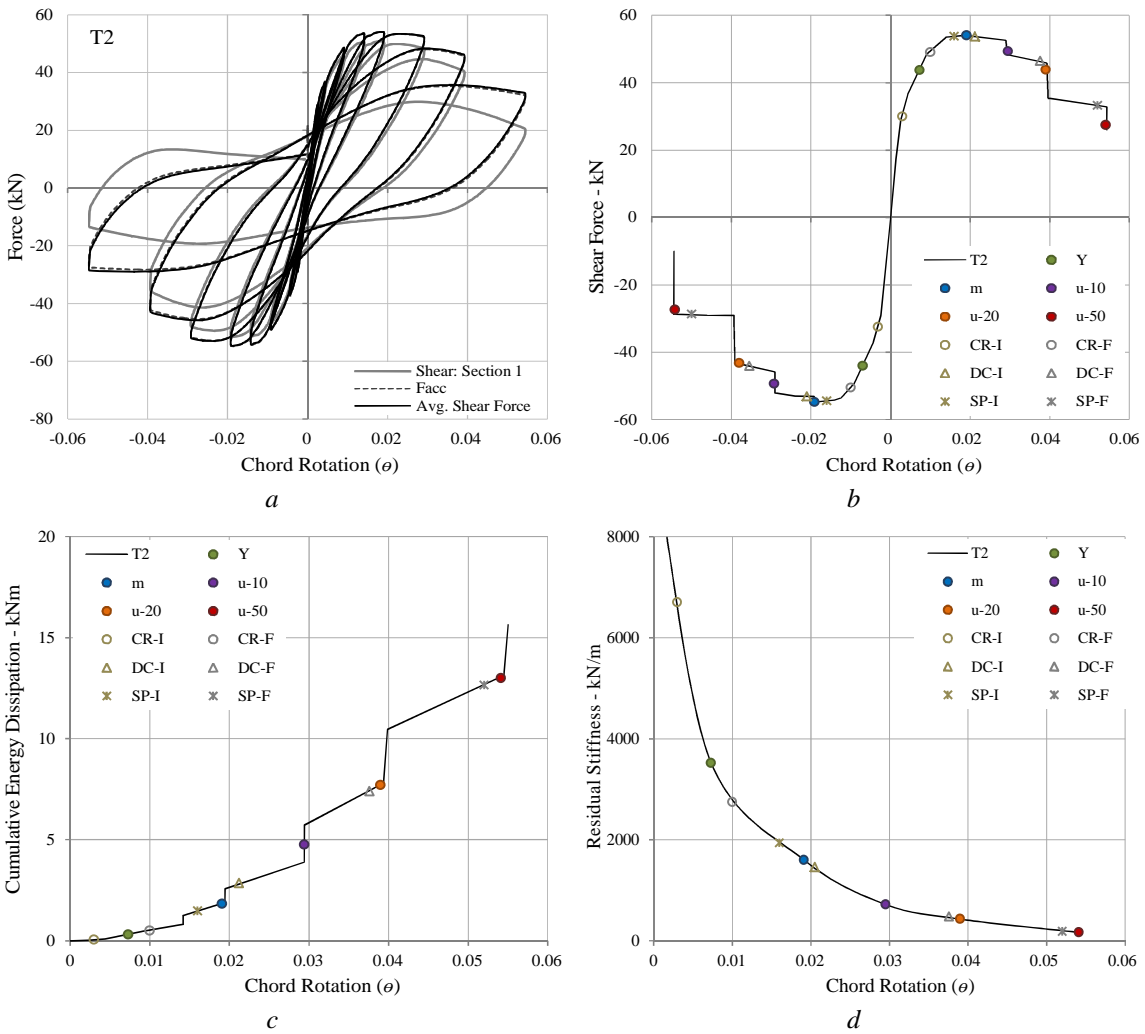


Figure D-24. Global EDP response of column T2, indicating different failure modes and damage levels: a) Force-Chord Rotation hysteresis; b) Shear Force-Chord Rotation envelope; c) Cumulative energy dissipation – Chord rotation; d) Residual Stiffness - Chord Rotation.

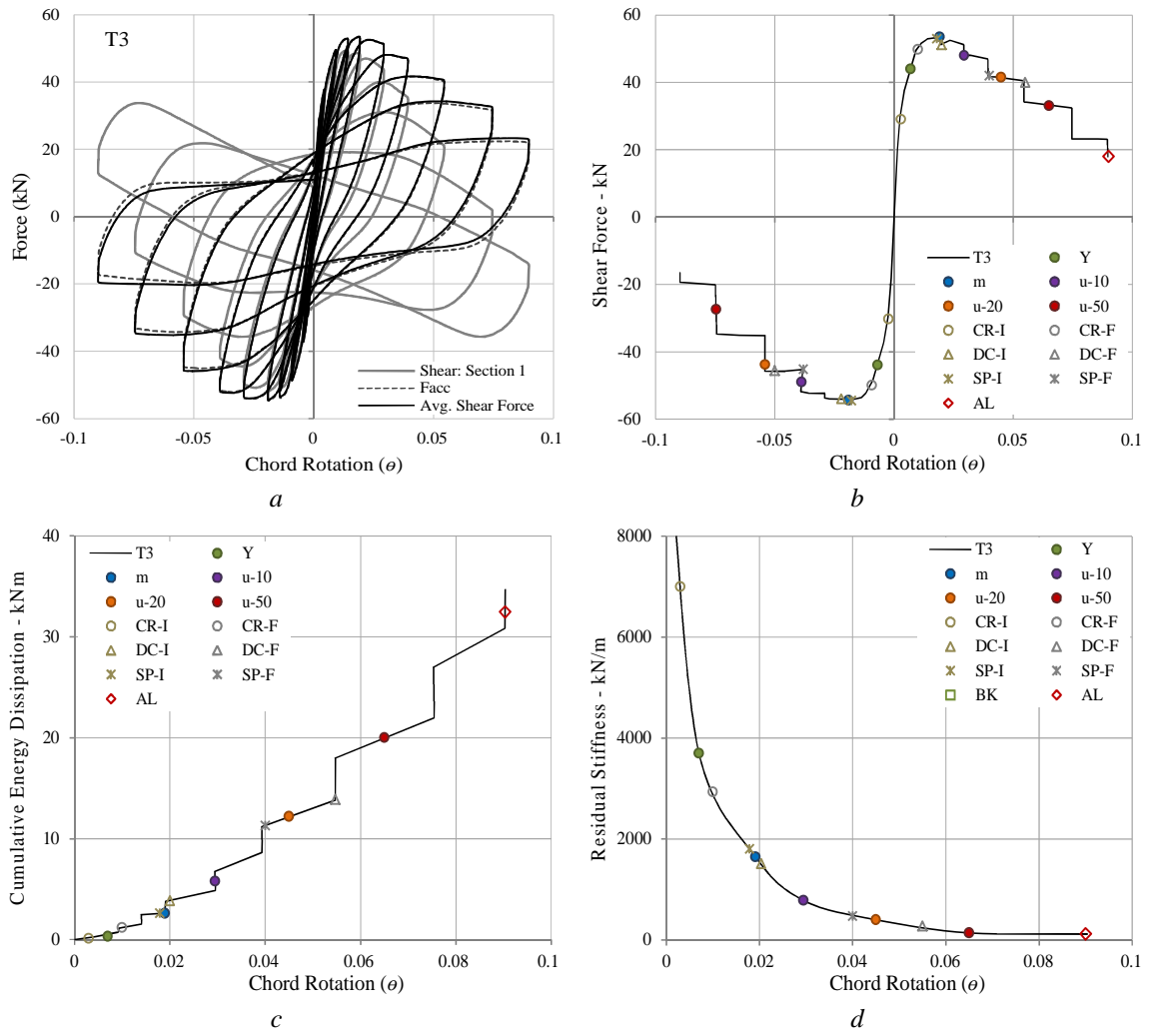


Figure D-25. Global EDP response of column T3, indicating different failure modes and damage levels: a) Force-Chord Rotation hysteresis; b) Shear Force-Chord Rotation envelope; c) Cumulative energy dissipation – Chord rotation; d) Residual Stiffness - Chord Rotation.

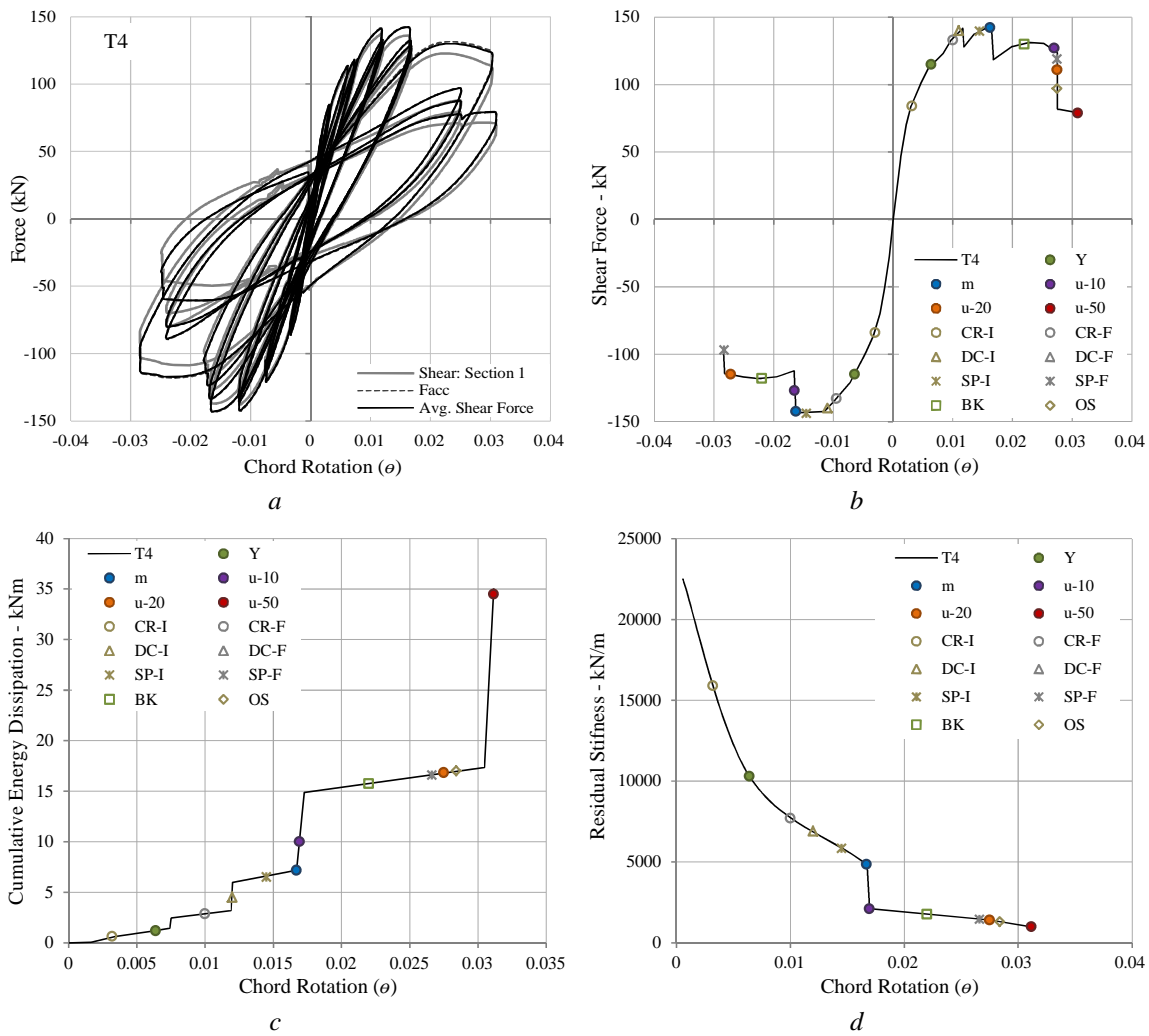


Figure D-26. Global EDP response of column T4, indicating different failure modes and damage levels: a) Force-Chord Rotation hysteresis; b) Shear Force-Chord Rotation envelope; c) Cumulative energy dissipation – Chord rotation; d) Residual Stiffness - Chord Rotation.

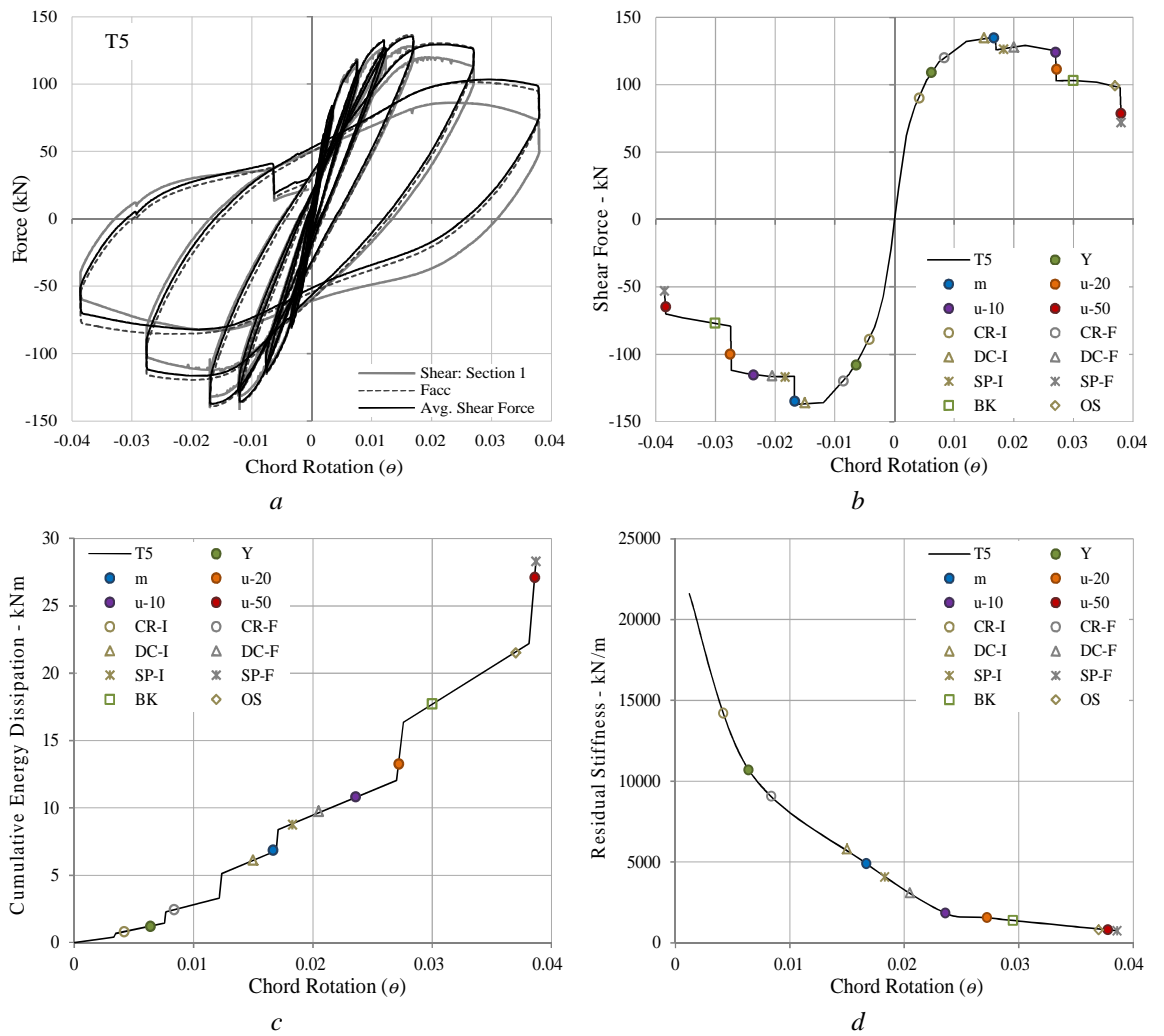


Figure D-27. Global EDP response of column T5, indicating different failure modes and damage levels: a) Force-Chord Rotation hysteresis; b) Shear Force-Chord Rotation envelope; c) Cumulative energy dissipation – Chord rotation; d) Residual Stiffness - Chord Rotation.

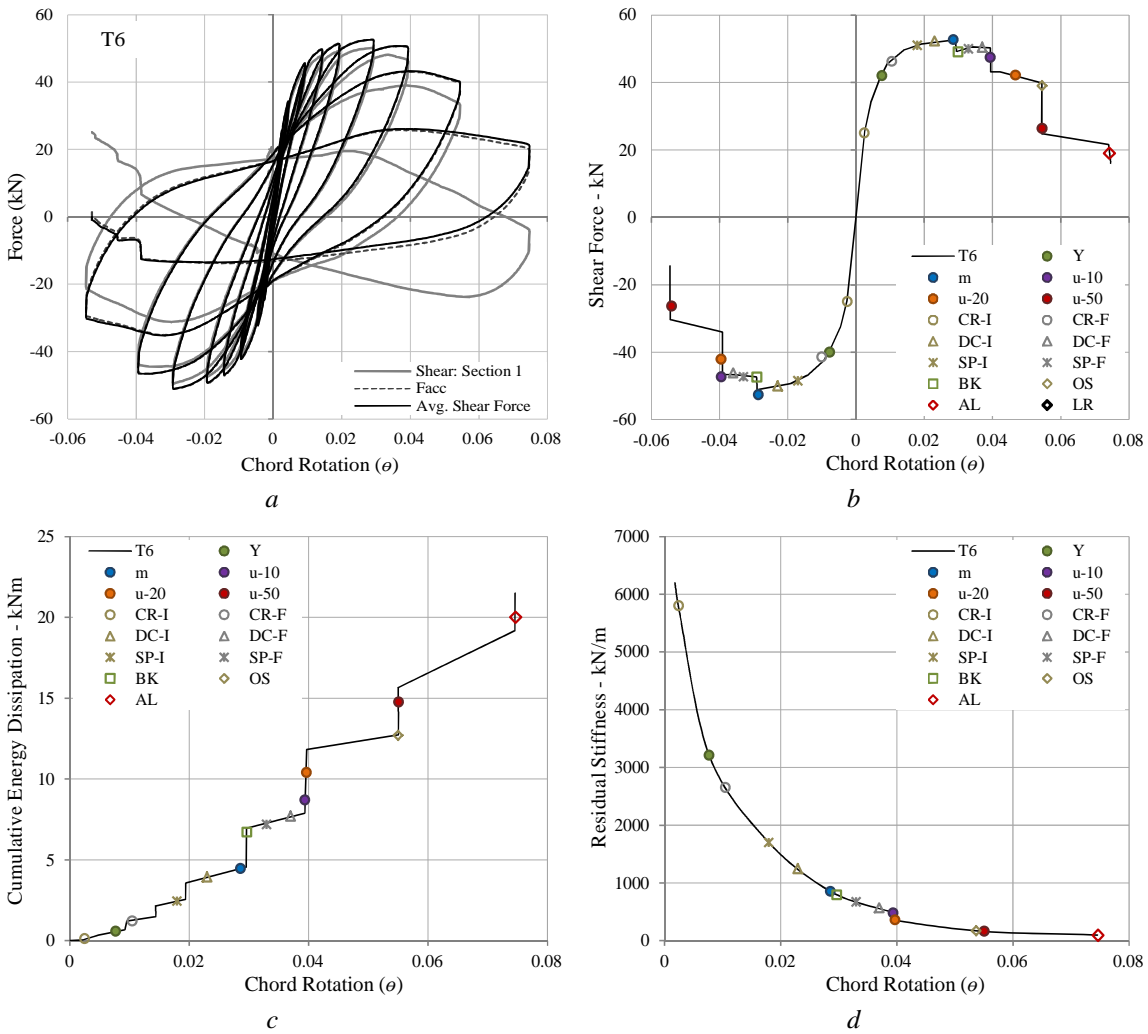


Figure D-28. Global EDP response of column T6, indicating different failure modes and damage levels: a) Force-Chord Rotation hysteresis; b) Shear Force-Chord Rotation envelope; c) Cumulative energy dissipation – Chord rotation; d) Residual Stiffness - Chord Rotation.

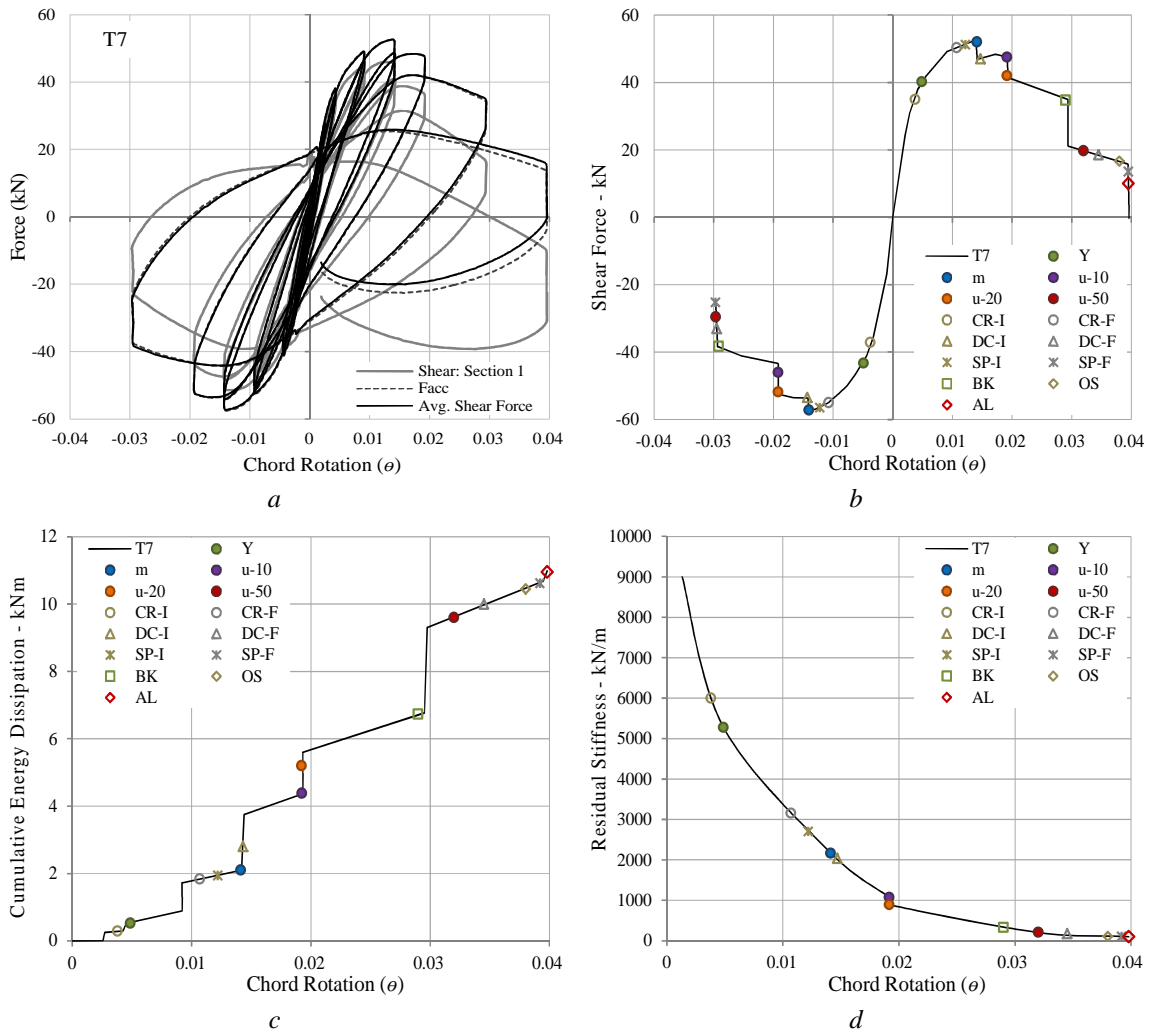
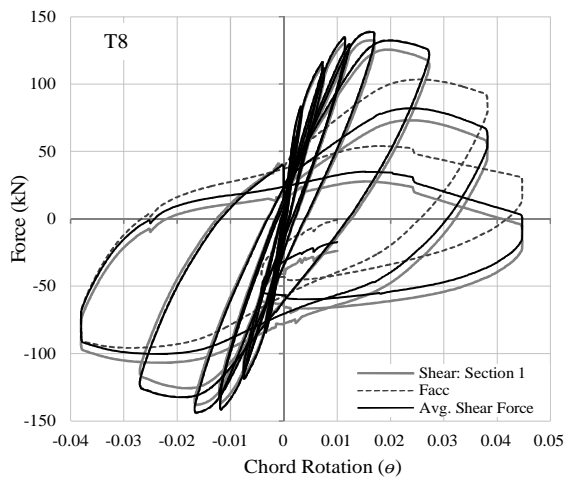
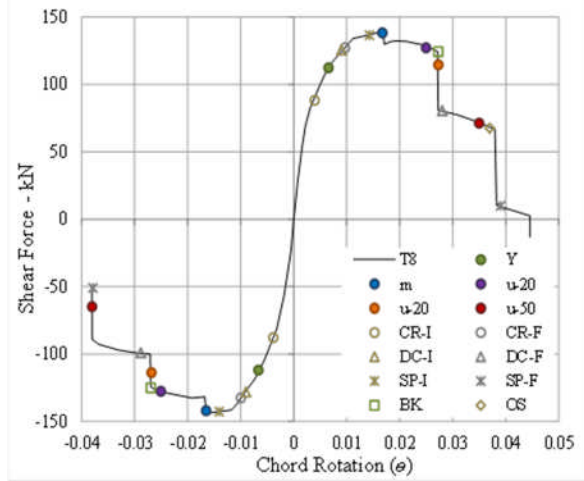


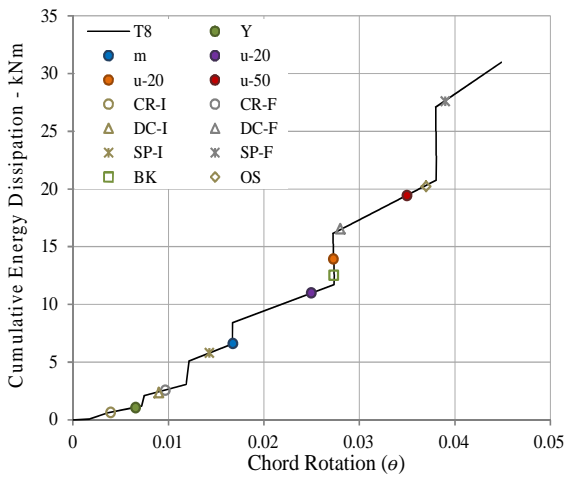
Figure D-29. Global EDP response of column T7, indicating different failure modes and damage levels: a) Force-Chord Rotation hysteresis; b) Shear Force-Chord Rotation envelope; c) Cumulative energy dissipation – Chord rotation; d) Residual Stiffness - Chord Rotation.



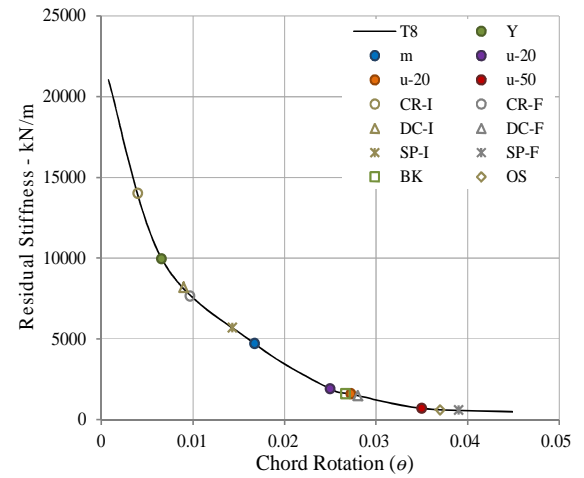
a



b



c



d

Figure D-30. Global EDP response of column T8, indicating different failure modes and damage levels: a) Force-Chord Rotation hysteresis; b) Shear Force-Chord Rotation envelope; c) Cumulative energy dissipation – Chord rotation; d) Residual Stiffness - Chord Rotation.

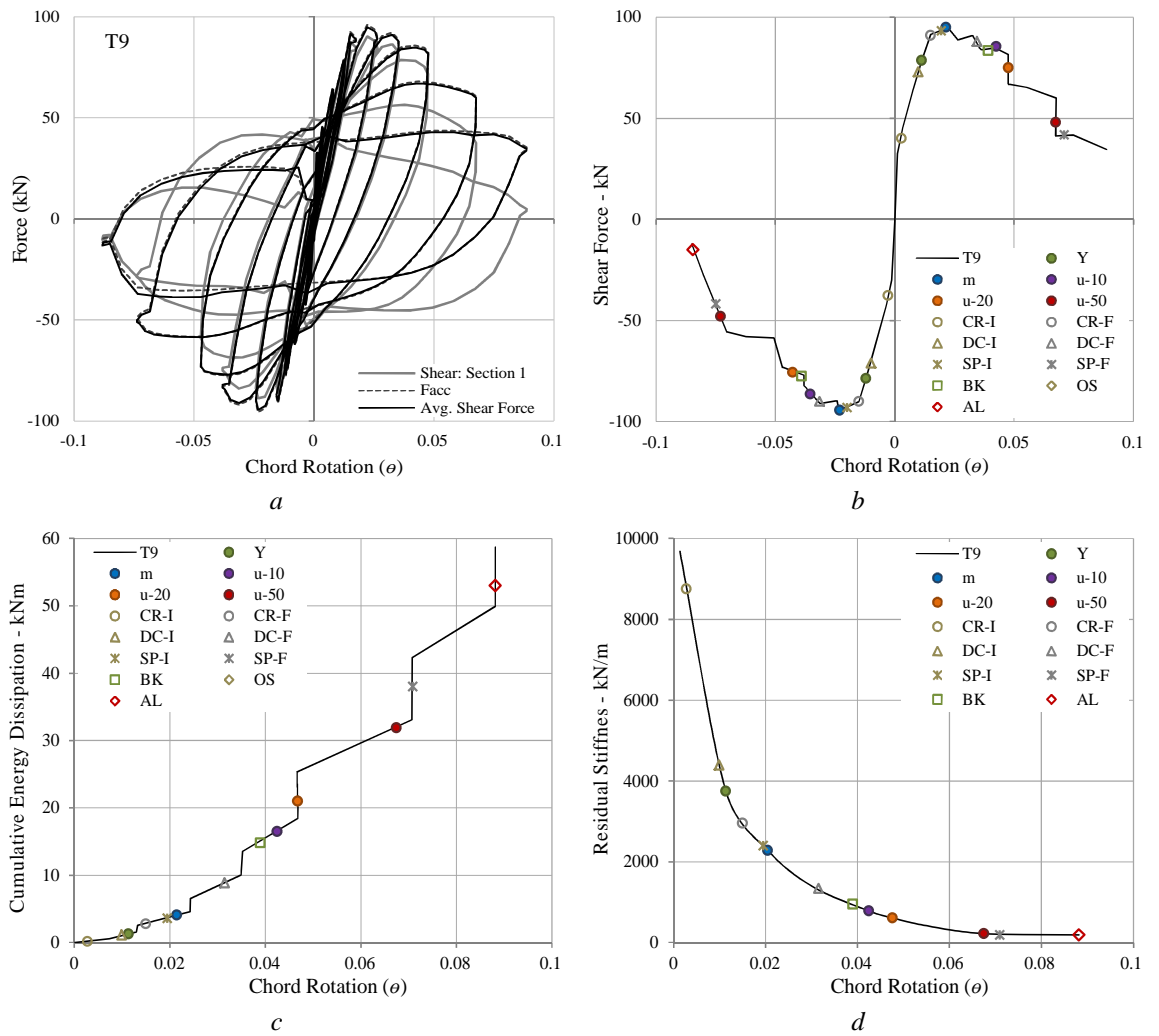


Figure D-31. Global EDP response of column T9, indicating different failure modes and damage levels: a) Force-Chord Rotation hysteresis; b) Shear Force-Chord Rotation envelope; c) Cumulative energy dissipation – Chord rotation; d) Residual Stiffness - Chord Rotation.

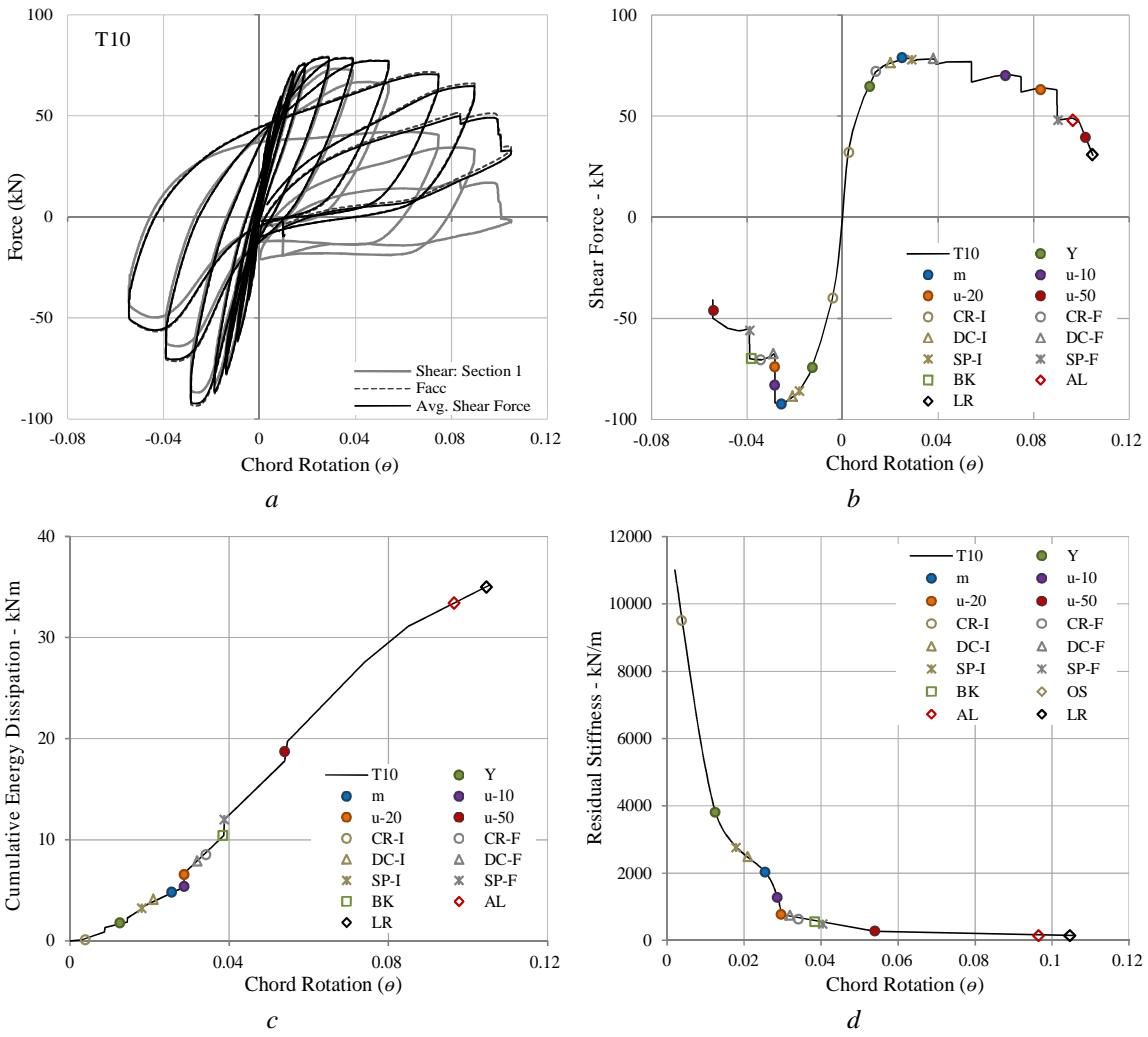


Figure D-32. Global EDP response of column T10, indicating different failure modes and damage levels: a) Force-Chord Rotation hysteresis; b) Shear Force-Chord Rotation envelope; c) Cumulative energy dissipation – Chord rotation; d) Residual Stiffness - Chord Rotation.

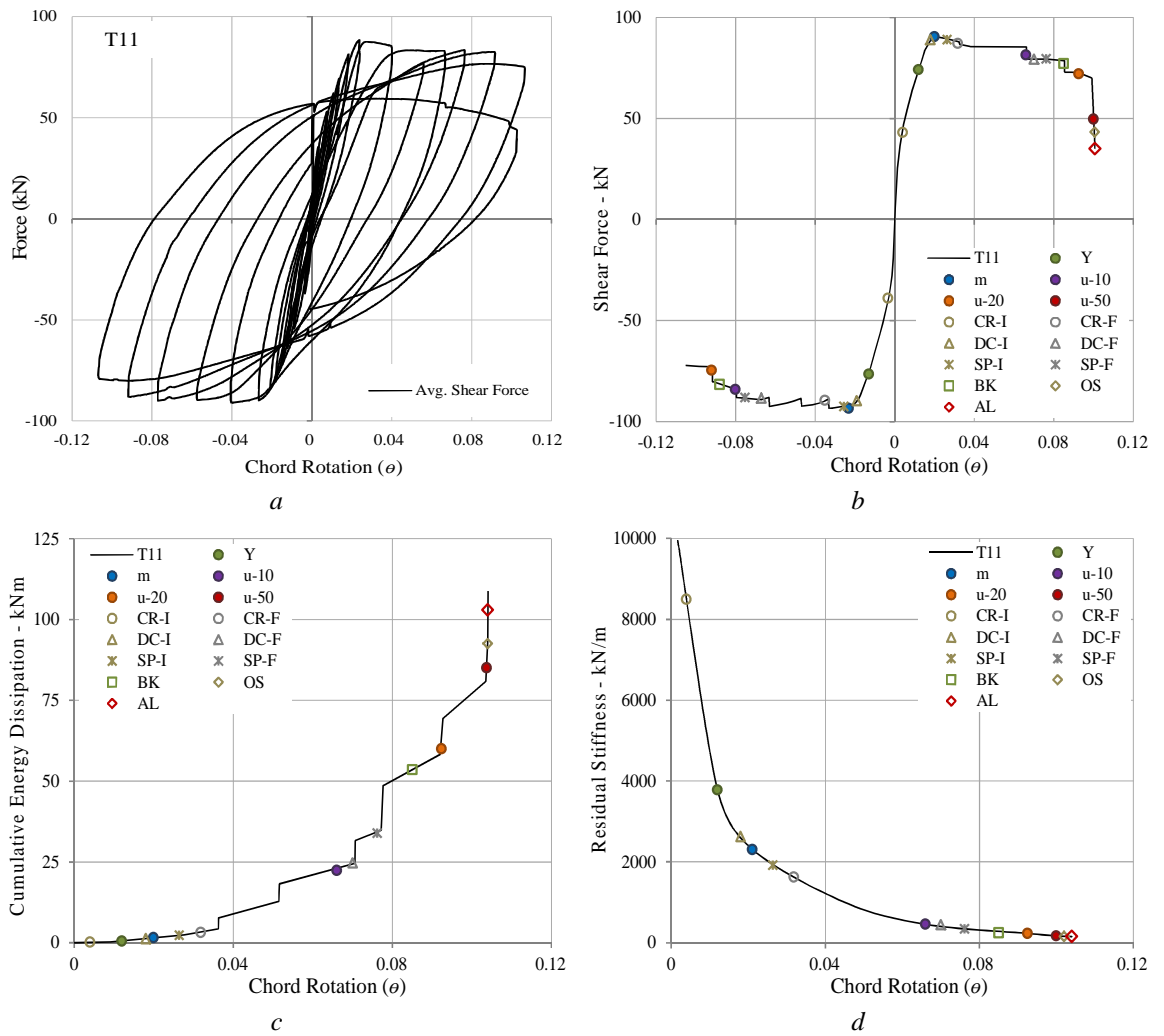


Figure D-33. Global EDP response of column T11, indicating different failure modes and damage levels: a) Force-Chord Rotation hysteresis; b) Shear Force-Chord Rotation envelope; c) Cumulative energy dissipation – Chord rotation; d) Residual Stiffness - Chord Rotation.

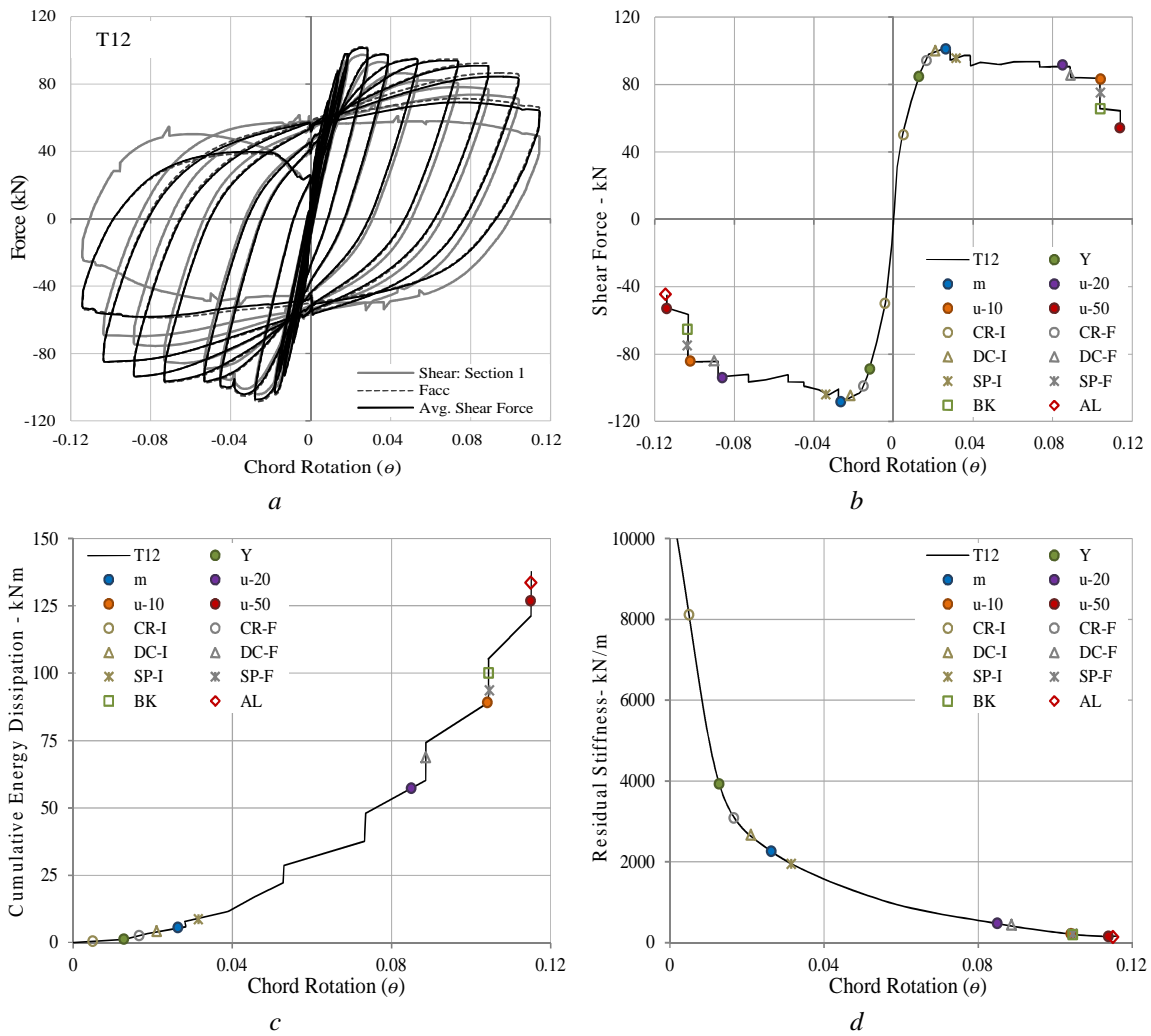


Figure D-34. Global EDP response of column T12, indicating different failure modes and damage levels: a) Force-Chord Rotation hysteresis; b) Shear Force-Chord Rotation envelope; c) Cumulative energy dissipation – Chord rotation; d) Residual Stiffness - Chord Rotation.

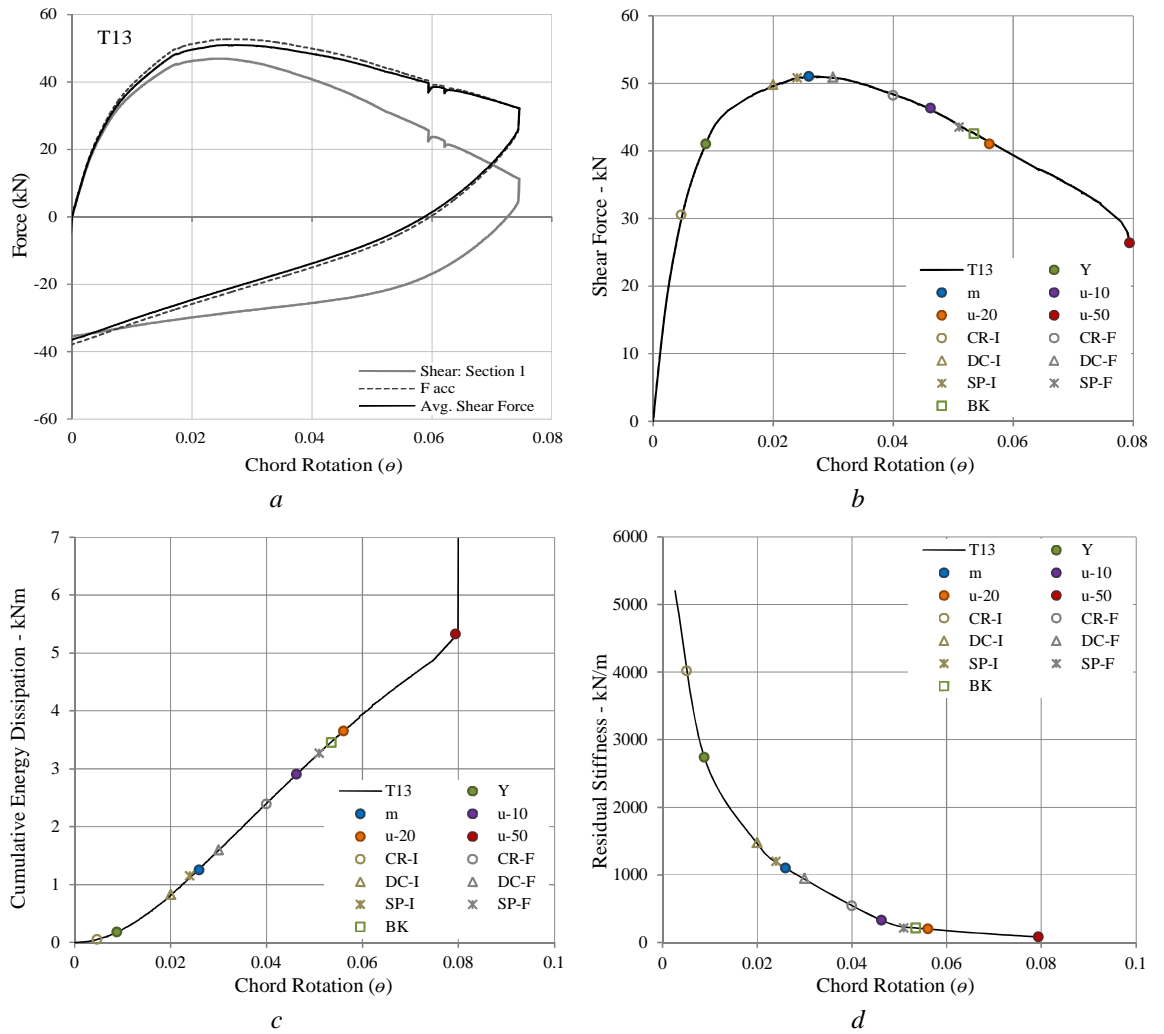


Figure D-35. Global EDP response of column T13, indicating different failure modes and damage levels: a) Force-Chord Rotation hysteresis; b) Shear Force-Chord Rotation envelope; c) Cumulative energy dissipation – Chord rotation; d) Residual Stiffness - Chord Rotation.

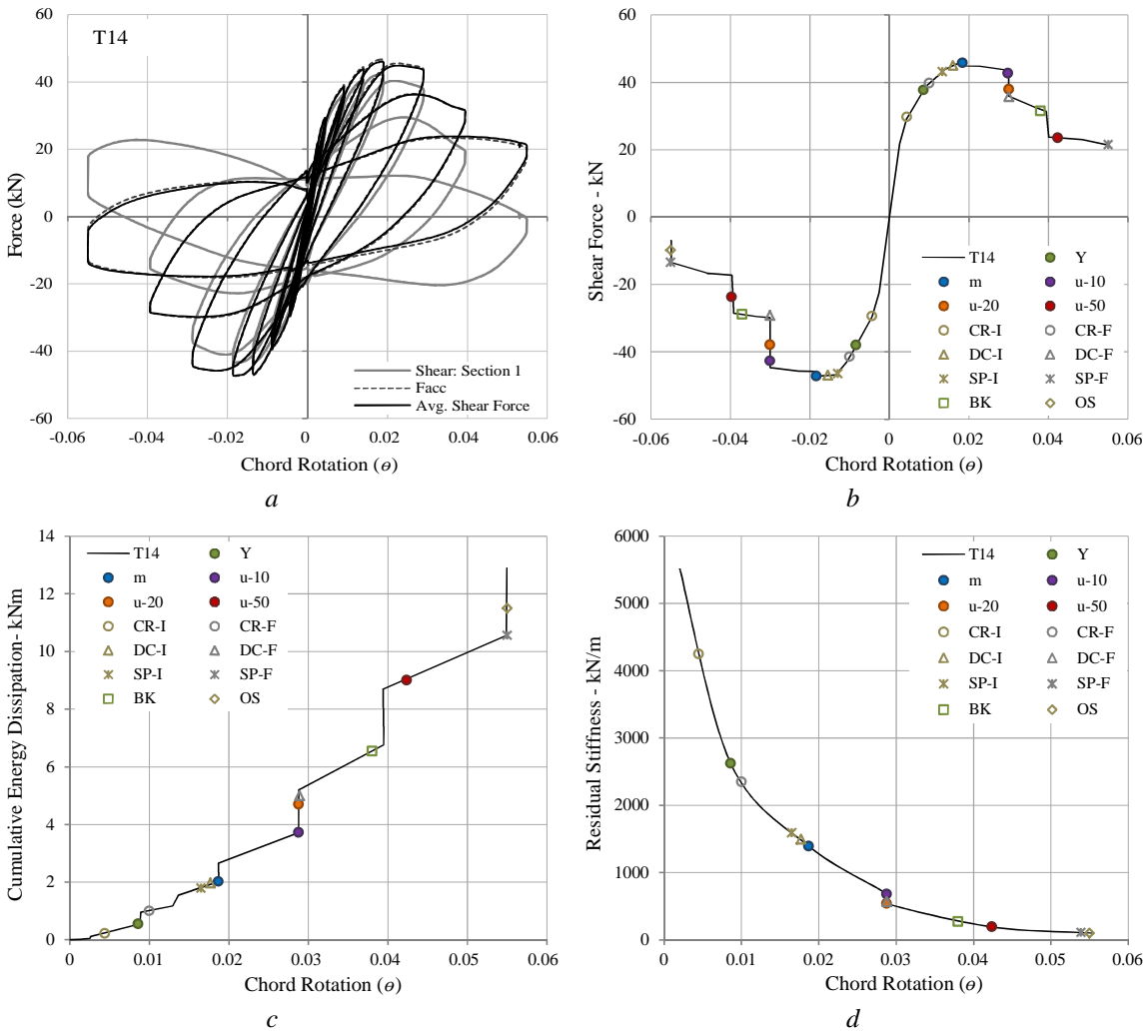


Figure D-36. Global EDP response of column T14, indicating different failure modes and damage levels: a) Force-Chord Rotation hysteresis; b) Shear Force-Chord Rotation envelope; c) Cumulative energy dissipation – Chord rotation; d) Residual Stiffness - Chord Rotation.

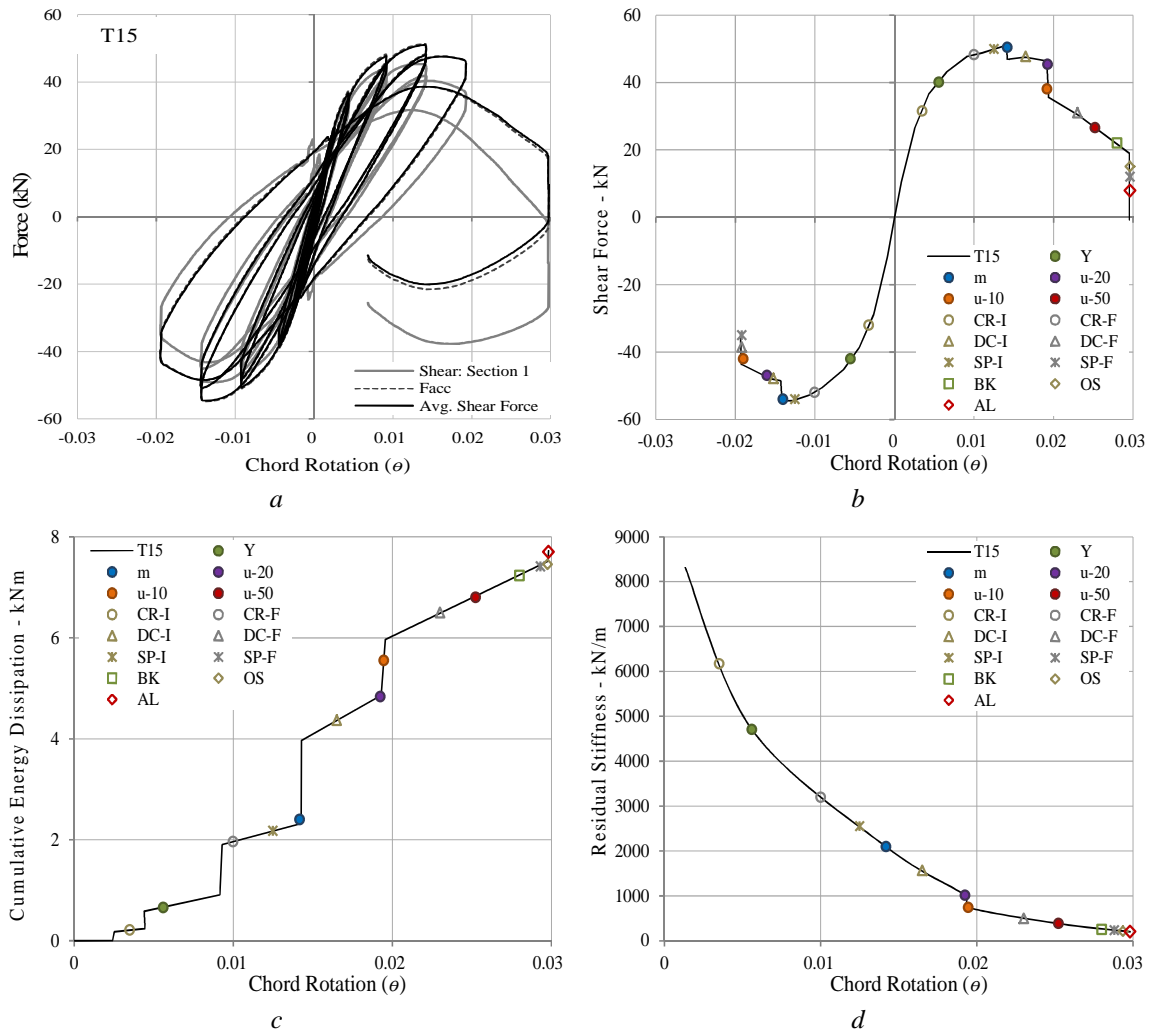
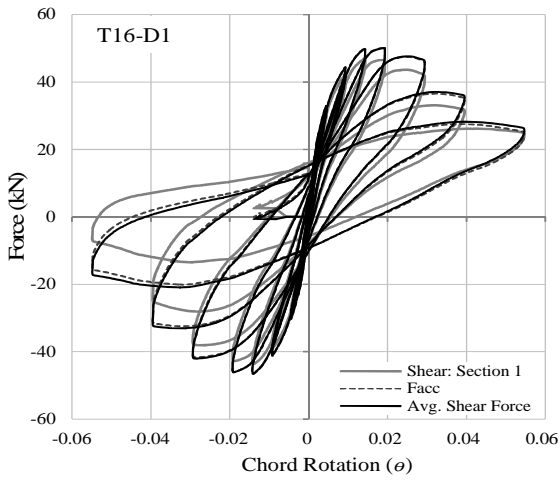
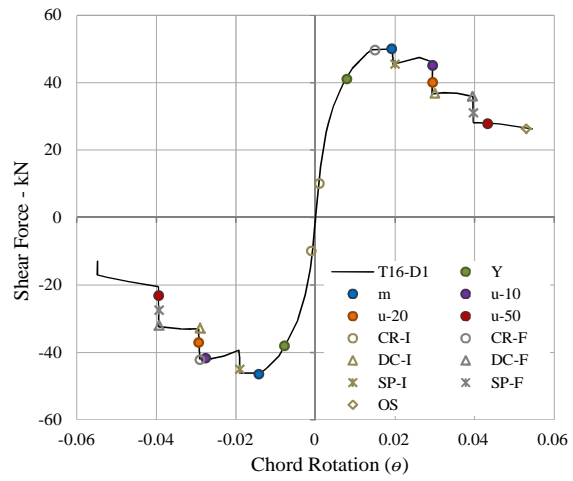


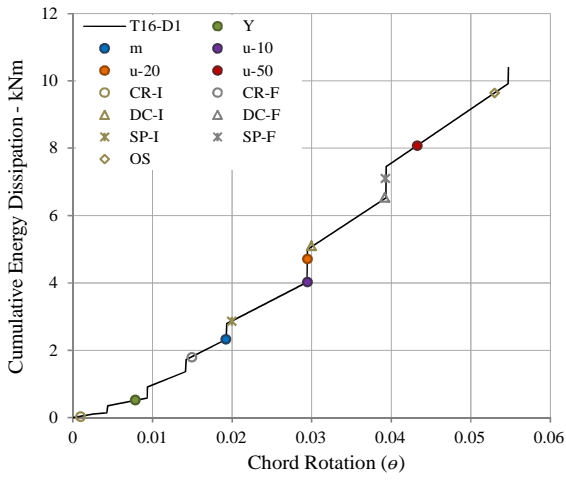
Figure D-37. Global EDP response of column T15, indicating different failure modes and damage levels: a) Force-Chord Rotation hysteresis; b) Shear Force-Chord Rotation envelope; c) Cumulative energy dissipation – Chord rotation; d) Residual Stiffness - Chord Rotation.



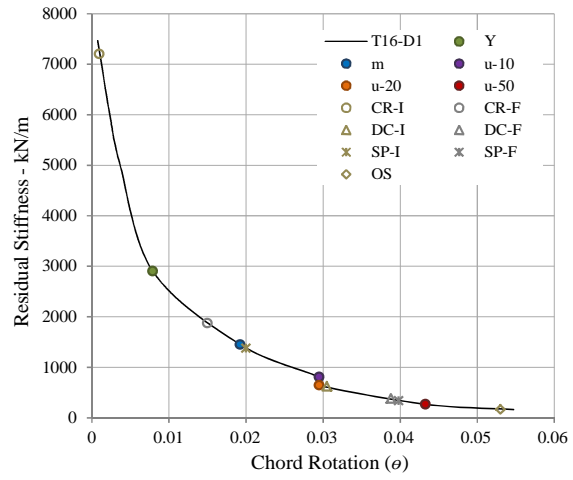
a



b



c



d

Figure D-38. Global EDP response of column T16-D1, indicating different failure modes and damage levels: a) Force-Chord Rotation hysteresis; b) Shear Force-Chord Rotation envelope; c) Cumulative energy dissipation – Chord rotation; d) Residual Stiffness - Chord Rotation.

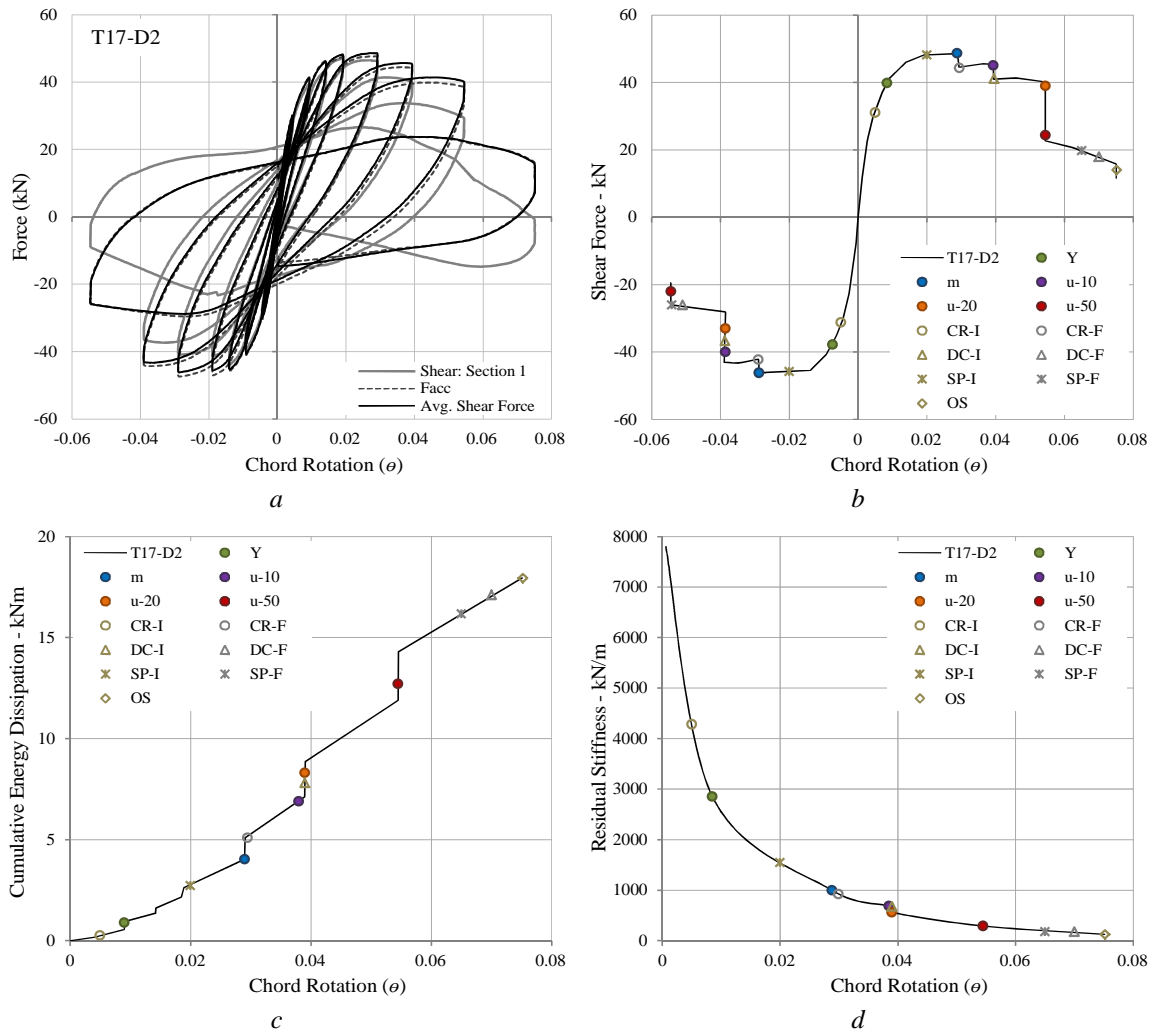


Figure D-39. Global EDP response of column T17-D2, indicating different failure modes and damage levels: a) Force-Chord Rotation hysteresis; b) Shear Force-Chord Rotation envelope; c) Cumulative energy dissipation – Chord rotation; d) Residual Stiffness - Chord Rotation.

D.3 Distribution of EDP Response of the Column Specimens

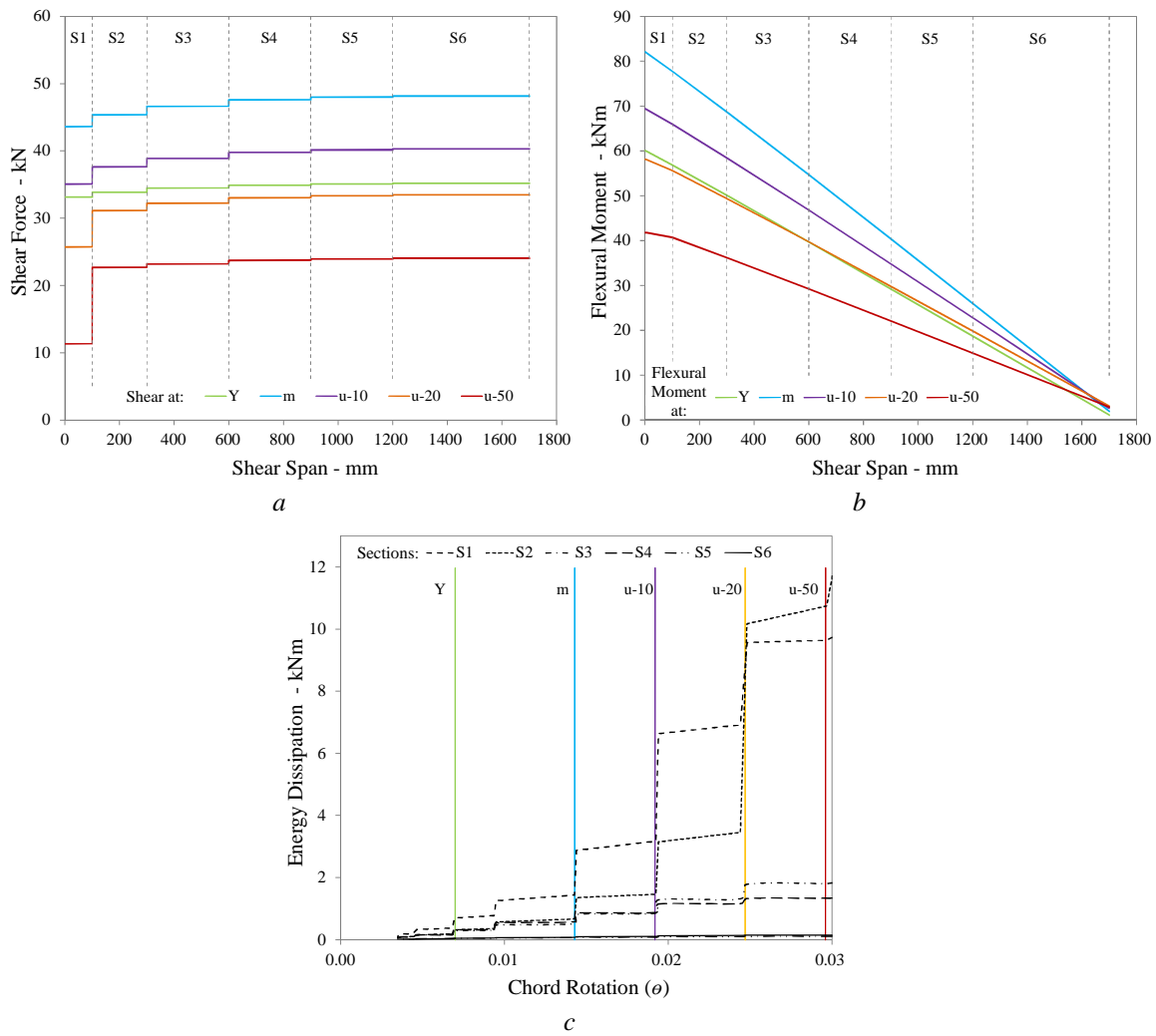


Figure D-40. EDP response at different sections along the shear span of column T1a for different damage levels: a) Shear Force-Shear Span; b) Flexural Moment – Shear Span; c) Energy Dissipation – Chord Rotation.

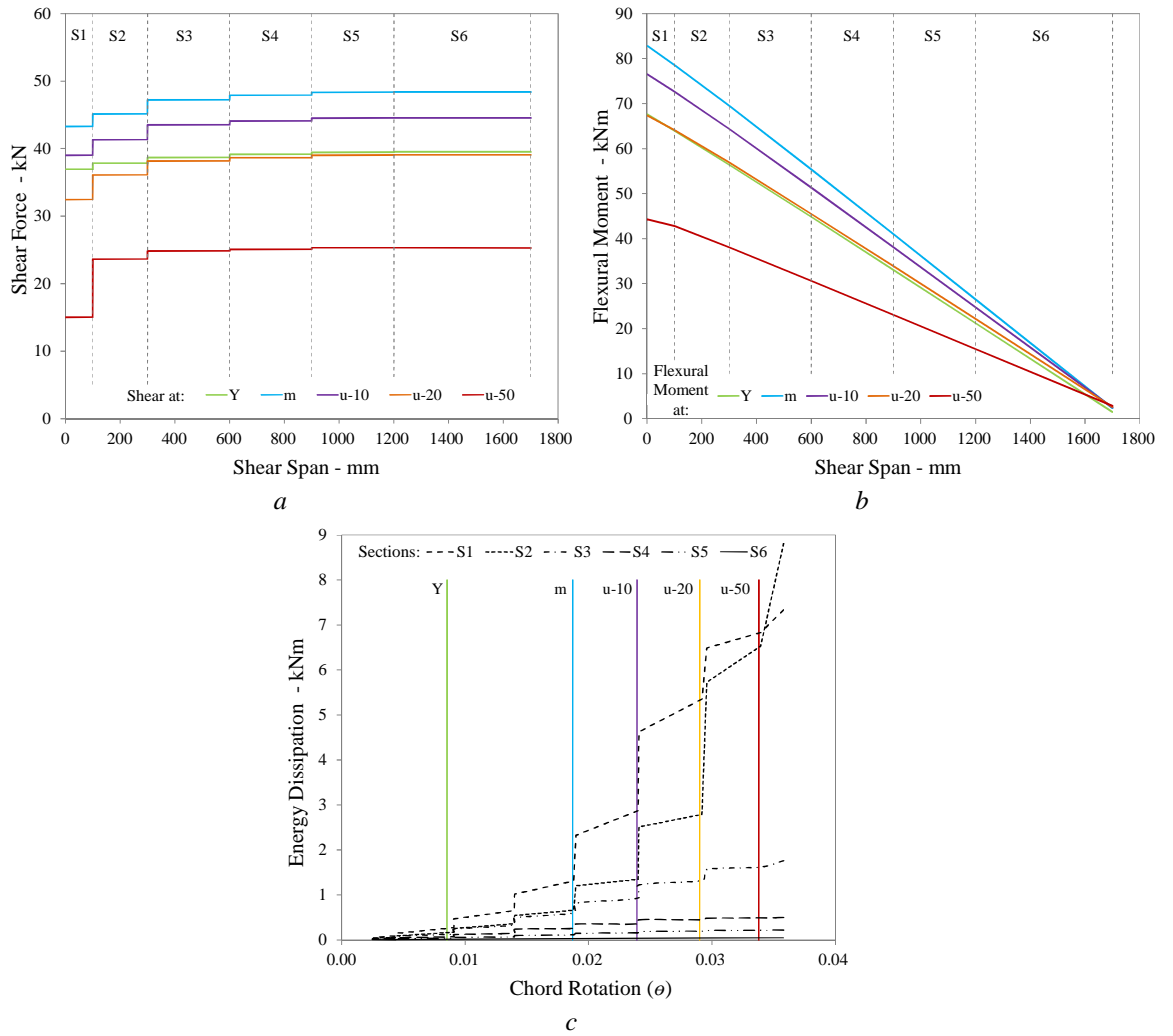


Figure D-41. EDP response at different sections along the shear span of column T1b for different damage levels: a) Shear Force-Shear Span; b) Flexural Moment – Shear Span; c) Energy Dissipation – Chord Rotation.

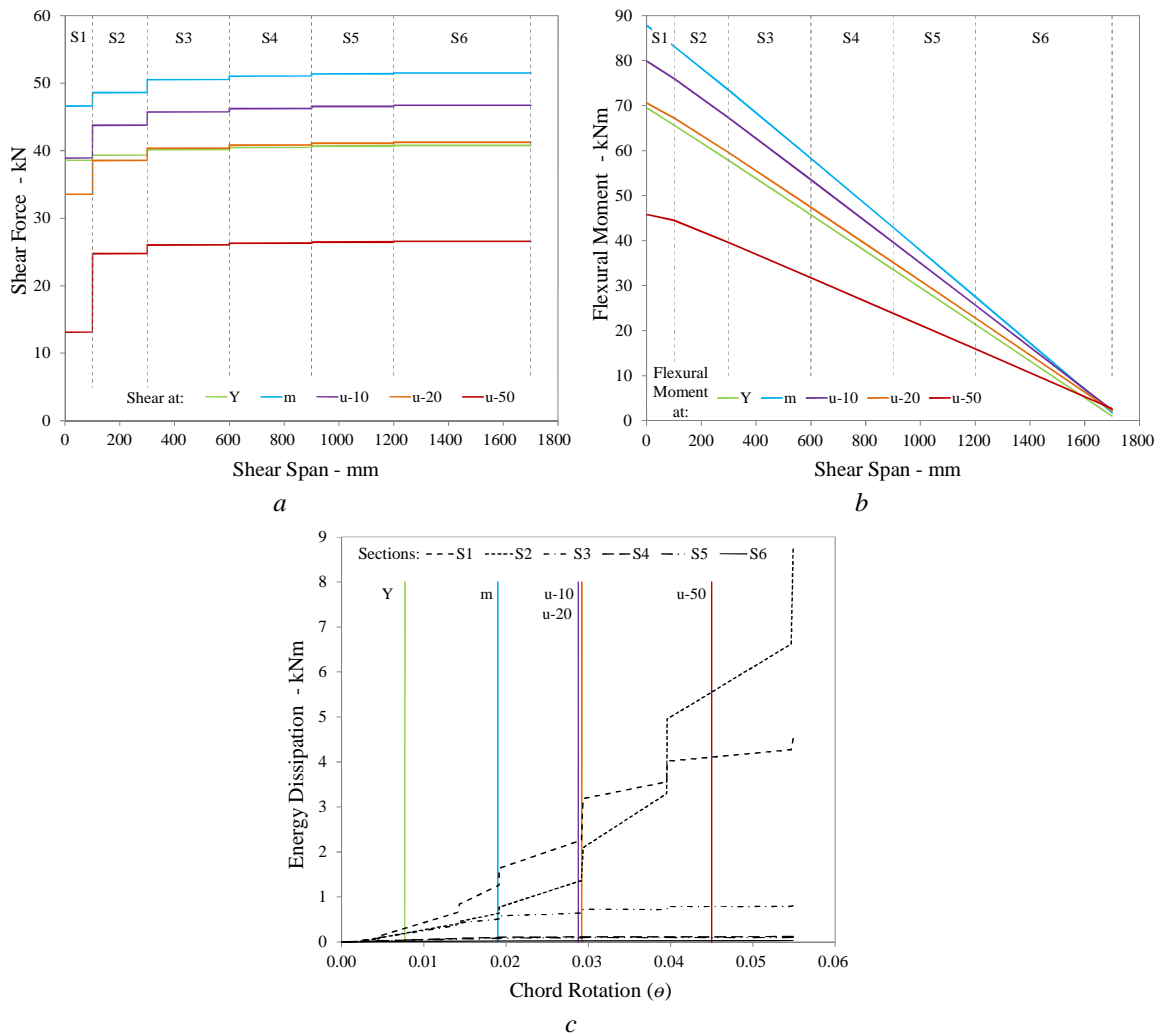


Figure D-42. EDP response at different sections along the shear span of column T1c for different damage levels: a) Shear Force-Shear Span; b) Flexural Moment – Shear Span; c) Energy Dissipation – Chord Rotation.

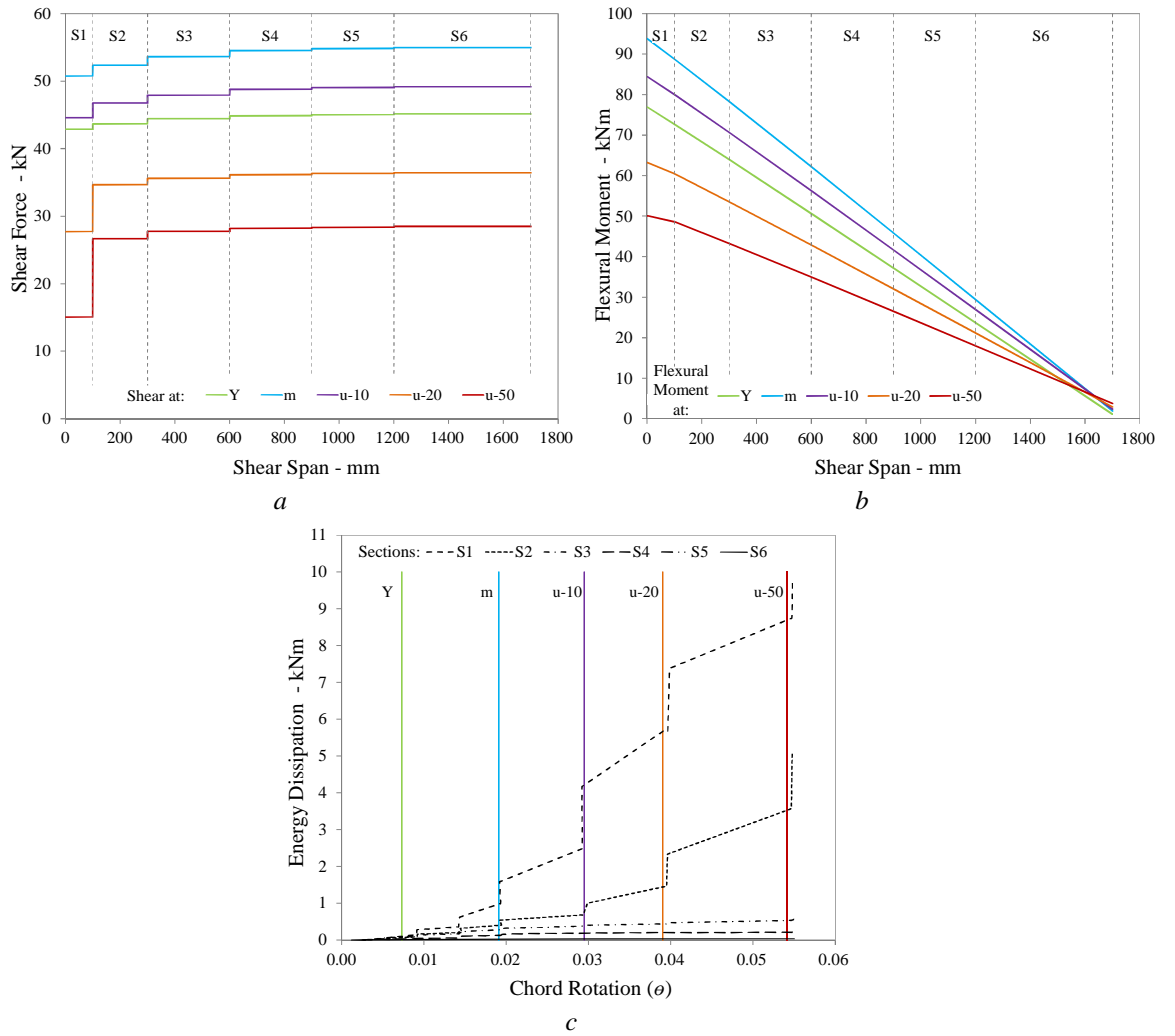


Figure D-43. EDP response at different sections along the shear span of column T2 for different damage levels: a) Shear Force-Shear Span; b) Flexural Moment – Shear Span; c) Energy Dissipation – Chord Rotation.

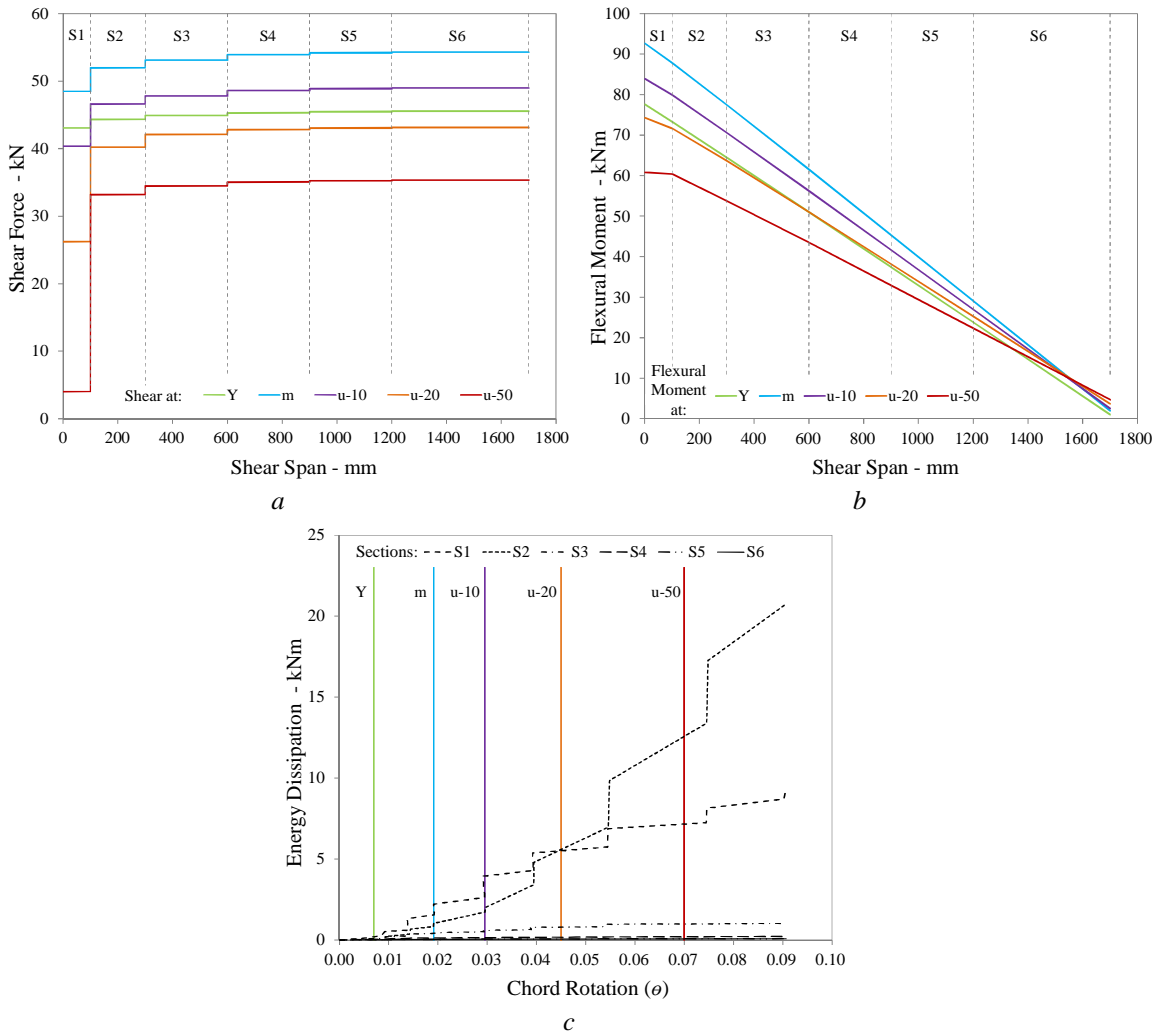


Figure D-44. EDP response at different sections along the shear span of column T3 for different damage levels: a) Shear Force-Shear Span; b) Flexural Moment – Shear Span; c) Energy Dissipation – Chord Rotation.

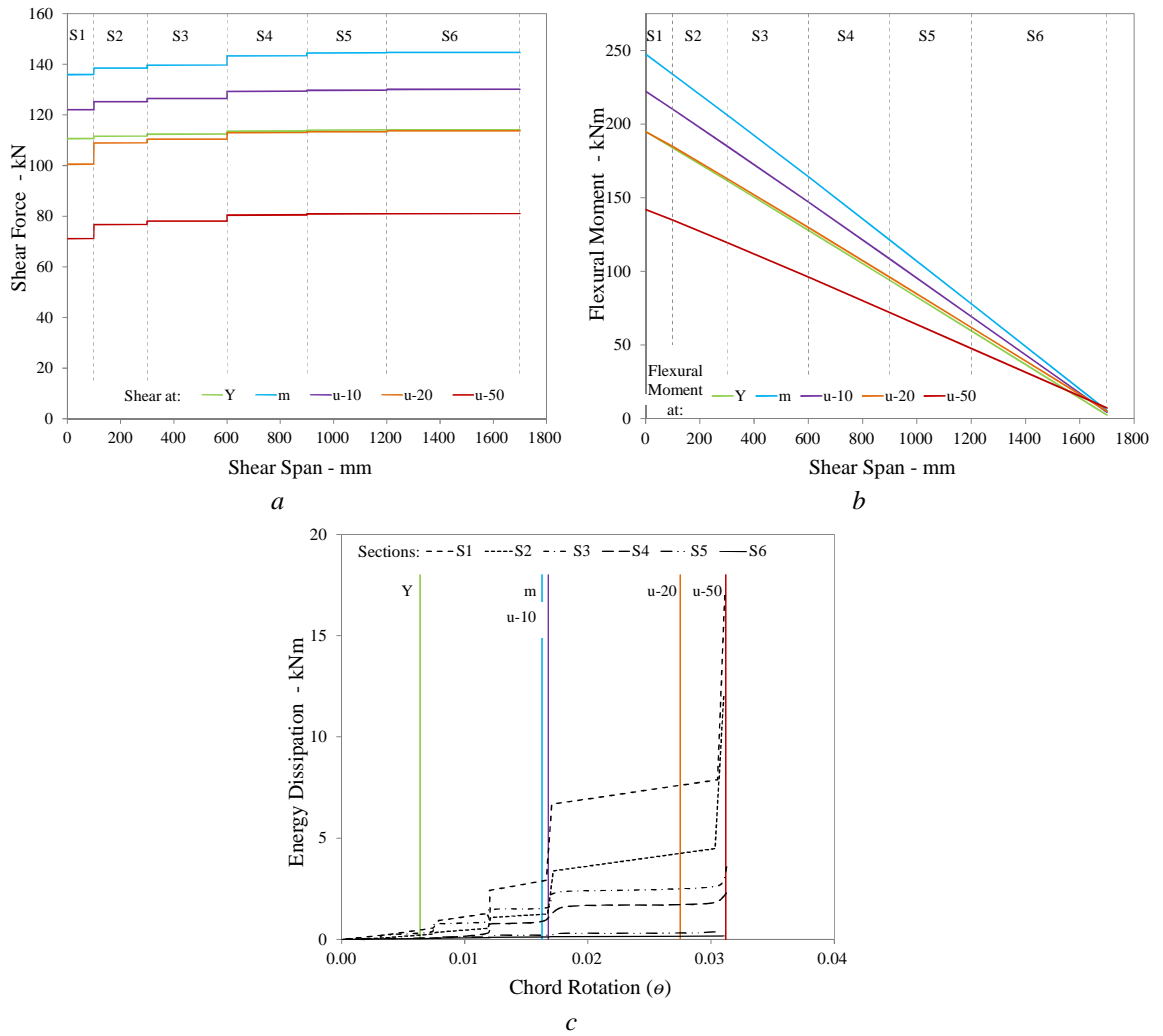


Figure D-45. EDP response at different sections along the shear span of column T4 for different damage levels: a) Shear Force-Shear Span; b) Flexural Moment – Shear Span; c) Energy Dissipation – Chord Rotation.

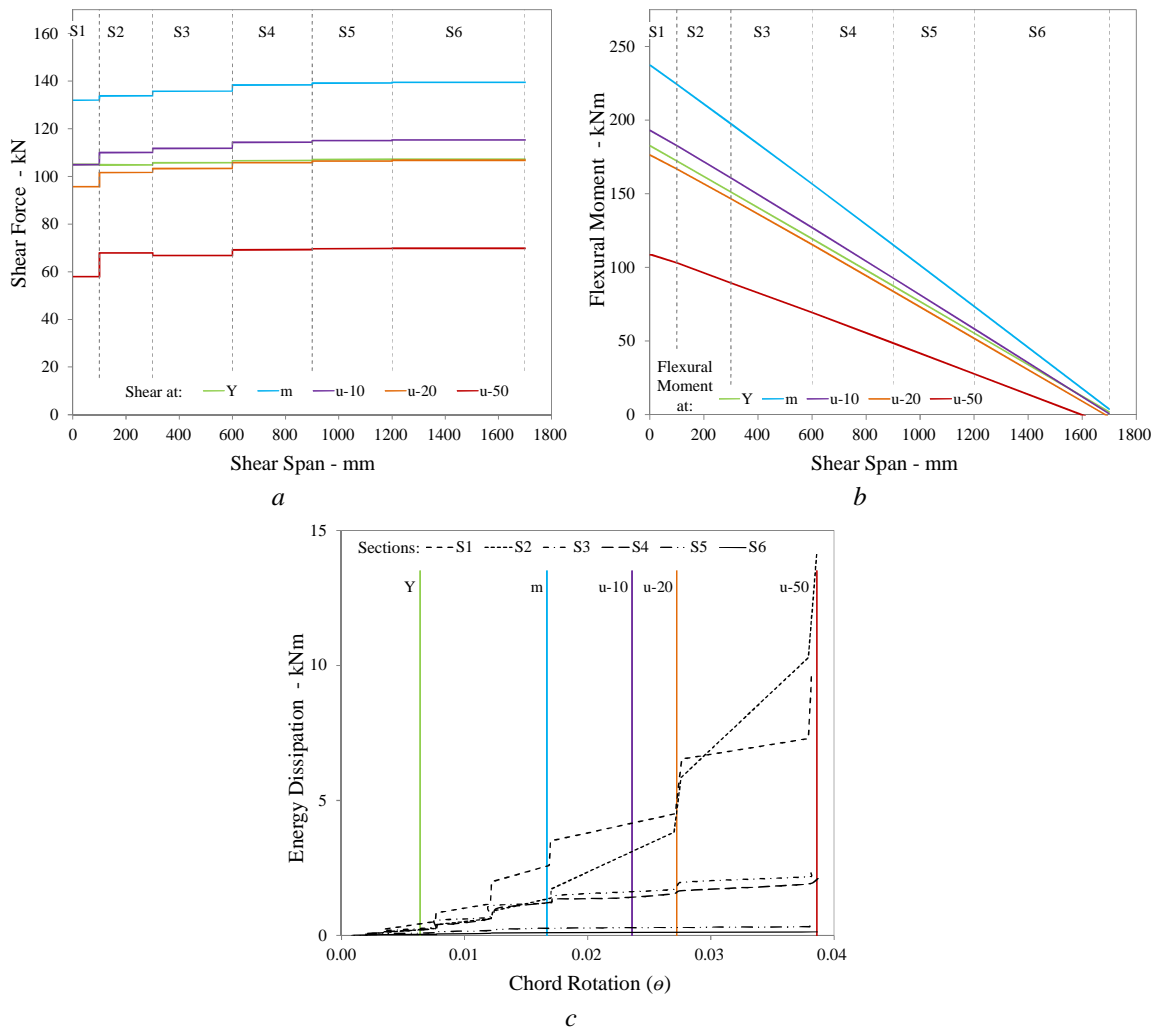


Figure D-46. EDP response at different sections along the shear span of column T5 for different damage levels: a) Shear Force-Shear Span; b) Flexural Moment – Shear Span; c) Energy Dissipation – Chord Rotation.

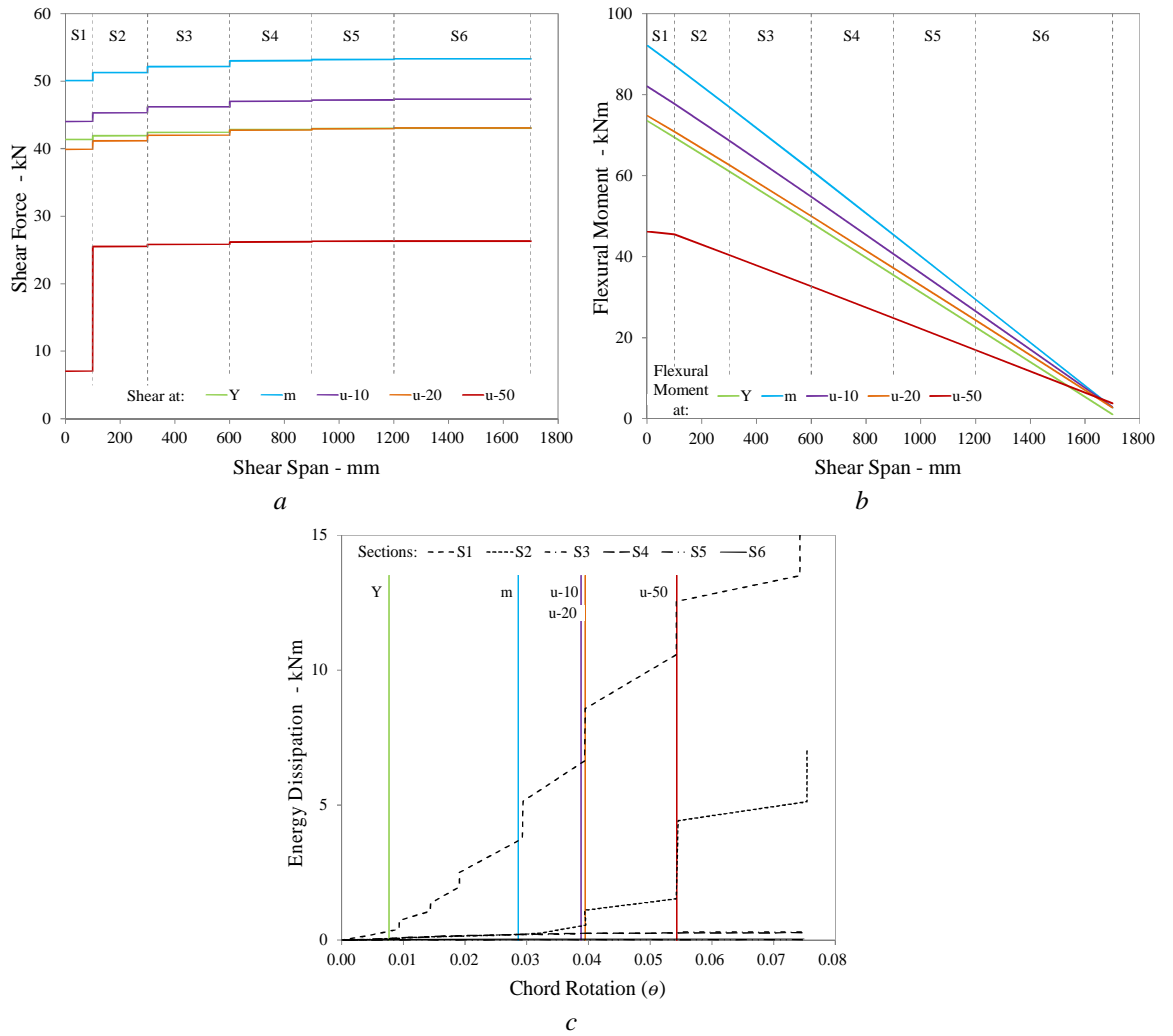


Figure D-47. EDP response at different sections along the shear span of column T6 for different damage levels: a) Shear Force-Shear Span; b) Flexural Moment – Shear Span; c) Energy Dissipation – Chord Rotation.

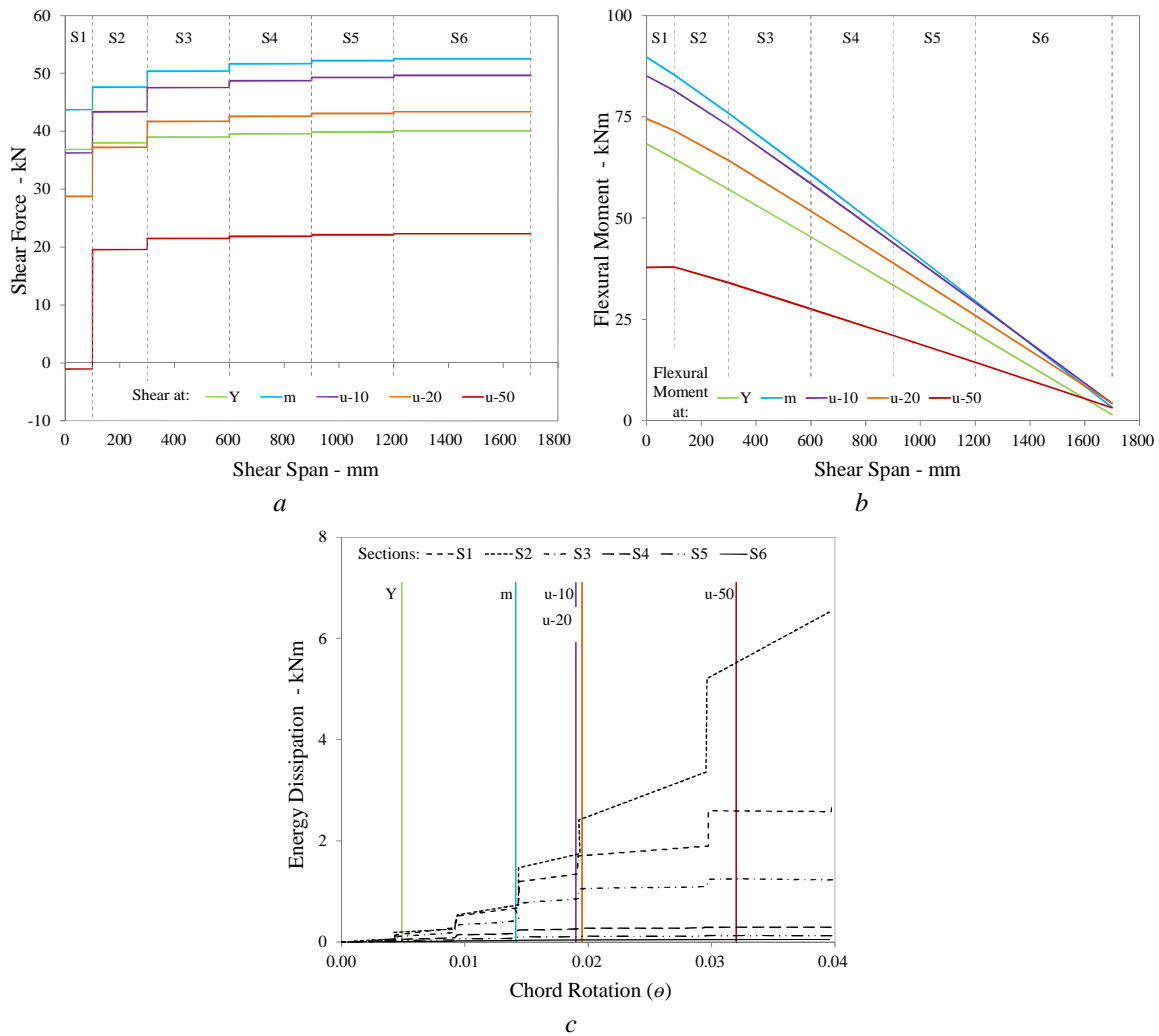


Figure D-48. EDP response at different sections along the shear span of column T7 for different damage levels: a) Shear Force-Shear Span; b) Flexural Moment – Shear Span; c) Energy Dissipation – Chord Rotation.

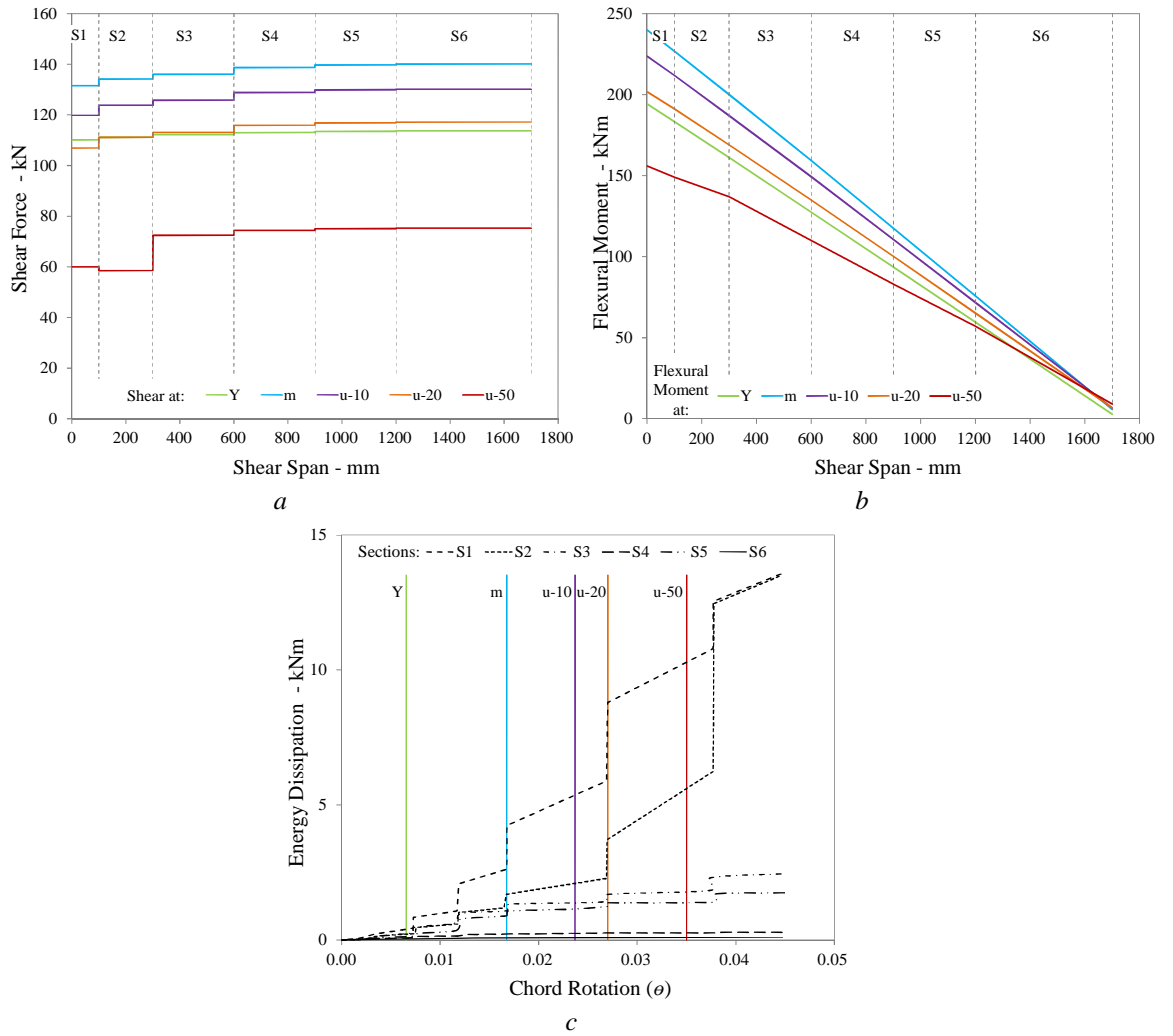


Figure D-49. EDP response at different sections along the shear span of column T8 for different damage levels: a) Shear Force-Shear Span; b) Flexural Moment – Shear Span; c) Energy Dissipation – Chord Rotation.

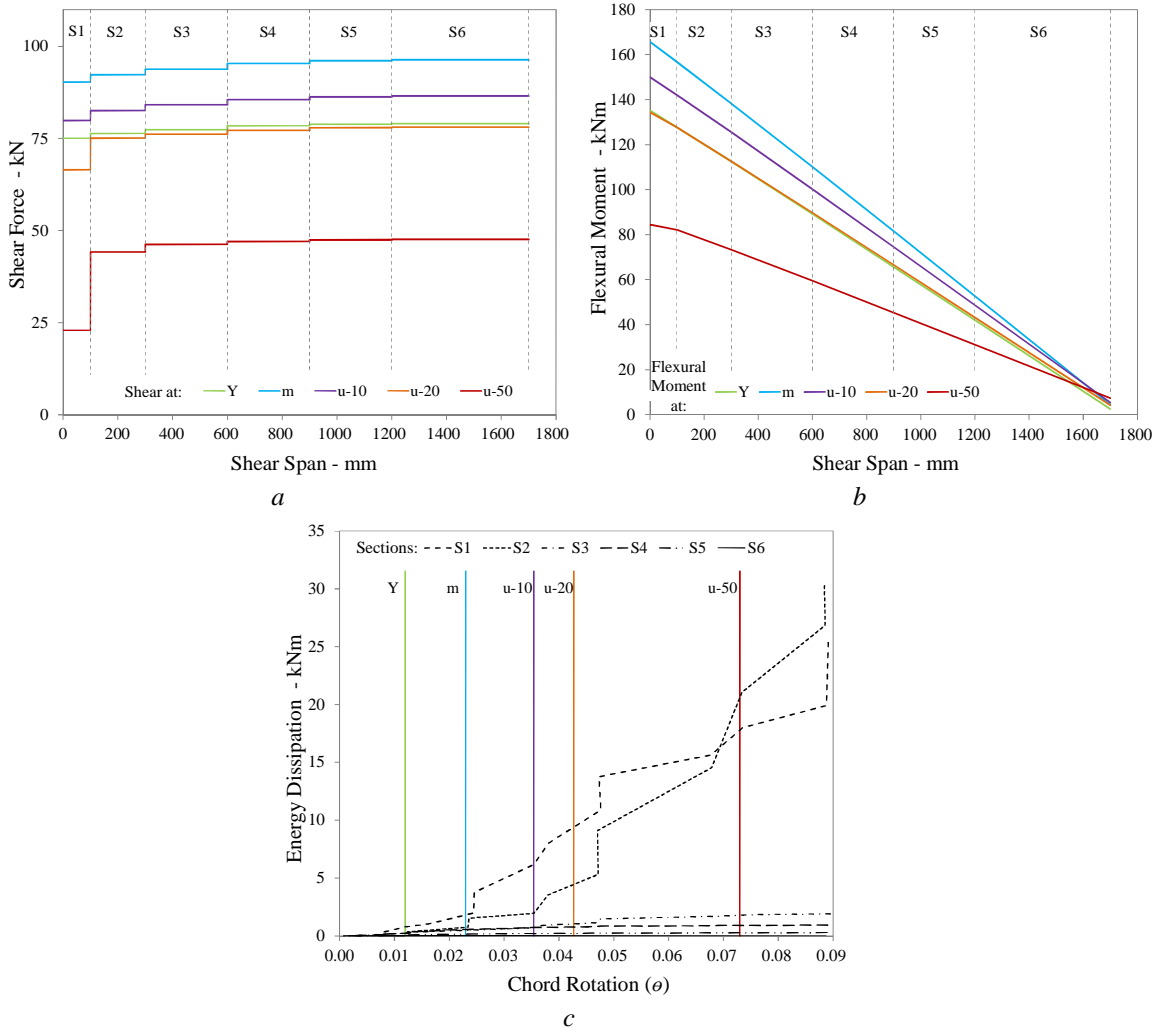


Figure D-50. EDP response at different sections along the shear span of column T9 for different damage levels: a) Shear Force-Shear Span; b) Flexural Moment – Shear Span; c) Energy Dissipation – Chord Rotation.

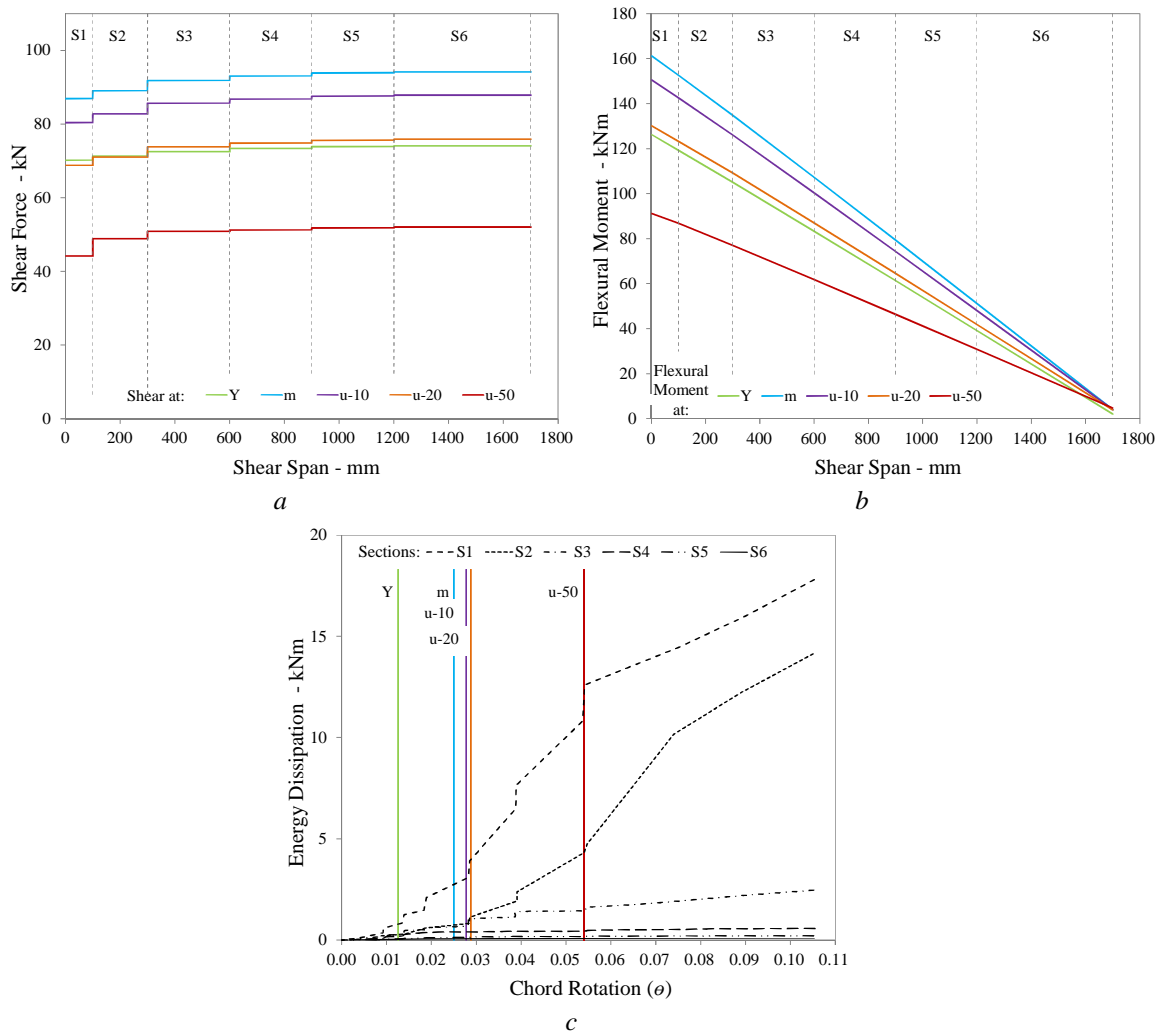


Figure D-51. EDP response at different sections along the shear span of column T10 for different damage levels: a) Shear Force-Shear Span; b) Flexural Moment – Shear Span; c) Energy Dissipation – Chord Rotation.

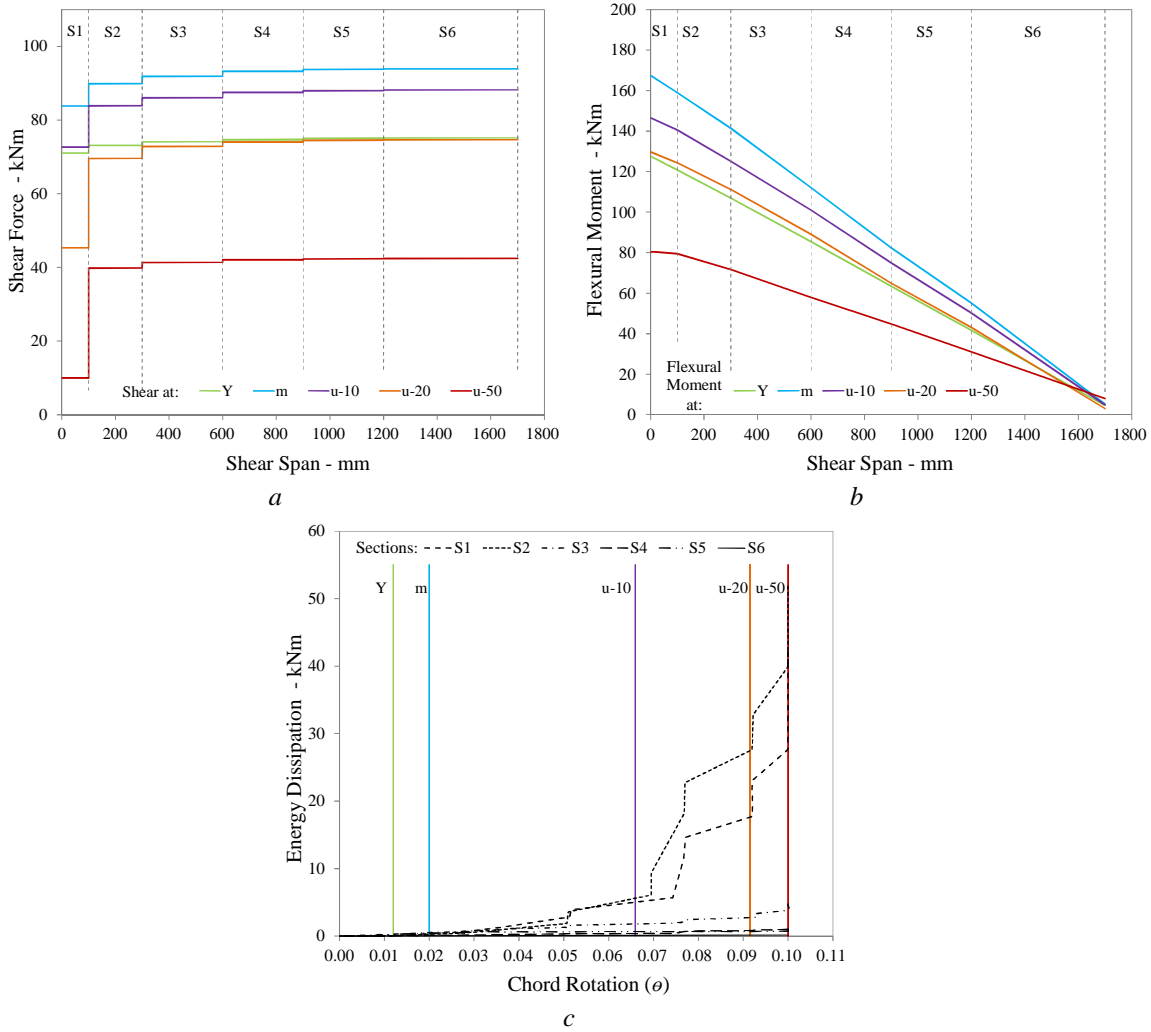


Figure D-52. EDP response at different sections along the shear span of column T11 for different damage levels: a) Shear Force-Shear Span; b) Flexural Moment – Shear Span; c) Energy Dissipation – Chord Rotation.

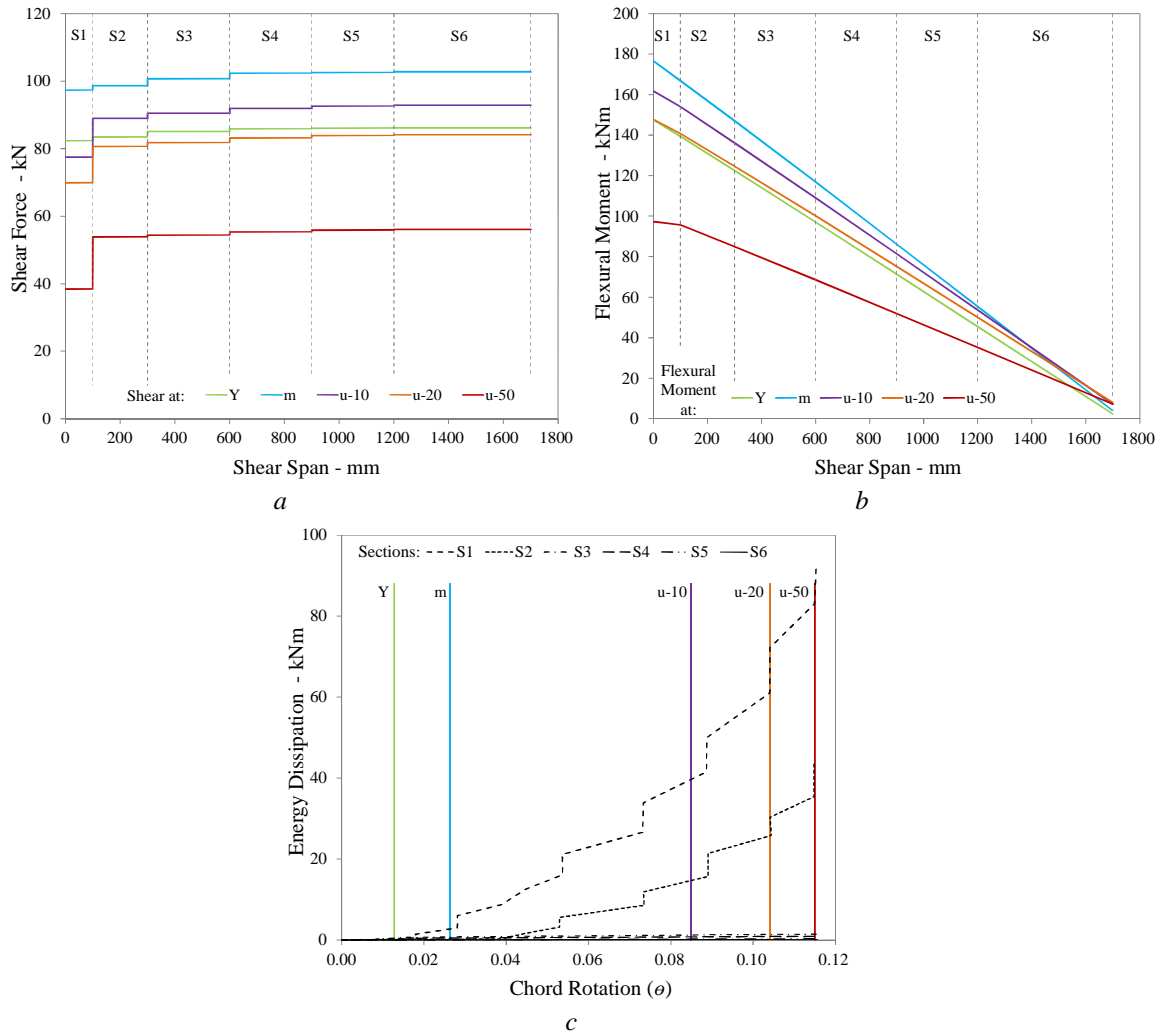


Figure D-53. EDP response at different sections along the shear span of column T12 for different damage levels: a) Shear Force-Shear Span; b) Flexural Moment – Shear Span; c) Energy Dissipation – Chord Rotation.

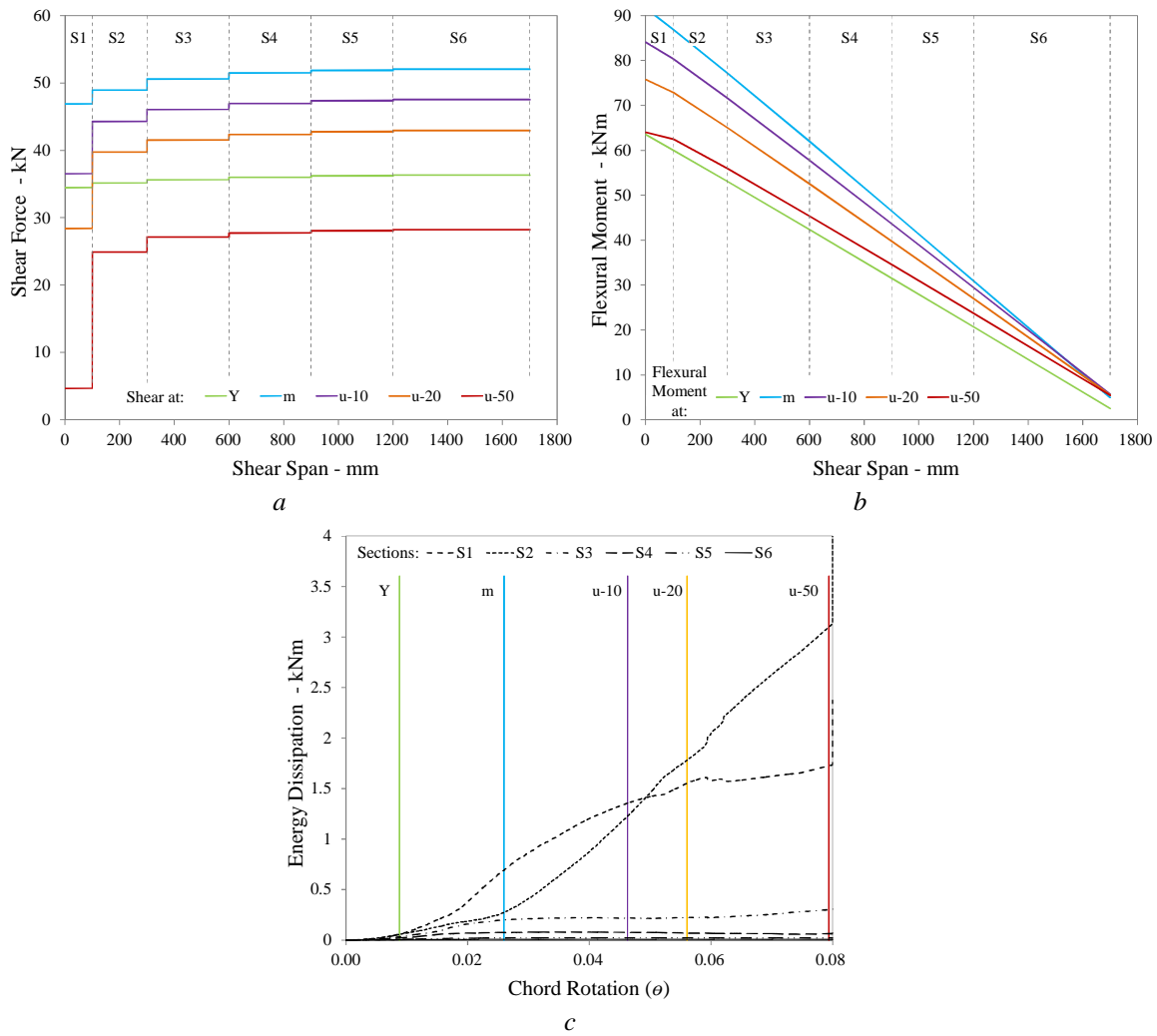


Figure D-54. EDP response at different sections along the shear span of column T13 for different damage levels: a) Shear Force-Shear Span; b) Flexural Moment – Shear Span; c) Energy Dissipation – Chord Rotation.

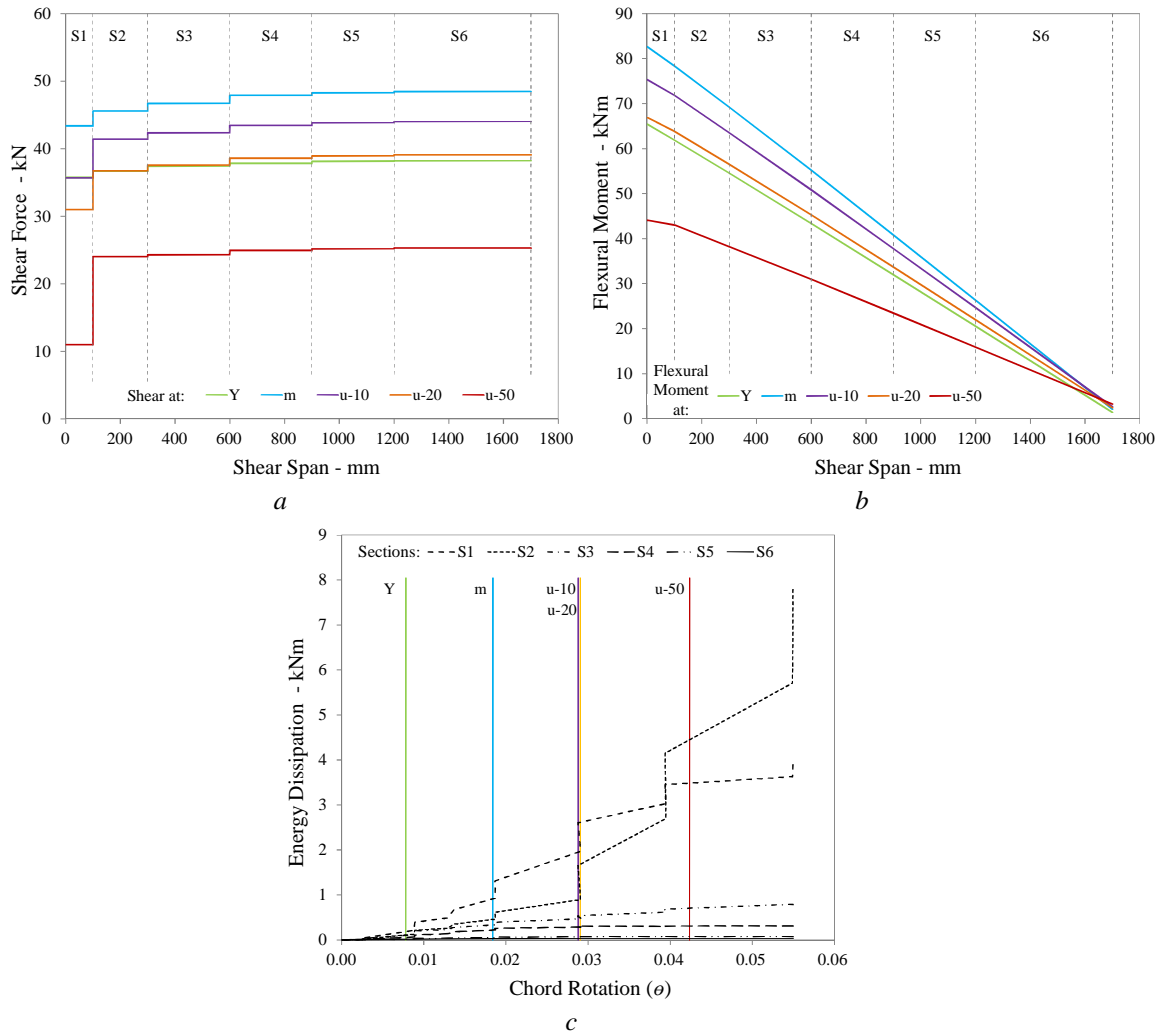


Figure D-55. EDP response at different sections along the shear span of column T14 for different damage levels: a) Shear Force-Shear Span; b) Flexural Moment – Shear Span; c) Energy Dissipation – Chord Rotation.

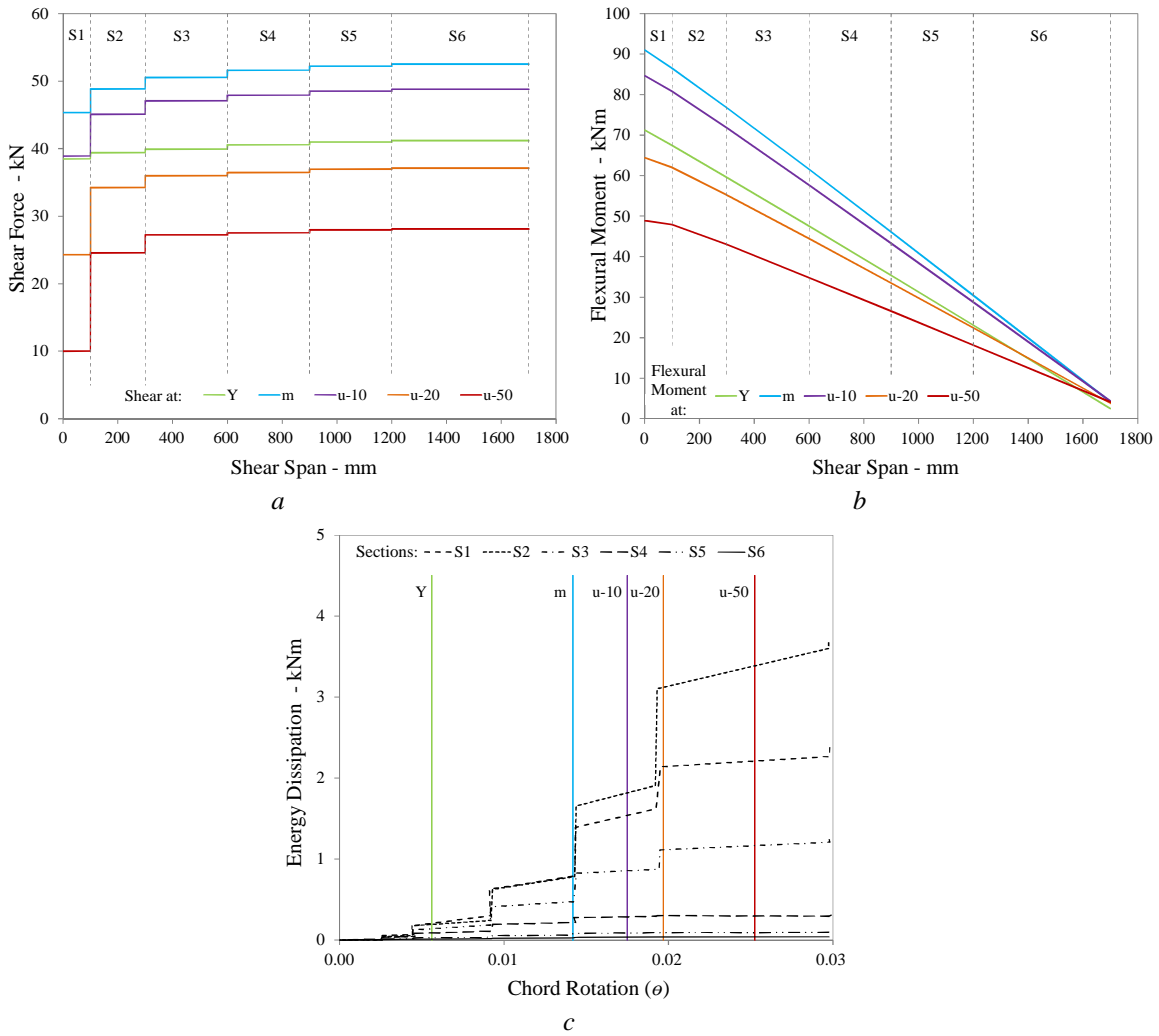


Figure D-56. EDP response at different sections along the shear span of column T15 for different damage levels: a) Shear Force-Shear Span; b) Flexural Moment – Shear Span; c) Energy Dissipation – Chord Rotation.

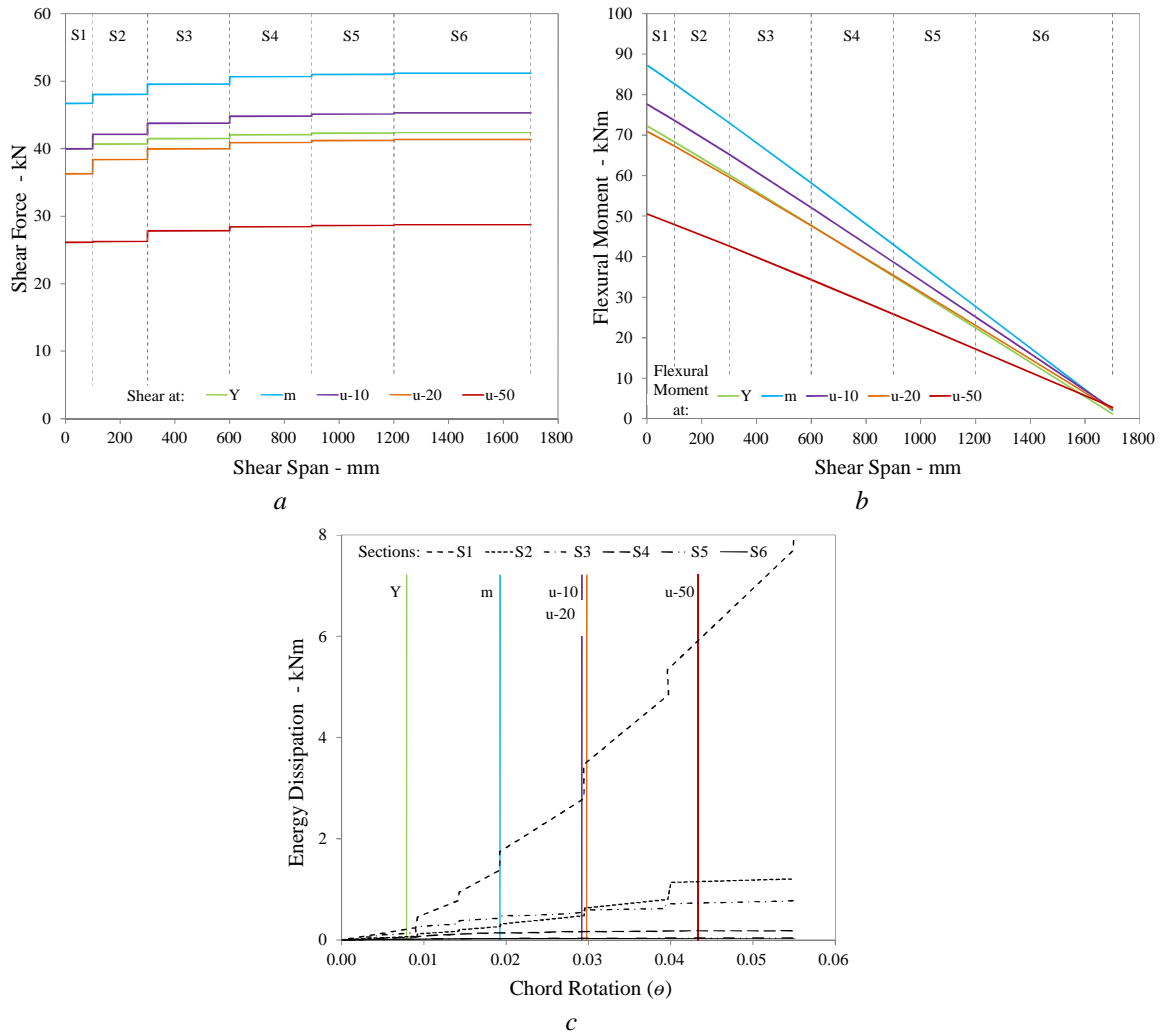


Figure D-57. EDP response at different sections along the shear span of column T16-D1 for different damage levels: a) Shear Force-Shear Span; b) Flexural Moment – Shear Span; c) Energy Dissipation – Chord Rotation.

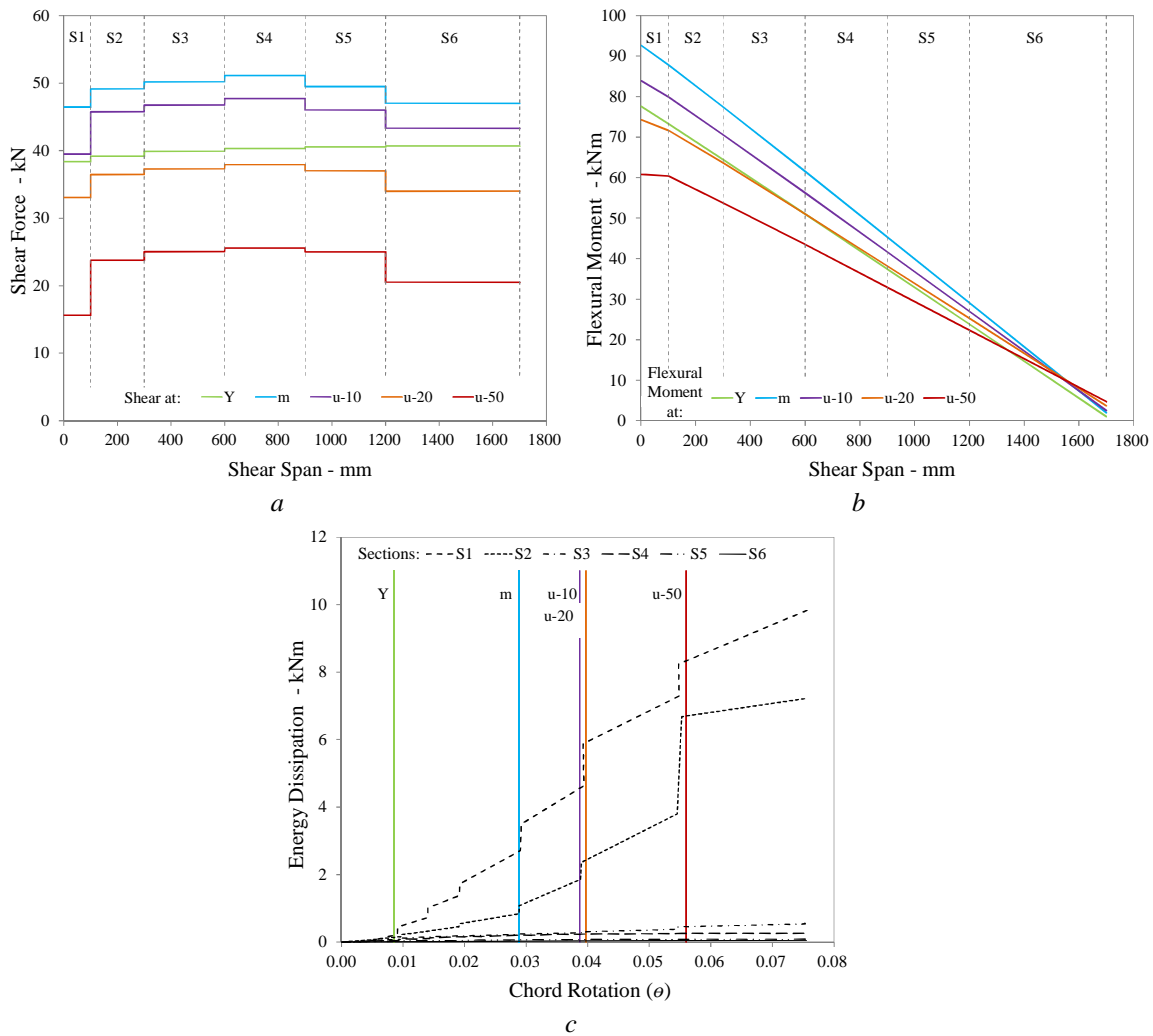
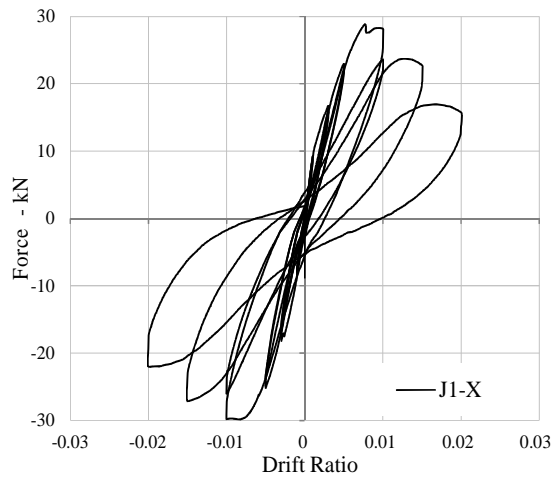
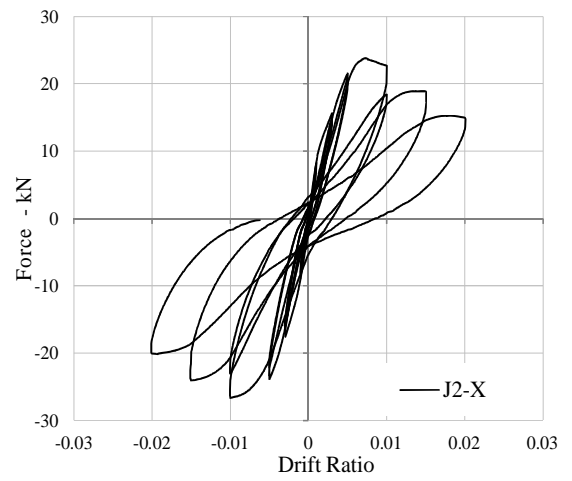


Figure D-58. EDP response at different sections along the shear span of column T17-D2 for different damage levels: a) Shear Force-Shear Span; b) Flexural Moment – Shear Span; c) Energy Dissipation – Chord Rotation.

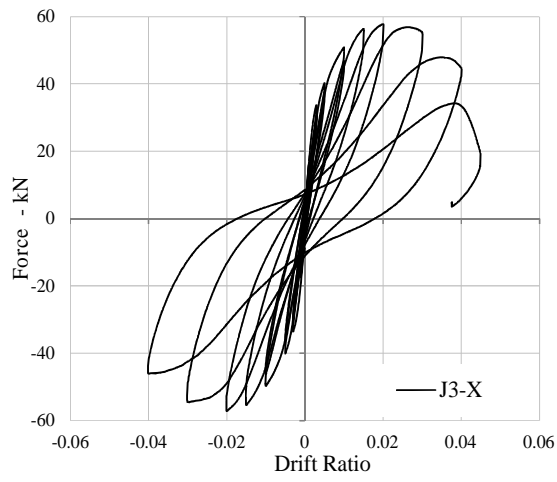
D.4 Distribution of EDP Response of the Column Specimens



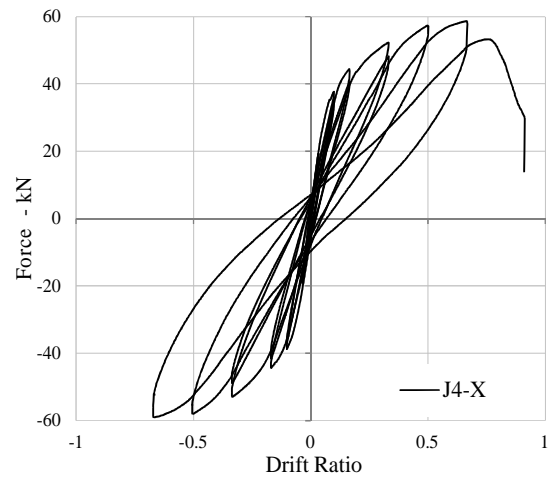
a



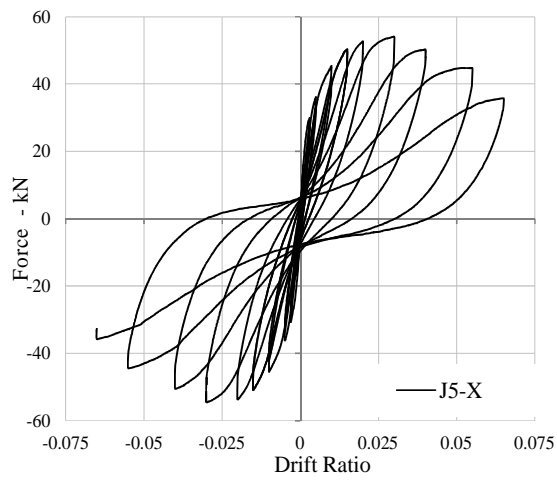
b



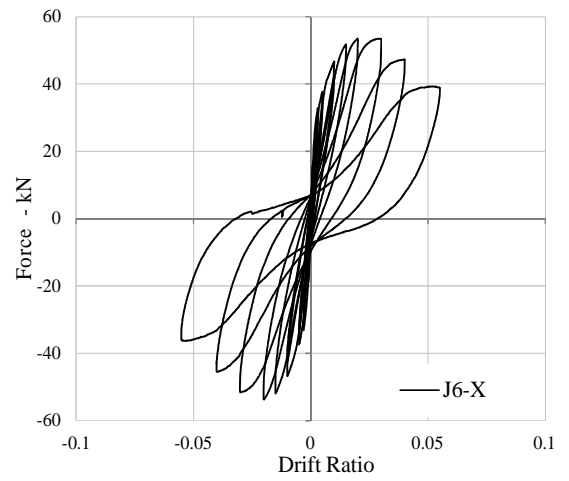
c



d



e



f

Continued...

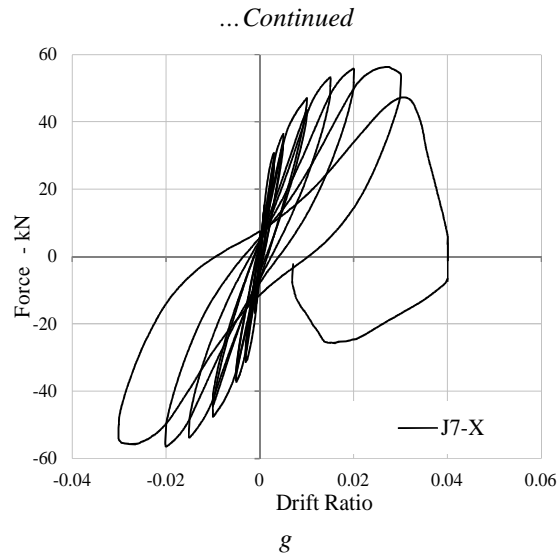
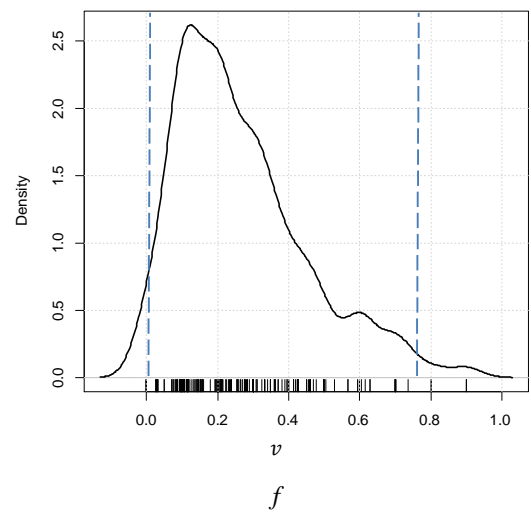
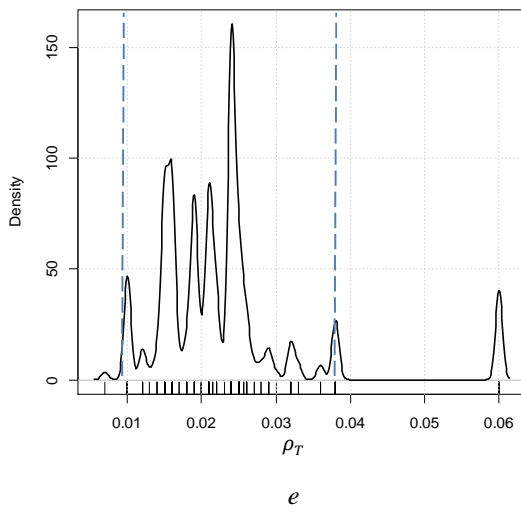
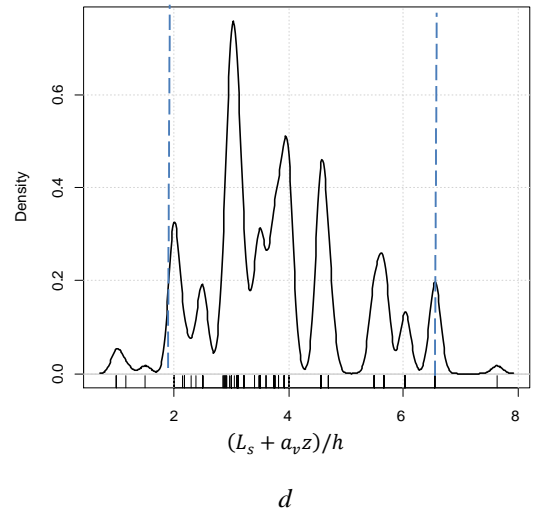
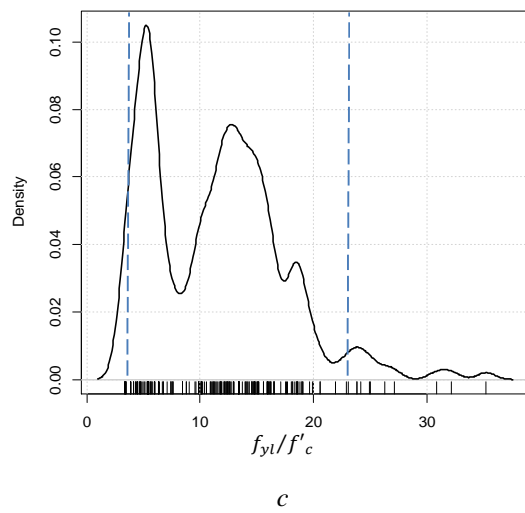
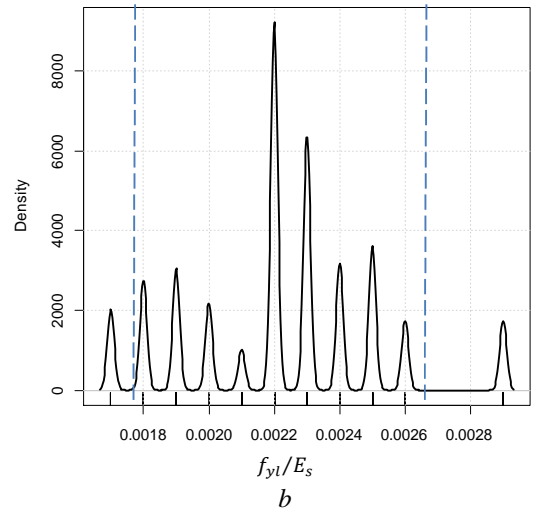
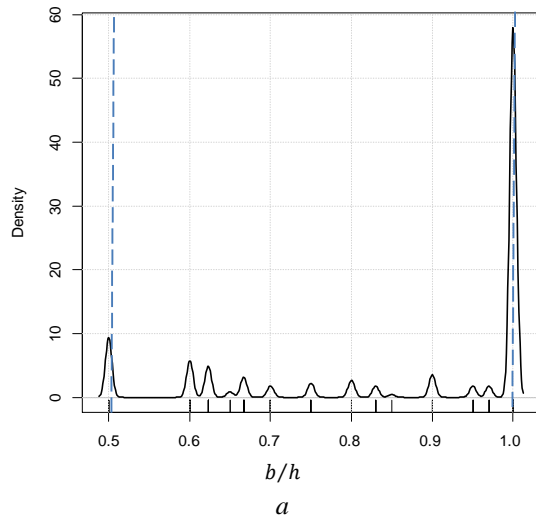


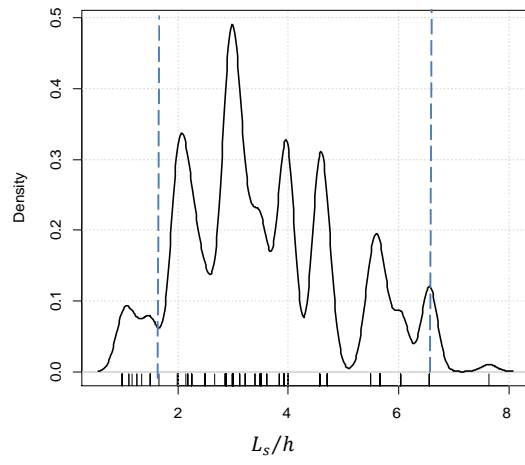
Figure D-59. Lateral force – drift response of the beam-column connections: a) J1-X, b) J2-X, c) J3-X, d) J4-X, e) J5-X, f) J6-X, g) J7-X.

Appendix E Distribution of Data of Regression Variables Using the Selected Database.



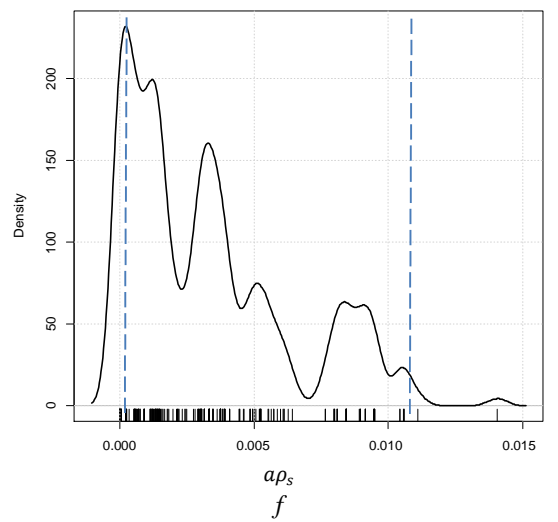
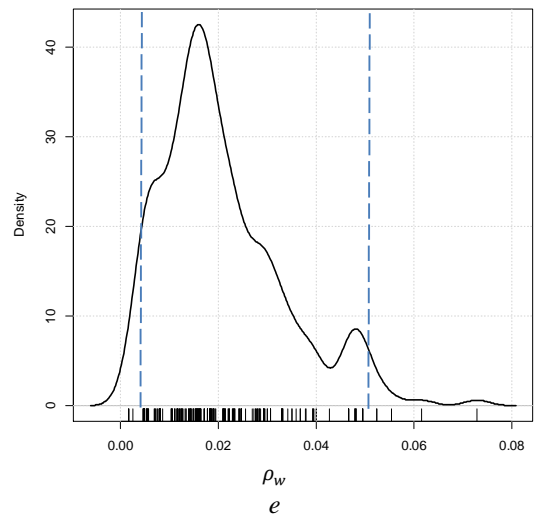
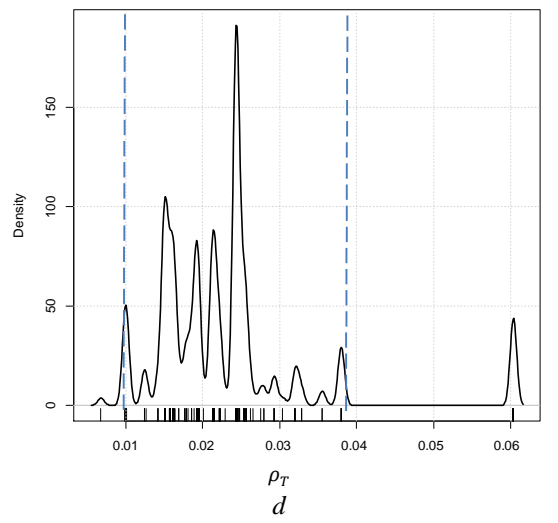
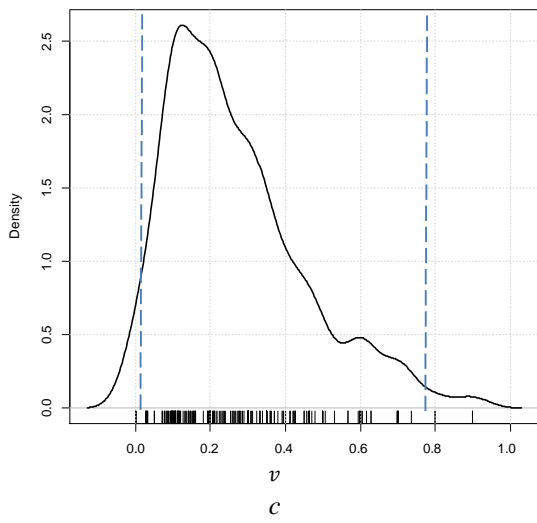
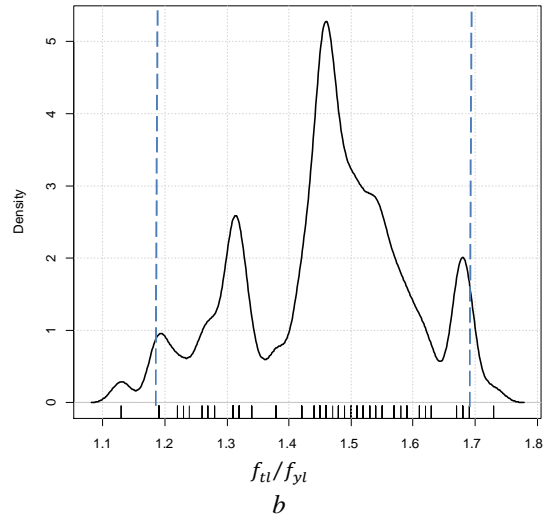
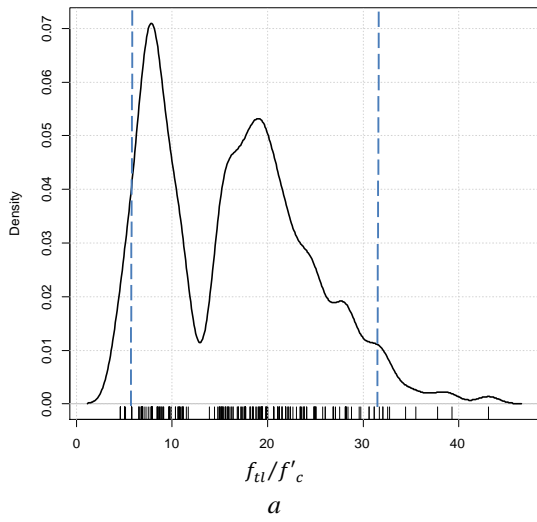
Continued...

...Continued



g

Figure E-1. *Distribution of explanatory variables used in the development of yield rotation and stiffness relations.*



Continued...

...Continued

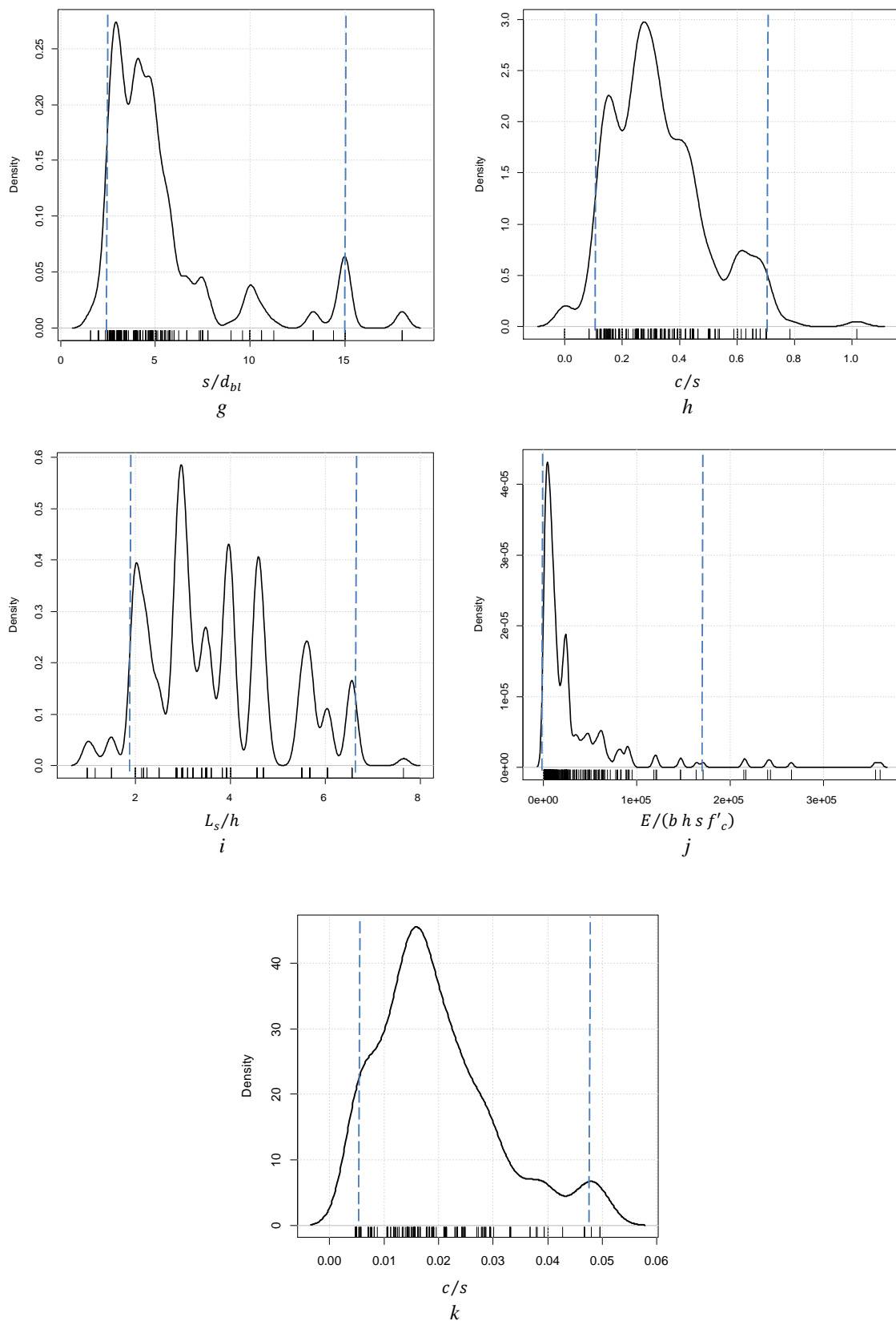
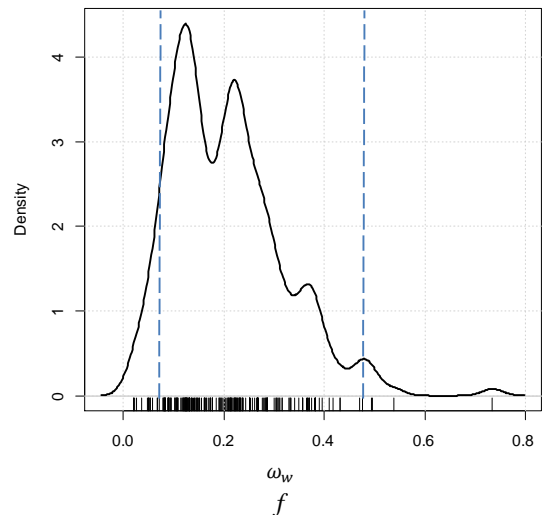
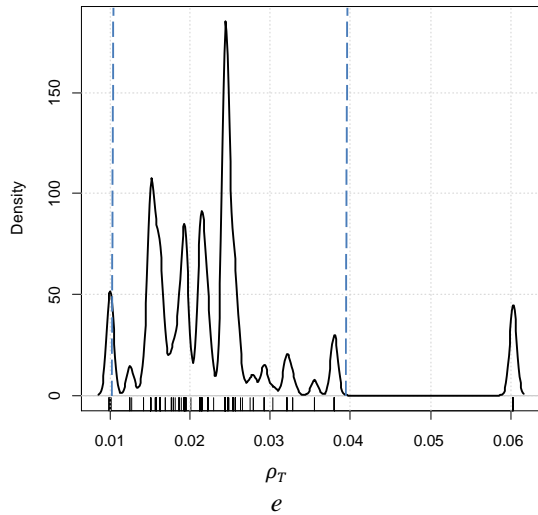
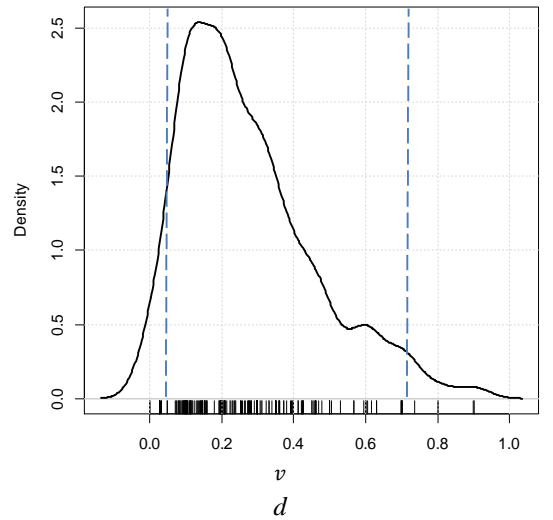
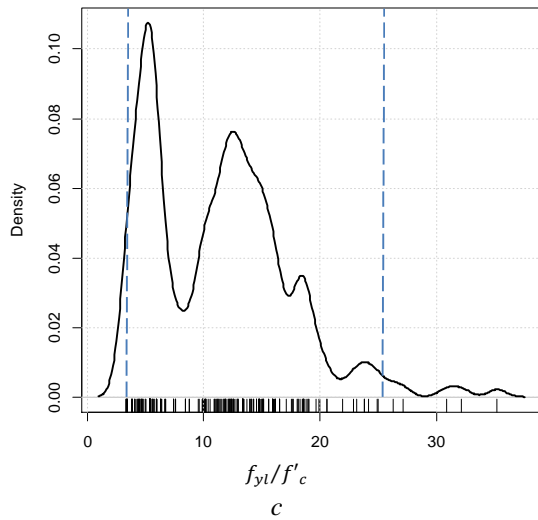
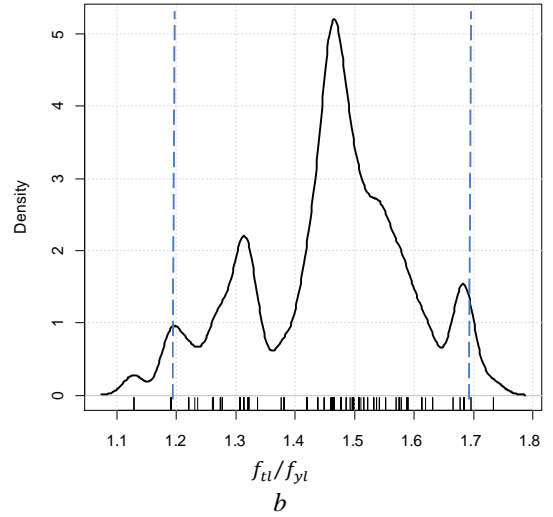
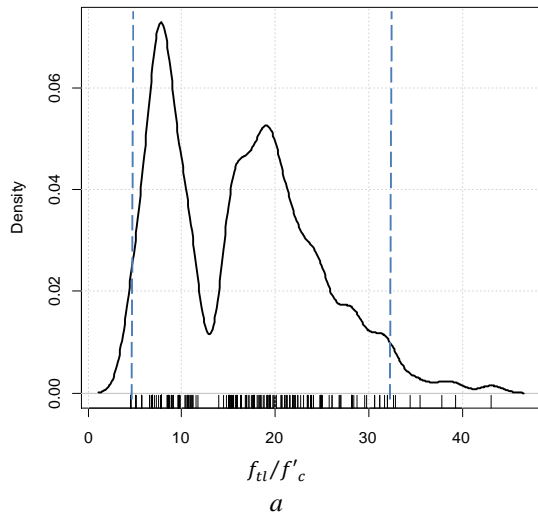
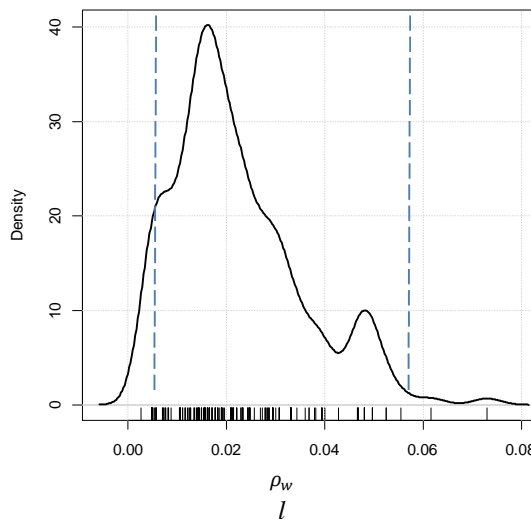
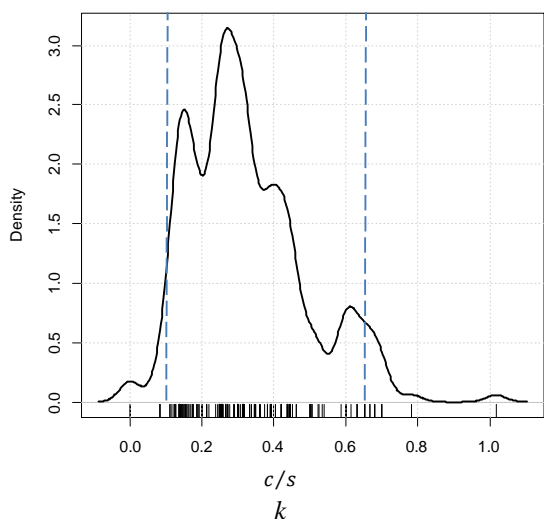
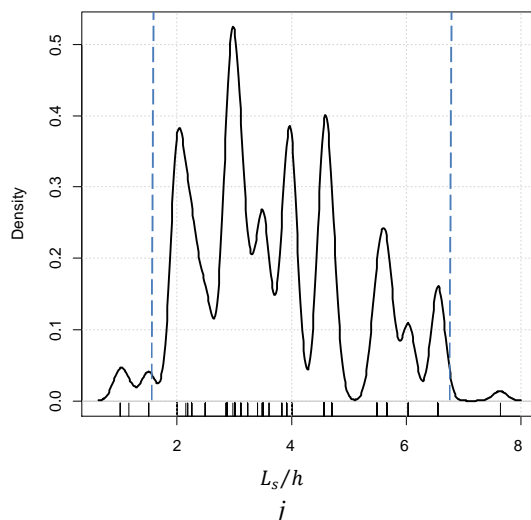
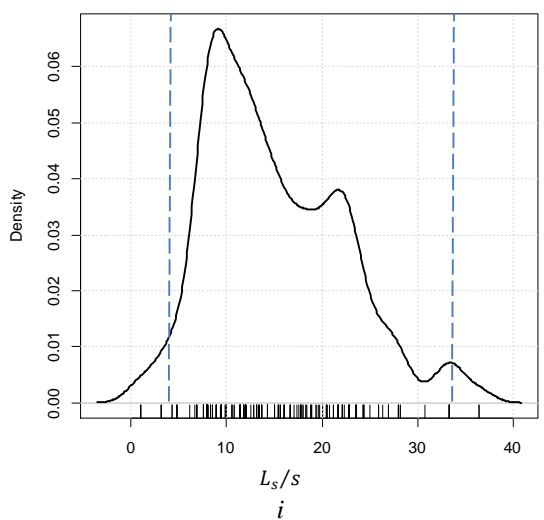
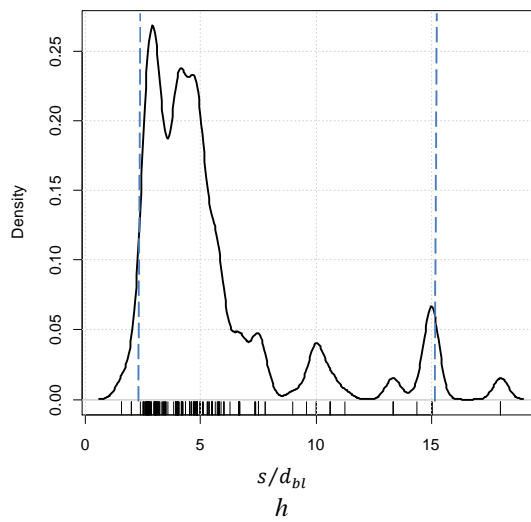
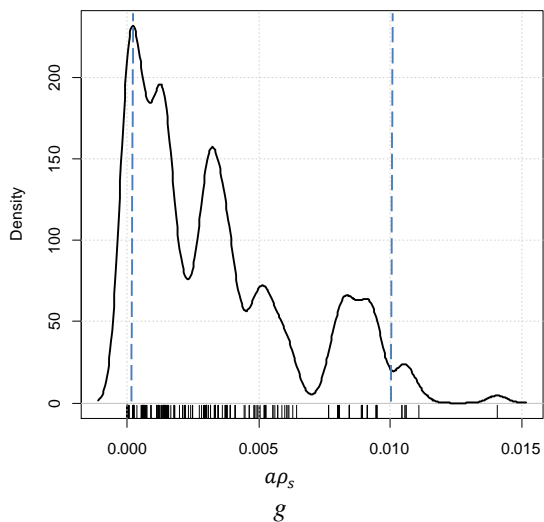


Figure E-3. Distribution of explanatory variables used in the development of rotation and stiffness relations at maximum force.



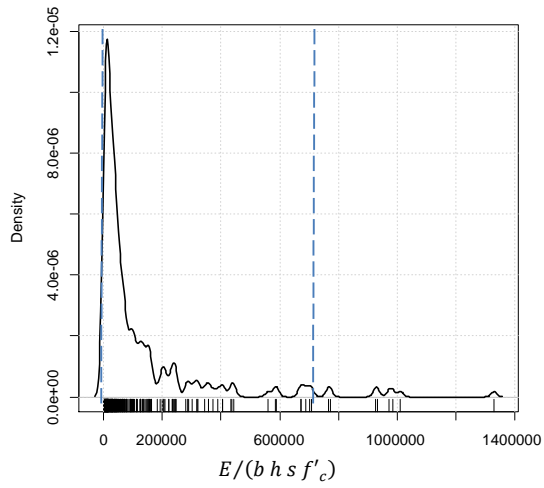
Continued ...

...Continued



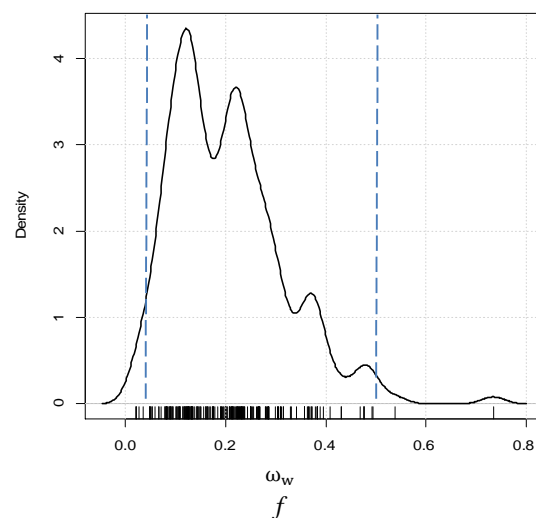
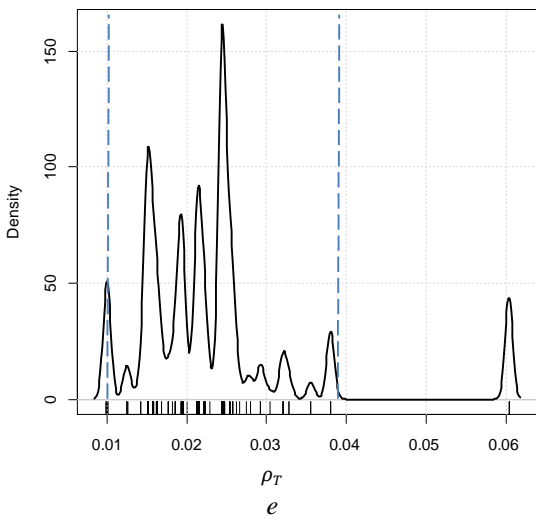
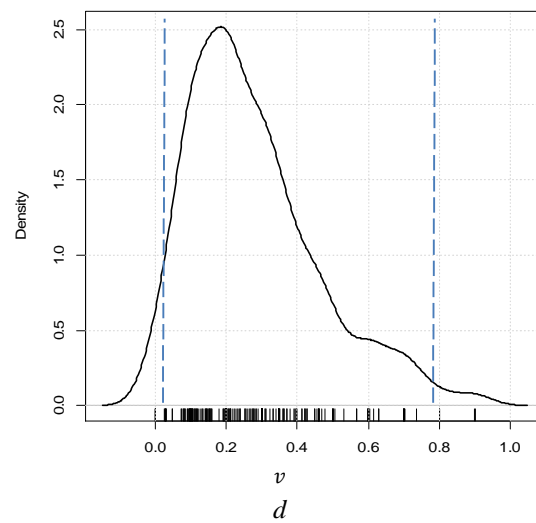
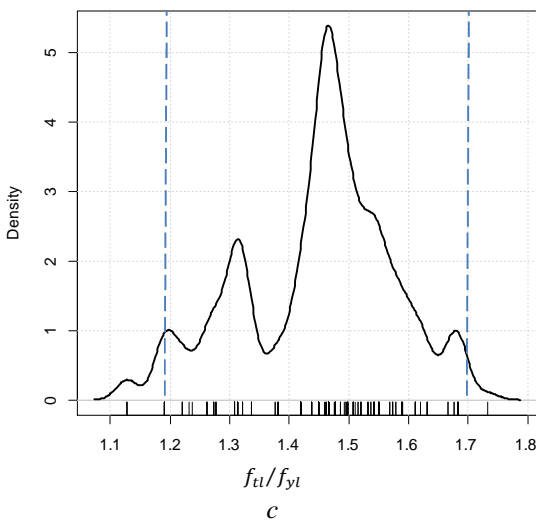
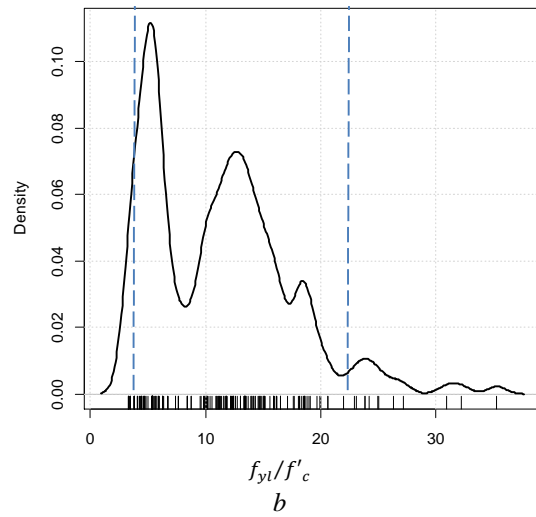
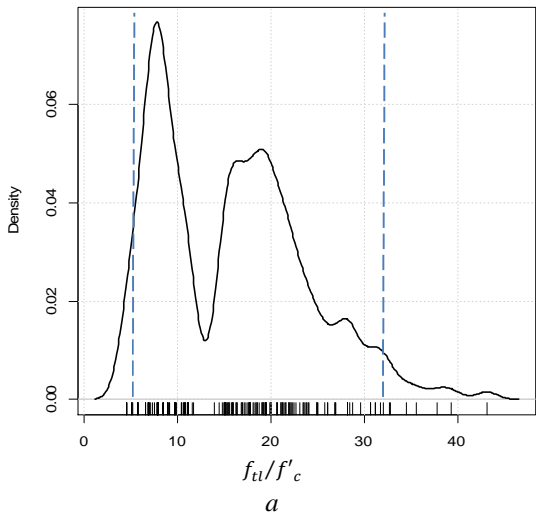
Continued...

...Continued



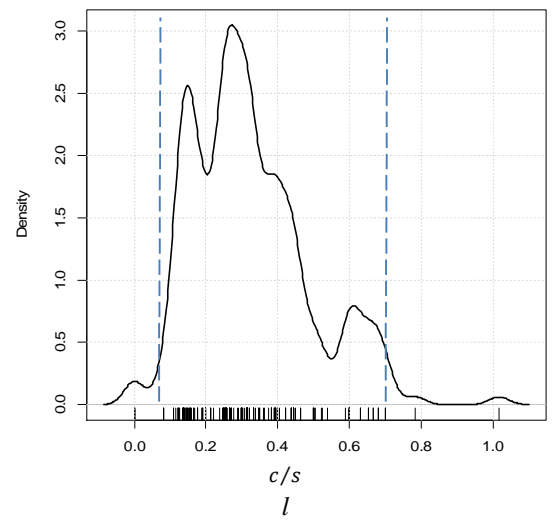
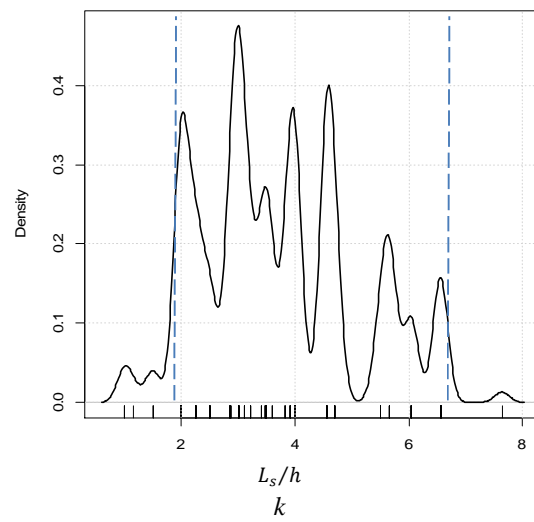
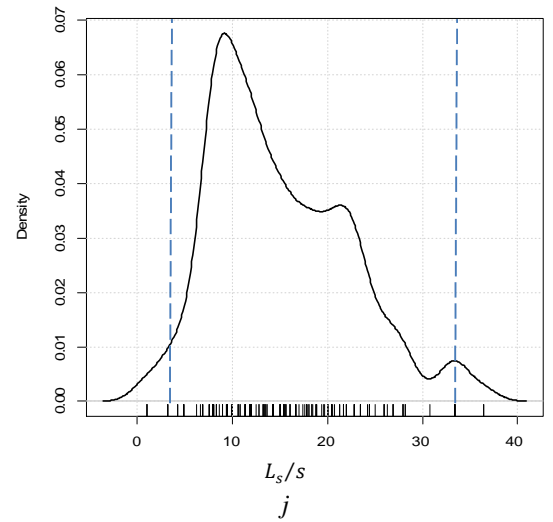
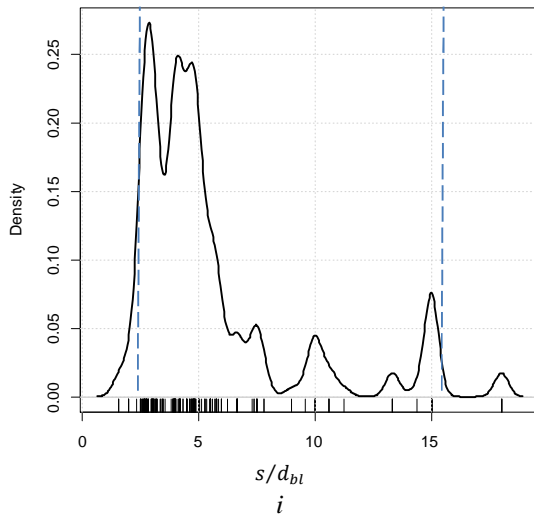
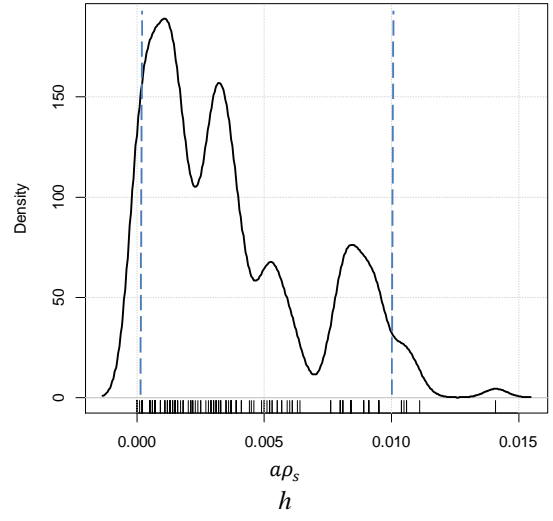
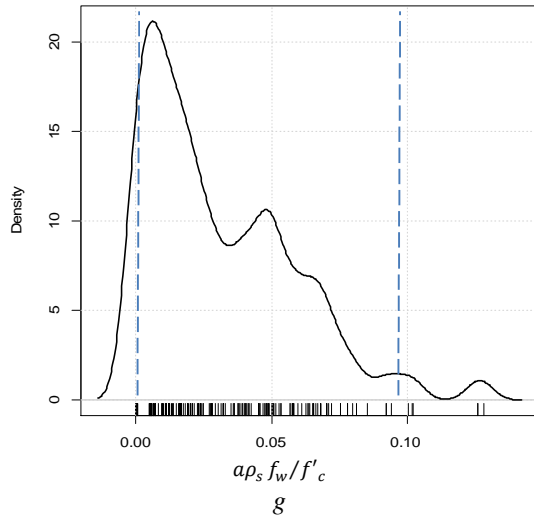
m

Figure E-4. Distribution of explanatory variables used in the development of rotation and stiffness relations at 10% reduction of maximum force.



Continued ...

...Continued



Continued...

...Continued

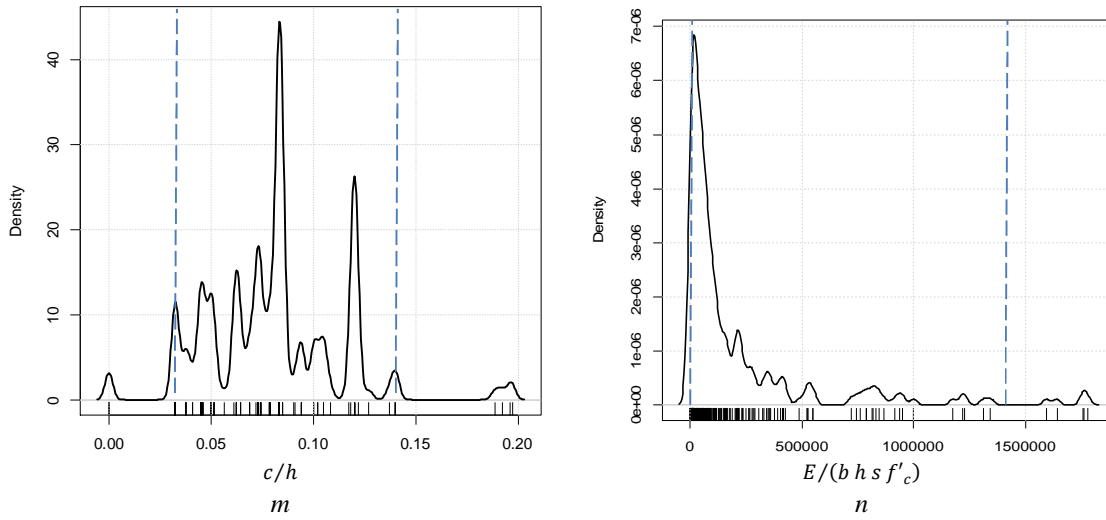
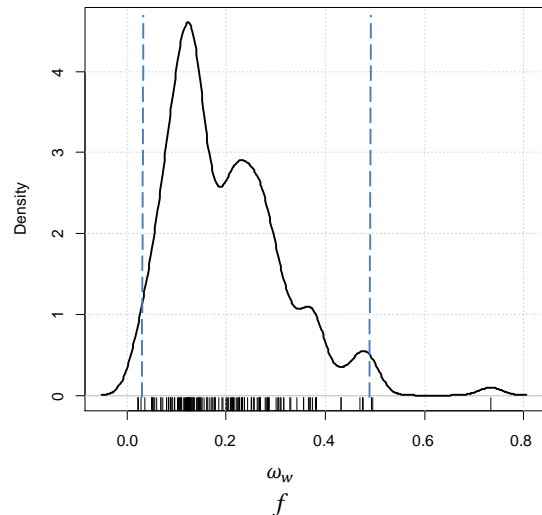
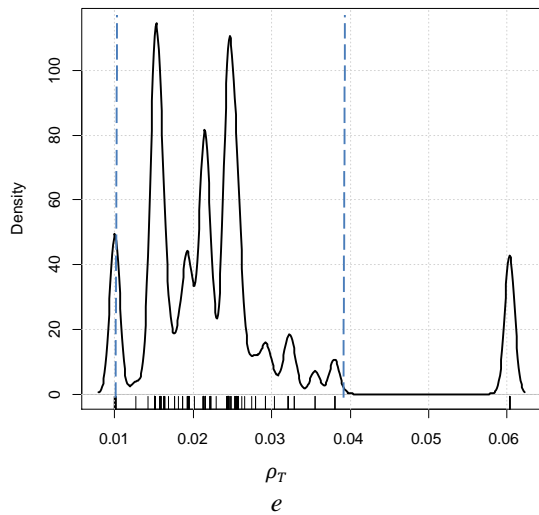
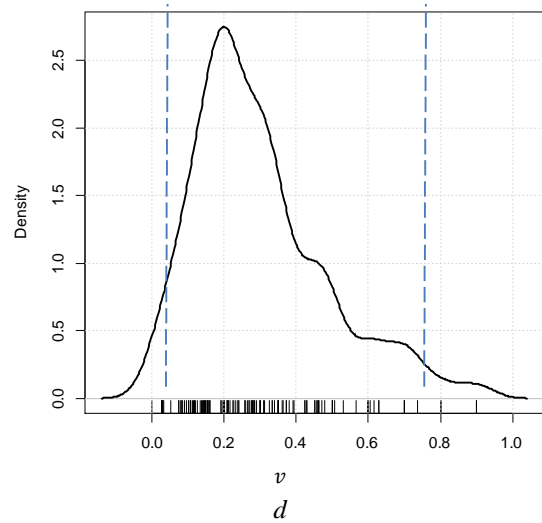
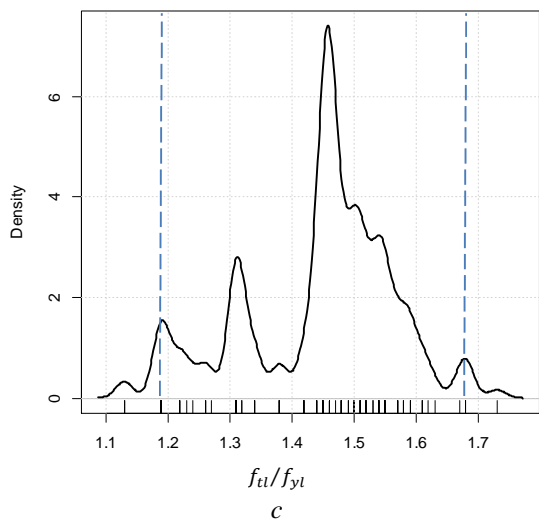
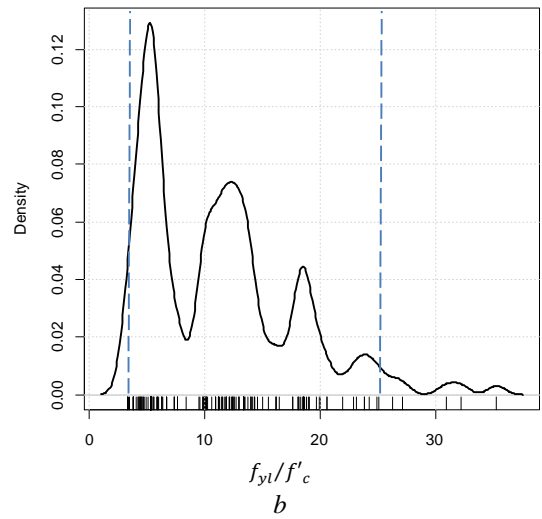
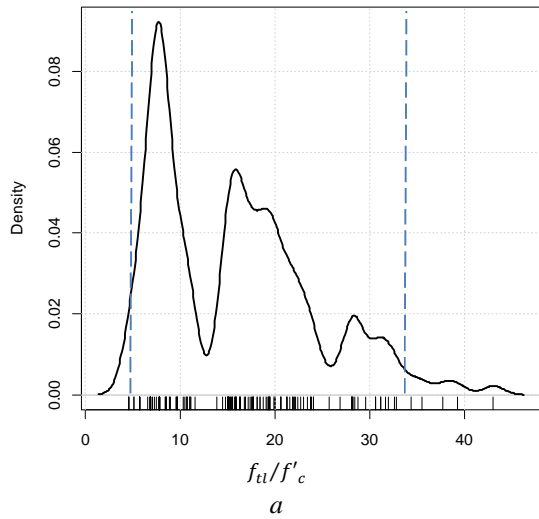
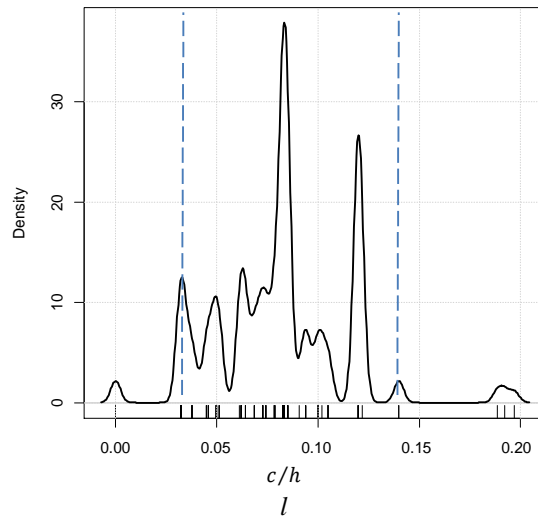
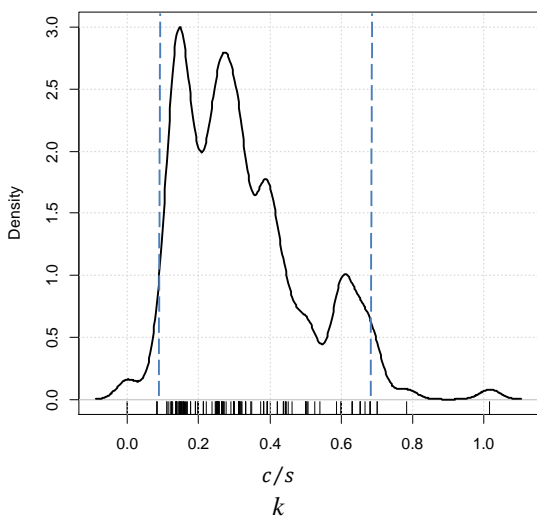
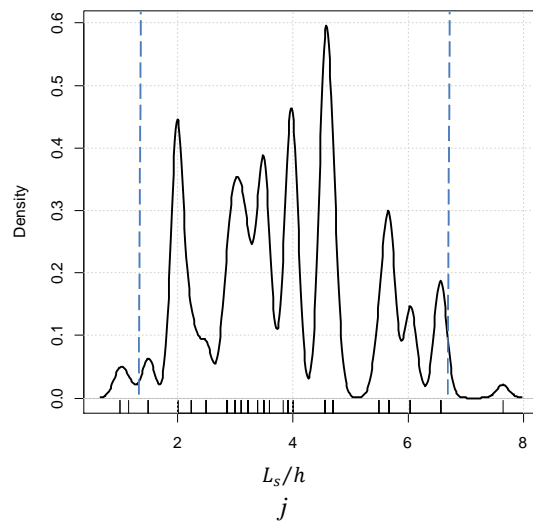
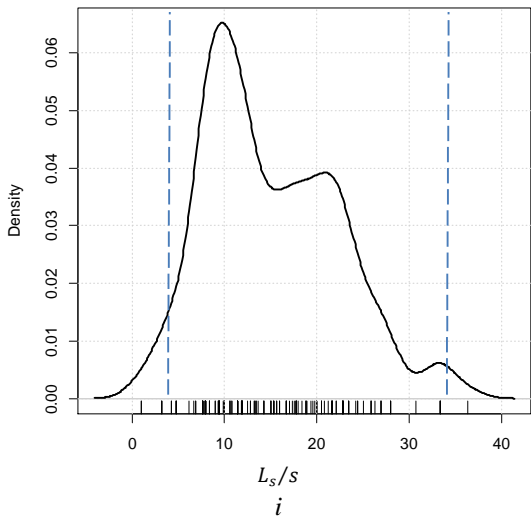
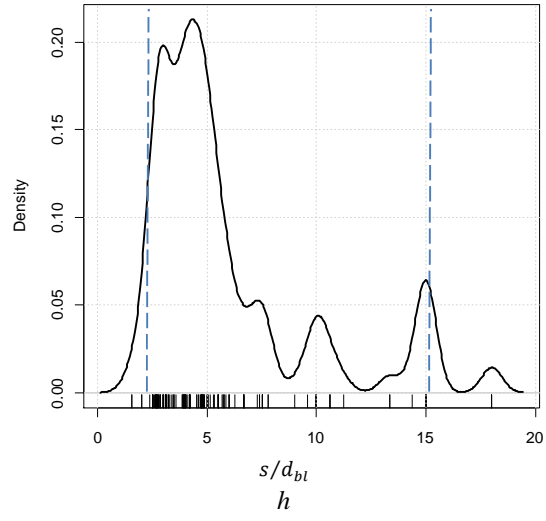
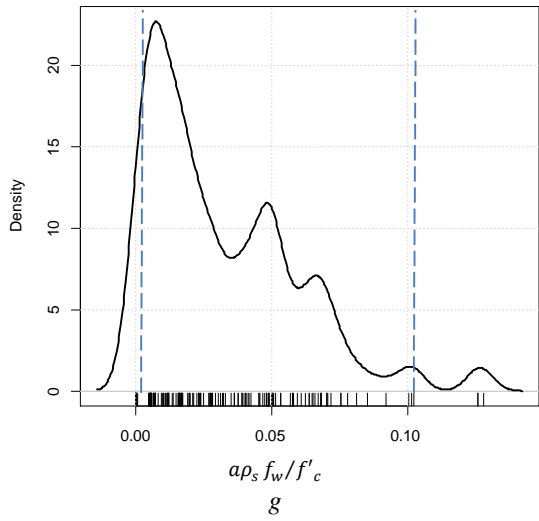


Figure E-5. Distribution of dependent variables used in the development of rotation and stiffness relations at 20% reduction of maximum force.



Continued ...

...Continued



Continued...

...Continued

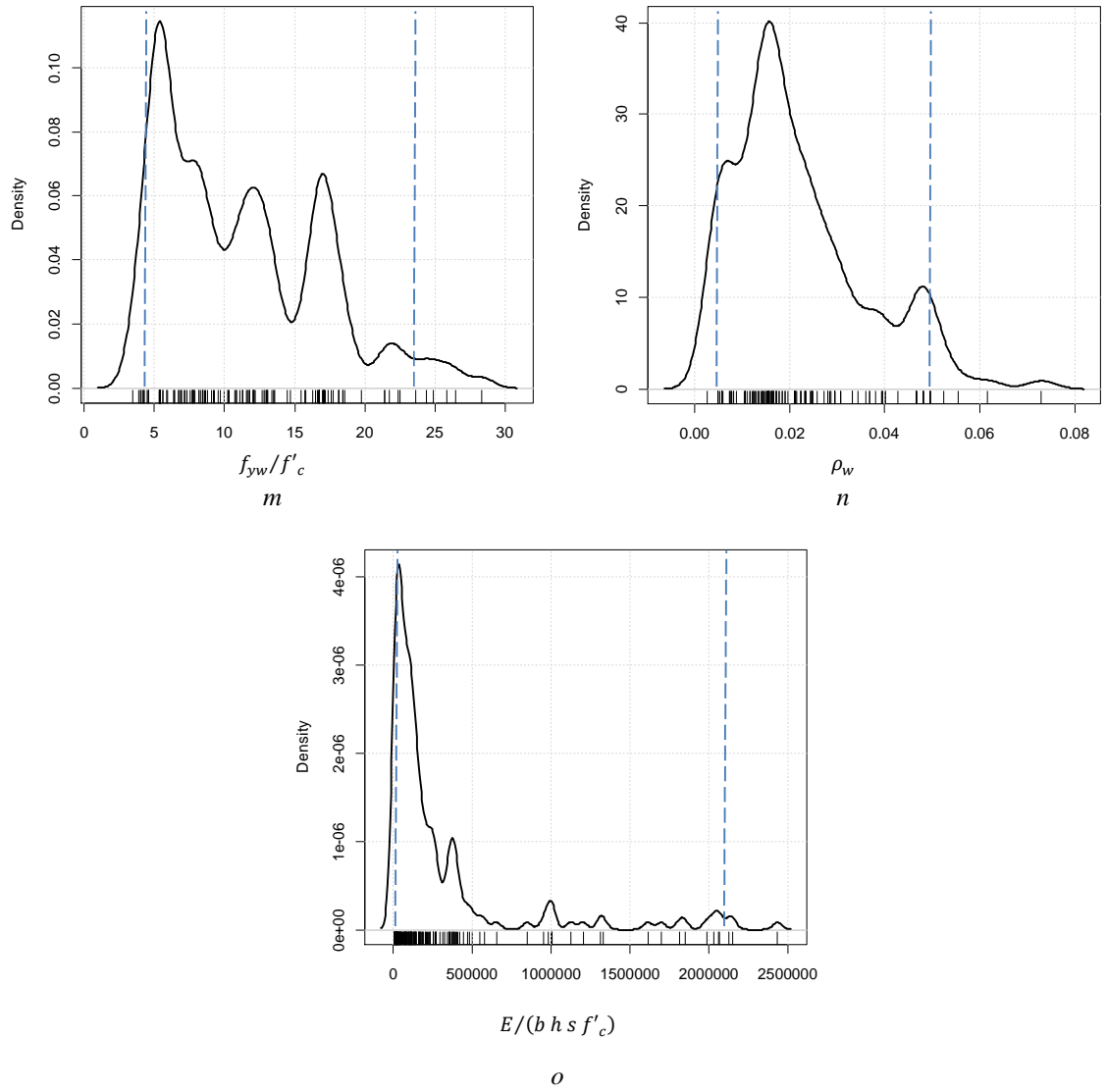


Figure E-6. Distribution of explanatory variables used in the development of rotation and stiffness relations at 50% reduction of maximum force.

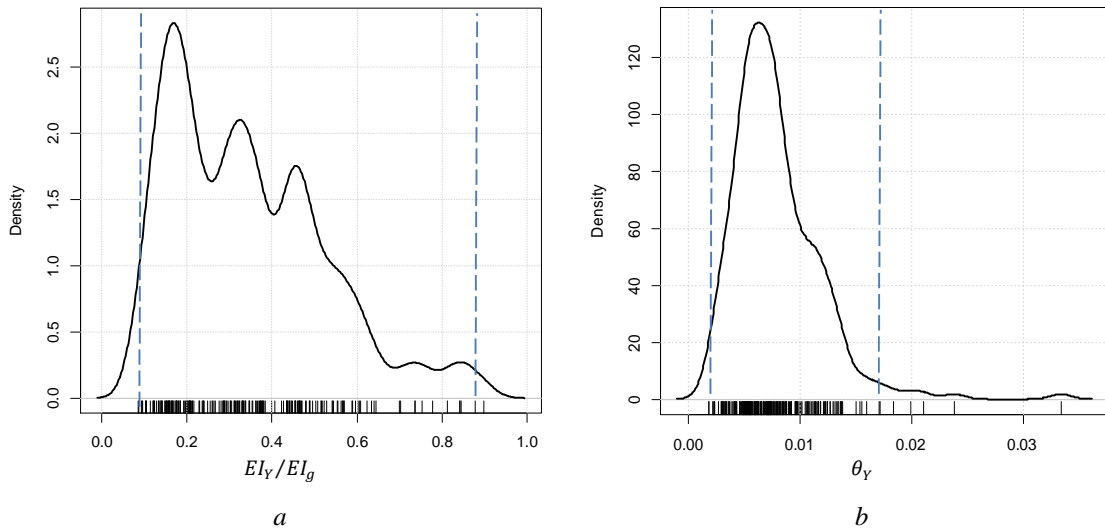


Figure E-7. Distribution of dependent variables used in the development of yield rotation and stiffness relations.

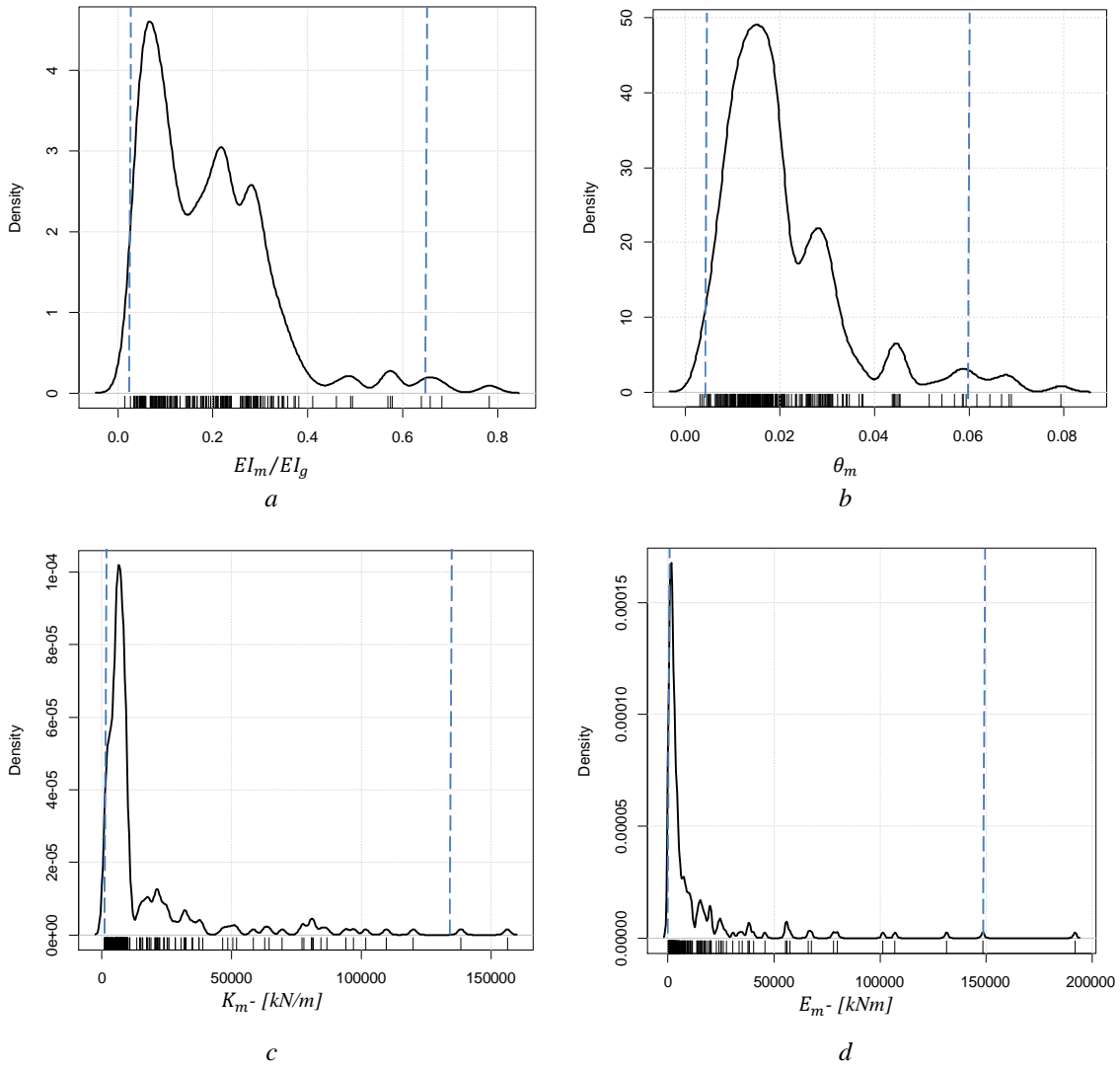


Figure E-8. Distribution of variables used in the development of rotation and stiffness relations at maximum force.

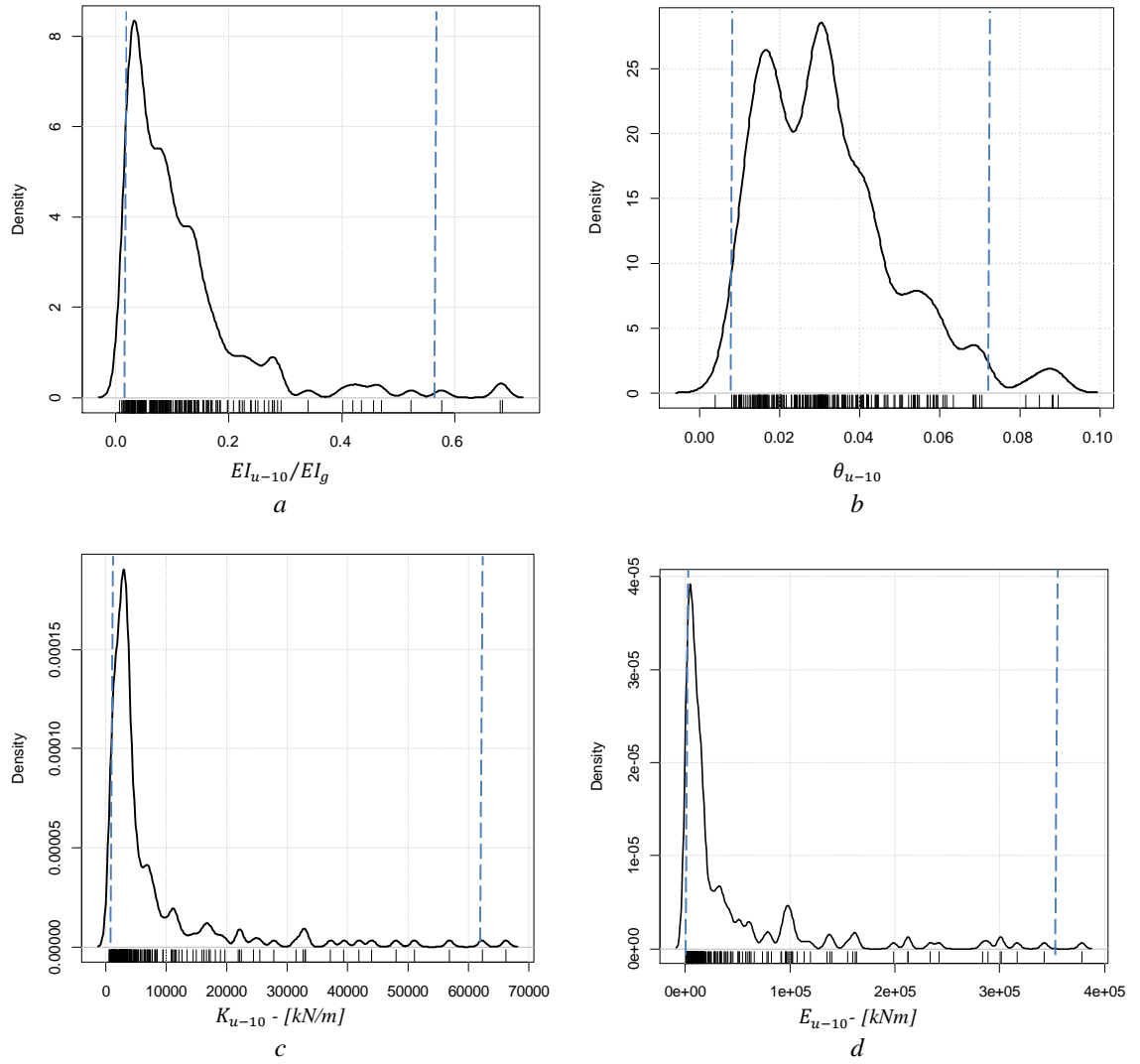


Figure E-9. Distribution of dependent variables used in the development of rotation and stiffness relations at 10% reduction of maximum force.

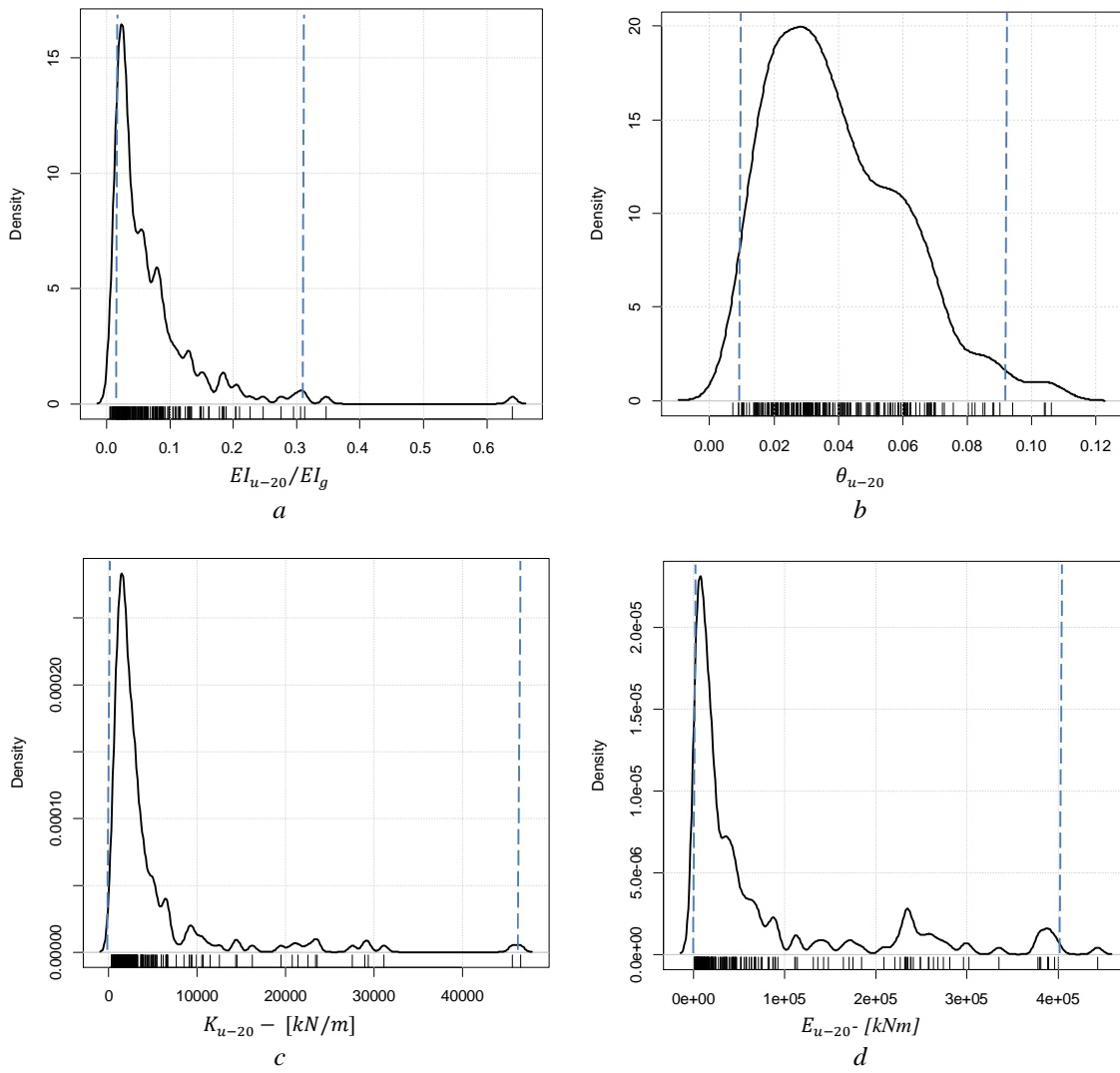


Figure E-10. Distribution of dependent variables used in the development of rotation and stiffness relations at 20% reduction of maximum force.

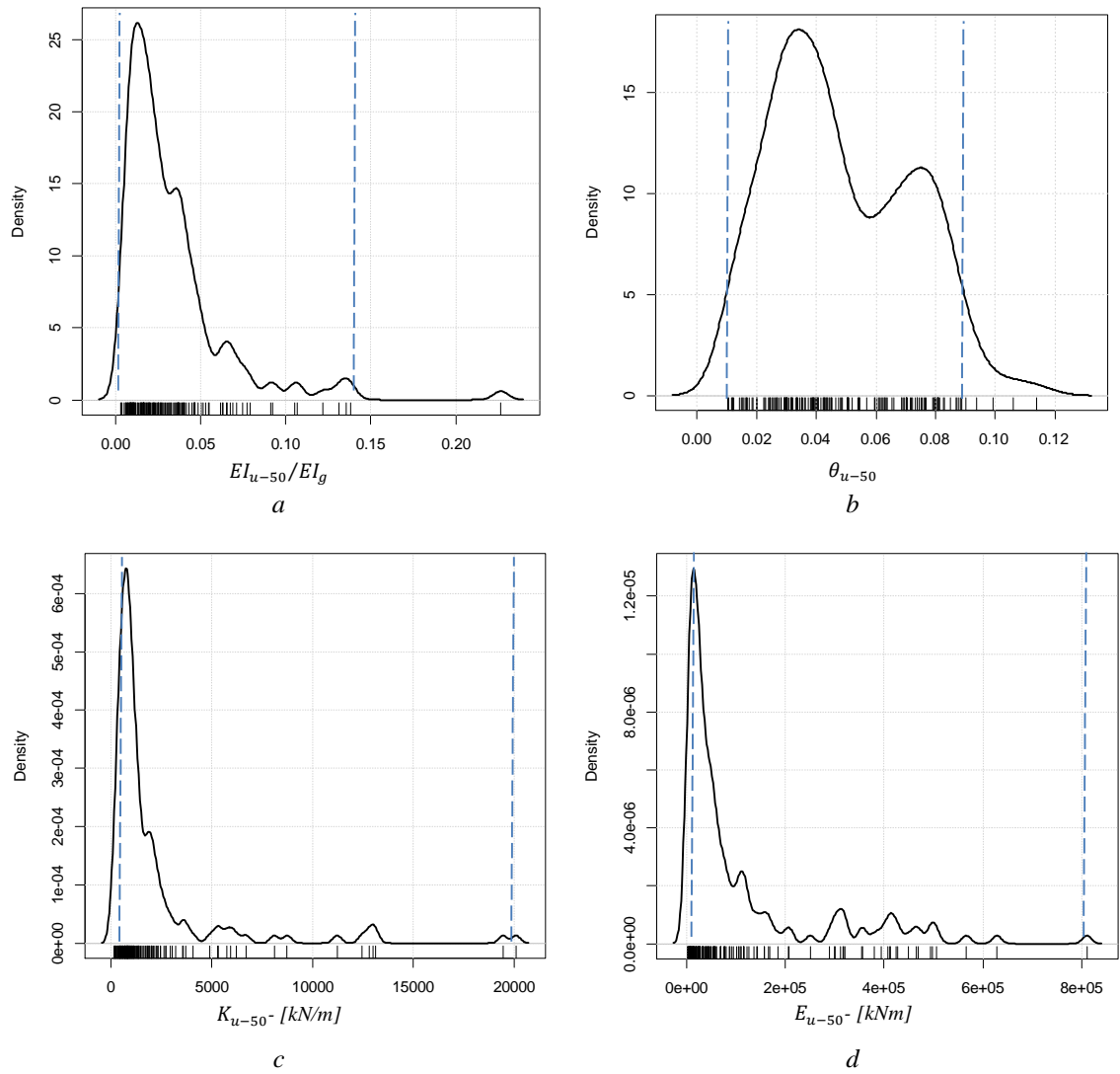


Figure E-11. Distribution of dependent variables used in the development of rotation and stiffness relations at 50% reduction of maximum force.

Appendix F Correlations of Explanatory Variables with Dependent Variables

For data in Tables F-1 to Table F-10, the value in italic refers to the form of the correlation that was actually considered in the regression analysis.

F.1 Correlations for Rotation Equations (θ_{dmg})

Table F-1. Correlation of explanatory variables with rotation at yield (θ_y).

EDP : X	Physical or material property (X)				
	f_{yl}/E_s	f_{yl}/f'_c	v	$(L_s + a_v z)/h$	ρ_T
$\theta_y : X$	0.33	0.04	-0.30	0.05	0.25
$\log \theta_y : X$	0.32	<u>0.16</u>	<u>-0.46</u>	<u>0.17</u>	<u>0.30</u>
$\theta_y : \log X$	0.39	0.08	-0.27	0.06	0.26
$\log \theta_y : \log X$	<u>0.39</u>	0.10	-0.25	0.13	0.28

Table F-2. Correlation of explanatory variables with rotation at maximum force (θ_m).

EDP : X	Physical or material property (X)									
	f_{tl}/f'_c	f_{tl}/f_{yl}	v	L_s/h	ρ_T	s/d_{bl}	ρ_w	$a\rho_s$	c/s	$E/(bhsf'_c)$
$\theta_m : X$	0.07	-0.04	-0.44	-0.21	0.12	-0.18	-0.07	-0.09	-0.02	0.65
$\log \theta_m : X$	0.09	-0.15	<u>-0.50</u>	-0.18	0.16	<u>-0.19</u>	-0.04	-0.11	<u>-0.12</u>	0.55
$\theta_m : \log X$	0.10	-0.04	-0.29	-0.20	0.18	-0.19	-0.13	-0.18	-0.06	0.54
$\log \theta_m : \log X$	<u>0.12</u>	<u>-0.16</u>	-0.28	<u>-0.20</u>	<u>0.22</u>	-0.17	<u>-0.12</u>	<u>-0.24</u>	-0.08	<u>0.62</u>

Table F-3. Correlation of explanatory variables with rotation at 10% maximum force reduction (θ_{u-10}).

EDP : X	Physical or material property (X)												
	f_{tl}/f'_c	f_{tl}/f_{yl}	f_{yl}/f'_c	v	L_s/h	L_s/s	ρ_T	s/d_{bl}	ρ_w	ω_w	$a\rho_s$	c/s	$E/(bhsf'_c)$
$\theta_{u-10} : X$	0.10	-0.14	0.11	-0.44	-0.15	0.20	0.16	-0.27	-0.03	0.06	0.05	0.12	0.58
$\log \theta_{u-10} : X$	0.15	-0.18	<u>0.19</u>	<u>-0.49</u>	-0.15	0.18	0.21	<u>-0.29</u>	-0.13	<u>0.17</u>	<u>-0.11</u>	<u>0.17</u>	0.52
$\theta_{u-10} : \log X$	0.15	-0.15	0.16	-0.18	-0.14	0.20	0.21	-0.28	-0.07	0.03	0.07	0.02	0.58
$\log \theta_{u-10} : \log X$	<u>0.21</u>	<u>-0.19</u>	<u>0.21</u>	-0.18	<u>-0.18</u>	<u>0.22</u>	<u>0.25</u>	-0.29	<u>-0.13</u>	0.11	-0.12	0.02	<u>0.60</u>

Table F-4. Correlation of explanatory variables with rotation at 20% maximum force reduction (θ_{u-20}).

EDP : X	Physical or material property (X)												
	f_{tl}/f'_c	f_{tl}/f_{yl}	f_{yl}/f'_c	v	L_s/h	L_s/s	ρ_T	s/d_{bl}	ω_w	$a\rho_s \frac{f_{yw}}{f'_c}$	c/s	$E/(bhsf'_c)$	
$\theta_{u-20} : X$	0.04	-0.13	0.04	-0.36	-0.18	0.26	0.18	-0.35	0.20	0.25	0.20	0.51	
$\log \theta_{u-20} : X$	0.10	-0.13	0.10	<u>-0.43</u>	-0.20	0.21	0.22	<u>-0.38</u>	<u>0.25</u>	<u>0.24</u>	<u>0.24</u>	0.48	
$\theta_{u-20} : \log X$	0.08	-0.14	0.10	-0.18	-0.17	0.21	0.23	-0.36	0.17	0.16	0.09	0.58	
$\log \theta_{u-20} : \log X$	<u>0.17</u>	<u>-0.17</u>	<u>0.15</u>	-0.17	<u>-0.20</u>	<u>0.24</u>	<u>0.27</u>	-0.38	<u>0.23</u>	0.11	0.09	<u>0.61</u>	

Table F-5. Correlation of explanatory variables with rotation at 50% maximum force reduction (θ_{u-50}).

EDP : X	Physical or material property (X)												
	f_{tl}/f'_c	f_{tl}/f_{yl}	f_{yl}/f'_c	v	L_s/h	L_s/s	ρ_T	s/d_{bl}	ω_w	$a\rho_s \frac{f_{yw}}{f'_c}$	c/s	$E/(bhsf'_c)$	
$\theta_{u-50} : X$	0.13	-0.18	0.13	-0.44	-0.20	0.23	0.23	-0.37	0.29	0.33	0.39	0.49	
$\log \theta_{u-50} : X$	0.13	<u>-0.19</u>	0.13	<u>-0.50</u>	-0.22	0.22	0.26	<u>-0.40</u>	0.29	<u>0.32</u>	<u>0.41</u>	0.45	
$\theta_{u-50} : \log X$	0.15	-0.18	0.15	-0.07	-0.21	0.25	0.29	-0.39	0.30	0.17	0.24	0.60	
$\log \theta_{u-50} : \log X$	<u>0.17</u>	-0.15	<u>0.16</u>	-0.07	<u>-0.23</u>	<u>0.26</u>	<u>0.31</u>	-0.38	<u>0.35</u>	0.15	0.23	<u>0.60</u>	

F.2 Correlations for Stiffness Equations (EI_{dmg}/EI_g)

Table F-6. Correlation of explanatory variables with stiffness ratio at yield (EI_Y/EI_g).

EDP : X	Physical or material property (X)			
	f_{yl}/f'_c	ν	L_s/h	b/h
$(EI_Y/EI_g):X$	-0.35	0.55	0.46	0.24
$\log(EI_Y/EI_g):X$	-0.40	<u>0.69</u>	0.48	0.38
$(EI_Y/EI_g):\log X$	-0.39	0.41	0.40	0.24
$\log(EI_Y/EI_g):\log X$	<u>-0.47</u>	0.61	<u>0.47</u>	<u>0.38</u>

Table F-7. Correlation of explanatory variables with stiffness ratio at maximum force (EI_m/EI_g).

EDP : X	Physical or material property (X)		
	f_{tl}/f'_c	ν	L_s/h
$(EI_m/EI_g):X$	-0.04	0.48	0.44
$\log(EI_m/EI_g):X$	-0.05	<u>0.64</u>	<u>0.55</u>
$(EI_m/EI_g):\log X$	-0.43	0.36	0.05
$\log(EI_m/EI_g):\log X$	<u>-0.52</u>	0.59	0.56

Table F-8. Correlation of explanatory variables with stiffness ratio at 10% reduction of maximum force (EI_{u-10}/EI_g).

EDP : X	Physical or material property (X)				
	f_{tl}/f'_c	v	L_s/h	$a\rho_s$	s/d_{bl}
$(EI_{u-10}/EI_g): X$	-0.37	0.41	0.48	-0.32	0.11
$\log(EI_{u-10}/EI_g): X$	<u>-0.43</u>	<u>0.62</u>	<u>0.56</u>	<u>-0.36</u>	0.19
$(EI_{u-10}/EI_g): \log X$	-0.16	0.10	0.17	-0.09	0.25
$\log(EI_{u-10}/EI_g): \log X$	-0.13	0.17	0.18	-0.20	<u>0.23</u>

Table F-9. Correlation of explanatory variables with stiffness ratio at 20% reduction of maximum force (EI_{u-20}/EI_g).

EDP : X	Physical or material property (X)					
	f_{tl}/f'_c	v	L_s/h	ρ_T	$a\rho_s$	c/h
$(EI_{u-20}/EI_g): X$	-0.39	0.44	0.51	0.01	-0.27	-0.16
$\log(EI_{u-20}/EI_g): X$	-0.42	<u>0.60</u>	<u>0.55</u>	<u>0.19</u>	<u>-0.31</u>	<u>-0.20</u>
$(EI_{u-20}/EI_g): \log X$	-0.42	0.37	0.47	0.05	-0.23	-0.08
$\log(EI_{u-20}/EI_g): \log X$	<u>-0.47</u>	0.60	0.51	0.12	-0.29	-0.14

Table F-10. Correlation of explanatory variables with stiffness ratio at 50% reduction of maximum force (EI_{u-50}/EI_g).

EDP : X	Physical or material property (X)					
	f_{tl}/f'_c	v	L_s/h	ρ_T	$a\rho_s f_{yw}/f'_c$	c/h
$(EI_{u-50}/EI_g): X$	-0.38	0.46	0.50	0.01	-0.09	-0.14
$\log(EI_{u-50}/EI_g): X$	-0.42	<u>0.59</u>	0.49	<u>0.19</u>	-0.18	-0.09
$(EI_{u-50}/EI_g): \log X$	-0.41	0.42	0.45	0.02	0.11	-0.08
$\log(EI_{u-50}/EI_g): \log X$	<u>-0.47</u>	0.60	<u>0.49</u>	0.19	<u>-0.24</u>	<u>-0.23</u>

Appendix G Scatter-plots of Regression Variables Using the Selected Database.

G.1 Scatter-plots of Explanatory Variables with Rotation (θ_{dmg}).

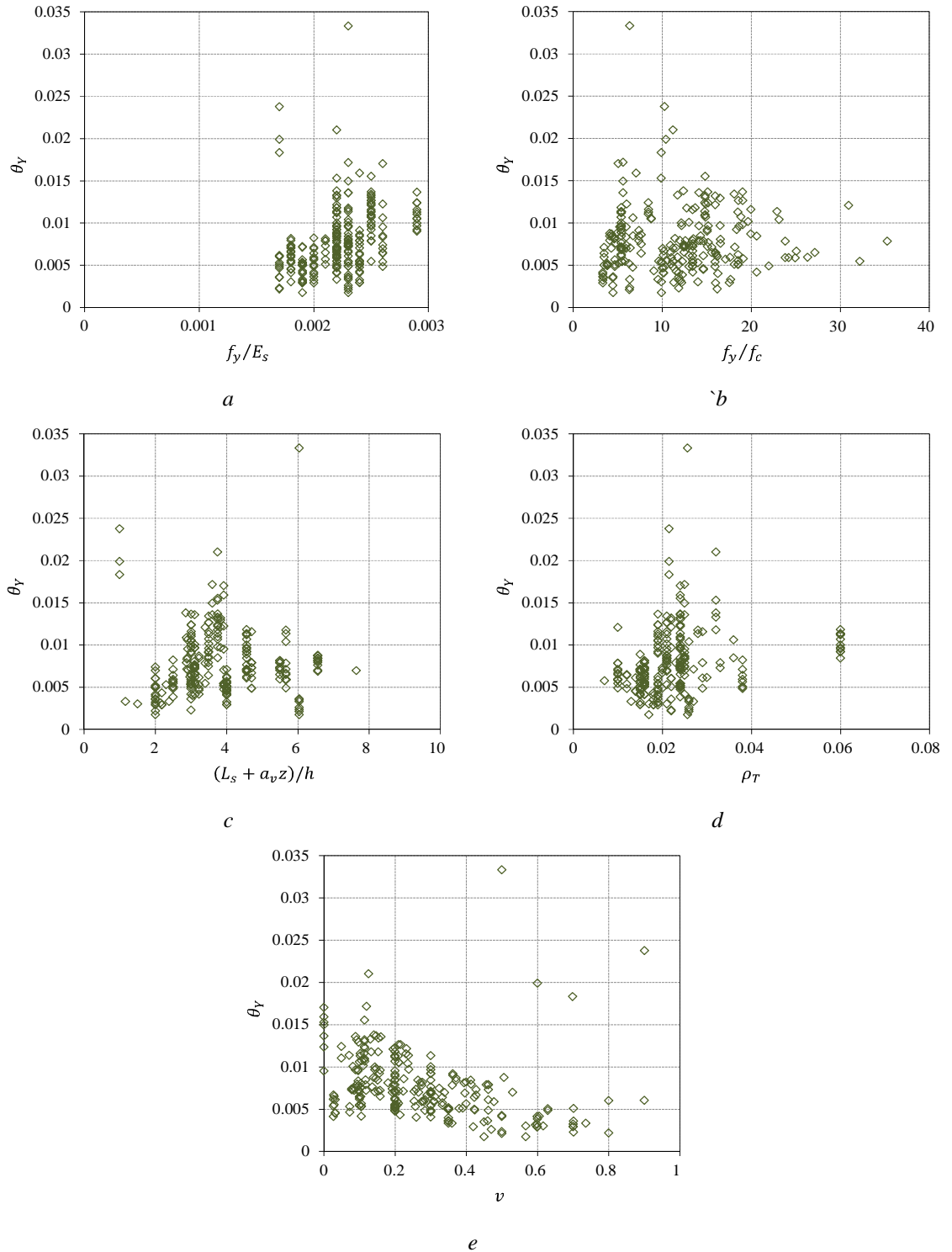
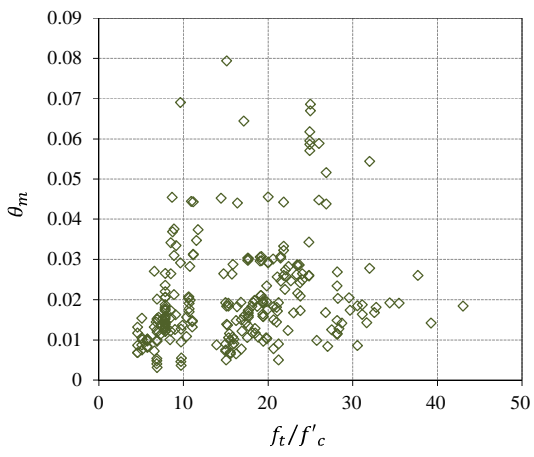
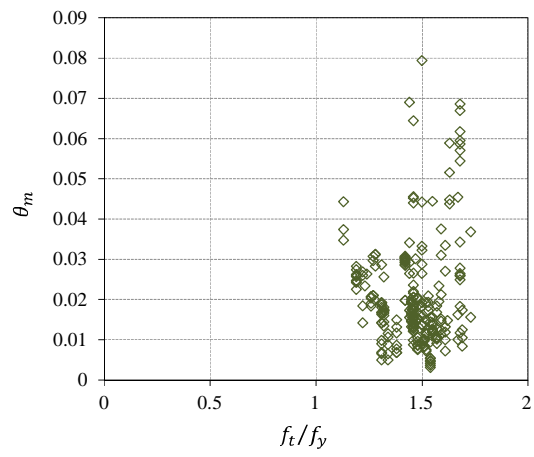


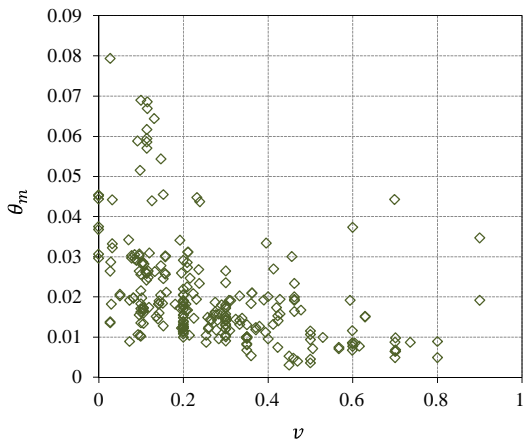
Figure G-1. Scatter plots showing trends between yield rotation (θ_y) and explanatory variables.



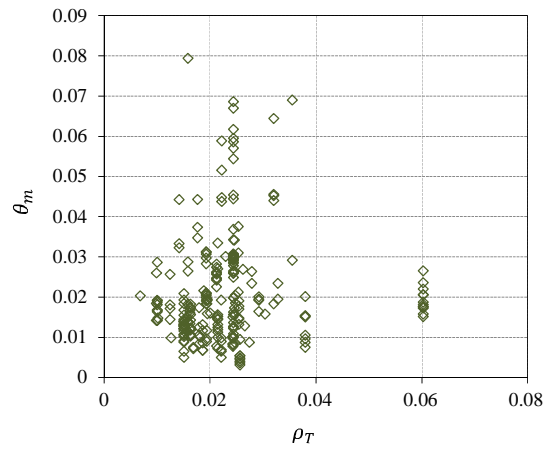
a



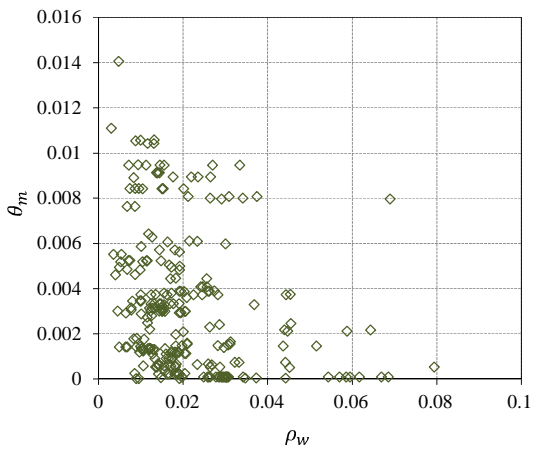
b



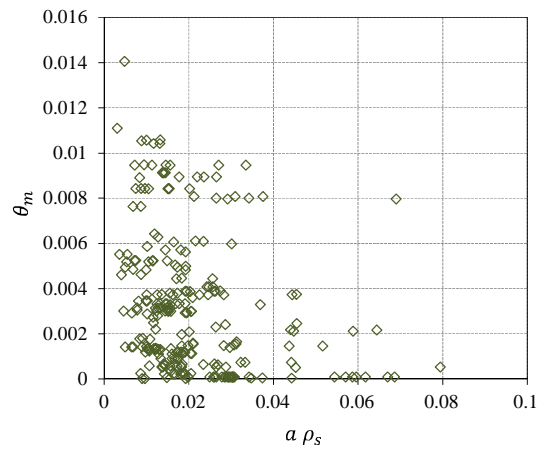
c



d



e



f

Continued...

...Continued

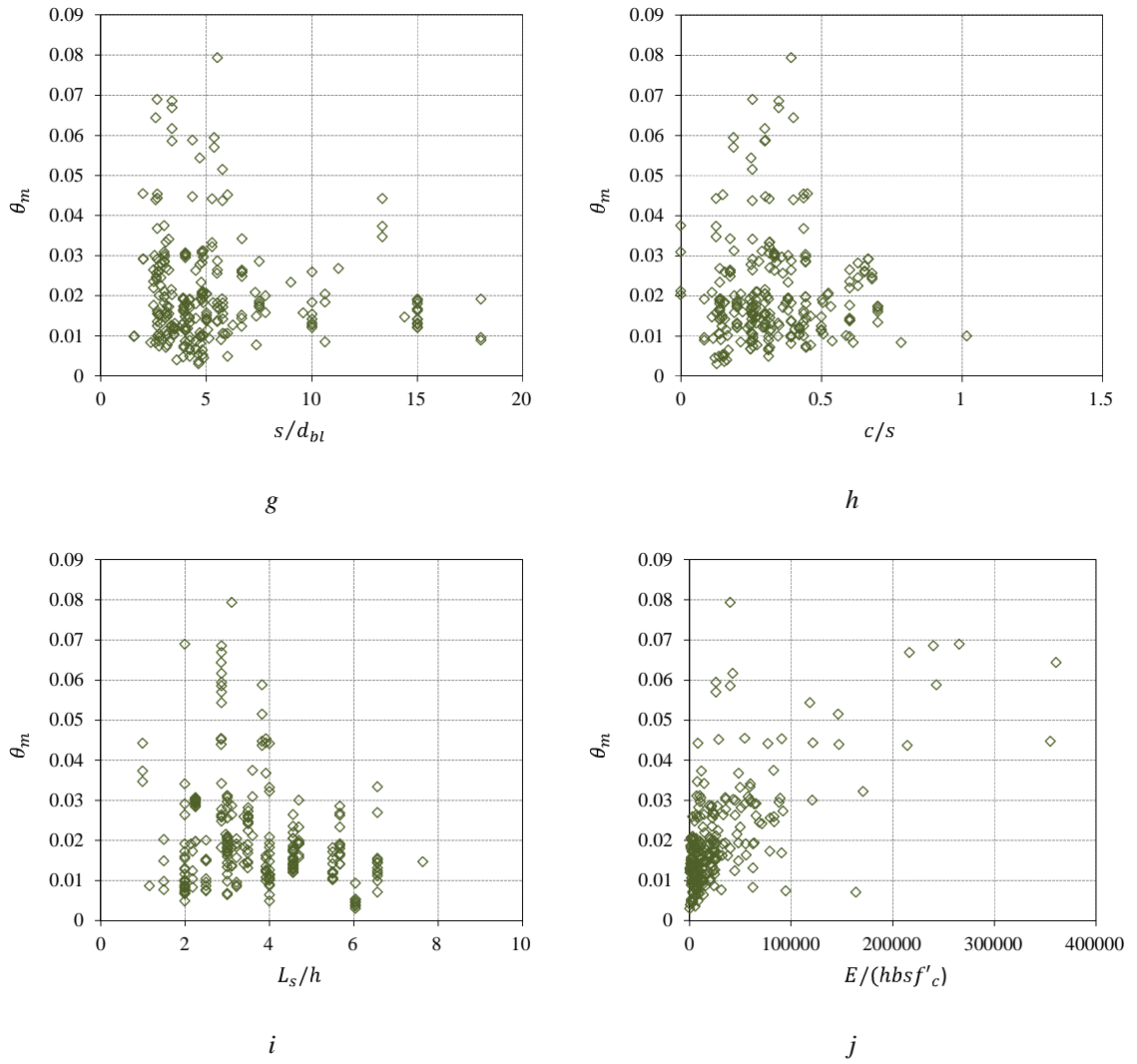
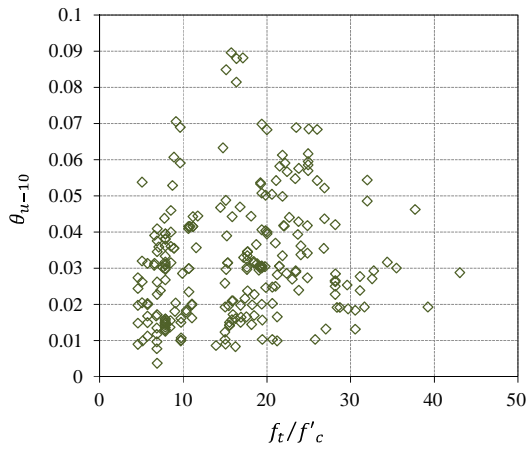
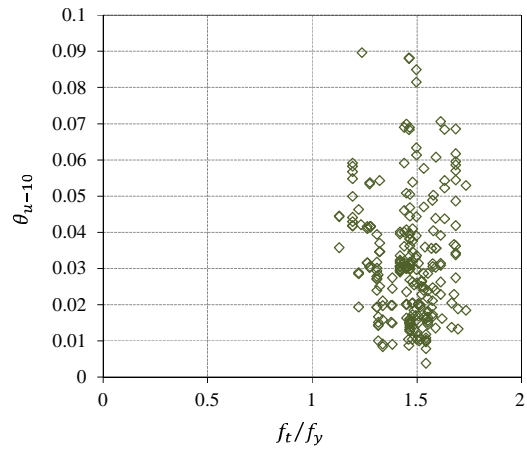


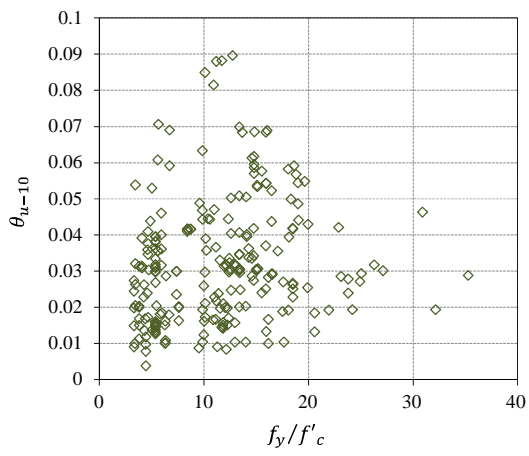
Figure G-2. Scatter plots showing trends between rotation at maximum force (θ_m) and explanatory variables.



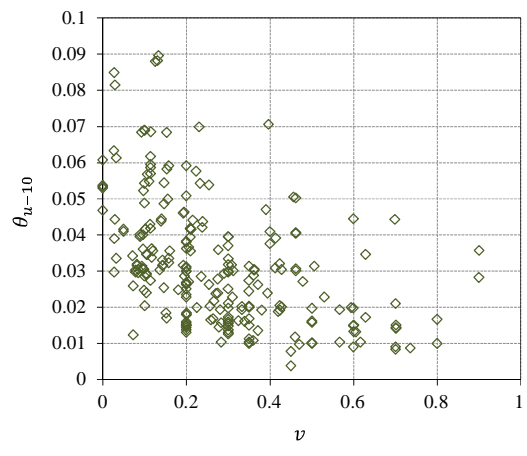
a



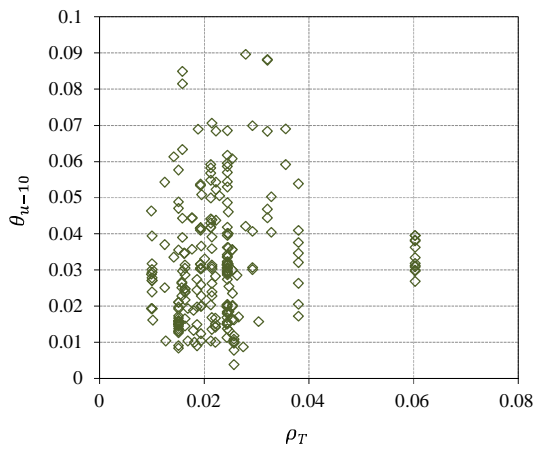
b



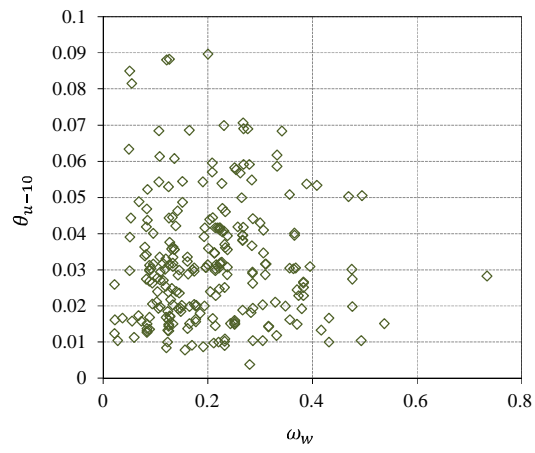
c



d



e



f

Continued ...

...Continued

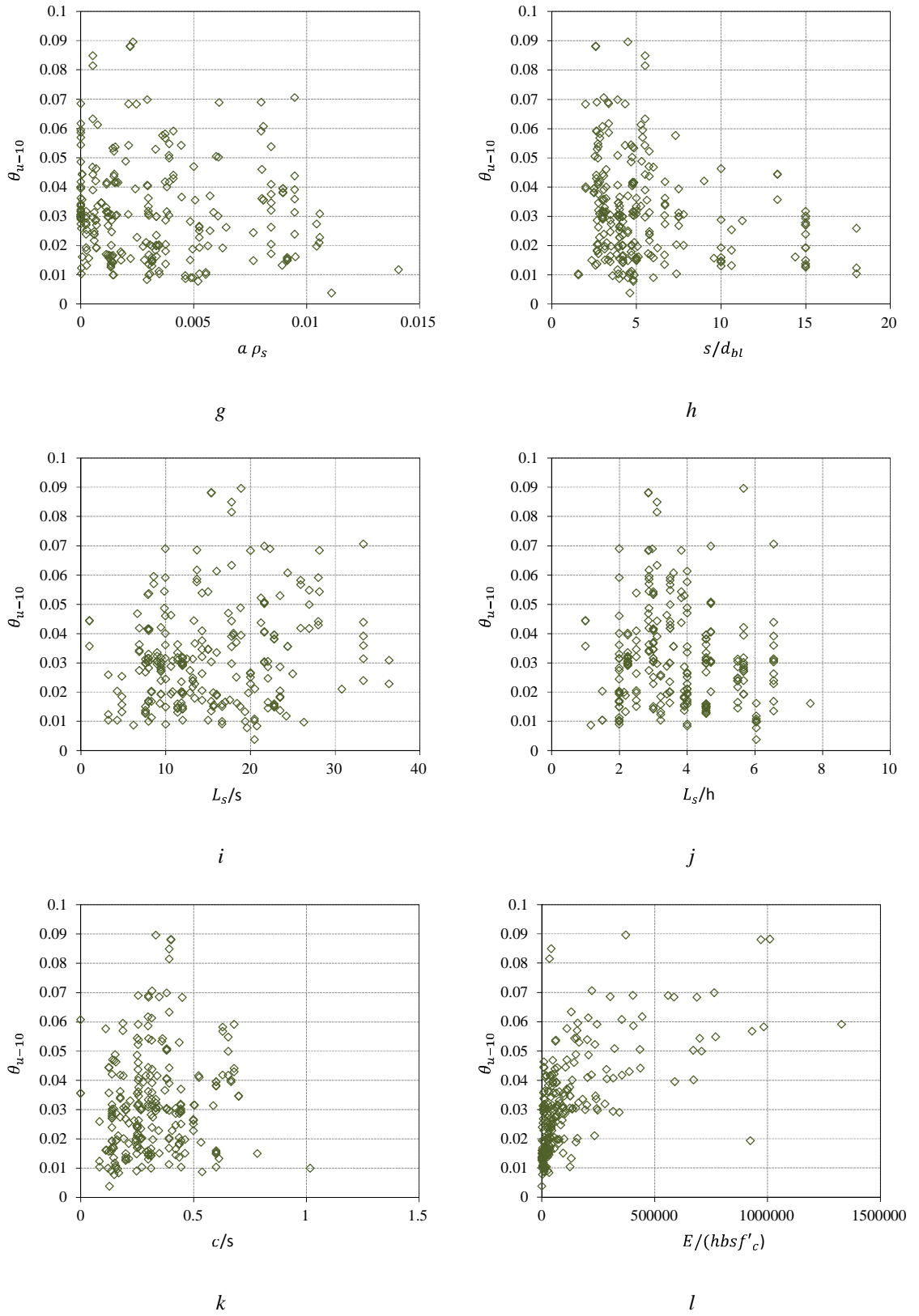
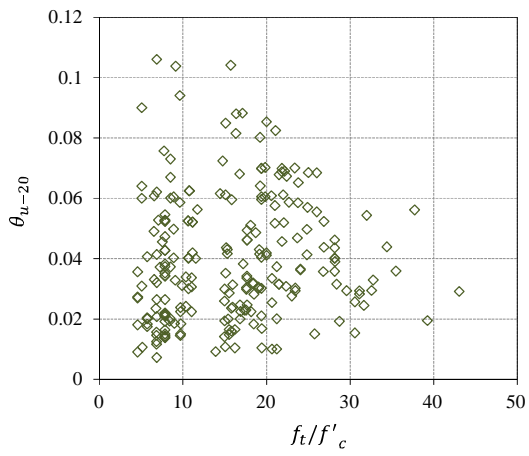
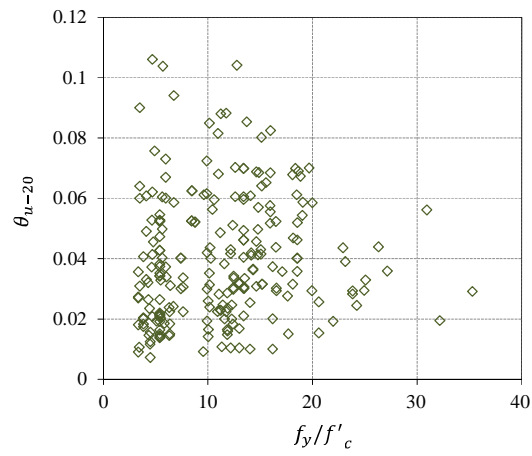


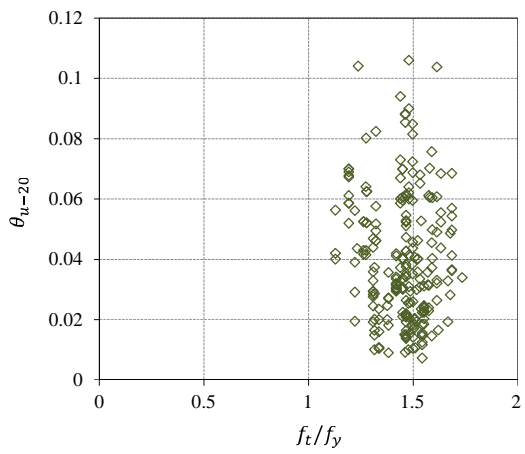
Figure G-3. Scatter plots showing trends between rotation at 10% maximum force reduction (θ_{u-10}) and explanatory variables.



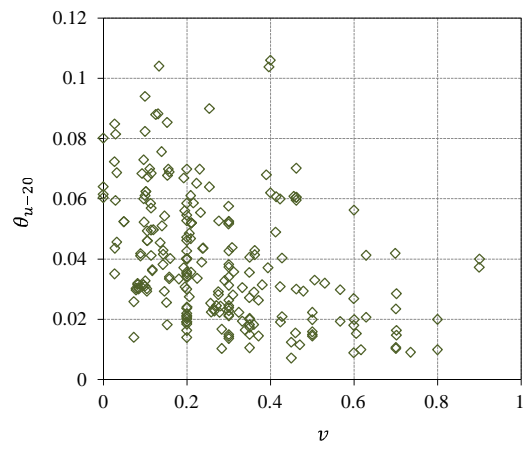
a



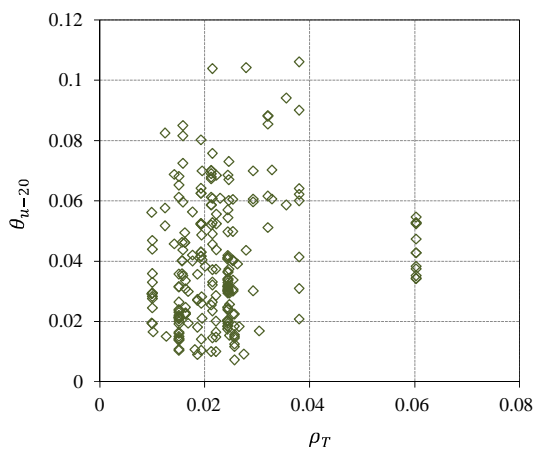
b



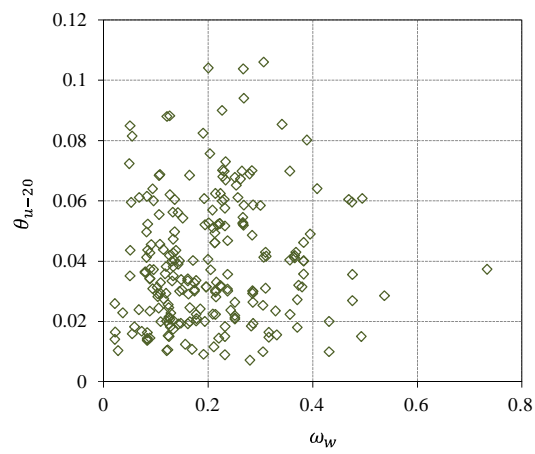
c



d



e



f

Continued ...

...Continued

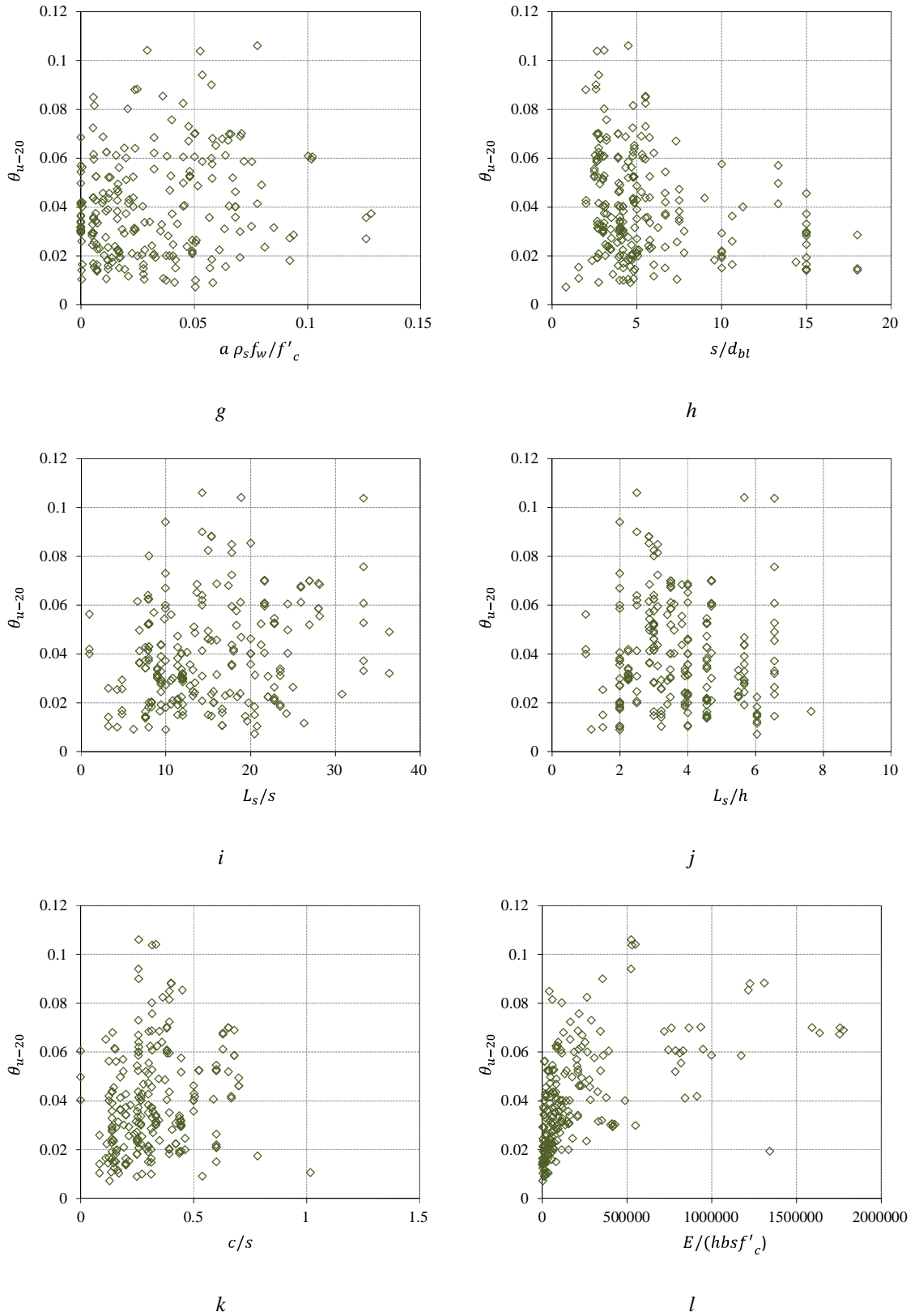
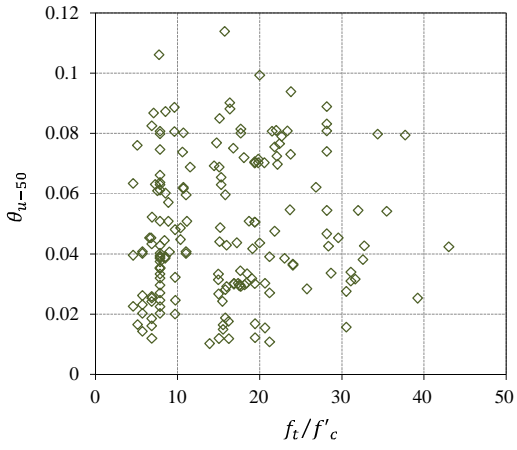
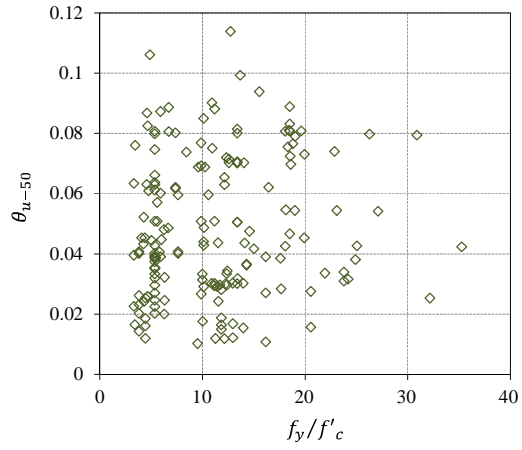


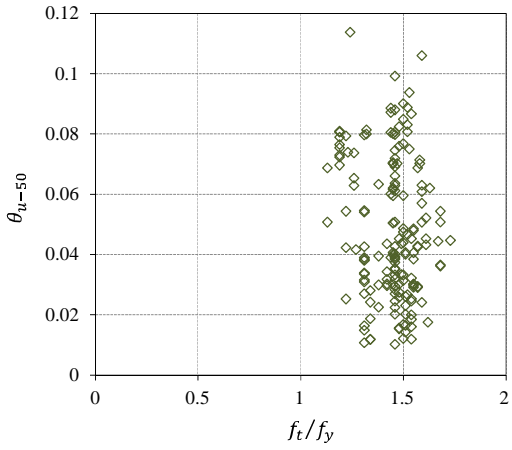
Figure G-4. Scatter plots showing trends between rotation at 20% maximum force reduction (θ_{u-20}) and explanatory variables.



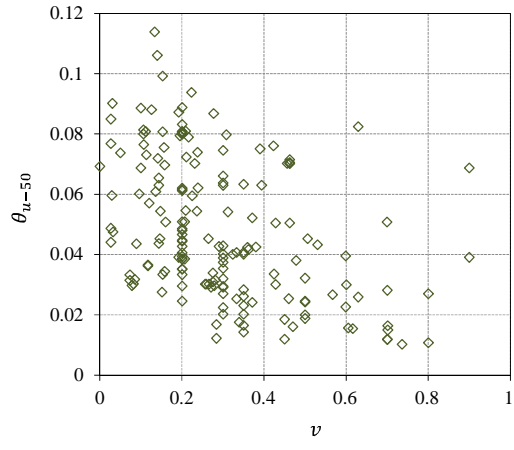
a



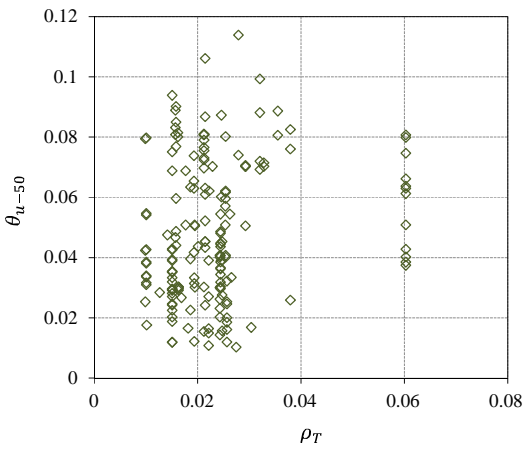
b



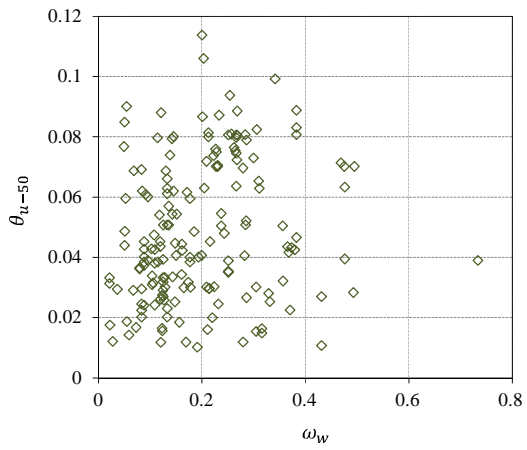
c



d



e



f

Continued ...

...Continued

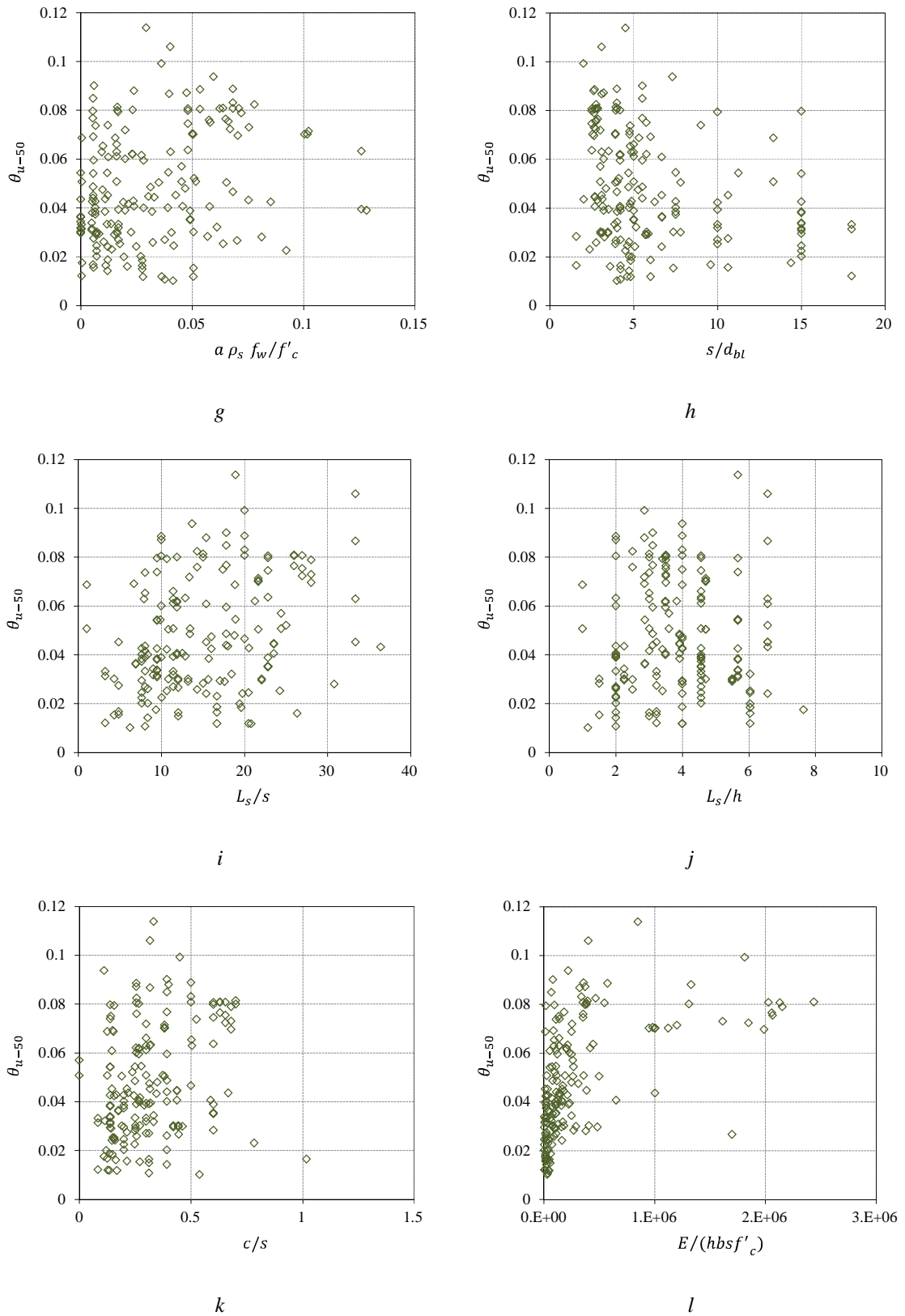


Figure G-5. Scatter plots showing trends between rotation at 50% maximum force reduction (θ_{u-50}) and explanatory variables.

G.2 Scatter-plots of Explanatory Variables with Stiffness Ratio (EI_{dmg}/EI_g).

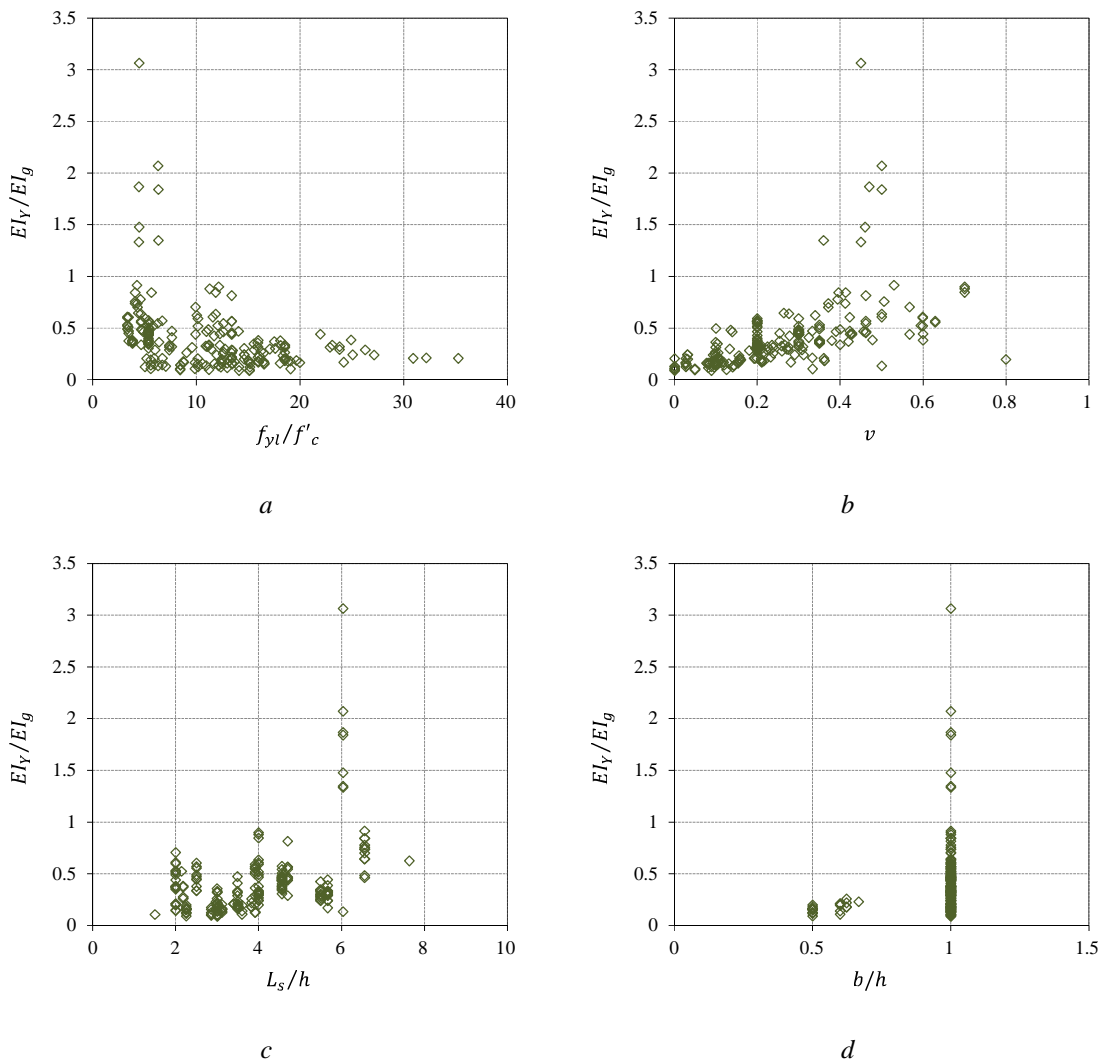


Figure G-6. Scatter plots showing trends between the stiffness ratio at yielding (EI_Y/EI_g) and explanatory variables.

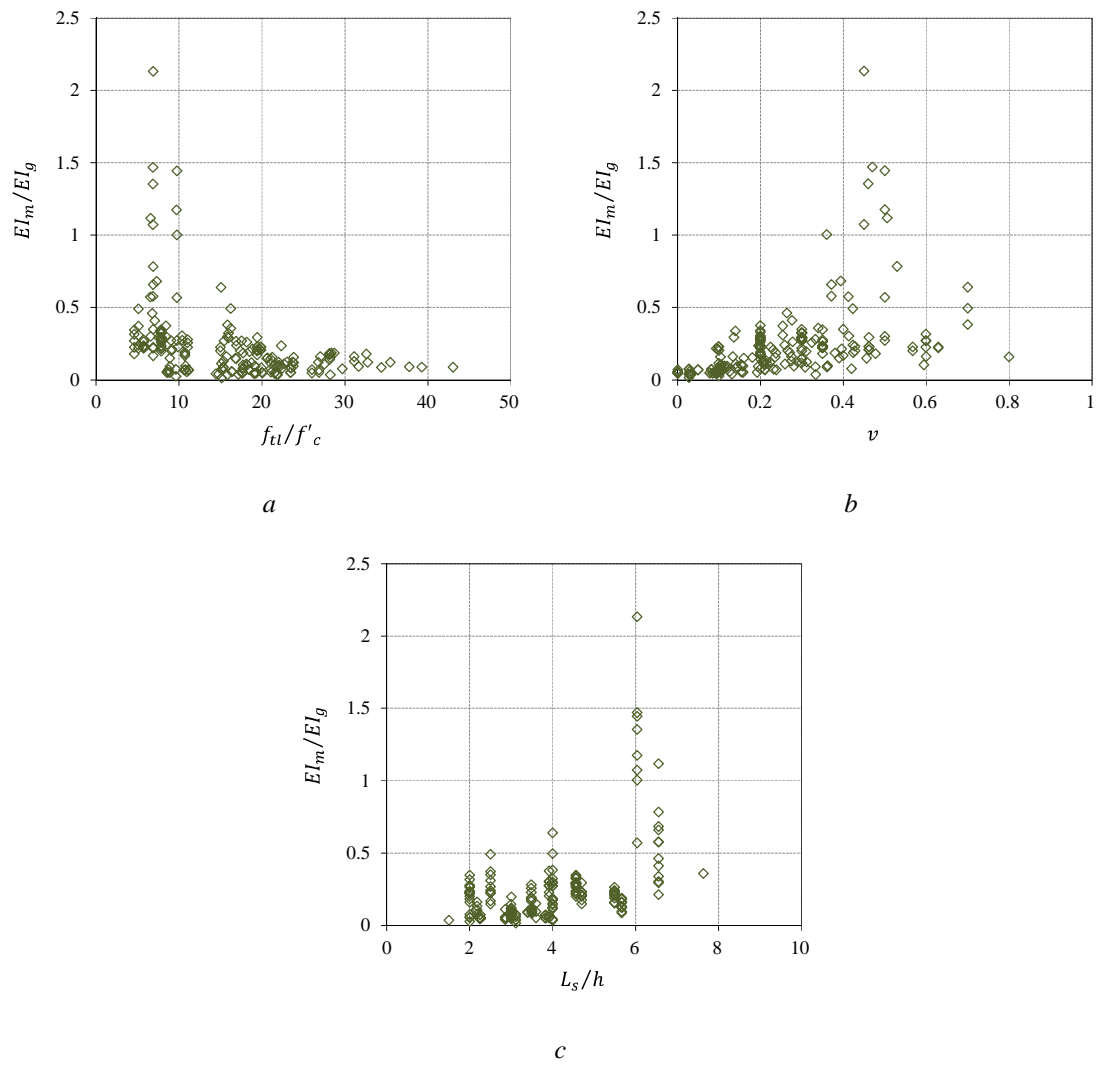
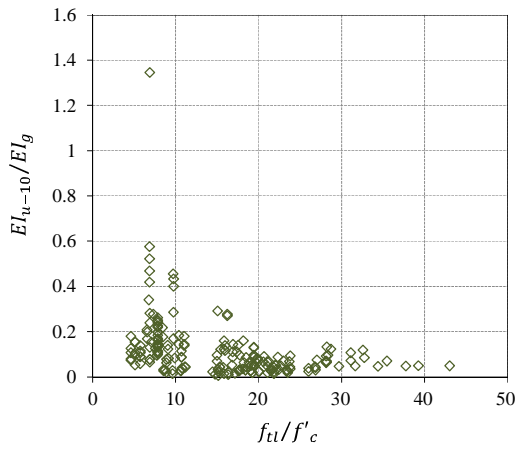
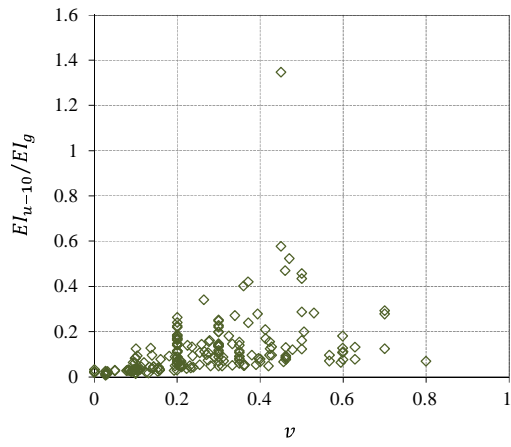


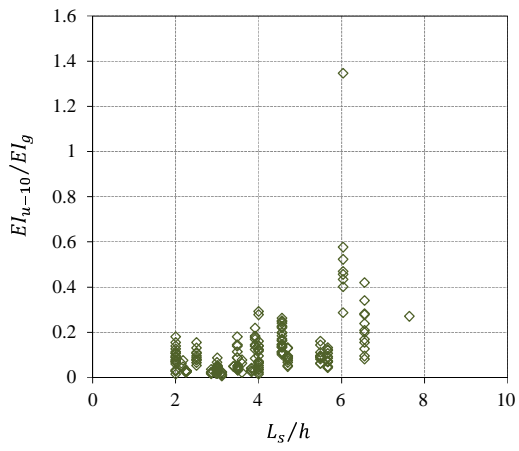
Figure G-7. Scatter plots showing trends between the stiffness ratio at maximum force (EI_m/EI_g) and explanatory variables.



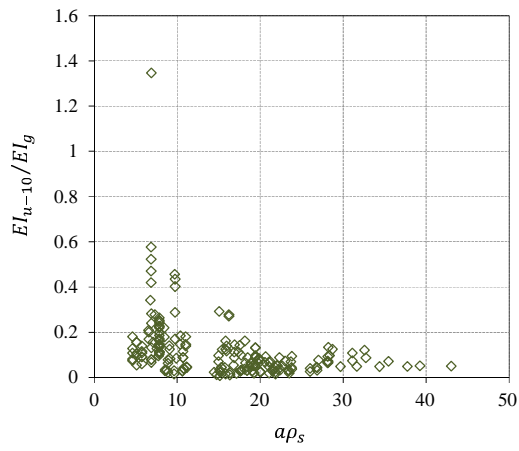
a



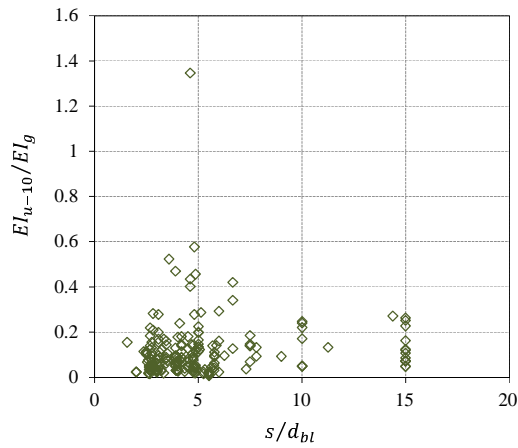
b



c

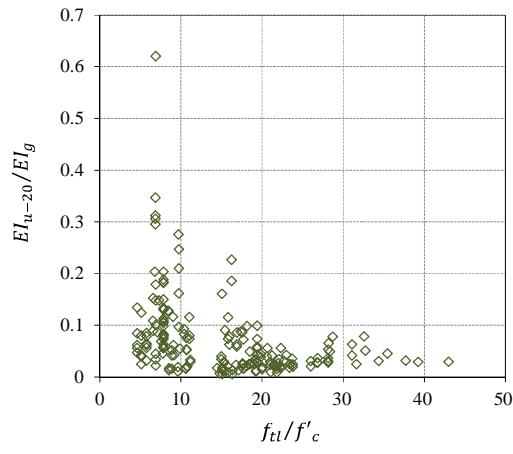


d

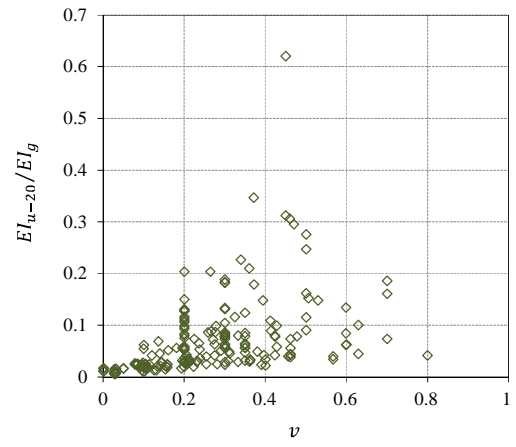


e

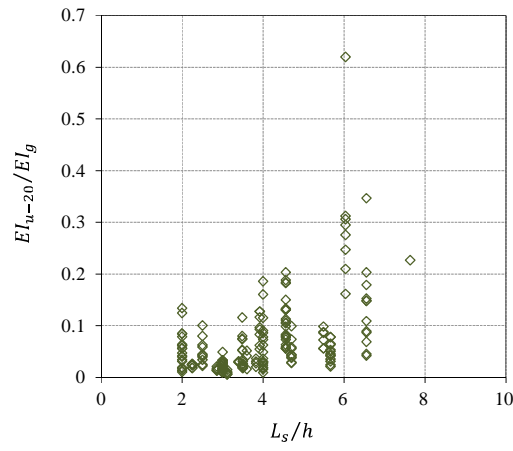
Figure G-8. Scatter plots showing trends between the stiffness ratio at 10% reduction of maximum force (EI_{u-10}/EI_g) and explanatory variables.



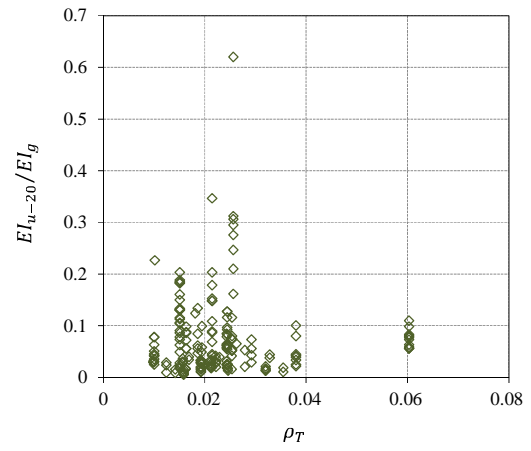
a



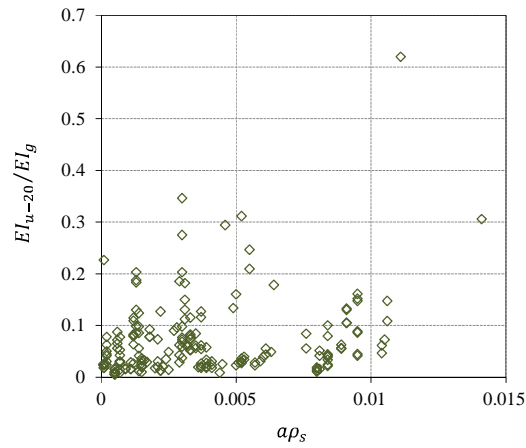
b



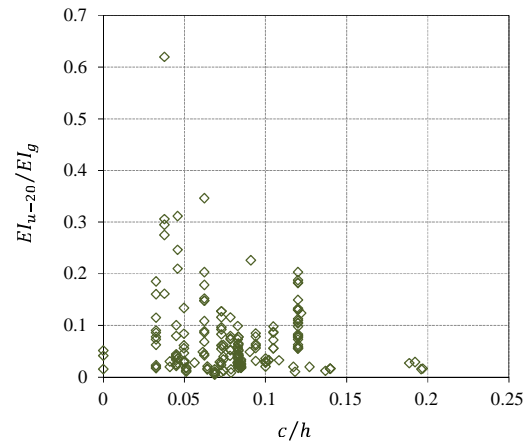
c



d

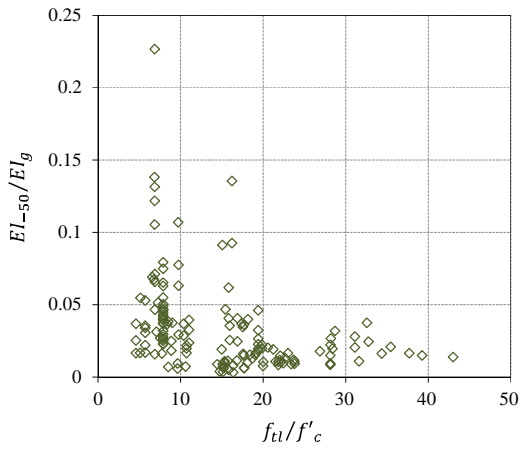


e

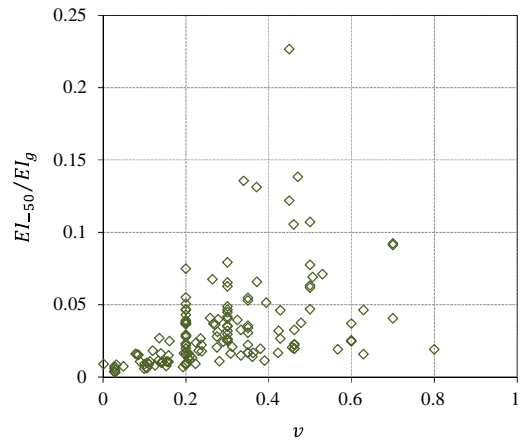


f

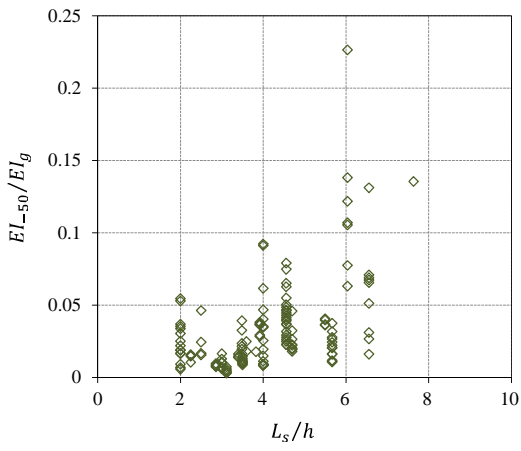
Figure G-9. Scatter plots showing trends between the stiffness ratio at 20% reduction of maximum force (EI_{u-20}/EI_g) and explanatory variables.



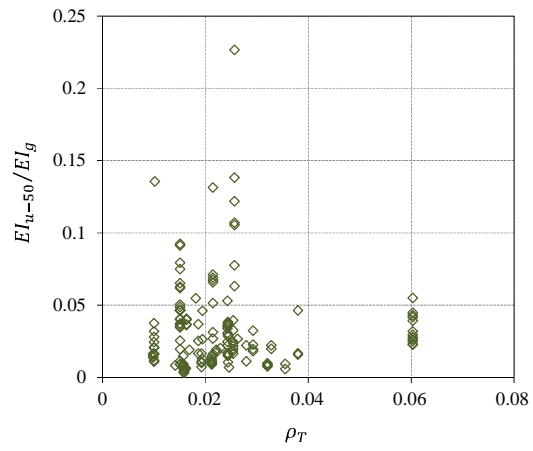
a



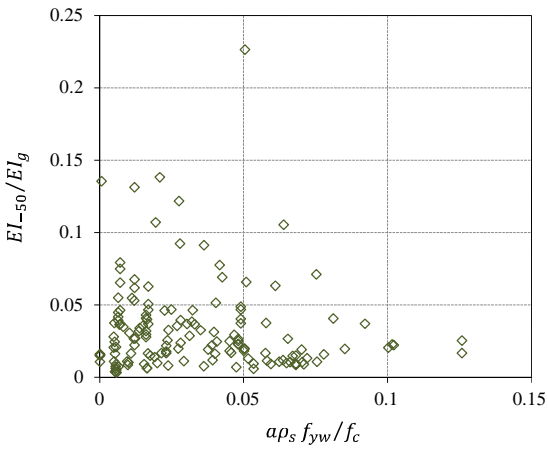
b



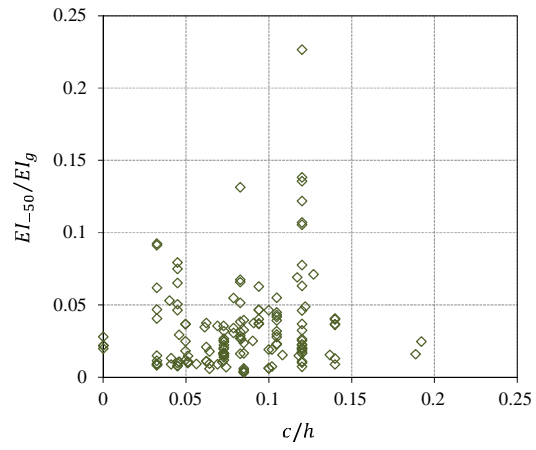
c



d



e



f

Figure G-10. Scatter plots showing trends between the stiffness ratio at 50% reduction of maximum force (EI_{u-50}/EI_g) and explanatory variables.

Appendix H Trends between Variables by Isolating Effects of Individual Variables.

H.1 Effects of Individual Explanatory Variables on Rotation (θ_{dmg}).

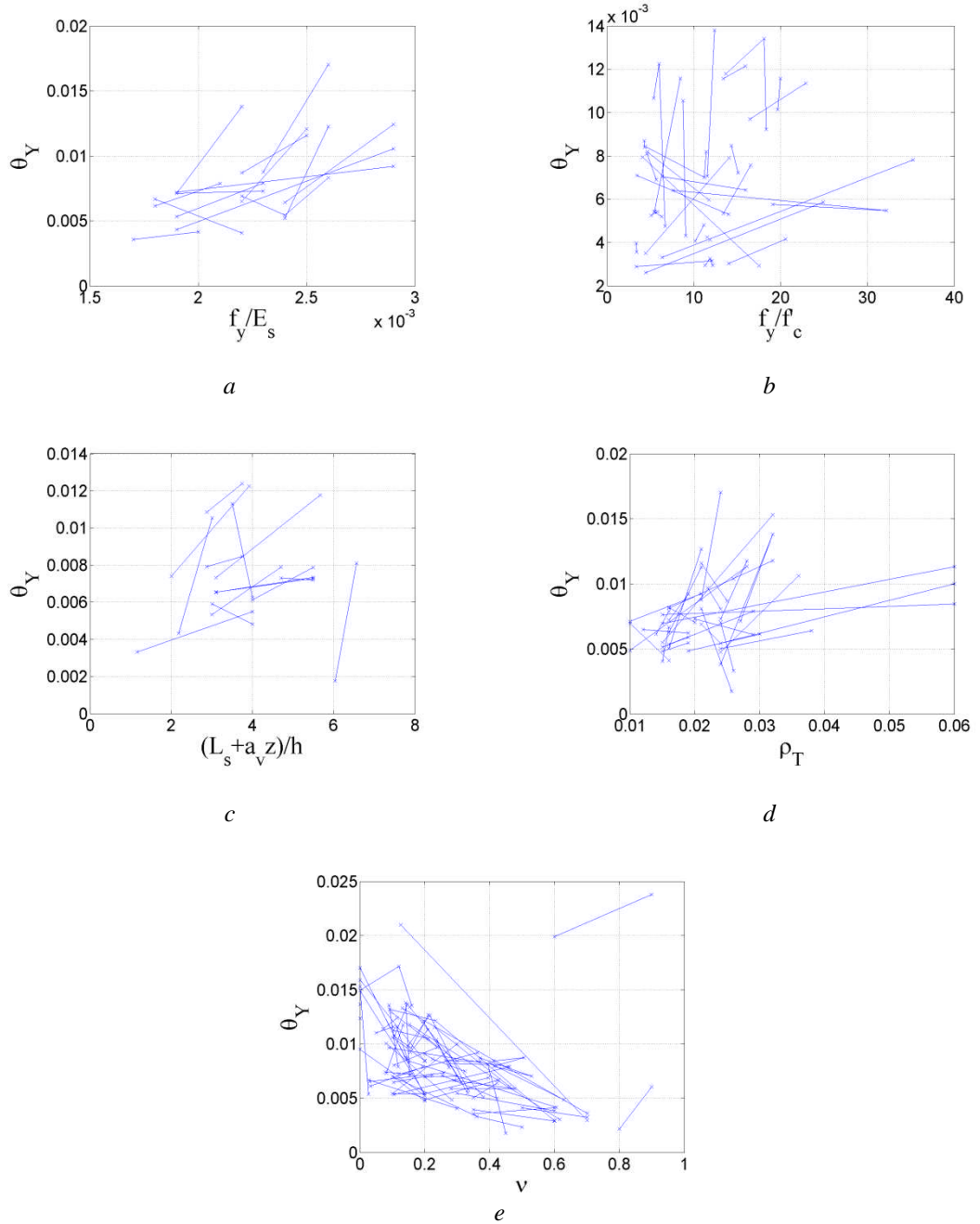
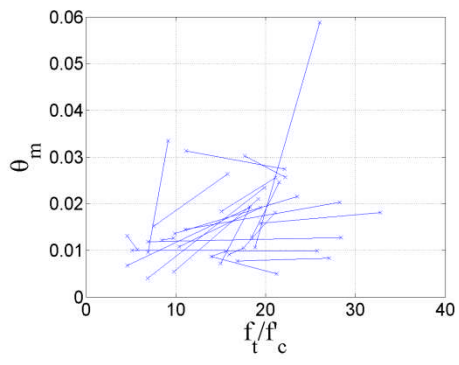
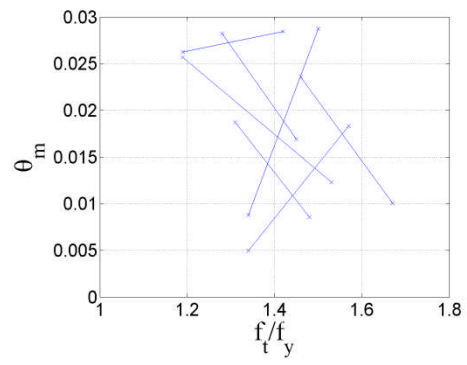


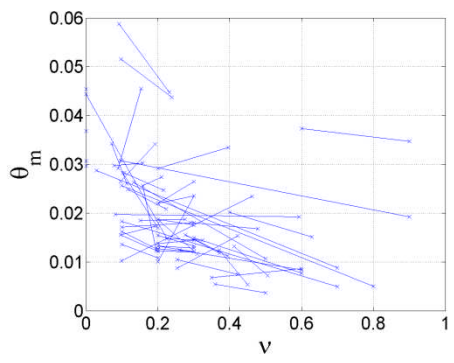
Figure H-1. Plot showing effects of individual variables on yield rotation (θ_Y).



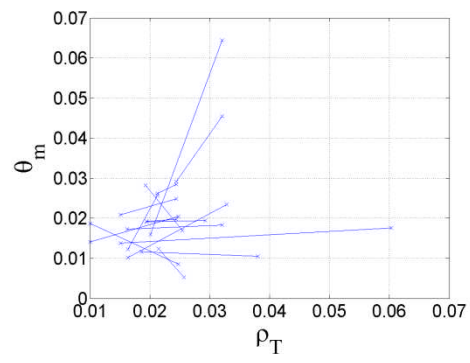
a



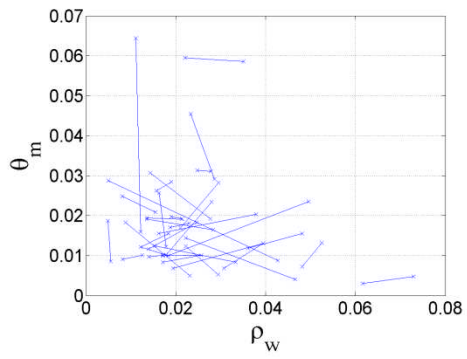
b



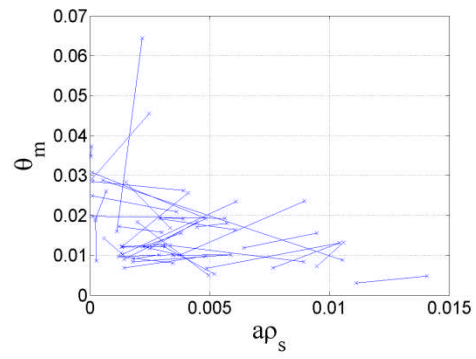
c



d



e



f

...Continued

... Continued

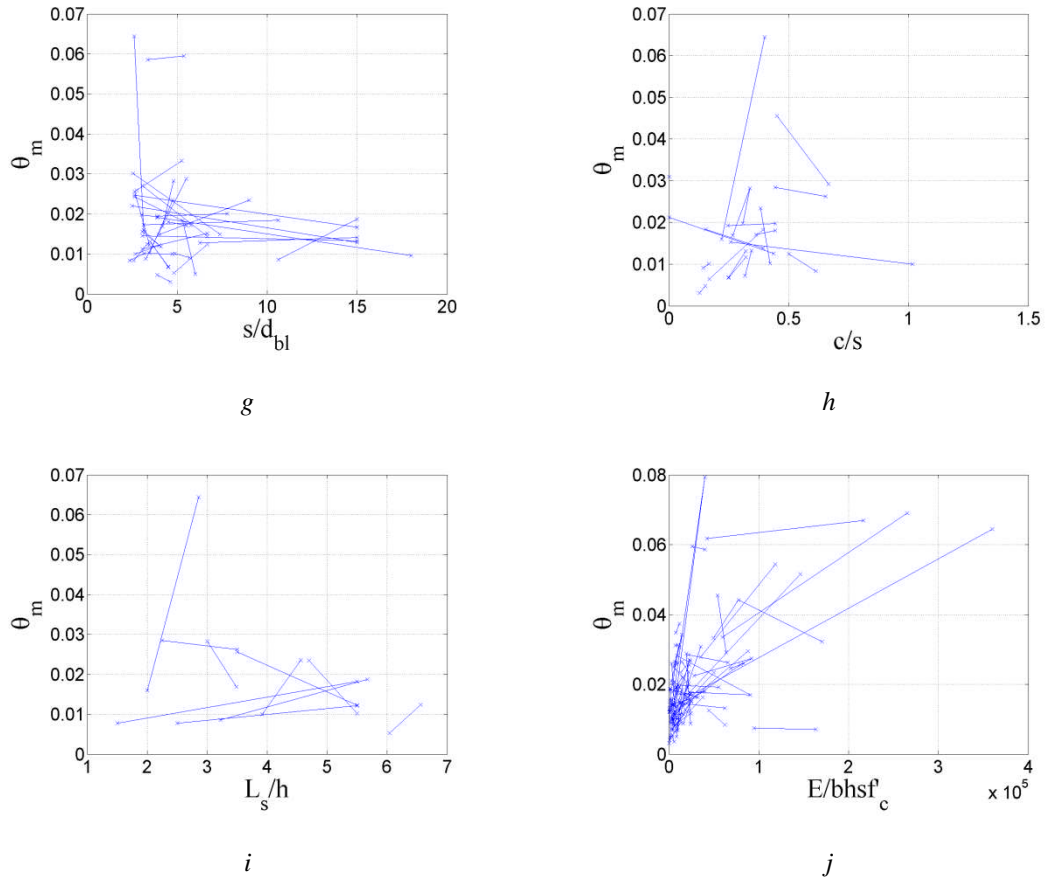
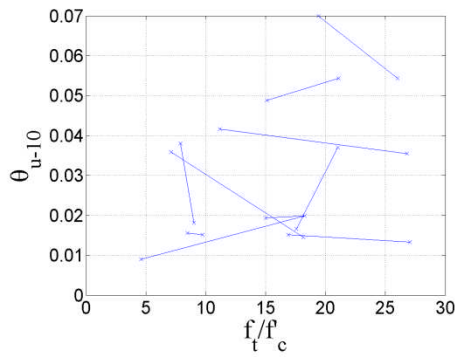
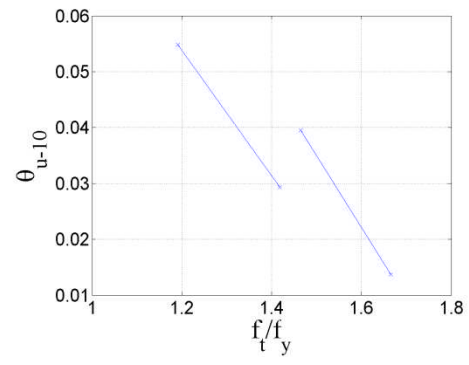


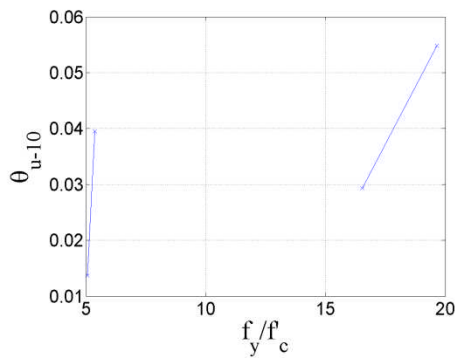
Figure H-2. Plot showing effects of individual variables on rotation at maximum force (θ_m).



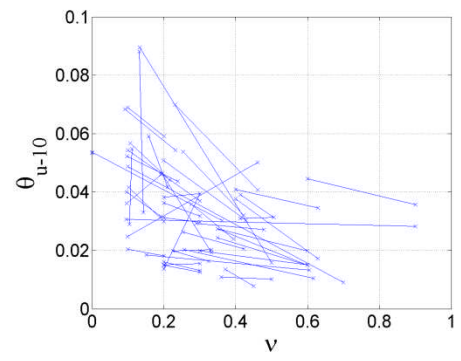
a



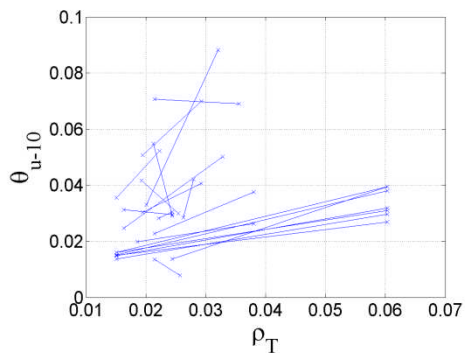
b



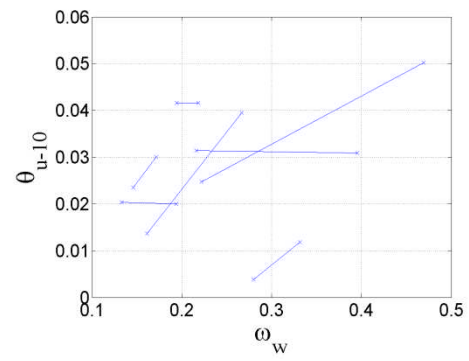
c



d



e



f

Continued...

...Continued

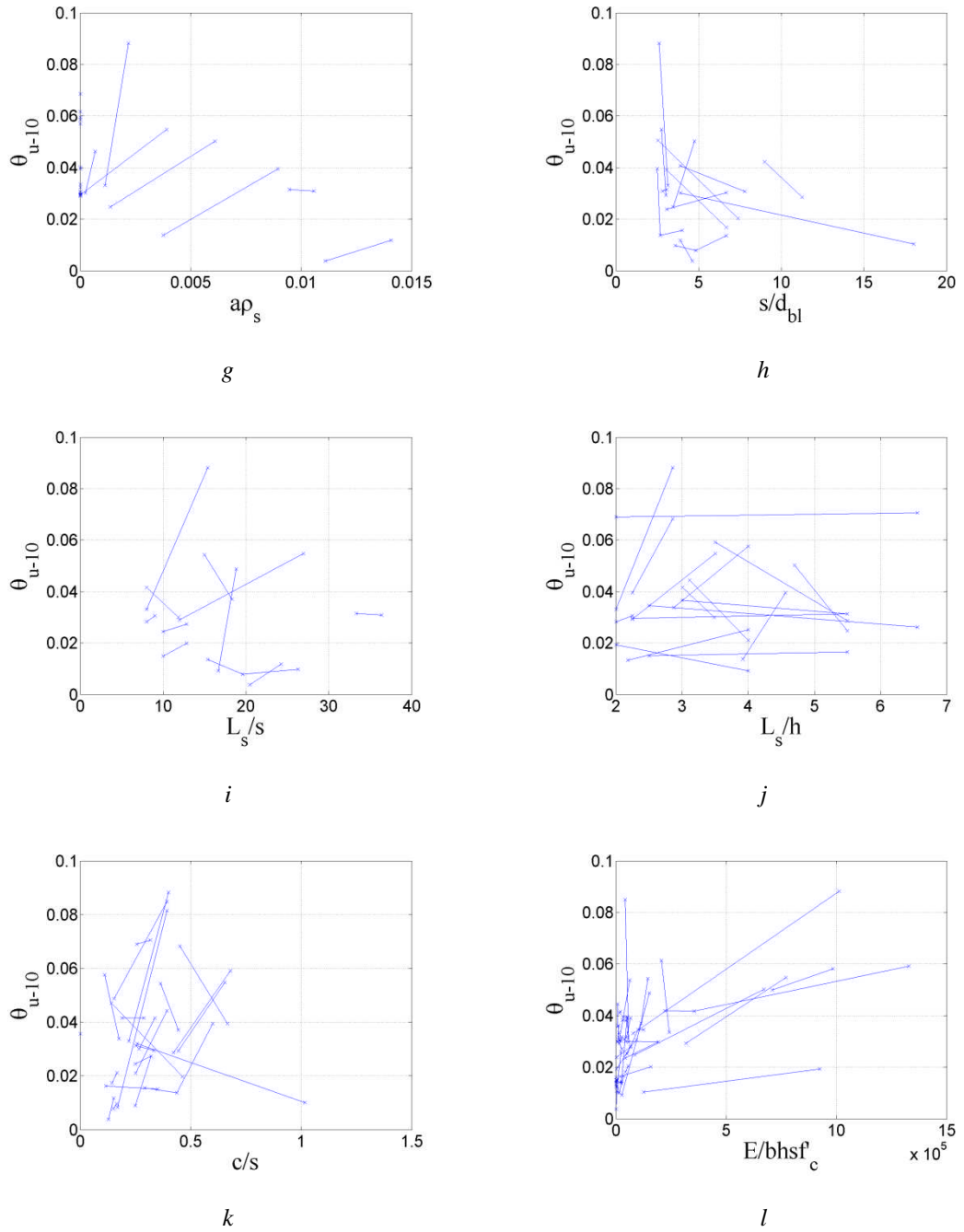
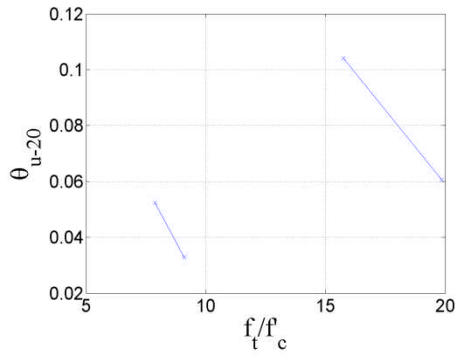
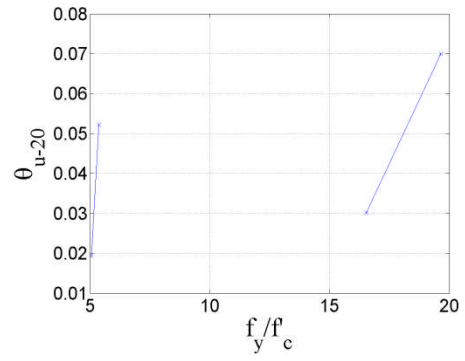


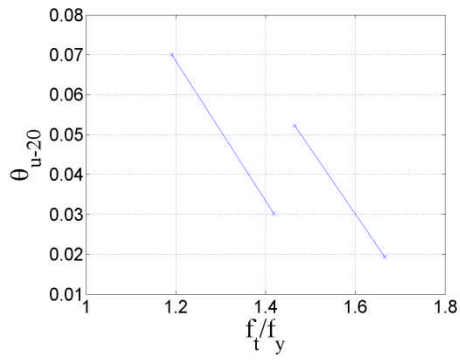
Figure H-3. Plot showing effects of individual variables on rotation at 10% reduction of maximum force (θ_{u-10}).



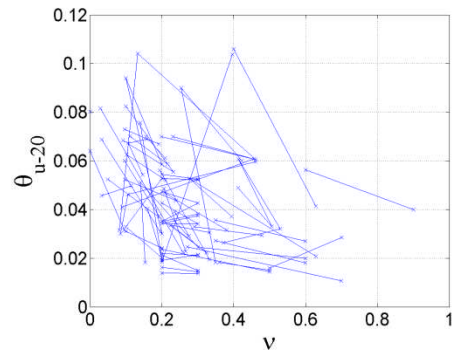
a



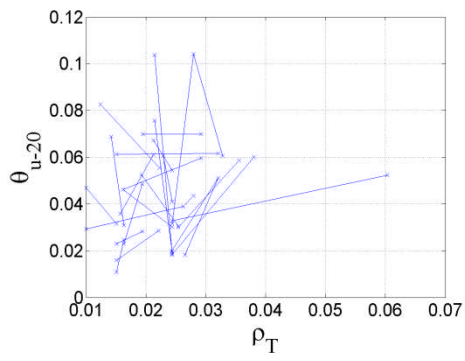
b



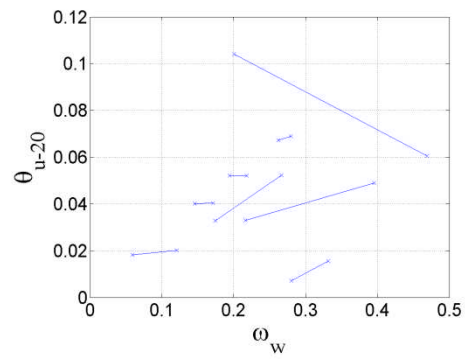
c



d



e



f

...Continued

... Continued

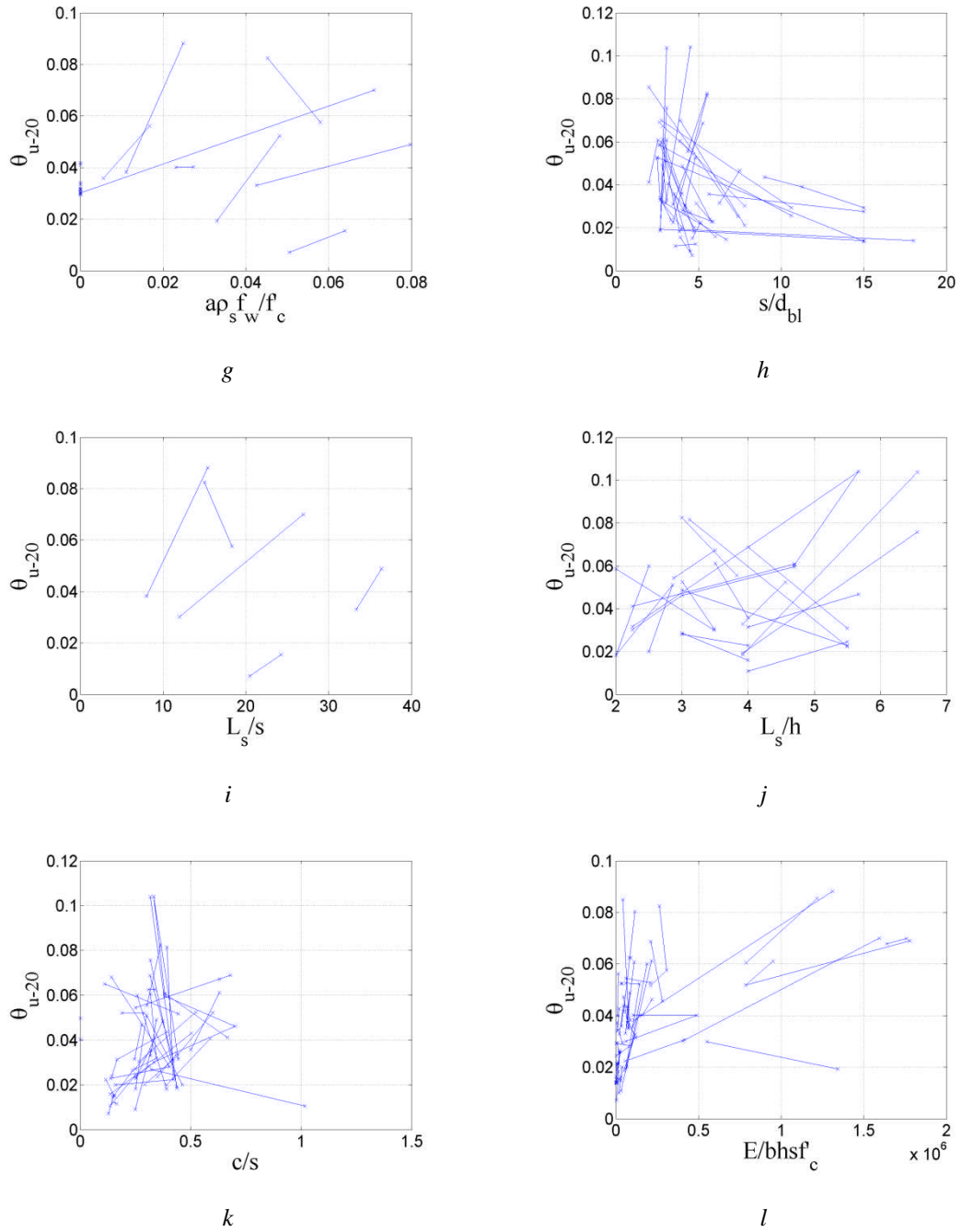
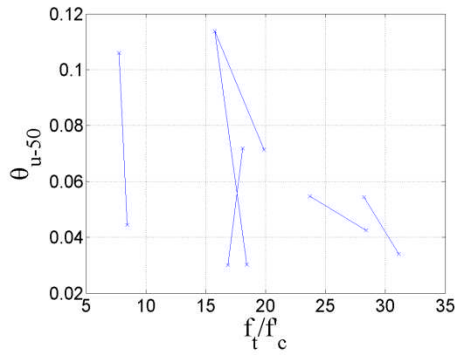
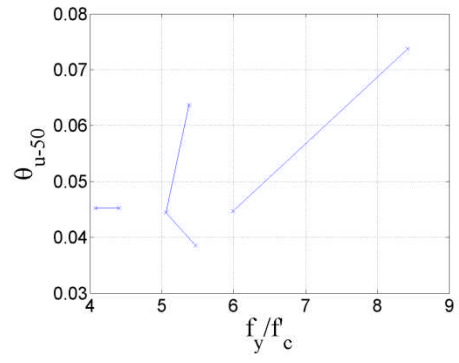


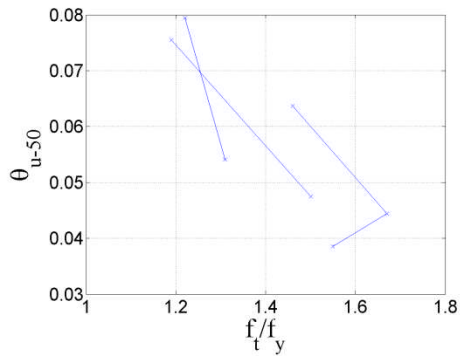
Figure H-4. Plot showing effects of individual variables on rotation at 20% reduction of maximum force (θ_{u-20}).



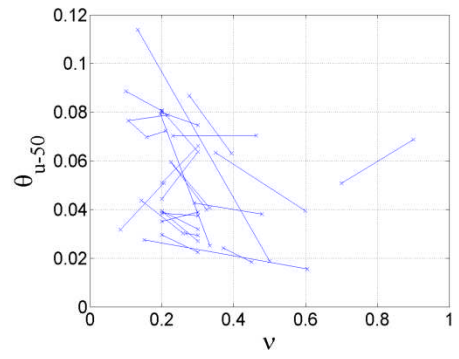
a



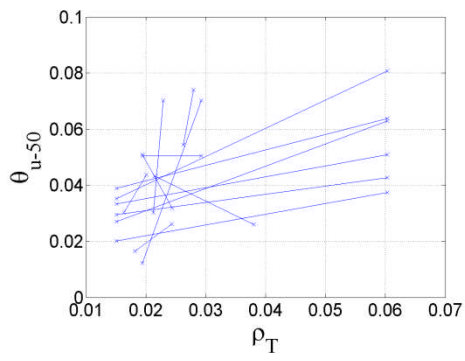
b



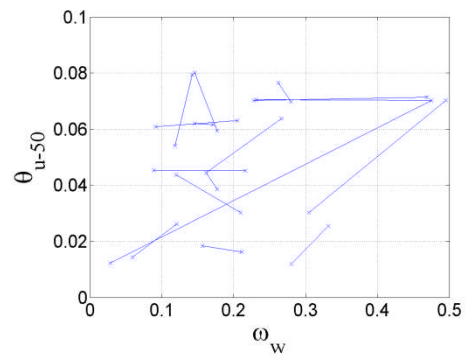
c



d



e



f

...Continued

... Continued

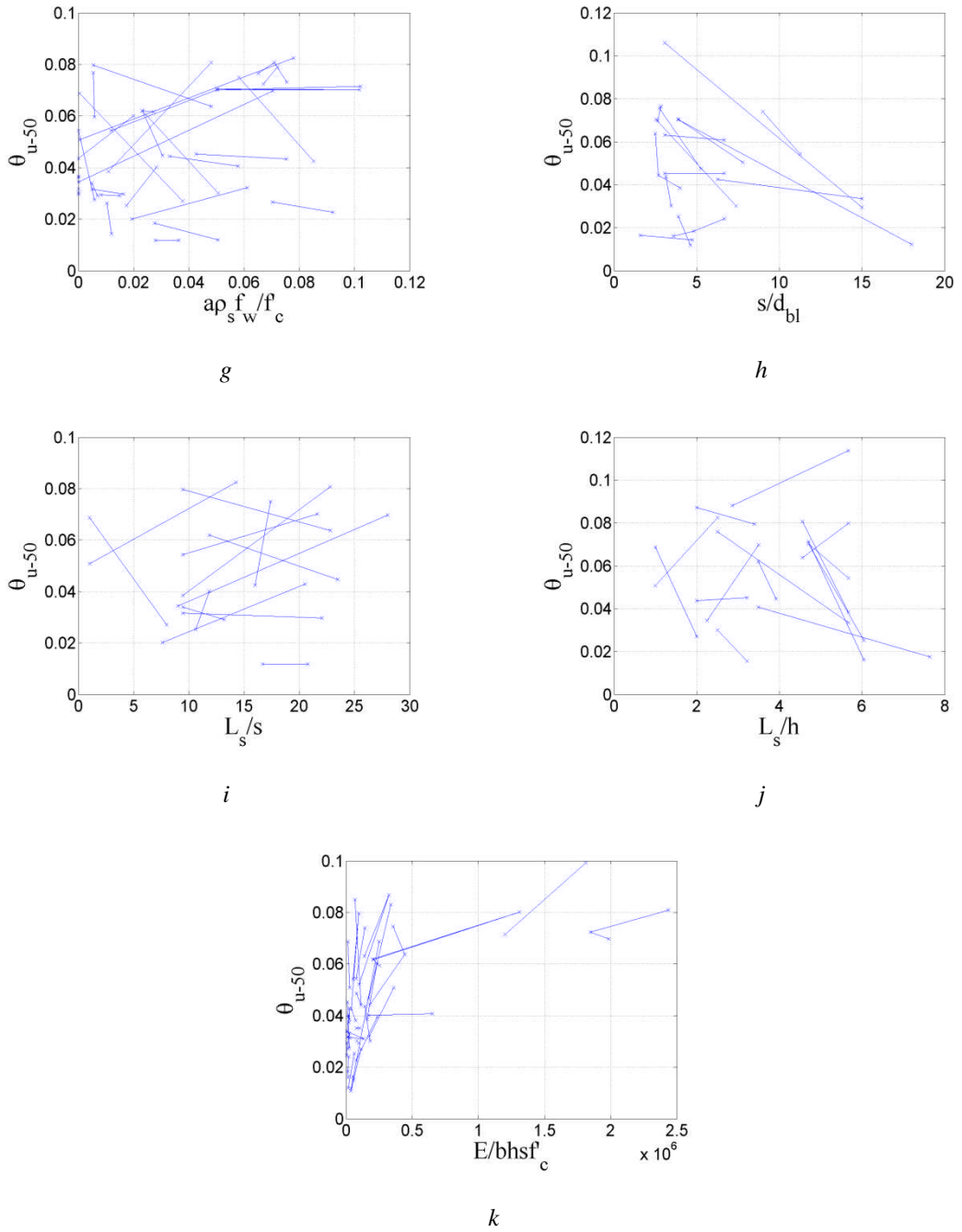


Figure H-5. Plot showing effects of individual variables on rotation at 50% reduction of maximum force (θ_{u-50}).

H.2 Effects of Individual Explanatory Variables on Stiffness Ratio (EI_{dmg}/EI_g).

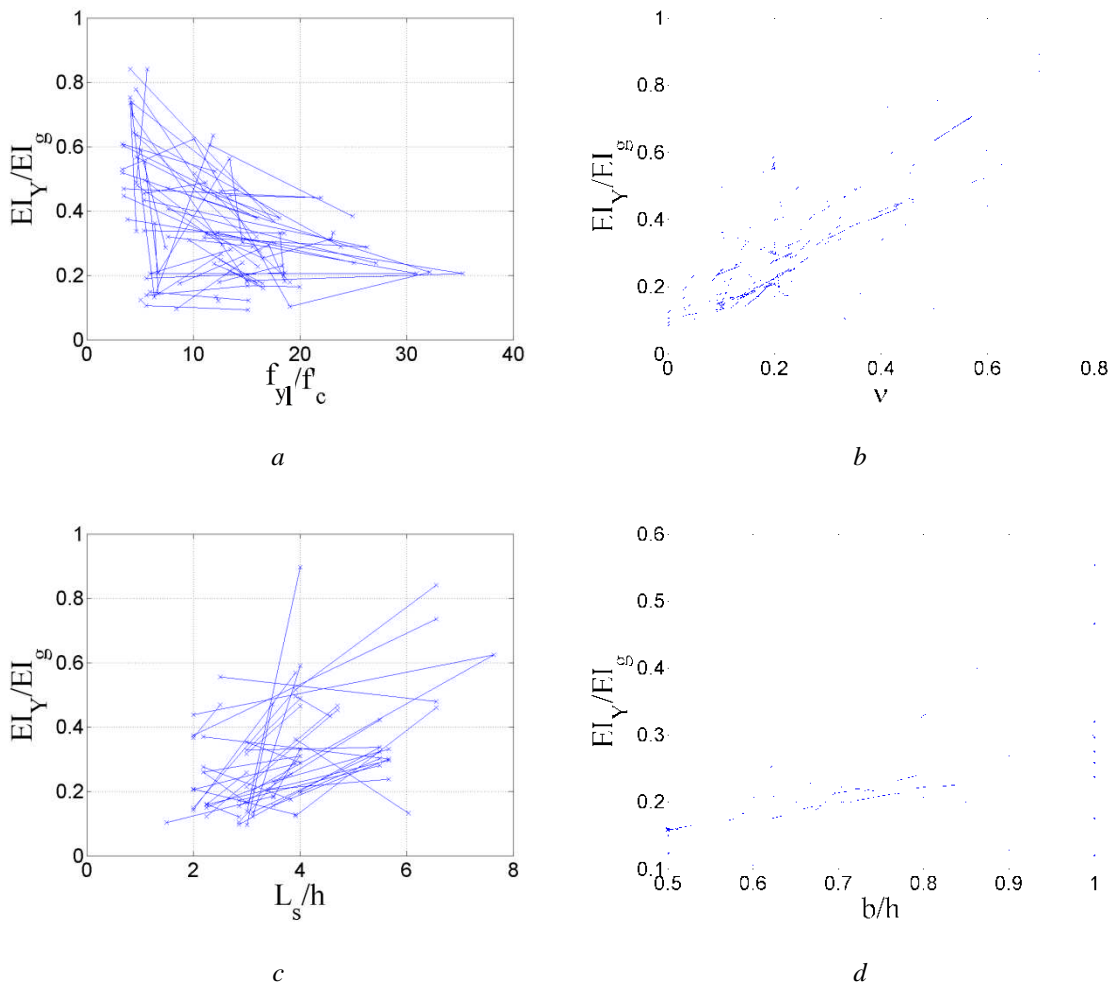
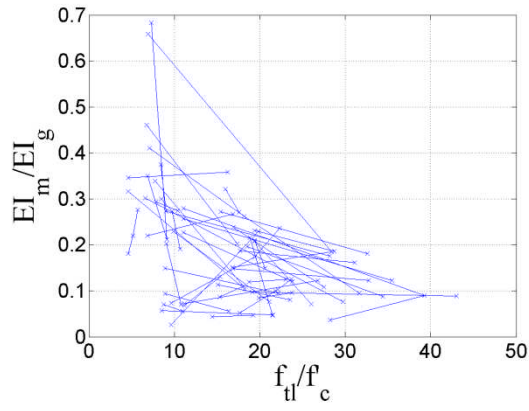
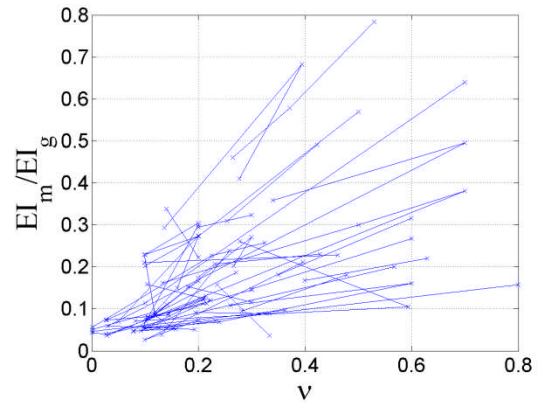


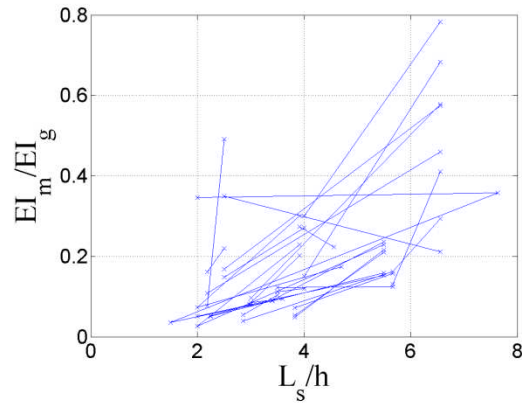
Figure H-6. Plot showing effects of individual variables on stiffness ratio at yield (EI_Y/EI_g).



a

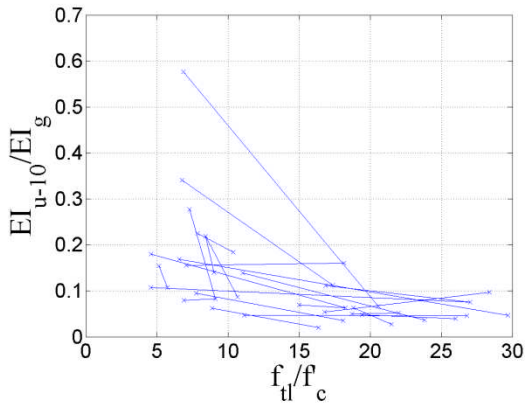


b

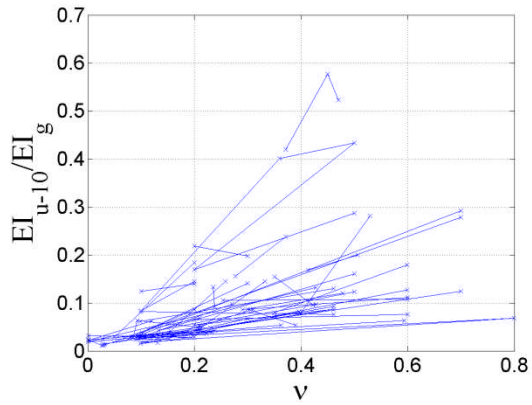


c

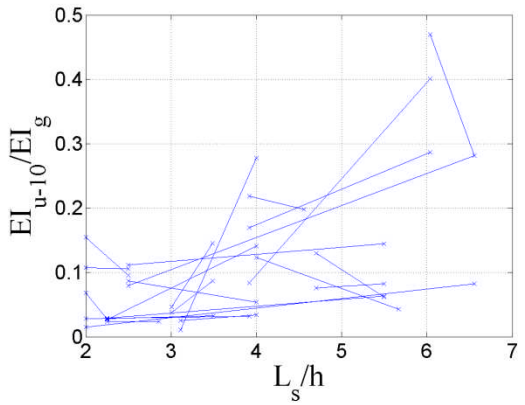
Figure H-7. Plot showing effects of individual variables on stiffness ratio at maximum force (EI_m/EI_g).



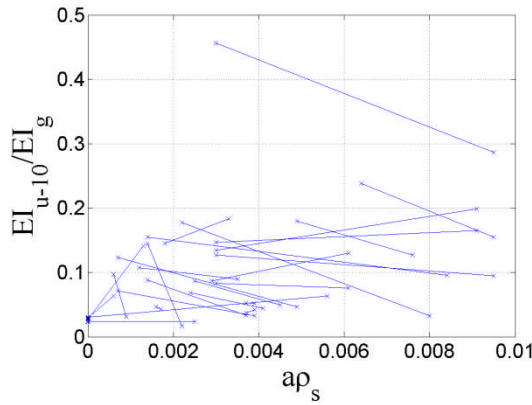
a



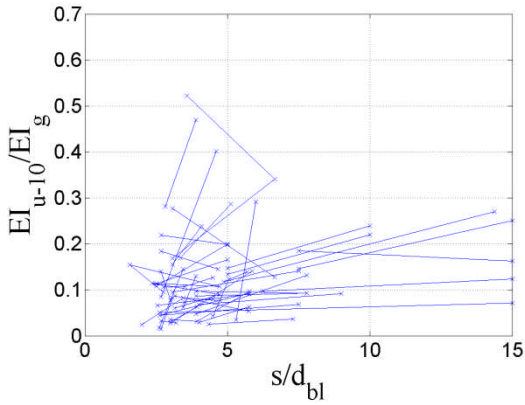
b



c

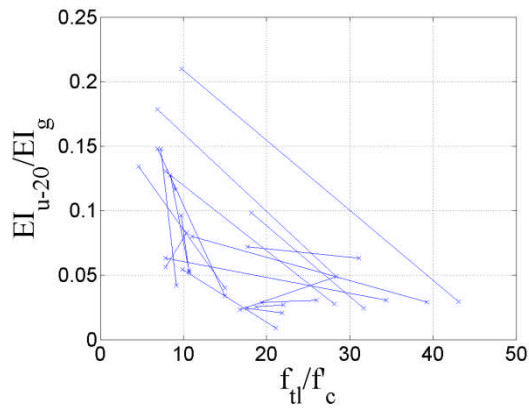


d

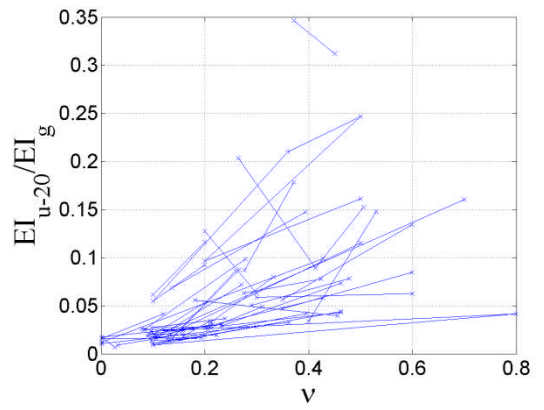


e

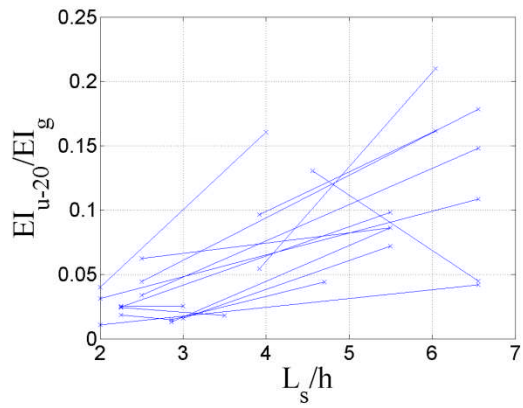
Figure H-8. Plot showing effects of individual variables on stiffness ratio at 10% reduction of maximum force (EI_{u-10}/EI_g).



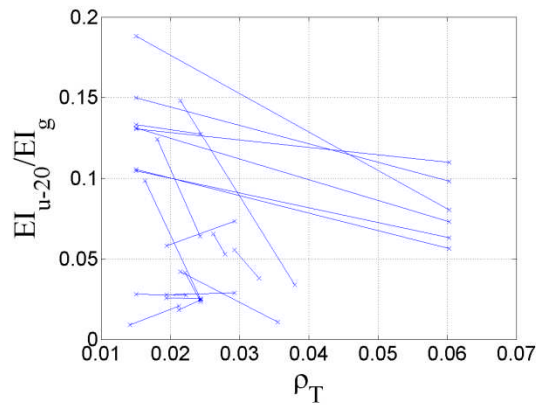
a



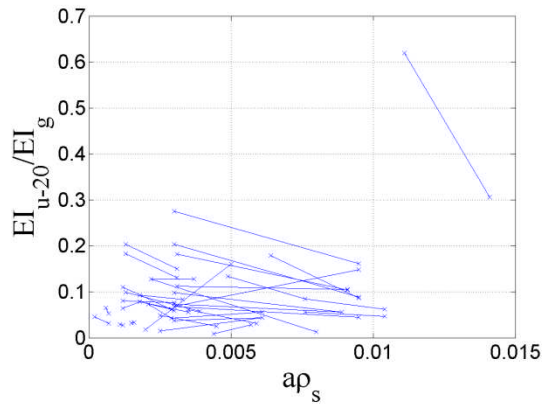
b



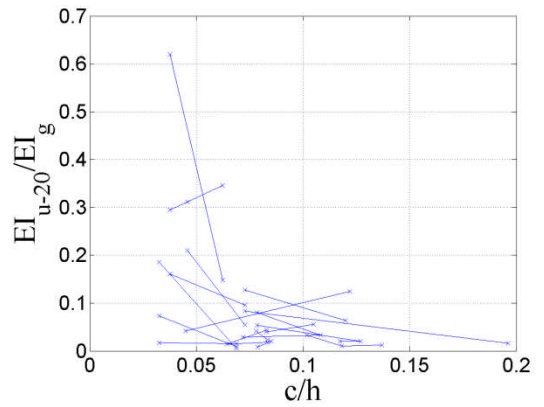
c



d

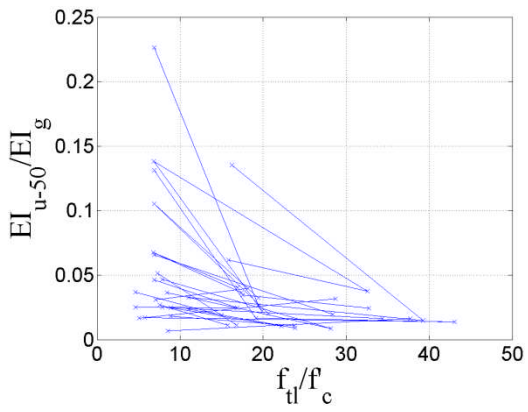


e

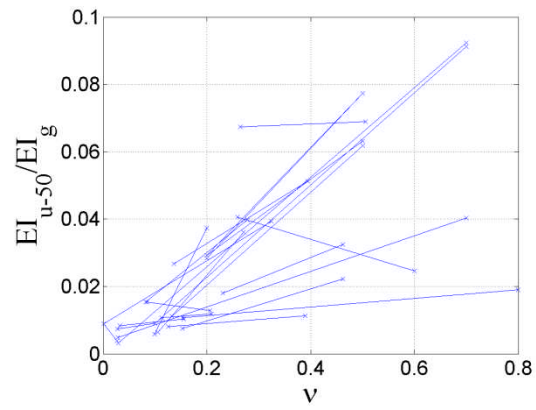


f

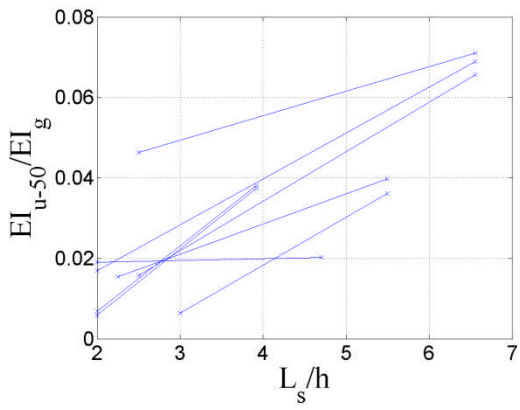
Figure H-9. Plot showing effects of individual variables on stiffness ratio at 20% reduction of maximum force (EI_{u-20}/EI_g).



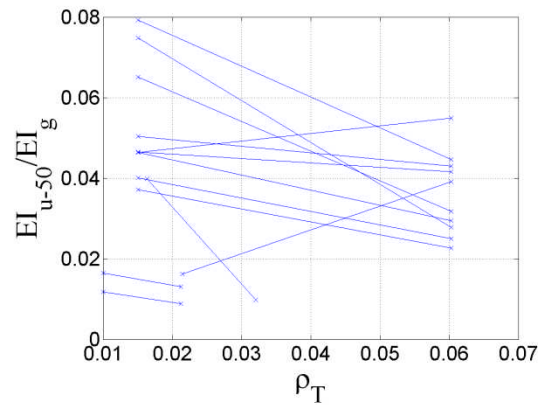
a



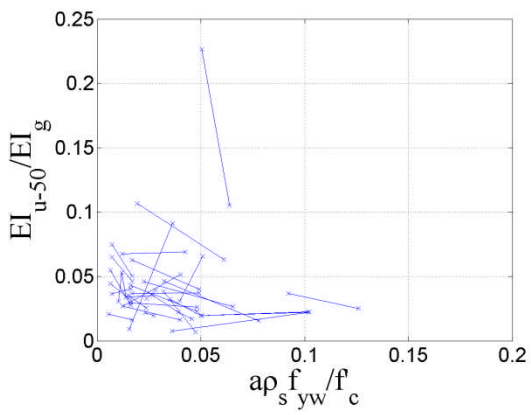
b



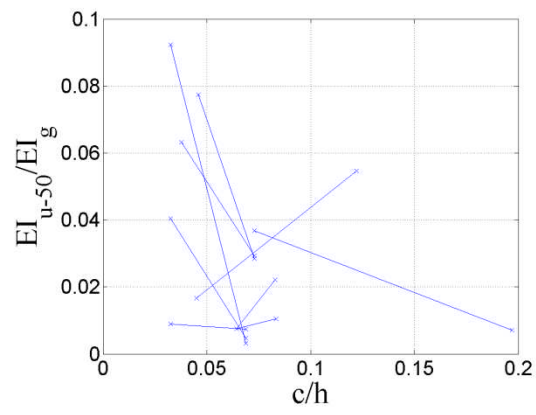
c



d



e



f

Figure H-10. Plot showing effects of individual variables on stiffness ratio at 50% reduction of maximum force (EI_{u-50}/EI_g).

Appendix I Diagnostics of the Statistical Regression Chord Rotation (θ_{dmg}) Models.

I.1 Diagnostics of the Chord Rotation Models at Yielding (θ_y).

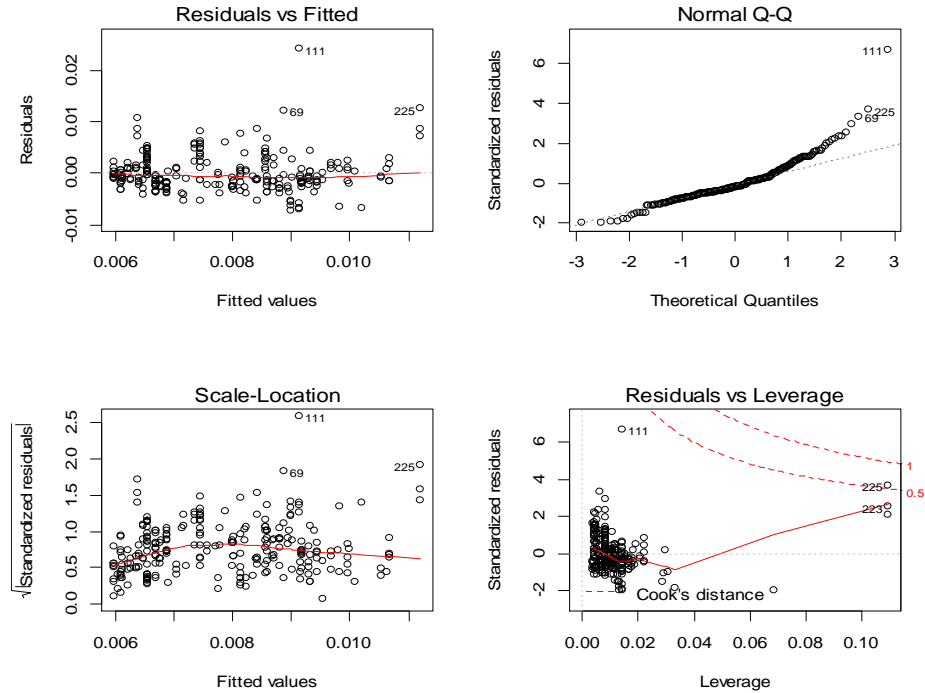


Figure I-1. Diagnostics of the chord rotation at yield (θ_y) regression model based on the semi-empirical form suggested by Biskinis *et al.*, 2010a. Outliers and extreme data-points are included in the regression analysis

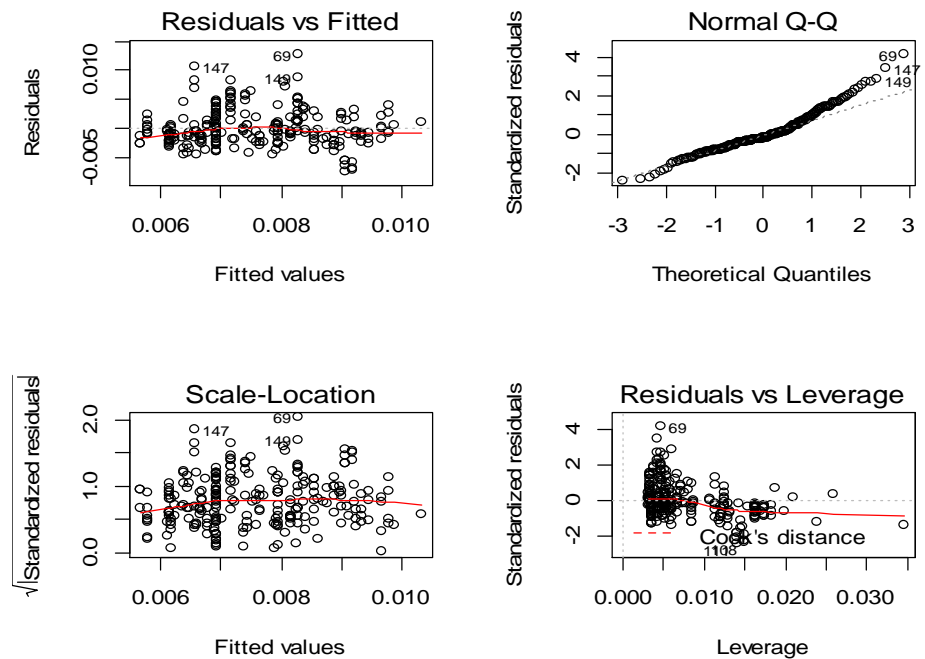


Figure I-2. Diagnostics of the chord rotation at yield (θ_y) regression model based on the semi-empirical form suggested by Biskinis *et al.*, 2010a. Outliers and extreme data-points are excluded from the regression analysis.

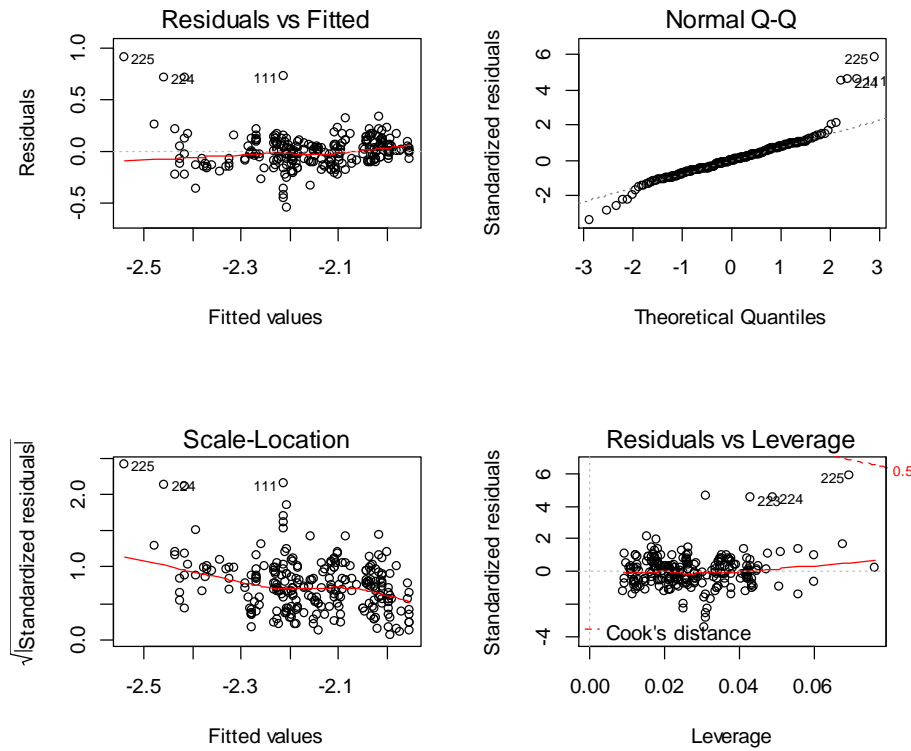


Figure I-3. Diagnostics of the chord rotation at yield (θ_y) regression model based on explanatory variables in literature or obtained from dimensional analysis. Outliers and extreme data-points are included in the regression analysis.

Table I-1. Diagnostics of the yield chord rotation (θ_y) model. Data includes all outliers and extreme values of variables.

Parameter	Estimate Coefficient	Standard Error	t-value	P(> t)
a_{sl}	0.736905	0.585868	1.258	0.20965
$\log(f_y/E_s)$	0.279010	0.220595	1.265	0.20713
f_y/f_c	0.006677	0.002006	3.328	0.00101
$\log \rho_T$	0.454646	0.07196	6.318	1.22E-09
v	-0.41043	0.058313	-7.038	1.90E-11
$(L_s + a_v z)/h$	0.009691	0.008388	1.155	0.24908
$a_{sl} \log(f_y/E_s)$	0.523943	0.042428	12.349	2.00E-16
Notes:	Residual standard error: 0.163 on 248 degrees of freedom Multiple R-squared: 0.7845, F-statistic: 6379 on 7 and 248 DF, p-value: < 2.2e-16			

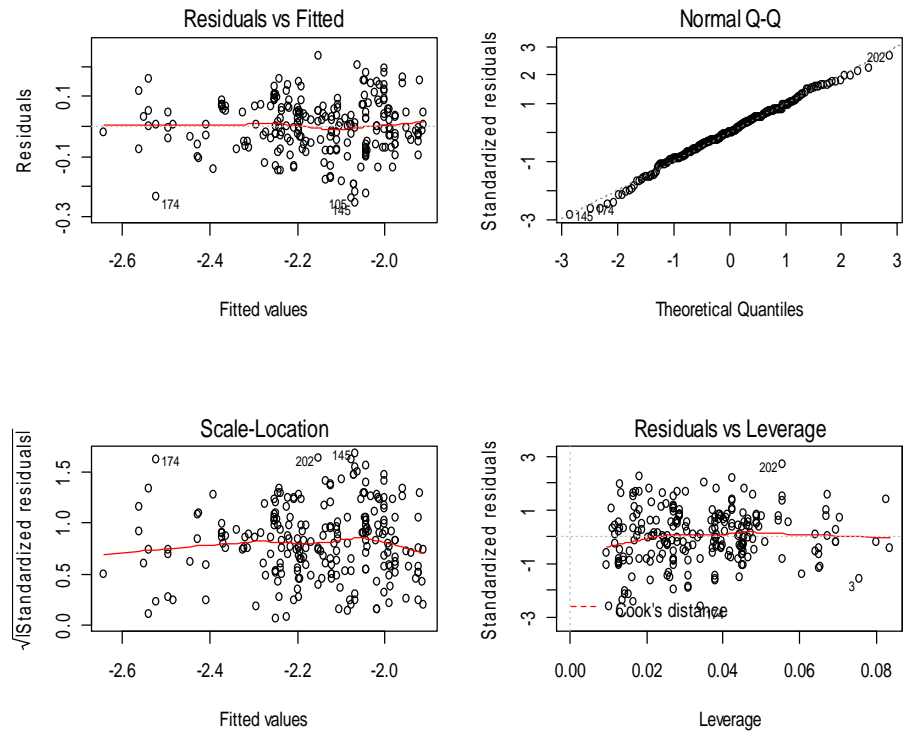


Figure I-4. Diagnostics of the chord rotation at yield (θ_y) regression model based on explanatory variables in literature or obtained from dimensional analysis. Outliers and extreme data-points are excluded from the regression analysis.

Table I-2. Diagnostics of the yield chord rotation (θ_y) model with variables obtained from dimensional analysis. Data does not include outliers and extreme values of variables.

Parameter	Estimate Coefficient	Standard Error	t-value	P(> t)
a_{sl}	1.996202	0.346048	5.769	2.61E-08
$\log(f_y/E_s)$	0.553849	0.024073	23.007	< 2e-16
f_y/f_c	0.004125	0.001146	3.6	0.000391
$\log\rho_T$	0.457207	0.041052	11.137	< 2e-16
ν	-0.53914	0.036548	-14.751	< 2e-16
$(L_s + a_\nu z)/h$	0.043354	0.005115	8.477	3.02E-15
$a_{sl} \log(f_y/E_s)$	0.748947	0.130414	5.743	2.98E-08
Notes:	Residual standard error: 0.09063 on 226 degrees of freedom			
	Multiple R-squared: 0.8122			
	F-statistic: 1.891e+04 on 7 and 226 DF, p-value: < 2.2e-16			

I.2 Diagnostics of the Chord Rotation Models at Maximum Force (θ_m).

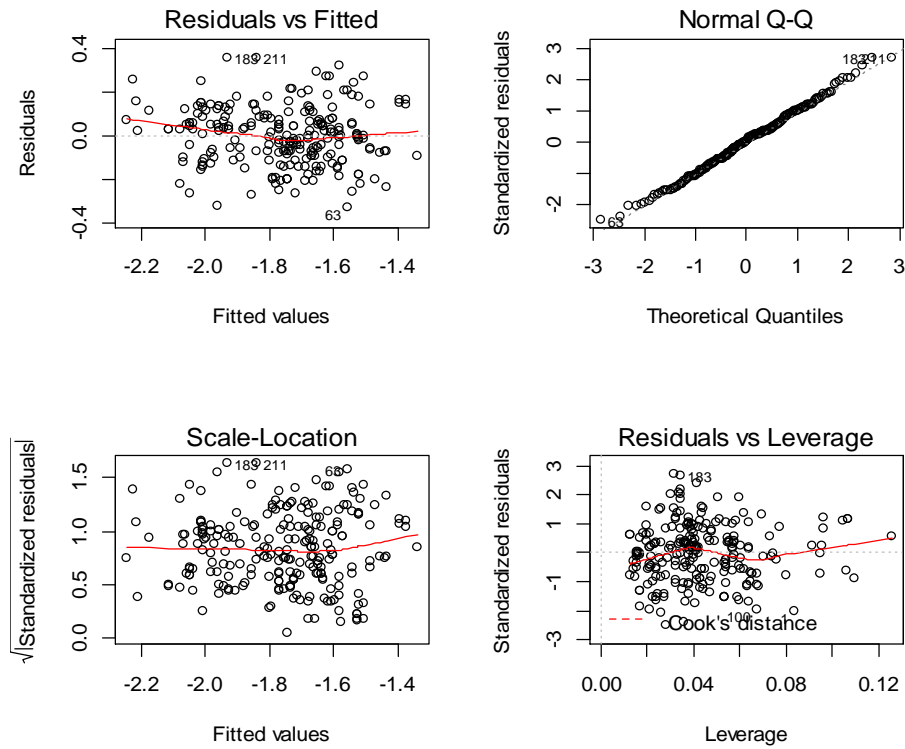


Figure I-5. Diagnostics of the chord rotation at maximum force (θ_m) regression model based on explanatory variables obtained from dimensional analysis. Outliers and extreme data-points are excluded from the regression analysis. An energy dissipation term is not considered.

Table I-3. Diagnostics of the chord rotation at maximum force (θ_m) model where variables are obtained from dimensional analysis. Outliers and extreme values of variables are excluded from the regression analysis. An energy dissipation term is not considered.

Parameter	Estimate Coefficient	Standard Error	t-value	P(> t)
$\log(f_t/f'_c)$	0.52369	0.04997	10.48	2.00E-16
ν	-0.8152	0.05458	-14.937	2.00E-16
$\log \rho_T$	0.56455	0.07311	7.722	3.98E-13
$\log \rho_w$	0.57845	0.06276	9.217	2.00E-16
c/s	-0.86567	0.10239	-8.455	3.87E-15
a_{sl}	-1.37517	0.17532	-7.844	1.88E-13
$a_{sl} \log(\rho_T)$	-0.44456	0.13486	-3.297	0.001141
$a_{sl} \log(\rho_w)$	-0.43738	0.08117	-5.388	1.83E-07
$a_{sl} \log(s/d_{bl})$	0.48184	0.14437	3.338	0.000992
$a_{sl} c/s$	-0.27938	0.11169	-2.501	0.001309
Notes:	Residual standard error: 0.1352 on 220 degrees of freedom Multiple R-squared: 0.754 F-statistic: 3923 on 10 and 220 DF, p-value: < 2.2e-16			

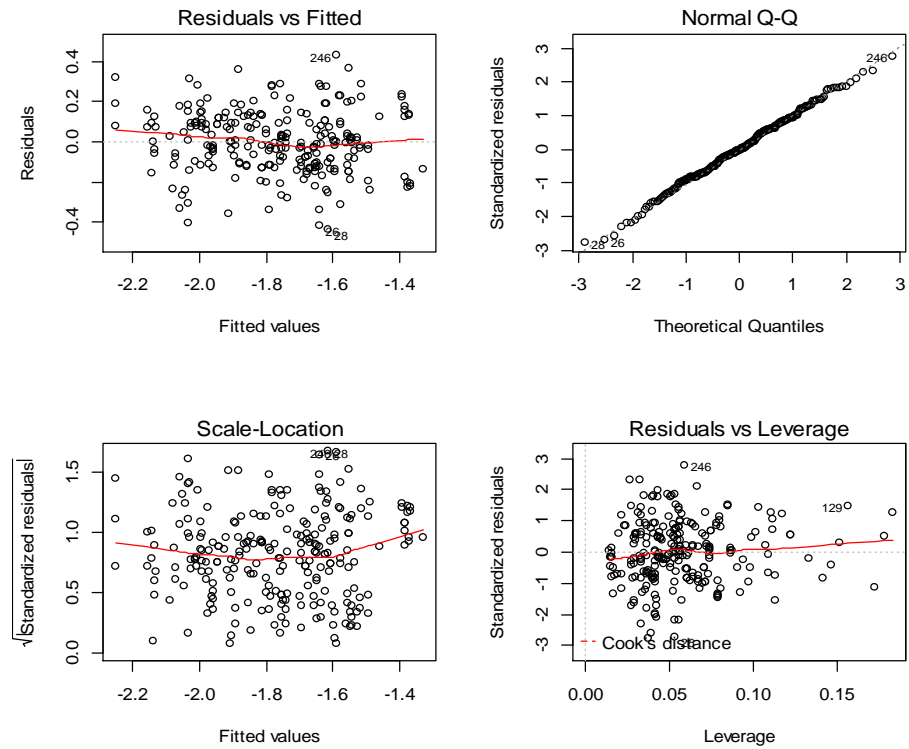


Figure I-6. Diagnostics of the chord rotation at maximum force (θ_m) regression model based on explanatory variables obtained from literature. Outliers and extreme data-points are excluded from the regression analysis. An energy dissipation term is not considered.

Table I-4. Diagnostics of the chord rotation at maximum force (θ_m) model with variables defined in literature. Outliers and extreme values of variables are excluded from the regression analysis. An energy dissipation term is not considered.

Parameter	Estimate Coefficient	Standard Error	t-value	P(> t)
$\log(f_t/f_y)$	-3.56E+00	5.80E-01	-6.139	3.50E-09
$\log(f_y/f'_c)$	2.04E-01	8.53E-02	2.393	0.007475
v	-8.88E-01	6.05E-02	-14.671	< 2e-16
$\log \rho_T$	4.58E-01	6.76E-02	6.781	9.58E-11
$\log(a \rho_s f_w/f'_c)$	-3.34E-04	6.50E-05	-5.136	5.90E-07
$\log(L_s/h)$	-6.64E-01	1.39E-01	-4.761	3.37E-06
a_{sl}	-1.09E+00	1.33E-01	-8.21	1.47E-14
$a_{sl} \log(L_s/h)$	5.93E-01	1.60E-01	3.704	0.000264
$a_{sl} \log(a \rho_s f_w/f'_c)$	3.53E-04	7.79E-05	4.528	9.45E-06
$a_{sl} \log(f_t/f_y)$	3.86E+00	7.17E-01	5.384	1.77E-07
$a_{sl} \log(f_y/f'_c)$	9.47E-03	3.93E-03	2.411	0.006661
<i>Notes:</i>	Residual standard error: 0.1587 on 235 degrees of freedom Multiple R-squared: 0.703 F-statistic: 2805 on 11 and 235 DF, p-value: < 2.2e-16			

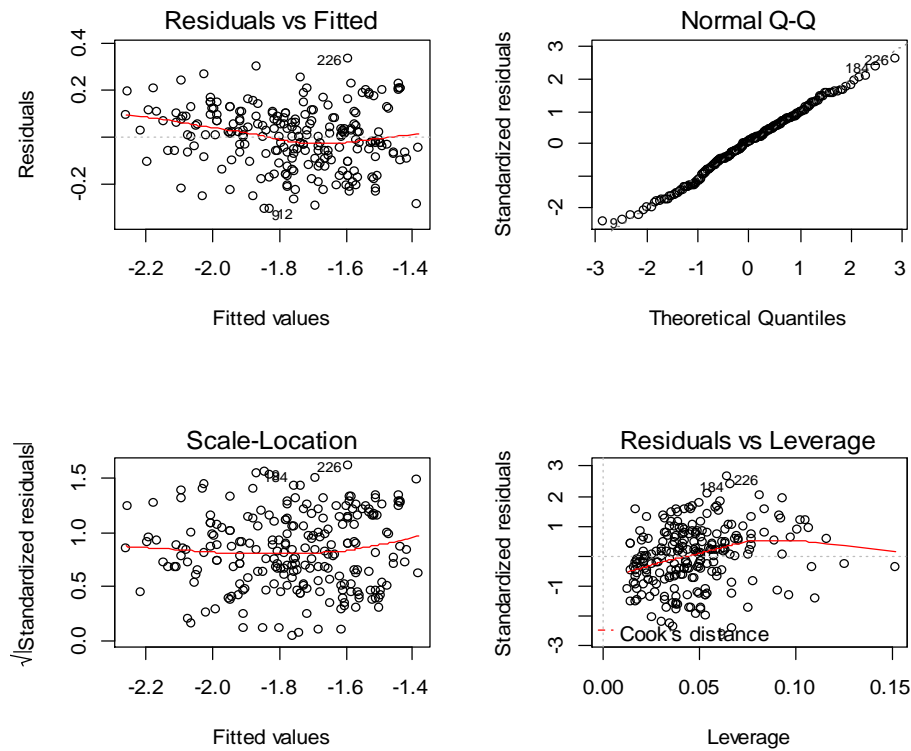


Figure I-7. Diagnostics of the chord rotation at maximum force (θ_m) regression model based on explanatory variables obtained from literature. Outliers and extreme data-points are excluded from the regression analysis. An energy dissipation term is considered.

Table I-5. Diagnostics of the chord rotation at maximum force (θ_m) model where variables are obtained from dimensional analysis. Outliers and extreme values of variables are excluded from the regression analysis. An energy dissipation term is considered.

Parameter	Estimate Coefficient	Standard Error	t-value	P(> t)
$\log(f_t/f'_c)$	0.415	0.049504	8.383	6.16E-15
ν	-0.80536	0.050948	-15.808	< 2e-16
$\log \rho_T$	0.521964	0.068379	7.633	6.89E-13
$\log \rho_w$	0.572155	0.06233	9.179	< 2e-16
c/s	-0.82191	0.098486	-8.345	7.85E-15
a_{sl}	-1.95564	0.187875	-10.409	< 2e-16
$\log(E/(hbsf'_c))$	0.008044	0.021656	0.371	1.32E-04
$a_{sl} \log(\rho_T)$	-0.45073	0.11338	-3.975	9.53E-05
$a_{sl} \log(\rho_w)$	-0.33514	0.073866	-4.537	9.38E-06
$a_{sl} c/s$	0.49624	0.121676	4.078	6.34E-05
$a_{sl} \log(E/(hbsf'_c))$	0.131953	0.029477	4.477	1.22E-05
Notes:	Residual standard error: 0.126 on 220 degrees of freedom Multiple R-squared: 0.802 F-statistic: 4130 on 11 and 220 DF, p-value: < 2.2e-16			

I.3 Diagnostics of the Chord Rotation Models at 10% Reduction of Maximum Force (θ_{u-10}).

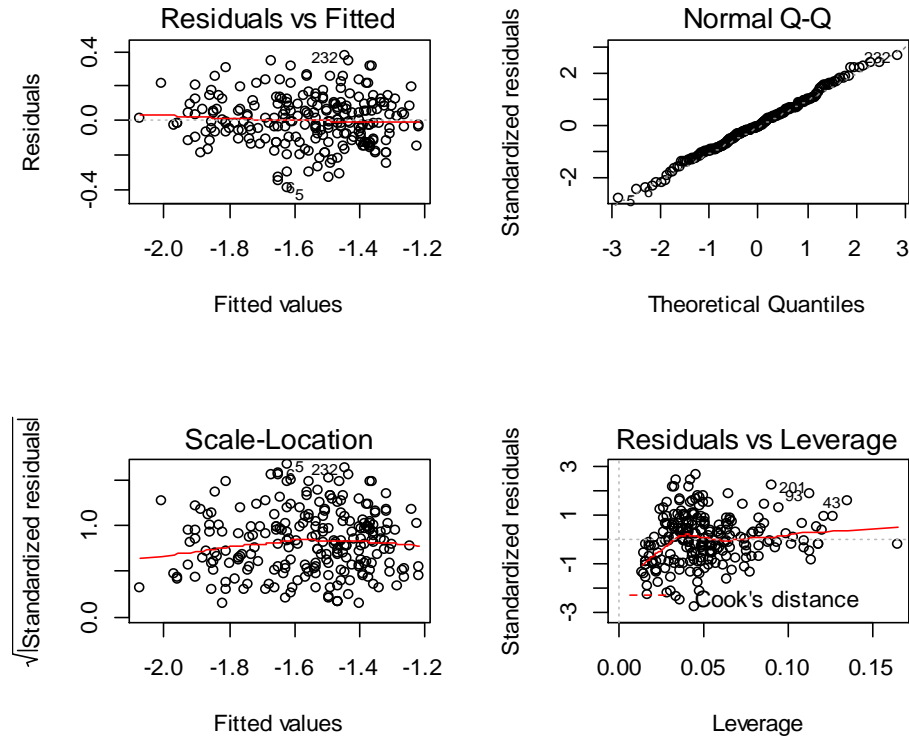


Figure I-8. Diagnostics of the chord rotation at 10% reduction of maximum force (θ_{u-10}) regression model based on explanatory variables obtained from dimensional analysis. Outliers and extreme data-points are excluded from the regression analysis. An energy dissipation term is not considered.

Table I-6. Diagnostics of the chord rotation at 10% reduction of maximum force (θ_{u-10}) model where variables are obtained from dimensional analysis. Outliers and extreme values of variables are excluded. An energy dissipation term is not considered.

Parameter	Estimate Coefficient	Standard Error	t-value	P(> t)
$\log(f_t/f'_c)$	-1.36415	0.276883	-4.927	1.63E-06
$\log(f_y/f'_c)$	1.634748	0.27109	6.03	6.73E-09
v	-0.79821	0.063188	-12.632	< 2e-16
$\log \rho_T$	0.584657	0.079999	7.308	4.78E-12
ω_w	0.640038	0.187739	3.409	0.000773
$\log(L_s/s)$	-0.25455	0.098326	-2.589	0.000026
c/s	-0.43917	0.075588	-5.81	2.14E-08
s/d_{bl}	-0.01794	0.004652	-3.857	0.00015
a_{sl}	-1.22685	0.182216	-6.733	1.39E-10
$a_{sl} \omega_w$	-0.53516	0.216616	-2.471	0.001424
$a_{sl} \rho_T$	-0.37506	0.114261	-3.283	0.001194
$a_{sl} \log(L_s/s)$	0.613878	0.104511	5.874	1.53E-08
Notes:	Residual standard error: 0.1352 on 220 degrees of freedom			
	Multiple R-squared: 0.784			
	F-statistic: 3923 on 10 and 220 DF, p-value: < 2.2e-16			

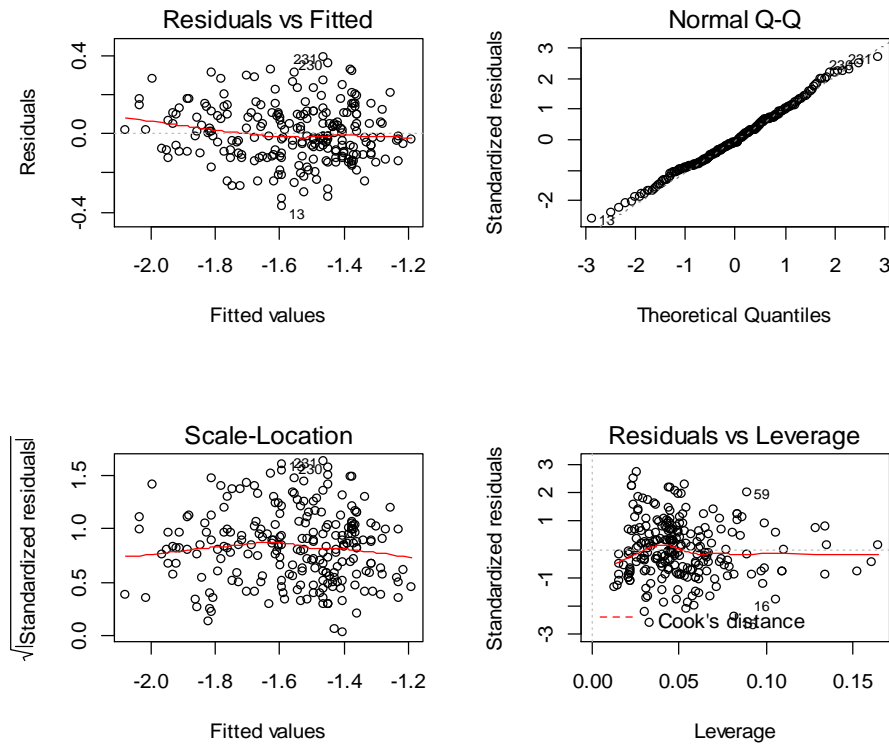


Figure I-9. Diagnostics of the chord rotation at 10% reduction of maximum force (θ_{u-10}) regression model based on explanatory variables obtained from literature. Outliers and extreme data points are excluded from the regression analysis. An energy dissipation term is not considered.

Table I-7. Diagnostics of chord rotation at 10% reduction of maximum force (θ_{u-10}) model with variables defined in literature. Outliers and extreme values of variables are excluded. An energy dissipation term is not considered.

Parameter	Estimate Coefficient	Standard Error	t-value	P(> t)
$\log(f_t/f_y)$	-1.23085	0.27211	-4.523	9.91E-06
$\log(f_y/f'_c)$	0.296258	0.072568	4.082	6.22E-05
v	-0.91466	0.068551	-13.343	< 2e-16
$\log \rho_T$	0.603069	0.071901	8.388	5.77E-15
$\log(a\rho_s)$	15.26124	4.507427	3.386	0.000839
s/d_{bl}	-0.0218	0.004374	-4.984	1.25E-06
c/s	-0.29557	0.07451	-3.967	9.83E-05
$\log(L_s/h)$	-0.50441	0.133704	-3.773	0.000207
a_{sl}	-1.03394	0.180597	-5.725	3.33E-08
$a_{sl} \log \rho_T$	-0.39016	0.120872	-3.228	0.001436
$a_{sl} \log(L_s/h)$	0.678367	0.150673	4.502	1.09E-05
Notes:	Residual standard error: 0.1467 on 222 degrees of freedom			
	Multiple R-squared: 0.743			
	F-statistic: 2217 on 12 and 222 DF, p-value: < 2.2e-16			

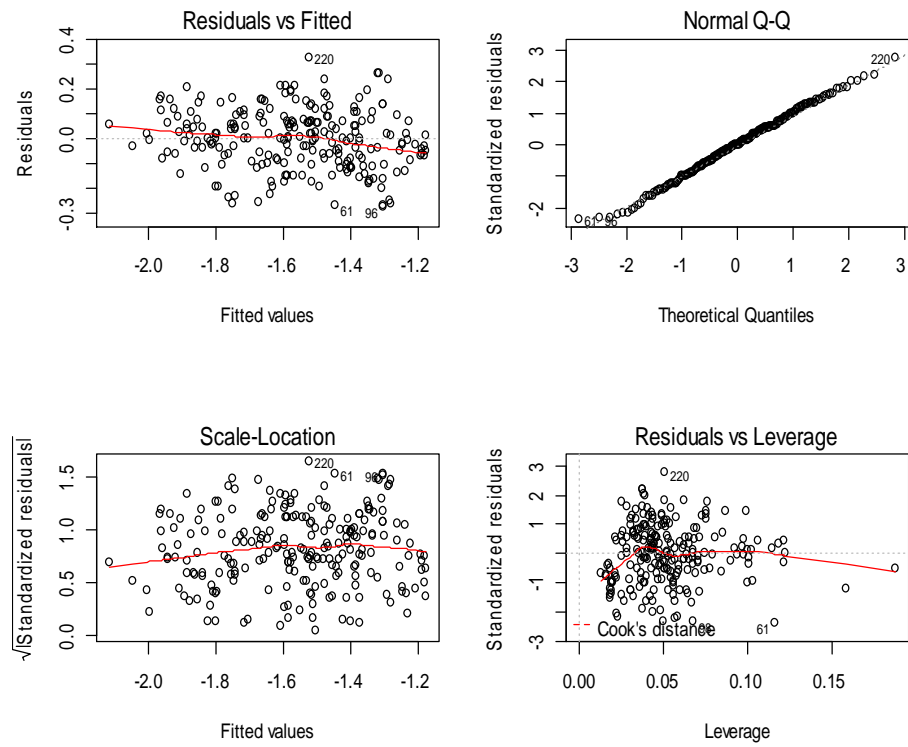


Figure I-10. Diagnostics of the chord rotation at 10% reduction of maximum force (θ_{u-10}) regression model based on explanatory variables obtained from literature. Outliers and extreme data-points are excluded from the regression analysis. An energy dissipation term is considered.

Table I-8. Diagnostics of the chord rotation at 10% reduction of maximum force (θ_{u-10}) equation where variables are obtained from dimensional analysis. Outliers and extreme values of variables are excluded. An energy dissipation term is not considered.

Parameter	Estimate Coefficient	Standard Error	t-value	P(> t)
$\log(f_t/f'_c)$	-0.45513	0.114107	-3.989	9.09E-05
f_y/f'_c	0.028462	0.004241	6.711	1.66E-10
v	-0.71207	0.049235	-14.463	< 2e-16
$\log \rho_w$	0.235294	0.041824	5.626	5.66E-08
$\log \rho_T$	0.549235	0.074754	7.347	4.05E-12
$\log(L_s/s)$	-0.4678	0.088045	-5.313	2.66E-07
c/s	-0.28437	0.063522	-4.477	1.22E-05
$\log(E/(hbsf'_c))$	0.169769	0.017918	9.475	< 2e-16
$\log(s/d_{bl})$	0.000571	0.080082	0.007	0.000532
a_{sl}	-1.3707	0.207042	-6.62	2.77E-10
$a_{sl} \log(\rho_T)$	-0.43448	0.117439	-3.7	0.000274
$a_{sl} \log(L_s/s)$	0.555638	0.089048	6.24	2.27E-09
Notes:	Residual standard error: 0.1467 on 222 degrees of freedom Multiple R-squared: 0.791 F-statistic: 2217 on 12 and 222 DF, p-value: < 2.2e-16			

I.4 Diagnostics of the Chord Rotation Models at 20% Reduction of Maximum Force (θ_{u-20}).

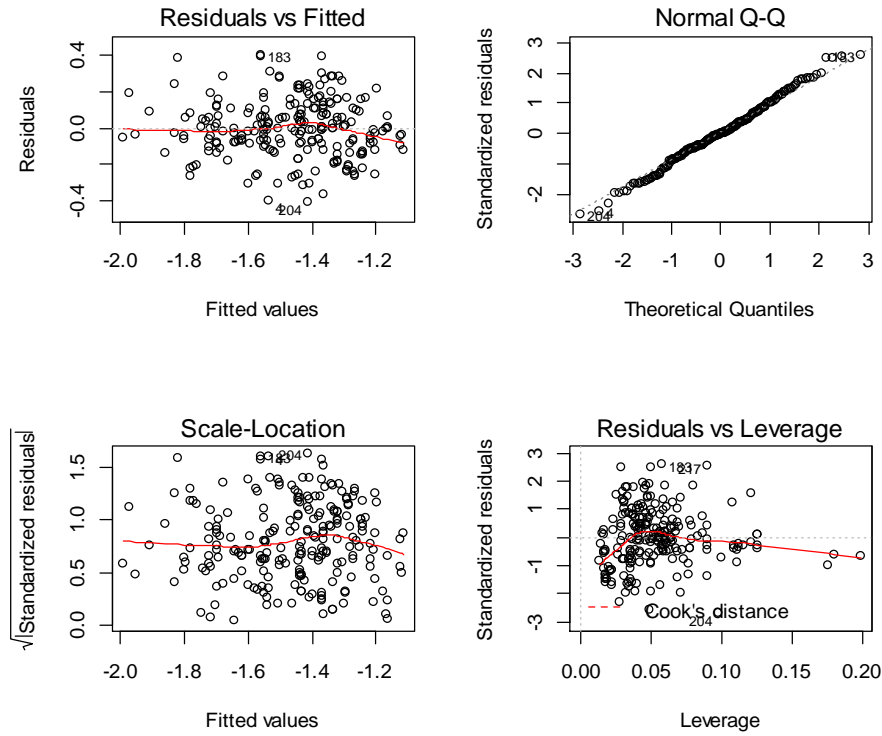


Figure I-11. Diagnostics of the chord rotation at 20% reduction of maximum force (θ_{u-20}) regression model based on explanatory variables obtained from dimensional analysis. Outliers and extreme data-points are excluded from the regression analysis. An energy dissipation term is not considered.

Table I-9. Diagnostics of the chord rotation at 20% reduction of maximum force (θ_{u-20}) model where variables are obtained from dimensional analysis. Outliers and extreme values of variables are excluded. An energy dissipation term is not considered.

Parameter	Estimate Coefficient	Standard Error	t-value	P(> t)
$\log(f_t/f'_c)$	-1.12899	0.362883	-3.111	0.000219
$\log(f_y/f'_c)$	1.328683	0.355877	3.734	0.000242
v	-0.77939	0.069331	-11.242	< 2e-16
$\log\omega_w$	0.164738	0.056813	2.9	0.000413
$\log\rho_T$	0.568576	0.088698	6.41	9.20E-10
$\log(L_s/s)$	0.02273	0.108005	0.21	0.833519
s/d_{bl}	-0.01778	0.005661	-3.14	0.000928
c/s	-0.35061	0.088088	-3.98	9.44E-05
a_{sl}	-1.34153	0.227403	-5.899	1.42E-08
$a_{sl}\rho_T$	-0.57894	0.137643	-4.206	3.83E-05
$a_{sl}\log(L_s/s)$	0.315837	0.110673	2.854	0.000546
Notes:	Residual standard error: 0.1608 on 213 degrees of freedom			
	Multiple R-squared: 0.760			
	F-statistic: 1709 on 11 and 213 DF, p-value: < 2.2e-16			

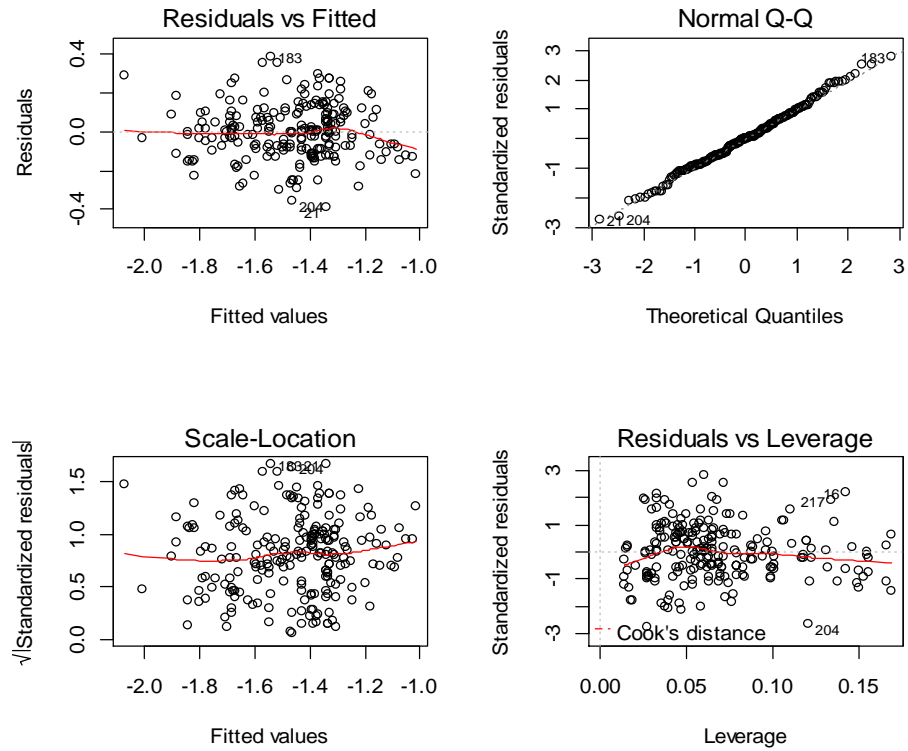


Figure I-12. Diagnostics of the chord rotation at 20% reduction of maximum force (θ_{u-20}) regression model based on explanatory variables obtained from literature. Outliers and extreme data-points are excluded from the regression analysis. An energy dissipation term is not considered.

Table I-10. Diagnostics of the chord rotation at 20% reduction of maximum force (θ_{u-20}) model with variables defined in literature. Outliers and extreme values of variables are excluded. An energy dissipation term is not considered.

Parameter	Estimate Coefficient	Standard Error	t-value	P(> t)
$\log(f_t/f_y)$	-1.0538	0.299916	-3.514	0.00054
$\log(f_y/f'_c)$	0.219283	0.047362	4.63	6.36E-06
v	-0.91515	0.064446	-14.2	< 2e-16
$\log \rho_T$	0.483601	0.07249	6.671	2.15E-10
$a \rho_s f_w/f'_c$	3.216501	0.458754	7.011	3.07E-11
$\log(L_s/h)$	-0.62922	0.16099	-3.908	0.000125
s/d_{bl}	-0.02023	0.004361	-4.639	6.10E-06
c/s	-0.17973	0.083828	-2.144	0.003316
a_{sl}	-1.3221	0.194518	-6.797	1.06E-10
$a_{sl} \log \rho_T$	-0.45892	0.130907	-3.506	0.000555
$a_{sl} \log(L_s/h)$	0.926487	0.17842	5.193	4.83E-07
Notes:	Residual standard error: 0.1438 on 213 degrees of freedom			
	Multiple R-squared: 0.719			
	F-statistic: 2140 on 11 and 213 DF, p-value: < 2.2e-16			

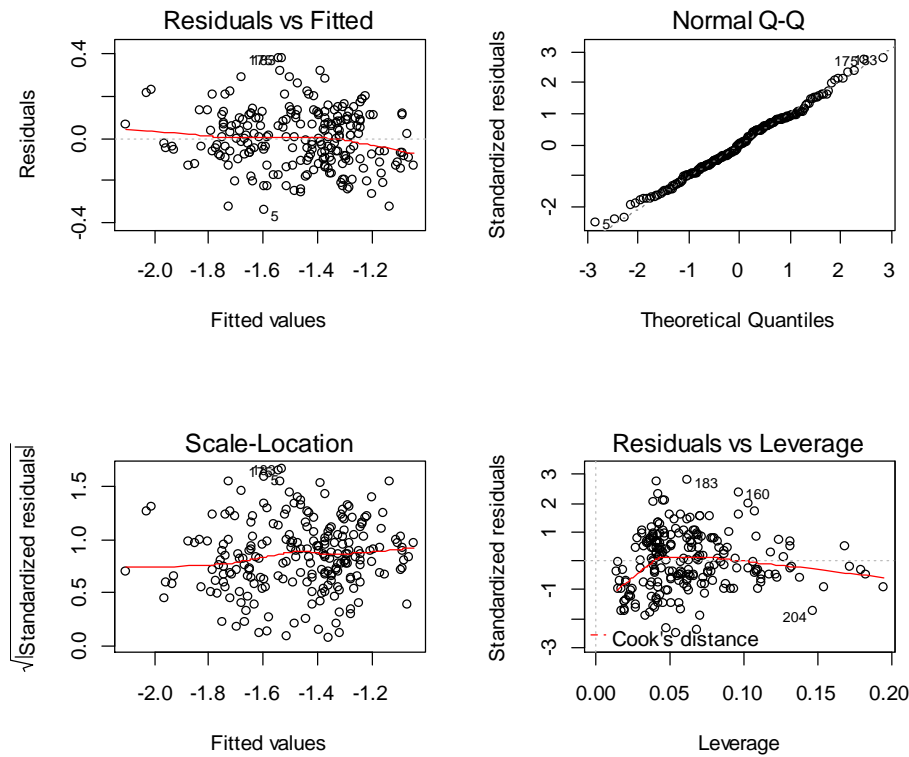


Figure I-13. Diagnostics of the chord rotation at 20% reduction of maximum force (θ_{u-20}) regression model based on explanatory variables obtained from literature. Outliers and extreme data-points are excluded from the regression analysis. An energy dissipation term is considered.

Table I-11. Diagnostics of chord rotation at 20% reduction of maximum force (θ_{u-20}) model where variables are obtained from dimensional analysis. Outliers and extreme values of variables are excluded. An energy dissipation term is considered.

Parameter	Estimate Coefficient	Standard Error	t-value	P(> t)
$\log(f_t/f'_c)$	-2.01515	0.313896	-6.42	8.94E-10
$\log(f_y/f'_c)$	1.985646	0.300305	6.612	3.08E-10
v	-0.73651	0.065043	-11.323	< 2e-16
$\log \rho_T$	0.50781	0.081339	6.243	2.34E-09
ω_w	1.243859	0.227492	5.468	1.29E-07
s/d_{bl}	-0.0136	0.004763	-2.854	0.00475
c/s	-0.51556	0.075269	-6.849	8.05E-11
$\log(L_s/s)$	-0.6009	0.122211	-4.917	1.77E-06
a_{sl}	-1.92042	0.213908	-8.978	< 2e-16
$\log(E/(hbsf'_c))$	0.137946	0.02009	6.866	7.31E-11
$a_{sl} \omega_w$	-1.13277	0.255267	-4.438	1.47E-05
$a_{sl} \log(\rho_T)$	-0.6431	0.124223	-5.177	5.27E-07
$a_{sl} \log(L_s/s)$	0.871515	0.11928	7.306	5.63E-12
Notes:	Residual standard error: 0.1405 on 210 degrees of freedom			
	Multiple R-squared: 0.813			
	F-statistic: 1897 on 13 and 210 DF, p-value: < 2.2e-16			

I.5 Diagnostics of the Chord Rotation Models at 50% Reduction of Maximum Force (θ_{u-50}).

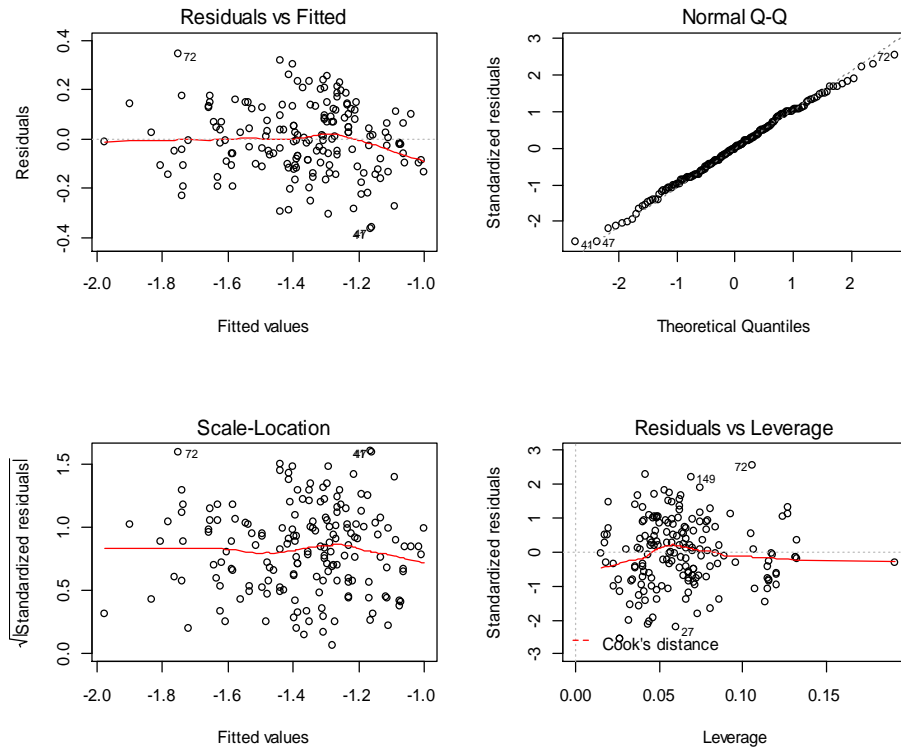


Figure I-14. Diagnostics of the chord rotation at 50% reduction of maximum force (θ_{u-50}) regression model based on explanatory variables obtained from dimensional analysis. Outliers and extreme data-points are excluded from the regression analysis. An energy dissipation term is not considered.

Table I-12. Diagnostics of chord rotation at 50% reduction of maximum force (θ_{u-50}) model where variables are obtained from dimensional analysis. Outliers and extreme values of variables are excluded. An energy dissipation term is not considered.

Parameter	Estimate Coefficient	Standard Error	t-value	P(> t)
$\log(f_t/f'_c)$	-0.88897	0.370769	-2.398	0.017654
$\log(f_y/f'_c)$	0.957016	0.355944	2.689	0.007934
v	-0.96157	0.071154	-13.514	< 2e-16
$\log \rho_T$	0.508514	0.085391	5.955	1.60E-08
$\log \omega_w$	0.371353	0.055045	6.746	2.63E-10
$\log(L_s/s)$	0.186248	0.106423	1.75	0.082023
c/s	-0.34781	0.080375	-4.327	2.65E-05
s/d_{bl}	0.001906	0.005403	0.353	0.72480
a_{sl}	-0.83526	0.225284	-3.708	0.00028
$a_{sl} \rho_T$	-0.35859	0.13011	-2.756	0.00253
$a_{sl} \log(L_s/s)$	S 0.225986	0.111058	2.035	0.00435
Notes:	Residual standard error: 0.1426 on 160 degrees of freedom Multiple R-squared: 0.740 F-statistic: 1462 on 11 and 160 DF, p-value: < 2.2e-16			

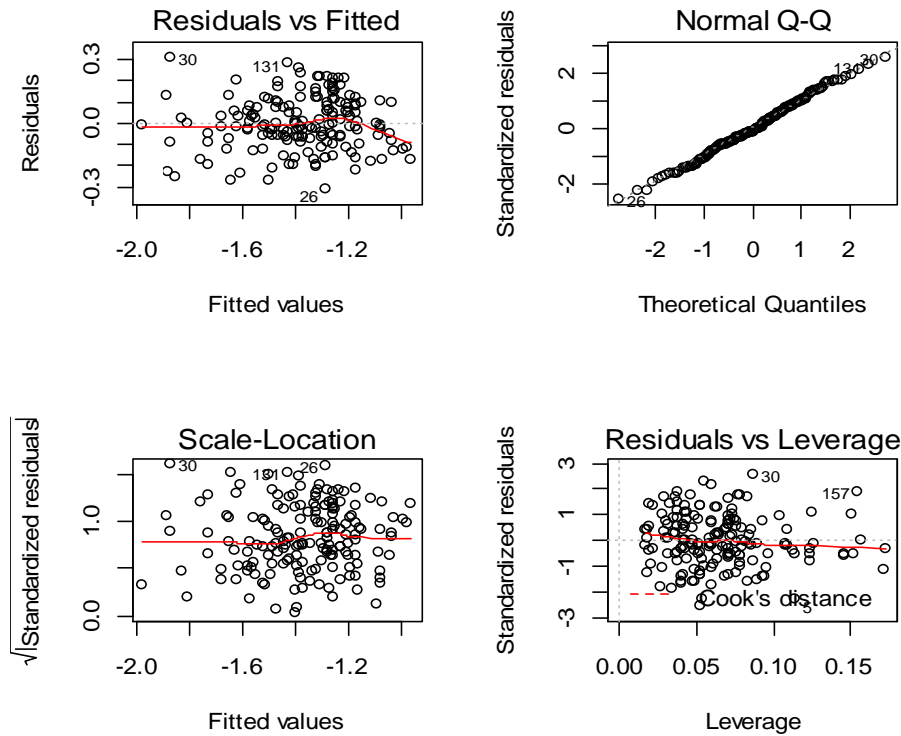


Figure I-15. Diagnostics of the chord rotation at 50% reduction of maximum force (θ_{u-50}) regression model based on explanatory variables obtained from literature. Outliers and extreme data points are excluded from the regression analysis. An energy dissipation term is not considered.

Table I-13. Diagnostics of chord rotation at 50% reduction of maximum force (θ_{u-50}) model with variables defined in literature. Outliers and extreme values of variables are excluded. An energy dissipation term is not considered.

Parameter	Estimate Coefficient	Standard Error	t-value	P(> t)
$\log(f_t/f_y)$	-0.35785	0.064462	-5.551	1.15E-07
v	-0.96024	0.063686	-15.078	< 2e-16
$a\rho_s f_w/f'_c$	3.610883	0.465732	7.753	9.83E-13
$\log\rho_T$	0.202253	0.055589	3.638	0.00037
$\log(L_s/h)$	-0.40494	0.176115	-2.299	0.00278
s/d_{bl}	-0.01253	0.004056	-3.089	0.00237
c/s	-0.08967	0.077178	-1.162	0.00247
a_{sl}	-0.50621	0.114997	-4.402	1.95E-05
$a_{sl} \log(L_s/h)$	0.886573	0.189397	4.681	6.05E-06
Notes:	Residual standard error: 0.1275 on 160 degrees of freedom Multiple R-squared: 0.702 F-statistic: 2202 on 9 and 160 DF, p-value: < 2.2e-16			

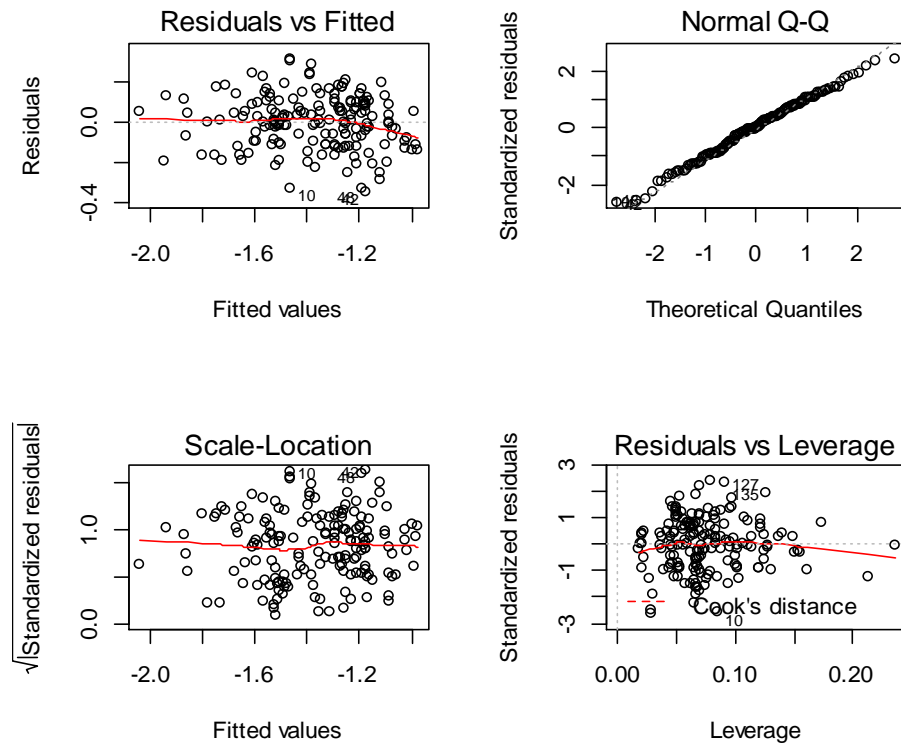


Figure I-16. Diagnostics of the chord rotation at 50% reduction of maximum force (θ_{u-50}) regression model based on explanatory variables obtained from literature. Outliers and extreme data-points are excluded from the regression analysis. An energy dissipation term is considered.

Table I-14. Diagnostics of chord rotation at 50% reduction of maximum force (θ_{u-50}) model where variables are obtained from dimensional analysis. Outliers and extreme values of variables are excluded. An energy dissipation term is not considered.

Parameter	Estimate Coefficient	Standard Error	t-value	P(> t)
$\log(f_t/f'_c)$	-1.92863	0.35102	-5.494	1.54E-07
$\log(f_y/f'_c)$	1.84325	0.3287	5.608	8.95E-08
v	-0.8428	0.07472	-11.28	< 2e-16
$\log \rho_T$	0.44107	0.08775	5.026	1.34E-06
ω_w	1.67312	0.2384	7.018	6.25E-11
$\log(L_s/s)$	-0.50985	0.14442	-3.53	0.000544
c/s	-0.51298	0.08311	-6.172	5.44E-09
$\log(E/(hbsf'_c))$	0.10834	0.02583	4.195	4.54E-05
$\log(s/d_{bl})$	-0.1187	0.07809	-1.52	0.00905
a_{sl}	-1.50785	0.24153	-6.243	3.79E-09
$a_{sl} \omega_w$	-1.38217	0.27555	-5.016	1.40E-06
$a_{sl} \log(\rho_T)$	-0.47213	0.12899	-3.66	0.000343
$a_{sl} \log(L_s/s)$	0.82195	0.13614	6.038	1.08E-08
<i>Notes:</i>	Residual standard error: 0.135 on 158 degrees of freedom Multiple R-squared: 0.785 F-statistic: 1386 on 13 and 158 DF, p-value: < 2.2e-16			

Appendix J Diagnostics of the Statistical Regression Stiffness Ratio (EI_{dmg}/EI_g) Models.

J.1 Diagnostics of the Stiffness Ratio Models at Yielding (EI_Y/EI_g).

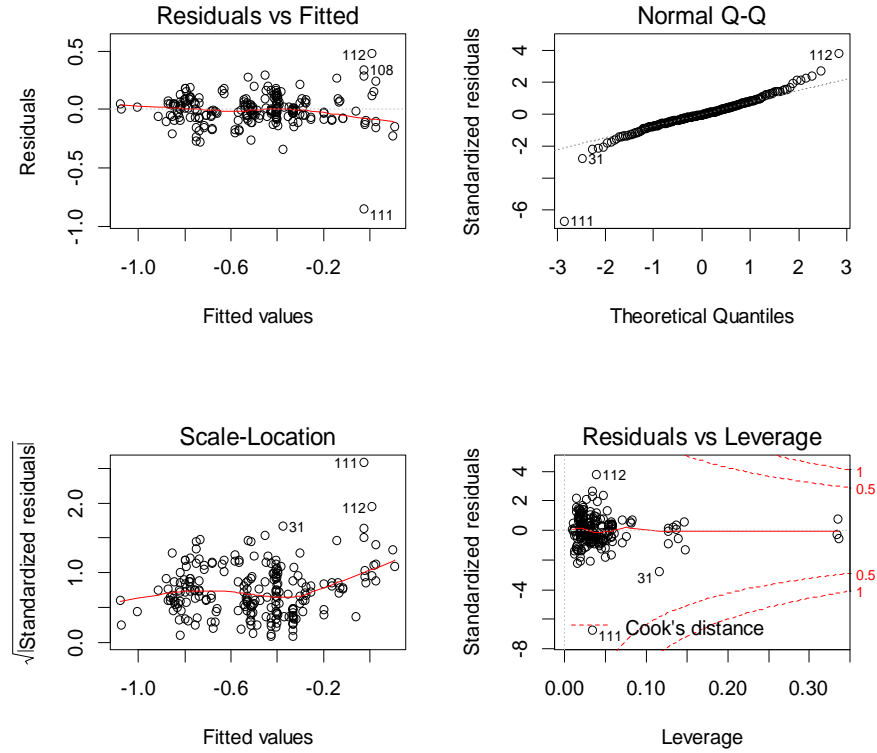


Figure J-1. Diagnostics of the stiffness ratio at yield (EI_Y/EI_g) regression model based on explanatory variables obtained from literature and dimensional analysis. Outliers and extreme data-points are included in the regression analysis. An energy dissipation term is not considered.

Table J-1. Regression statistics of stiffness ratio at yielding (EI_Y/EI_g) model where variables are obtained from literature and dimensional analysis. Outliers and extreme values of variables are included in the regression analysis. An energy dissipation term is not considered.

Parameter	Estimate Coefficient	Standard Error	t-value	P(> t)
l	-0.5904	0.06413	-9.206	< 2e-16
$\log(f_{yl}/f'_c)$	-0.20722	0.06303	-3.288	0.00118
v	0.71405	0.0792	9.016	< 2e-16
$\log(L_s/h)$	0.29515	0.10815	2.729	0.00689
$\log(b/h)$	1.51819	0.35344	4.296	2.66E-05
$a_{sl} \log(f_{yl}/f'_c)$	0.09888	0.02572	3.845	0.00016
$a_{sl} \log(v)$	-0.2787	0.06942	-4.014	8.29E-05
$a_{sl} \log(L_s/h)$	0.50648	0.11197	4.523	1.02E-05
$a_{sl} \log(b/h)$	-1.69351	0.36988	-4.579	8.02E-06
Notes:	Residual standard error: 0.1292 on 210 degrees of freedom			
	Multiple R-squared: 0.7909			
	F-statistic: 99.32 on 8 and 210 DF, p-value: < 2.2e-16			

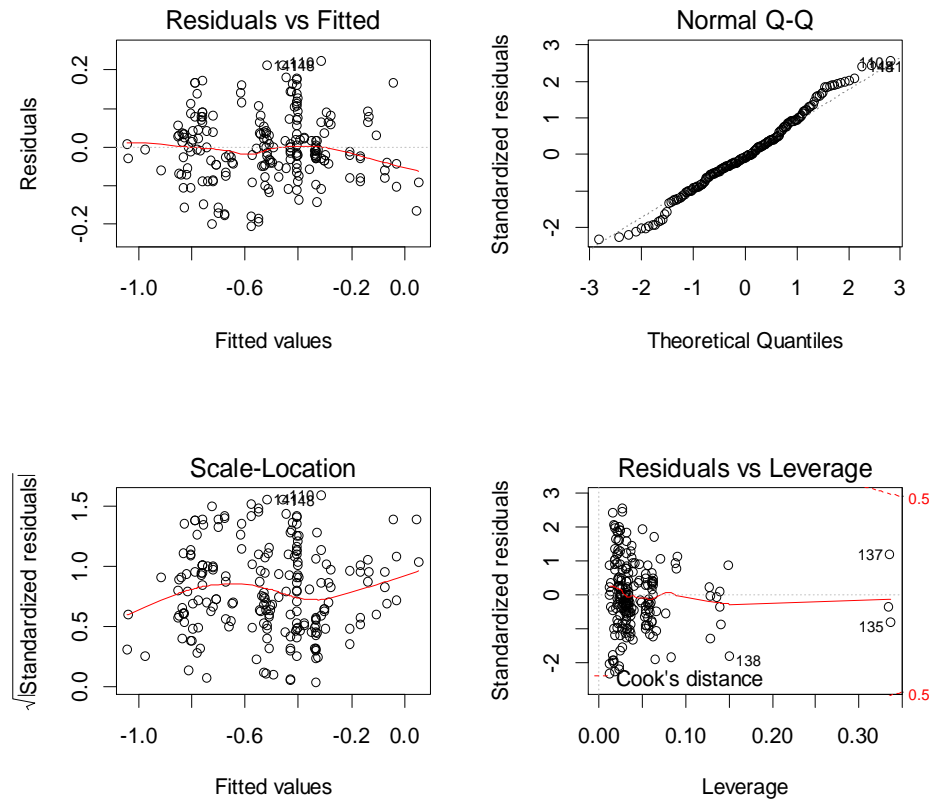


Figure J-2. Diagnostics of the stiffness ratio at yield (EI_Y/EI_Q) regression model based on explanatory variables obtained from literature and dimensional analysis. Outliers and extreme data-points are excluded from the regression analysis. An energy dissipation term is not considered.

Table J-2. Regression statistics of stiffness ratio at yielding (EI_Y/EI_Q) model where variables are obtained from literature and dimensional analysis. Outliers and extreme values of variables are excluded from the regression analysis. An energy dissipation term is not considered.

Parameter	Estimate Coefficient	Standard Error	t-value	P(> t)
I	-0.59436	0.04488	-13.244	< 2e-16
$\log(f_{yl}/f'_c)$	-0.20342	0.04333	-4.694	5.03E-06
ν	0.70575	0.05785	12.199	< 2e-16
$\log(L_s/h)$	0.29968	0.07454	4.02	8.30E-05
$\log(b/h)$	1.521	0.24299	6.26	2.40E-09
$a_{sl} \log(f_{yl}/f'_c)$	-0.22261	0.0488	-4.562	8.96E-06
$a_{sl} \log(\nu)$	0.09176	0.01774	5.172	5.72E-07
$a_{sl} \log(L_s/h)$	0.39455	0.07945	4.966	1.49E-06
$a_{sl} \log(b/h)$	-1.63082	0.25527	-6.389	1.20E-09
Notes:	Residual standard error: 0.0886 on 195 degrees of freedom Multiple R-squared: 0.8675, F-statistic: 159.5 on 8 and 195 DF, p-value: < 2.2e-16			

J.2 Diagnostics of the Stiffness Ratio Models at Maximum Force (EI_m/EI_g).

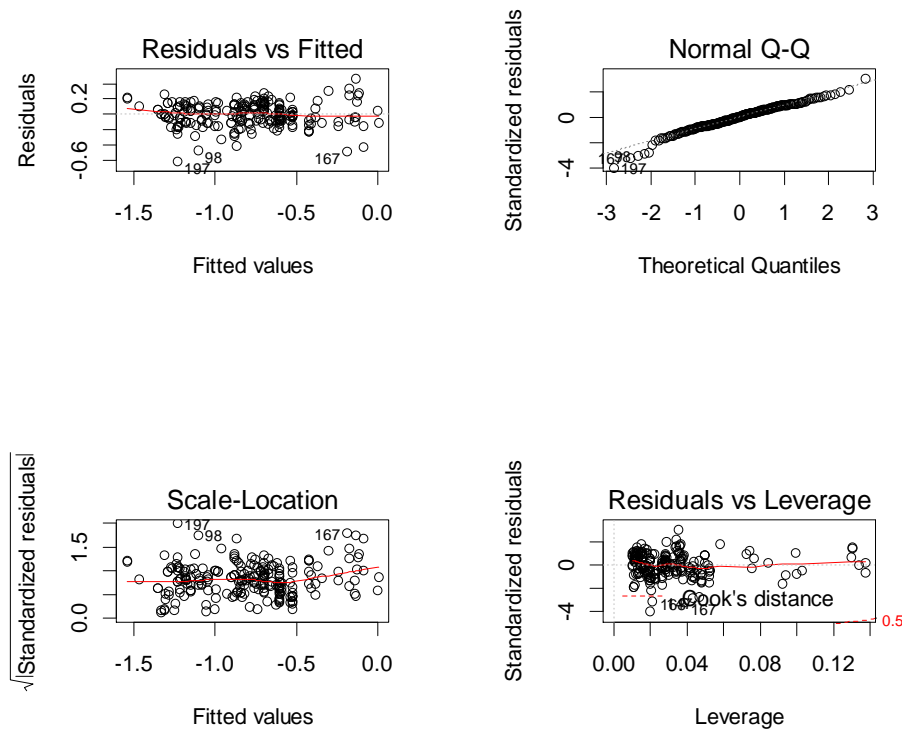


Figure J-3. Diagnostics of the stiffness ratio at maximum force (EI_m/EI_g) regression model based on explanatory variables obtained from literature and dimensional analysis. Outliers and extreme data-points are included in the regression analysis. An energy dissipation term is not considered.

Table J-3. Regression statistics of stiffness ratio at maximum force (EI_m/EI_g) model where variables are obtained from literature and dimensional analysis. Outliers and extreme values of variables are included in the regression analysis. An energy dissipation term is not considered.

Parameter	Estimate Coefficient	Standard Error	t-value	P(> t)
I	-0.80912	0.082249	-9.837	< 2e-16
$\log(f_{tl}/f'_c)$	-0.40825	0.074189	-5.503	1.07E-07
ν	0.791355	0.090218	8.772	5.83E-16
L_s/h	0.090937	0.012183	7.464	2.14E-12
$a_{sl} f_{tl}/f'_c$	-0.00922	0.002485	-3.709	0.000265
$a_{sl} \log(\nu)$	0.138375	0.030098	4.597	7.34E-06
$a_{sl} L_s/h$	0.037284	0.011384	3.275	0.001233
Notes:	Residual standard error: 0.1548 on 212 degrees of freedom Multiple R-squared: 0.8254 F-statistic: 167.1 on 6 and 212 DF, p-value: < 2.2e-16			

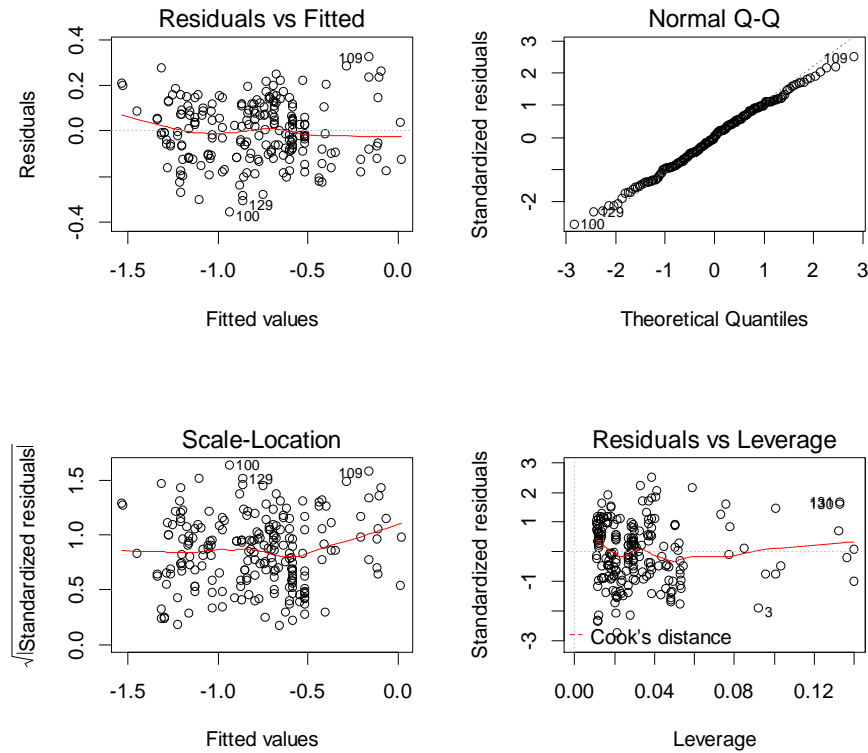


Figure J-4. Diagnostics of the stiffness ratio at maximum force (EI_m/EI_g) regression model based on explanatory variables obtained from literature and dimensional analysis. Outliers and extreme data-points are excluded from the regression analysis. An energy dissipation term is not considered.

Table J-4. Regression statistics of stiffness ratio at maximum force (EI_m/EI_g) model where variables are obtained from literature and dimensional analysis. Outliers and extreme values of variables are excluded from the regression analysis. An energy dissipation term is not considered.

Parameter	Estimate Coefficient	Standard Error	t-value	P(> t)
I	-0.75879	0.071557	-10.604	< 2e-16
$\log(f_{tl}/f'_c)$	-0.41417	0.063656	-6.506	5.74E-10
ν	0.714648	0.078799	9.069	< 2e-16
L_s/h	0.08708	0.010484	8.306	1.31E-14
$a_{sl} f_{tl}/f'_c$	-0.0102	0.002141	-4.763	3.60E-06
$a_{sl} \log(\nu)$	0.146397	0.026088	5.612	6.41E-08
$a_{sl} L_s/h$	0.043514	0.009889	4.4	1.73E-05
Notes:	Residual standard error: 0.1326 on 206 degrees of freedom Multiple R-squared: 0.8597, F-statistic: 210.4 on 6 and 206 DF, p-value: < 2.2e-16			

J.3 Diagnostics of the Stiffness Ratio Models at 10% Reduction of Maximum Force (EI_{u-10}/EI_g).

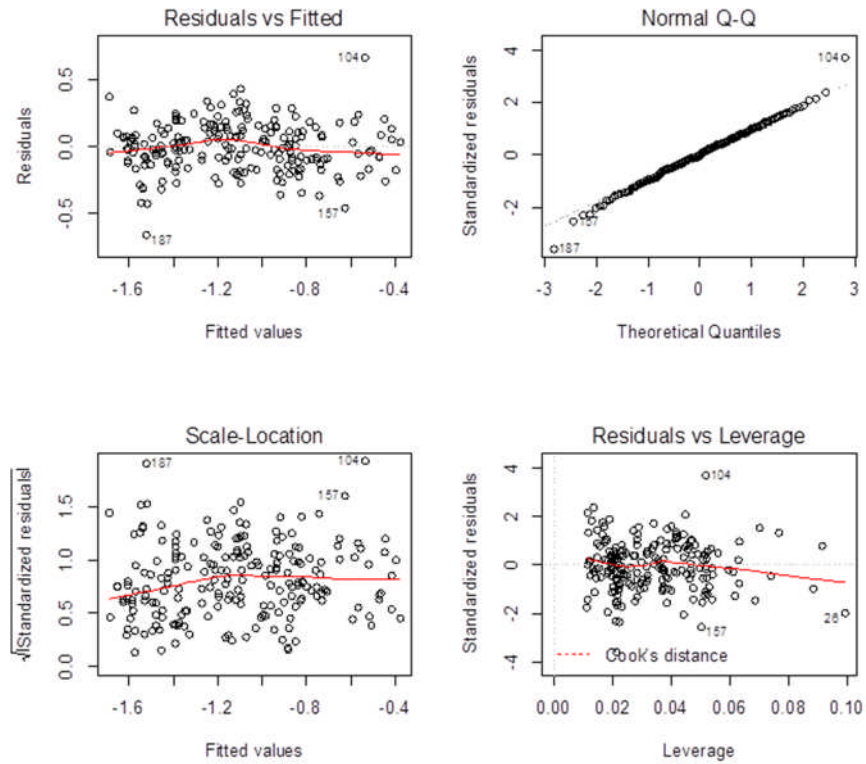


Figure J-5. Diagnostics of the stiffness ratio at 10% reduction of maximum force (EI_{u-10}/EI_g) regression model based on explanatory variables obtained from literature and dimensional analysis. Outliers and extreme data-points are included in the regression analysis. An energy dissipation term is not considered.

Table J-5. Regression statistics of stiffness ratio at 10% reduction of maximum force (EI_{u-10}/EI_g) model where variables are obtained from literature and dimensional analysis. Outliers and extreme values of variables are included in the regression analysis. An energy dissipation term is not considered.

Parameter	Estimate Coefficient	Standard Error	t-value	P(> t)
l	-1.75268	0.062609	-27.994	< 2e-16
f_{tl}/f'_c	1.201839	0.087785	13.691	< 2e-16
ν	-0.01896	0.001824	-10.394	< 2e-16
L_s/h	0.155028	0.010316	15.028	< 2e-16
$a\rho_s$	-14.5282	5.075055	-2.863	0.004644
$\log(s/d_{bl})$	0.182681	0.061626	2.964	0.003398
$a_{sl} L_s/h$	-0.02468	0.006611	-3.733	0.000246
Notes:	Residual standard error: 0.1841 on 202 degrees of freedom Multiple R-squared: 0.7697, F-statistic: 112.5 on 6 and 202 DF, p-value: < 2.2e-16			

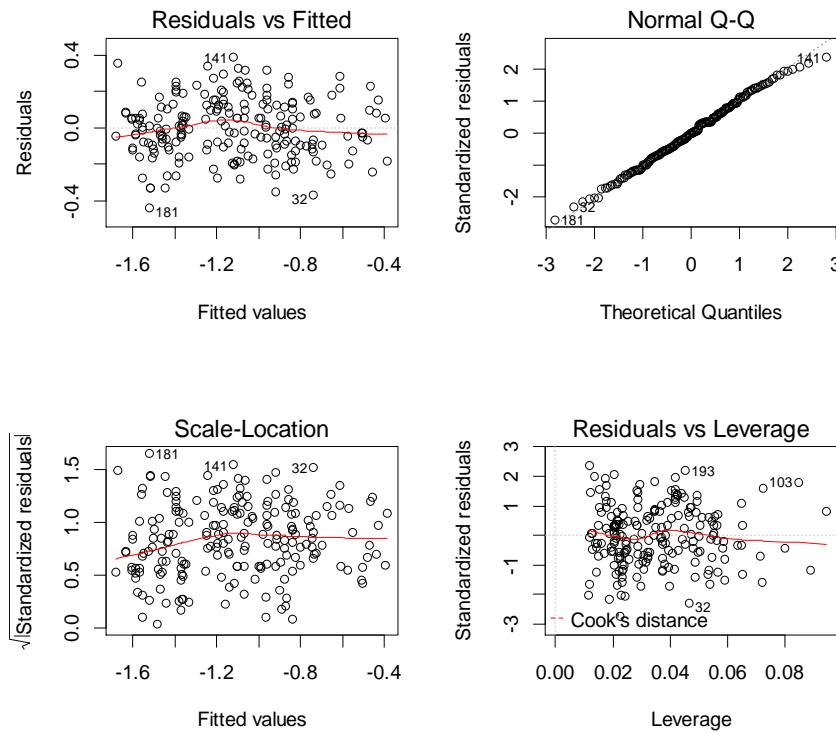


Figure J-6. Diagnostics of the stiffness ratio at 10% reduction of maximum force (EI_{u-10}/EI_g) regression model based on explanatory variables obtained from literature and dimensional analysis. Outliers and extreme data-points are excluded from the regression analysis. An energy dissipation term is not considered.

Table J-6. Regression statistics of stiffness ratio at 10% reduction of maximum force (EI_{u-10}/EI_g) model where variables are obtained from literature and dimensional analysis. Outliers and extreme values of variables are excluded from the regression analysis. An energy dissipation term is not considered.

Parameter	Estimate Coefficient	Standard Error	t-value	P(> t)
l	-1.6988	0.056765	-29.927	< 2e-16
f_{tl}/f'_c	-0.01888	0.001626	-11.612	< 2e-16
ν	1.222541	0.081758	14.953	< 2e-16
L_s/h	0.150349	0.009289	16.186	< 2e-16
$a\rho_s$	-17.6191	4.609318	-3.823	0.000177
$\log(s/d_{bl})$	0.139252	0.055081	2.528	0.001225
$a_{sl} L_s/h$	-0.0238	0.005941	-4.007	8.74E-05
Notes:	Residual standard error: 0.1633 on 196 degrees of freedom Multiple R-squared: 0.8001, F-statistic: 130.7 on 6 and 196 DF, p-value: < 2.2e-16			

J.4 Diagnostics of the Stiffness Ratio Models at 20% Reduction of Maximum Force (EI_{u-20}/EI_g).

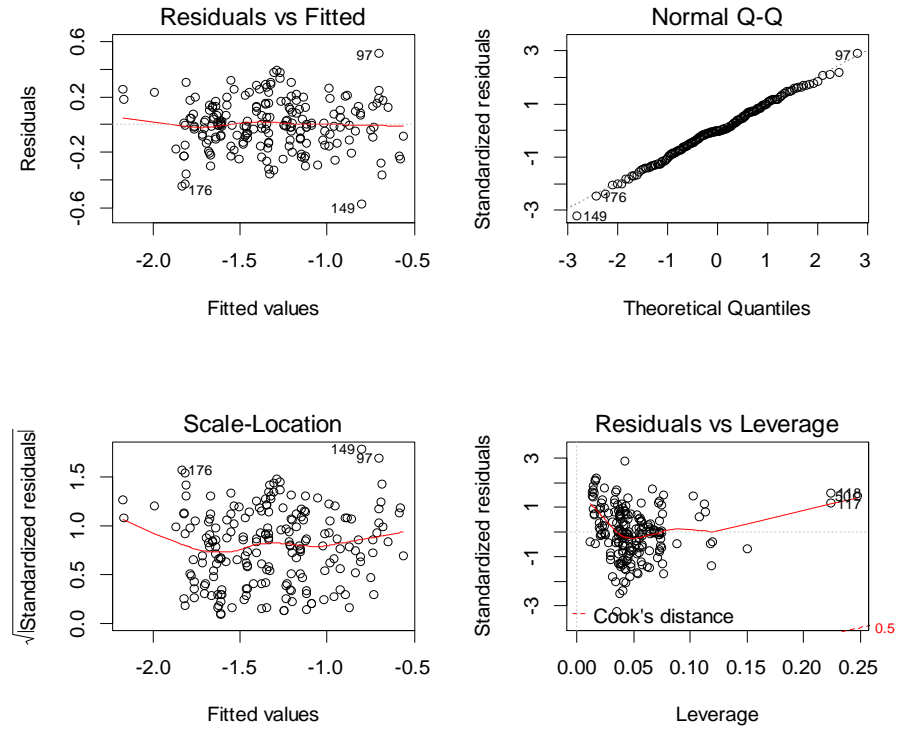


Figure J-7. Diagnostics of the stiffness ratio at 20% reduction of maximum force (EI_{u-20}/EI_g) regression model based on explanatory variables obtained from literature and dimensional analysis. Outliers and extreme data-points are included in the regression analysis. An energy dissipation term is not considered.

Table J-7. Regression statistics of stiffness ratio at 20% reduction of maximum force (EI_{u-20}/EI_g) model where variables are obtained from literature and dimensional analysis. Outliers and extreme values of variables are included in the regression analysis. An energy dissipation term is not considered.

Parameter	Estimate Coefficient	Standard Error	t-value	P(> t)
I	-1.46179	0.11742	-12.449	< 2e-16
$\log(f_{tl}/f'_c)$	-0.70376	0.06632	-10.612	< 2e-16
ν	0.92041	0.1184	7.774	4.67E-13
L_s/h	0.12284	0.01055	11.648	< 2e-16
ρ_T	-6.28369	1.39689	-4.498	1.19E-05
$\log(a\rho_s)$	-0.07654	0.01524	-5.023	1.17E-06
c/h	2.69728	0.59009	4.571	8.73E-06
$a_{sl} \log \nu$	0.14214	0.04536	3.134	0.002
$a_{sl} \rho_T$	10.29056	2.23955	4.595	7.87E-06
$a_{sl} c/h$	-3.02913	0.68916	-4.395	1.84E-05
Notes:	Residual standard error: 0.1814 on 190 degrees of freedom Multiple R-squared: 0.7831, F-statistic: 76.24 on 9 and 190 DF, p-value: < 2.2e-16			

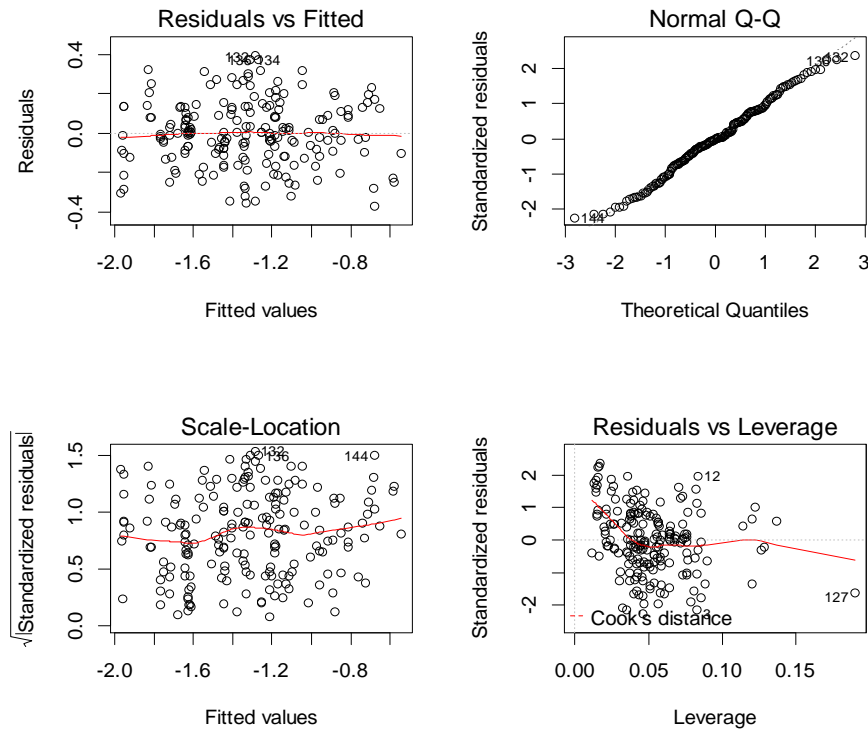


Figure J-8. Diagnostics of the stiffness ratio at 20% reduction of maximum force (EI_{u-20}/EI_g) regression model based on explanatory variables obtained from literature and dimensional analysis. Outliers and extreme data-points are excluded from the regression analysis. An energy dissipation term is not considered.

Table J-8. Regression statistics of stiffness ratio at 20% reduction of maximum force (EI_{u-20}/EI_g) model where variables are obtained from literature and dimensional analysis. Outliers and extreme values of variables are excluded from the regression analysis. An energy dissipation term is not considered.

Parameter	Estimate Coefficient	Standard Error	t-value	P(> t)
I	-1.33763	0.113641	-11.771	< 2e-16
$\log(f_{tl}/f'_c)$	-0.71579	0.061971	-11.55	< 2e-16
ν	0.673615	0.126527	5.324	2.94E-07
L_s/h	0.123688	0.009948	12.434	< 2e-16
ρ_T	-6.65153	1.298434	-5.123	7.56E-07
$\log(a\rho_s)$	-0.08885	0.014478	-6.137	5.03E-09
c/h	2.026795	0.571626	3.546	0.000497
$a_{sl} \log \nu$	0.35262	0.06831	5.162	6.30E-07
$a_{sl} \rho_T$	11.34263	2.137847	5.306	3.20E-07
$a_{sl} c/h$	-1.89425	0.695026	-2.725	0.001221
Notes:	Residual standard error: 0.1681 on 184 degrees of freedom Multiple R-squared: 0.8042, F-statistic: 53.09 on 10 and 154 DF, p-value: < 2.2e-16			

J.5 Diagnostics of the Stiffness Ratio Models at 50% Reduction of Maximum Force (EI_{u-50}/EI_g).

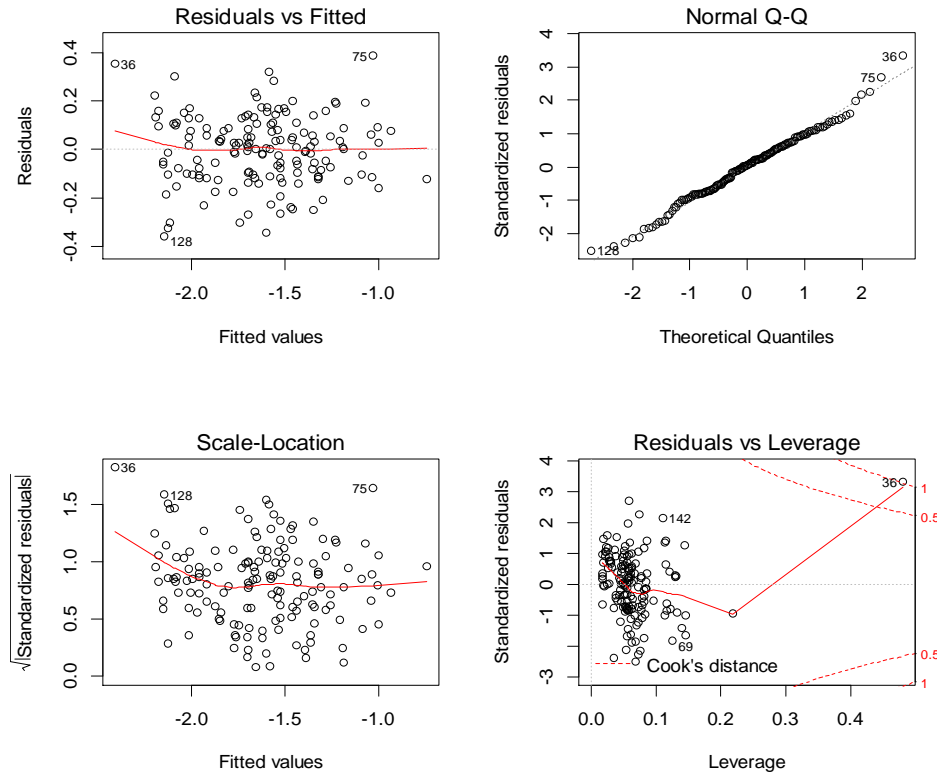


Figure J-9. Diagnostics of the stiffness ratio at 50% reduction of maximum force (EI_{u-50}/EI_g) regression model based on explanatory variables obtained from literature and dimensional analysis. Outliers and extreme data-points are included in the regression analysis. An energy dissipation term is not considered.

Table J-9. Regression statistics of stiffness ratio at 50% reduction of maximum force (EI_{u-50}/EI_g) model where variables are obtained from literature and dimensional analysis. Outliers and extreme values of variables are included in the regression analysis. An energy dissipation term is not considered.

Parameter	Estimate Coefficient	Standard Error	t-value	P(> t)
I	-2.36086	0.151	-15.635	< 2e-16
$\log(f_{tl}/f'_c)$	-0.69728	0.05707	-12.218	< 2e-16
v	0.96965	0.11276	8.599	1.34E-14
$\log(L_s/h)$	1.77108	0.18706	9.468	< 2e-16
ρ_T	-4.03004	1.13674	-3.545	0.000532
$\log(a\rho_s f_{yw}/f'_c)$	-0.18637	0.0227	-8.21	1.22E-13
$a_{sl} \log(v)$	0.22168	0.05293	4.188	4.91E-05
$a_{sl} L_s/h$	-0.09414	0.0228	-4.129	6.18E-05
$a_{sl}\rho_T$	8.94748	2.61342	3.424	0.000808
$a_{sl} \log(c/h)$	-0.25999	0.09805	-2.652	0.000221
Notes:	Residual standard error: 0.1474 on 142 degrees of freedom Multiple R-squared: 0.8364, F-statistic: 80.64 on 9 and 142 DF, p-value: < 2.2e-16			

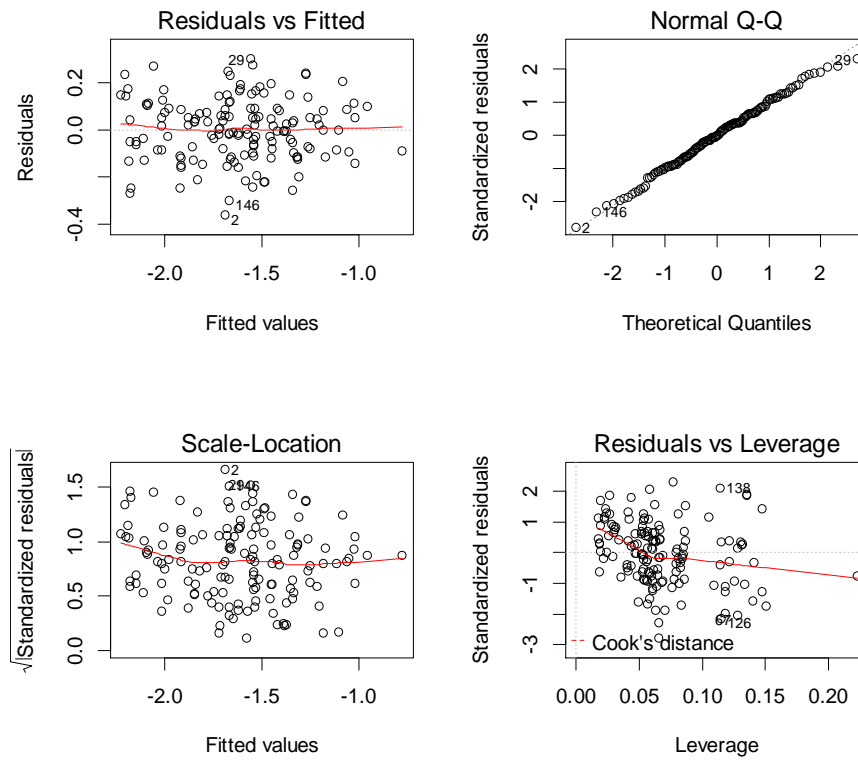


Figure J-10. Diagnostics of the stiffness ratio at 50% reduction of maximum force (EI_{u-50}/EI_g) regression model based on explanatory variables obtained from literature and dimensional analysis. Outliers and extreme data-points are excluded from the regression analysis. An energy dissipation term is not considered.

Table J-10. Regression statistics of stiffness ratio at 50% reduction of maximum force (EI_{u-50}/EI_g) model where variables are obtained from literature and dimensional analysis. Outliers and extreme values of variables are excluded from the regression analysis. An energy dissipation term is not considered.

Parameter	Estimate Coefficient	Standard Error	t-value	P(> t)
I	-2.2002	0.14424	-15.254	< 2e-16
$\log(f_{tl}/f'_c)$	-0.67022	0.05239	-12.792	< 2e-16
ν	0.80856	0.11611	6.963	1.24E-10
$\log(L_s/h)$	1.56763	0.17921	8.747	6.77E-15
ρ_T	-4.40903	1.0388	-4.244	4.00E-05
$\log(a\rho_s f_{yw}/f'_c)$	-0.19034	0.02086	-9.123	7.88E-16
$a_{sl} \log(\nu)$	0.33737	0.06672	5.056	1.34E-06
$a_{sl} L_s/h$	-0.07803	0.02139	-3.649	0.000373
$a_{sl}\rho_T$	7.54113	2.40802	3.132	0.000212
$a_{sl} \log(c/h)$	-0.26637	0.09056	-2.941	0.000835
Notes:	Residual standard error: 0.1341 on 138 degrees of freedom Multiple R-squared: 0.8525, F-statistic: 88.65 on 9 and 138 DF, p-value: < 2.2e-16			

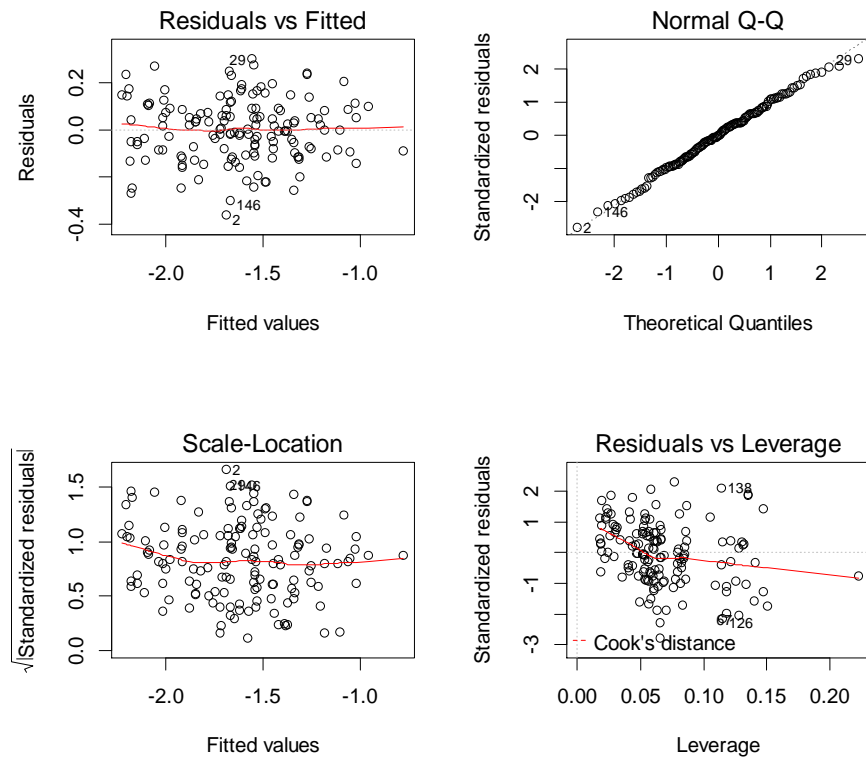


Figure J-11. *Diagnostics of the stiffness ratio at 50% reduction of maximum force (EI_{u-50}/EI_g) regression model based on explanatory variables obtained from literature and dimensional analysis. Outliers and extreme data-points are excluded from the regression analysis. An energy dissipation term is not considered.*

Appendix K Diagnostics of the Statistical Regression Models relating Chord Rotation (θ_{dmg}), Energy Dissipation (E_{dmg}) and Stiffness (K_{dmg}).

K.1 Diagnostics of the Chord Rotation, Energy dissipation and stiffness at Maximum force.

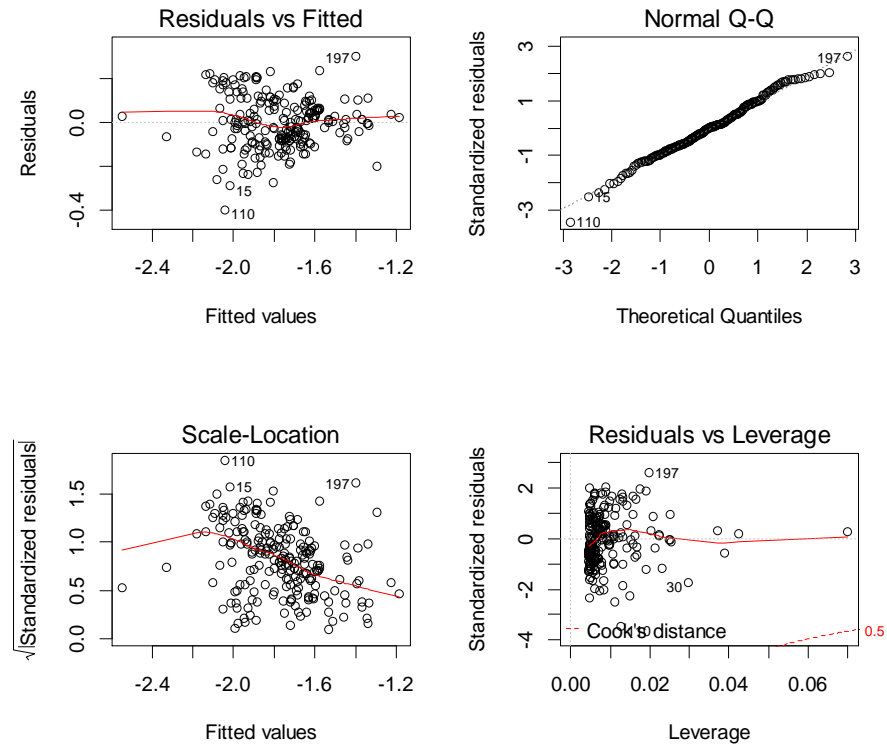


Figure K-1. Diagnostics of the regression model relating the chord rotation (θ_m), energy dissipation (E_m), and stiffness (K_m) using non-dimensional terms. Outliers and extreme data-points are included in the regression analysis.

Table K-1. Regression statistics of model relating the chord rotation (θ_m), energy dissipation (E_m), and stiffness (K_m) using non-dimensional terms. Outliers and extreme data-points are included in the regression analysis.

Parameter	Estimate Coefficient	Standard Error	t-value	P(> t)
I	-1.631665	0.009577	-170.37	< 2e-16
$\log(E_m/[K_m L_s^2])$	0.308786	0.011945	25.85	< 2e-16
<i>Notes:</i>	Residual standard error: 0.1165 on 217 degrees of freedom Multiple R-squared: 0.7549, F-statistic: 668.2 on 1 and 217 DF, p-value: < 2.2e-16			

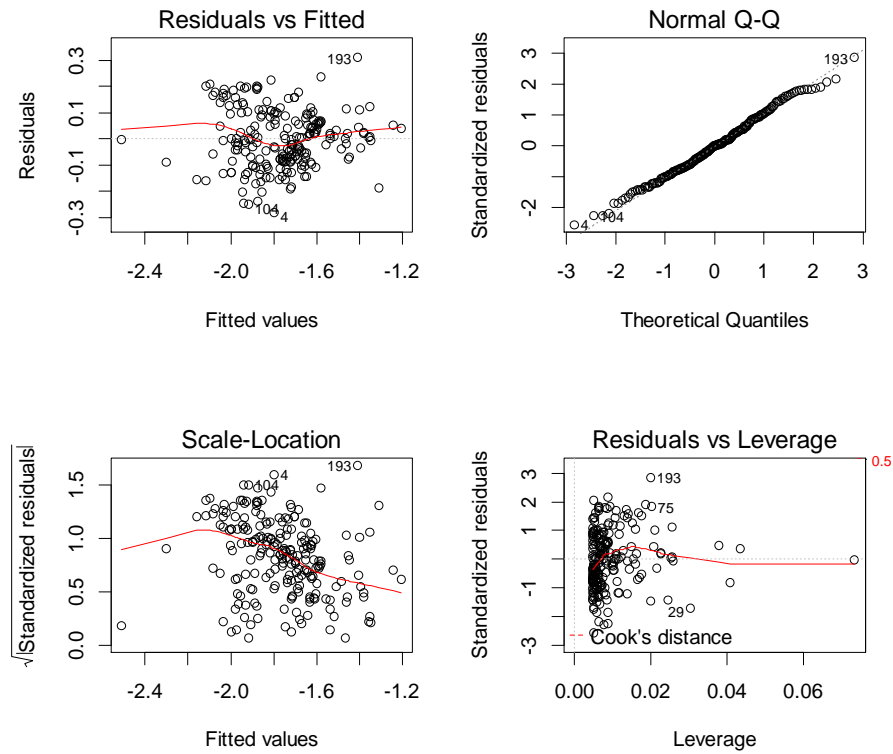


Figure K-2. Diagnostics of the regression model relating the chord rotation (θ_m), energy dissipation (E_m), and stiffness (K_m) using non-dimensional terms. Outliers and extreme data-points are excluded in the regression analysis.

Table K-2. Regression statistics of model relating the chord rotation (θ_m), energy dissipation (E_m), and stiffness (K_m) using non-dimensional terms. Outliers and extreme data-points are excluded in the regression analysis.

Parameter	Estimate Coefficient	Standard Error	t-value	P(> t)
I	-1.63129	0.00903	-180.66	<2e-16
$\log(E_m/[K_m L_s^2])$	0.29735	0.01146	25.95	<2e-16
<i>Notes:</i>	Residual standard error: 0.1098 on 213 degrees of freedom Multiple R-squared: 0.7597, F-statistic: 673.4 on 1 and 213 DF, p-value: < 2.2e-16			

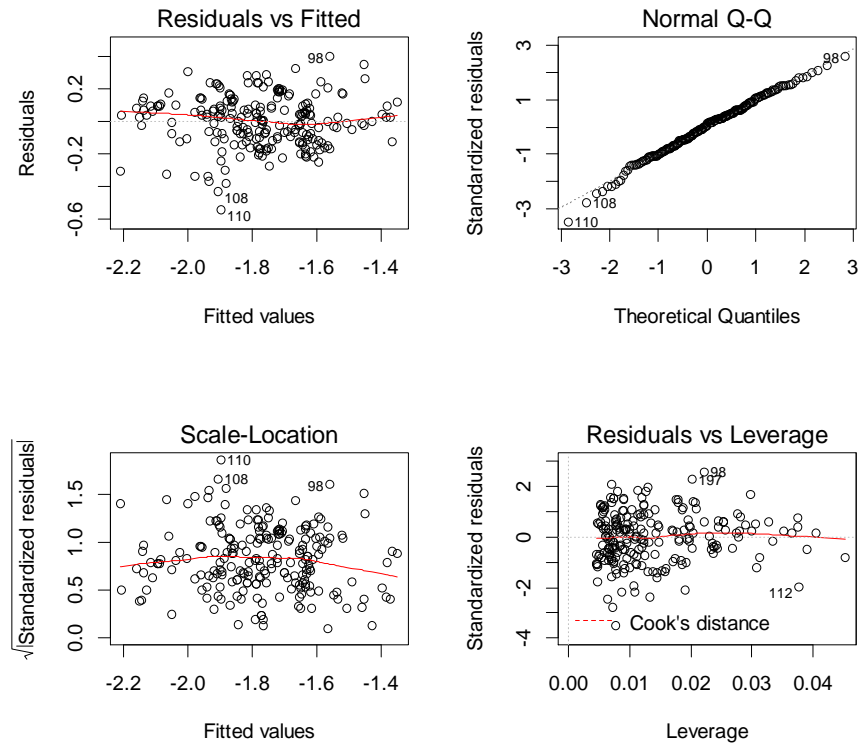


Figure K-3. Diagnostics of the regression model relating the chord rotation (θ_m), energy dissipation (E_m), and stiffness (K_m) using dimensional terms. Outliers and extreme data-points are included in the regression analysis.

Table K-3. Regression statistics of model relating the chord rotation (θ_m), energy dissipation (E_m), and stiffness (K_m) using dimensional terms. Outliers and extreme data-points are included in the regression analysis.

Parameter	Estimate Coefficient	Standard Error	t-value	P(> t)
I	-1.19728	0.11305	-10.59	<2e-16
$\log(E_m)$	0.17444	0.01699	10.27	<2e-16
$\log(K_m)$	-0.30372	0.02366	-12.84	<2e-16
<i>Notes:</i>	Residual standard error: 0.1567 on 216 degrees of freedom Multiple R-squared: 0.5586, F-statistic: 136.7 on 2 and 216 DF, p-value: < 2.2e-16			

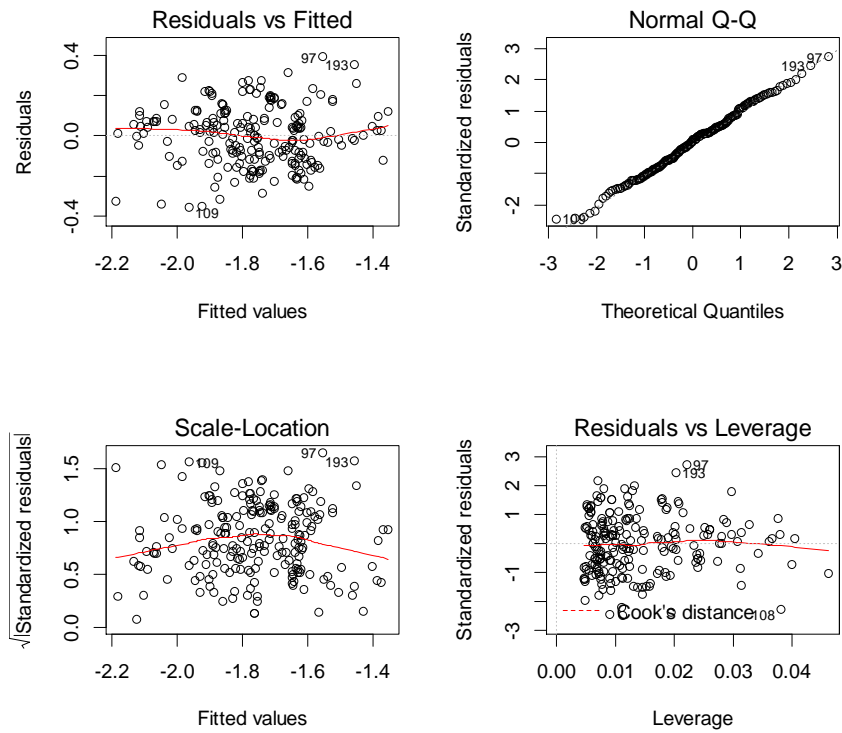


Figure K-4. Diagnostics of the regression model relating the chord rotation (θ_m), energy dissipation (E_m), and stiffness (K_m) using dimensional terms. Outliers and extreme data-points are excluded in the regression analysis.

Table K-4. Regression statistics of model relating the chord rotation (θ_m), energy dissipation (E_m), and stiffness (K_m) using dimensional terms. Outliers and extreme data-points are excluded in the regression analysis.

Parameter	Estimate Coefficient	Standard Error	t-value	P(> t)
I	-1.23968	0.10562	-11.74	<2e-16
$\log(E_m)$	0.17210	0.01583	10.87	<2e-16
$\log(K_m)$	-0.28884	0.02218	-13.02	<2e-16
<i>Notes:</i>	Residual standard error: 0.1458 on 212 degrees of freedom Multiple R-squared: 0.5784, F-statistic: 145.4 on 2 and 212 DF, p-value: < 2.2e-16			

K.2 Diagnostics of the Chord Rotation, Energy dissipation and stiffness at 10% Maximum Force Reduction.

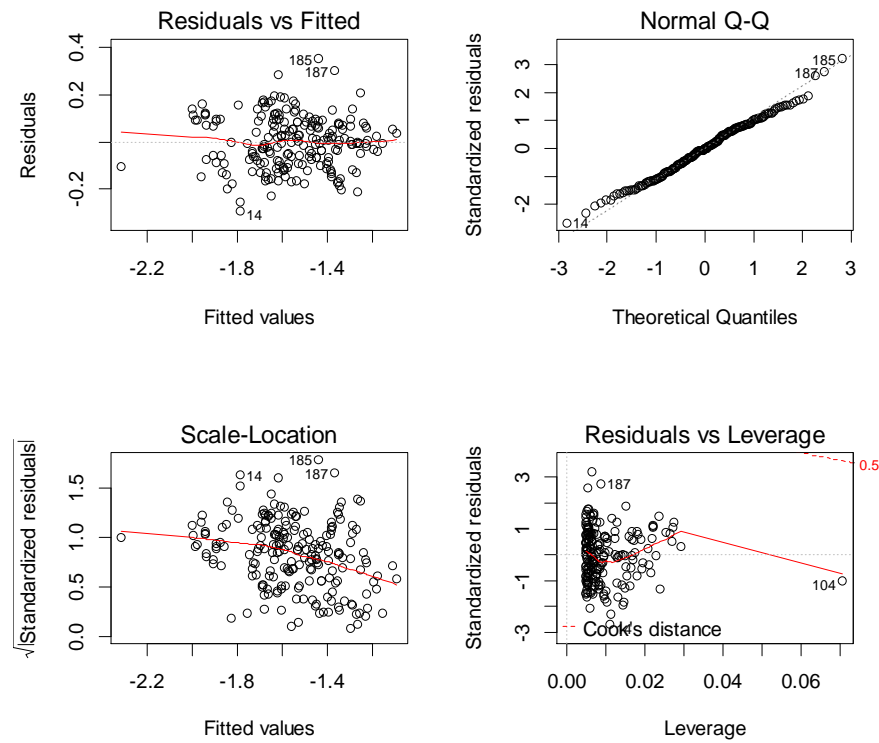


Figure K-5. Diagnostics of the regression model relating the chord rotation (θ_{u-10}), energy dissipation (E_{u-10}), and stiffness (K_{u-10}) using non-dimensional terms. Outliers and extreme data-points are included in the regression analysis.

Table K-5. Regression statistics of model relating the chord rotation (θ_{u-10}), energy dissipation (E_{u-10}), and stiffness (K_{u-10}) using non-dimensional terms. Outliers and extreme data-points are included in the regression analysis.

Parameter	Estimate Coefficient	Standard Error	t-value	P(> t)
I	-1.673581	0.008784	-190.53	<2e-16
$\log(E_{u-10}/[K_{u-10}L_s^2])$	0.275115	0.010141	27.13	<2e-16
<i>Notes:</i>	Residual standard error: 0.1095 on 207 degrees of freedom			
	Multiple R-squared: 0.7805			
	F-statistic: 736 on 1 and 207 DF, p-value: < 2.2e-16			

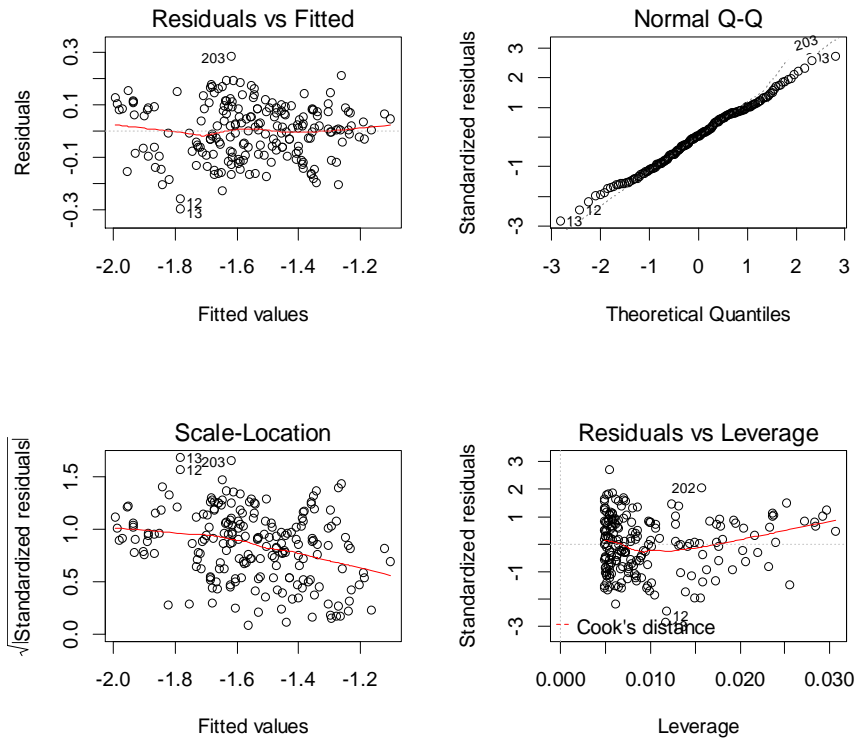


Figure K-6. Diagnostics of the regression model relating the chord rotation (θ_{u-10}), energy dissipation (E_{u-10}), and stiffness (K_{u-10}) using non-dimensional terms. Outliers and extreme data-points are excluded in the regression analysis.

Table K-6. Regression statistics of model relating the chord rotation (θ_{u-10}), energy dissipation (E_{u-10}), and stiffness (K_{u-10}) using non-dimensional terms. Outliers and extreme data-points are excluded in the regression analysis.

Parameter	Estimate Coefficient	Standard Error	t-value	P(> t)
I	-1.672750	0.008619	-194.08	<2e-16
$\log(E_{u-10}/[K_{u-10}L_s^2])$	0.268763	0.010095	26.62	<2e-16
Notes:	Residual standard error: 0.105 on 203 degrees of freedom			
	Multiple R-squared: 0.7774			
	F-statistic: 708.8 on 1 and 203 DF, p-value: < 2.2e-16			

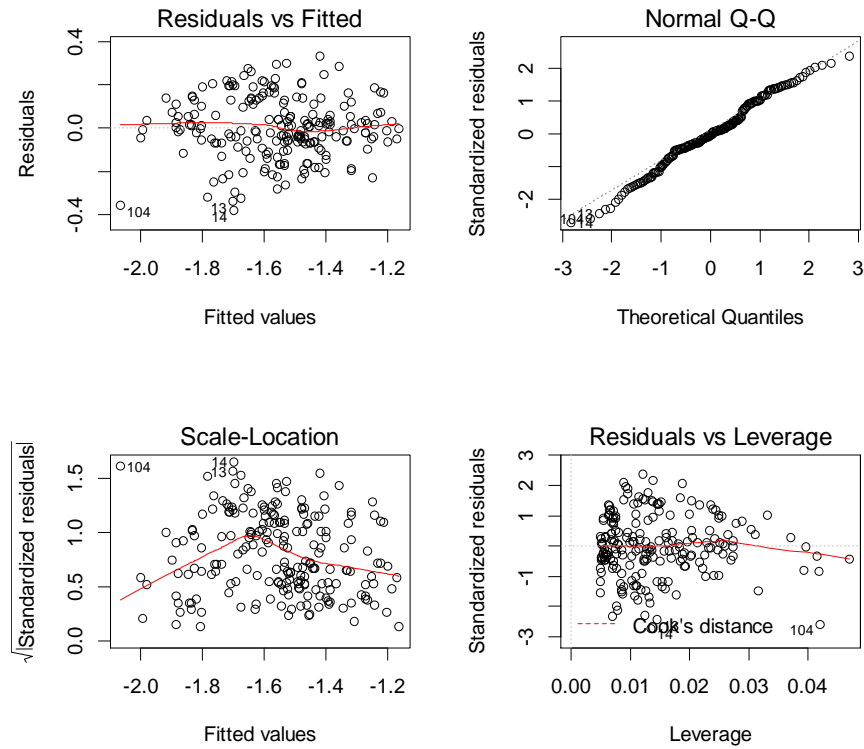


Figure K-7. Diagnostics of the regression model relating the chord rotation (θ_{u-10}), energy dissipation (E_{u-10}), and stiffness (K_{u-10}) using dimensional terms. Outliers and extreme data-points are included in the regression analysis.

Table K-7. Regression statistics of model relating the chord rotation (θ_{u-10}), energy dissipation (E_{u-10}), and stiffness (K_{u-10}) using dimensional terms. Outliers and extreme data-points are included in the regression analysis.

Parameter	Estimate Coefficient	Standard Error	t-value	P(> t)
I	-1.42545	0.11097	12.85	<2e-16
$\log(E_{u-10})$	0.19884	0.01489	13.35	<2e-16
$\log(K_{u-10})$	-0.26373	0.02272	-11.61	<2e-16
Notes:	Residual standard error: 0.1404 on 206 degrees of freedom			
	Multiple R-squared: 0.6412			
	F-statistic: 184.1 on 2 and 206 DF, p-value: < 2.2e-16			

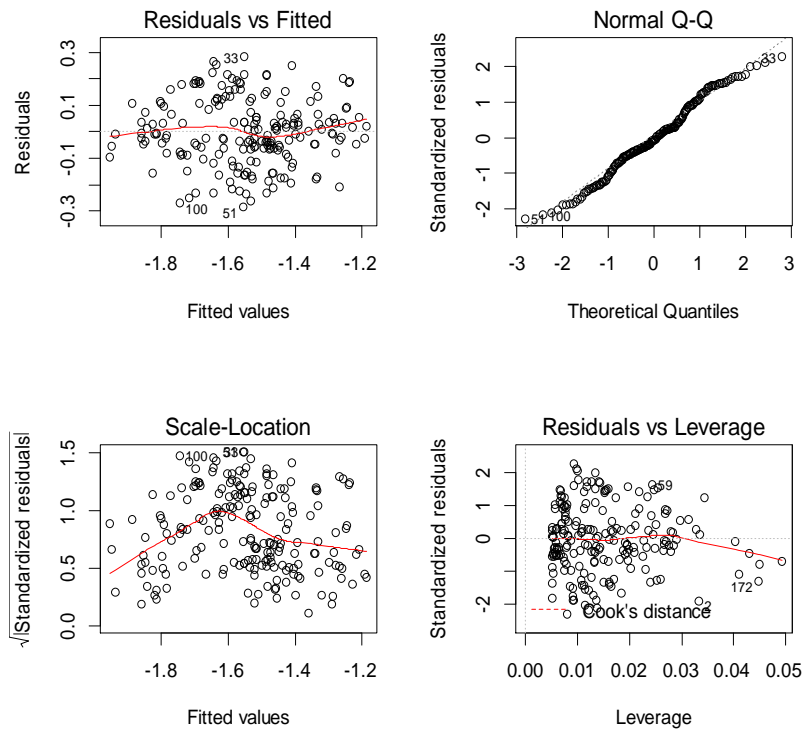


Figure K-8. Diagnostics of the regression model relating the chord rotation (θ_{u-10}), energy dissipation (E_{u-10}), and stiffness (K_{u-10}) using dimensional terms. Outliers and extreme data-points are excluded in the regression analysis.

Table K-8. Regression statistics of model relating the chord rotation (θ_{u-10}), energy dissipation (E_{u-10}), and stiffness (K_{u-10}) using dimensional terms. Outliers and extreme data-points are excluded in the regression analysis.

Parameter	Estimate Coefficient	Standard Error	t-value	P(> t)
I	-1.47982	0.10014	-14.78	<2e-16
$\log(E_{u-10})$	0.18734	0.01345	13.93	<2e-16
$\log(K_{u-10})$	-0.23392	0.02070	-11.30	<2e-16
<i>Notes:</i>	Residual standard error: 0.1243 on 197 degrees of freedom			
	Multiple R-squared: 0.6532			
	F-statistic: 185.5 on 2 and 197 DF, p-value: < 2.2e-16			

K.3 Diagnostics of the Chord Rotation, Energy dissipation and stiffness at 20% Maximum Force Reduction.

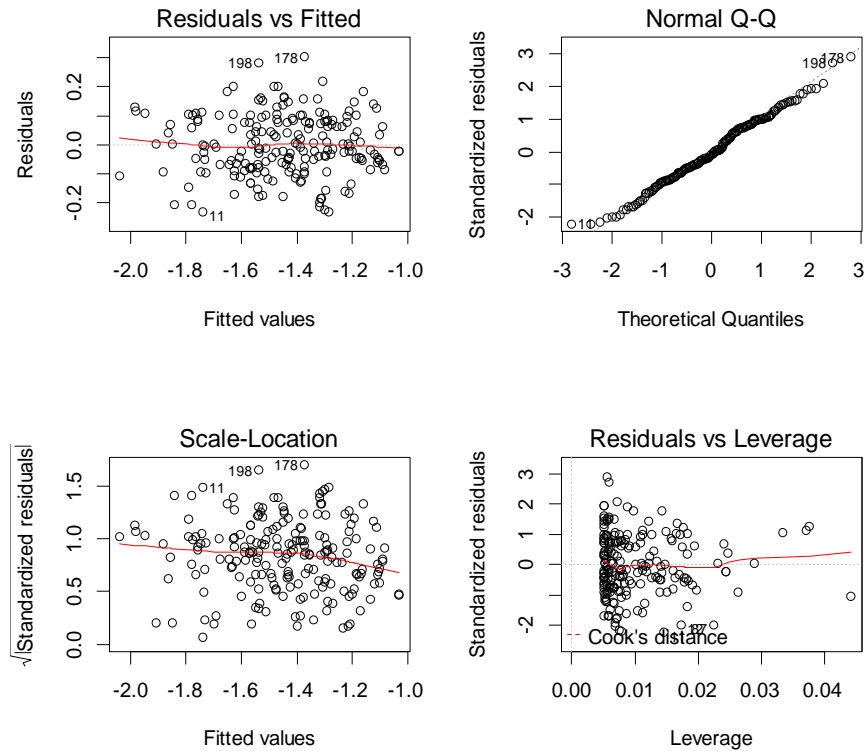


Figure K-9. Diagnostics of the regression model relating the chord rotation (θ_{u-20}), energy dissipation (E_{u-20}), and stiffness (K_{u-20}) using non-dimensional terms. Outliers and extreme data-points are included in the regression analysis.

Table K-9. Regression statistics of model relating the chord rotation (θ_{u-20}), energy dissipation (E_{u-20}), and stiffness (K_{u-20}) using non-dimensional terms. Outliers and extreme data-points are included in the regression analysis.

Parameter	Estimate Coefficient	Standard Error	t-value	P(> t)
I	-1.71717	0.01208	-142.21	<2e-16
$\log(E_{u-20}/[K_{u-20}L_s^2])$	0.29328	0.01034	28.37	<2e-16
<i>Notes:</i>	Residual standard error: 0.105 on 198 degrees of freedom			
	Multiple R-squared: 0.8026			
	F-statistic: 805 on 1 and 198 DF, p-value: < 2.2e-16			

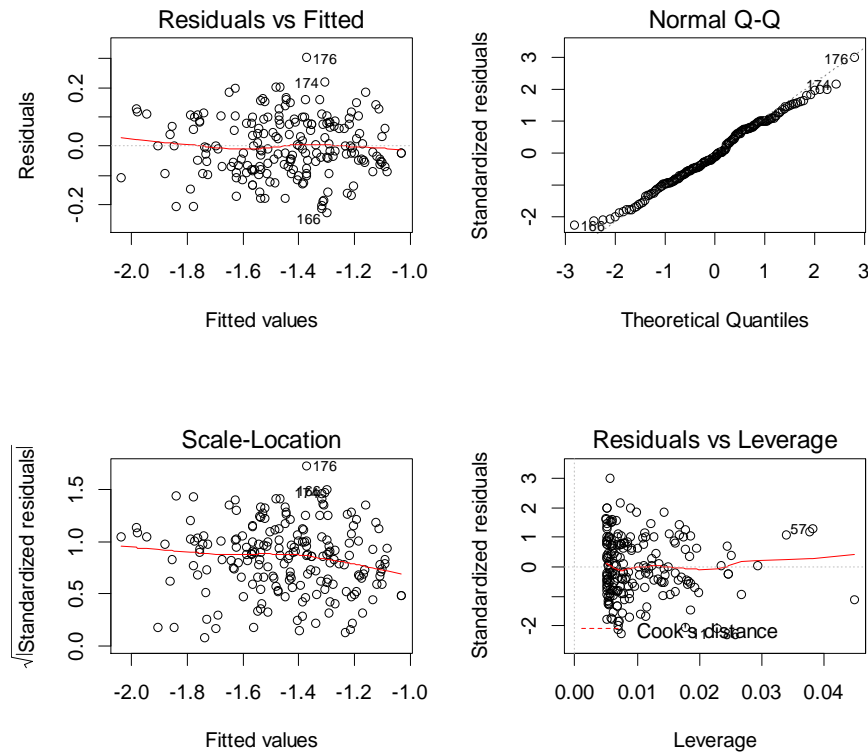


Figure K-10. Diagnostics of the regression model relating the chord rotation (θ_{u-20}), energy dissipation (E_{u-20}), and stiffness (K_{u-20}) using non-dimensional terms. Outliers and extreme data-points are excluded in the regression analysis.

Table K-10. Regression statistics of model relating the chord rotation (θ_{u-20}), energy dissipation (E_{u-20}), and stiffness (K_{u-20}) using non-dimensional terms. Outliers and extreme data-points are excluded in the regression analysis.

Parameter	Estimate Coefficient	Standard Error	t-value	P(> t)
I	-1.71612	0.01174	-146.12	<2e-16
$\log(E_{u-20}/[K_{u-20}L_s^2])$	0.29311	0.01002	29.24	<2e-16
Notes:	Residual standard error: 0.1011 on 195 degrees of freedom Multiple R-squared: 0.8143, F-statistic: 855 on 1 and 195 DF, p-value: < 2.2e-16			

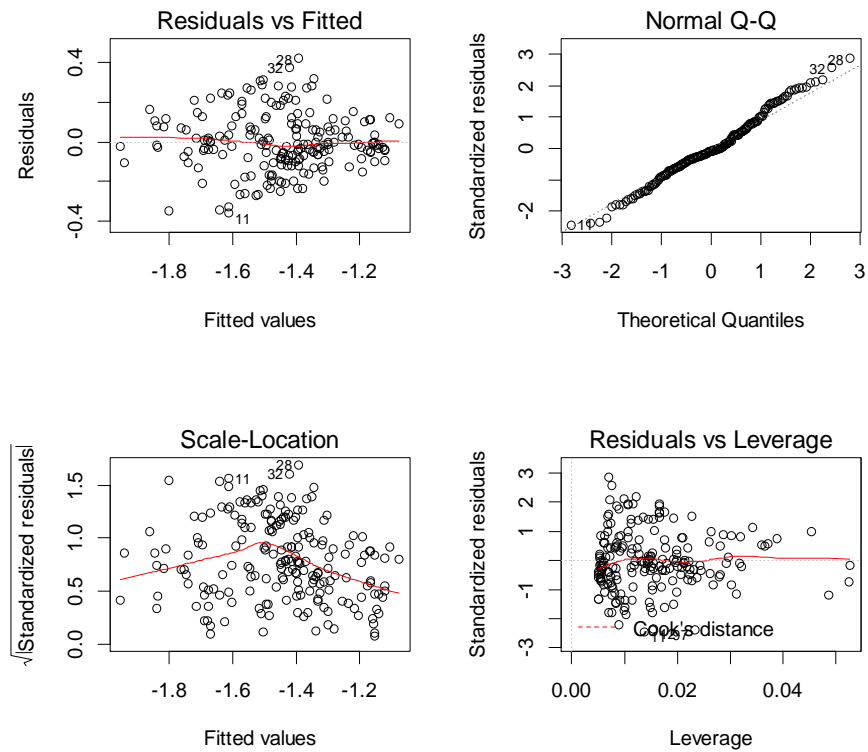


Figure K-11. Diagnostics of the regression model relating the chord rotation (θ_{u-20}), energy dissipation (E_{u-20}), and stiffness (K_{u-20}) using dimensional terms. Outliers and extreme data-points are included in the regression analysis.

Table K-11. Regression statistics of model relating the chord rotation (θ_{u-20}), energy dissipation (E_{u-20}), and stiffness (K_{u-20}) using dimensional terms. Outliers and extreme data-points are included in the regression analysis.

Parameter	Estimate Coefficient	Standard Error	t-value	P(> t)
I	-1.51271	0.12288	-12.311	<2e-16
$\log(E_{u-20})$	0.20709	0.01645	12.587	<2e-16
$\log(K_{u-20})$	-0.24965	0.02508	-9.956	<2e-16
<i>Notes:</i>	Residual standard error: 0.147 on 197 degrees of freedom			
	Multiple R-squared: 0.6149			
	F-statistic: 157.3 on 2 and 197 DF, p-value: < 2.2e-16			

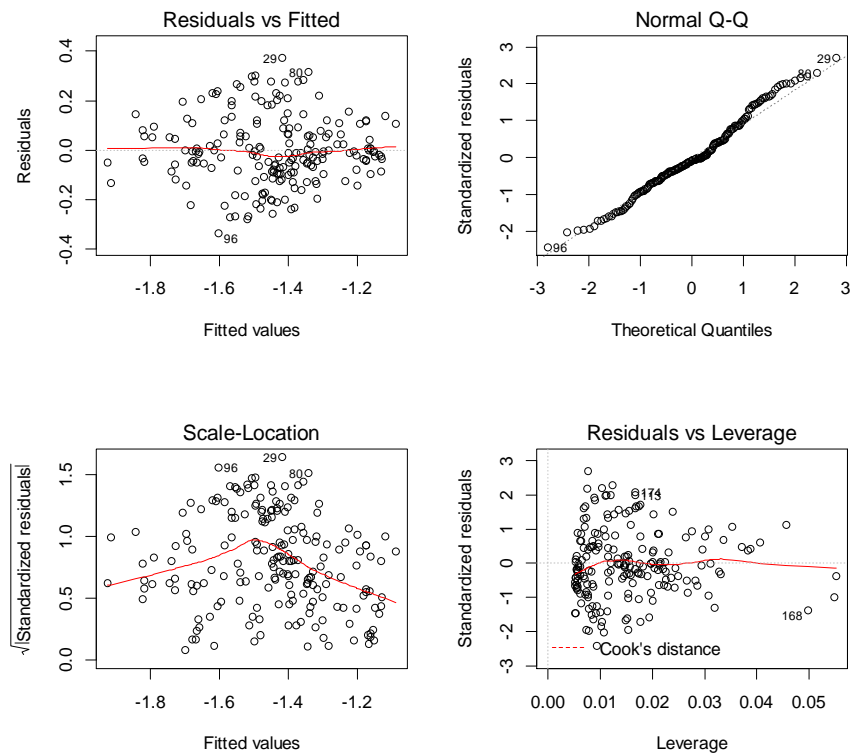


Figure K-12. Diagnostics of the regression model relating the chord rotation (θ_{u-20}), energy dissipation (E_{u-20}), and stiffness (K_{u-20}) using dimensional terms. Outliers and extreme data-points are excluded in the regression analysis.

Table K-12. Regression statistics of model relating the chord rotation (θ_{u-20}), energy dissipation (E_{u-20}), and stiffness (K_{u-20}) using dimensional terms. Outliers and extreme data-points are excluded in the regression analysis.

Parameter	Estimate Coefficient	Standard Error	t-value	P(> t)
I	-1.53662	0.11631	-13.211	<2e-16
$\log(E_{u-20})$	0.20137	0.01558	12.921	<2e-16
$\log(K_{u-20})$	-0.23425	0.02395	-9.781	<2e-16
<i>Notes:</i>	Residual standard error: 0.1386 on 193 degrees of freedom Multiple R-squared: 0.6211, F-statistic: 158.2 on 2 and 193 DF, p-value: < 2.2e-16			

K.4 Diagnostics of the Chord Rotation, Energy dissipation and stiffness at 50% Maximum Force Reduction.

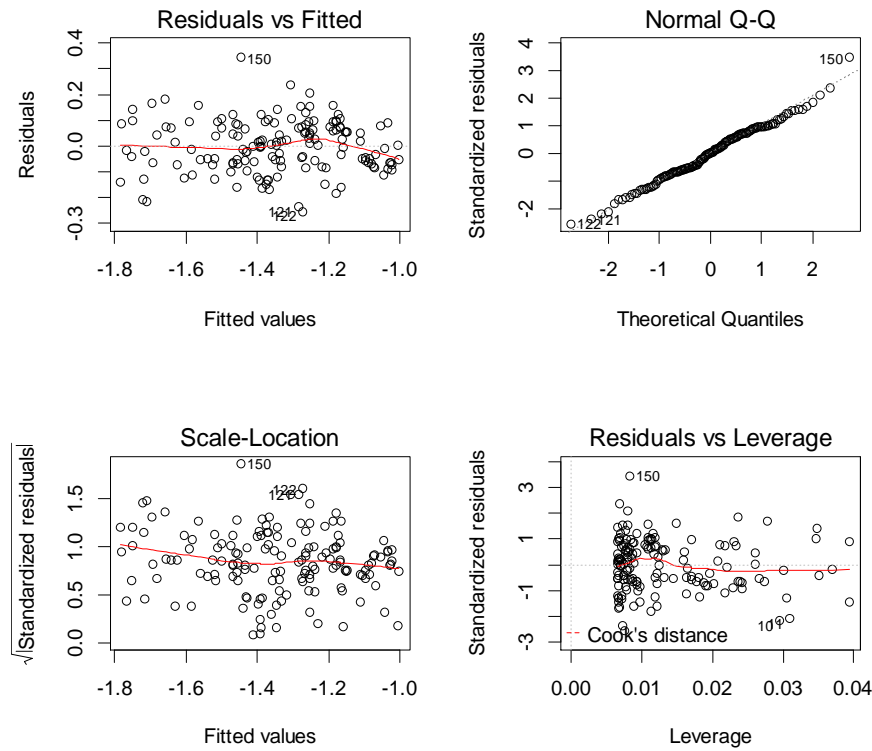


Figure K-13. Diagnostics of the regression model relating the chord rotation (θ_{u-20}), energy dissipation (E_{u-50}), and stiffness (K_{u-50}) using non-dimensional terms. Outliers and extreme data-points are included in the regression analysis.

Table K-13. Regression statistics of model relating the chord rotation (θ_{u-50}), energy dissipation (E_{u-50}), and stiffness (K_{u-50}) using non-dimensional terms. Outliers and extreme data-points are included in the regression analysis.

Parameter	Estimate Coefficient	Standard Error	t-value	P(> t)
I	-1.79238	0.02023	-88.62	<2e-16
$\log(E_{u-50}/[K_{u-50}L_s^2])$	0.30718	0.01269	24.21	<2e-16
<i>Notes:</i>	Residual standard error: 0.09987 on 150 degrees of freedom			
	Multiple R-squared: 0.7962			
	F-statistic: 586.1 on 1 and 150 DF, p-value: < 2.2e-16			

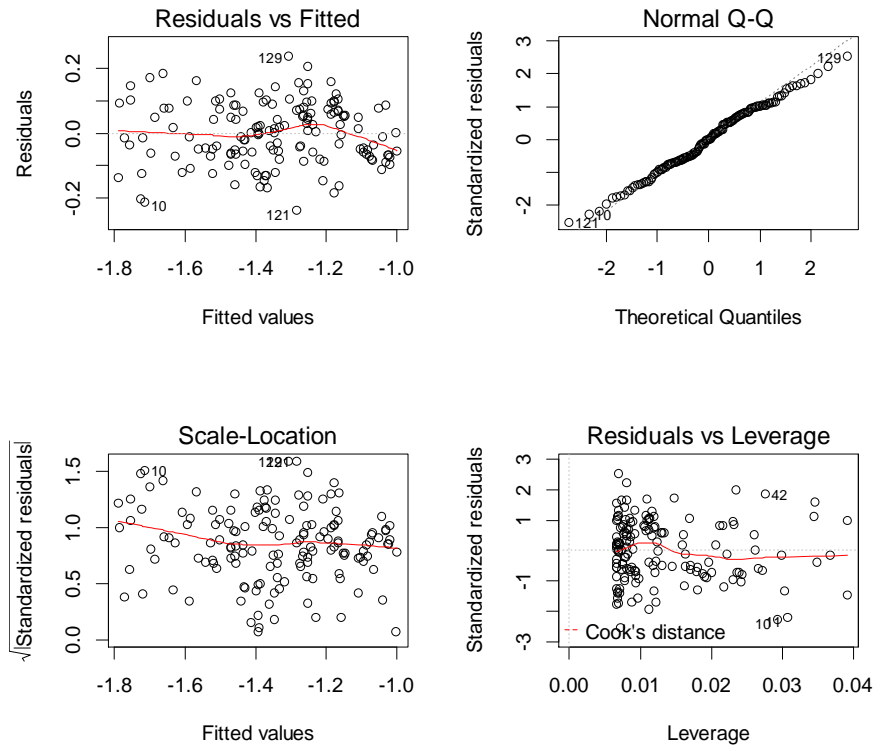


Figure K-14. Diagnostics of the regression model relating the chord rotation (θ_{u-50}), energy dissipation (E_{u-50}), and stiffness (K_{u-50}) using non-dimensional terms. Outliers and extreme data-points are excluded in the regression analysis.

Table K-14. Regression statistics of the model relating the chord rotation (θ_{u-50}), energy dissipation (E_{u-50}), and stiffness (K_{u-50}) using non-dimensional terms. Outliers and extreme data-points are excluded in the regression analysis.

Parameter	Estimate Coefficient	Standard Error	t-value	P(> t)
I	-1.79777	0.01898	-94.72	<2e-16
$\log(E_{u-50}/[K_{u-50}L_s^2])$	0.31028	0.01192	26.03	<2e-16
<i>Notes:</i>	Residual standard error: 0.09391 on 149 degrees of freedom			
	Multiple R-squared: 0.8198			
	F-statistic: 677.7 on 1 and 149 DF, p-value: < 2.2e-16			

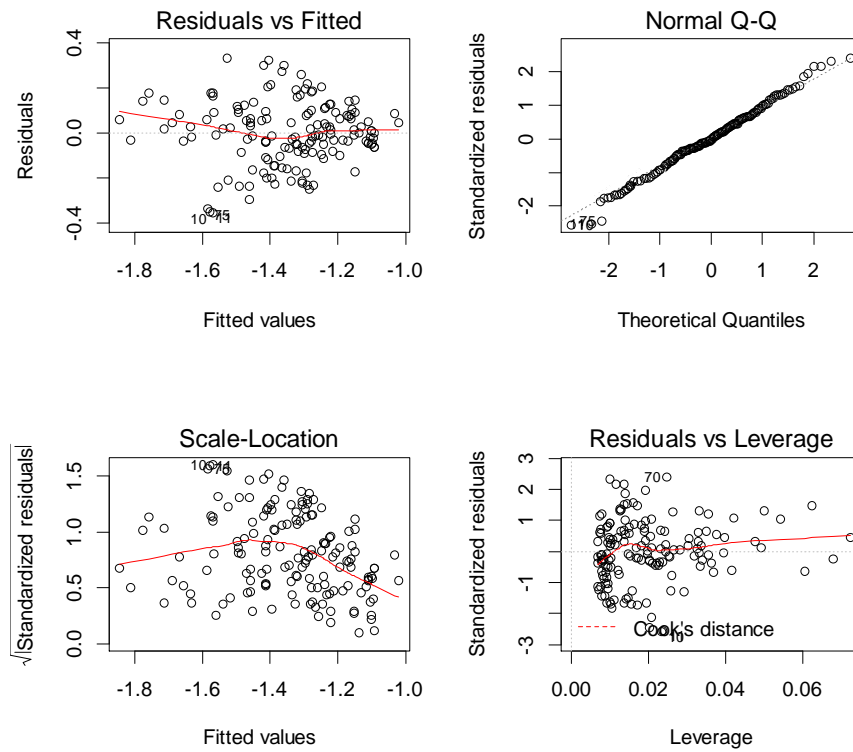


Figure K-15. Diagnostics of the regression model relating the chord rotation (θ_{u-50}), energy dissipation (E_{u-50}), and stiffness (K_{u-50}) using dimensional terms. Outliers and extreme data-points are included in the regression analysis.

Table K-15. Regression statistics of model relating the chord rotation (θ_{u-50}), energy dissipation (E_{u-50}), and stiffness (K_{u-50}) using dimensional terms. Outliers and extreme data-points are included in the regression analysis.

Parameter	Estimate Coefficient	Standard Error	t-value	P(> t)
I	-1.50239	0.13043	-11.518	<2e-16
$\log(E_{u-50})$	0.20302	0.01931	10.514	<2e-16
$\log(K_{u-50})$	-0.25831	0.02710	-9.532	<2e-16
<i>Notes:</i>	Residual standard error: 0.1394 on 149 degrees of freedom			
	Multiple R-squared: 0.6056			
	F-statistic: 114.4 on 2 and 149 DF, p-value: < 2.2e-16			

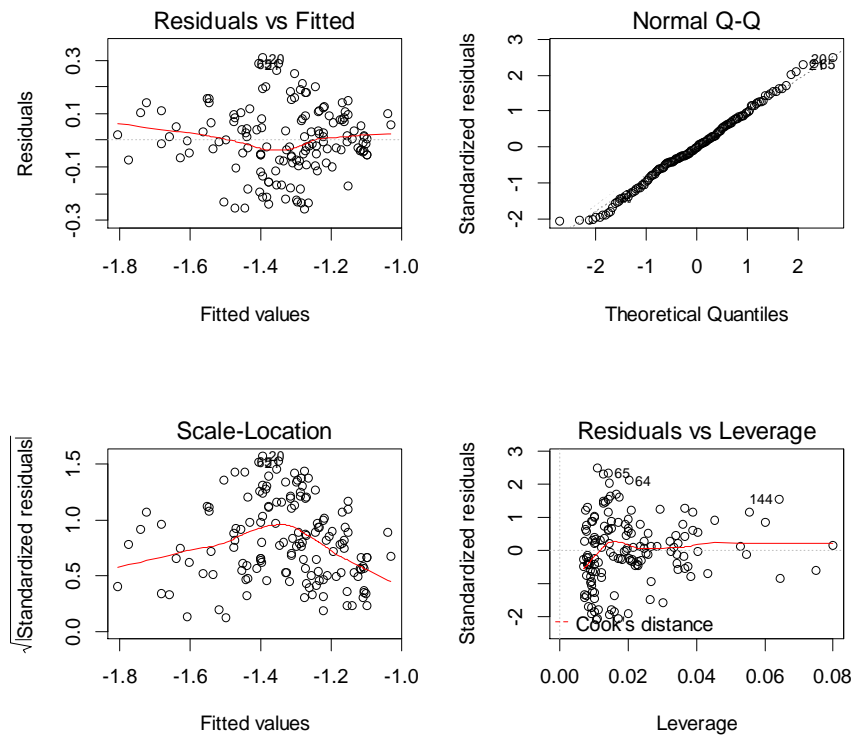


Figure K-16. Diagnostics of the regression model relating the chord rotation (θ_{u-50}), energy dissipation (E_{u-50}), and stiffness (K_{u-50}) using dimensional terms. Outliers and extreme data-points are excluded in the regression analysis.

Table K-16. Regression statistics of model relating the chord rotation (θ_{u-50}), energy dissipation (E_{u-50}), and stiffness (K_{u-50}) using dimensional terms. Outliers and extreme data-points are excluded in the regression analysis.

Parameter	Estimate Coefficient	Standard Error	t-value	P(> t)
I	-1.47367	0.11907	-12.376	<2e-16
$\log(E_{u-50})$	0.18853	0.01761	10.704	<2e-16
$\log(K_{u-50})$	-0.24259	0.02518	-9.632	<2e-16
<i>Notes:</i>	Residual standard error: 0.1254 on 143 degrees of freedom			
	Multiple R-squared: 0.618			
	F-statistic: 115.7 on 2 and 143 DF, p-value: < 2.2e-16			